The Measurement of Volume Fraction and Velocity Profiles in Vertical and Inclined Multiphase Flows.

James Cory

December 1999

A thesis submitted to the University of Huddersfield in partial fulfilment of the requirements for the degree of Doctor of Philosophy.

The University of Huddersfield in collaboration with The Engineering & Physical Sciences Research Council and Schlumberger Cambridge Research Ltd.

Declaration

No portion of the work referred to in this thesis has been submitted in support of an application for another degree or qualification of this or any other university or other institute of learning.

Acknowledgements

I would like to express my gratitude to my supervisor, Gary Lucas, for giving me the opportunity to carry out this research. I would also like to thank him for his support and advice during the research, and for reading all the draft copies of this thesis.

I would like to thank the technicians at the University of Huddersfield for their help in manufacturing, and repairing, the varied equipment that I have needed. I would particularly like to thank David Bray for putting up with my seemingly insatiable desire to spill water. As part of the parallel research program at UMIST I would like to thank Weng Wah Loh, and the other members of the Process Tomography Unit, for the development of the dual-plane ERT system.

Outside work I would like to acknowledge the support of my friends and family who I know always meant well even if I didn't show it. Last, but by no means least, I would like to thank Claire for her almost endless support and patience throughout the research. It must be hard sometimes to put up with someone for whom pumping plastic balls through a pipe is a fulfilling day at the office.

I would like to acknowledge the financial assistance of EPSRC (grant no. GR/L59088) and Schlumberger Cambridge Research.

Abstract

The nature of solids-liquid flows often results in non-uniform profiles of solids volume fraction and axial solids velocity across the flow cross-section. In order to measure the solids volumetric flow rate in these situations it is necessary to measure the profiles of the local solids volume fraction and axial solids velocity and to obtain mean values of the solids volume fraction, solids axial velocity and solids volumetric flow rate by integration of these profiles over the flow cross-section.

This thesis describes the development of a local conductivity measurement probe capable of acquiring measurements of the local solids volume fraction and the local axial solids velocity in non-uniform solids-liquid flows. Techniques enabling mean values of the solids volume fraction, axial solids velocity and solids volumetric flow rate to be obtained are described. Flow modelling is described that also allows the prediction of the water volumetric flow rate.

Extensive sensitivity modelling and modelling validation is reported that allows the probe to be optimised to acquire measurements of local solids volume fraction and local axial solids velocity. This includes the optimisation of the device to allow two axially displaced sensors to function simultaneously without exhibiting "cross-talk".

Extensive experimental profiles of local solids volume fraction and local axial solids velocity acquired in vertical and inclined solids-liquid flows are presented. These are qualitatively compared with profiles obtained using a dual-plane Electrical Resistance Tomography system developed as part of a parallel research program at UMIST. Integrated values of the solids volume fraction, axial solids velocity and solids volumetric flow rate have been compared with reference measurement data and possible error sources have been identified and investigated. Finally flow modelling has been described which allows the water volumetric flow rate to be predicted to the same order of accuracy as the solids volumetric flow rate was calculated.

Table of contents.

List of figures.

List of tables.

Nomenclature.

a	Axial field electrode length
A	Cross-sectional area of a conductor applied to the solids hopper water level meter (see 6.3.1.3)
A	Cross-sectional area of pipe

b	Radius of the probe

c	Coefficient in Won's relationship, equal to $.0.5(f - s_\alpha)$
C_D	Drag coefficient
$C_{dl,1}$, $C_{dl,2}$	Double layer capacitances for electrodes 1 and 2

d	Internal diameter of the nylon rings
d_1	Width of the solids hopper water level meter strips
d_2	Length of the current path between the solids hopper water level meter strips
d_p	Particle diameter
D	Pipe diameter

e	Percentage error
e_{abs}	Absolute error
e_w	Error between ΔV_{WON} and ΔV_{FEA}

f	Frequency
f	Field electrode separation of a SEMM array
f	Rotational frequency of the turbine meter (see Section 6.3.2)
f	Friction factor (see Chapters 6 and 7)
F_1, F_2	Field electrodes
F_D	Drag force resisting the motion of a particle
F_g	Downward force on a particle due to gravity

g	Acceleration due to gravity
h	Height of water in the solids hopper
i	Electrical current
j	Physical sensor separation
k	Rectifier gain
k	Coefficient in Machon's conductivity relationship
K^A, K^B, K^C	Cell constants of sensors A, B and C
l	Length of the measuring section over which the pressure gradient is measured
L	Effective axial sensor separation of cross-correlation sensors
L	Length of a conductor applied to the solids hopper water level meter (see Section 6.3.1.3)
m	Coefficient in the De La Rue & Tobias' conductivity relationship (see Chapter 2)
m	Axial distance from the datum to electrode 1 in the Won relationship (see Section 3.2.4)
m	Wetted length of the solids hopper water level meter strips (see Section 6.3.1.3)
m	Meter factor of the turbine meter (see Section 6.3.2)
$\dot{M}$	Mass flow rate
M_s	Mass of solids in the hopper
M_w	Mass of water in the hopper
n	Coefficient in Slawinski's conductivity relationship (see Chapter 2)
n	Axial distance from the datum to electrode 2 in the Won relationship (see Section 3.2.4)
n	Coefficient in the Richardson-Zaki hindered settling model (see Chapter 8)

o	Axial distance from the datum to point P

p	Coefficient in Slawinski's conductivity relationship
ΔP	Pressure difference
ΔP_{PE}	Pressure difference due to the change in potential energy of the flow
ΔP_F	Pressure difference due to frictional losses

q	Coefficient in the Zuber hindered settling model
Q	Volumetric flow rate
Q_c	Volumetric flow rate of drillings cuttings
Q_s	Solids volumetric flow rate
Q_w^*	Volumetric flow rate of water into the solids hopper
Q_w	Water volumetric flow rate

r	Radial distance from the probe wall to a point P in the Won relationship (see Section 3.2.4)
r	Radial position of the nylon ring relative to the probe wall in the simulated particle testing (see Chapters 3 and 5)
r	Radial co-ordinate of probe applied to the traverse (see Section 4.3) and the experimental procedure (see Section 6.4).
r	Radius of the solids hopper at the water level applied to the solids hopper water level meter (see Section 6.3.1.3)
r^*	Relative radial position of the probe
R	Resistance
ΔR	Resistance change
R^A, R^B, R^C	Resistances across sensors A, B, and C
R_f	Fluid resistance
R_{max}	Maximum measured resistance with the probe at any radial position {wall proximity testing}
R_{max}	Maximum measured resistance for any position of the nylon ring {simulated particle testing}

$R_{n,xy}(\tau)$	Normalised cross-correlation
$R_{p,1}$, $R_{p,2}$	Polarisation resistances for electrodes 1 and 2
R^R	Resistance across the reservoir water conductivity meter
R_{r^*}	Measured resistance with the probe at r^*
R_{ref}	Reference resistor in the solids hopper water level meter
R^{ref}	Reference resistance
$R^{R,ref}$	Reference resistance in the reservoir water conductivity meter
$R_{(r,z)}$	Measured resistance with a nylon ring at position (r,z) relative to the probe
$R_{s,1}$, $R_{s,2}$	Surface film resistances for electrodes 1 and 2
R_u	Measured resistance with the probe at the pipe centre
R_w	Measured resistance with no nylon ring resistance
R_x	Resistance between the strips of the hopper water level meter
$R_{xx}(\tau)$	Auto-correlation of signal x(t)
$R_{xy}(n)$	FFT cross-correlation function of signals x(t) and y(t)
$R_{xy}(\tau)$	Cross-correlation function of signals x(t) and y(t)
$R_{yy}(\tau)$	Auto-correlation of signal y(t)

s	Coefficient in the Mooney viscosity relationship
s_α	Sense electrode separation for the single sensor of a 4-electrode SEMM array, or sensor C of a 6-electrode SEMM array
s_v	Sense electrode separation for sensors A and B of either a 6-electrode SEMM array or an 8-electrode probe
S_1, S_2, S_3, S_4	Sense electrodes

t	Time
T	Total time period over which correlation is calculated
ΔT	Refers to elapsed time in the hopper control program
T_w	Water temperature

u	Mean velocity
u_c	Critical velocity
u_h	Homogeneous velocity

u_p	Particle velocity
u_s	Mean axial solids velocity
$u_{s,i}$	Local axial solids velocity
u_w	Mean axial water velocity
$u_{w,i}$	Local axial water velocity

v_a	Actual velocity
v_{est}	Estimated velocity from cross-correlation
v_{slip}	Mean axial slip velocity
$v_{slip,i}$	Axial slip velocity
v_t	Terminal settling velocity of a single particle
V	Potential
V^A, V^B, V^C	Rectified potential differences across R^A, R^B and R^C
V_{conv}	Potential difference across the electrodes in the convergence model
V_f	Potential difference across R_f
V_p	Potential at a point P
V^R	Rectified potential difference across R^R
V_{ref}	Rectified potential difference across R_{ref}
$V_{(i)}^{ref}$, $V_{(j)}^{ref}$	Potentials measured in the reference circuit at points (i) and (j)
$V^{R,ref}$	Rectified potential difference across $R^{R,ref}$
V_s	Voltage response of the solids hopper load cell
V_w	Voltage response of the water hopper load cell
V_x	Rectified potential difference across R_x
ΔV^A, ΔV^B, ΔV^C	Sinusoidal potential differences across R^A, R^B and R^C
ΔV_{FEA}	Potential difference between S_1 and S_2 predicted by the FE model
ΔV_{inf}	Measured potential difference when the array is in an infinite tank
ΔV_{max}	Maximum measured potential difference for any position of the nylon ring
ΔV_p	Measured potential difference with a nylon ring at point P
$\Delta V_{perspex}$	Measured potential difference with a perspex pipe wall
ΔV^R	Sinusoidal potential difference across R^R
ΔV_{ref}	Sinusoidal potential difference across R_{ref}
ΔV^{ref}	Sinusoidal potential difference across R^{ref}

$\Delta V^{R,ref}$	Sinusoidal potential difference across $R^{R,ref}$
ΔV_{steel}	Measured potential difference with a steel pipe wall
ΔV_u	Measured potential difference with no nylon ring present
ΔV_{WON}	Potential difference between S_1 and S_2 predicted by Won's relationship
ΔV_x	Sinusoidal potential difference across R_x

x(t)	Input signal for cross-correlation
X	Refers to the value of a parameter
X_i	Refers to the initial value of a property
X(k)	FFT of signal x(t)
X_r	Refers to the relative value of a property
X_t	Refers to the value of a property at time t

y	Axial co-ordinate of probe
y(t)	Input signal for cross-correlation
$Y^*(k)$	Complex conjugate of the FFT of signal y(t)

z	Axial position of the nylon ring relative to the probe wall
Z	Contact impedance in chapter 3
Z	Vertical axis in the pipe in chapter 7 and chapter 8

Greek symbols

α_s	Mean solids volume fraction
$\alpha_{s,i}$	Local solids volume fraction
δ	Time delay between two signals being cross-correlated
ϕ	Field variable in the Laplace equation
Φ	Relative sensitivity to the proximity of the pipe wall
γ	Coefficient in Famularo & Happel's hindered settling model
η	Resistivity of the fluid
λ	Radial size of finite elements
θ	The angle of the hopper cone in {water level meter}

θ	Angular co-ordinate of probe in {traverse + procedure}
ρ	Density
$\sigma^A, \sigma^B, \sigma^C$	Measured conductivities at sensor A, B, and C
σ_m	Mixture conductivity
$\sigma_{m,i}$	Local mixture conductivity
σ^R	Measured conductivity at the reservoir water conductivity meter
τ	Time period of cross-correlation device
υ_w^*	Volume of water in the solids hopper
υ_{wet}	Volume of the solids hopper in which water is present
ω	Electrode separation ratio
Ψ	Relative sensitivity to the nylon ring

Subscripts

0	Refers to the value at the start of the experimental test
(1)	Refers to time 1
(2)	Refers to time 2
actual	Refers to an actual value
corr	Refers to a corrected value of effective sensor separation, L
estimated	Refers to an estimated value
f	Refers to the value at the end of the experimental test
(l)	Refers to the lower boundary limit in the hopper control system
m	Refers to a value pertaining to or obtained in the solids-liquid mixture
n	Refers to a normalisation value
n1	Refers to the closest preceding normalisation value
n2	Refers to the closest following normalisation value
ran	Refers to the random error, or the standard deviation of the error
s	Refers to a value pertaining to the solid
sys	Refers to the systematic, or mean, error
t	Refers to the value at time t during the experimental test
(u)	Refers to the upper boundary limit in the hopper control system
w	Refers to a value pertaining to or obtained in water

Superscripts

#	Refers to data involving reference measurements of volume fraction which have been corrected for increasing $e_{abs}^{probe,\alpha}$ with increasing α_s^{ref}
*	Refers to data involving local probe volume fraction measurements which have been corrected for increasing $e_{abs}^{probe,\alpha}$ over time
α	Refers to errors in solids volume fraction values
A	Refers to values calculated using the two layer slip model A
B	Refers to values calculated using the two layer slip model B
B-R	Refers to values calculated using the Brinkman-Roscoe viscosity relationship
corr	Refers to a value which has been corrected for the variation of water conductivity during the experimental test
corr1	Refers to a value which has been corrected by the normalisation values
ERT	Refers to values obtained from the ERT system
L={number}	Refers to data involving an estimate of solids velocity from the local probe calculated using L={number}
Mny	Refers to values calculated using the Mooney viscosity relationship
pred	Refers to the predicted value from an iterative routine
pred,max	Maximum predicted value of Q_w
pred,min	Minimum predicted value of Q_w
probe	Refers to values obtained from the local probe
Q	Refers to errors in solids volumetric flow rate errors
ref	Refers to values obtained from reference devices
u	Refers to errors in solids velocity values

1. Introduction.

The primary objective of this research was to develop a device capable of measuring the local solids volume fraction, $\alpha_{s,i}$, and the local solids axial velocity, $u_{s,i}$, in highly non-uniform solids-liquid flows. Initially this technology was required to validate images of $\alpha_{s,i}$ and $u_{s,i}$ obtained using a tomographic device being developed as part of a parallel research program. However it was also intended to explore other applications of this technology, and to investigate its development as an industrial and laboratory tool.

A solids-liquid flow is a multiphase flow where both a solid and a liquid component are present. However multiphase flows can comprise any combination of flowing phases, e.g. gas-liquid, gas-solids, solids-gas-liquid. In addition they share many features with multi-component flows where more than one component of the same phase is present, e.g. liquid-liquid. In this chapter some of the basic properties of these flows are presented in order to show the type of measurements that need to be made in order to achieve the research objectives. Following this some industrial applications are presented in order to show the need for this research. Finally the layout of the thesis is explained in order to allow easier understanding of the work.

1.1 Properties of a multiphase flow.

In order to understand the types of flows encountered in this research, and the measurements that need to be made within them, it is necessary to introduce some of the basic properties of multiphase flows. Figure 1-1 shows a schematic representation of a flowing mixture of solid particles and liquid in a cylindrical pipe.

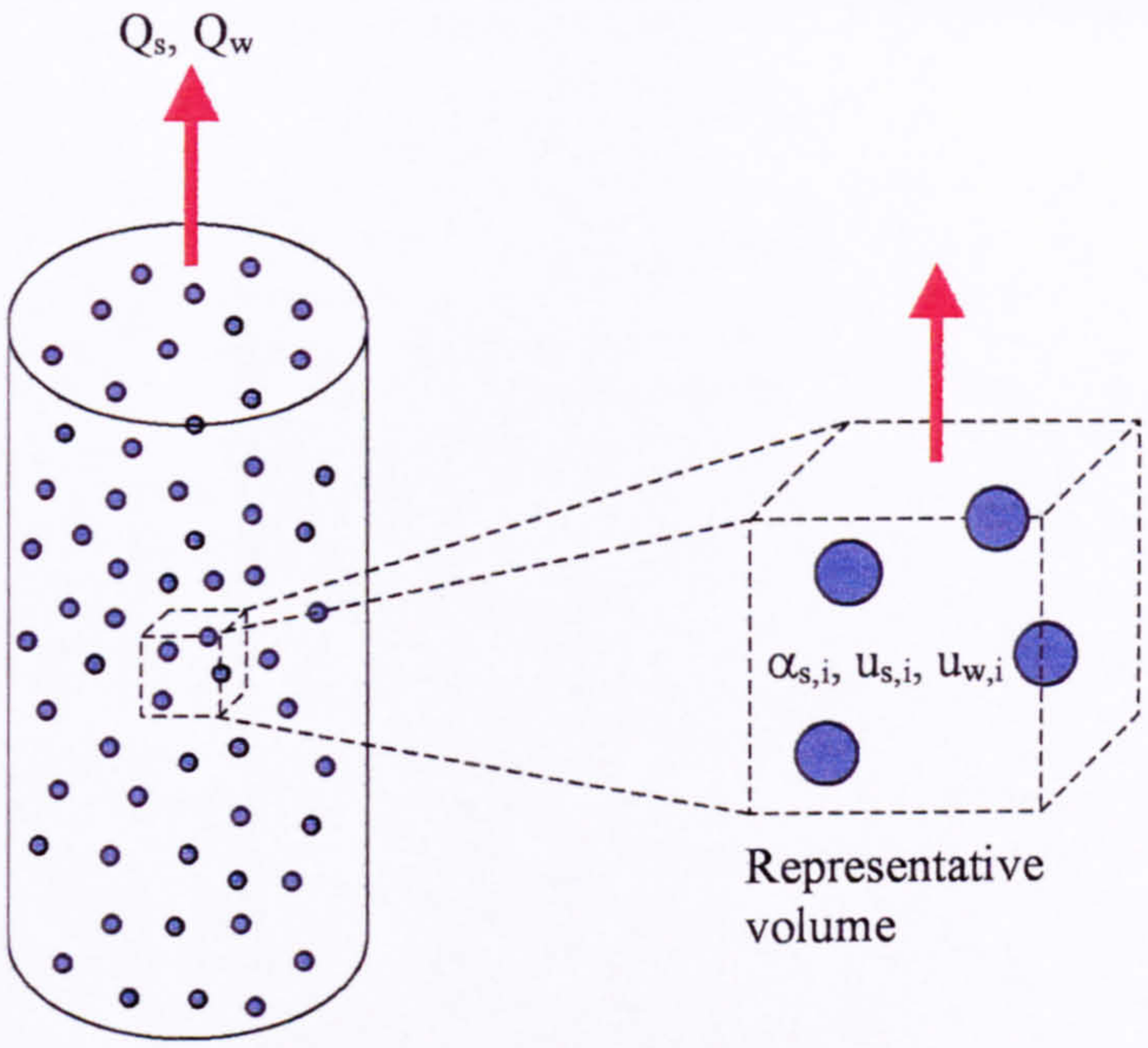

Figure 1-1. Schematic representation of a multiphase flow.

From Figure 1-1 the volumetric flow rates of the solid particles and the water are Q_s and Q_w respectively. In terms of local time averaged properties Q_s and Q_w can be calculated using Equation 1-1 and Equation 1-2 where A is the cross-sectional area of the pipe.

$$Q_s = \int_A u_{s,i}\alpha_{s,i}\,dA$$

Equation 1-1

$$Q_w = \int_A u_{w,i}\left(1-\alpha_{s,i}\right)dA$$

Equation 1-2

In Equation 1-1 and Equation 1-2 $\alpha_{s,i}$ is the local solids volume fraction. Figure 1-1 shows a small, representative volume in the flowing mixture. The local solids volume fraction, $\alpha_{s,i}$, at a point i in the flow is given by the volume of solids in the representative volume divided by the total volume of the representative volume.

Also in Equation 1-1 and Equation 1-2 $u_{s,i}$ and $u_{w,i}$ are the local axial velocities of the solid particles and the water respectively. The difference between these local velocities is referred to as the local axial slip velocity, $v_{slip,i}$. This is defined in Equation 1-3.

$$v_{slip,i} = u_{w,i} - u_{s,i}$$

Equation 1-3

Using a similar method to Equation 1-1 and Equation 1-2 it is possible to define an area averaged solids volume fraction, α_s. This is given by Equation 1-4.

$$\alpha_s = \frac{1}{A}\int_A \alpha_{s,i} dA$$

Equation 1-4

It is also possible to define an area averaged mean solids velocity, u_s given by Equation 1-5, and an area averaged mean liquid velocity, u_w given by Equation 1-6.

$$u_s = \frac{\int_A \alpha_{s,i} u_{s,i} dA}{\int_A \alpha_{s,i} dA} = \frac{Q_s}{A\alpha_s}$$

Equation 1-5

$$u_w = \frac{\int_A (1-\alpha_{s,i}) u_{w,i} dA}{\int_A (1-\alpha_{s,i}) dA} = \frac{Q_w}{A(1-\alpha_s)}$$

Equation 1-6

Although many other properties of multiphase flows are discussed in this thesis, an understanding of these basic terms will allow a good general understanding. Other properties will be developed from those presented here.

1.2 The measurements needed in the present investigation.

In a uniform flow $\alpha_{s,i}$ and $u_{s,i}$, will be constant across the flow cross-section. In this case α_s is equal to $\alpha_{s,i}$. In a similar way u_s will be equal to $u_{s,i}$. In this case a global flow measurement device, that measures the mean values of $\alpha_{s,i}$ and $u_{s,i}$ across either a chord or a cross-section of the pipe, will give an accurate measurement of α_s and u_s. These can then be used to give a measurement of Q_s using Equation 1-1 rearranged as shown in Equation 1-7.

$$Q_s = A\alpha_{s,i} u_{s,i}$$

Equation 1-7

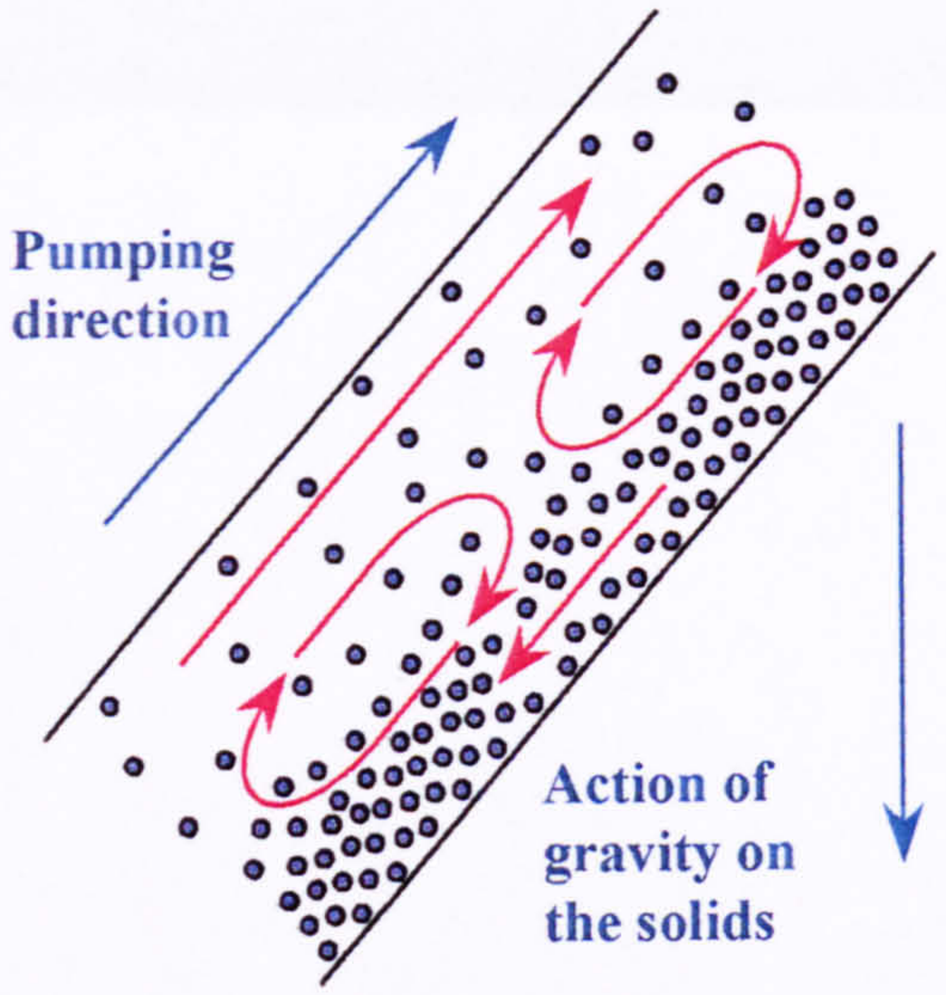

Figure 1-2. An inclined solids-liquid flows in a pipe.

However in a real flow the flow parameters are generally not uniform and the solution is not so simple. A good example is the inclined flow shown schematically in Figure 1-2. In an inclined flow the distribution of the solids is highly non-uniform. The action of gravity tends to cause the dense solid particles to sink to the bottom of the pipe. This can cause a layer of solids to develop at the bottom of the pipe. At the same time the upward flowing liquid tends to lift the solid particles from the top of this layer and re-suspend them. The result of these two conflicting forces is a flow where the time averaged local solids volume fraction shows a variation from a high value at the bottom of the pipe to a much lower value at the top of the pipe. The time averaged solids axial velocity profile in an inclined flow is similarly complex. If the dense solids bed on the bottom of the pipe becomes thick enough it will flow backwards down the pipe. At the same time the layer at the top of the pipe, with a much lower solids volume fraction, will move rapidly up the pipe.

In non-uniform flows it is assumed that $Q_s \neq A\alpha_{s,i}u_{s,i}$. It is assumed that a complete profile of $\alpha_{s,i}$ and $u_{s,i}$ must be acquired in order to calculate Q_s using Equation 1-1. One aim of the current investigation will be to show that this hypothesis is correct. It is therefore necessary to develop a device that will measure $\alpha_{s,i}$ and $u_{s,i}$ within the cross-section of the pipe.

1.3 Possible applications of this technology.

In this section possible applications of a device capable of measuring the local properties of a solids-liquid pipe flow will be described. It is not intended that this be an exhaustive listing of applications. Its purpose is merely to show the range of areas in which the current research

could be applicable. Before introducing possible applications of a solids-liquid flow measurement device, it is important to note the generic nature of some of the current investigation.

The intended application is for a solids-liquid flow. However, depending on the measurement method, the device could also have applications in solids-gas flow. If the device developed is non-intrusive other applications will exist in the fields of gas-liquid and liquid-liquid flows. This is because some of the flow patterns found in these flows are very similar. If the device developed is intrusive this is unlikely to be the case. Intrusive devices for measuring fluid-fluid flows usually monitor the penetration of the different phases by the device. An intrusive device for measuring solids-liquid flow must monitor the passage of the different phases close to the device.

The technology may also be applicable in areas which do not actually involve flowing mixtures. A device which can measure the local solids volume fraction in a flowing mixture can also be used in a static mixture. Finally the technology may be applicable in areas which do not involve a pipe geometry.

1.3.1 Oil and gas industry applications.

Part of the original funding for this research came from the oil industry and the original intended application is within this field. Traditionally the oil and gas industry has been one of the largest funders of multiphase flow research. Much equipment developed within these industries is then devolved for other applications at a later date. Within the oil and gas industry there are two main fields of operation. These are discussed separately below.

1.3.1.1 Drilling for oil and gas.

The following application is the one for which this technology was originally intended. As such it has already attracted funding from both public and industrial sources which suggests that it is a viable market.

During oil well drilling operations a fluid, known as drilling mud, is pumped into the well. This fluid passes down the drill pipe, past the cutting bit, and then back up the well bore. As the fluid returns to the surface it carries the drilling cuttings produced at the base of the well

with it. This returning mixture is a solids-liquid flow. This operation is shown schematically in Figure 1-3.

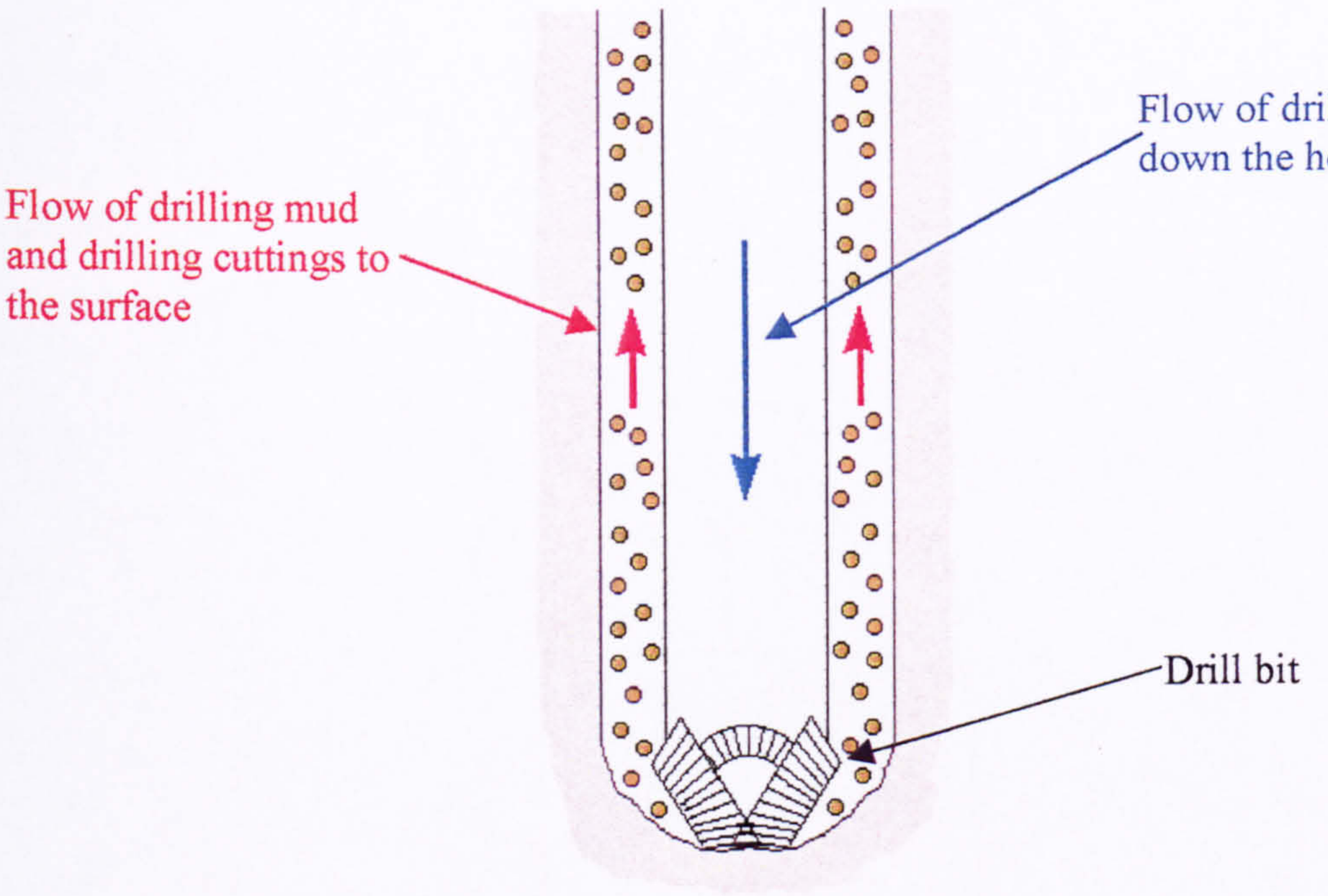

Figure 1-3. Schematic representative of the oil well drilling operation.

The rate at which an oil well is being drilled is known. Therefore it should be possible to predict the volumetric flow rate, Q_c, at which the rock cuttings will return to the surface. However this expected volumetric flow rate does not always occur. If Q_c falls below the expected value it is possible that the rock cuttings are becoming jammed in the well. In the worst cases this can lead to the entire drilling head becoming stuck in the well. Similarly if Q_c is higher than the expected value then this could indicate that the well is collapsing. As either of these outcomes could entail a cost of several million pounds they need to be avoided if possible. Therefore there is a need for a technology capable of monitoring these flows.

1.3.1.2 Oil and gas production.

A producing oil or gas well does not produce a single phase product. Often oil, gas, and water can be produced from the same well, although in many cases the predominant flow is two phase. Therefore a multiphase flow measurement application exists. Indeed oil and gas production is probably the largest area in current multiphase flow measurement research. Within this field there are three main areas of possible application.

The first area, and the one in which most research is currently taking place, is well testing. As an oil well ages the relative fractions of oil, water and gas will vary. If the fraction of the desired product, whether oil or gas, drops too low the costs of operating the well will outweigh the income from the product. Therefore well testing needs to be carried out at regular intervals.

At present the most common way to check a well's production is to transport a test separator to the well-head. This device is attached to the production line. It separates the phases and then individually meters each one. Test separation is an expensive method of well testing. As an example Priddy [1] reports that for BP Exploration Operating Company Ltd. to carry out seventy-five well tests in a year on their Cusiana oil field in Colombia, which has eleven wells producing up to 500 thousand barrels of oil per day, cost £2.25million in operating costs. Added to this test separators require the well to be off line during testing. Thorn et al [2] report that approximately 2% of production is lost due to test separation procedures. Also, as the test separators do not operate at full production flow rates, and introduce a pressure drop of up to 100psi onto the well, the flow conditions can not be considered representative of those during production. Jamieson [3] reports that Shell UK Exploration and Production have saved £40million in capital expenditure alone due to installing 4 multiphase flow meters offshore in the North Sea. He reports that Shell UK Exploration and Production expect to save between £180million and £280million in capital expenditure by 2010. Jamieson [3] suggests that the market for the technology will be worth £1billion, or approximately 10000 multiphase flow meters between now and 2010. He estimates that the subsea market in the North Sea will be worth £20million between now and 2010.

The measurement device developed in the current investigation does not comprise a full multiphase flow meter. To make a full multiphase flow measurement it is necessary to measure the velocities of all the components and the phase fractions of (n-1) components in a flow of n components. However it is possible that the technology may be capable of carrying out some of the necessary measurements.

A sub application within the field of well testing is downhole testing. Oil wells will often produce flow from a number of different strata along their length. Inserting a flow meter downhole allows the flow from each individual layer to be monitored. In this way layers which are not producing oil can be identified and sealed off. Jamieson [3] reports that the

advantage of this area for multiphase metering is that gas is usually condensed at the pressures downhole. Thorn et al [2] report that downhole pressures can reach 850bar and temperatures can reach 150°c. This results in a two phase flow which would be more suitable for the technology developed in the current investigation. However these same harsh conditions result in a need for a very robust device.

The third major application is allocation metering. Modern oil fields often produce relatively small amounts of oil. In many cases this can make them economically unviable. Because of this oil companies will often combine production facilities and pipeline facilities to lower the operating costs and manpower requirements. Priddy [1] reports that the Eastern Trough Area Project (ETAP) in the North sea groups together seven oil and gas fields. Two operating companies are responsible for the fields but in total seven major oil companies are partners in the project. It is important in these types of situations to accurately meter each partner's allocation of oil or gas. Accuracies in this area are higher because the there is a need for fiscal quality monitoring. Thorn et al [2] estimate that well testing requires an accuracy of ±10% relative error whilst allocation monitoring can require accuracies of greater than ±5% relative error.

In addition to these production multiphase flow measurement requirements Jamieson [3] and Priddy [1] both report a need for accurate laboratory facilities. Both Shell UK Exploration and Production and BP Exploration Operating Company Ltd. use test separators to calibrate multiphase flow meters at the well-head. However both Jamieson [3] and Priddy [1] have reported that the measurements from these devices are not satisfactory. Therefore they both suggest that specialist laboratory facilities and instruments will become more important as the field for multiphase flow meters becomes larger. This could be a more easily attainable application for the technology developed in the present investigation. As reported at the beginning of this chapter, an intrusive device for solids-liquid flow measurement is unlikely to be applicable in fluid-fluid flows. However Akagawa et al [4] report simulating fluid-fluid flows in the lab with solids-liquid flows. This allows strict control of the properties of the flow, particularly the particle/bubble diameter. Therefore even a device unsuitable for making measurements in a fluid-fluid flow can be applied in this field.

1.3.2 Hydraulic transport applications.

Hydraulic transport is the movement of solid material, usually in a pipe, using a liquid as a carrying medium. The main area of application of hydraulic transport is the transport of minerals, sometimes over large distances. After their extraction minerals usually need to be transported to other sites either for their use or ongoing shipment. Traditionally this was achieved by road or rail transport. However hydraulic transport is now often a more attractive option. As reported by Constantini & Parsons [5] and Goosen & Cooke [6] hydraulic transport usually results in a lower environmental impact and lower costs. For example Constantini & Parsons [5] estimate that a proposed 900 mile potash pipeline in Western Canada capable of transporting 6 million tons of potash per year would cost one third of the equivalent rail transport network.

In order to successfully hydraulically transport a material the pumping load necessary to overcome the pressure drop per unit length must be known. Additionally it must be ensured that the solids remain adequately suspended in the flow during operation. Correct prediction of the pressure drop and the suspension velocity during the design of a hydraulic transport pipeline can result in savings in both building and operating costs. As the size of hydraulic transport pipelines increases this becomes more important. As an example Constantini & Parsons [5] report a proposed 1000 mile coal pipeline in the USA capable of transporting 37 million tons of coal per year. The estimated cost to build the pipeline is reported as $650 million. The estimated operating cost is reported as $137 million per annum. If improved knowledge of the pumping loads could result in even a 1% operating cost reduction this would result in a saving of $1.37 million per annum. Because of these potential savings a wide range of investigation of these flows is continually reported. However a survey of the literature showed that examples of local measurements acquired in these flows are uncommon. The device developed in the current investigation could be extremely useful in this field.

A second requirement within this field is the measurement of the flows themselves in an industrial environment. Kakka [7] reports a 53 mile iron-ore pipeline in Tasmania used for transporting the mineral from the mine to waiting cargo ships. In this application the requirement for an instrument capable of measuring both the solids volume fraction and velocity in order to calculate the volumetric flow rate of ore into the ships is stated. It is

possible that the device developed in the current investigation could be used in this application.

A further possible area of application is in the field of dredging and underwater mining. Ljubicic et al [8] report an application where coal is cut from the sea floor and then sucked onto a waiting vessel. Similar techniques without the cutting tool are used for the collection of aggregates at sea. It is important in this process to ensure that the solids are efficiently removed from the sea bed. Ljubicic et al [8] report the results of substantial experimentation surrounding the design of the suction system. It is clear that improved knowledge of the flow in the suction pipe would be valuable. The device developed in the current investigation could be used for this purpose.

1.3.3 Process industry applications.

Within the process industries many applications exist for solids-liquid measurement devices. A particular field which has been investigated is water treatment. Water treatment processes involve removing the solids from solids-liquid flows. This can be achieved in a number of ways including belt press separation and centrifugal filtering. However, as reported by Chu & Lee [9], not all of the water can be removed by mechanical methods. This water is referred to as bound water as its molecules are bound to those of the solid. In order to release this water a polymer flocculant is added to the process stream. The quantity of polymer that must be added to the process stream will vary with the type and volume fraction of the solids. If too little polymer is added the separated sludge will contain a high water volume fraction. If too much polymer is added Abu-Orf & Dentel [10] report that the resulting liquid stream can contain polluting levels of polymer. Chu & Lee [9] report that the dewettability of the process stream will decrease again if too much polymer is added. Finally the addition of too much polymer incurs unnecessary costs. Abu-Orf & Dentel [10] report that the U.S.A. produced 5.3 million tons of dry solids from municipal wastewater treatment alone in 1993 and that to achieve this production approximately $130million was spent on polymer flocculants. Even a 1% reduction in polymer usage could result in substantial saving.

Traditionally the quantity of polymer to be added is determined by visual inspection of the separated sludge. However as reported by Abu-Orf & Dentel [10] and Chou et al [11] the condition of the incoming stream can vary hourly and the traditional methods are not adequate. Therefore there is a requirement for more knowledge of these flows and for

instruments capable of determining the solids content of the flow on-line. It is considered that the device developed in the current investigation could have applications either in laboratory simulations of these flows or as a possible on-line measurement instrument.

The water treatment application described above could also be analogous to many other solids-liquid pipeline flows within the process industries. However there are other areas where the technology could be applicable. Grieve et al [12] report research into applying solids-liquid measurement technology to level and moisture content measurements within filters. As the operating filter and the resulting filter cake are both solids-liquid mixtures there is a possible application of the technology here. Fluidised beds are a very common type of reaction vessel in process applications. In a fluidised bed a solids-liquid mixture is continually circulated inside the bed. Examples of research to investigate the solids volume fraction and velocity within fluidised beds are the work reported by Wei et al [13] and Yang & Gautam [14]. It is considered that the technology developed here could be directly applicable in these areas. Finally within the field of separation there are a wide range of possible applications of the technology. Examples are the measurement of the local solids volume fraction inside hydrocyclones as reported by Bond et al [15] and the measurement of component interface positions within a settling tank as reported by Schüller et al [16]. It is likely that there are applications of the technology developed here in these areas.

1.3.4 Geophysical applications.

Although the current investigation aims to develop a device capable of making solids volume fraction measurements in pipe flows it may be applicable to other fields where a measurement of solids volume fraction is required. A number of these can be found within the field of Geophysics. A good example of this is the measurement of sediment density on the sea bed which is reported by Hulbert et al [17]. A similar application involving the measurement of sediment density in a bore-hole is reported by Lauer-Leredde et al [18]. The density of a sediment is directly related to its solids volume fraction and therefore this is a possible application of the current research. A similar application is the detection of sediment height on the sea bed. The sediment level is usually measured by detecting the point at which the local sediment volume fraction drops to zero. An example of this application is reported by Ridd [19]. It is likely that the device developed in the current investigation will be applicable in these areas.

Many geophysical applications involve the measurement of conductivities, densities, or water volume fractions over large areas or the pinpointing of anomalous areas in an otherwise even material. A good introduction to this field is given by Griffiths & King [20]. Particular applications include the detection of layer interfaces within soils reported by Lagace et al [21] and the detection of leaks from storage ponds or pipes reported by Binley et al [22] and Jordana et al [23]. Although the current research is unlikely to be directly applicable in these areas it is possible that it could be developed for the applications.

1.4 The format of the thesis.

It is useful at this stage to explain the format of the thesis. The thesis is generally laid out to present the research in a chronological order. However this arrangement has not been strictly adhered to. Each chapter is intended to be a reasonably self contained report on one area of the research. However it may be necessary to refer back to earlier sections of the work in some cases before a full understanding can be achieved. This section is intended to allow the reader to identify areas of interest within the research and therefore the relevant chapters.

Chapter 2 This chapter reports the results of the initial literature surveys carried out in the present investigation. These involve the selection of the measurement principle of the instrument and further research into detailed areas of this measurement principle. Also the measurement principle used in the parallel research program introduced at the beginning of Chapter 1 is investigated.

Chapter 3 This chapter reports the design and optimisation of the measurement device. This includes the mechanical design and construction of the instrument. It also includes the results of finite element modelling designed to optimise the device.

Chapter 4 This chapter reports on the design and construction of all the electronic measurement hardware and software. It also presents the design and construction of the ancillary mechanical and electrical components.

Chapter 5 This chapter presents the results of static experimental testing using the equipment described in Chapter 3 and Chapter 4. This experimental testing was carried out to validate the finite element modelling presented in Chapter 3.

Chapter 6 The development of the University of Huddersfield multiphase flow loop is described. This includes all the reference measurement devices and calibrations. In addition the experimental procedure is described. This covers the use of the

developed device and the reference measurement instruments.

Chapter 7 All experimental results are presented in this section. Results from both the device developed as part of this investigation, and the device developed in the parallel investigation, are presented. Any errors in the results are discussed and possible improvements are suggested.

Chapter 8 In this chapter the results of modelling carried out to predict the liquid volumetric flow rate of the flow are presented.

2. Literature review.

2.1 Solids-liquid flow measurement methods.

As described in Chapter 1, the aim of the current investigation was to measure $\alpha_{s,i}$, and $u_{s,i}$ in upward solids-liquid flows in pipes. It was intended to use these measurements to calculate area averaged measurements of Q_s, α_s, and u_s. It was also intended to use these measurements to validate a non-intrusive flow meter developed as part of a parallel research program, and to use the results to attempt to predict Q_w. This section of the literature review is devoted to describing measuring techniques that can be used to acquire local measurements in multiphase flows. A number of detailed reviews of multiphase flow measurement devices already exist in the literature. Where possible this section provides only a brief discussion of these techniques and the reader is referred to existing sources if more information is required. It should be noted at this point that the measurement technique used in the parallel research program was Electrical Resistance Tomography (ERT). A review of this technique has been included in this section whilst a description of the device used in the parallel investigation is included in Chapter 6.

A wide range of different techniques have been used to acquire local measurements in multiphase flows. Different techniques are used to acquire measurements in different types of flow and also to acquire measurements of different parameters. For the current investigation only methods which could give a local measurement in a pipe cross-section are considered. Techniques such as gamma ray attenuation, which give measurements averaged along a chord of the cross-section are not discussed. Similarly global measurement techniques are not discussed. The theoretical and practical basis of some of the different techniques is discussed. Applications of each are then presented. The suitability of each technique to application in the particular solids-liquid flow used during this investigation is then critically discussed. In conclusion this section will show why one technique was chosen for development and application to the current investigation.

2.1.1 Optical methods.

A variety of techniques can be considered as optical methods. This section briefly describes the technical basis behind some of the techniques which could be applied to the flow conditions in the current investigation. Applications in which each technique has been used

are then introduced. Finally the possible application of each method to the current investigation has been critically examined.

2.1.1.1 Velocimetric methods.

Velocimetry involves tracking the paths of individual particles or bubbles. The simplest velocimetric measuring technique is photography. A review of previous research on multiphase flow techniques including photographic and cinematographic methods is reported by Chaouki et al [24]. Additionally cinematographic techniques have been applied by Scarlett & Grimley [25] in solids-liquid flows and by Gunn & Al-Doori [26], and Polonsky et al [27], in gas-liquid flows.

In a solids-liquid flow cinematography can be used to follow the path of a small number of tracer particles within the flow. In order to be able to visualise the tracer particles the rest of the flow must be invisible to the camera. In order to achieve this the liquid component and the bulk of the solid particles must be translucent and have matched refractive indices. In addition, if the experiments are carried out in a cylindrical pipe, a liquid filled square box must be constructed around the pipe in order to eliminate refraction effects due to the round pipe. Finally, in order to visualise the motion of the tracer particles in 3 dimensions, images must be acquired at two perpendicular positions and then reconstructed. A diagram showing the experimental set-up of Scarlett & Grimley [25] is shown below. Using this system the probability of tracer particles passing through designated pixels in the pipe cross-section was measured. If it is assumed that the tracer particles are well mixed in the flow this measurement can be used to give the solids volume fraction profile.

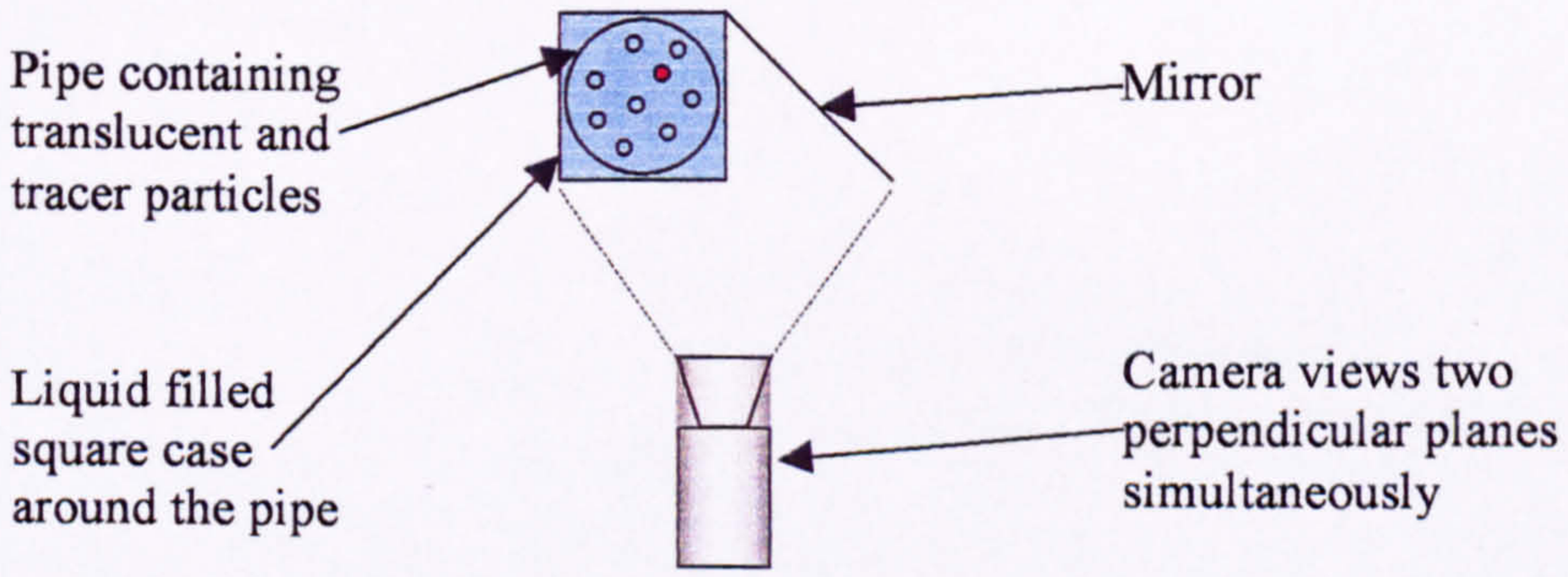

Figure 2-1. The optical method of Scarlett & Grimley.

In gas-liquid flows Yamamoto et al [28] incorporated a sophisticated image analysis system into their method. Using two perpendicular images, like those in the method of Scarlett & Grimley, they were able to individually track bubbles in three dimensions, in flows with much

higher volume fractions than previously achieved. Apart from this application this method has mostly been used to visualise the deformation of gas bubbles as they rise through a liquid column. In this case the total gas volume fraction must be low in order that individual bubbles can be imaged clearly. The system of Gunn & Al-Doori [26] used high speed video cameras to record the passage of bubbles through a column of water only 15mm thick. Polonsky et al [27] used video cameras to record the movement of large Taylor, or "cap", bubbles which cover almost the entire cross-section of the pipe. In both these applications the possibility of capturing more than one bubble in the direct line of sight of the camera was low. The system of Gunn & Al-Doori [26] was also used to record the interaction of an intrusive probe with rising bubbles.

Obviously this method cannot be applied directly to industrial applications. Even as a laboratory tool it requires an expensive experimental configuration and analysis of the data can be extremely time consuming. Additionally, in order to achieve a reasonable level of accuracy, high speed cameras must be used. The camera used by Scarlett & Grimley [25] could be operated at speeds of up to 3000 frames per second. Because of these disadvantages, photographic methods were not considered suitable for the current investigation.

Another form of velocimetry is laser velocimetry. In laser velocimetry a sheet of laser light is shone across the flow. The particles, or bubbles, in the path of the light sheet reflect the light and therefore appear to shine. A camera aimed perpendicularly at the light sheet can record the positions of these particles, assuming that the remainder of the flow between the camera and the sheet is relatively translucent. A good review of this technique is given by Chaouki et al [24]. It is generally carried out with translucent particles. These are invisible to the camera whilst still, if the material is chosen carefully, reflecting the laser light. There are a number of variations of this technique. In streak velocimetry, as reported by Hassan & Blanchet [29], the laser light is pulsed twice for each exposure of the camera. This results in each image showing a streak following the path of each particle. The length of each streak gives the velocity of the particle if the pulse rate of the laser is known. In speckle velocimetry, as reported by Yamamoto et al [28], each image records the instantaneous position of the particle only. Analysis of a series of these images allows the particle tracks to be calculated. In both of these variations the solids volume fraction is measured using a counting technique.

The advantage of laser velocimetry over conventional velocimetry is that higher volume fraction flows can be used without having to introduce tracers. However the technique still requires a relatively translucent flow, and a large quantity of specialist hardware and software. Again it is also not easily applicable in an industrial environment. For these reasons it was decided that this technique was also not suitable for the current investigation.

2.1.1.2 Laser Doppler Anemometry (LDA).

Laser Doppler Anemometry (LDA) relies on the Doppler effect. In LDA a laser beam is focussed onto a control volume in the cross-section of the multiphase flow. The beam is scattered by either particles or bubbles in the flow. This modifies the frequency of the laser light. The modified frequency of the light is proportional to the velocity of the object which caused the scattering. In addition the solids volume fraction can be calculated by counting the number of particles which pass through the control volume. A good review of LDA is given by Chaouki et al [24]. It has also been reviewed briefly by Jones & Delhaye [30], and Sheng & Irons [31].

An important requirement for LDA is a clear optical path to the control volume. Therefore it is usually limited to flows of a low concentration. In addition Sheng & Irons reported from their literature review that it is not usually successful if the particle size exceeds 4mm diameter. A number of researchers have attempted to circumnavigate the low concentration condition. Marié [32], in gas-liquid flow, installed nozzles at a point below the control volume. Using these a jet of gas could be injected into the regions of flow between the laser source and the control volume, and between the laser receptor and the control volume. However this could have a severe effect on the flow conditions and was not considered to be practical. In solids-liquid flow both Chen & Kadambi [33], and Yianneskis & Whitelaw [34], used a matched refractive index system and a small number of tracer particles. This has been explained in Section 2.1.1.1. Finally Wei et al [13] optimised the tip of a local LDA probe in order to reduce the distance between the measuring window and the control volume. This reduced the chance of particles passing between the two.

In conclusion LDA suffers from many of the problems identified with velocimetric techniques. Again, specialist, high cost, equipment is required, and there is no real possibility of developing the technique for industrial use. For these reasons it was decided that LDA was not a suitable technique for the current investigation.

2.1.1.3 Fibre-optic probes.

It is possible to acquire a true local measurement in a two-phase flow, using optical methods, regardless of the disperse phase volume fraction. In general these intrusive probes determine which phase the tip of the device is immersed in at a given time. As such the flow must be fluid-fluid. In these devices light is transmitted down an optical fibre to an open tip within the flow. Some of the light is reflected, either back up the same fibre or up a parallel fibre. The remainder of the light is transmitted out into the flow. The relative proportion of light which is reflected depends on the refractive index of the material surrounding the tip of the probe.

A second type of optical probe can be used in a solids-liquid flow. Akagawa et al [4] reported an intrusive optical probe where light was transmitted into the flow through an optical fibre as before. However the receiving fibre was positioned perpendicularly to the first fibre in such a way that light was reflected into it by particles passing close to the pair. Two axially displaced sensors of this type were used in order to measure the solids velocity. This type of device would be applicable to the current investigation although this method requires relatively complex equipment and analysis.

The first type of device is unsuitable for the current investigation because it requires a fluid-fluid flow. However, because the probes are intrusive, research has been carried out into the optimum shape of probe in order to minimise the flow disturbance. Reviews of this research are given by Mendes de Moura & Marvillet [35], Cartellier & Achard [36], and Jones & Delhaye [30]. If the method selected for this investigation is an intrusive one then work in this area may be useful.

2.1.2 Tracer methods.

Tracer methods are most commonly used to measure mean solids velocity only. Radioactive tracers or positron emitting tracers can be injected into a flow and the time taken for them to reach a downstream detector can be measured. This gives a measure of the tracer velocity along the length of pipe. This method was used by Tallon et al [37] to measure the flow of solids in a pneumatic transport application by making the properties of the tracer similar to the properties of the solid component. However this method has been extended by some researchers to give local measurements. Tracer particles are mixed with the solid component of the flow as if a global estimate was to be made. However instead of using one detector

downstream of the injection point, a carefully positioned array of detectors is used. This allows the local position and trajectory of each tracer particle to be measured at a given cross-section of pipe. Therefore the solids velocity is known, and the solids volume fraction can be measured using a counting method. A review of research in this area is given by Chaouki et al [24]. It was decided that it was unsuitable for this investigation due to the high cost and complexity of the necessary equipment.

2.1.3 Sampling methods.

Sampling involves removing some of the flowing mixture from the pipe. The simplest way to acquire a local measurement in this way is to put a small pitot tube at the relevant position in the flow. Miller & Gidaspow [38] successfully used this technique in gas-solids flows. Some researchers, including Nasr-El-Din & Shook [39], have claimed that the pitot will affect the flow and that solids will tend to be deflected around the pitot rather than entering it. These researchers recommend isokinetic sampling. In isokinetic sampling, in order to ensure that the flow enters the pitot, fluid is drawn out through the rear of the probe in such a way that the static pressure at the mouth of the pitot is identical to that which would exist at the same point in the flow in the absence of the probe. Whichever method is used to acquire the sample, the analysis is the same. The withdrawn sample is separated and measured off line allowing the volumetric flow rate of each phase to be measured.

Unfortunately this does not allow the solids volume fraction or the solids velocity to be directly determined. This is because the volumetric flow rate at a point is proportional to the product of these properties and the variables cannot be independently determined without additional information. Rao & Dukler [40] acquired this extra information using an isokinetic-momentum probe. The pitot tube was mounted on a sensitive strain gauge. It was then possible to measure the force applied by the solids as they struck a sharp 90° bend in the pitot. This extra information allowed the solids volume fraction and solids velocity to be measured.

A principle factor in accurate sampling is the pitot diameter. The pitot must be large enough to ensure that a relatively undisturbed flow enters it. Rao & Dukler [40] used solid particles 0.065mm in diameter with a pitot 1.6mm in diameter. This ensured that a representative flow of solids entered the pitot. Miller & Gidaspow [38] claimed accurate results using a 0.47mm diameter pitot with 0.075mm diameter solid particles. In the present investigation the solid particles are 4mm in diameter. In order to achieve the same order ratios of pitot to solids

diameter as Rao & Dukler [40] and Miller & Gidaspow [38] the pitot would have to be between 25mm and 100mm in diameter. As the working section of the flow loop is only 80mm in diameter these sizes of intrusion would make this method unsuitable.

2.1.4 Electrical methods.

Electrical measurement methods applied to two phase flows rely on the electrical properties of the phases being significantly different. The electrical properties most frequently measured are the conductivity and permittivity of the phases. In the present investigation the conductivities of the two phases differ significantly. The conductivity of the water is approximately $150\mu Scm^{-1}$. The solid particles are effectively insulators, i.e. their conductivity is negligible. This high difference means that conductivity methods are more applicable in the current investigation. Therefore only conductivity measurement techniques are discussed in this section. Many global techniques exist to measure the electrical properties of two phase flows. However as these do not meet the needs of the present investigation they are not considered here. In order to make direct local electrical measurements in a two phase flow an intrusive device must be used.

2.1.4.1 Local conductivity probes for fluid-fluid flows.

The majority of research that has been carried out on local conductivity measurement probes for flow measurement has been in the area of fluid-fluid flows. These devices use a penetration principle similar to that employed by local optical probes as described in Section 2.1.1.3. The probe consists of a conducting needle tip encased in, but insulated from, a conducting holder. This arrangement is shown in Figure 2-2. The needle electrode is held at a potential and the conducting casing is grounded. If the probe tip is immersed in a conducting medium current flows. If the tip is immersed in a non-conducting medium current does not flow. After signal analysis the measured potential difference across the two electrodes gives an almost digital response with a low output if the probe is immersed in the conducting phase and a high output when the probe is immersed in the non-conducting phase. By measuring the relative time that the probe is immersed in each phase an estimate of the disperse phase volume fraction is achieved. This technique has also been extended to give bubble velocities by mounting two needle electrodes axially separated in the same casing, and then cross-correlating the two signals. Cross-correlation applied to flow measurement is described in Section 2.3.

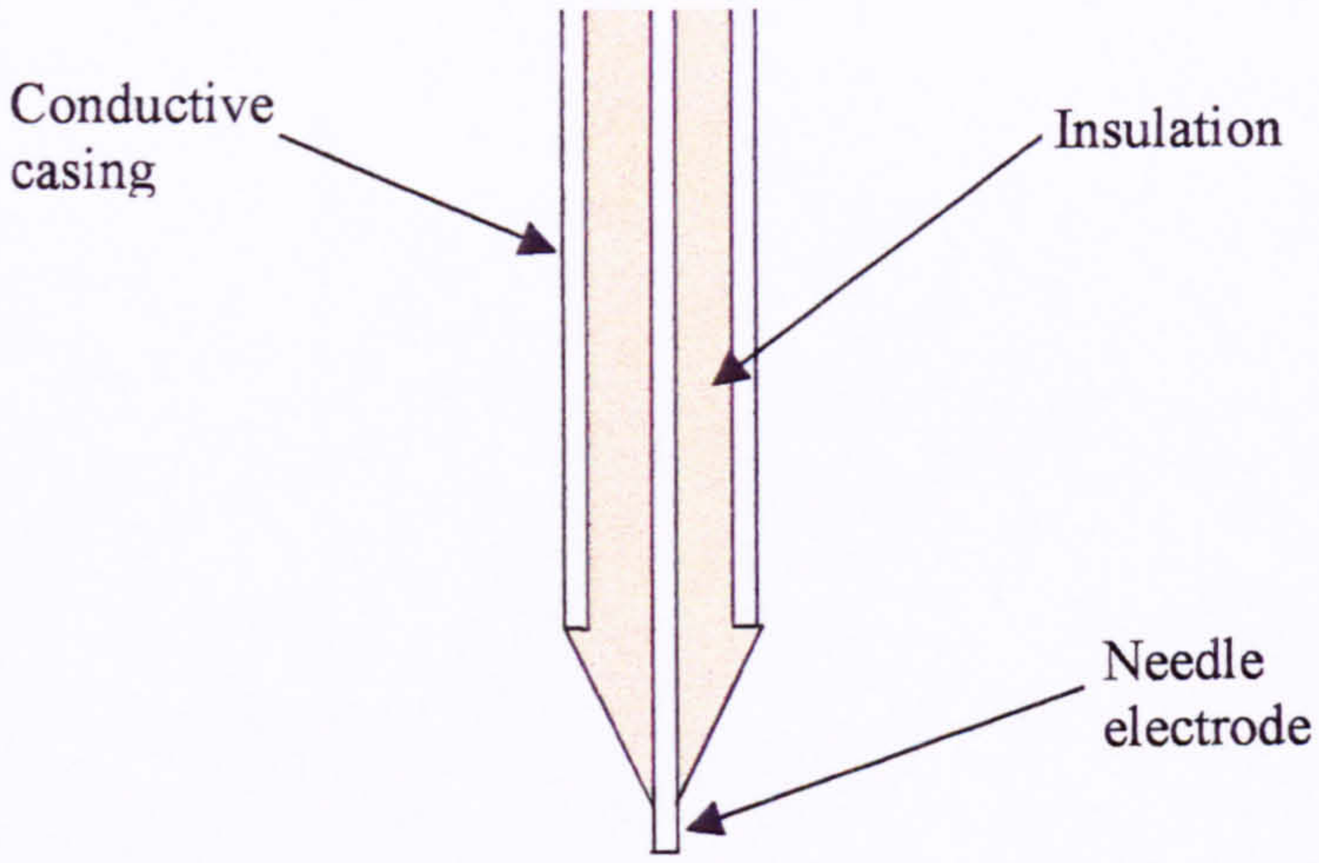

Figure 2-2. General representation of a penetration type conductivity probe tip.

Obviously this technique cannot be applied to solids-liquid flow measurement. However researchers in this field have carried out a wide variety of tests to discover the disturbance effects of local probes on two phase flow fields, the properties of electrical fields in two phase flows, the optimal probe parameters for cross-correlation flow measurement, and also the possible methods of constructing the local probes. This research could be applicable to the current investigation and therefore it is briefly reported here.

Reviews of penetration type local probe techniques are given by Jones & Delhaye [30] and Mendes de Moura & Marvillet [35]. A review carried out by Cartellier & Achard [36] includes a presentation of the relative accuracies in local disperse phase volume fraction measurement of a wide variety of local penetration probes. As some errors in any local probe measurement will be introduced by the probe intrusion this is an interesting reference. Probes are reported showing relative accuracies of between ±5% and ±20%. This suggests that this particular type of probe could achieve the accuracy needed for the industrial applications reported in Chapter 1. However a review by Ceccio & George [41] reports some researchers finding considerable deflection of the flow by the probe.

As well as reviews of research work, individual research was examined in order to investigate the areas listed above. Many of the probes reported used only single sensors. Angeli & Hewitt [42] reported the use of a probe 0.86mm in diameter in a pipe 25.4mm in diameter. Vigneaux et al [43] and Clark et al [44] reported the successful use of single sensor probes although they did not give any dimensions for their devices. Sheng & Irons [31] reported the use of a 1.5mm diameter probe in a model of a large steel making ladle. Teyssedou et al [45] reported more detailed tests on a 1mm diameter probe used in a 19mm pipe. They varied the sharpness of the

probe tip which varied the distance between the needle electrode and the casing. They discovered that with a large separation the probe gave an artificially high reading when positioned near the pipe wall. They concluded that the large electrode separation caused the electric field around the probe to penetrate further into the flow. They suggested that this allowed the pipe wall to affect the field and therefore alter the reading.

Penetration probes with two sensors, designed to allow a disperse phase velocity estimate to be made using cross-correlation, are also reported in the literature. However the probe velocity estimates are not generally compared with any reference measurement. Thang & Davis [46] reported using a 1.6mm diameter probe in a 50mm diameter pipe. The axial distance between the two sensors was ≈5mm. Van der Welle [47] reported using a dual sensor probe with a sensor separation of 10mm although the other dimensions of the probe were not presented. Revankar & Ishii [48] reported the use of a probe 0.7mm in diameter in a 5mm pipe. This device had a sensor separation of 4mm. In an often referenced paper on gas-liquid flow Serizawa et al [49] used a 1.8mm diameter probe in a 60mm diameter pipe. This device had a sensor separation of 5mm. Castello-Branco & Schwerdtfeger [50] reported using a dual sensor penetration device in large bubble plumes in casting ladles. In this case a 1.8mm diameter probe was used with a 2mm sensor separation. Sun et al [51] reported the use of a probe employing a sensor separation of 2mm although the overall diameter of the device was not given. Finally Gunn & Al-Doori [26] investigated the effect of this type of probe on the flow field by photographing the flow around the probe. These experiments used two 4mm diameter probes separated by an axial distance of 11mm. They were carried out in a 15mm deep slot so that the probe was visible to the camera at all times. Their conclusions were that bubbles were deformed as they struck the probe. However they concluded that the overall flow was not affected by the probe.

In conclusion probes with diameters of between 0.7mm and 4mm have been used by researchers in this field. The ratio of probe diameter to pipe diameter in these cases varied between 0.03 and 0.14. This suggests a wide range of opinion on the ideal probe diameter to minimise flow disturbance. However the literature reviewed suggested that although probes affect bubbles they actually penetrate, they do not affect the overall flow field. The sensor separations used in these devices varied from 2mm to 11mm with no authors reporting substantial errors in their velocity estimates. Finally the majority of the probes examined had

been constructed by bonding the components together with an epoxy resin. This gave the necessary strength whilst also insulating the components from each other.

2.1.4.2 Local conductivity probes for solids-liquid flows.

Compared to fluid-fluid penetration probes, little research has been carried out involving local conductivity measurement probes in solids-liquid flows. In a solids-liquid application the probe cannot penetrate the particles. Instead the probe is usually designed to measure the mixture conductivity, σ_m, over a small volume around itself. A known electrical current, i, is established between two electrodes. The potential difference, V, is then measured either between these two electrodes, or between two other electrodes in the vicinity. σ_m is then proportional to i and V as shown in Equation 2-1.

$$\sigma_m \propto \frac{i}{V}$$

Equation 2-1

The conductivity of a two phase mixture is related to the conductivity of each phase and the relative volume fractions of each phase. If the electrical conductivity of each of the two phases and of the mixture is known, the disperse phase volume fraction can be estimated. Many relationships have been developed to give this estimate. A review of these is given in Section 2.2.

Nasr-El-Din et al [52] developed a 4.8mm diameter probe of this type for use in pipe flows. The probe used a four electrode configuration where current was injected between two "field" electrodes and the resulting potential difference was measured across two "sense" electrodes. Using this configuration the author claimed that electrochemical effects were negated. He also claimed that this configuration negated variations in the conductivity reading due to varying mixture velocity. The arrangement of the electrodes in the probe is shown in Figure 2-3. The field electrodes were both formed from areas of the casing whilst the sense electrodes were the cut ends of 0.3mm diameter wire. The separation of the sense electrodes was 1mm. As with the penetration probes the components were bonded together, and insulated from each other, with an epoxy resin.

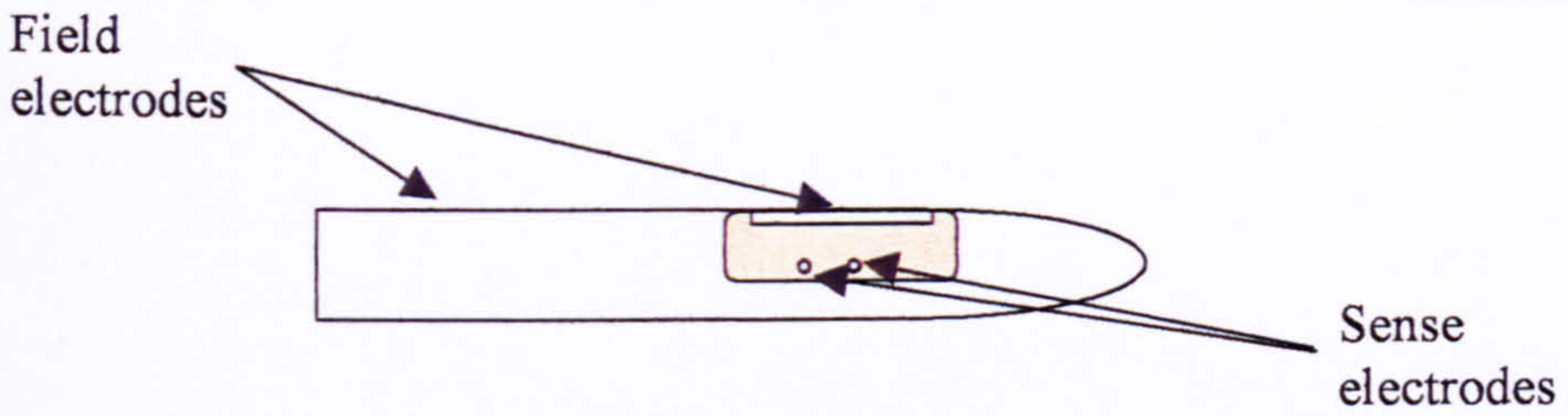

Figure 2-3. Local conductivity probe of Nasr-El-Din et al.

Using this probe Nasr-El-Din et al acquired measurements in a 50mm pipe, and presented profiles of solids volume fraction across the pipe. Whilst the results were not validated against any reference measurements, some factors were noted which could be applicable to the present investigation. It was noted that the conductivity measurement varied with the orientation of the probe relative to the pipe wall. Considering the asymmetrical nature of the design this is not surprising. This type of wall effect was also noted by Teyssedou et al [45] with a penetration probe. A wide variation of the measured mixture conductivity with varying temperature in the pipe was also noticed. As the liquid conductivity varies with temperature this is also not surprising. Finally an effect was noticed as the particle diameter increased. As the particle diameter increased above the sense electrode separation the probe began to underestimate the solids volume fraction. No explanation was given for this but it was suggested as a guideline for the design of this type of probe.

MacTaggart et al [53] extended the work of Nasr-El-Din et al by developing a probe for measuring the solids volume fraction in a tank containing a solids-liquid mixture. Again the probe used a four electrode measurement technique. However in this case the arrangement of the electrodes was as shown in Figure 2-4. The probe was 4.8mm in diameter and the sense electrodes were separated by 1mm.

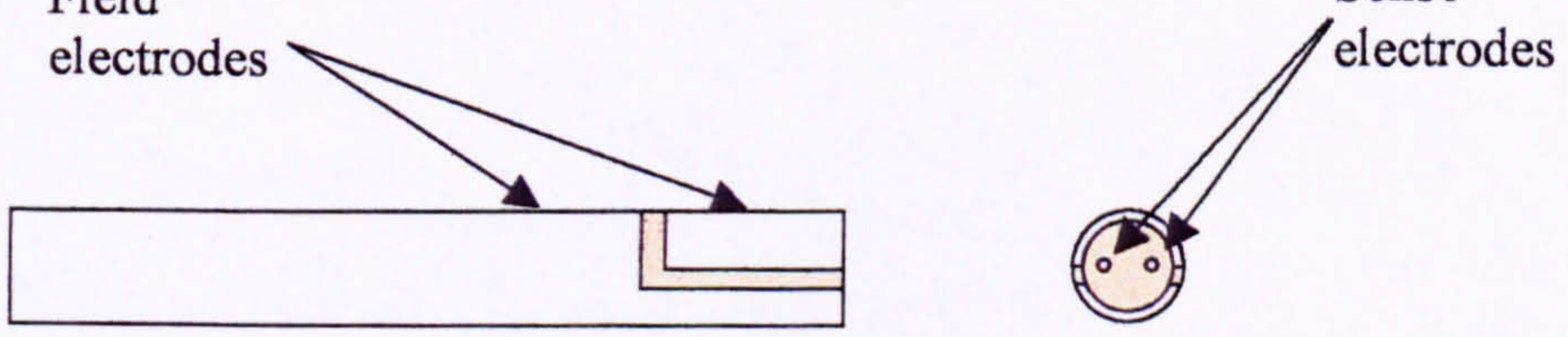

Figure 2-4. Local conductivity probe of MacTaggart et al.

Using this device profiles of local solids volume fraction were presented for a large mixing vessel. Most of the conclusions reached were similar to those of Nasr-El-Din et al [52]. However MacTaggart et al extended the experimentation with different probe orientations. In

their work it was reported that the solids volume fraction estimate also varied depending on which field electrode was facing the wall. It was concluded that the area of the field electrode closest to the wall had an effect on the measurement. No explanation of this was given, it was merely presented as a guideline for the design of this type of probe.

Asakura et al [54] reported a 3mm diameter probe that differed from those mentioned above in that it did not use a four electrode measurement technique. It could also be used to measure solids velocity as well as solids volume fraction. Unfortunately very few details of the device, or the measurement technique, were presented. However the probe possessed three ring shaped electrodes formed from 0.3mm diameter wire. These were arranged as shown in Figure 2-5 with each electrode separated by 10mm.

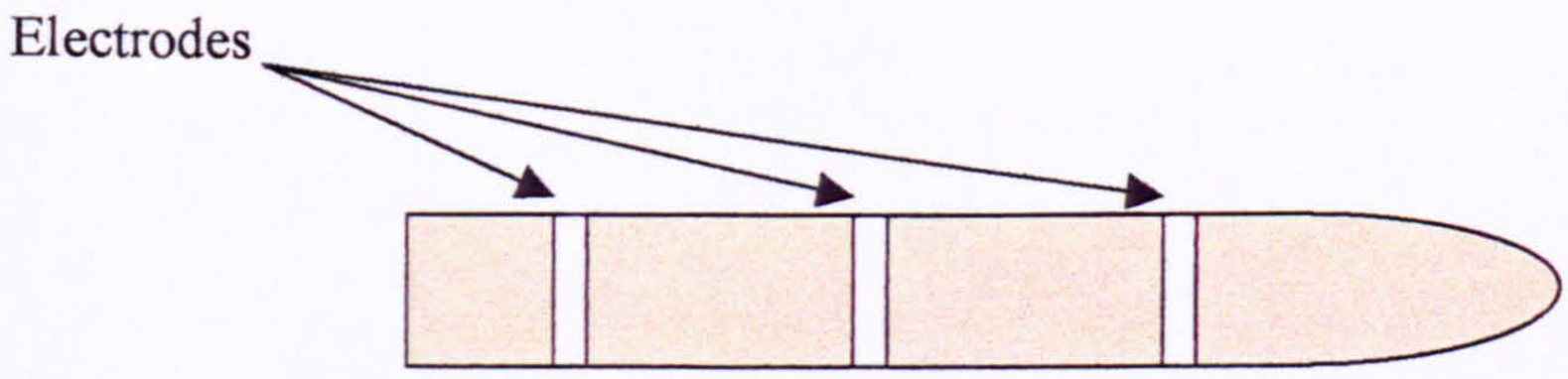

Figure 2-5. The local conductivity probe of Asakura et al.

The most obvious measurement technique that could be used with this device would be to inject current from the centre electrode to each of the outer electrodes. This would result in two measurable potential differences which could be cross correlated to give a solids velocity estimate. The signal from either of these two sensors could then also be used to give a solids volume fraction measurement. Using this device Asakura et al acquired and presented profiles of solids volume fraction and solids velocity across a 51mm pipe. However the measurements were not validated against any reference devices and no discussion of any possible errors was presented.

The final appearance in the literature of this type of device is the six electrode probe developed by Xie et al [55]. This device was developed in order to measure the velocity of a flow of blood, which can be considered a solids-liquid flow. No details of the dimensions of this device were reported. However its configuration is shown in Figure 2-6.

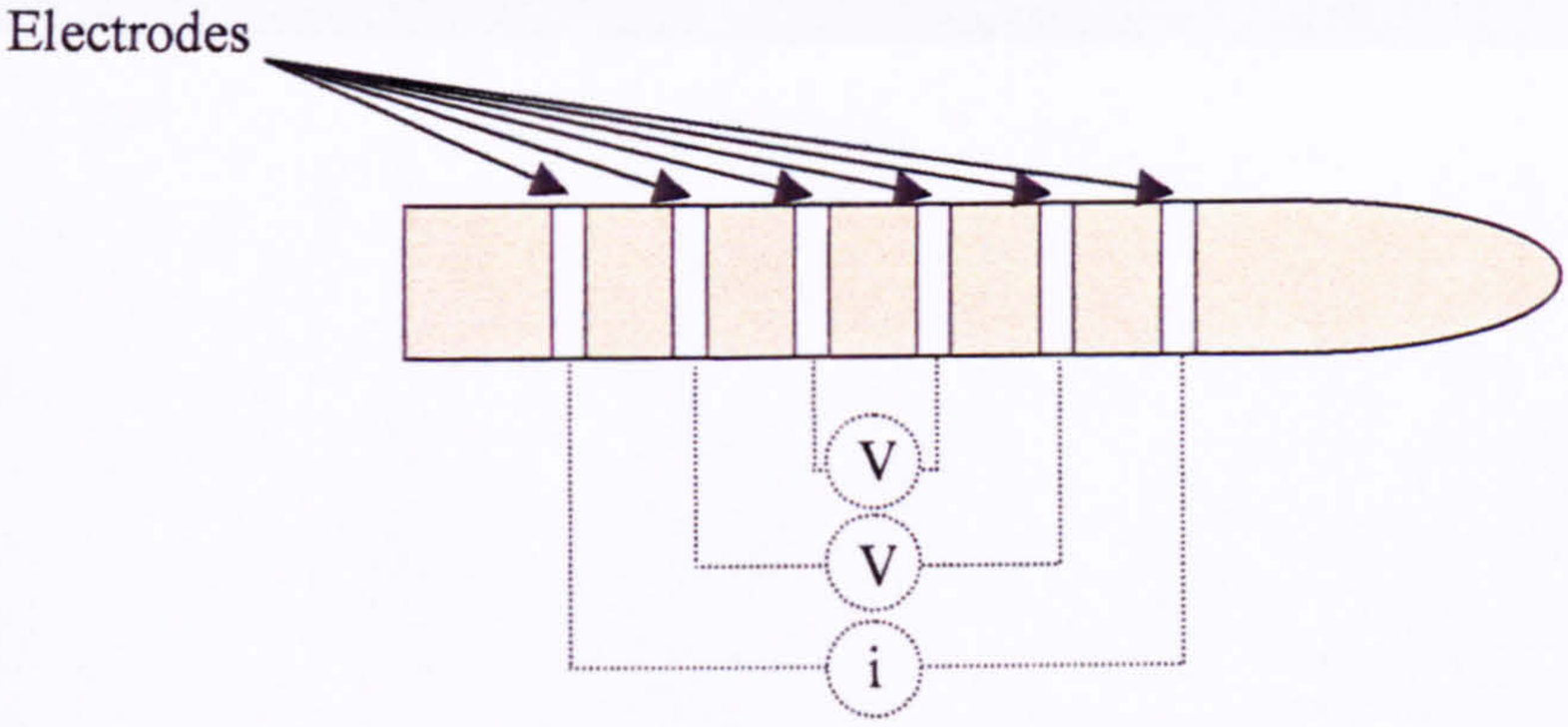

Figure 2-6. The local conductivity probe of Xie et al.

By establishing an alternating current across the outermost electrode pair and measuring the resulting potential differences as shown in Figure 2-6 Xie at al claimed that a measurement of the resistivity of the blood could be made. However a number of assumptions were made in order to justify this. Xie et al then claimed that the resistivity was proportional to the velocity of the blood due to the changing alignment of the blood cells. Calibration results referenced against an unspecified "speedometer" were presented to support this. Clearly this effect will not be present in the current investigation as the solid particles are regular spheres.

In conclusion conductivity probes appear in the literature that allow local values of solids volume fraction and solids velocity to be acquired. These devices involve relatively inexpensive equipment, and can be constructed with a variety of different geometries for different applications. The simplicity of the probes allows them to be constructed in a robust form for industrial applications. The probes presented varied in diameter from 3mm to 4.8mm giving ratios of probe diameter to pipe diameter of between 0.06 and 0.1. Two probes were presented that allowed a velocity measurement to be made. One of these used a velocity measurement method that cannot be applied in the current investigation. The measurement method used by the other was not specified. The major disadvantage of these devices is that they are intrusive. However the work of Gunn & Al-Doori [26] suggested that the effects of this were negligible.

After examining the literature in detail it was decided that this type of device would be most suitable for the present investigation. It has a number of advantages over the other techniques presented. In addition little previous research has been carried out which means that the current research will be novel.

2.1.5 Tomographic methods.

As discussed at the beginning of this chapter, one of the intended uses of the device developed in the present investigation was the validation of a solids flow meter developed in a parallel research program. The measurement technique used in this parallel program was Electrical Resistance Tomography (ERT). Because of this it had already been decided not to use a tomographic principle in the present investigation. However in order to become familiar with the technique it was investigated in the existing literature at this stage. For the same reason the results of this investigation are briefly presented here. A description of the device developed for this application is given in Chapter 6 and in published work by Loh [56] and Lucas et al [57,58].

Tomography is the imaging of the interior of a body using sensors positioned around its boundary. A large number of measurements are acquired across different parts of the body. These are then reconstructed, using a mathematical algorithm, to give an image of the interior. Using this broad outline different types of tomography, involving measurements of different properties of the body, have been developed. A good introduction to tomography is given by Dickin et al [59] where the different tomographic methods are divided into hard field, where the sensitivity is not influenced by the flow being imaged, and soft field, where the flow can affect the sensitivity of the sensors. A brief description of some of the hard field and soft field techniques is given in the following sections.

2.1.5.1 Hard field tomographic methods.

Generally the hard field tomographic techniques are nuclear based. Nuclear based techniques can be divided into two areas, particle tracking methods, and ray transmission methods. A good review of both of these techniques is given by Chaouki et al [24]. This includes a comprehensive survey of the published literature.

Positron emission particle tracking (PEPT) involves injecting radioactive tracers into the flow. The nuclei of these tracers decay emitting two back to back gamma rays simultaneously. If both of these rays can be detected a line of sight to the radioactive particle can be calculated. In order to detect the emitted gamma rays banks of detectors are constructed around the body being imaged. This technique is mostly used in laboratory applications although short lived tracers are used in medical applications. The laboratory applications have included the

percolation of tracers through rock and the extrusion of materials into moulds, as well as pipe flow applications. The advantage of the technique is that the position of each tracer particle can be located very accurately as the gamma rays always travel in a straight line. The disadvantages of the technique are the complexity of the equipment and the time taken to build up a full flow profile. Added to this there is often significant resistance to the use of radioactive tracers in industrial applications for health and safety reasons.

The ray transmission methods involve transmitting a ray of energy through the flow. X-rays, gamma rays, and neutron beams have all been used in this way. When a ray, for example an X-ray, passes through a medium it is attenuated by the material through which it passes. Materials of different density attenuate the ray to different degrees. If a detector is positioned on the opposite side of the body from the transmitter this attenuation can be measured. In this way the integral of the density distribution along the path of the ray can be calculated. In order to obtain a complete image of the flow rays must be transmitted across a number of chords of the pipe. The density distribution within the pipe can then be reconstructed using a mathematical algorithm. As with PEPT the advantage of this method is that the rays always travel in a straight line through the flow. Because of this the spatial resolution that can be achieved is high. However this method also involves a large amount of specialist equipment and problems with health and safety issues regarding radioactivity cannot be overlooked.

2.1.5.2 Soft field tomographic methods.

Soft field tomography includes optical, sonic, and electrical methods. It is the fastest growing area of tomography within process applications. This is mostly due to reasons of cost, safety and speed of data acquisition. Within the soft field techniques electrical methods are generally the most popular. There are three main types of electrical tomography, electromagnetic, capacitance, and resistance. This section will concentrate on Electrical Resistance Tomography (ERT) as this is the method employed by the solids flow meter validated by the device developed in the current investigation. Reviews of this and other soft field tomographic methods are give by Chaouki et al [24] and Dickin et al [59]. A review of ERT including reconstruction methods is given by Ceccio & George [41]. A description of the principles of ERT is given by Yang [60].

In ERT a map of the conductivity across the interior of the vessel is measured using an array of electrodes at its boundary. In order to do this, in the device developed in the parallel

program, alternating current is injected into the interior of the vessel via an adjacent pair of the electrodes. The potential difference is then measured across all the other adjacent pairs of electrodes. Alternating current is then injected via the next adjacent pair of electrodes and the potential difference is again measured across all the other adjacent pairs. This process is repeated until all the adjacent pairs of electrodes have been excited. In a 16 electrode ring this corresponds to 104 individual measurements. This excitation configuration, which is described in detail by Dickin et al [59], is referred to as the adjacent pairs methodology. It should be noted that other excitation configurations exist.

Once all the measurements have been obtained they must be reconstructed using a mathematical algorithm to give the image of the flow. A wide variety of different algorithms exist. They vary in speed and in the quality of the image they allow to be reconstructed. In the current parallel program two algorithms are used. The first is the linear back projection method. This is a high speed algorithm but it does not allow an accurate image to be reconstructed. The second is the modified Newton-Raphson technique. This is a far more computationally intensive algorithm but it allows a much more accurate image to be reconstructed. Both these algorithms are discussed in more detail by Loh [56].

ERT has previously been used in a wide range of applications. Only a few references have been mentioned here as examples. In the field of pipe flow measurement it was developed for high speed pattern recognition by Peng et al [61], and was used to make more accurate solids volume fraction measurements by Primrose & Qiu [62]. It was used to image the insides of pressure filters by Grieve et al [12], and to image foam densities in froth flotation vessels by Cilliers et al [63]. The advantages of soft field tomography, and ERT in particular, are that it is fast, safe, and does not require large amounts of specialist hardware. The disadvantage lies in it soft field nature. The electric field, and therefore the calibration of the device, will be affected by the conductivity distribution that is being measured. Finite element sensitivity testing is used to minimise this drawback, but the final images can never possess the high spatial definition of hard field tomographic techniques.

2.2 Relating mixture conductivity, σ_m, to α, the solids volume fraction.

As described in Section 2.1, and Section 2.1.4.2 in particular, it was decided that a local conductivity probe would be the most suitable instrument to acquire the measurements of $\alpha_{s,i}$ and $u_{s,i}$ in the current investigation. Estimating $\alpha_{s,i}$ using a measurement of $\sigma_{m,i}$, the local

mixture conductivity, is a relatively simple and economical method which yields accurate results. The method relies on the fact that the electrical conductivity of a solids-liquid mixture depends on the conductivity and the relative volume of each of the phases. In the current investigation the liquid, water, is conductive whilst the solid particles are non-conductive. Therefore as $\alpha_{s,i}$ increases $\sigma_{m,i}$ will fall.

In order to obtain an accurate estimate of $\alpha_{s,i}$ it is necessary to be able to accurately relate it to $\sigma_{m,i}$. Many expressions have been developed for this relationship. A review of some is given in this section. Additionally, summaries of some have been reported by Nasr-El-Din et al [52] and also by MacTaggart et al [53]. Experimental testing of some has been reported by De La Rue & Tobias [64].

Maxwell's [65] relationship was one of the earliest developed. It is given by Equation 2-2.

$$\frac{\sigma_m - \sigma_w}{\sigma_m + 2\sigma_w} = \alpha_s \frac{\sigma_s - \sigma_w}{\sigma_s + 2\sigma_w}$$

Equation 2-2

Here α_s is the solids volume fraction. σ_m , σ_w and σ_s are the conductivities of the mixture, the continuous phase (water), and the dispersed phase (solids) respectively. Maxwell's relationship assumes that the particles are evenly sized spheres and that they are in an ordered arrangement at a low volume fraction. This low volume fraction condition allowed Maxwell to assume that the electrical field around each particle was unaffected by any other particles. In the current investigation σ_s is effectively zero. Therefore Maxwell's relationship reduces to Equation 2-3.

$$\sigma_m = \sigma_w \frac{2(1-\alpha_s)}{(2+\alpha_s)}$$

Equation 2-3

Nasr-El-Din et al [52] and De La Rue & Tobias [64] reported that a number of other researchers have developed theoretical relationships that match this reduction of Maxwell's relationship. Additionally Turner [66] and Neale & Nader as reported by Nasr-El-Din et al [52] showed that Maxwell's relationship accurately fits experimental data for solids volume fractions up to 0.55. De La Rue & Tobias [64] also reported experimental work by a number of researchers that suggested that Maxwell's relationship is reliable.

Bruggeman [67] extended Maxwell's relationship to fit spheres of random size and distribution. This means that Bruggeman's relationship should apply to mixtures with solids volume fractions approaching 1. Bruggeman's relationship is given by Equation 2-4.

$$(\sigma_m - \sigma_s)\left(\frac{\sigma_m}{\sigma_w}\right)^{-1/3} = (1-\alpha_s)(\sigma_w - \sigma_s)$$

Equation 2-4

The variables used in Equation 2-4 have previously been defined for Equation 2-2. For the present investigation, where σ_s is effectively zero, Bruggeman's relationship reduces to Equation 2-5.

$$\sigma_m = \sigma_w(1-\alpha_s)^{3/2}$$

Equation 2-5

De La Rue & Tobias [64] showed that above solids volume fractions of 0.25 Maxwell's assumption that the field around the particles is unaffected by other particles is not true. From experimental testing of suspensions of non-conducting spheres, random grains, and rods, they developed Equation 2-6.

$$\sigma_m = \sigma_l(1-\alpha_s)^m$$

Equation 2-6

For suspensions where $0.45 \le \alpha_s \le 0.75$ they gave m=1.5. Therefore, in the current investigation the relationship of De La Rue & Tobias is equivalent to Bruggeman's relationship. De La Rue & Tobias also reported experimental work carried out by Pearce. Pearce measured the conductivity of 2D arrangements of spheres and found that if the arrangement of spheres was an ordered lattice σ_m was given by Maxwell's relationship. However if the arrangement was random the mixture conductivity was given by Bruggeman's relationship.

MacTaggart et al [53] reported the work of Prager who extended Maxwell's relationship to fit a random arrangement of arbitrary shaped non-conducting particles. Prager also set the condition that none of the particles could overlap. Prager's relationship is given in Equation 2-7.

$$\sigma_m = \sigma_w \frac{(1-\alpha_s)(3-\alpha_s)}{3}$$

Equation 2-7

Nasr-El-Din et al [52], MacTaggart et al [53] and De La Rue & Tobias [64] all recommended either one or more of the above relationships following qualitative and quantitative comparisons. However other relationships have been presented. Nasr-El-Din et al [52] reported the theoretical relationship developed by Begovich & Watson which is given in Equation 2-8, and the relationship developed by Machon, based purely on experimental data, which is given by Equation 2-9.

$$\sigma_m = \sigma_w(1-\alpha_s)$$

Equation 2-8

$$\sigma_m = \sigma_w(1-k\alpha_s)$$

Equation 2-9

De La Rue & Tobias [64] also reported two relationships based purely on experimental data. They reported Mashovert's relationship which is given by Equation 2-10. However they suggested that the range of experimental data used to generate this relationship was low. They also presented the relationship developed by Slawinski, given in Equation 2-11. This relationship was developed to give an improved fit at high solids volume fractions. However it was acknowledged that this results in a poor fit at low solids volume fractions.

$$\sigma_m = \sigma_w(1-1.78\alpha_s+\alpha_s^2)$$

Equation 2-10

$$\sigma_m = \sigma_w\left\{1+\left(\frac{\alpha_s}{p}\right)\left[\frac{(1+0.3219p)^2}{(1-p)-1}\right]\right\}^2 \quad \text{where} \quad p = n\cdot\alpha_s^{2/3}$$

Equation 2-11

In the current investigation the solids volume fraction was not expected to exceed 0.3 in vertical flow and cannot exceed close packing in inclined flow. Experimental testing showed that the close packed volume fraction ≈0.62. Additionally the solid particles are regular spheres. Therefore, after examining the comparisons carried out by Nasr-El-Din et al [52], MacTaggart et al [53], and De La Rue & Tobias [64], it was decided that Maxwell's [65] relationship should give a good fit to the data. However the possibility still remains to use a different relationship at a later point in the research if this seems advisable.

2.3 Cross-correlation applied to flow measurement.

In order to measure the solids velocity using local conductivity measurements the fluctuations in electrical conductivity caused by particles passing two axially displaced local conductivity sensors are measured and recorded. As a particle passes the upstream sensor it causes a change in its output signal. The same particle will then cause a similar change in the output signal from the downstream sensor as it passes it. The time delay between these changes in output signal will be equal to the time taken for the particle to travel between the sensors. This is proportional to the particle velocity. Therefore in order to calculate the solids velocity the time lag between the changes in output signal measured at the upstream and downstream sensors must be estimated.

This is done by cross-correlation. Cross-correlation is the process of matching two similar signals as a function of the time delay between them. A comprehensive introduction to cross-correlation is given by Beck & Plaskowski [68]. The principle involves calculating the sum of the differences between the two signals at every acquired point. This gives a measurement of the agreement between the two signals for a zero time shift. One signal is then shifted in time by a time τ. The summing process is then repeated to give a measurement of the agreement between the curves when the time lag is assumed to be τ. This process can be summarised by Equation 2-12.

$$R_{xy}(\tau) = \frac{1}{T}\int_0^T x(t)y(t+\tau)dt$$

Equation 2-12

In Equation 2-12 $R_{xy}(\tau)$ is defined as the cross-correlation function and the two sensors are referred to as x and y. T is the total time period for which data was acquired. In practice this function gives a measurement of the cross-correlation that is proportional to the magnitudes of the input signals. The cross-correlation is therefore usually normalised. This is done by incorporating the auto-correlation of each output signal, $R_{xx}(\tau)$ and $R_{yy}(\tau)$ and the mean values of each output signal. The autocorrelation is the correlation between each output signal and itself. The resulting normalised cross correlation is given by Equation 2-13.

$$R_{n,x,y}(\tau) = \frac{R_{xy}(\tau) - \left(\overline{x(t)}\right)\left(\overline{y(t)}\right)}{\sqrt{\left[R_{xx}(0) - \overline{x(t)}^2\right]\left[R_{yy}(0) - \overline{y(t)}^2\right]}}$$

Equation 2-13

This yields a value of 1 for a perfect correlation and a value of 0 for no correlation. Equation 2-12 and Equation 2-13 show the arithmetic theory of cross-correlation. In practice Fast Fourier Transforms (FFT) can also be used to carry out the process. This is detailed by Beck & Plaskowski [68]. Using the FFT method the cross correlation function is given by Equation 2-14.

$$R_{xy}(n) = \mathrm{IFFT}\left(X(k)Y^{*}(k)\right)$$

Equation 2-14

In Equation 2-14 X(k) is the FFT of the signal from the X sensor and $Y^{*}(k)$ is the complex conjugate of the FFT of the signal from sensor Y. The FFT method is often used in practice as it can be implemented efficiently using digital computers.

Cross correlation has been used by a wide variety of researchers in flow measurement. Reviews of applications using a variety of measurement principles are given by Beck & Plaskowski [68], Jones & Delhaye [30] and Rajan et al [69]. Cross-correlation of electrical conductivity measurements was used to measure global average velocities by Lucas & Albusaidi [70], Longoni et al [71], and Gu & Liu [72]. As discussed in Section 2.1.4.1 cross correlation was used with local penetration probes by Thang & Davis [46], Van der Welle [47], Revankar & Ishii [48], Serizawa et al [49], Castello-Branco & Schwerdtfeger [50], Gunn & Al-Doori [26], and Sun et al [51]. However in the field of local probe measurements in solids-liquid flows only one reference to the use of cross-correlation was found. This is the work of Asakura et al [54]. Therefore it was thought that the current investigation would be novel.

In cross-correlation flow measurement two linked design parameters of the device are critical. These are the axial separation of the two sensors, L, and the sample period τ. It should be noted that τ is equal to $\frac{1}{f}$ where f is the sampling frequency of the device. The accuracy of the estimate of the time delay, δ, between the output signals from the two sensors will only be equal to $\delta \pm \tau$, unless curve fitting techniques are used. At the same time δ will reduce as L reduces. In this way the accuracy of the cross-correlation velocity estimate is dependent on both L and τ. Equation 2-15 shows the relationship between the actual velocity, v_a, the estimated velocity, v_{est}, and the meter parameters as described above.

$$v_{est} = \frac{v_a}{1 \pm \left(\frac{\tau v_a}{L} \right)}$$

Equation 2-15

This relationship is discussed in detail by Beck & Plaskowski [68]. In the local conductivity devices reviewed in this chapter L varied between 2mm and 11mm. In most cases the sampling frequency was not given. Therefore the achievable accuracy of the devices could not be calculated. In the current investigation it was decided that this relationship, and the relative accuracy of the cross-correlation device, would be investigated fully.

2.4 Conductivity measurement devices.

Aside from the field of two phase flow measurement electrical conductivity measurement has been used in a variety of other fields. It was decided that research carried out in these other areas could be applicable to the present investigation. Additionally it was important to identify any other fields in which the current research could be applied. Therefore a review of conductivity measurement in other fields was carried out and is presented in this section.

2.4.1 Electrolyte conductivity measurement devices.

The area of application most closely related to two-phase flow measurement is the measurement of the conductivity of electrolytes and other liquids. This is purely a single phase application, but apart from that the instruments are identical. Volanschi et al [73] have reported the use of a two electrode instrument manufactured using a solid state device referred to as an ISFET. The ISFET is a device used for measuring pH. Therefore the instrument could be used for a dual purpose. Using this device Volanschi et al reported considerable electrochemical effects and drifting of the measurements. In a later paper Volanschi et al [74] investigated these effects and concluded that a four electrode measurement technique, where current was injected through two electrodes and potential was measured across two others, negated them. This four electrode technique has previously been introduced in Section 2.1.4.2 where it was applied by Nasr-El-Din et al [52] and MacTaggart et al [53] for the same reasons.

Ncube et al [75] reported the use of a two electrode probe with one electrode having an area $0.001mm^2$ and the other having an area $500mm^2$. They claimed that this caused the measurement to be localised at the small electrode. However they reported substantial drift

over time using this system. A calibration procedure was presented. However Nasr-El-Din et al [52] and Volanschi et al [74] suggested that this behaviour is caused by electrochemical effects and could be negated using a four electrode system.

In a closely related field Holtzknecht et al [76] reported the use of a four electrode probe where each electrode was a spring mounted pin. This device was used to measure the conductivity of solid electrodes. It was optimised for measuring extremely high conductivities. This involved some differences in the electronic design of the instrument.

2.4.2 Geophysical devices.

Electrical conductivity measurement is widely used in geophysics. It is used within a number of areas to fulfil different requirements. In its simplest form electrical conductivity measurements are used to give the resistivity of soils or ocean sediments locally around a probe. Hulbert et al [17] reported a probe consisting of four spike electrodes. The electrode array was driven into the sea bed and therefore the conductivity of the sediment was measured. In order to calibrate this simple device it was used in a laboratory environment with sediments of known conductivity.

Lauer-Leredde et al [18] presented a more complicated instrument to carry out this measurement. Their device consisted of a ring of small circular electrodes around a cylindrical probe. Current was injected through these and sunk through a ground electrode a relatively large distance away. In this way the resistivity of the material at a number of points around the probe was measured. In use the device was slowly driven into the sea bed and therefore the measurements gave a map of the sediment conductivity around the probe at different depths. Lauer-Leredde et al [18] also reported finite element modelling carried out on this device to optimise the penetration of the measurement away from the probe body. A similar device was also reported by Daily & Ramirez [77]. They used a similar mapping tool to measure the electrical conductivity of rock around the wall of a bore-hole. This data was used to identify the porosity of the rock, i.e. the air volume fraction of a solids-gas mixture. This instrument was used to determine the geological suitability of sites for the storage of nuclear waste.

Ridd [19] presented another device for use in ocean sediments. The 1m long cylindrical probe had ring electrodes formed around it at equal separations along its length. It was driven into

the sea bed. Selection of different sets of four electrodes allowed the density of the sediment at different depths to be measured. Additionally the sudden conductivity change as the electrodes were exposed to the water above the sediment layer allowed the sediment deposition rate to be determined. In addition Ridd [78] presented theoretical modelling work designed to increase understanding of the behaviour of a ring electrode. Won [79] also presented modelling work of this type.

The other major use of electrical conductivity measurement within Geophysics is geophysical prospecting. A detailed introduction to geophysical prospecting is given by Griffiths & King [20]. In geophysical prospecting a variety of different electrode arrays can be used to measure the conductivity of rock formations at some depth from the device. The closest of these to two phase flow measurement devices are the Wenner array and the Schlumberger array. Both devices use a four electrode measurement technique to inject current through the rock, and to measure the resulting potential difference. The difference between the arrays is the relative separation of the electrodes. The principle of geophysical prospecting involves adjusting the overall separation of the electrodes. This adjusts the depth of penetration of the measurement. By carrying out this procedure at different points over a landscape, and utilising reconstruction algorithms, like those presented by Griffiths & King [20] and Lagace et al [21], a map of the conductivity of the rock formations below the landscape can be reconstructed.

Much experimental work appears to have been carried out to optimise the depth of penetration of the arrays and to decide which offers the best performance. Some of this can be applicable to the current investigation although the results are for a greatly different scale of measurement as the electrode separations used in geophysics can be hundreds of meters. This large scale has led to another large area of research in the field. As the electrodes are separated over such great distances very long cabling is needed. Because of this, noise and coupling between wires can be a problem. Much modelling and experimental work, for example by Ma & Dawalibi [80] and Gasulla-Forner et al [81], has been carried out in this area which could also be useful in the present investigation.

This technology has been used in wide variety of areas as well as pure geophysical mapping. Jordana et al [23] used Wenner and Schlumberger arrays to detect leaks from pipes. The conductivity of the soil changes dramatically if large amounts of water are present in it. By prospecting along the path of an underground pipe the position of any leaks were pinpointed.

In a similar area, but using a different array, Binley et al [22] positioned a large number of voltage measurement electrodes around the perimeter of a sealed waste storage pond. Current was injected at a point a relatively large distance away. By measuring the soil conductivity around the pool the position of any leaks was pinpointed.

In conclusion conductivity measurements have been used in a wide variety of fields apart from two phase pipe flow measurement. It is possible that the instrument developed and research carried out in this investigation could be useful in another field. Similarly it is possible that research already carried out in another field could be useful in the present investigation. Because of this it was decided that it was important to follow developments in a wide range of research fields.

3. Design and finite element modelling of the probe.

3.1 Design of the probe.

3.1.1 Fundamental measurement method.

As discussed in Chapter 2, conductivity measurements have been used successfully in a wide variety of multiphase flow metering applications. Measurement of the properties of multiphase flow by electrical conductivity methods relies on the fact that the electrical conductivity of a multiphase mixture depends on the conductivity and the relative volume fractions of each of the phases.

In order to measure $\alpha_{s,i}$ by measuring $\sigma_{m,i}$ the relationship between the two variables must be accurately known. Many expressions have been developed for this relationship and these have been discussed and compared in detail in Section 2.2. For this investigation Maxwell's [65] relationship was selected. Maxwell's relationship and how it can be applied to a suspension of non-conducting solids in a conducting liquid is explained in Section 2.2.

In order to measure $u_{s,i}$ the fluctuations in electrical conductivity caused by particles passing two axially separated conductivity sensors are recorded. These signals are then cross-correlated. Cross-correlation applied to flow measurement is described in Section 2.3.

3.1.2 Probe shape.

Intrusive probes have been found to affect the flow in their vicinity. This can lead to inaccuracies in measurements. Published work showing this has been reviewed in Sections 2.1.1.3 and 2.1.4. In the case of a solids-liquid flow this results in the particles being deflected away from the probe before they can be sensed. This can lead to an artificially low measurement of $\alpha_{s,i}$. In order to minimise the flow disturbance the probes must have a small diameter compared to that of the pipe. This ratio of probe diameter to pipe diameter is referred to as the relative probe diameter. A survey of previous work was carried out to see if there was agreement on the relative diameter of probe that should be used. This review showed that there appeared to be a wide range of different opinions as to the effect of probe size. At one extreme Revankar & Ishii [48] claimed accurate results using a relative probe diameter of 0.14. Since the pipe diameter in the current investigation is 80mm this would allow the use of

a probe 11mm in diameter in the current work. At the other extreme Coulson and Richardson [82] state that in the context of a pitot tube, "for the flow not to be appreciably disturbed, the diameter of the instrument must not be more than 2% of the diameter of the pipe". In the present investigation this would mean using a probe no larger than 1.6mm in diameter. In the light of this lack of agreement it was simply decided that the final probes should be made as small as possible using the available manufacturing facilities.

3.1.3 Electrode shape and configuration.

3.1.3.1 The combined excitation and measurement method.

The simplest arrangement for a local probe is to have two electrodes in each sensor. This arrangement is shown in Figure 3-1.

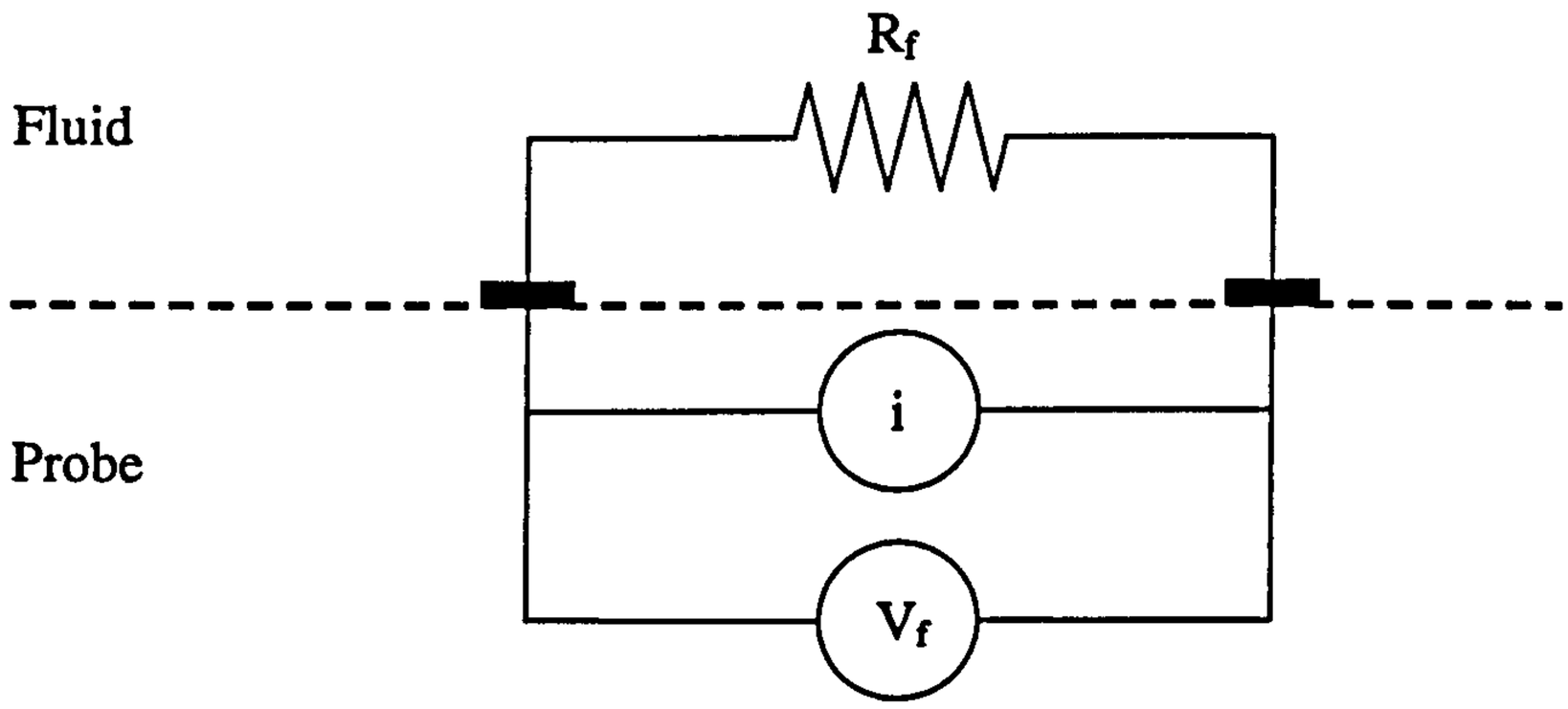

Figure 3-1. Schematic representation of a two electrode conductivity measurement.

Current is injected across the electrodes. If the resulting voltage drop, V_f, and the applied current, i, are measured then the mixture resistance, R_f, can be calculated according to Ohm's law. This relationship is shown in Equation 3-1.

$$R_f = \frac{V_f}{i}$$

Equation 3-1

R_f can now be related to the solids volume fraction using relationships such as Maxwell's [65], as discussed in Section 2.2. However there are significant disadvantages to this system.

Most of these disadvantages arise as a result of the contact impedance, Z, at the interface between the fluid and the electrodes. The contact impedance can be explained by looking at an equivalent electrical circuit for the system. The equivalent circuit shown in Figure 3-2 is

based on circuits given by Trethewey & Chamberlain [83], and Volanschi et al [74]. Tretheway & Chamberlain state that this model was originally proposed by Randles.

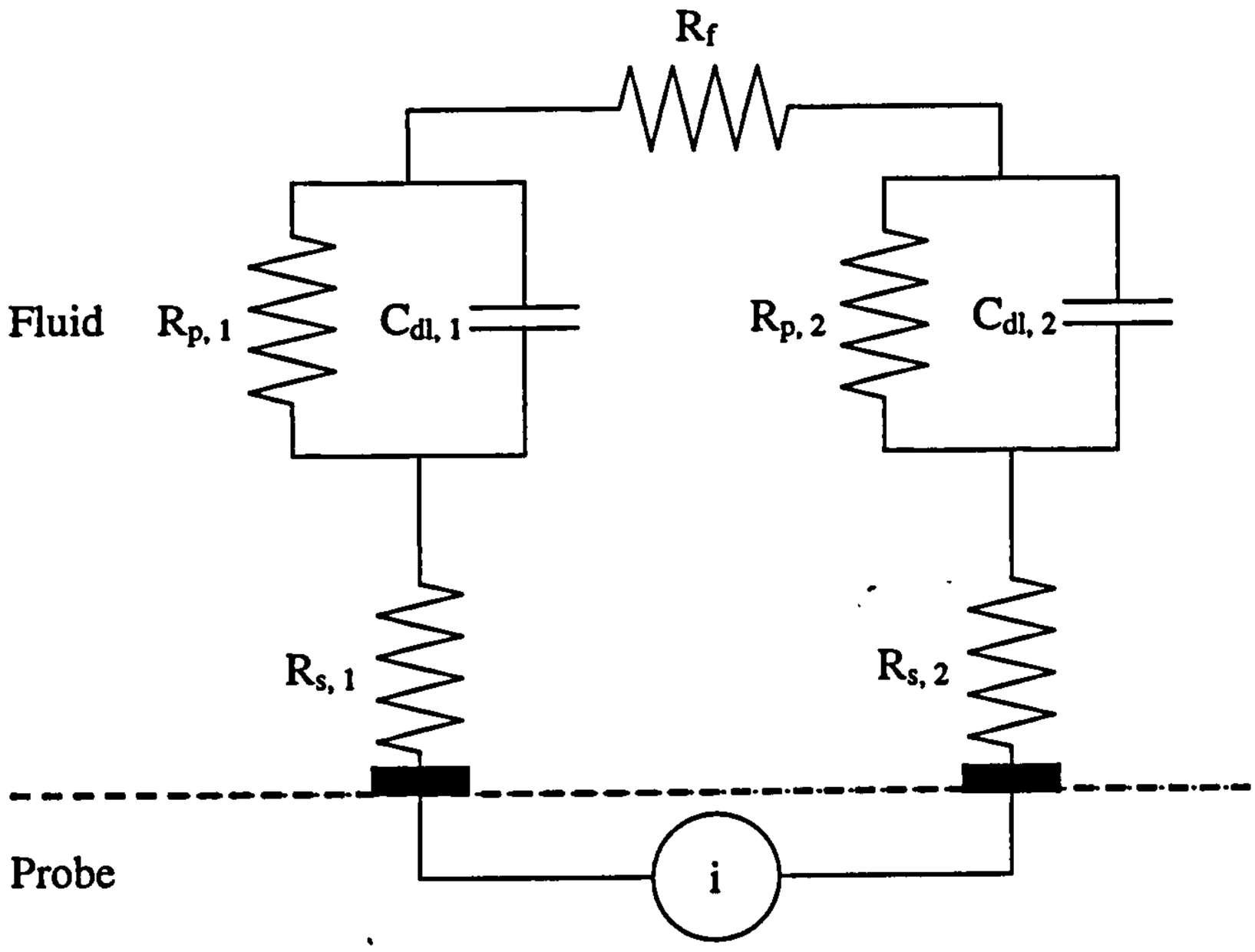

Figure 3-2. Equivalent electrical circuit for current passing through a fluid between two electrodes.

In Figure 3-2 an AC current is passed between two electrodes, 1 and 2, across a fluid with resistance R_f. The contact impedance for each electrode is represented by R_p, C_{dl}, and R_s. These are each explained below.

R_s, the surface film resistance is the resistance to current flow caused by any build-up of deposits on the surface of the electrodes. Even if no electrical current flows the surface of the electrode will become fouled as a result of impurities and biological growths in the water. However if an electrical current is flowing additional deposits will form on the electrodes due to electrolysis.

If a DC current is applied across the electrodes one will be the negative electrode and one will be the positive electrode. In a battery the positive terminal is referred to as the anode and the negative terminal is referred to as the cathode. In an aqueous corrosion cell this nomenclature is reversed, i.e. the negative terminal is referred to as the anode, and the positive terminal is referred to as the cathode. In this analysis the standard nomenclature for an aqueous corrosion cell has been adopted. Negatively charged electrons flow through the wiring of the circuit from the cathode (+) to the anode (-). Therefore the anode (-) corrodes by loss of electrodes

with the result that solid corrosion products form on its surface. These corrosion products have a very high resistance. Simultaneously the cathode (+) consumes these electrodes. This will usually not damage the electrode. The overall result of the corrosion is that R_s will significantly increase on the anode (-). If an AC current is applied the electrodes alternately act as anode and cathode as their polarity changes. This has the effect of causing each electrode to be alternately corroded. Although this is preferable to the consequences of DC excitation both electrodes will still suffer corrosion damage.

R_p, the polarisation resistance or charge transfer resistance, and C_{dl}, the double layer capacitance arise due to the passage of electrical current across the phase interface between the electrode and the fluid. When electrical current passes through an infinite medium charge is distributed homogeneously within the medium. However this is not the case when current passes across a solid-liquid interface. In the electrode charge is carried by electrons. However in the liquid the charge is carried by positive and negative ions. At the electrode-liquid interface the charge is transferred from electrons to ions. This causes a charge distribution referred to as a double layer. This distribution is shown schematically in Figure 3-3.

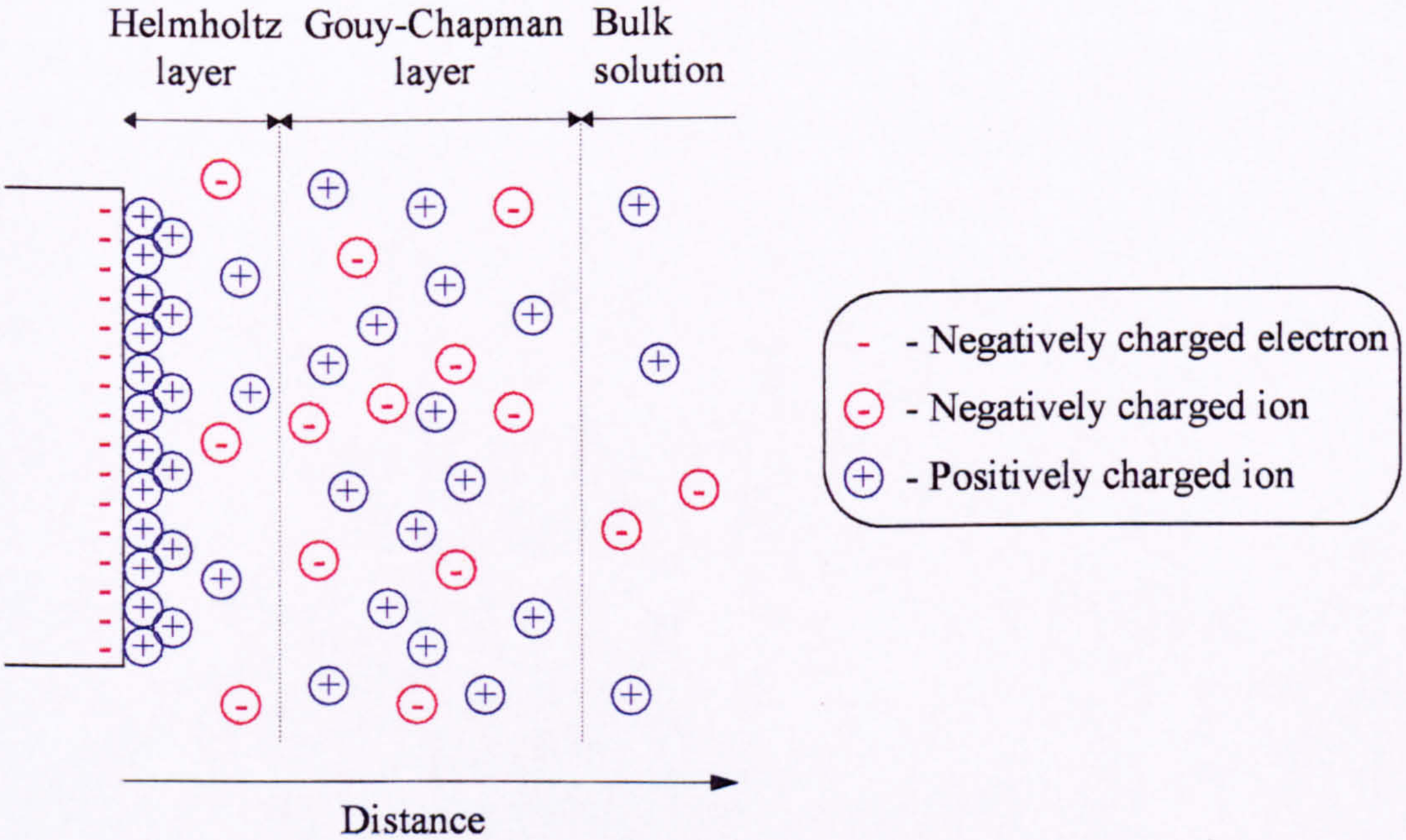

Figure 3-3. Schematic representation of the double layer distribution at a solids-liquid interface.

The Helmholtz layer, or compact layer, occurs closest to the electrode surface. In this region the distribution of charge changes linearly with distance from the electrode surface. The Gouy-Chapman layer, or diffuse layer, occurs further from the electrode surface. In this layer

the distribution of charge changes exponentially with distance from the electrode. Finally in the bulk solution the charge is distributed homogeneously. Because of this arrangement there is a separation of charge which results in an effective resistance and capacitance across the double layer. These are the polarisation resistance, R_p, and the double layer capacitance, C_{dl}.

If these impedances are too large they can become a significant fraction of the total impedance measurement. Volanschi et al [74] showed that they can be reduced by increasing the electrode surface area. This would require a two electrode sensor to have relatively large electrodes which would make the conductivity measurement less local. The size of the double layer capacitance can also be reduced by using a DC excitation. However this would result in an imbalanced electrolytic effect across the electrodes. This effect has been discussed in more detail on the previous page. The double layer capacitance, C_{dl}, can also be short-circuited by using a very high frequency excitation. If this capacitance is short-circuited then no current will flow through the polarisation resistance, R_p. Therefore both impedances are negated. However the frequency required is of the order of hundred's of kilohertz which complicates the measurement system.

In addition to these disadvantages Lee et al [84] reported that curves of solids volume fraction plotted against mixture resistance acquired with a two electrode measurement system were velocity dependent although no reasons were given. Nasr-El-Din et al [52] claimed that this is because the polarisation resistance, R_p, is velocity dependent although they offered no proof for this.

3.1.3.2 The separated excitation and measurement method.

As a result of their findings Nasr-El-Din et al [52] and Volanschi et al [74] used a configuration of electrodes that separated the excitation from the measurement. The electrodes in their research are arranged to form an array using a Separated Excitation and Measurement Method (SEMM). In an SEMM array electrical current is applied across two "field" electrodes. This creates an electric field around the electrode array. The potential difference between a separate pair of "sense" electrodes within the field is then measured using a high input impedance circuit. This arrangement is shown schematically in Figure 3-4.

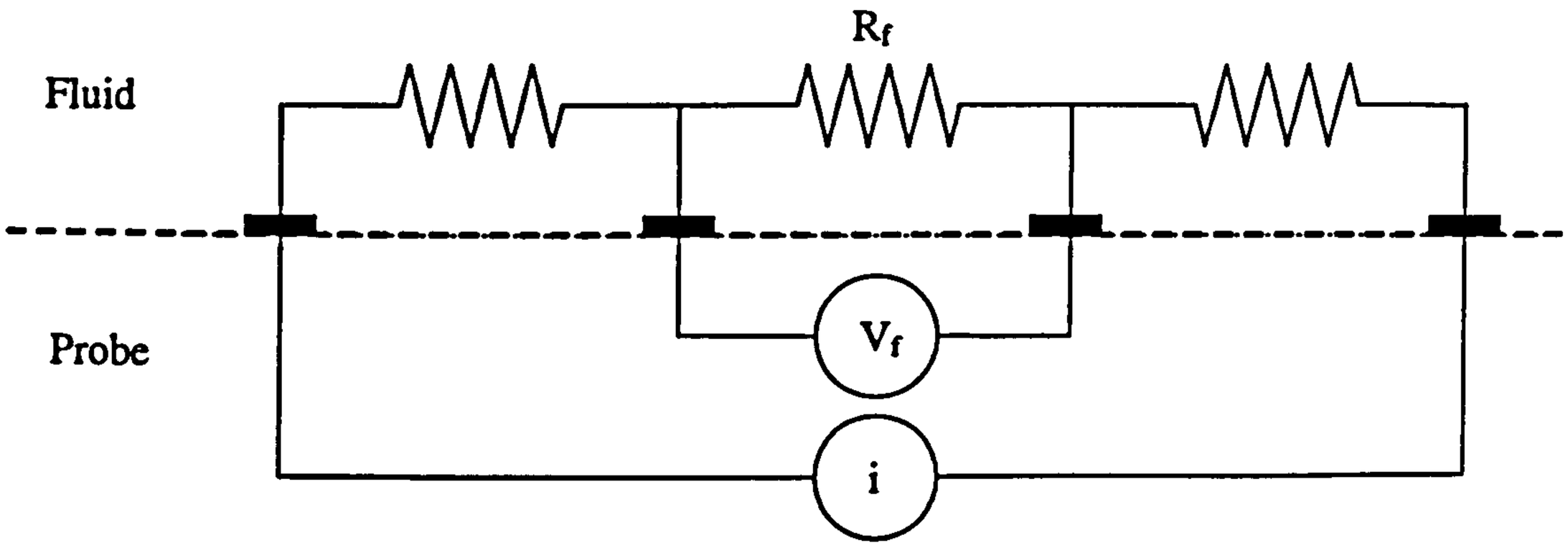

Figure 3-4. Schematic representation of a four electrode conductivity measurement.

If the applied current, i, and the potential difference, V_f, are measured then the mixture resistance at the sense electrodes, R_f, can be calculated using Ohm's law (Equation 3-1) in the same way as with the two electrode measurement. Because the impedance of the voltage measurement circuit is very high the current flow through the sense electrodes is very small. This means that there is negligible charge transfer at the sense electrodes. Therefore the contact impedance, Z, is minimised. Additionally any electrolytic effects on the sense electrodes are minimised also. To minimise electrolytic effects on the field electrodes, which could accelerate their corrosion, an alternating current is used for the excitation. This results in an alternating potential difference being measured at the sense electrodes. In this case it is necessary to measure the amplitude of this potential difference in order to calculate the mixture resistance, R_f. Sensors using SEMM arrays have also been used in oceanographic research by Ridd [19] and they are extensively used in geophysical surveying as described by Griffiths & King [20]. Because of the advantages of this configuration it was chosen for the probe design in the present study.

The electrode arrays constructed by Nasr-El-Din et al [52], MacTaggart et al [53] and Volanschi et al [74] used the simplest possible SEMM array. This consists of two field electrodes with two separate sense electrodes positioned between them. The probes built by Nasr-El-Din et al [52] used field electrodes on opposite sides of the probe and circular sense electrodes approximately 0.5mm in diameter mounted on one side of the probe as shown in Figure 2-3. The probes developed by MacTaggart et al [53] used the same arrangement of field electrodes but with the two sense electrodes in the end of the steel tube probe as shown in Figure 2-4. The configurations used by Nasr-El-Din et al and MacTaggart et al resulted in probes that were asymmetrical. Consequently they behaved differently depending on their orientation in the pipe. This was particularly noticeable when coupled with the effects of

approaching a boundary, such as the pipe wall. To avoid this problem in the current investigation ring electrodes were used to give a symmetrical design. Ring electrodes configured as an SEMM array have previously been used by Ridd [19]. A four electrode array with ring electrodes is shown in Figure 3-5. By using this electrode shape the probe should be able to approach the pipe wall from any direction and have the same response.

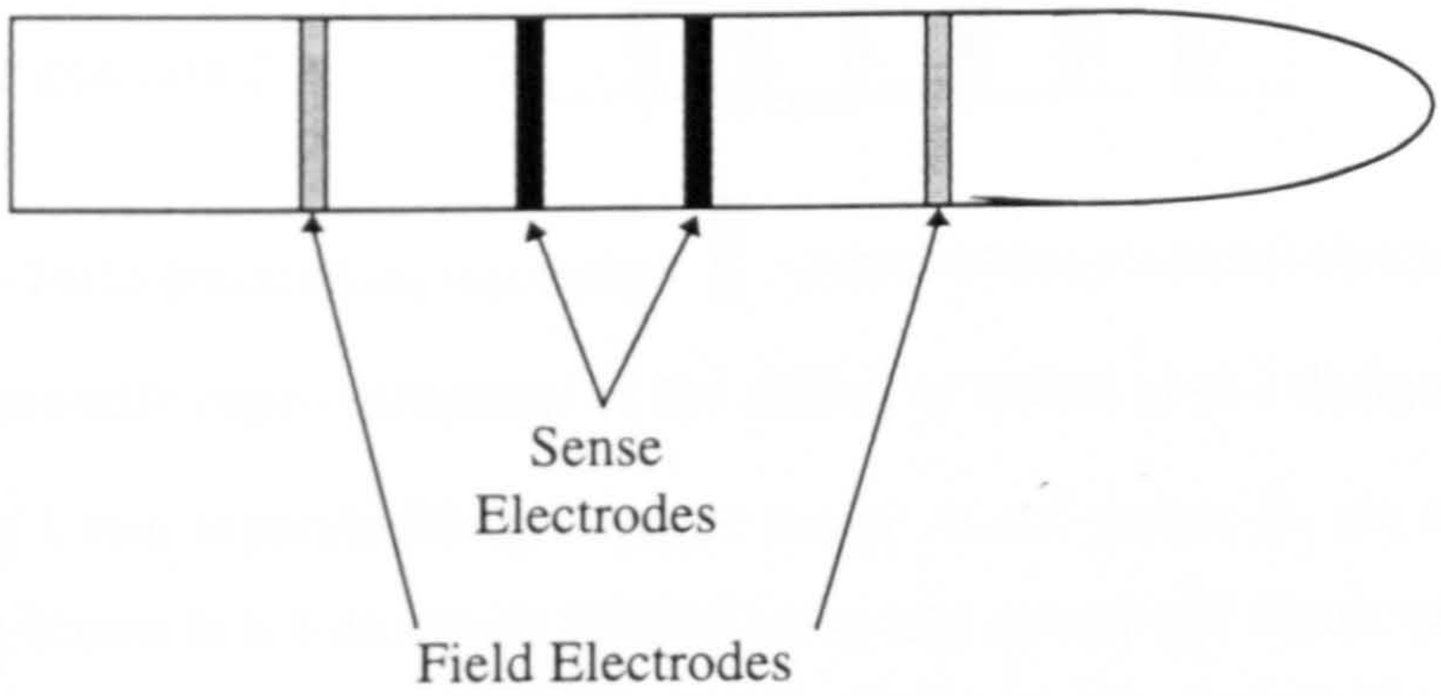

Figure 3-5. A symmetric probe design using an SEMM array.

3.1.3.3 Applying the SEMM to combined solids volume fraction and solids velocity measurement.

A common factor in the previous work is that it generally only deals with volume fraction measurements. To measure velocity, signals from two axially separated sensors must be cross-correlated. Therefore the probes designed for the current investigation must contain two axially displaced sensors.

The major design criteria for the probe can now be summarised. The probes must have ring electrodes arranged to form two axially displaced sensors using the SEMM principle. Two basic designs were developed from this specification. They are shown schematically in Figure 3-6.

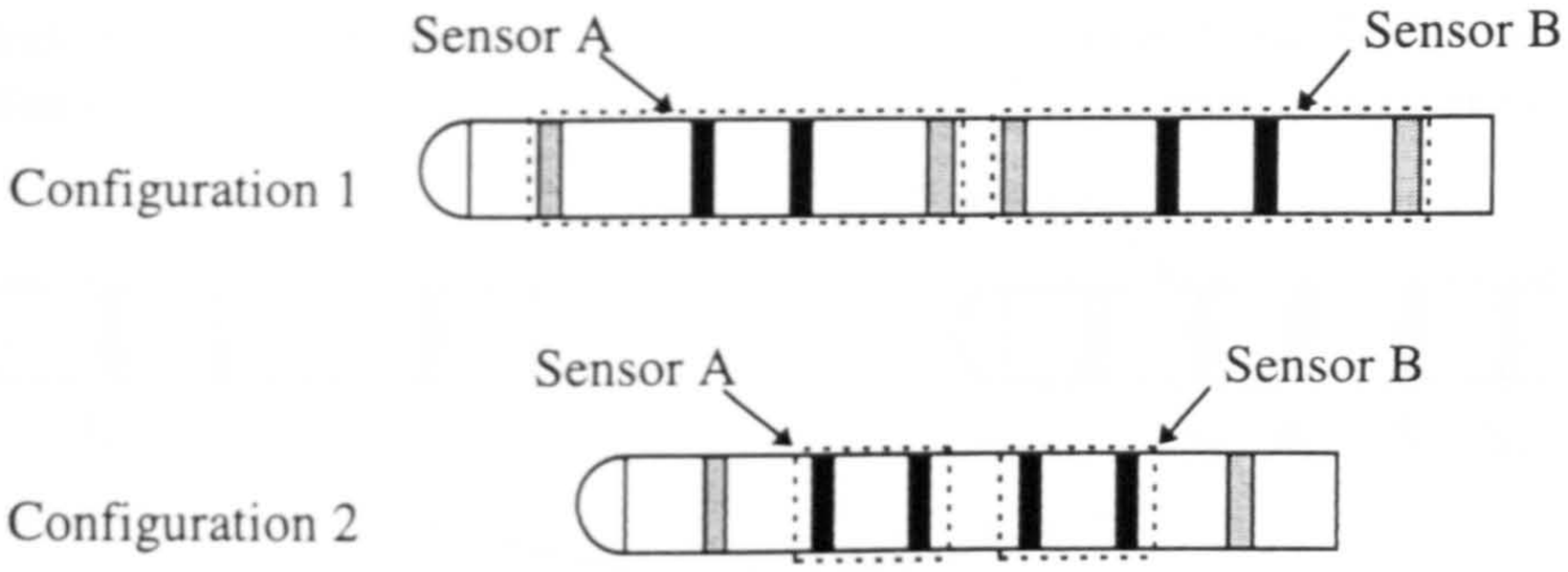

Figure 3-6. Schematic representations of the different initial probe designs.

In configuration 1 two separate SEMM arrays, sensor A and sensor B, are incorporated into the probe. Each sensor is a 4-electrode SEMM array and consists of a pair of field electrodes and a pair of sense electrodes. The signal from either sensor could be used to give a measurement of $\alpha_{s,i}$. The combined signals from sensor A and sensor B would be cross-correlated to give a measurement of $u_{s,i}$. It was unclear how a probe of this design would behave. If the sensors were operated simultaneously interference between them is possible. Because the sensors are separate this could possibly be reduced by some sort of shielding. However this shielding effect could not be simply quantified.

In configuration 2 a single 6-electrode SEMM array is used. There is one pair of field electrodes. In order to create two axially displaced sensors the array contains two pairs of sense electrodes which are configured as sensor A and sensor B as shown in Figure 3-7. The potential difference across any pair of the sense electrodes is measured to give a measurement of $\alpha_{s,i}$. Potential difference measurements from sensor A and sensor B are cross-correlated to give a measurement of $u_{s,i}$. Figure 3-7 shows how the different measurements can be acquired from the electrodes.

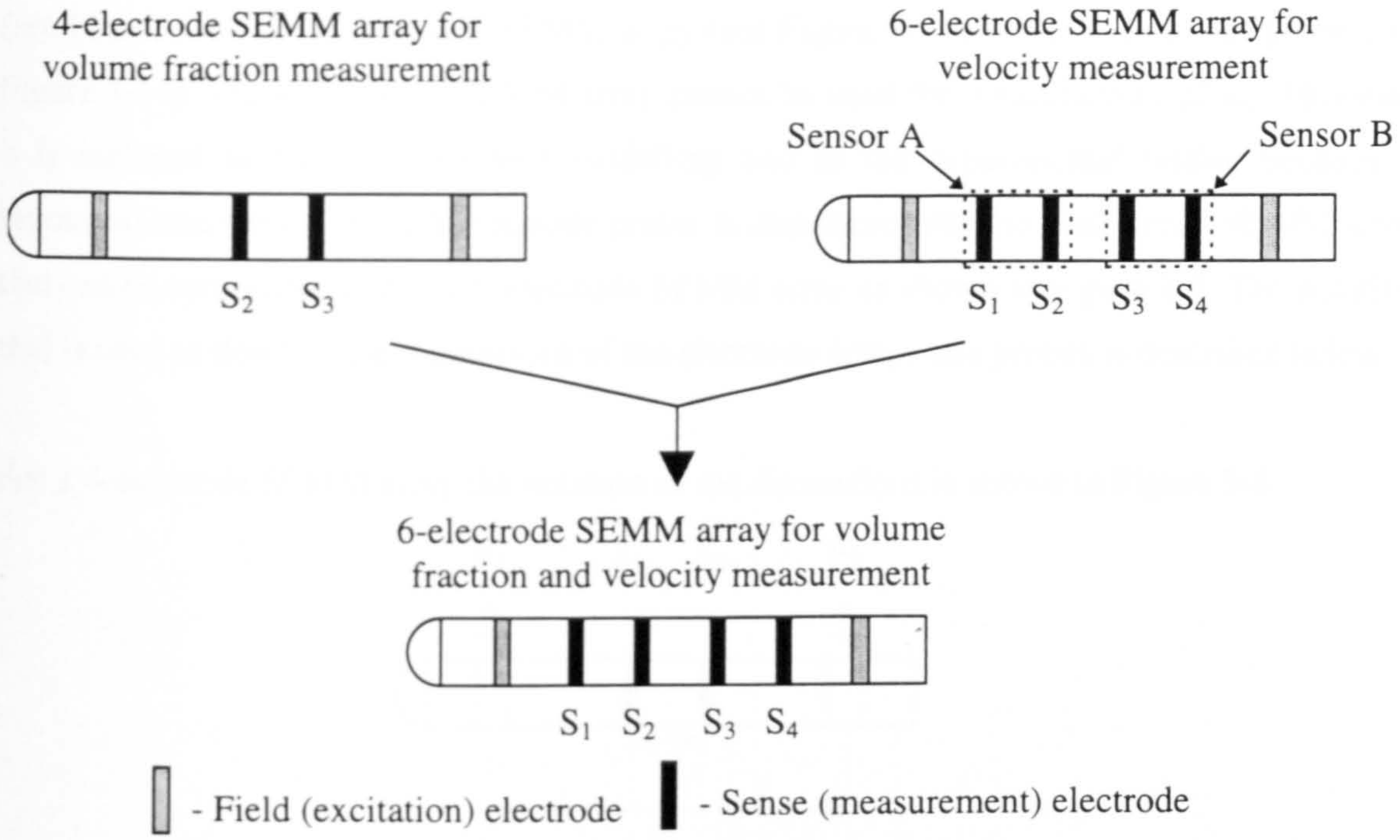

Figure 3-7. Schematic representations of how multiple measurements can be acquired from one six electrode probe.

The use of only two field electrodes means that only one excitation current is needed. This cuts down on the electrical complexity of the probe and also reduces its size. It should also be noted that the presence of sense electrodes S_1 and S_4 will not affect the potential difference measured between sense electrodes S_2 and S_3. This is because the sense electrodes draw negligible current. Therefore they are electrically invisible to each other.

3.2 Finite element modelling of the probe.

3.2.1 Probe geometry and configuration notation.

Within the following sections, which describe finite element modelling of the probe, and in later sections of this thesis, a wide variety of probe geometries and configurations will be referenced. In order to make these variations easier to understand it is useful to define a common notation.

In Section 3.1.3.2 and Section 3.1.3.3 two types of SEMM array were described. These are the 4-electrode SEMM array (see Figure 3-8) and the 6-electrode SEMM array (see Figure 3-9). Using these SEMM arrays three configurations of array have been simulated using finite element analysis and built for experimental testing. These are the 4-electrode SEMM array

(see Figure 3-8), the 6-electrode SEMM array (see Figure 3-9) and the 8-electrode probe (see Figure 3-10). The 4-electrode SEMM array cannot be used for measurement of $u_{s,i}$. However it is included in the finite element modelling and in the experimental testing because it represents one sensor of the 8-electrode probe. It also represents the 4-electrode SEMM array that can be configured within a 6-electrode SEMM array as shown in Figure 3-7. The notation that is used to describe the dimensions of the electrode arrays and probes is described below.

For a 4-electrode SEMM array the notation of the dimensions is shown in Figure 3-8.

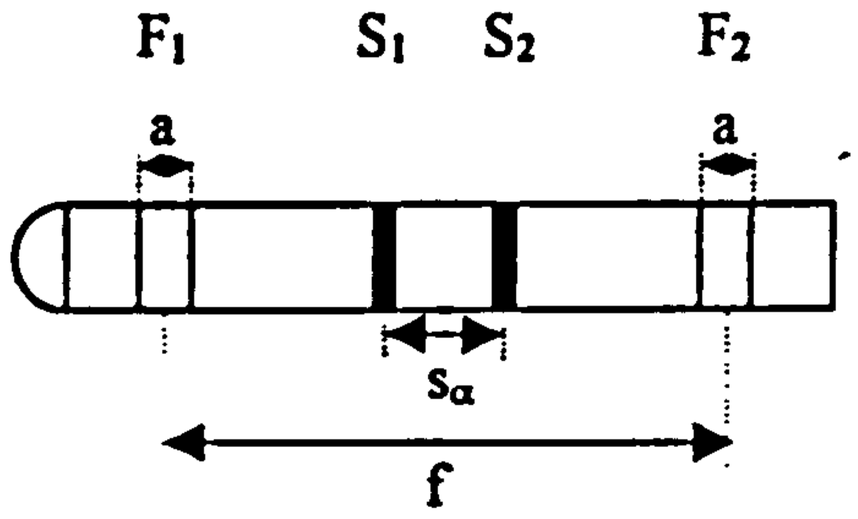

Figure 3-8. Notation used for a 4-electrode SEMM array.

s_α - This the sense electrode separation. It is the separation, centre to centre, between the sense electrodes. These are S_1 and S_2.

f - This is the field electrode separation. It is the separation, centre to centre, between the field electrodes. These are F_1 and F_2.

a - This is the axial length of the field electrodes.

For a 6-electrode SEMM array the notation of the dimensions is shown in Figure 3-9.

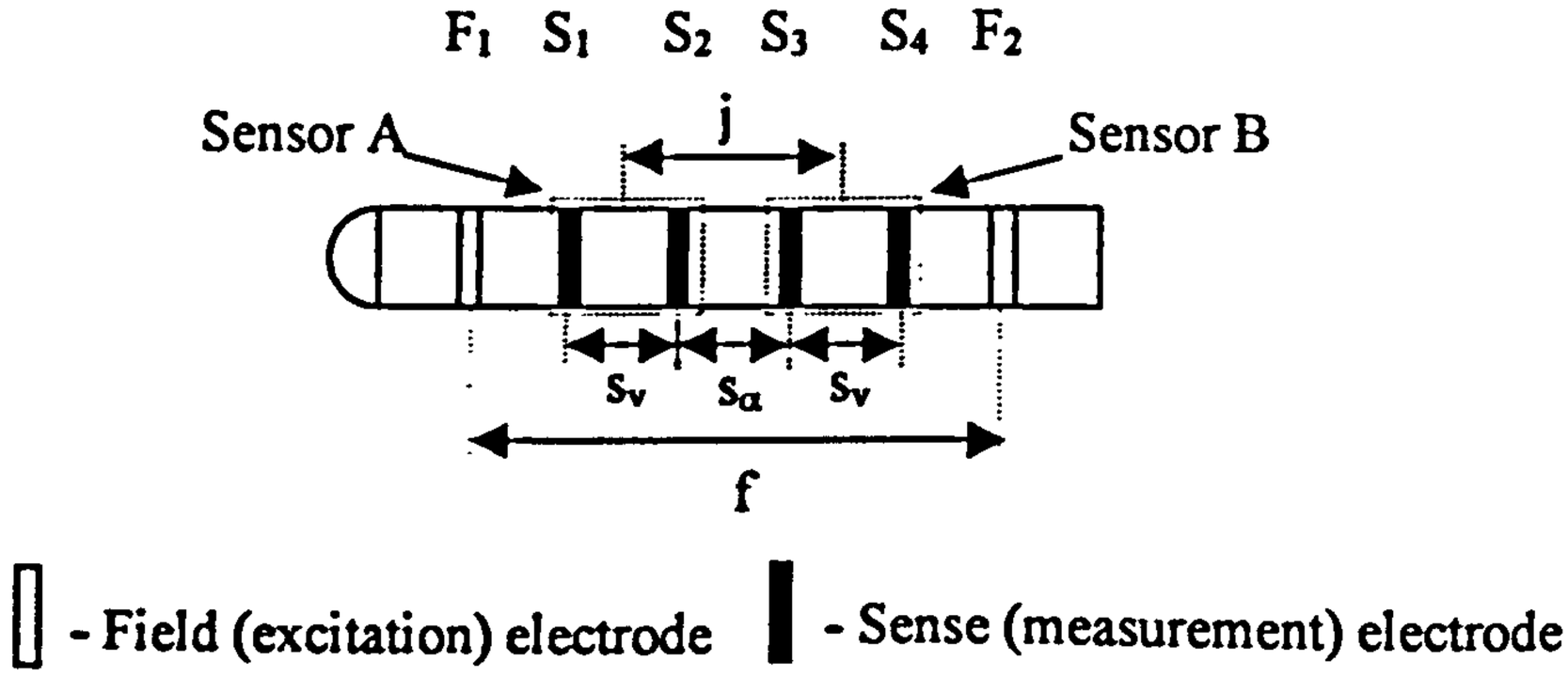

Figure 3-9. Notation used for a 6-electrode SEMM array.

s_v - This the sense electrode separation for the two sensors, A and B, used to acquire

the measurement of $u_{s,j}$. It is the separation, centre to centre, between the sense electrodes in each sensor. These are S_1 and S_2 for sensor A, and S_3 and S_4 for sensor B.

s_α - This the sense electrode separation for sensor C which can be used to acquire a measurement of $\alpha_{s,j}$ (see Figure 3-7). It is the separation, centre to centre, between the sense electrodes S_2 and S_3.

f - This is the field electrode separation. It is the separation, centre to centre, between the field electrodes F_1 and F_2.

j - This is the sensor separation. It is the separation, centre to centre, between the two sensors A and B.

For an 8-electrode probe the notation is shown in Figure 3-10.

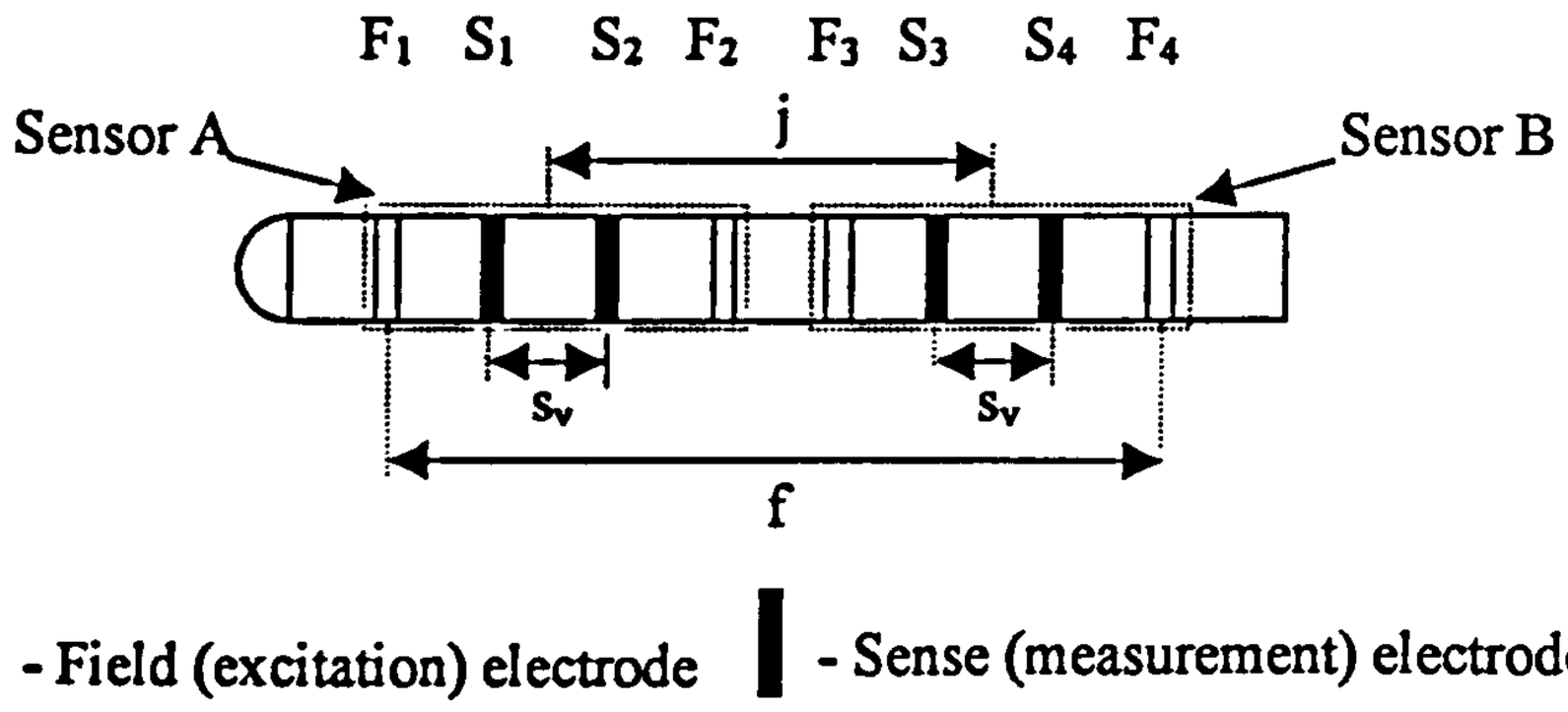

Figure 3-10. Notation used for an 8-electrode probe.

s_v - This the sense electrode separation for the two sensors, A and B. It is the separation, centre to centre, between the sense electrodes in each sensor. These are S_1 and S_1 for sensor A, and S_3 and S_4 for sensor B.

f - This is the field electrode separation. It is the separation, centre to centre, between the field electrodes. These are F_1 and F_2.

j - This is the sensor separation. It is the separation, centre to centre, between the two sensors A and B.

This common notation will be used wherever possible throughout this thesis in order to aid understanding of the probe, and to make comparing the finite element modelling and experimental testing simpler.

3.2.2 The reasons for finite element modelling of the probe.

In order to understand the responses of the chosen electrode array configurations they were modelled using a finite element solver. The aim of the modelling was to define the electric field around the probe when using different configurations and separations of the electrodes. The finite element solver used was PAFEC, which is a structural and thermal finite element solver. PAFEC was not ideal for the task as it does not directly allow modelling of electrical fields. However the equations that govern thermal problems can also be applied to electrical problems. In this case voltage is analogous to temperature and electrical current is analogous to heat flux. The potential distribution within the model is solved using the Laplace equation, as given in Rao [85] and shown in Equation 3-2.

$$\nabla^2\phi = 0$$

Equation 3-2

In Equation 3-2 ϕ is the field variable that is being solved for. In the current investigation this is the electrical potential. In order to solve the Laplace equation certain conditions must be adhered to at the boundary of the system. In this case a mixture of boundary conditions is used. These are explained below.

Over part of the boundary the Dirichlet condition is applied. Rao [85] states that the Dirichlet condition requires that the potential is proscribed at the boundary. As previously mentioned, in an SEMM array current is passed between two field electrodes. In this investigation this is accomplished by applying a current to one field electrode and setting the potential to zero volts at the other. This is the case in the finite element models and in the experimental probe. Therefore the Dirichlet condition is met at the grounded field electrode. Additionally, the outside wall of the pipe itself is assumed to be grounded. Therefore the Dirichlet condition is met at this boundary also.

Over the remainder of the boundary the Cauchy condition is applied. Rao [85] states that the Cauchy condition requires that the electrical current is known at the boundary. If the electrical current is zero then the Cauchy boundary condition can be called the Neumann condition. As mentioned in the paragraph above electrical current is applied to one of the field electrodes in an SEMM array. Therefore at this field electrode the Cauchy condition is met. The remainder of the boundary consists of the probe wall, constructed of Nylon, and the axial limits of the

modelled pipe section. At these boundaries it is assumed that no current flows. Therefore the Neumann condition is met at these points.

Initially the probe response predicted by the finite element model was compared with the probe response predicted by published mathematical models for a ring electrode. This allowed the finite element model to be validated. Following this, finite element modelling was carried out to investigate the following situations.

- **Wall Effects.** The response of probes configured with a single 4-electrode SEMM array (see Figure 3-8) to the proximity of both steel and plastic pipe walls was investigated.
- **Single Sensors.** The response of probes configured with a single 4-electrode SEMM array (see Figure 3-8) to a moving particle was investigated. This is analogous to a probe which could be used to measure $\alpha_{s,i}$. It should be noted that the response of an individual 4-electrode SEMM array can be considered to be the same as that of the 4-electrode SEMM array that is assumed to be contained within 6-electrode SEMM array (see Figure 3-7).
- **Dual Sensors.** The response of probes configured with two 4-electrode SEMM arrays (see Figure 3-10) and configured with a single 6-electrode SEMM array (see Figure 3-9) to a moving particle was investigated. These are analogous to probes that could be used to measure $u_{s,i}$.

3.2.3 Finite element model design.

Finite element modelling is a powerful analytical tool. However it can be extremely computationally time consuming. To simplify the model, and minimise the time consumption, it was based around a 2D axisymmetric model of a pipe. The way in which the axisymmetric model is rotated, by the finite element solver, to represent the complete pipe section is shown in Figure 3-11. For symmetric cases, such as those used for comparisons with mathematical models, this model is accurate. However in asymmetric cases, such as models involving simulated particles, or probes positioned away from the centre of the pipe, it is not a true representation of the geometry. For example a solid particle, modelled in the axisymmetric model, actually represents a ring of solid material. This is shown in Figure 3-11. Similarly modelling the probe closer to the pipe wall in an axisymmetric model actually represents a probe in a smaller diameter pipe. However simplifying the model from 3D to 2D reduced the number of elements from ≈50000 to ≈1500. This obviously reduced the computation time

significantly. In order to verify the accuracy of the simplified models interesting results were all verified experimentally (see Chapter 5).

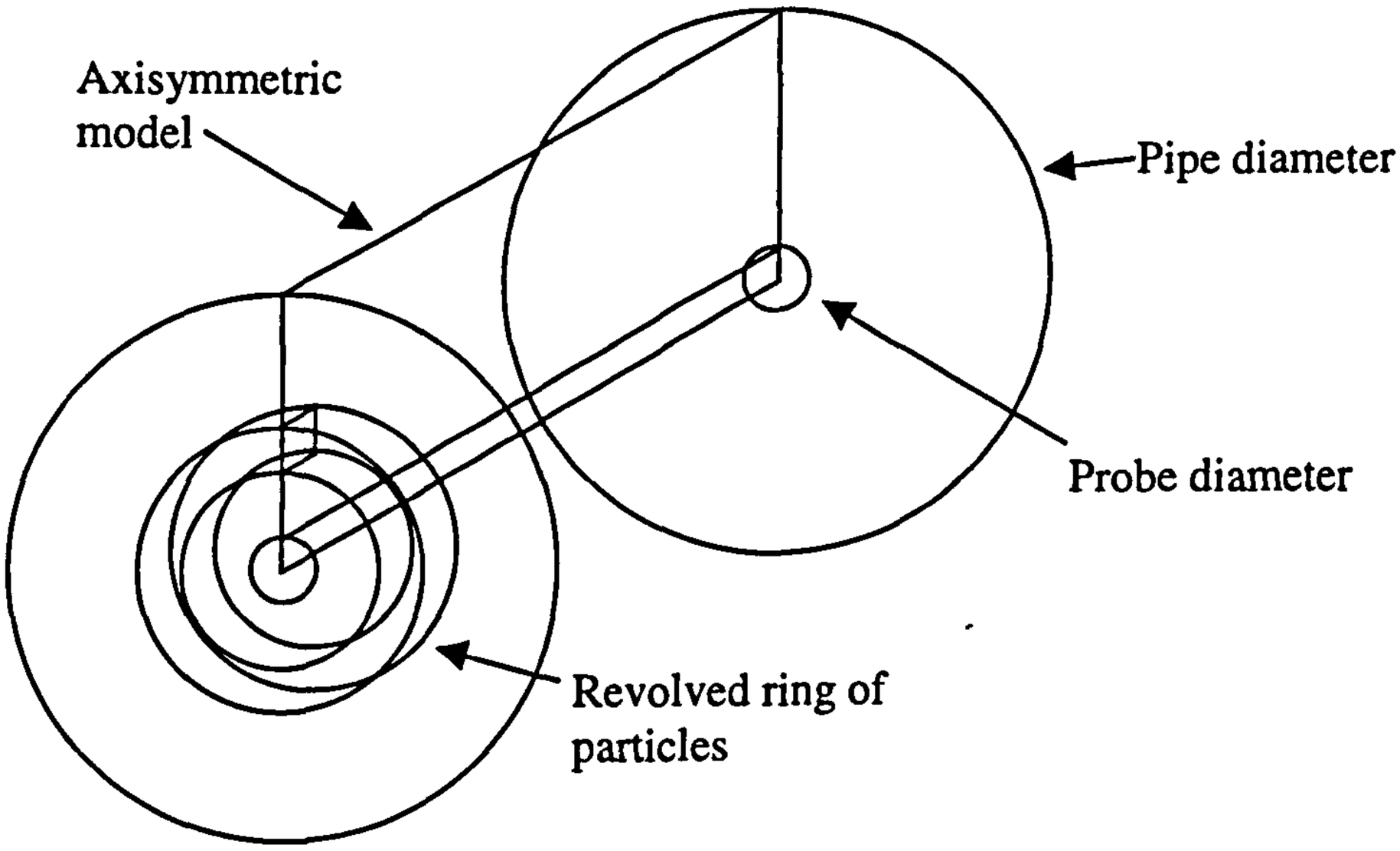

Figure 3-11. Revolution of the axisymmetric PAFEC model to give the actual modelled shape.

3.2.3.1 Convergence testing.

In order to determine the optimum element sizes for the F.E. models convergence tests were carried out. Some FEA software carries out these tests automatically. In order to recreate them in PAFEC axisymmetric models were created of a probe with two electrodes separated by 13mm in a 50mm radius vessel. The axial size of the elements was fixed at 1mm. The radial size, λ, of the elements was then incrementally reduced whilst a current was established between the electrodes and the resulting potential difference, V_{conv}, was measured. As λ reduced, and the model became more accurate, the measured response of the probe converged upon the exact value. Initially λ was set to 10mm over the entire vessel. λ was then reduced to 1mm between 0mm and 10mm radial distance from the probe resulting in a substantial change in V_{conv}. λ was then reduced to 1mm between 10mm and 20mm radial distance from the probe. This resulted in a negligible change in V_{conv}. This suggested that the radial element size at a radial distance greater than 10mm from the electrodes was not critical.

The bulk of the convergence therefore concentrated on the element sizes between 0mm and 10mm radial distance from the probe. Figure 3-12 shows the results of this testing. A key to the element size configurations is given in Table 3-1.

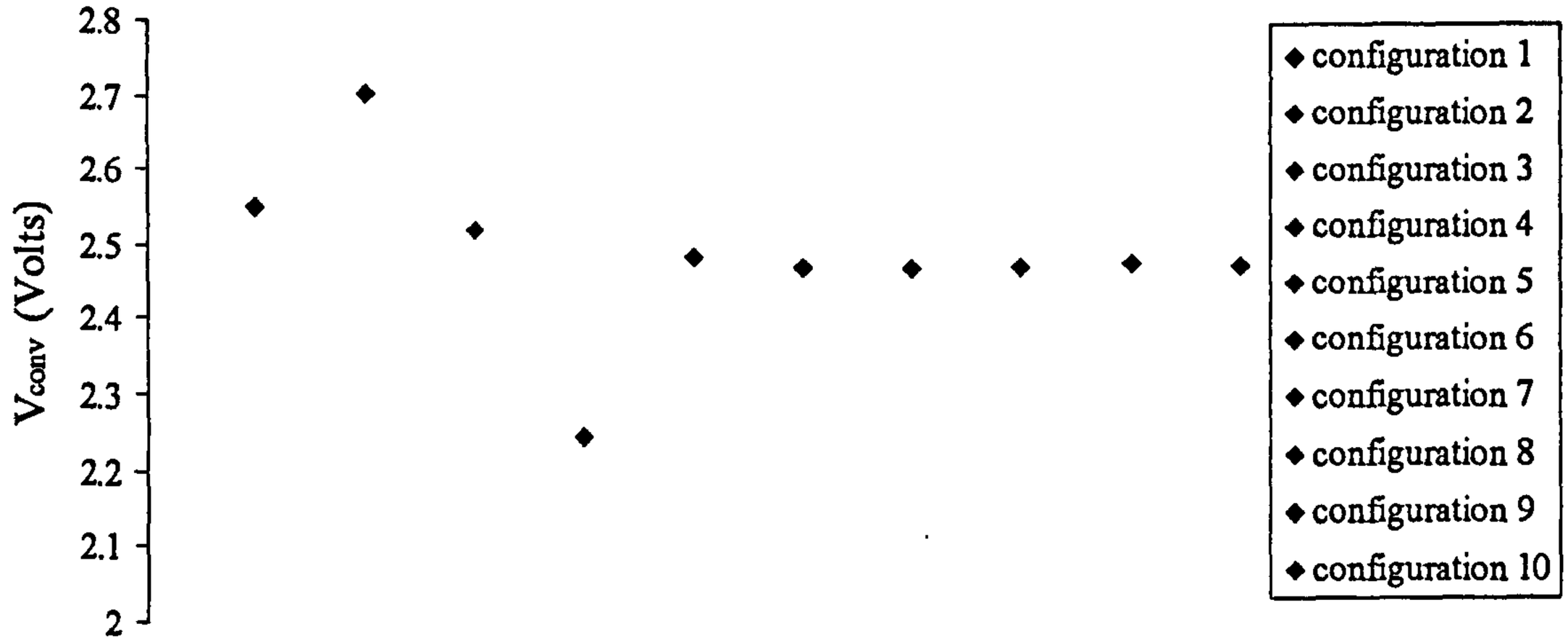

Figure 3-12. Plot to show the results of convergence testing on the axisymmetric PAFEC mesh.

Table 3-1. Key to the element size configurations plotted in Figure 3-12.

	Radial distance from the probe, (mm)									
	→1	→2	→3	→4	→5	→6	→7	→8	→9	→10
Element configuration	λ, (mm)									
Configuration 1	10									
Configuration 2	5									
Configuration 3	2									
Configuration 4	1				5					
Configuration 5	1									
Configuration 6	0.5				1					
Configuration 7	0.25				1					
Configuration 8	0.20				1					
Configuration 9	0.20					1				
Configuration 10	0.10				1					

Figure 3-12 shows that if λ was reduced below 1mm the change in V_{conv} was small. Therefore it was considered that λ=1mm over the first 10mm radial distance from the probe would give an accurate model. The earlier testing had showed that beyond 10mm radial distance from the probe the value of λ was less critical. Therefore it would be acceptable to use a larger element at this point.

3.2.3.2 Development of the FEA model to allow simulated movement of particles.

A limiting factor of the finite element analysis software was that it could only be used to analyse the response of the probe to a static situation. For investigating the response of the ring electrodes in water, and investigating the response of the probe to the proximity of the pipe wall, this is not a problem. However, it does mean that a single model is unable to predict the response of the probe to a particle moving past it. To simulate the effect of a particle moving past a probe a number of models had to solved, with the particle in a different position in each one. This ignores the effect of velocity on the measurement. However Nasr-El-Din et al [52] showed that velocity has a negligible effect when using sensors configured as SEMM arrays.

It was decided that the finite element mesh should be identical for each modelled position of the particle. This would mean that any errors resulting from the model design would be identical for all cases. In order to meet this requirement the model shown in Figure 3-13 was used. The mesh has a rectangular grid of 1mm × 1mm elements over the area where particles were positioned. The remainder of the mesh is graded away from this area. Using this mesh the material properties of different elements in the grid section can be changed to represent water or solid particles. This allows a large number of different particle positions to be modelled. It should be emphasised again that because the mesh is axisymmetric each modelled position of the particle actually represents a ring of solid material encircling the probe (see Figure 3-11).

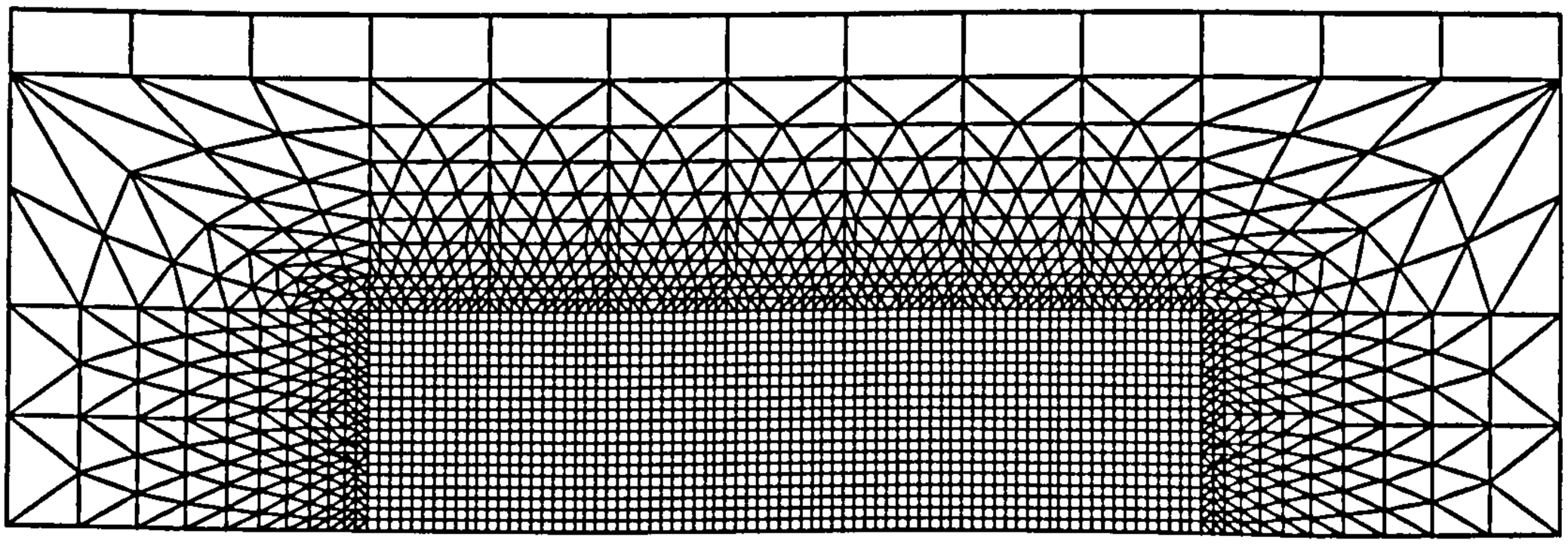

Figure 3-13. The axisymmetric finite element mesh

3.2.3.3 Control Software.

For a given probe geometry, to simulate the motion of a particle the material properties of the elements had to be changed sequentially to represent each particle position. Also the correct field electrode positions and configuration had to be set. After solution the potentials at the sense electrodes had to be extracted. Each model took 6 minutes to solve and there were between 75 and 800 models to solve for each probe geometry, depending on the number of particle positions modelled. To do this manually would have been extremely time consuming. Therefore control software was written in UNIX to generate the sequential models and automate their solution. This software allowed four weeks processing to be set up in half an hour and then left to run unattended.

3.2.4 Analysis of the electric potential around the ring electrodes.

It was decided to check the finite element model results against mathematical models. A review of the literature showed that Won [79] and Ridd [78] have developed analytical models of ring electrodes. Won developed a logarithmic model which is simple to simulate. Ridd's model is more precise and also more complex. However Ridd estimated that the Won model only introduces an error of 5%. As the finite element modelling was only intended to give guidelines for optimising the probe, and as all interesting results were validated experimentally (see Chapter 5), it was decided that it would be acceptable to use the Won model for comparisons.

The Won model [79] was used to make two comparisons. First it was used to calculate maps of the electric field between two ring electrodes, 1 and 2. This was intended to enable a qualitative comparison of the predicted electric fields. The model was rearranged to give the voltage V_P at a point P between the electrodes as shown in Figure 3-14 and Equation 3-3.

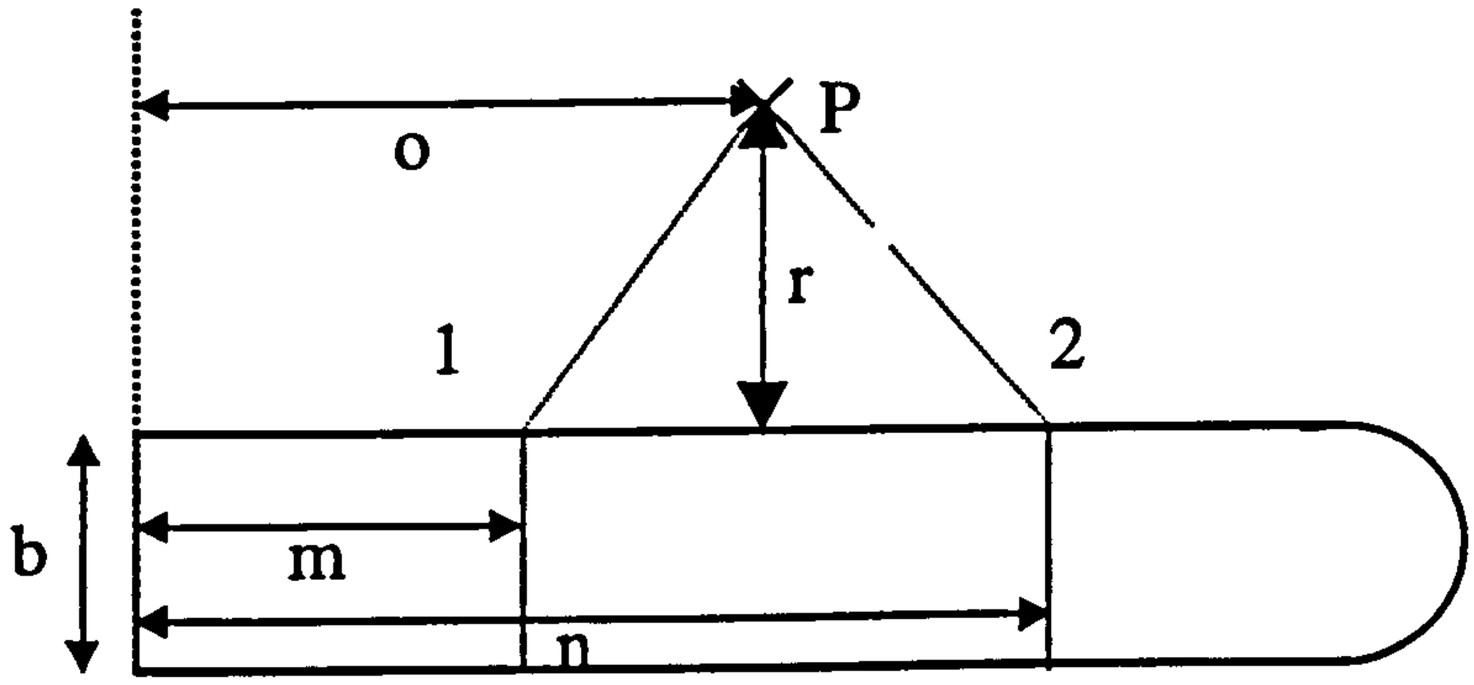

Figure 3-14. Notation used to represent two ring electrodes around a cylindrical probe for solution of the Won model.

$$V_P = \frac{i\eta}{4\pi^2 b}\left\{\ln\left[1+\frac{\pi}{2}\cdot\frac{2b}{\sqrt{(r-2b)^2+(o-m)^2}}\right]-\ln\left[1+\frac{\pi}{2}\cdot\frac{2b}{\sqrt{(r-2b)^2+(o-n)^2}}\right]\right\}$$

Equation 3-3

i = current

η = resistivity of the fluid in which the probe is immersed

r = radial distance of P from the probe centre

b = diameter of the probe

Equation 3-3 assumes that electrode 1 is held at a potential of +V Volts and that electrode 2 is held at a potential of -V Volts. This results in a symmetrical electric field between the electrodes, with 0V at a centre line between them. In the electrode system in the present investigation one of the field electrodes is held at 0V. This is the case in both the finite element models and with the experimental probe. To represent this, an offset was applied to the Won model so that the potential at the low field electrode is raised to 0V.

Using Equation 3-3 "potential maps" were calculated to show the predicted electric field between two ring electrodes with different separations (shown by distance n-m in Figure 3-14). Similar potential maps were then also created using the finite element model. Potential maps are shown for a model where the ring electrodes are 3mm apart in Figure 3-15.

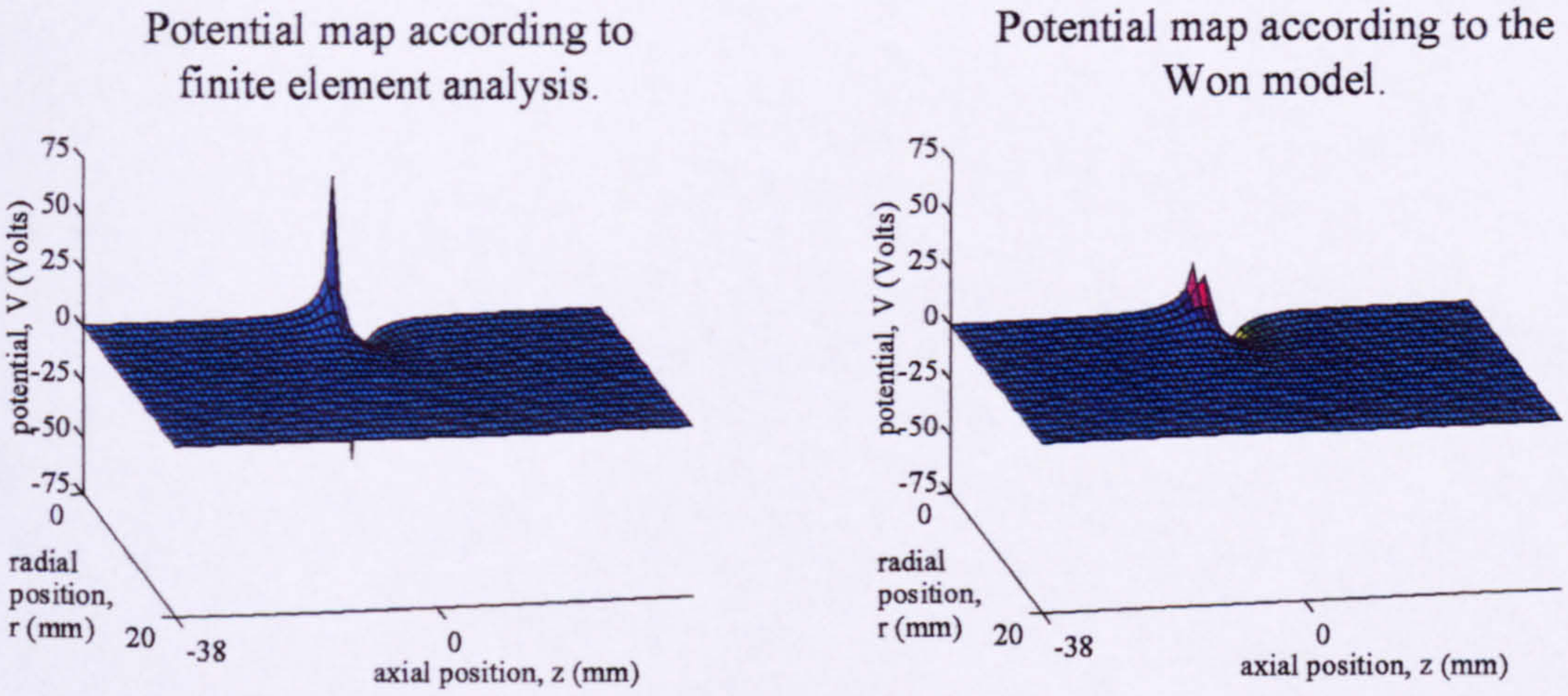

Figure 3-15. Potential maps calculated using FEA and the Won relationship, and a map of the error between the two.

Figure 3-15 shows that the predicted potential fields are qualitatively similar. The main difference is that the Won model predicts infinite potentials at the electrodes which is not practically achievable and is not predicted by the finite element analysis.

A quantitative comparison was also made between the Won model and FEA. The potential difference between sense electrodes S_1 and S_2 was calculated using both the Won model, ΔV_{won}, and the finite element model, ΔV_{fea}, for probes configured as 4-electrode SEMM arrays with varying f and s_α (see Figure 3-8). However the results also represent the response of the 4-electrode SEMM array that can be assumed to be contained within a six electrode probe as shown in Figure 3-7. The probes were assumed to be immersed in fluid at the centre of a pipe. A schematic representation of this arrangement is shown in Figure 3-16. The rearranged version of the Won model is shown in Equation 3-4

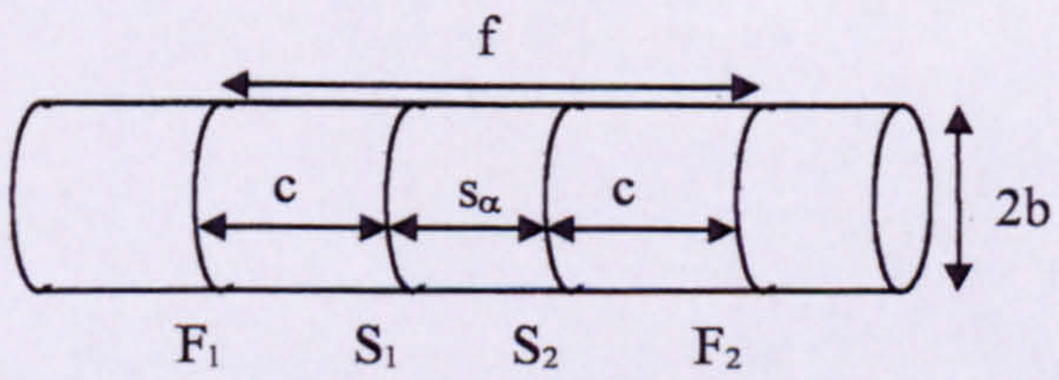

Figure 3-16. Notation used to represent a 4-electrode SEMM array for solution using the Won model.

$$\Delta V_s = \frac{i\eta}{2\pi^2 b}\left\{\ln\left[1+\frac{\pi b}{2c}\right]-\ln\left[1+\frac{\pi b}{2(c+s_\alpha)}\right]\right\}$$

Equation 3-4

F_1 and F_2 - field electrodes

S_1 and S_2 - sense electrodes

i = current

η = resistivity of the fluid in which the probe is immersed

The percentage error between the ΔV_{won} and ΔV_{fea} is plotted in Figure 3-17 .In this case error is defined as in Equation 3-5.

$$e_w = \frac{\Delta V_{fea} - \Delta V_{won}}{\Delta V_{won}} \times 100$$

Equation 3-5

Five lines are plotted in Figure 3-17. These correspond to s_α of between one and nine millimetres. Each line is a plot of e_w against f.

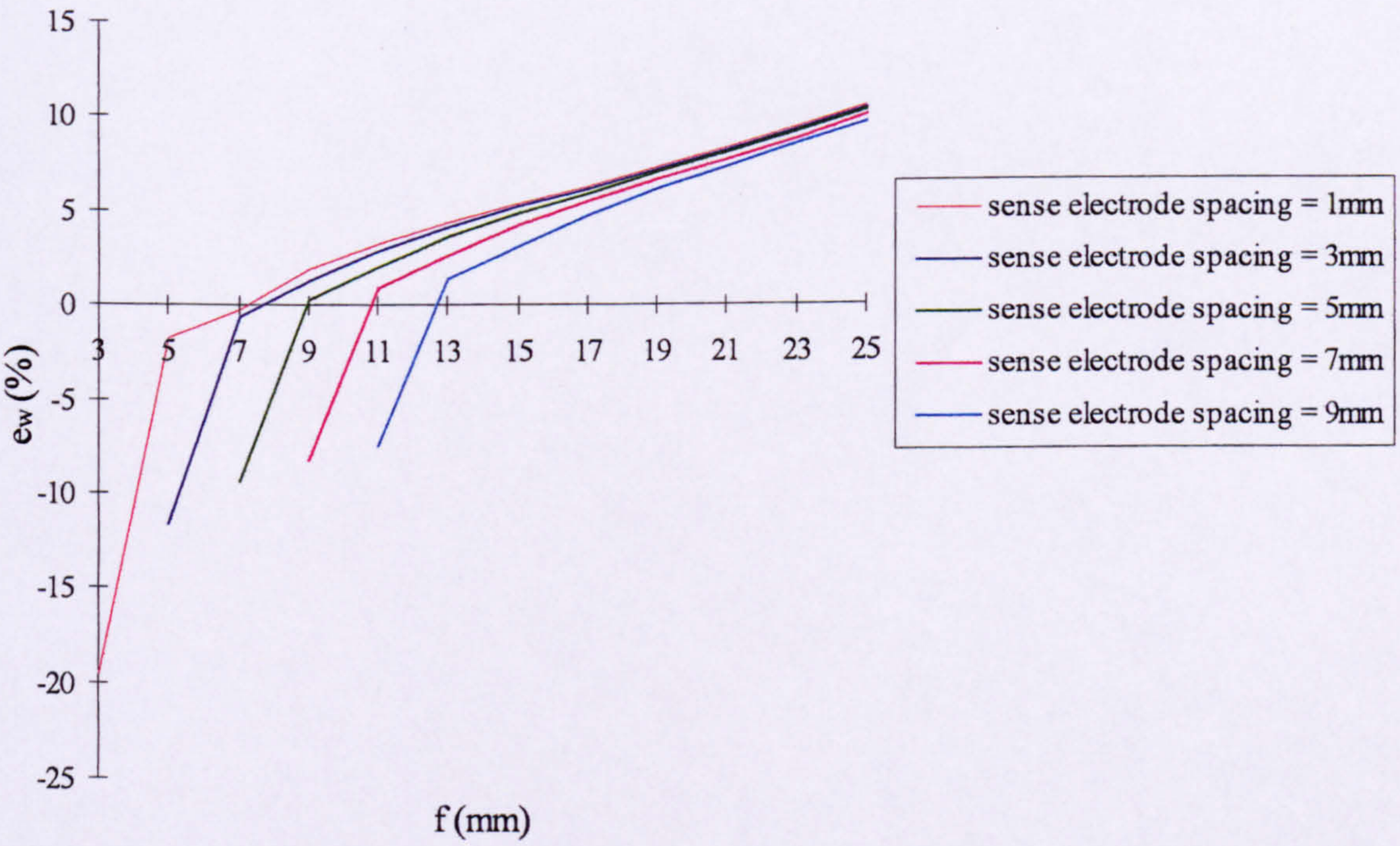

Figure 3-17. e_w plotted against f and s_α,

Figure 3-17 shows considerable variation in e_w for different electrode configurations with a maximum value of the order of 20%. However, in the FEA results presented later in this chapter, the dimensions of most interest (see Section 3.2.6.2) are $11\text{mm} \leq f \leq 17\text{mm}$ and $s_\alpha \leq 7\text{mm}$. For these cases Figure 3-17 shows e_w up to 5%. As the finite element modelling was only intended to give guidelines for optimising the probe, and as all interesting results

were validated experimentally (see Chapter 5), it was decided that this was an acceptable error.

3.2.5 Wall effects.

Models were created of probes in pipes of different radii, with both steel (conducting) and Perspex (non-conducting) walls. The aim of this modelling was to discover whether one type of pipe material had a greater effect on the probe response than the other. As with the previous mathematical model comparisons, these models were solved using a probe with a 4-electrode SEMM array (see Figure 3-8). However, as before, they also represent the response of the 4-electrode SEMM array that can be assumed to be contained within a 6-electrode SEMM array as shown in Figure 3-7.

Initially a model was set up which assumed the probe to be immersed in an effectively infinite tank. The potential difference between the sense electrodes in this case was ΔV_{inf} . ΔV_{inf} is plotted in Figure 3-18 as a straight dotted line. Models were then solved which assumed the probe to be immersed in pipes with diameters decreasing from 80mm. This is not an exact simulation of the probe approaching a single pipe wall but the results were only intended to be qualitative. The potential difference between the sense electrodes, ΔV_s has been plotted against pipe diameter in Figure 3-18 for both steel, ΔV_{steel} and perspex, $\Delta V_{perspex}$, pipes.

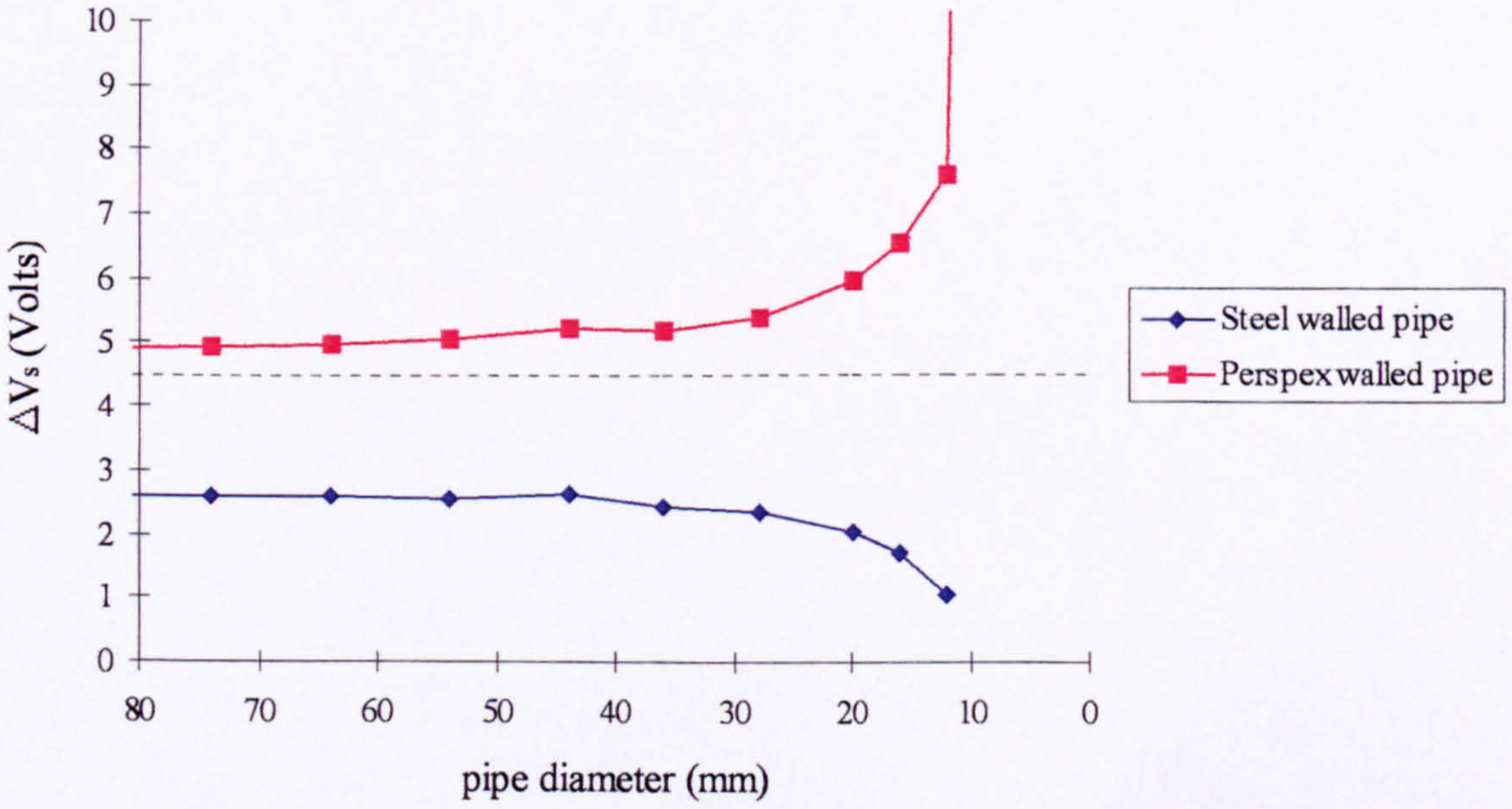

Figure 3-18. The effects of different pipe wall materials on the response of the probe.

Figure 3-18 shows that over the majority of the range of pipe diameter both ΔV_{steel} and $\Delta V_{perspex}$ show a fairly constant deviation from ΔV_{inf}. At low pipe diameters both ΔV_{steel} and $\Delta V_{perspex}$ show a large deviation from ΔV_{inf} with $\Delta V_{perspex}$ showing the largest change. This is due to the pipe wall affecting the electric field around the probe. With a non-conducting pipe wall none of the supplied current can sink to the pipe. Reducing the pipe diameter therefore causes the electric field to be compressed. This increases the current density around the probe and therefore increases the value of $\Delta V_{perspex}$. With a conducting pipe wall some of the supplied current sinks to the wall. This causes the offset in ΔV_{steel} from ΔV_{inf} which is present even at large pipe diameters. Reducing the pipe diameter causes more of the supplied current to sink to the pipe wall. This reduces the current density around the probe and therefore reduces ΔV_{steel}.

It is important to note that the changes in ΔV_{steel} and $\Delta V_{perspex}$ shown in Figure 3-18 are larger than would be obtained for the real probe. In the axisymmetric geometry used in the finite element modelling the probe is simultaneously converged upon by the pipe wall from all sides causing a large change in response. If the real probe were traversed towards a pipe wall its opposite side would be moving away from the opposite pipe wall. Therefore a smaller change in response would be expected.

In conclusion the results show that the effect of both materials can be large as the probe approaches the pipe wall. However a conducting pipe wall appears to draw some of the probe current at all pipe diameters. The effect of this is to reduce the current density around the probe and therefore to reduce its sensitivity to local events. The conducting pipe wall also increases the current load of the device which has implications for the electronic circuit design. Given these possible complications, and recognising that a translucent Perspex pipe wall allows easy visual observation of the flow and the probe, it was decided that a non-conducting Perspex pipe was preferable for the current investigation.

3.2.6 Simulated particle modelling of the probe.

3.2.6.1 Introduction to the simulated particle modelling.

The following sections describe the results of modelling that simulated the movement of a non-conducting particle past a probe. It should be reiterated at this point that because the

finite element model is axisymmetric each modelled position of the particle actually represents a ring of particles circling the probe (Figure 3-11). Also, as the radial position of the particle moves away from the probe, the volume of solid material in the resulting ring will increase (see Figure 3-11). This will affect the sensitivity results but it was considered that the results would still offer valuable information regarding the optimisation of the probe. For each probe configuration a number of different particle positions were tested. For each of these a position dependent relative sensitivity, Ψ, was calculated as below.

$$\Psi = \frac{(\Delta V_P - \Delta V_u)}{(\Delta V_{max} - \Delta V_u)} \times \frac{100}{1}$$

Equation 3-6

ΔV_P = Potential difference between the sense electrodes with a particle modelled at position P for a given probe configuration.

ΔV_{max} = Largest observed potential difference between the sense electrodes for all positions of the particle for the given probe configuration.

ΔV_u = Potential difference between the sense electrodes for the given probe configuration with no particles modelled.

For each position of the particle Ψ was plotted against the particle co-ordinates to give a surface plot such as that shown in Figure 3-19. Figure 3-19 represents the "sensitivity volume" for the probe. The probe shown schematically in Figure 3-19 is a 4-electrode SEMM array. However this method of representing the sensitivity volume of the probe can be used for any probe configuration.

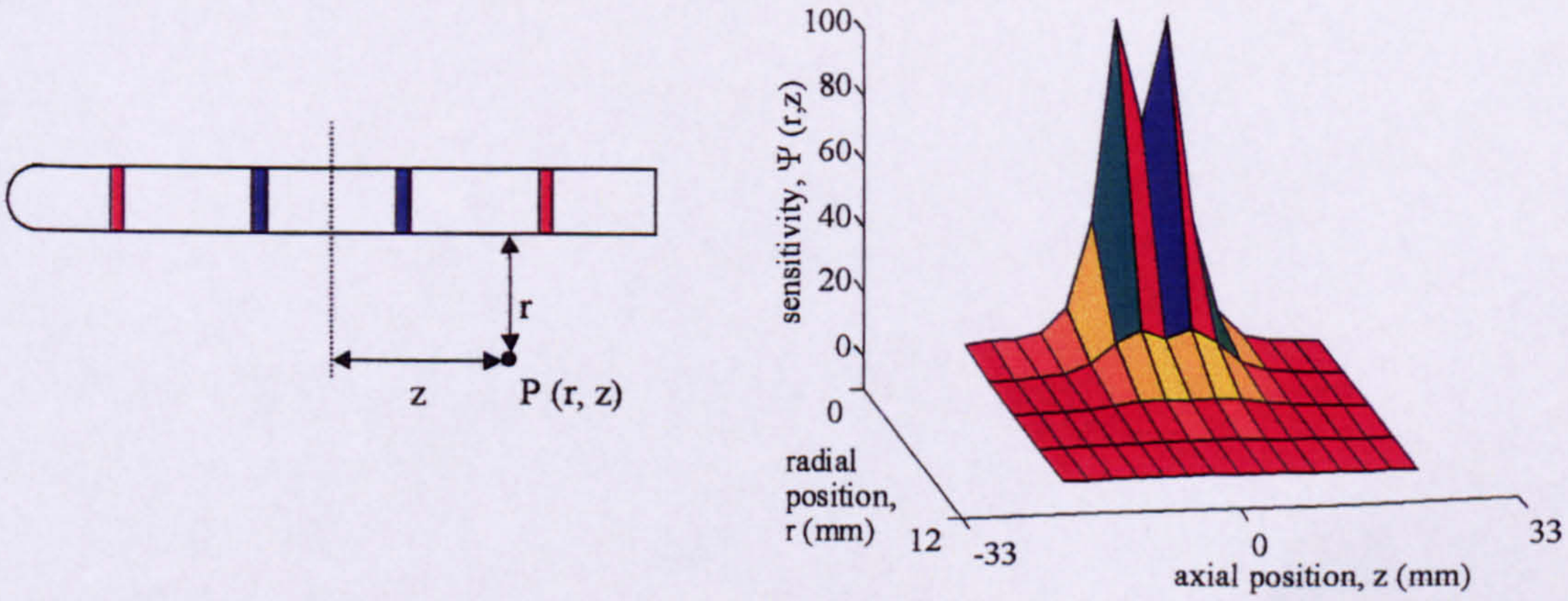

Figure 3-19. The format of the simulated particle results.

The sensitivity volumes presented in this chapter give a qualitative representation. As Ψ is a relative value no quantitative impression of the response of a probe can be deduced. A quantitative understanding of the behaviour of the probes can be gained from the experimental static test results presented in Chapter 5.

3.2.6.2 Modelling of 4-electrode SEMM arrays.

Using the format described in Section 3.2.6.1 models were analysed consisting of single 4-electrode SEMM arrays (see Figure 3-8). These were analogous to the devices to be used for measurement of $\alpha_{s,i}$. The results also apply to the 4-electrode SEMM array that can be assumed to be contained within a 6-electrode SEMM array (see Figure 3-7) and they can apply to each 4-electrode SEMM array contained within an 8-electrode probe (see Figure 3-10), provided that only one is active at any time. The modelling was designed to discover the effects of varying the dimensions of the probe. The dimensions that were varied for this modelling were s_α, f and a (see Figure 3-8).

Before the modelling began it was important to define an optimal sensitivity volume shape for measurement of $\alpha_{s,i}$. The purpose of the 4-electrode SEMM array was to acquire a measurement of $\sigma_{m,i}$. If the probe interrogates a volume that is small compared to the individual particle volume it will respond to individual particles passing the sensing array, but will not acquire a representative measurement of $\sigma_{m,i}$. Therefore it was decided that the array should have uniform sensitivity over a volume that is large compared with the volume of the individual particles. This translates into a large sensitivity volume that has relatively constant high value of Ψ.

As discussed in Section 3.2.3.2 the format of the finite element modelling requires a separate model to be solved for each simulated position of the particle. Initially 75 simulated particle positions were solved for each configuration of the probe which corresponds to increments of 3mm in the radial and axial position of the particle (see Figure 3-19). This results in what will be referred to as a "rough" sensitivity volume. However some results were examined in more detail by solving 513 simulated particle positions which corresponds to increments of 1mm in the radial and axial position of the particle (see Figure 3-19). This gives what will be referred to as a "detail" sensitivity volume. In order to reduce the time taken for the modelling detail sensitivity volumes were not acquired for all the configurations of the array. Where possible

detail sensitivity volumes are presented. However Figure 3-20 shows that the key features of the detail sensitivity volume are reproduced in the rough sensitivity volume.

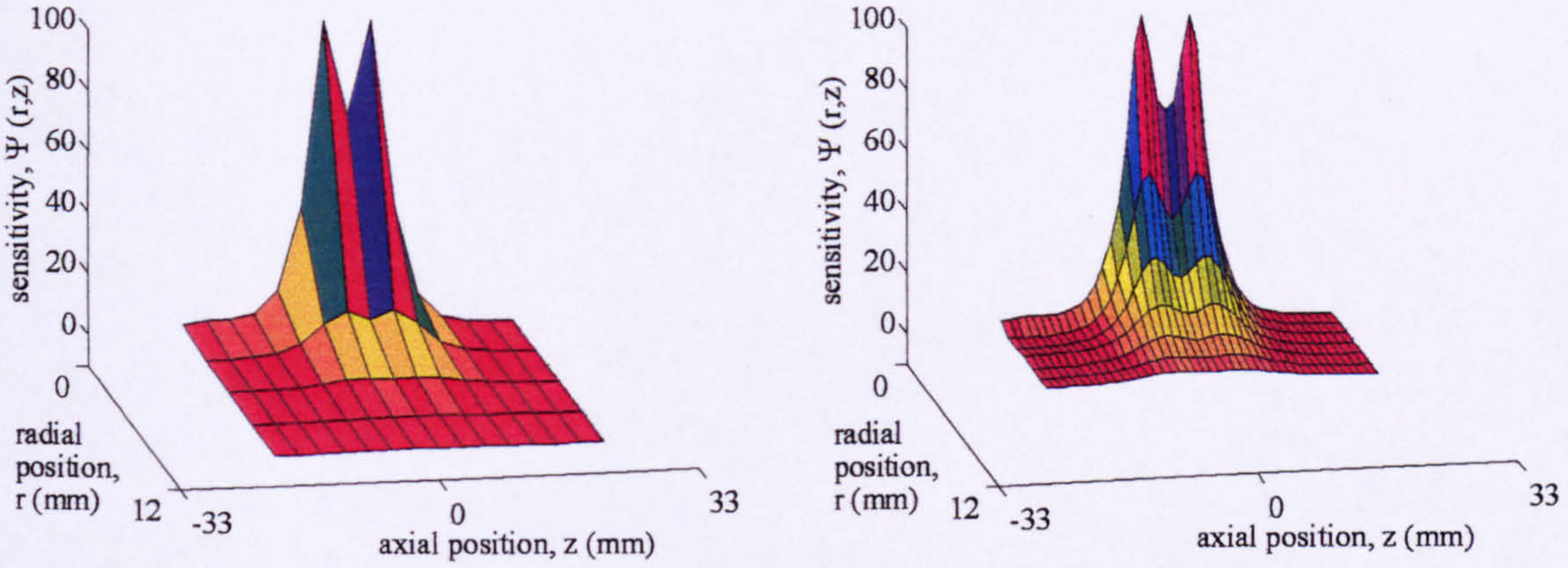

Figure 3-20. Comparison of "rough" and "detail" sensitivity volumes for a 4-electrode SEMM array.

The effect on the sensitivity volume shape of varying the field electrode axial length, a

Sensitivity volumes were constructed for 4-electrode SEMM arrays with a (see Figure 3-8) of 6mm, 4mm, 2mm, and point source. A point source exists when the electrode consists of a single node in the FE model. When an axisymmetric point source is rotated to form the full three-dimensional model (see Figure 3-11) it becomes a ring with zero axial length. Figure 3-21 shows the effect on the sensitivity volume of varying a for two configurations of the array. Each column of Figure 3-21 shows sensitivity volumes for 4-electrode SEMM arrays with constant values of f and s_α. Each row of Figure 3-21 then shows the sensitivity volume for that array configured with different a.

Figure 3-21 shows that as a increases the symmetry of the sensitivity volume decreases. It can be seen in Figure 3-21 that this also has the effect of slightly reducing the size of the sensitivity volume as a increases. In Section 3.2.6.2 it was decided that the optimum sensitivity volume for a 4-electrode SEMM array should be large relative to the particle volume. Therefore this result suggests that the axial length of the field electrodes should be minimised. However it is possible that this effect is a result of the electrode loading in the FE model. As a is increased the electrical current must be distributed over more nodes of the FE model. The distribution is calculated arbitrarily and it is possible that this introduced errors into the model. Therefore this result has been investigated experimentally in Chapter 5.

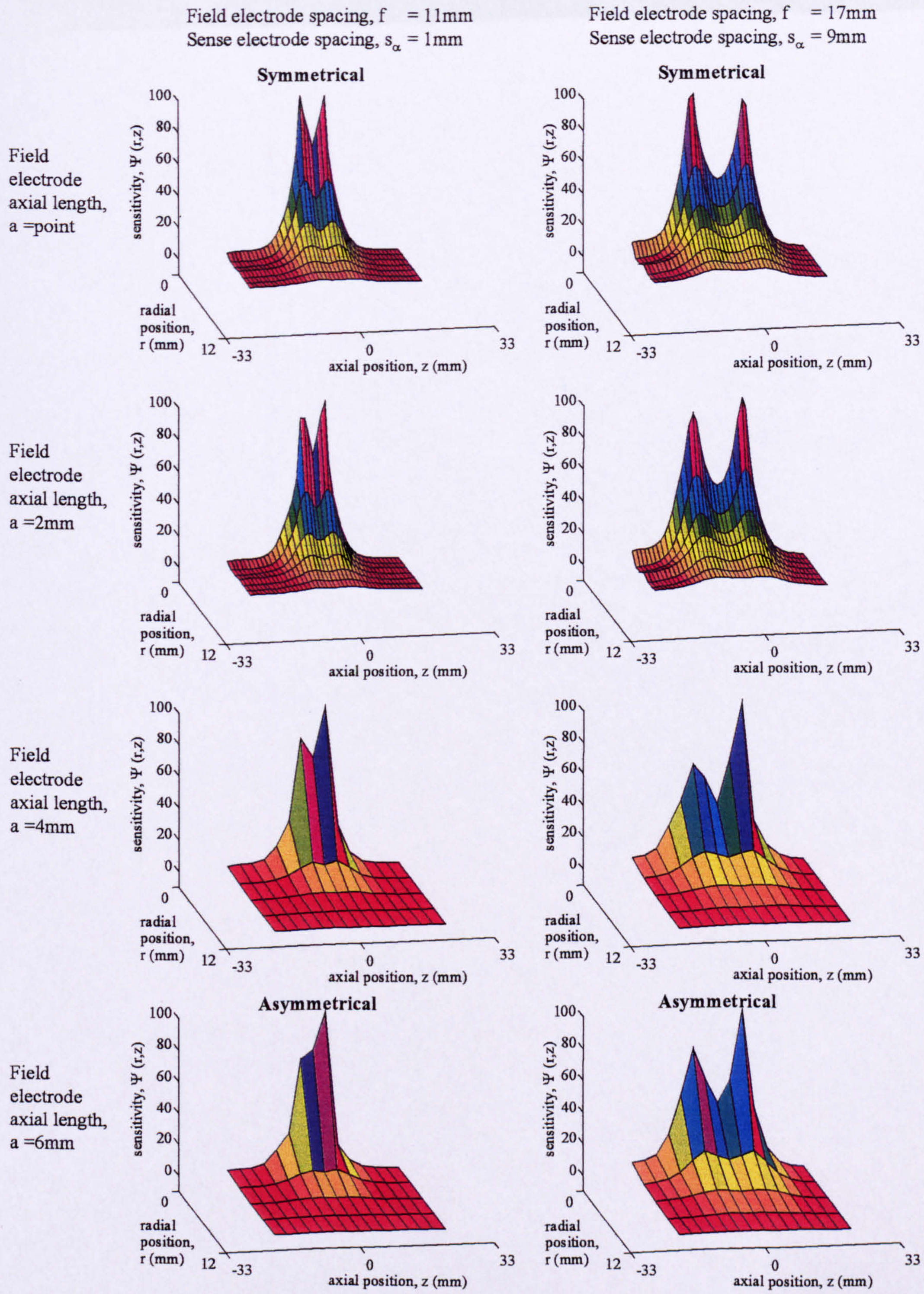

Figure 3-21. The effect on the sensitivity volume shape of varying a.

The effect on the sensitivity volume shape of varying the field electrode separation, f

Sensitivity volumes were constructed for 4-electrode SEMM arrays with 12 values of f (see Figure 3-8) between 3mm and 29mm. The lower limit of 3mm represents the smallest separation that could be constructed whilst still allowing 2 sense electrodes to be configured. It was felt that above the upper limit of 29mm the probe would not be rigid enough for use in the current investigation. Representative sensitivity volumes, for arrays with a set as a point source, are shown in Figure 3-22. These show definite trends which are described in this section. There are three distinct shapes of sensitivity volume as described below;

Shape 1. At low f the sensitivity volume shows a twin peaked shape. The positions of the peaks roughly coincide with the field electrode positions. The size of the sensitivity volume increases with increasing f.

Shape 2. As f is increased the shape evolves into a single peak. The peak covers a large volume around the probe at high Ψ. This sensitivity volume only retains this shape for a narrow range of f.

Shape 3. As f increases further the single peak breaks down. The sensitivity volume now becomes very uneven with high Ψ at a single position and with smaller separate peaks in Ψ on either side of this main peak.

As stated at the beginning of Section 3.2.6.2, for making a measurement of $\alpha_{s,i}$, the sensitivity volume should be large relative to the individual particle volume. It should also have a high sensitivity over as large an area as possible. From the results shown in Figure 3-22, a shape 2 sensitivity volume would be the most ideal. The results suggest that the sensitivity of the probe can be altered substantially by changing f. This behaviour could not be found in the literature and to confirm the findings it was decided that it should be investigated experimentally. This work is reported in Chapter 5.

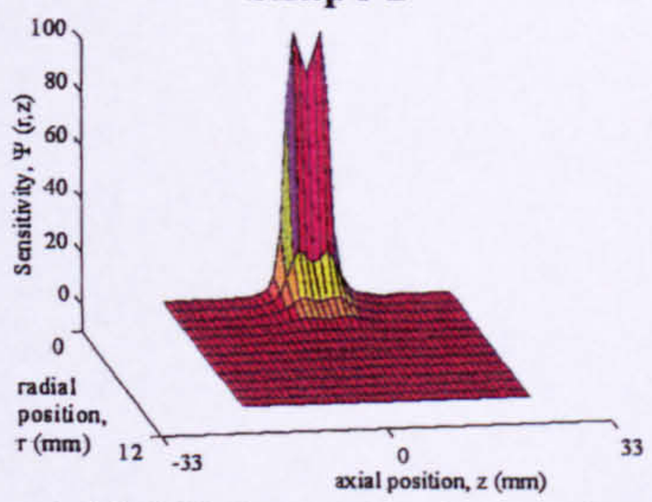

Axial field electrode length, a = point
Field electrode spacing, f = 3mm
Sense electrode spacing, s_α = 1mm

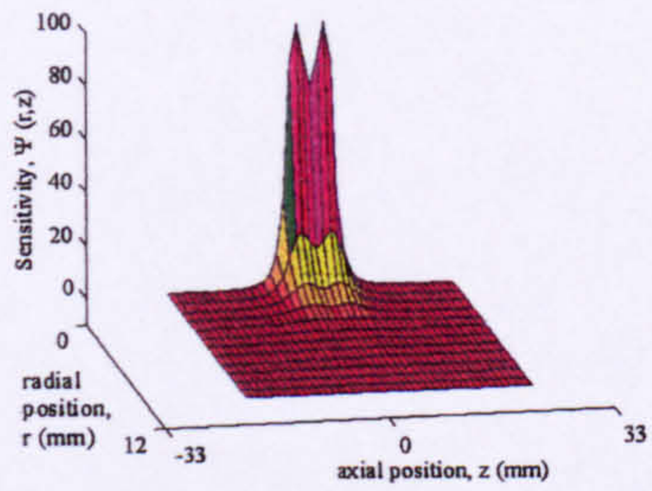

Axial field electrode length, a = point
Field electrode spacing, f = 5mm
Sense electrode spacing, s_α = 1mm

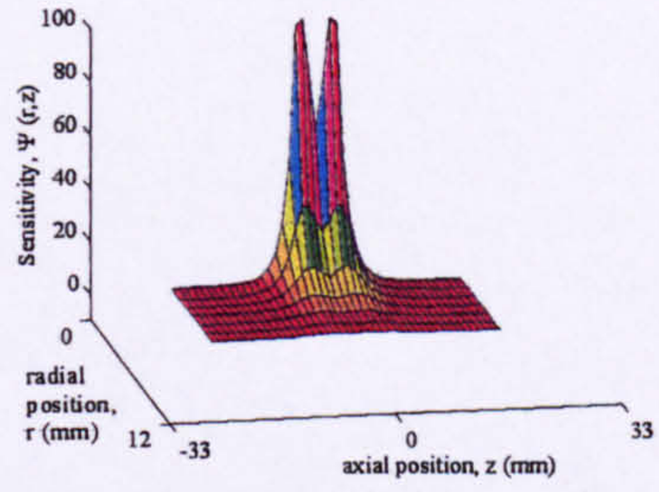

Axial field electrode length, a = point
Field electrode spacing, f = 7mm
Sense electrode spacing, s_α = 1mm

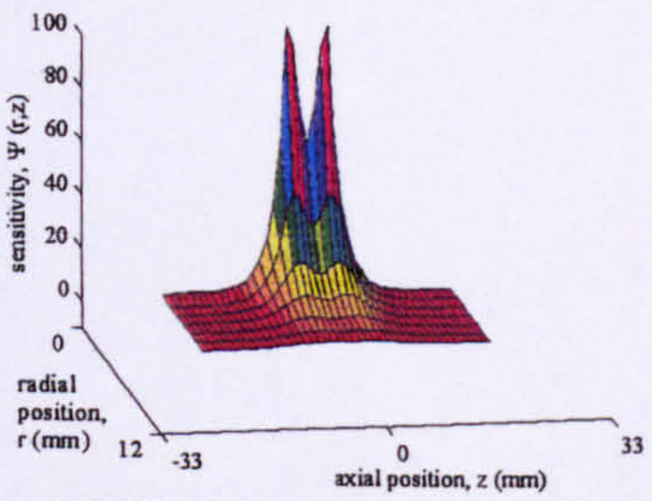

Axial field electrode length, a = point
Field electrode spacing, f = 9mm
Sense electrode spacing, s_α = 1mm

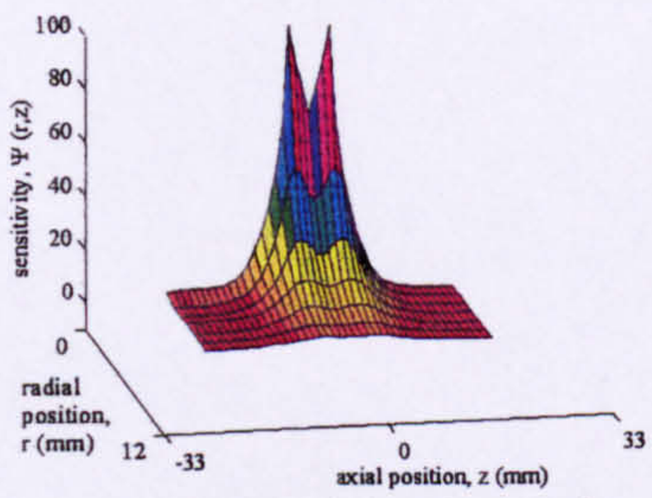

Axial field electrode length, a = point
Field electrode spacing, f = 11mm
Sense electrode spacing, s_α = 1mm

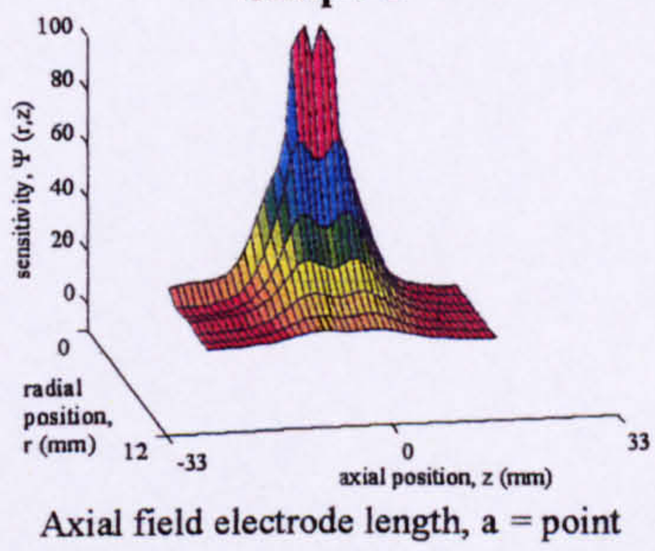

Axial field electrode length, a = point
Field electrode spacing, f = 13mm
Sense electrode spacing, s_α = 1mm

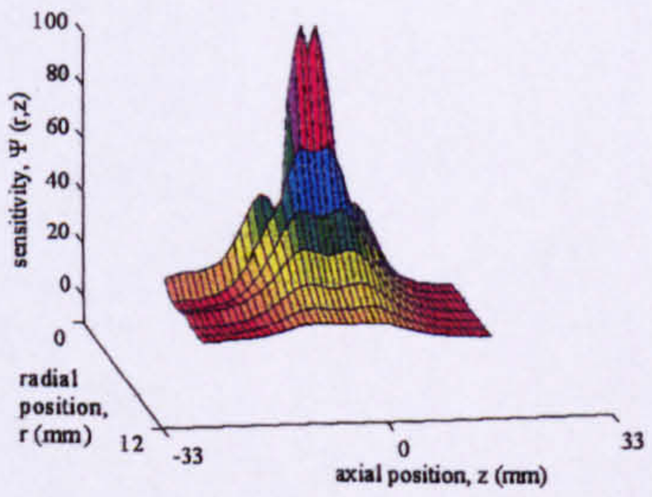

Axial field electrode length, a = point
Field electrode spacing, f = 15mm
Sense electrode spacing, s_α = 1mm

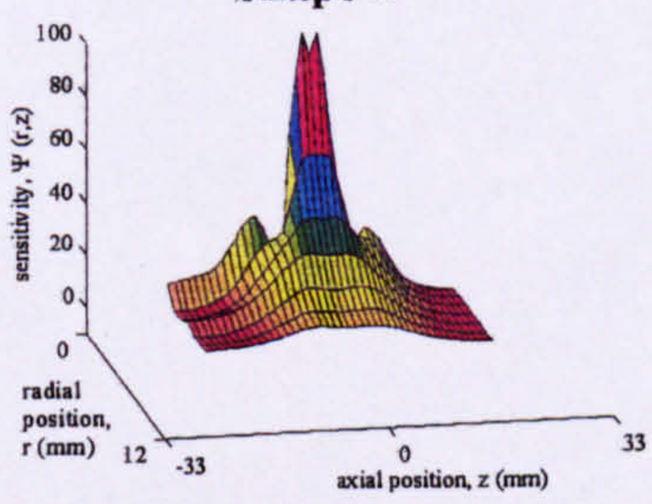

Axial field electrode length, a = point
Field electrode spacing, f = 17mm
Sense electrode spacing, s_α = 1mm

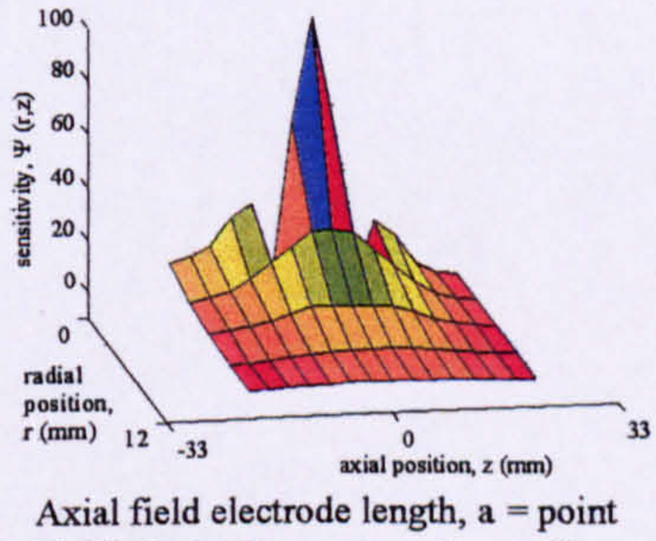

Axial field electrode length, a = point
Field electrode spacing, f = 19mm
Sense electrode spacing, s_α = 1mm

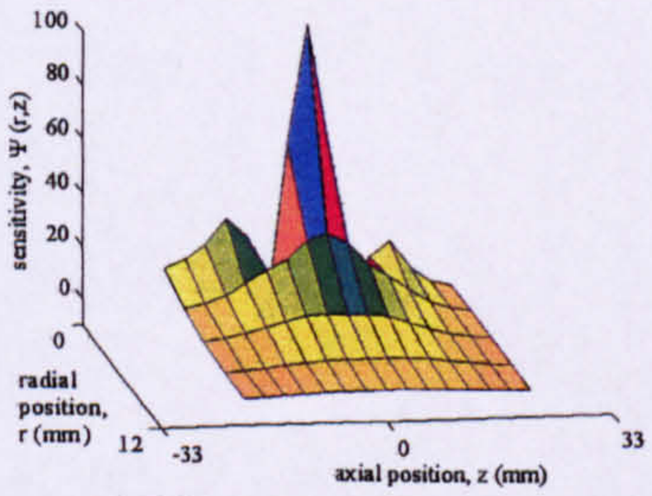

Axial field electrode length, a = point
Field electrode spacing, f = 21mm
Sense electrode spacing, s_α = 1mm

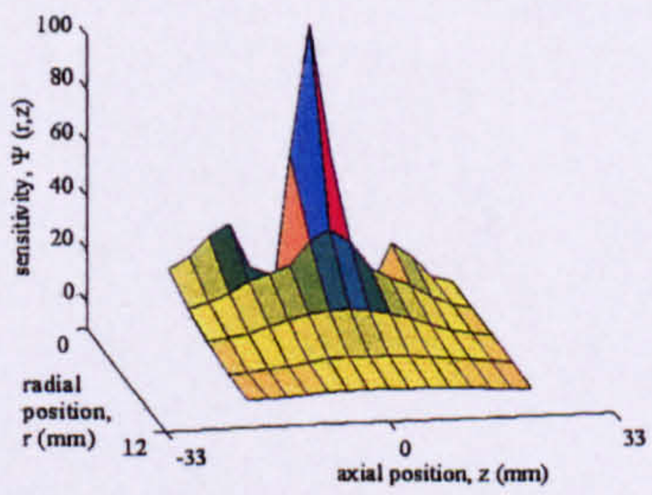

Axial field electrode length, a = point
Field electrode spacing, f = 23mm
Sense electrode spacing, s_α = 1mm

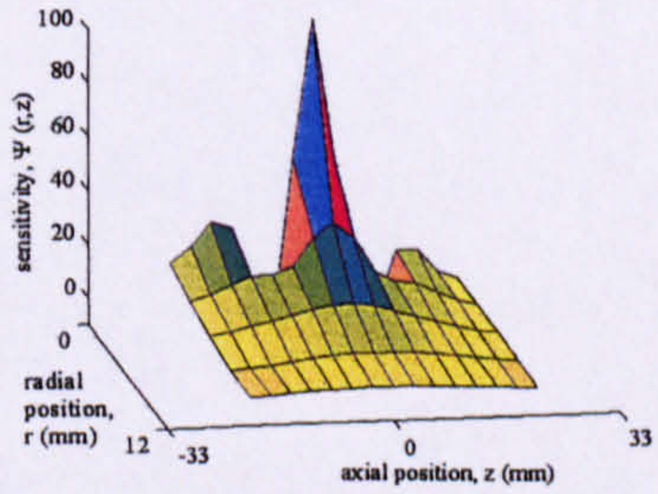

Axial field electrode length, a = point
Field electrode spacing, f = 25mm
Sense electrode spacing, s_α = 1mm

Figure 3-22. The effect on the sensitivity volume shape of increasing f.

The effect on the sensitivity volume shape of varying the sense electrode separation, s_α

Sensitivity volumes were constructed for 4-electrode SEMM arrays with s_α, of 1mm, 3mm, 5mm, 7mm, and 9mm. The lower limit of 1mm represents the smallest separation that could

be constructed using the available manufacturing facilities. The upper limit of 9mm was selected during the modelling as above this value the optimum sensitivity volume shape selected in the previous section could not easily be identified. The results of the modelling show that the three sensitivity volume shapes observed in the previous section (see Figure 3-22) occur at larger f as s_α is increased. Because of this it is useful to define each combination of f and s_α using an electrode separation ratio, ω, which is defined in Equation 3-7.

$$\omega = \frac{s_\alpha}{f}$$

Equation 3-7

Representative results showing the effects of variation of ω on the sensitivity volume shape are shown in Figure 3-23. Figure 3-23 is arranged with s_α constant in each column, and f constant in each row. Therefore ω increases from left to right, and decreases from top to bottom.

Figure 3-23 shows that as ω decreases the sensitivity volume shape changes from shape 1 through to shape 3. However Figure 3-23 also shows that the sensitivity volume shape cannot be predicted by defining ω alone. For example if f is 13mm a shape 2 sensitivity volume occurs at $\omega = 0.08$. This is shown in the top row of Figure 3-23. However if f is 19mm a shape 2 sensitivity volume occurs at $\omega = 0.47$. This is shown in the bottom row of Figure 3-23.

When the full range of finite element analysis results were examined it became apparent that the value of ω required to achieve a shape 2 sensitivity volume increased almost linearly between 0.08 and 0.47 as f increased between 13mm and 19mm. This suggests that a direct relationship exists between the two dimensions. In the current investigation there are an inadequate number of results to define this relationship accurately. However the results do show that both f and s_α, are important for predicting the sensitivity volume shape accurately.

ω = 0.08, shape 2

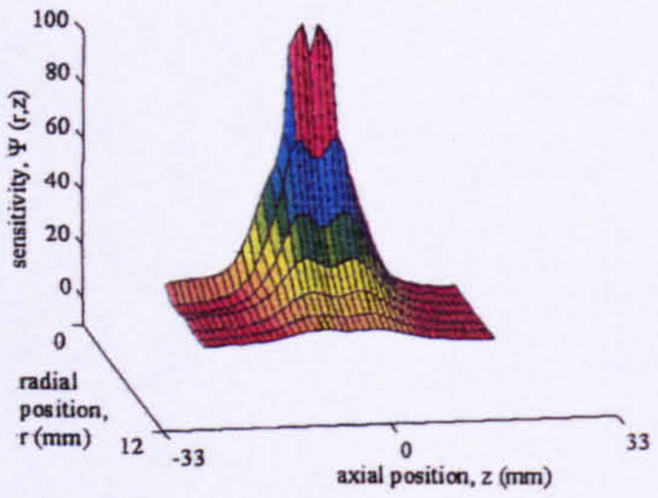

Axial field electrode length, a = point
Field electrode spacing, f = 13mm
Sense electrode spacing, s_α = 1mm

ω = 0.38, shape 1

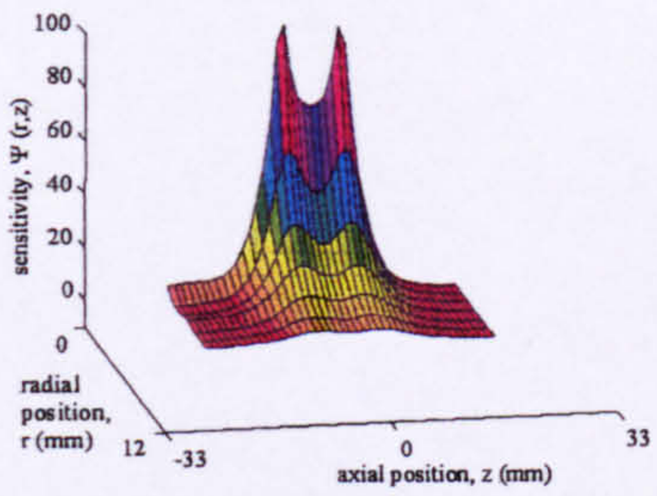

Axial field electrode length, a = point
Field electrode spacing, f = 13mm
Sense electrode spacing, s_α = 5mm

ω = 0.69, shape 1

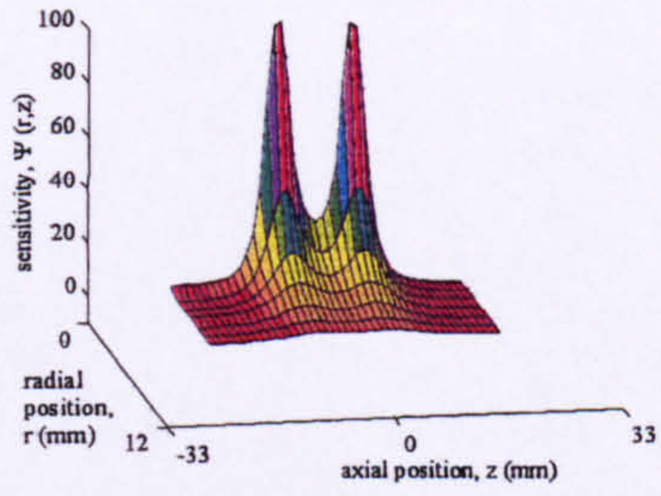

Axial field electrode length, a = point
Field electrode spacing, f = 13mm
Sense electrode spacing, s_α = 9mm

ω = 0.07, shape 2/3

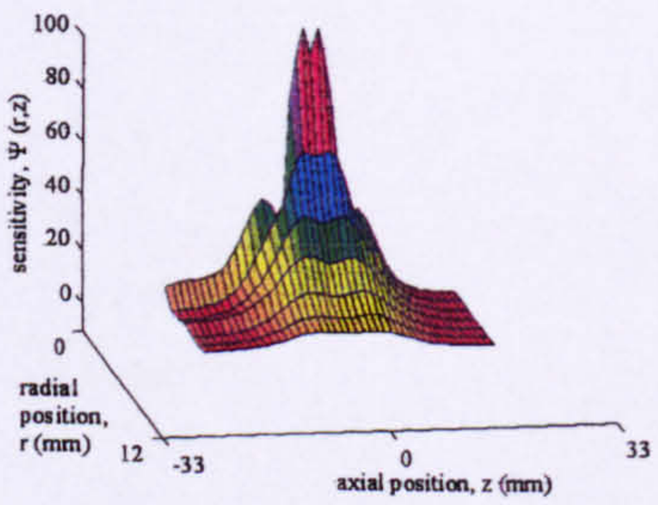

Axial field electrode length, a = point
Field electrode spacing, f = 15mm
Sense electrode spacing, s_α = 1mm

ω = 0.33, shape 2

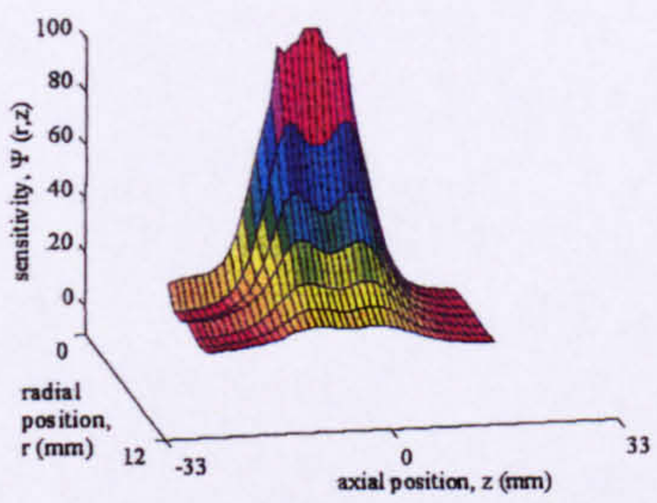

Axial field electrode length, a = point
Field electrode spacing, f = 15mm
Sense electrode spacing, s_α = 5mm

ω = 0.60, shape 1

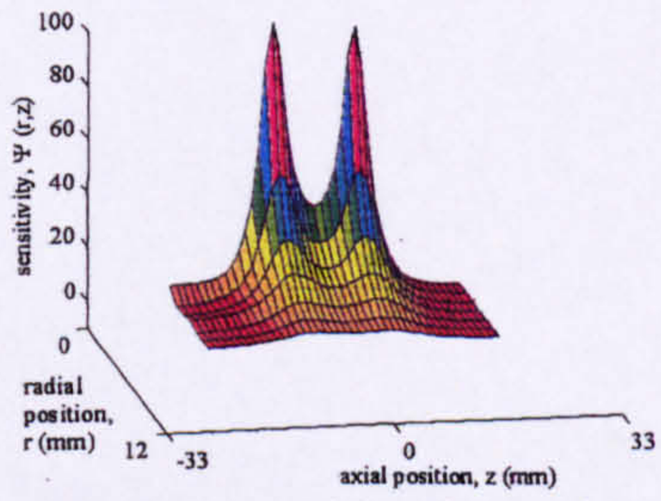

Axial field electrode length, a = point
Field electrode spacing, f = 15mm
Sense electrode spacing, s_α = 9mm

ω = 0.06, shape 3

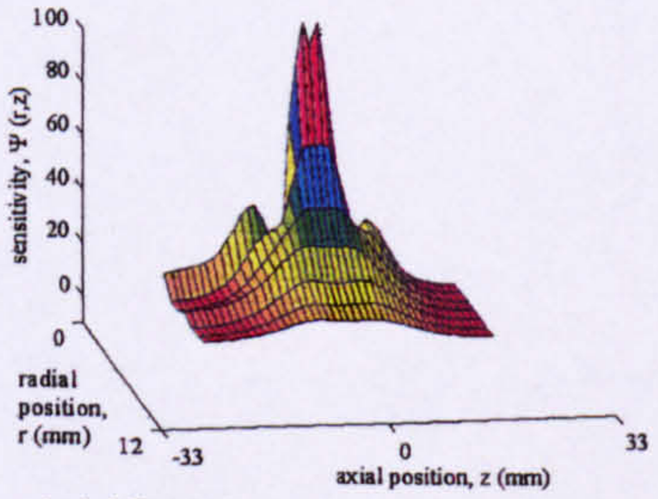

Axial field electrode length, a = point
Field electrode spacing, f = 17mm
Sense electrode spacing, s_α = 1mm

ω = 0.18, shape 2/3

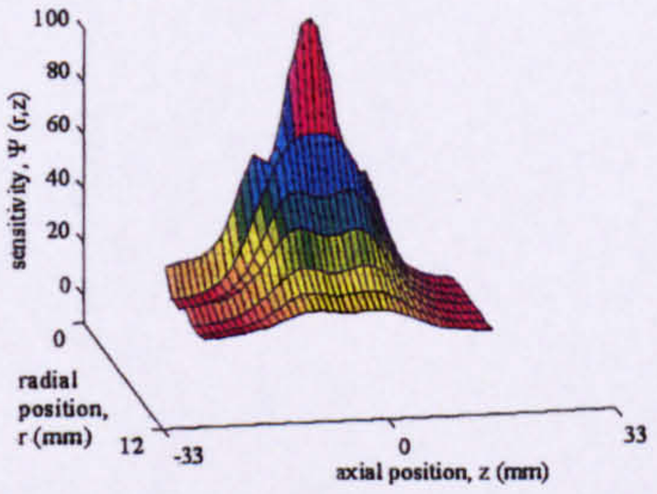

Axial field electrode length, a = point
Field electrode spacing, f = 17mm
Sense electrode spacing, s_α = 5mm

ω = 0.53, shape 1

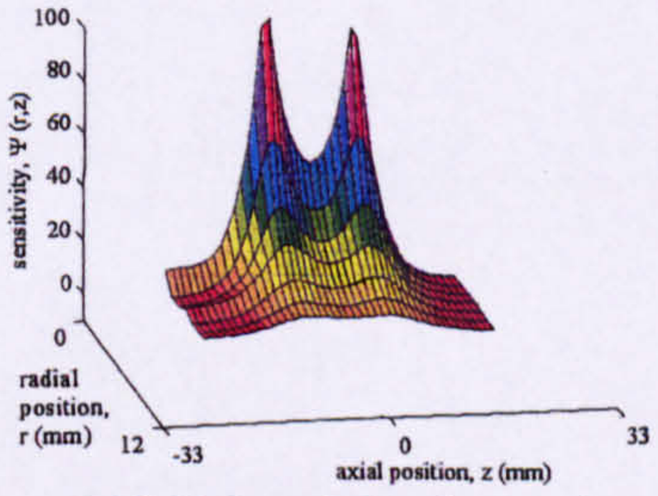

Axial field electrode length, a = point
Field electrode spacing, f = 17mm
Sense electrode spacing, s_α = 9mm

ω = 0.05, shape 3

Axial field electrode length, a = point
Field electrode spacing, f = 19mm
Sense electrode spacing, s_α = 1mm

ω = 0.26, shape 3

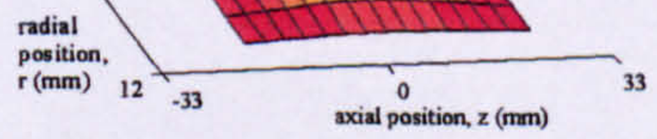

Axial field electrode length, a = point
Field electrode spacing, f = 19mm
Sense electrode spacing, s_α = 5mm

ω = 0.47, shape 2

Axial field electrode length, a = point
Field electrode spacing, f = 19mm
Sense electrode spacing, s_α = 9mm

Figure 3-23. The effect on the sensitivity volume shape of varying the electrode separation ratio, ω.

It is interesting to note parallels with geophysical prospecting tools at this point. Different configurations of geophysical conductivity measurement tool were discussed in Chapter 2. In particular this included the Wenner array and the Schlumberger array, described by Griffiths & King [20]. These are arranged as 4-electrode SEMM arrays. The principle difference between these arrays is their electrode separation ratio. The Wenner array uses $\omega = 0.33$, whilst the Schlumberger array uses $\omega = 0.10$. Much debate exists in the literature about the relative depths of investigation of these instruments. It may be possible to apply some of the conclusions from the current research although further work would need to be carried out to determine the effects of scaling up the dimensions, as the value of f used in a geophysical array can be of the order of tens of meters.

In conclusion the finite element modelling of 4-electrode SEMM arrays has allowed the identification of an ideal sensitivity volume shape, defined as shape 2 here. It has shown some of the combinations of f and s_α necessary to achieve a shape 2 sensitivity volume shape. Finally it has identified that f and s_α should be maximised, whilst retaining one of the given combinations, in order to maximise the size of the sensitivity volume.

3.2.6.3 Modelling of velocity measurement probes.

Using the format described in Section 3.2.5.1 sensitivity volumes were constructed for probes configured as 6-electrode SEMM arrays (see Figure 3-9) and 8-electrode probes (see Figure 3-10). These probes can be used to acquire measurements of $u_{s,i}$. The way in which this can be achieved is detailed in Section 3.1.3.3. It is important that in this section it is assumed that the two 4-electrode SEMM arrays of the 8-electrode probe are assumed to be operating simultaneously, at the same frequency and in phase. If they are operated separately the modelling of 4-electrode SEMM arrays reported in Section 3.2.6.2 can be applied.

The modelling reported in this section was carried out to determine the effect, on the sensitivity volumes of both configurations of probe, of varying the probe geometry. From this it was intended to determine which configuration and geometry would be most suitable for acquiring a measurement of $u_{s,i}$. In order to do this it was important to define the ideal sensitivity volume shape for the measurement of $u_{s,i}$. It was decided that for the probe to give an accurate cross-correlation velocity estimate, the signals from each sensor must have a high frequency content. Signals with high frequency content have been shown by Lucas [86] to give sharp, narrow correlation peaks which allow a more accurate estimate of the location of

the maximum to be made. Additionally, by minimising the flow volume interrogated by the sensors, the sensors will only respond to the motion of individual particles. A number of researchers, including Lucas [87], and Kytomaa & Brennen [88], have noticed that sensors with large sensitivity volumes tend to respond to the passage of large structures, such as waves, which may be present in the flow.

The sensor separation, j, between Sensor A and Sensor B is also important. Beck and Plaskowski [68] have shown that as j decreases the accuracy of the cross-correlation velocity estimate is affected in two ways.

1. The measured time delay, δ, between a particle passing sensor A and Sensor B will decreases as j decreases. For a constant sampling rate this will increase the error in the estimate of δ and therefore in the estimate of $u_{s,i}$. This effect can be countered by increasing the sampling rate. In the current investigation a sample rate of up to 3750Hz could be achieved. Therefore this affect can be effectively negated.

2. The peak value of the normalised cross-correlation function increases as j is decreased. This makes it easier to determine the exact position of the peak and results in increasing accuracy of the cross-correlation velocity estimate. This effect is caused by flow pattern dispersion. Serizawa et al [89] have measured bubble dispersion in bubbly air-water flow. Their results showed motion of the disperse phase is by no means purely axial. Therefore j should be minimised. In the current modelling 16mm is the maximum value of j that has been used.

The field electrode axial length, a, was not varied in this modelling. In Section 3.2.6.2 modelling was carried out to investigate the effect on the sensitivity volume shape of a 4-electrode SEMM array of varying a. Although an effect was noticed it was decided that it could have been caused by the electrode loading in the model. Additionally the effect did not appear to substantially alter the sensitivity volume shape. Therefore a was fixed as single point in all the modelling in this section....

3.2.6.3.1 Observations made from the results of modelling both 6-electrode SEMM arrays and 8-electrode probes.

One trend was immediately identified from the sensitivity volumes constructed. The three sensitivity volume shapes identified from the modelling of 4-electrode SEMM arrays (see 3.2.6.2) can be identified in the modelling of both 6-electrode SEMM arrays and the modelling of 8-electrode probes. However the sensitivity volume for each sensor appears to be compressed by the proximity of the second sensor in each configuration. Examples of this effect in a 6-electrode SEMM array and an 8-electrode probe are shown in Figure 3-24.

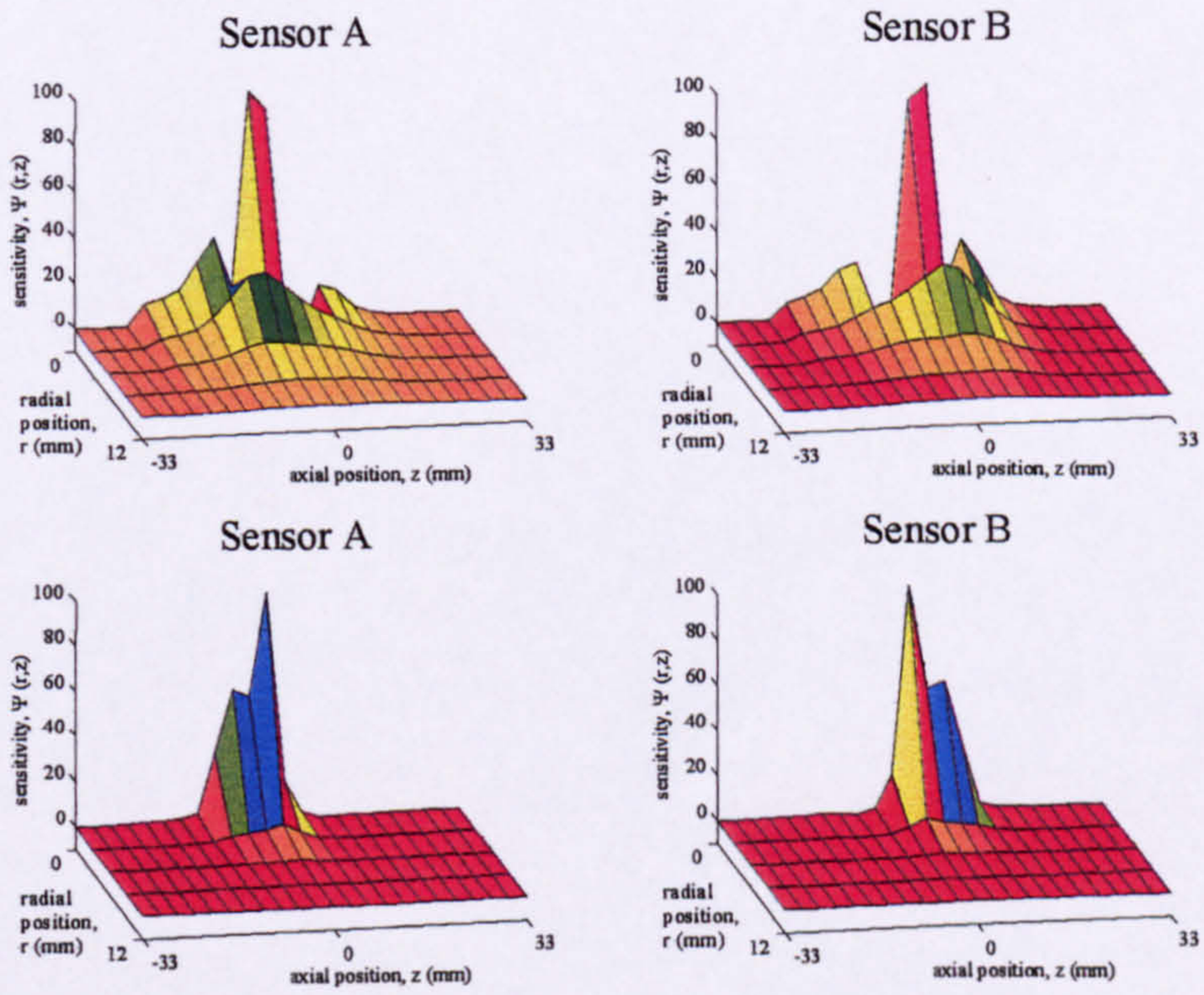

Figure 3-24. Appearance of the 4-electrode SEMM array sensitivity volume shapes in the sensitivity volumes of 6-electrode SEMM arrays and 8-electrode probes.

One effect of this compression is to reduce the size of the sensitivity volumes towards the single point desired for the velocity measurement sensors. These results suggest that operating two sensors in tandem could result in a probe that is better optimised for the measurement of $u_{s,i}$. This effect was investigated experimentally (see Chapter 5).

3.2.6.3.2 Modelling of 8-electrode probes.

This configuration of the probe uses two 4-electrode SEMM arrays as shown in Figure 3-10. As such it has two pairs of field electrodes. Using two pairs of field electrodes there are three patterns in which the electrodes can be excited as shown in Figure 3-25.

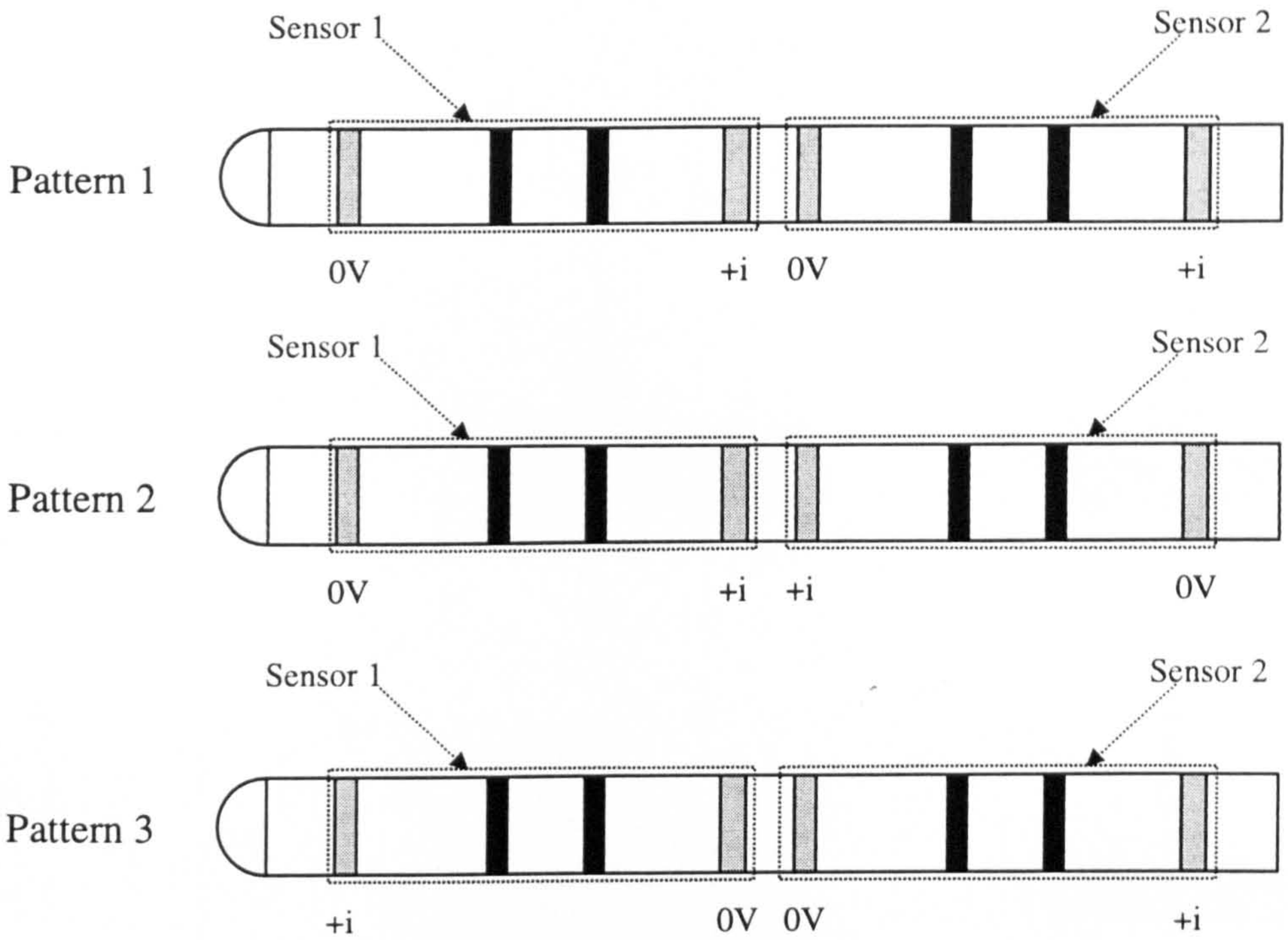

Figure 3-25. Possible excitation patterns for an 8-electrode probe.

The effect on the sensitivity volume shapes of varying the excitation pattern.

Sensitivity volumes were constructed for 8-electrode probes using all three excitation patterns. An example of the effect of each of the three excitation patterns on the sensitivity volumes is shown in Figure 3-26.

Using excitation pattern 1 resulted in similar sensitivity volumes for each sensor. If the excitation patterns are examined (see Figure 3-25) it can be seen that the excitation of Sensor B uses the same orientation as the excitation of Sensor A for excitation pattern one. Therefore it would be expected that the sensitivity volume would be similar.

Using excitation patterns 2 and 3 resulted in sensitivity volumes from each sensor that were approximate mirror images of each other. If the excitation patterns are again examined (see Figure 3-25) it can be seen that the excitation orientation of Sensor B is a mirror image of the excitation orientation of Sensor A for excitation patterns two and three, and that therefore sensitivity volumes that are mirror images of each other would be expected.

Close examination of the modelling results showed that if the differences attributed to the excitation pattern were set aside, the trends in sensitivity volume shape with varying geometry

of the probe were similar with all three excitation patterns. Therefore in the remainder of this section only sensitivity volumes for excitation pattern one have been presented.

Excitation pattern 1
Sensor separation, j = 10mm
Field electrode spacing, f = 7mm
Sense electrode spacing, s_v = 5mm

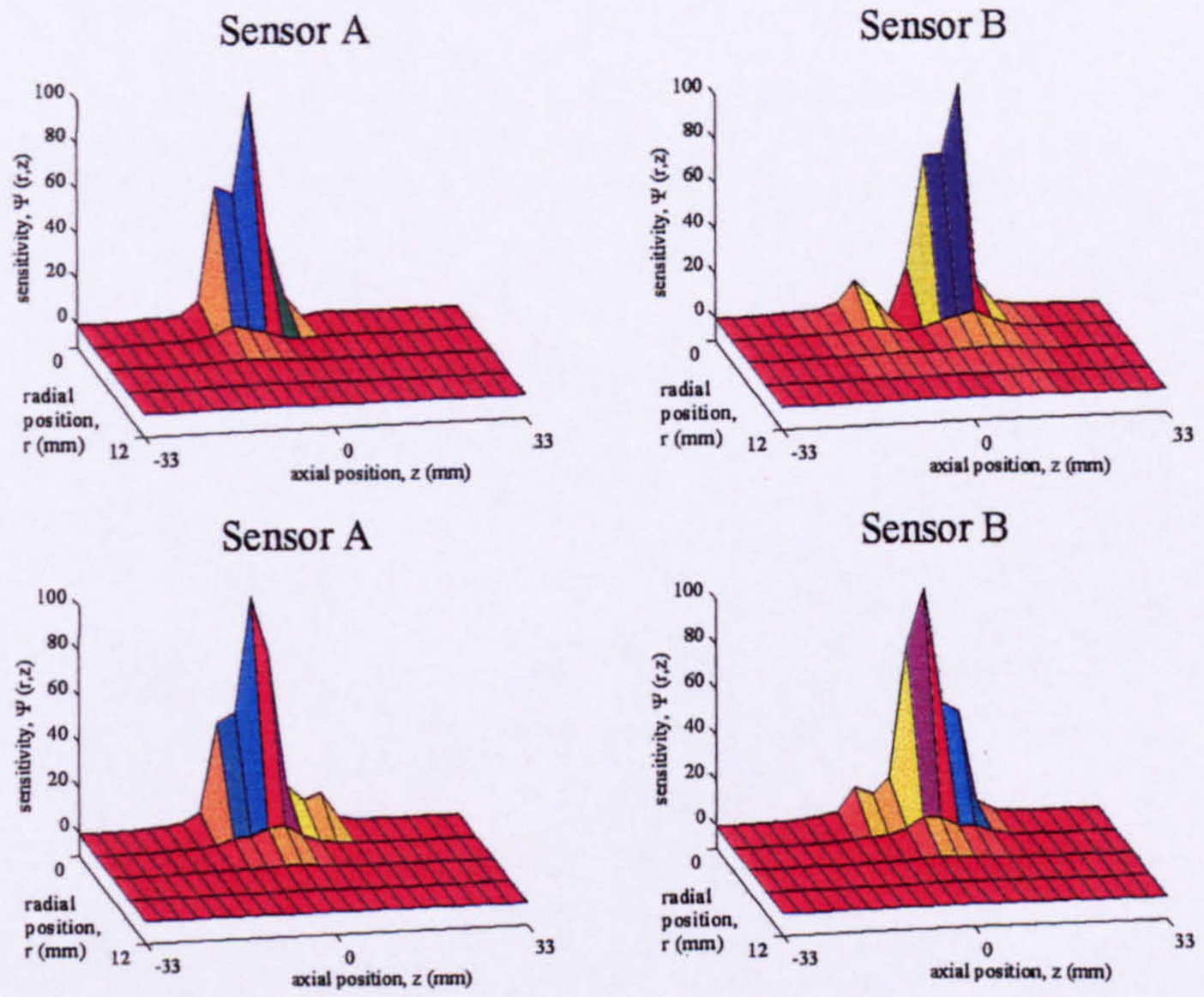

Excitation pattern 2
Sensor separation, j = 10mm
Field electrode spacing, f = 7mm
Sense electrode spacing, s_v = 5mm

Excitation pattern 3
Sensor separation, j = 10mm
Field electrode spacing, f = 7mm
Sense electrode spacing, s_v = 5mm

Figure 3-26. The effect on the sensitivity volume shapes of an 8-electrode probe of varying the excitation pattern.

<u>The effects on the sensitivity volume shapes of varying the sensor separation, j.</u>

Sensitivity volumes were constructed for 8-electrode probes with the two 4-electrode SEMM arrays separated by sensor separations, j, of between 4 and 16mm. The minimum limit of 4mm was represents the smallest 8-electrode probe that could be constructed. The selection of the maximum limit was discussed in Section 3.2.6.3. Representative sensitivity volumes for these probes are presented in Figure 3-27.

Sensor separation, j = 4mm
Field electrode spacing, f = 3mm
Sense electrode spacing, s_v = 1mm

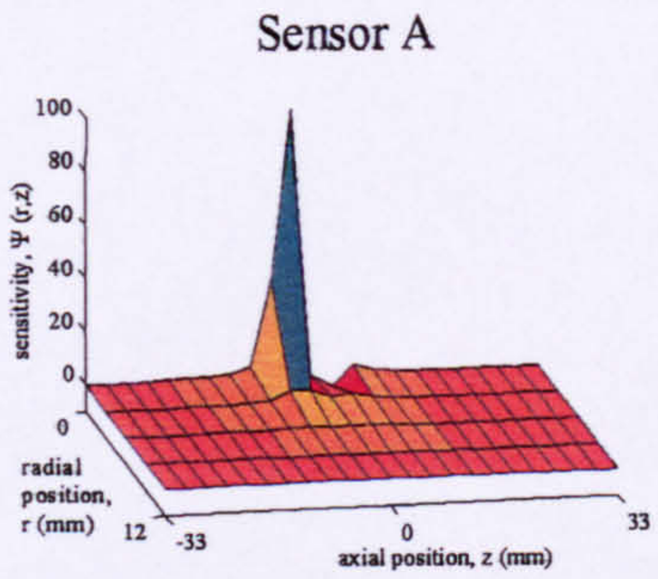

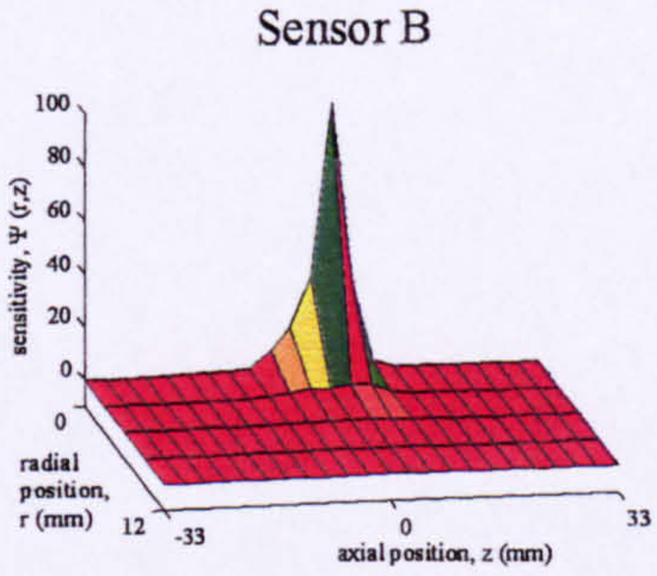

Sensor separation, j = 6mm
Field electrode spacing, f = 3mm
Sense electrode spacing, s_v = 1mm

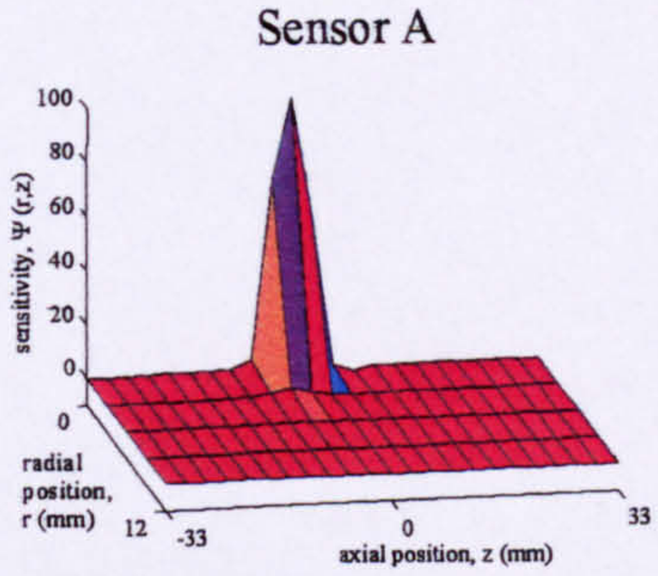

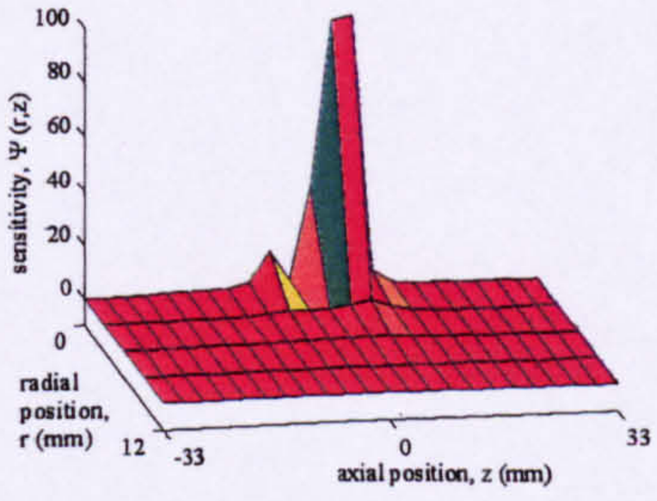

Sensor separation, j = 8mm
Field electrode spacing, f = 3mm
Sense electrode spacing, s_v = 1mm

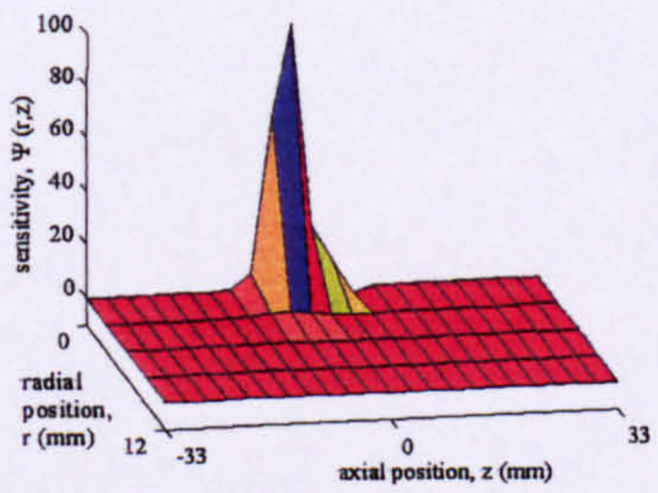

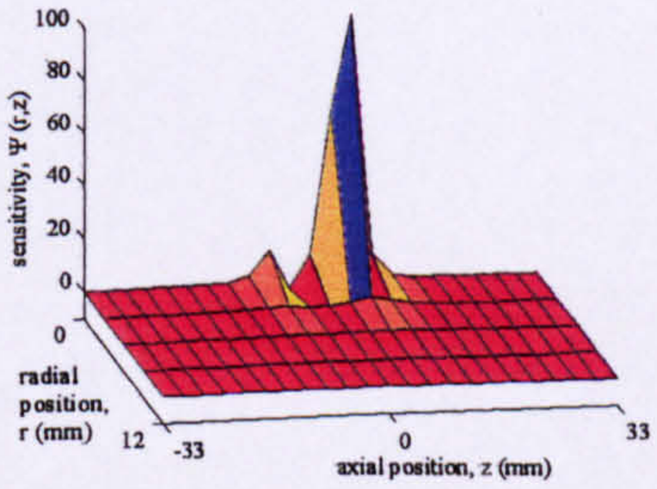

Sensor separation, j = 10mm
Field electrode spacing, f = 3mm
Sense electrode spacing, s_v = 1mm

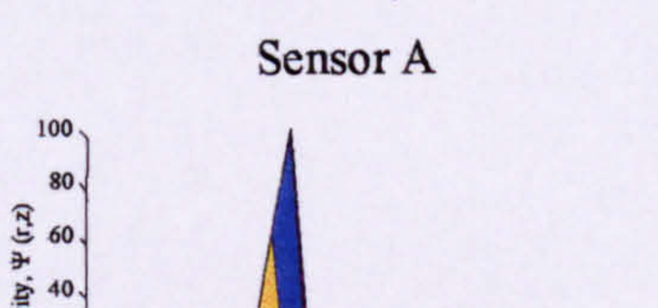

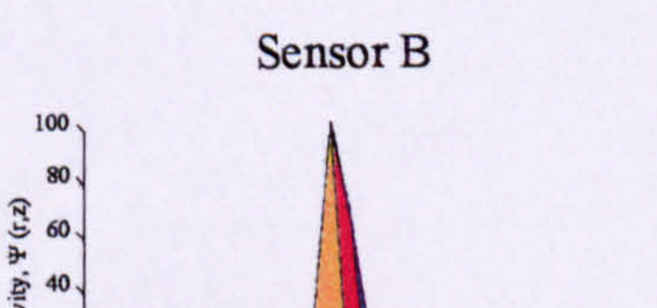

Sensor separation, j = 16mm
Field electrode spacing, f = 3mm
Sense electrode spacing, s_v = 1mm

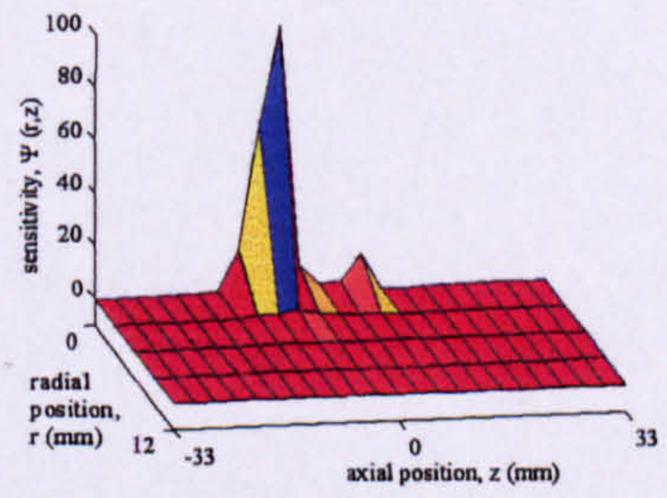

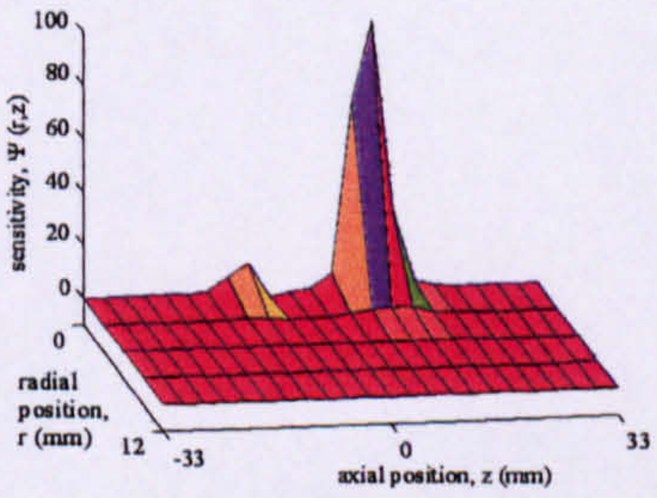

Figure 3-27. The effect on the sensitivity volume shapes of an 8-electrode probe of varying j.

The results in Figure 3-27 show that as j is increased the axial separation between the sensitivity volumes for each sensor increases. This is as expected as axial separation between the two sensors is being increased. Figure 3-27 also shows interference, or "cross-talk", appearing in the sensitivity volumes as j is increased. Cross-talk is an effect which can occur when two sensors, using the same excitation, are placed close together. It is caused by a particle passing one sensor causing a fluctuation in the response of the other. This is shown by the sensitivity volume for each sensor having two distinct peaks separated by an axial distance. The effect of cross-talk is to degrade the cross-correlation of the signals. This is because either peak in the response of sensor A could correlate with either peak in the response of sensor B. It is important to minimise cross-talk in the current investigation and therefore it would be important to minimise j.

<u>The effect on the sensitivity volume shapes of varying the field electrode separation, f.</u>

Sensitivity volumes were constructed for 8-electrode probes with f between 3mm and 11mm. The minimum value of 3mm represents the smallest 8-electrode probe that could be constructed. The maximum value of 11mm is the largest value of f that could integrated with the fixed maximum value of j of 16mm Representative sensitivity volumes from these modelling are presented in Figure 3-28.

From Figure 3-28 it can be seen that varying f has little effect on the sensitivity volume shapes. Although the axial and radial size of the sensitivity volume change, there is no fundamental change shape. This was expected and can be explained by looking at the sensitivity volumes for 4-electrode SEMM arrays with varying f shown in Figure 3-22. From Figure 3-22 it can be seen that the sensitivity volume shape does not change fundamentally as f varies from 3mm to 11mm. In conclusion these results suggest that the field electrode separation is not important for the prediction of the sensitivity volume shape of this type of sensor for the size range considered here.

Sensor separation, j = 16mm
Field electrode spacing, f = 3mm
Sense electrode spacing, s_v = 1mm

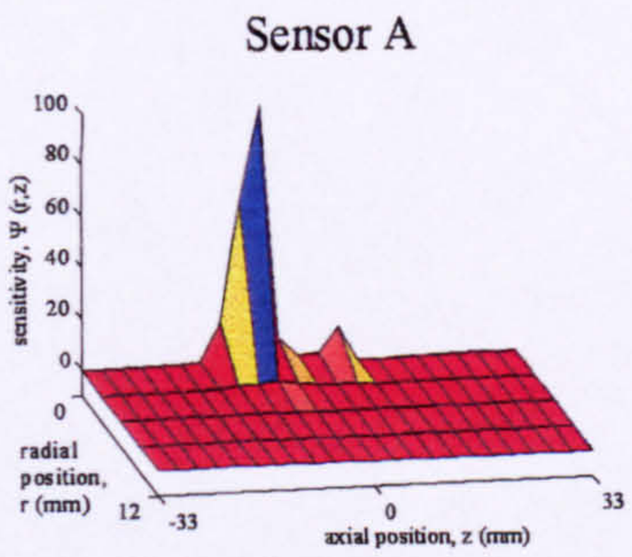

Sensor separation, j = 16mm
Field electrode spacing, f = 5mm
Sense electrode spacing, s_v = 1mm

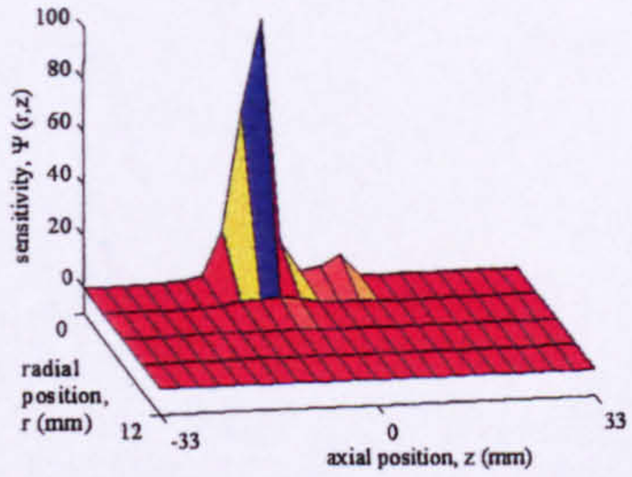

Sensor separation, j = 16mm
Field electrode spacing, f = 7mm
Sense electrode spacing, s_v = 1mm

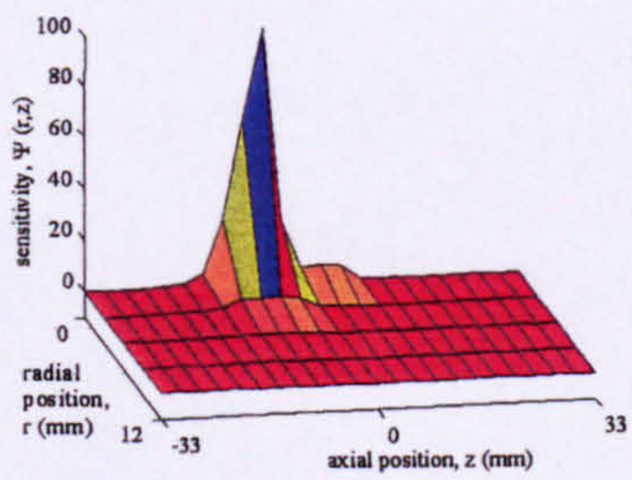

Sensor separation, j = 16mm
Field electrode spacing, f = 9mm
Sense electrode spacing, s_v = 1mm

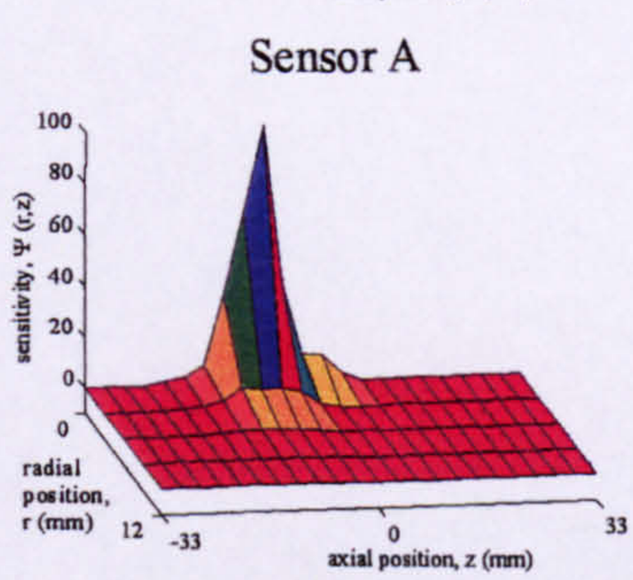

Sensor separation, j = 16mm
Field electrode spacing, f = 11mm
Sense electrode spacing, s_v = 1mm

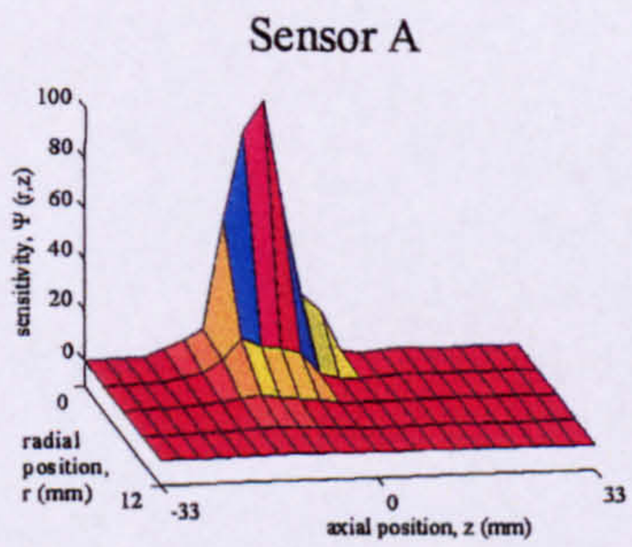

Figure 3-28. The effect on the sensitivity volume shapes of an 8-electrode probe of varying f.

The effect on the sensitivity volume shapes of varying the sense electrode separation, s_v.

Sensitivity volume were constructed for 8-electrode probes with s_v varying between 1mm and 9mm. The minimum value of 1mm represents the smallest 8-electrode probe that could be constructed. The maximum value of 9mm is the largest value of f that could integrated with the fixed maximum value of f of 11mm Representative sensitivity volumes from this modelling are presented in Figure 3-29. For each value of s_v the equivalent sensitivity volume for a 4-electrode SEMM array is also presented.

Figure 3-29 shows that a significant change in the sensitivity volume shape occurs as s_v is altered. At low s_v the sensitivity volume shape is a relatively sharp peak. As s_v is increased the sensitivity volume shape begins to resemble that of the equivalent 4-electrode SEMM array. This leads to the conclusion that s_v should be kept as low as possible if this configuration of sensor is to be used for measurement of $u_{s,i}$.

Sensor separation, j = 16mm
Field electrode spacing, f = 11mm
Sense electrode spacing, s_v= 1mm

Sensor A

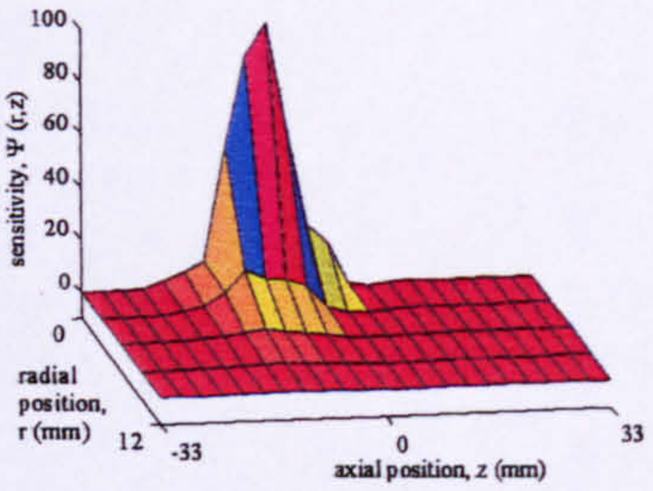

Sensor B

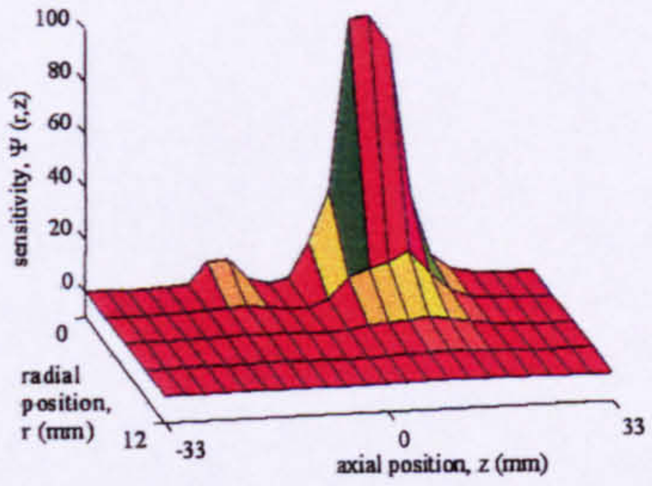

Isolated 4 electrode SEMM array

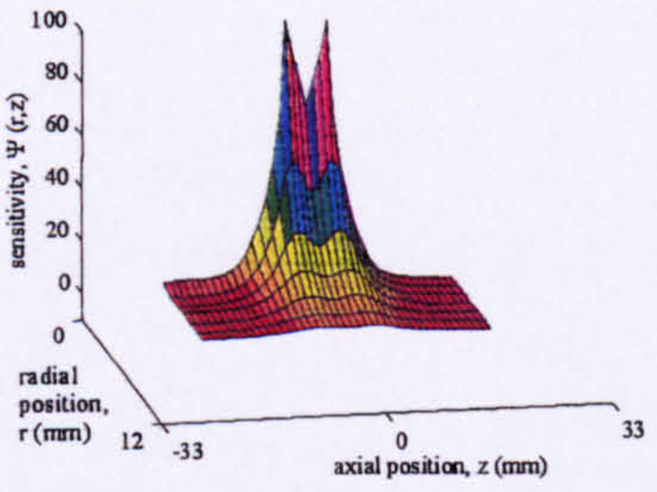

Sensor separation, j = 16mm
Field electrode spacing, f = 11mm
Sense electrode spacing, s_v= 3mm

Sensor A

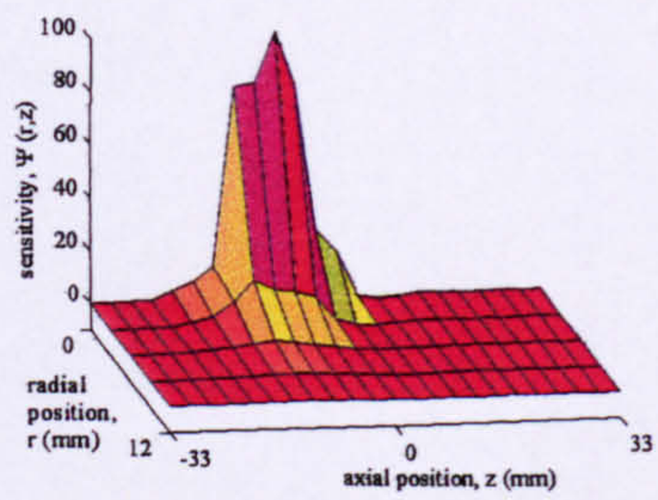

Sensor B

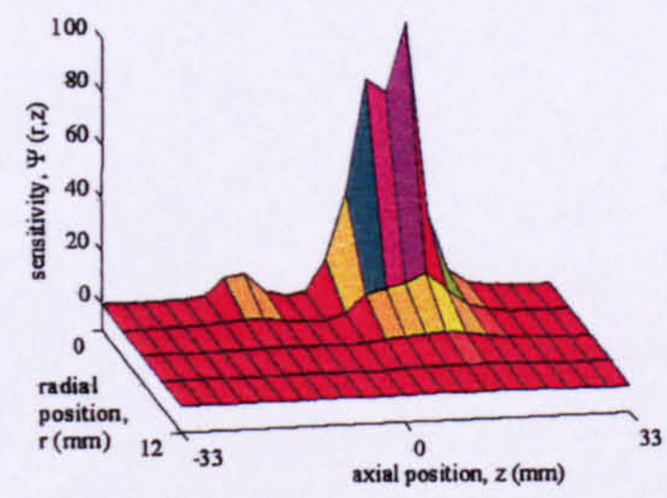

Isolated 4 electrode SEMM array

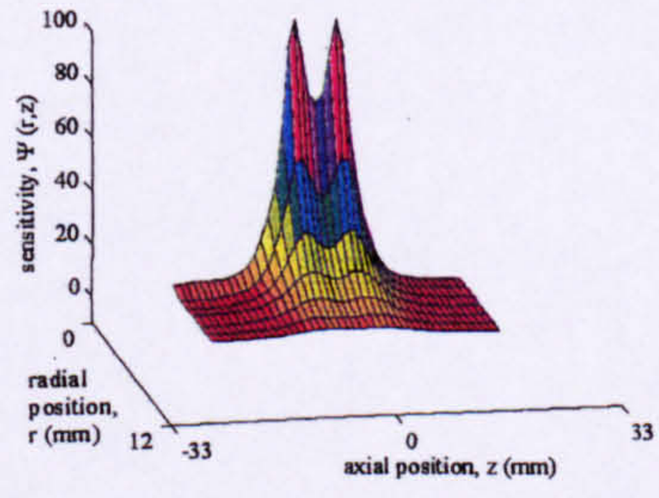

Sensor separation, j = 16mm
Field electrode spacing, f = 11mm
Sense electrode spacing, s_v= 5mm

Sensor A

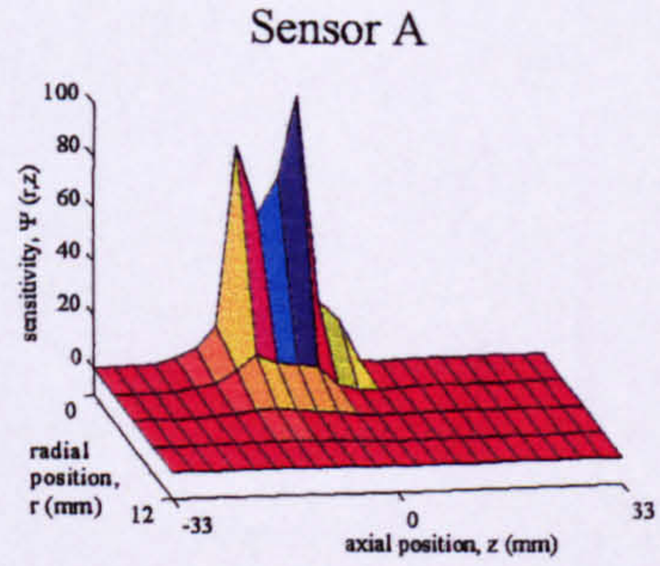

Sensor B

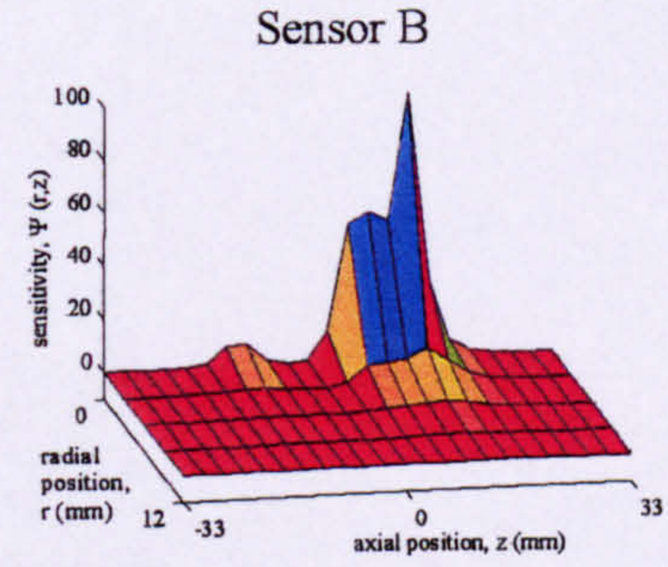

Isolated 4 electrode SEMM array

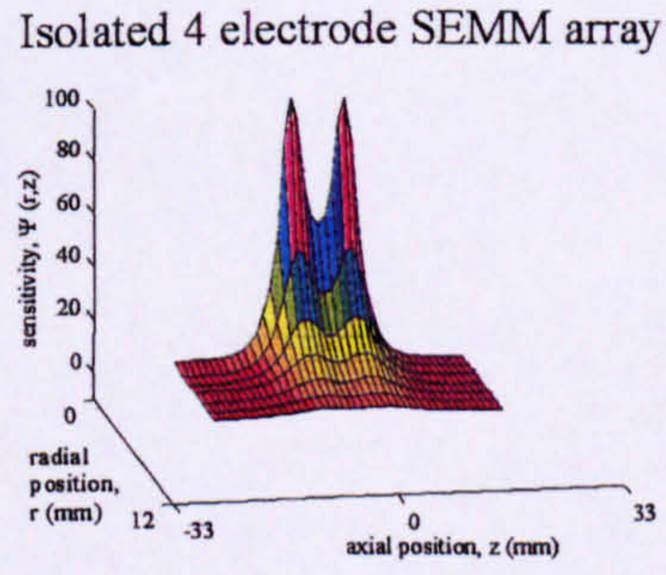

Sensor separation, j = 16mm
Field electrode spacing, f = 11mm
Sense electrode spacing, s_v= 7mm

Sensor A

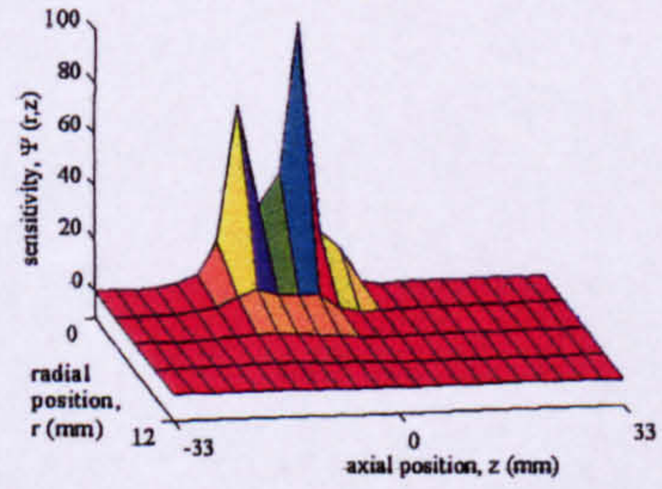

Sensor B

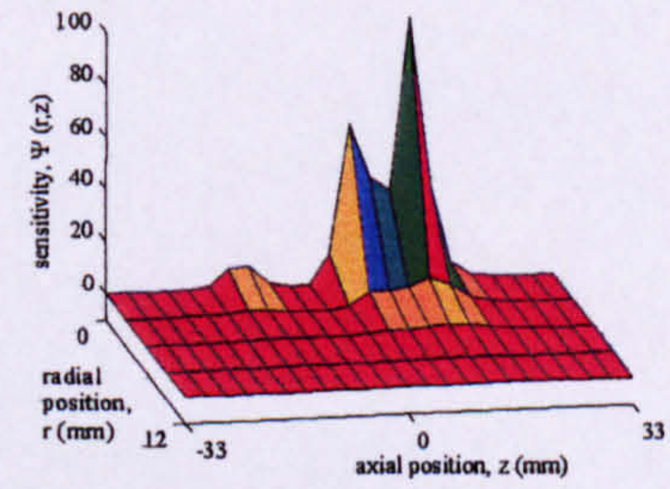

Isolated 4 electrode SEMM array

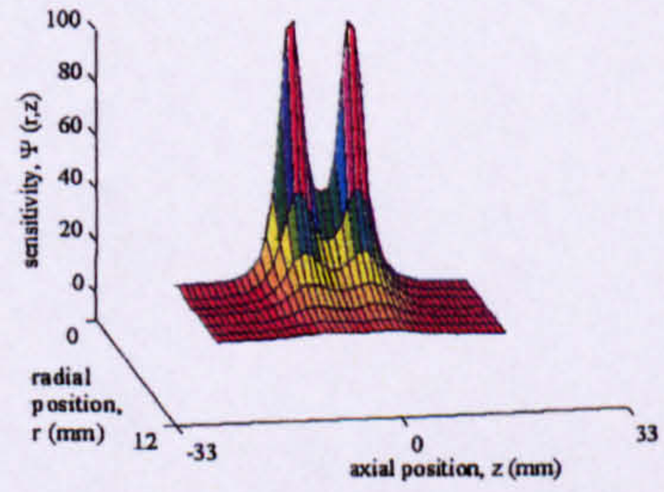

Figure 3-29. The effect on the sensitivity volume shapes of an 8-electrode probe of varying s_v.

3.2.6.3.3 Modelling of 6-electrode SEMM arrays.

The aim of this section of the modelling was to determine the optimum geometry for a 6-electrode SEMM array (see Figure 3-9) for measurement of $u_{s,i}$. This modelling does not relate to the 4-electrode SEMM array that can be assumed to be contained within a 6-electrode SEMM array as shown in Figure 3-7. The effect on the sensitivity volumes of varying three dimensions is presented. These are the sensor separation, j, the field electrode separation, f and the sense electrode separation for the velocity sensors, s_v (see Figure 3-9).

<u>The effect on the sensitivity volume shapes of varying the sensor separation, j.</u>

Sensitivity volumes were constructed for 6-electrode SEMM arrays with j between 2mm and 10mm. The minimum value of 2mm represents the smallest 6-electrode SEMM array that could be constructed. The maximum value of 10mm is the largest value of j that could integrated with a fixed maximum value of f of 19mm. 19mm was selected as the maximum value of f as it is the largest f at which a shape 2 sensitivity volume shape could easily be identified in Section 3.2.6.2. Therefore if the array were used to acquire combination measurements of $\alpha_{s,i}$ and $u_{s,i}$ as shown in Figure 3-7, 19mm is the largest value of f that would be selected. Representative sensitivity volumes from this modelling are presented in Figure 3-30.

Figure 3-30 shows that as j is increased the axial and radial width of the sensitivity volumes decreases. This suggests that j should be maximised. However, as discussed at the beginning of Section 3.2.6.3, j should be minimised in order to reduce the effects of flow pattern dispersion. Therefore it was important to determine whether variation of any of the other dimensions of the array could help to achieve an optimum sensitivity volume shape at low j.

Sensor separation, j **= 2mm**
Field electrode spacing, f = 13mm
Sense electrode spacing, s_v = 1mm

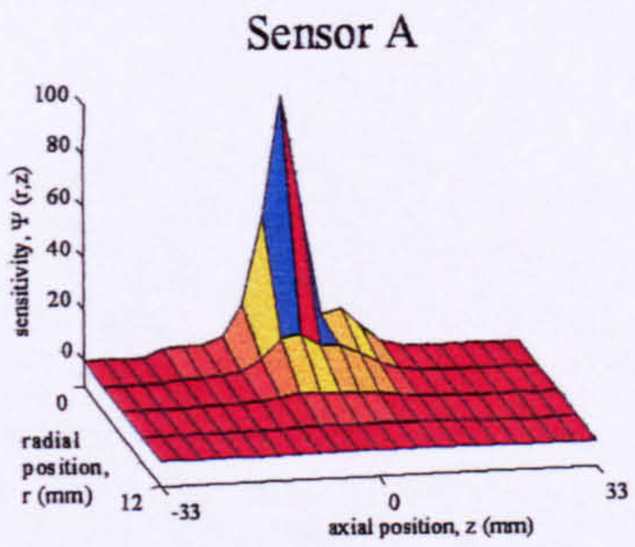

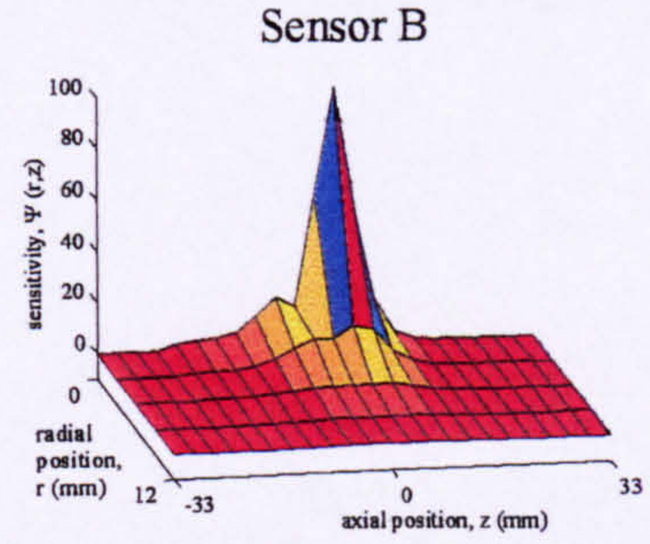

Sensor separation, j **= 4mm**
Field electrode spacing, f = 13mm
Sense electrode spacing, s_v = 1mm

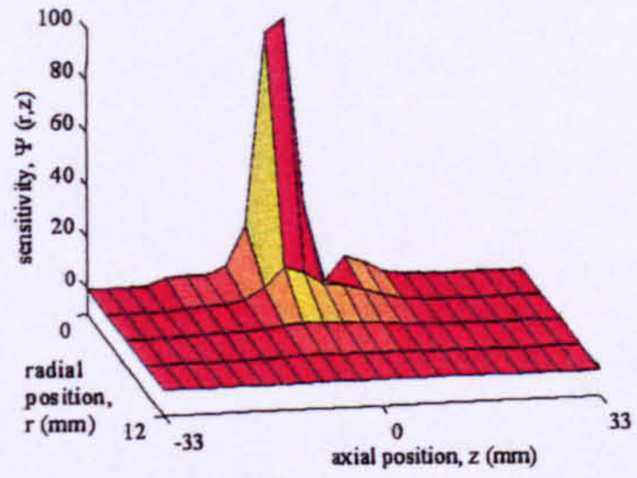

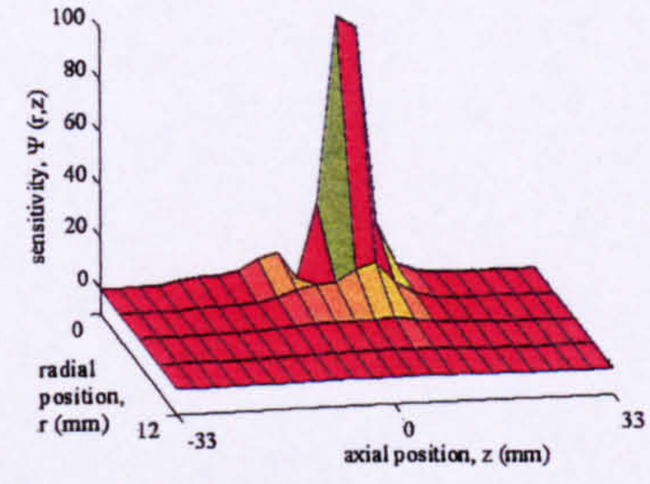

Sensor separation, j **= 6mm**
Field electrode spacing, f = 13mm
Sense electrode spacing, s_v = 1mm

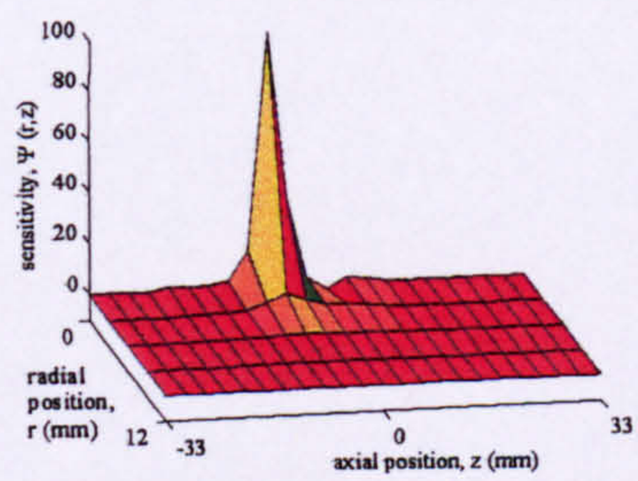

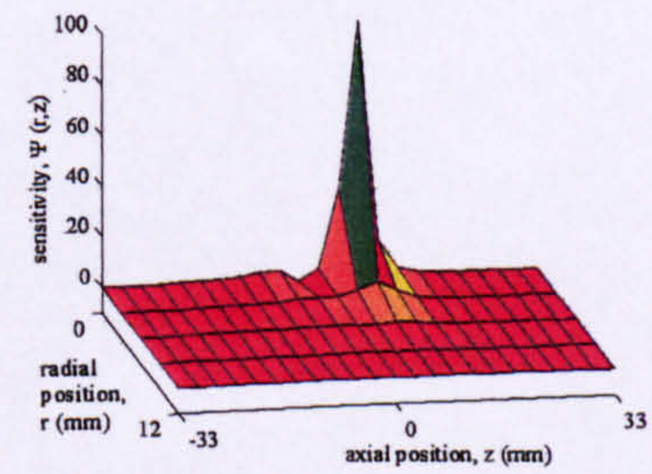

Sensor separation, j **= 8mm**
Field electrode spacing, f = 13mm
Sense electrode spacing, s_v = 1mm

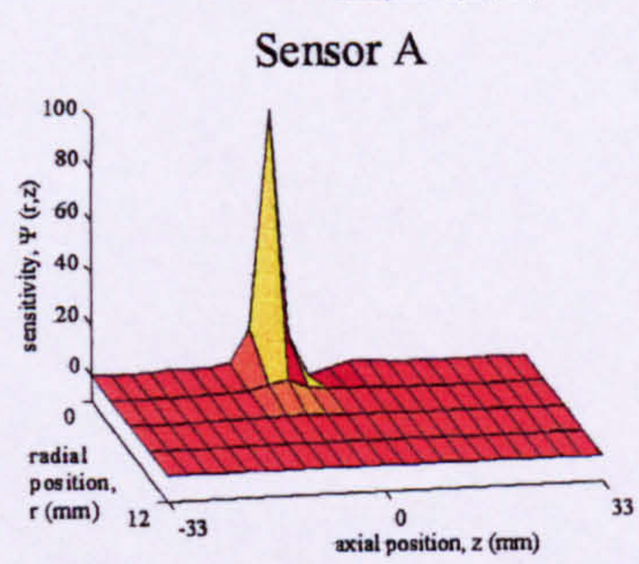

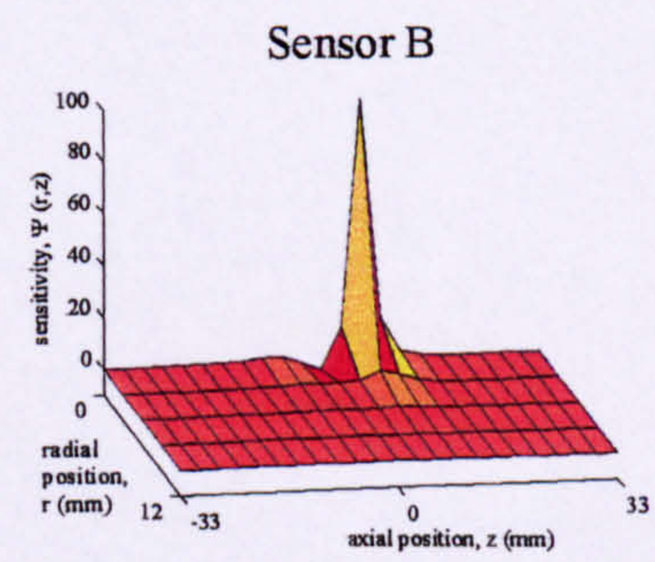

Sensor separation, j **= 10mm**
Field electrode spacing, f = 13mm
Sense electrode spacing, s_v = 1mm

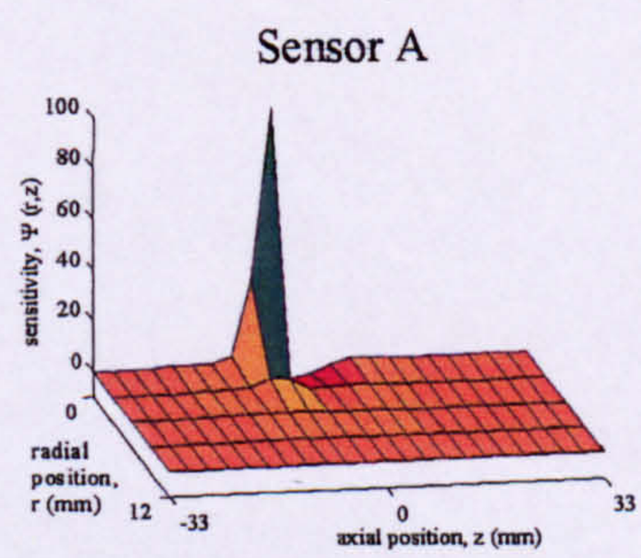

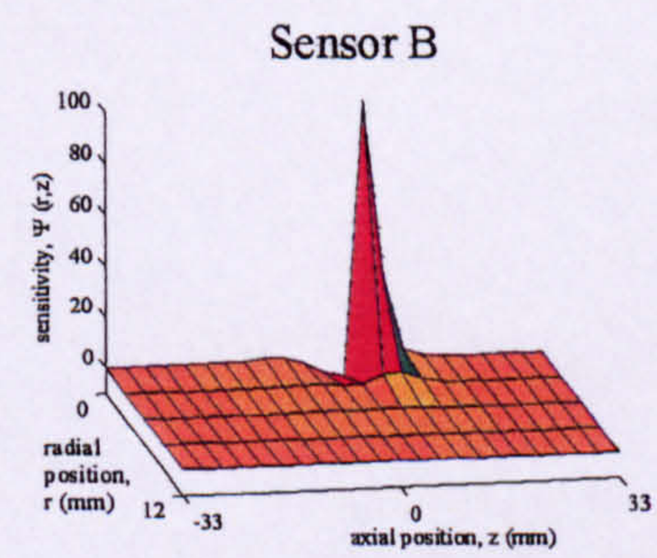

Figure 3-30. The effect on the sensitivity volumes shapes of a 6-electrode SEMM array of varying j.

The effect on the sensitivity volume shapes of varying the field electrode separation, f.

Sensitivity volumes were constructed for 6-electrode SEMM arrays with f between 5mm and 19mm. The minimum value of 5mm represents the smallest 6-electrode SEMM array that could be simulated. The selection of the maximum value of 19mm has been discussed previously. Representative sensitivity volumes from this modelling are shown in Figure 3-31.

Figure 3-31 shows that the size of the sensitivity volume increases as f is increased. However the sensitivity volume shape cannot be predicted from the value of f alone. It has already been shown in Figure 3-30 that the sensitivity volume shape is optimised as j is increased. Therefore the combined results show that the sensitivity volume shapes of a 6-electrode SEMM array are optimised if f is minimised with respect to j.

Sensor separation, j = 4mm
Field electrode spacing, f = 11mm
Sense electrode spacing, s_v = 3mm

Sensor separation, j = 4mm
Field electrode spacing, f = 13mm
Sense electrode spacing, s_v = 3mm

Sensor separation, j = 4mm
Field electrode spacing, f = 15mm
Sense electrode spacing, s_v = 3mm

Sensor separation, j = 4mm
Field electrode spacing, f = 17mm
Sense electrode spacing, s_v = 1mm

Sensor separation, j = 4mm
Field electrode spacing, f = 19mm
Sense electrode spacing, s_v = 1mm

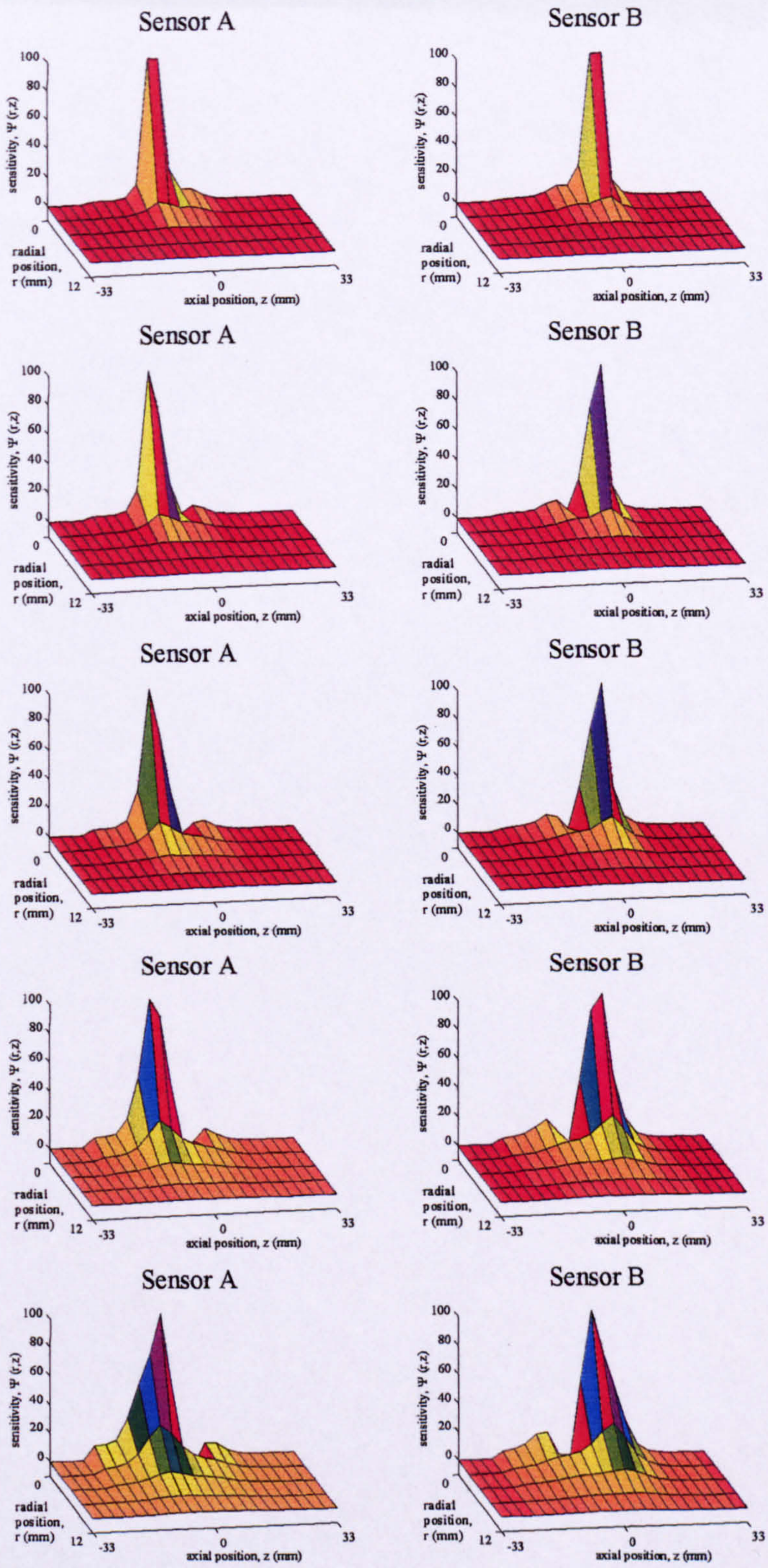

Figure 3-31. The effect on the sensitivity volume shapes of a 6-electrode SEMM array of varying f.

The effect on the sensitivity volume shape of varying the sense electrode separation, s_v.

Sensitivity volumes were constructed for 6-electrode SEMM arrays with s_v of 1mm, 3mm, 5mm and 7mm. The minimum value of 1mm is the smallest value that could be simulated. The largest value 7mm represents the largest value of s_v that could be accommodated within the fixed maximum value of f of 19mm. Representative results from this modelling are presented in Figure 3-32.

Sensor separation, j = 8mm
Field electrode spacing, f = 19mm
Sense electrode spacing, s_v= 1mm

Sensor separation, j = 8mm
Field electrode spacing, f = 19mm
Sense electrode spacing, s_v= 3mm

Sensor separation, j = 8mm
Field electrode spacing, f = 19mm
Sense electrode spacing, s_v= 5mm

Sensor separation, j = 8mm
Field electrode spacing, f = 19mm
Sense electrode spacing, s_v= 7mm

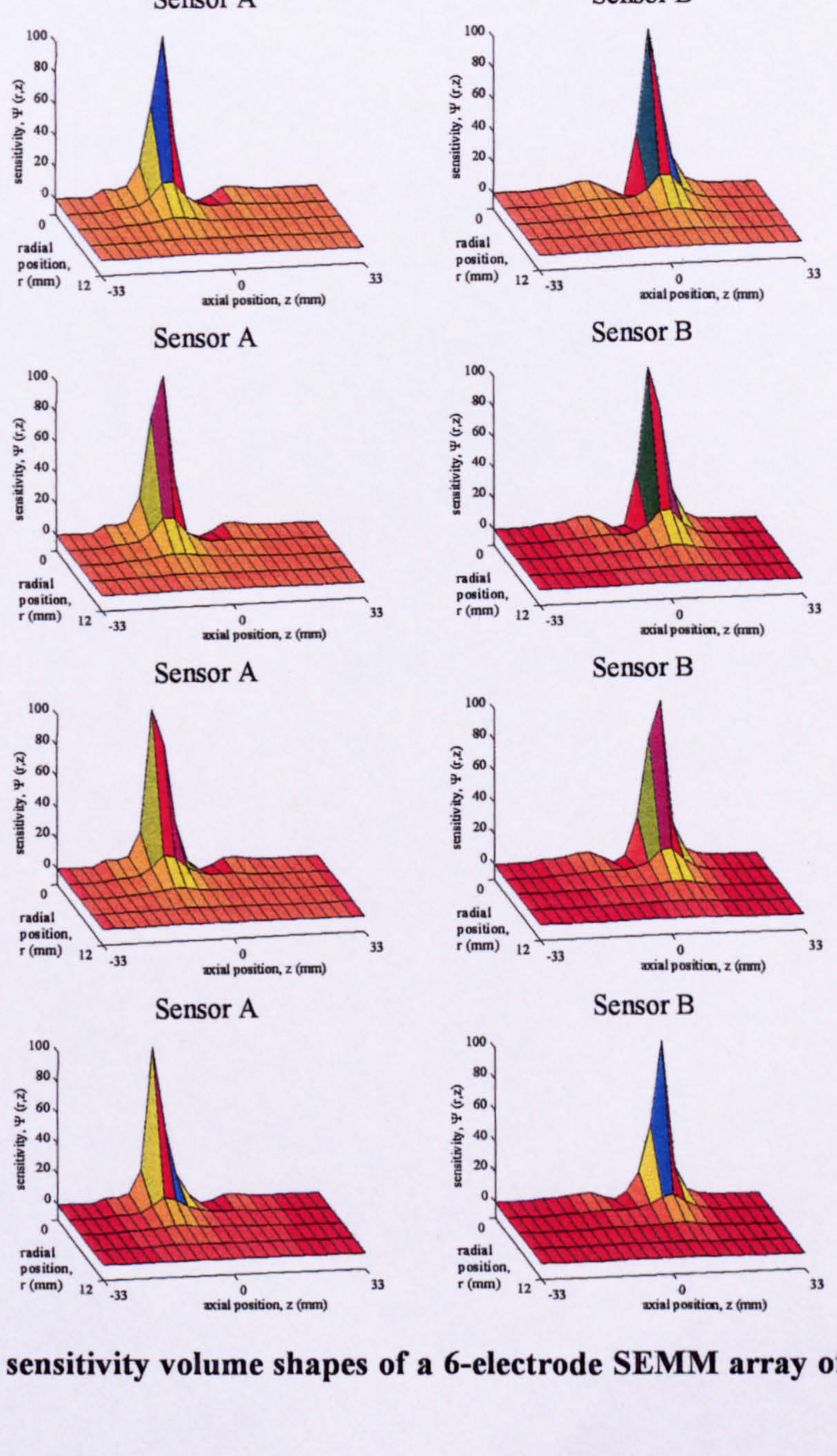

Figure 3-32. The effect on the sensitivity volume shapes of a 6-electrode SEMM array of varying s_v.

Figure 3-32 shows variation of s_v appears to have little effect on the sensitivity volume shapes. Therefore it can be concluded that the only dimensions that should be carefully controlled when optimising a 6-electrode SEMM array for measurement of $u_{s,i}$ are j and f.

3.2.7 Conclusions of the finite element modelling of the probe.

It is important to note that the results of the finite element modelling are qualitative. In order to validate them experimental testing has been carried out (see Chapter 5). However the modelling results did suggest a number of guidelines for the optimisation of 4-electrode SEMM arrays, 6-electrode SEMM arrays and 8-electrode probes.

For a 4-electrode SEMM array, for measurement of $\alpha_{s,i}$, it was decided that the sensitivity volume shape should be large relative to the volume of the individual particles, and should have high, uniform sensitivity over as much of the sensitivity volume as possible. In Section 3.2.6.2 it was shown that it is important to select the combination of f and s_α carefully in order to achieve the optimum sensitivity volume shape. The results suggested that a direct relationship existed between the optimal values of f and s_α. However there were an inadequate number of results to predict this relationship.

The modelling of 6-electrode SEMM arrays and 8-electrode probes for cross correlation solids velocity measurement gave more surprising results. It was decided in Section 3.2.6.3 that the optimum sensitivity volume shape for this measurement would have high sensitivity over as small an area as possible. Much of the previous work in the literature in this area has concentrated on isolating the two axially displaced sensors, Sensor A and Sensor B, from each other to prevent cross-talk. The finite element modelling carried out in the present investigation, and presented in 3.2.6.3, suggested that cross-talk can be minimised without isolating the sensors. It also suggested that if the sensors are not isolated from each other their interaction can actually improve the sensitivity volume shape.

Optimum sensitivity volume shapes for the measurement of $u_{s,i}$ were achieved for both 6-electrode SEMM arrays and for 8-electrode probes. However it was important to be able to make measurements of both $u_{s,i}$ and $\alpha_{s,i}$ in the current investigation. It was stated above that the interference between Sensor A and Sensor B could improve the sensitivity volume shapes for measurement of $u_{s,i}$ for both configurations. However this has the effect of rendering both

sensors unsuitable for measurement of $\alpha_{s,i}$ as the optimum sensitivity volume shapes for each measurement are very different. In the case of the 8-electrode probe this means that a third, isolated, sensor for measurement of $\alpha_{s,i}$ would be required. However this is not the case for the 6-electrode SEMM array. In Section 3.1.3.3 and Figure 3-7 a method by which three independent measurements could be acquired from one 6-electrode SEMM array was outlined. This involves configuring sense electrodes S_1 and S_2 as Sensor A, and sense electrodes S_3 and S_4 as Sensor B. The measurements acquired from these sensors are cross-correlated to give a measurement of $u_{s,i}$. Sense electrodes S_2 and S_3 are configured as Sensor C which can be used to make an independent measurement of $\alpha_{s,i}$. As this would allow both measurements to be acquired simultaneously it was decided that this would be the optimum configuration for the current investigation.

In order for the combined solids volume fraction and solids velocity measurement to be possible it is important to be able to optimise the sensitivity volumes of sensor A, sensor B and sensor C. For sensor C it is important that both f and s_α, should be chosen carefully (see Section 3.2.6.2). For sensors A and B it is important that both j and f be chosen carefully, whilst the value of s_v is not critical (see Section 3.2.6.3.3). Therefore there are three critical dimensions, j, f and s_α, that must be combined in order to give a 6-electrode SEMM array that is optimised for combination measurement of both $\alpha_{s,i}$ and $u_{s,i}$. The finite element modelling results suggested four optimum geometries. The dimensions of these are presented in Table 3-2. The relevant sensitivity volumes are presented in Figure 3-33.

Table 3-2. Optimum array geometries for combination measurement of $\alpha_{s,i}$ and $u_{s,i}$.

Sensor Separation (j), (mm)	Field electrode separation (f), (mm)	Sense electrode separation (s_α), (mm)	Sense electrode separation (s_v), mm
6	13	1	5
6	13	3	3
6	15	5	1
8	15	5	3

Sensor α

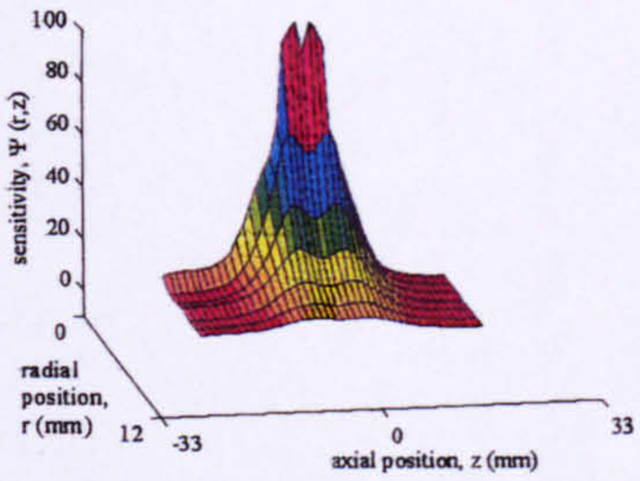

Sensor separation, j = 6mm
Field electrode spacing, f = 13mm
Sense electrode spacing, s_α = 1mm
Sense electrode spacing, s_v = 5mm

Sensor A

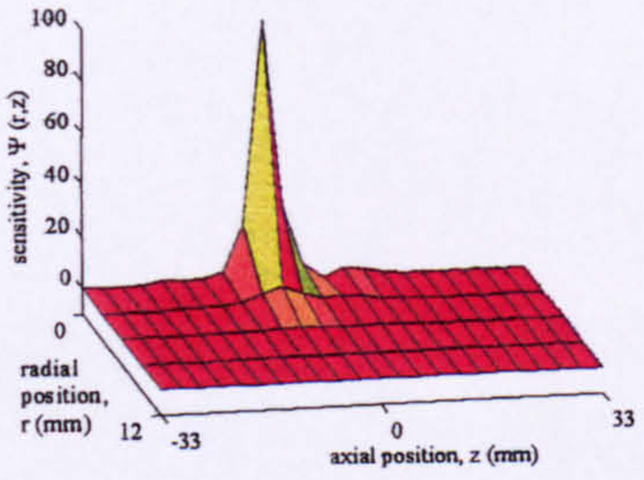

Sensor B

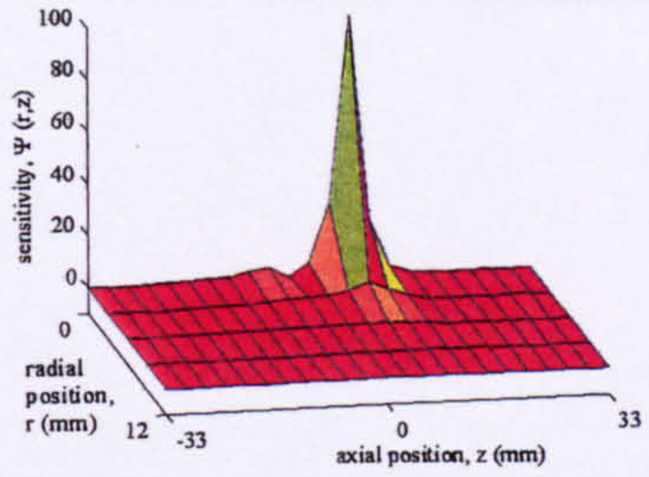

Sensor α

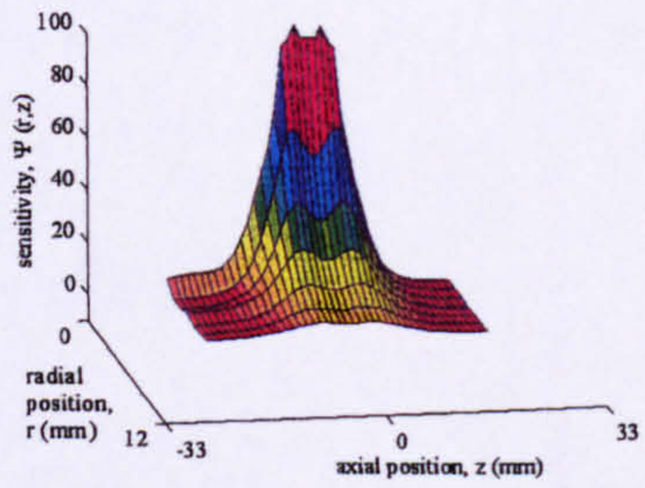

Sensor separation, j = 6mm
Field electrode spacing, f = 13mm
Sense electrode spacing, s_α = 3mm
Sense electrode spacing, s_v = 3mm

Sensor A

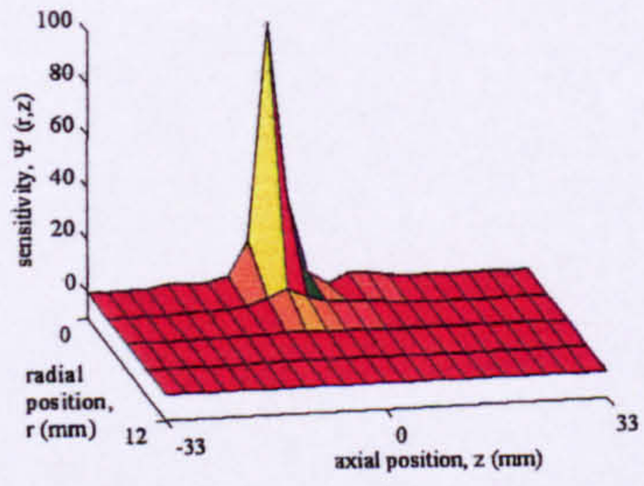

Sensor B

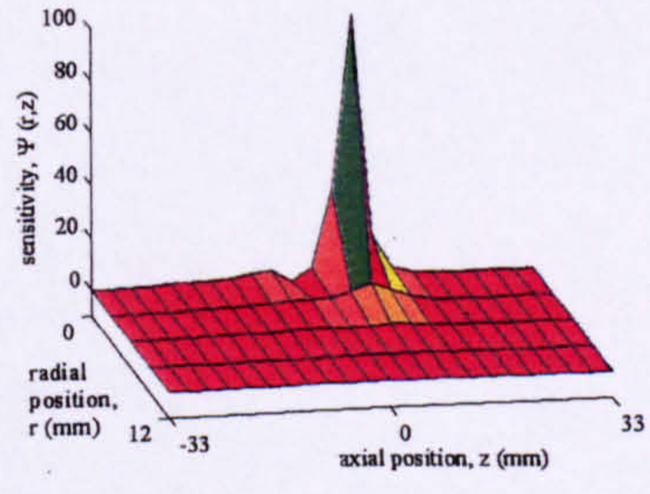

Sensor α

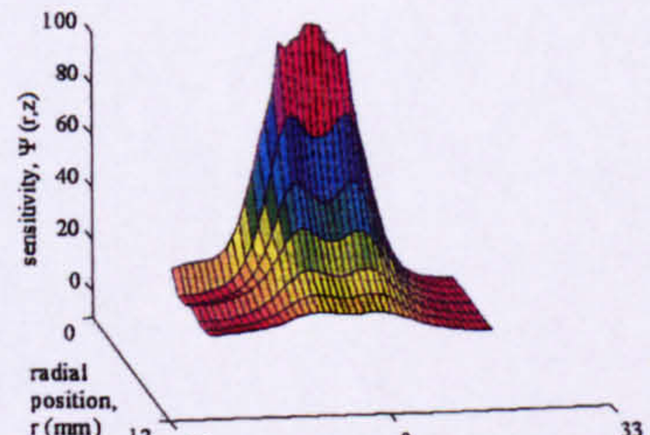

Sensor separation, j = 6mm
Field electrode spacing, f = 15mm
Sense electrode spacing, s_α = 5mm
Sense electrode spacing, s_v = 1mm

Sensor A

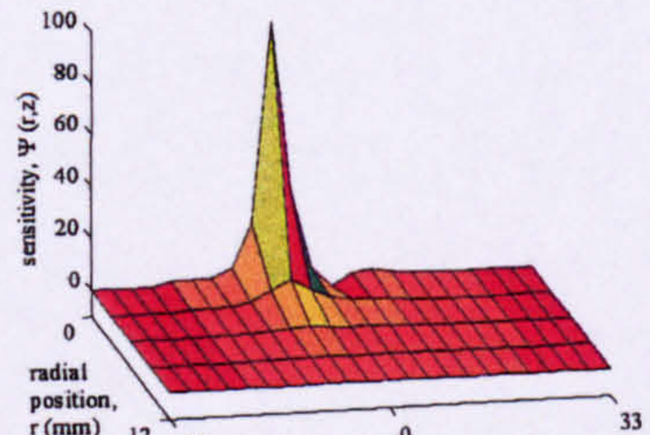

Sensor B

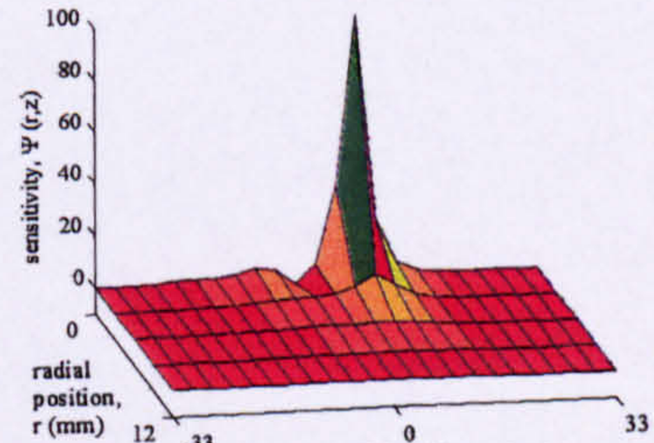

Sensor α

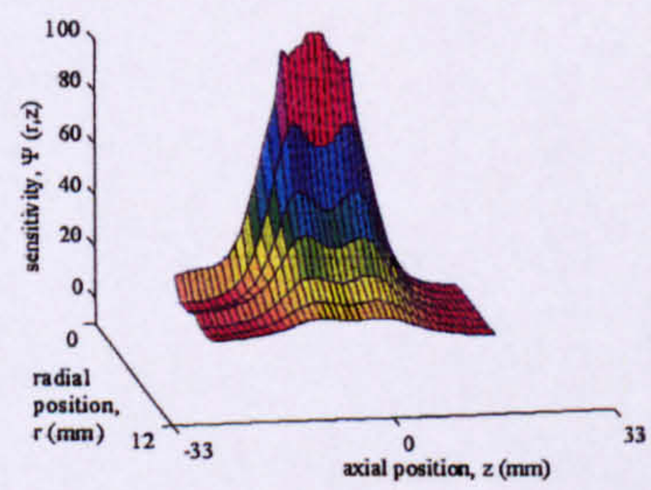

Sensor separation, j = 8mm
Field electrode spacing, f = 15mm
Sense electrode spacing, s_α = 5mm
Sense electrode spacing, s_v = 3mm

Sensor A

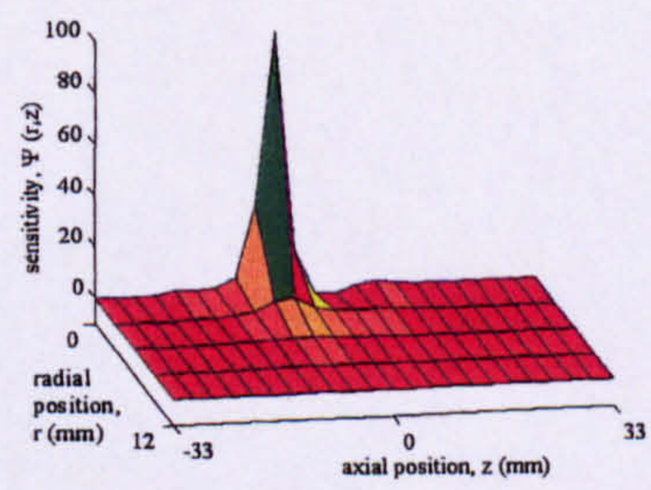

Sensor B

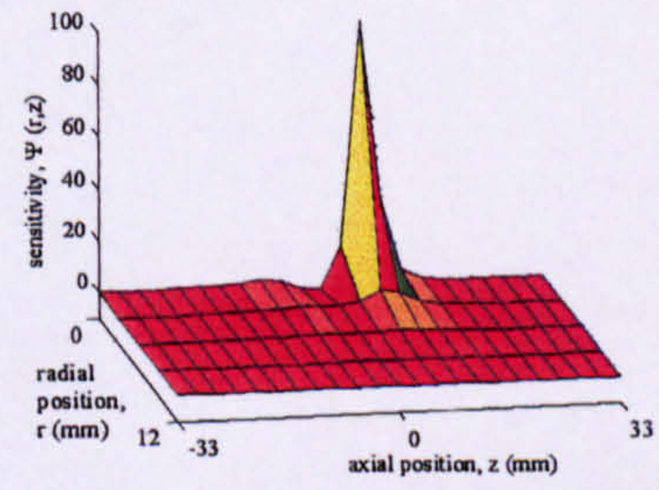

Figure 3-33. Optimum configurations of 6-electrode SEMM array for combination solids volume fraction and velocity measurement.

4. Construction of the local probe and ancillaries.

4.1 The local probe.

The main problem with manufacturing the measurement probes was achieving a small enough overall size. It had been decided (see Chapter 2) that the probes had to have the smallest diameter realistically possible in order to present minimal interference to the flow. The finite element analysis (see Chapter 3) had suggested that the probe should be configured as a 6-electrode SEMM array and that the length of the array should be no more than 15mm. The finite element analysis had also indicated a number of ways in which the behaviour of the probe would change as the electrode separations and configuration were changed. In order to experimentally test these alternative probe configurations (see chapter 5) a different probe would be required for each configuration. This meant that a relatively large number of different probes were required.

Making such small probes out of separate components would be time consuming and would involve intricate machining. A better solution was to mould each probe as a solid device. This is a method that has been used by a number of researchers, including Nasr-El-Din et al [52] and Thang & Davis [46] who constructed probes for monitoring pipe flow, and Ridd [19] who used this method of manufacture to construct oceanographic probes with ring electrodes. Moulding the probes gives high strength for a relatively small size. It also allows a wide variety of configurations to be constructed with very little tooling because probes with different configurations and geometries can be manufactured in the same mould. For the current investigation a low viscosity epoxy resin, CIBA CY1301, was chosen as the moulding material and a steel mould was designed and manufactured. The probe construction method is described below and shown in Figure 4-1.

1. A "former" is cut from nylon tube with a 4mm outside diameter. Ring grooves are cut around the former at the desired positions of the electrodes and a hole is drilled through the former at each of these positions. The nylon former allows the electrodes to be accurately positioned and forms their ring shape.

2. The electrode wires are positioned around the former at the ring grooves. The insulated remainder of each electrode wire runs through the hole in the former, up through the

former and through a stainless steel L-shaped probe carrier. The wires are 0.25mm diameter silver plated copper single conductor with Tefzel insulation. The L-shaped probe carrier is a stainless steel tube with a 4mm outside diameter.

3. This assembly is clamped into the mould and the epoxy resin is injected into it, encapsulating the wiring and the former. The resin also bonds the former to the probe carrier and creates a smooth profile. Following the moulding the external surface of the electrodes is cleaned of any traces of epoxy resin.

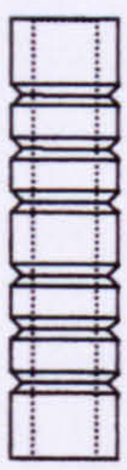

1. The electrode grooves are cut into the former.

2. The wire electrodes are fixed to the former and the assembly is placed in one half of the mould with the stainless steel probe holder.

3. The two halves of the mould are clamped together and epoxy resin is injected into it. The final probe is small, rigid, and has a smooth profile.

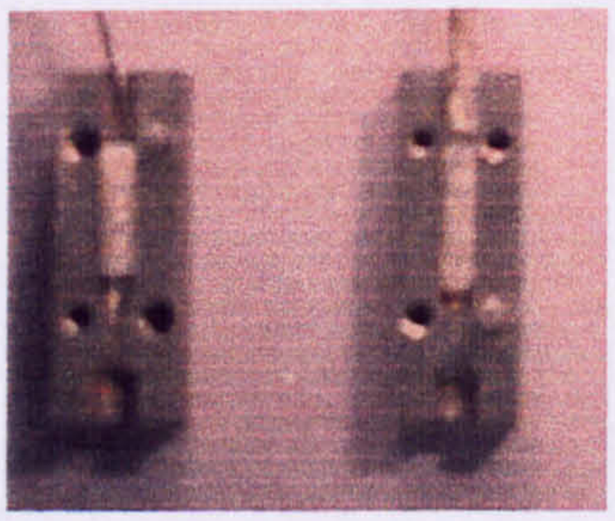

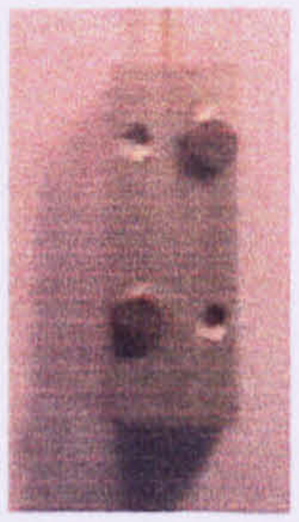

Figure 4-1. The probe construction method shown schematically and by photograph.

4.2 The measurement electronics.

4.2.1 Electronics design for the 6-electrode SEMM array.

As described in Chapter 3, the completed local probe design consists of a 6-electrode SEMM array as shown in Figure 4-2. An AC excitation is applied between the two outermost, field, electrodes, F_1 and F_2. Voltages are measured between different combinations of pairs of the four inner, sense, electrodes, S_1-S_4, in order to measure $\alpha_{s,i}^{probe}$, the local solids volume fraction and $u_{s,i}^{probe}$, the local solids axial velocity.

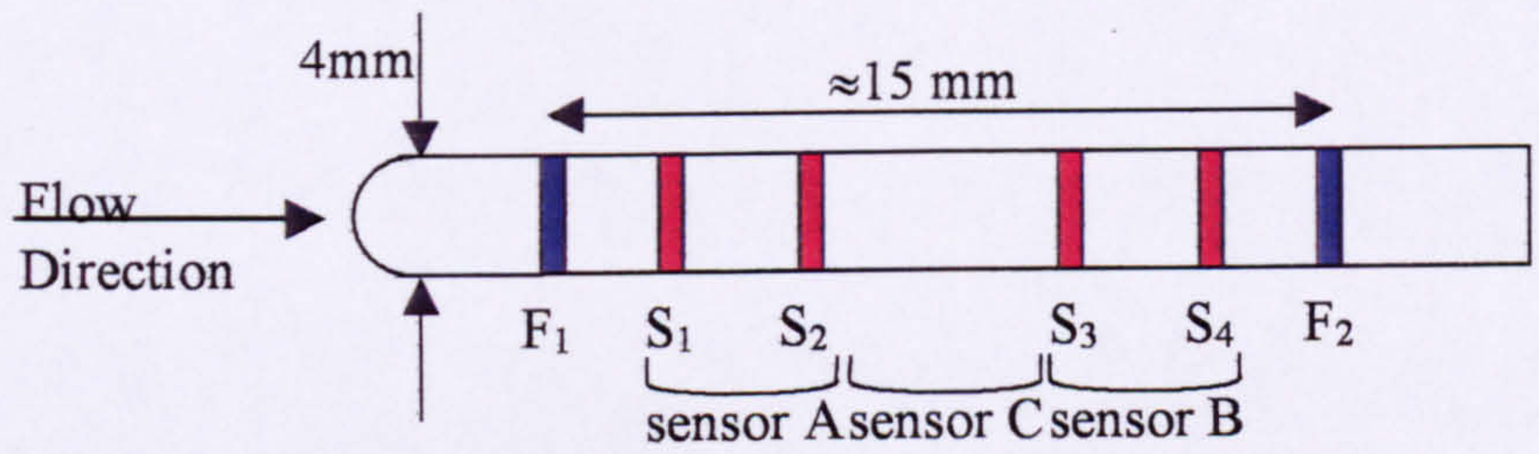

Figure 4-2. Schematic representation of a 6-electrode SEMM array.

The electrical principle for the excitation and voltage measurement is shown in Figure 4-3.

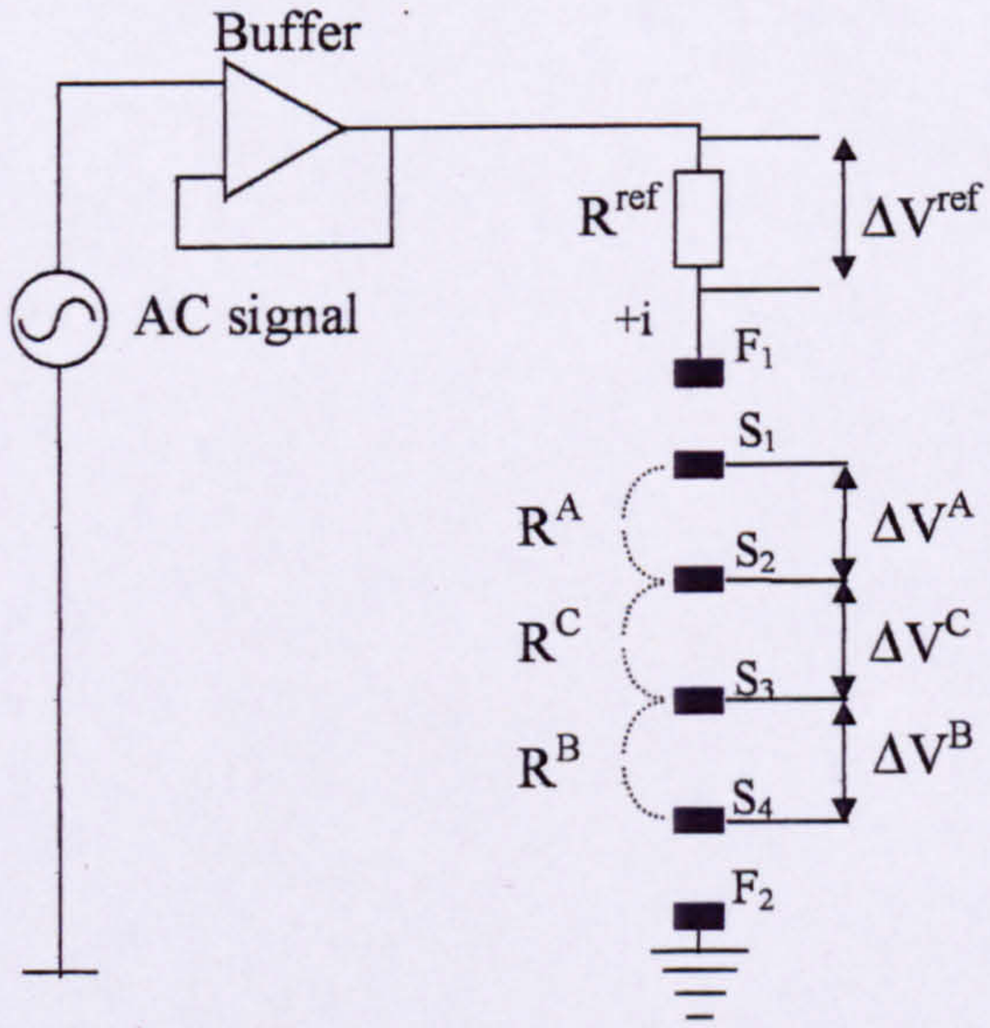

Figure 4-3. The electrical principle of the measurement used in the local probe.

An AC excitation is applied to field electrode F_1. Field electrode F_2 is held at earth potential. The applied excitation signal gives rise to a sinusoidally varying current i, as shown in Figure 4-3, which causes the sinusoidal voltage drops shown in Figure 4-3 as ΔV^A, ΔV^B, ΔV^C and ΔV^{ref}. As all the loads are effectively purely resistive these voltage drops are all in phase with the excitation signal. The amplitudes of ΔV^A, ΔV^B, and ΔV^C are proportional to the fluid

resistances, R^A, R^B, and R^C, between each respective pair of sense electrodes as shown in Figure 4-3 and Equation 4-1. The amplitude of ΔV^{ref} is similarly proportional to R^{ref}.

$$\text{(i)}\, R^A = \frac{|\Delta V^A|}{|i|} \quad \text{(ii)}\, R^B = \frac{|\Delta V^B|}{|i|} \quad \text{(iii)}\, R^C = \frac{|\Delta V^C|}{|i|} \quad \text{(iv)}\; R^{ref} = \frac{|\Delta V^{ref}|}{|i|}$$

Equation 4-1

R^A, R^B, and R^C are respectively inversely proportional to the electrical conductivities, σ_m^A, σ_m^B, and σ_m^C, of the fluid mixture between the pairs of sense electrodes as shown in Figure 4-3 and Equation 4-2. As described in Section 2.2 the mixture conductivities can be related to the solids volume fraction of the fluid between each pair of sense electrodes. In Equation 4-2 K^A, K^B, and K^C are referred to as the cell constants of the sensor pairs.

$$\text{(i)}\frac{1}{R^A} = K^A\sigma_m^A \qquad \text{(ii)}\frac{1}{R^B} = K^B\sigma_m^B \qquad \text{(iii)}\frac{1}{R^C} = K^C\sigma_m^C$$

Equation 4-2

The electronic measurement hardware, which is described in Section 4.2.2, rectifies the sinusoidal voltage drops, ΔV^A, ΔV^B, ΔV^C, and ΔV^{ref}, and gives a DC output, referenced to ground, that is proportional to their amplitudes as shown in Equation 4-3. As all the rectifier circuits were matched during construction it was assumed that the rectifier gain, *k*, was equal for all four measurements.

$$\text{(i)}\, V^A = k|\Delta V^A| \quad \text{(ii)}\; V^B = k|\Delta V^B| \quad \text{(iii)}\; V^C = k|\Delta V^C| \quad \text{(iv)}\; V^{ref} = k|\Delta V^{ref}|$$

Equation 4-3

4.2.1.1 Measurement of solids velocity.

In order to measure the velocity of a particle passing the probe the DC output voltage, V^A, between electrodes S_1 and S_2 is taken as being the output from sensor A. Similarly, the DC output voltage, V^B, between electrodes S_3 and S_4 is taken as being the output from sensor B. As solid particles pass sensor A and then sensor B they cause fluctuations in the conductivity of the fluid at each sensor, σ_m^A and σ_m^B. From Equation 4-1, Equation 4-2 and Equation 4-3 it can be seen that this will cause fluctuations in V^A and V^B. By cross-correlating V^A and V^B an estimate of the solids velocity, $u_{s,i}^{probe}$, can be made. V^A and V^B can be cross-correlated directly

without having to calculate R^A and R^B because it is the time delay between the signals which is of interest.

4.2.1.2 Solids volume fraction measurement.

The local solids volume fraction measured by the local probe, $\alpha_{s,i}^{probe}$, is given by Maxwell's relationship which is shown in Equation 2-3. Maxwell's relationship can be rearranged to give Equation 4-4.

$$\alpha_{s,i}^{probe} = \frac{1-\left(\frac{\sigma_m^C}{\sigma_w^C}\right)}{1+0.5\left(\frac{\sigma_m^C}{\sigma_w^C}\right)}$$

Equation 4-4

From Equation 4-4 it is clear that both σ_m^C, which is the mixture conductivity at sensor C, and σ_w^C, which is the water conductivity measured at sensor C, are required in order to calculate $\alpha_{s,i}^{probe}$. Substituting this nomenclature into Equation 4-2 Equation 4-5 can be derived.

$$\text{(i)}\ \frac{1}{R_m^C} = K^C\sigma_m^C \qquad \text{(ii)}\ \frac{1}{R_w^C} = K^C\sigma_w^C$$

Equation 4-5

If Equation 4-1 and Equation 4-3 are combined Equation 4-6 can be derived.

$$\text{(i)}\ R_m^C = R^{ref}\left(\frac{V^C}{V^{ref}}\right)_m \qquad \text{(ii)}\ R_w^C = R^{ref}\left(\frac{V^C}{V^{ref}}\right)_w$$

Equation 4-6

Now combining Equation 4-5 and Equation 4-6 gives Equation 4-7.

$$\text{(i)}\ \sigma_m^C = \left(\frac{V^{ref}}{V^C}\right)_m \frac{1}{R^{ref}K^C} \qquad \text{(ii)}\ \sigma_w^C = \left(\frac{V^{ref}}{V^C}\right)_w \frac{1}{R^{ref}K^C}$$

Equation 4-7

Finally combining Equation 4-7(i) and Equation 4-7(ii) gives Equation 4-8.

$$\frac{\sigma_m^C}{\sigma_w^C} = \left(\frac{V^{ref}}{V^C}\right)_m \left(\frac{V^C}{V^{ref}}\right)_w$$

Equation 4-8

From Equation 4-8 and Equation 4-4 it is clear that the measurements $\left(\frac{V^C}{V^{ref}}\right)_m$, acquired in the mixture, and $\left(\frac{V^C}{V^{ref}}\right)_w$, acquired in water, can be used to calculate $\alpha_{s,i}^{probe}$, the local solids volume fraction. It should be noted that the value of K^C will vary as the distance between the probe and the pipe wall varies. Therefore $\left(\frac{V^C}{V^{ref}}\right)_m$ and $\left(\frac{\dot{V}^C}{V^{ref}}\right)_w$ must be acquired with the probe at the same distance from the pipe wall for Equation 4-8 to be true.

4.2.2 The voltage measurement circuit.

The circuit used to measure V^{ref}, V^A, V^B, and V^C is an extension of an existing design by Al-Kurdi [90]. For this application it was modified so that it could be built as a modular system in a standard laboratory equipment rack. A schematic diagram of the circuit is shown in Figure 4-4. It is made up of two main stages as below;

1. Reference resistance measurement stage to measure V^{ref}.
2. Fluid resistance measurement stages to measure V^A, V^B, and V^C.

As both stages are essentially the same it is only necessary to describe one in detail. In this case the reference resistance measurement stage will be considered. It is explained below (see Figure 4-4 also);

a) Voltages $V_{(i)}^{ref}$ and $V_{(j)}^{ref}$ were applied, via a high input impedance buffer, to a differential amplifier with unity gain. The buffer ensured that negligible current was drawn by the measurement circuit. The output of the differential amplifier was as defined in Equation 4-9.

$$\Delta V^{ref} = V_{(i)}^{ref} - V_{(j)}^{ref}$$

Equation 4-9

b) ΔV^{ref} was now fed into an AD630 integrated circuit. The output of this stage is a full-wave rectified signal.

c) This signal was then fed into a low pass Butterworth filter with cut-off frequency 15Hz. This removed the high frequency carrier wave content from the signal to give a DC output voltage V^{ref} which was proportional to $|\Delta V^{ref}|$ as in Equation 4-10 where k is the gain of the circuit.

$$V^{ref} = k|\Delta V^{ref}|$$

Equation 4-10

d) The final stage of the circuit allows the DC offset of V^{ref} to be adjusted.

The fluid resistance measurement stages, A, B and C, follow the same principle giving DC output voltages, V^A, V^B and V^C, proportional to $|\Delta V^A|$, $|\Delta V^B|$ and $|\Delta V^C|$, respectively. All of the measurement stages were closely matched in order to ensure that k was the same for each circuit.

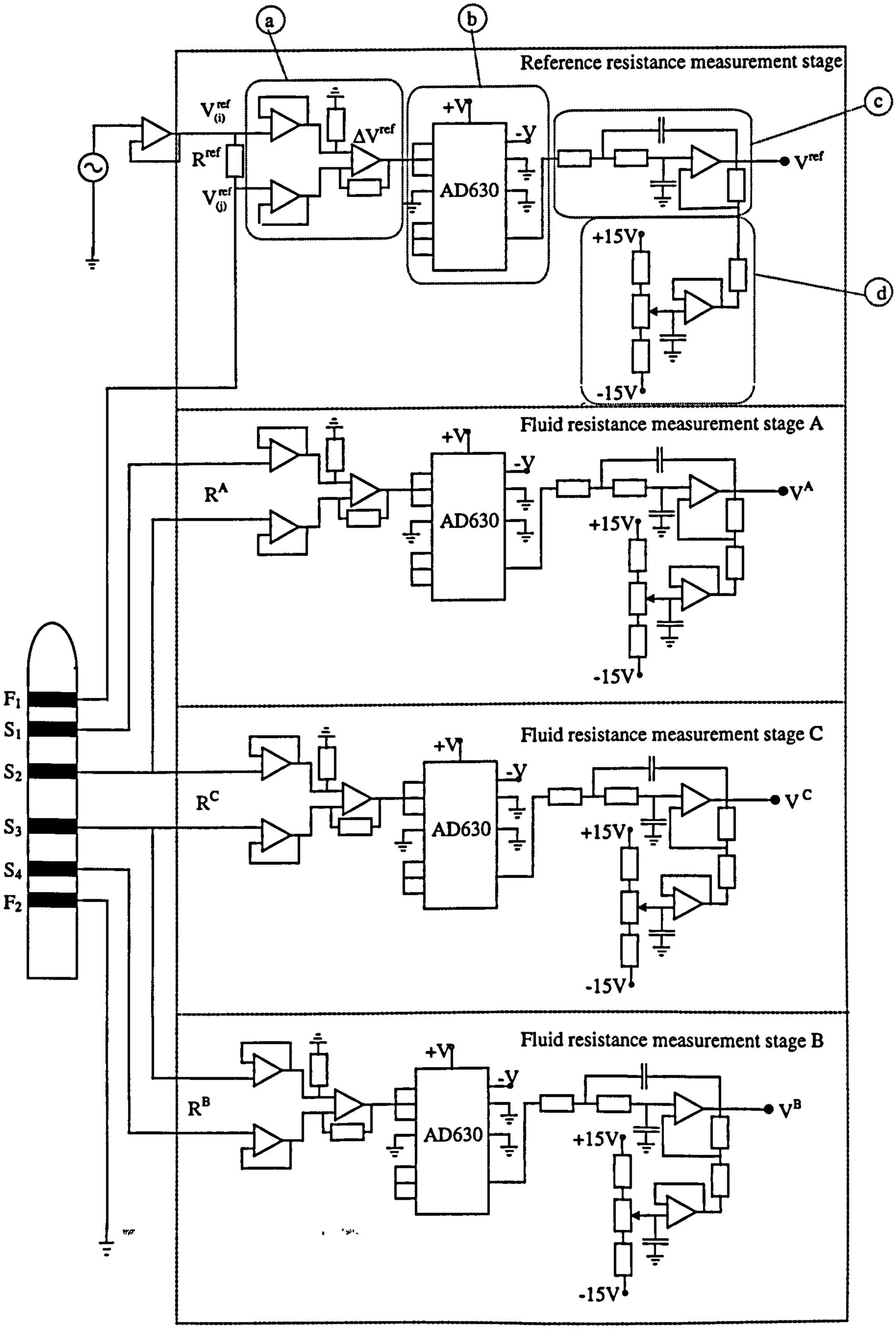

Figure 4-4. Schematic diagram of the local probe measurement circuitry.

4.2.3 The modular design of the measurement system.

The measurement system was built in modules resulting in the reference resistance measurement stage, and each fluid resistance measuring stage, being built on a separate card in a racking system. This was done for two reasons:

- As all the signal connections to each measurement stage are external, the modular system allowed different combinations of reference measurement and fluid measurement stages to be assembled. In this investigation three different fluid measurements, V^A, V^B, and V^C, were acquired whilst only one reference measurement, V^{ref}, was acquired (see Figure 4-4). However the modular system allowed flexibility in case different configurations of probe, such as an 8-electrode probe, had to be tested.
- The modular system enabled each measurement to be acquired by a dedicated circuit on a separate card. This resulted in a system where it was easier to trace any faults. It also allowed the system to be built into a standard laboratory equipment rack. This reduced electrical noise and made the system portable. For this reason the power supply and oscillator, to generate the AC input signal, were also built into the same racking system.

The final system consisted of the modules and connections shown in Figure 4-5. It gave four DC voltage outputs, V^A, V^B, V^C and V^{ref}, referenced to ground, which were directly interfaced to a Data Translation DT2812A data acquisition card. The Power supply card supplied ±15V DC and 0V DC to the other cards. The oscillator card contained two adjustable sine wave generators. The frequency of the sinusoidal output was set at 10kHz. The amplitude could be adjusted by a potentiometer on the card. It should be noted that reference resistance measurement card b was surplus in the current investigation.

Figure 4-5. Schematic diagram and photograph of the measurement hardware.

4.3 The computer controlled two axis probe traversing system.

In order to acquire the necessary measurements in the flow loop the probe had to be positioned accurately at any given point within the cross-section of the pipe. This required movement in two axes. Since the pipe had a circular cross-section a radial co-ordinate system was easier to implement than a Cartesian co-ordinate system. In a radial co-ordinate system movement is in the r and θ directions as shown in Figure 4-6.

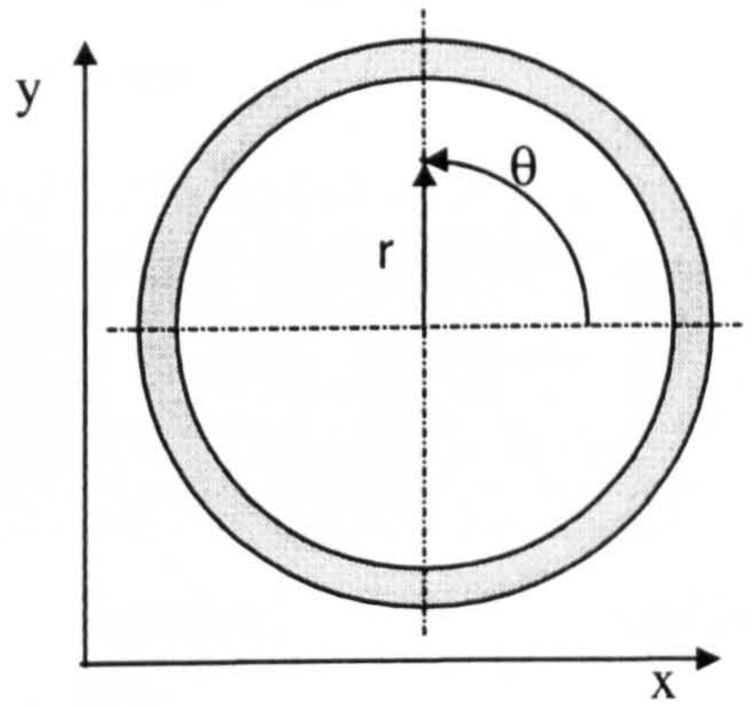

Figure 4-6. Radial co-ordinate system applied to a circular pipe cross-section.

In order to be able to carry out the radial and angular movement two separate traversing systems were required as below:

1. **Linear Traverse.** A device capable of varying the radial co-ordinate, r, of the probe.
2. **Rotary Traverse.** A device capable of rotating the linear traverse around the circumference of the pipe, enabling the angular co-ordinate, θ, of the probe to be varied.

The design of these two systems is given in the following sections.

4.3.1 The linear traverse.

A stepper motor controlled device was designed and constructed to carry out the linear traversing. A photograph of the device is shown in Figure 4-7. A linear stepper motor drove the traversing yoke along two guide rails which kept the motion of the yoke linear. Guide rails were chosen to support the motor and traversing yoke instead of using a solid linear slideway as this reduced the weight of the mechanism considerably. In order to support the weight of the mechanism it was attached to a large clamp on the pipe wall. This spread the load over a 100mm long section of pipe. The probe carrier was sealed through the clamp with O-rings to prevent any leakage. A junction box allowed the short wires from the electrodes to be connected to long screened co-axial leads connected to the measurement hardware. The junction box and the probe carrier were electrically isolated from the traverse and stepper motor to minimise electrical noise on the probe signals. The linear traverse was capable of crossing the pipe in steps of 0.025mm.

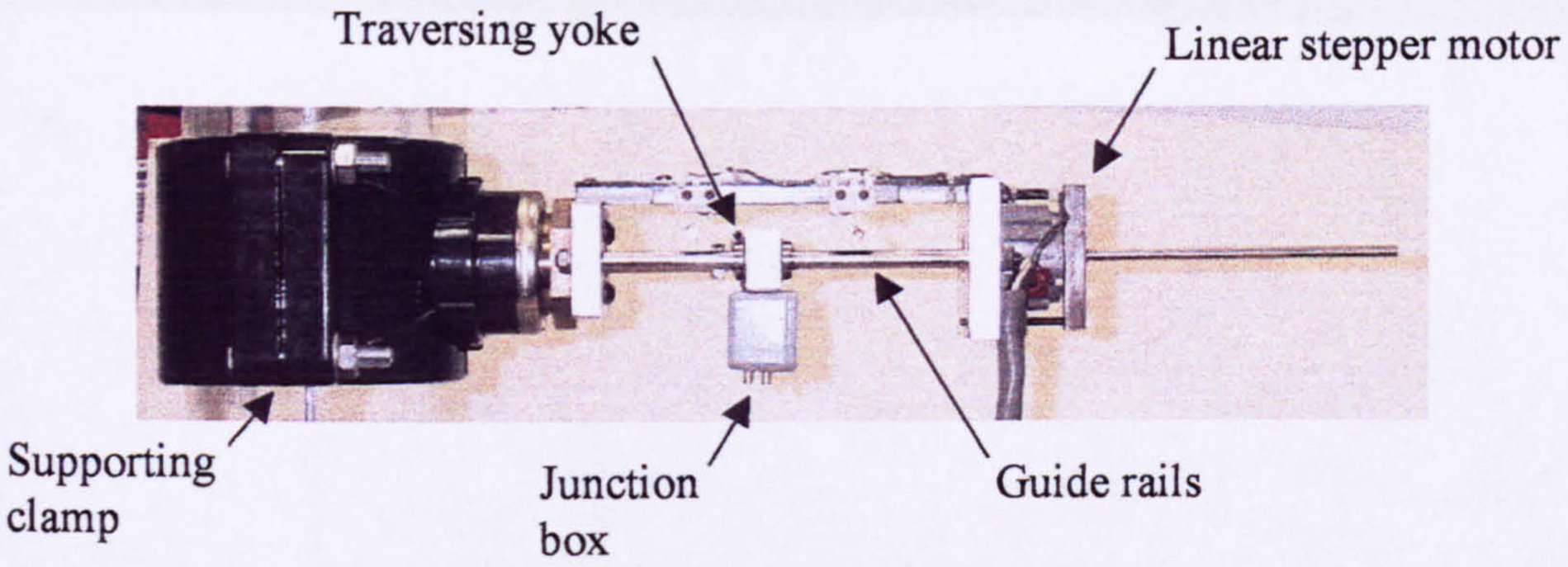

Figure 4-7. The linear traverse.

4.3.2 The rotary traverse.

The design of the rotary traverse was more complicated. The traverse had to be capable of rotating a section of pipe approximately 600mm long. This length was chosen so that none of the traverse hardware would obscure viewing of the measurement probe itself. Before the traverse was designed, existing devices were examined to ensure that any obvious pitfalls were avoided. An existing rotary traverse of a similar size installed at the laboratories of Schlumberger Cambridge Research (SCR) had problems with leakage. It was thought that this was due to inadequate rigidity and sealing. The sealing of the rotating pipe on the SCR traverse was by O-rings and it was constructed of standard thin wall pipe.

To avoid this sealing problem in the current investigation the rotating section of pipe was machined from acrylic tube with 15mm wall thickness. This is three times the wall thickness of standard acrylic pipe and gives a much more rigid section (as the stiffness of a tube is proportional to the square of its wall thickness). In order to support and seal this heavy piece of pipe o-rings were not sufficient. Instead sealed stainless steel bearings were used to support the rotating section, and spring loaded double lip seals were used to seal the joint. These were mounted in flanges machined from Delrin, a free-machining nylon.

The rotating section was driven by a worm and wheel (see Figure 4-8). The worm and wheel allowed more torque to be easily transmitted to the pipe than conventional gears or a belt drive. This is because there is a high tooth contact area at all times. The wheel used was manufactured from Delrin to reduce its weight and to allow it to be easily bonded to the rotating pipe section. The steel worm was supported by two roller bearings and was driven by a conventional stepper motor. The worm and motor were both attached to the lower Delrin

flange section. This system allowed angular steps of 0.015° to be made. The rotary traverse with the linear traverse already attached is shown in Figure 4-8.

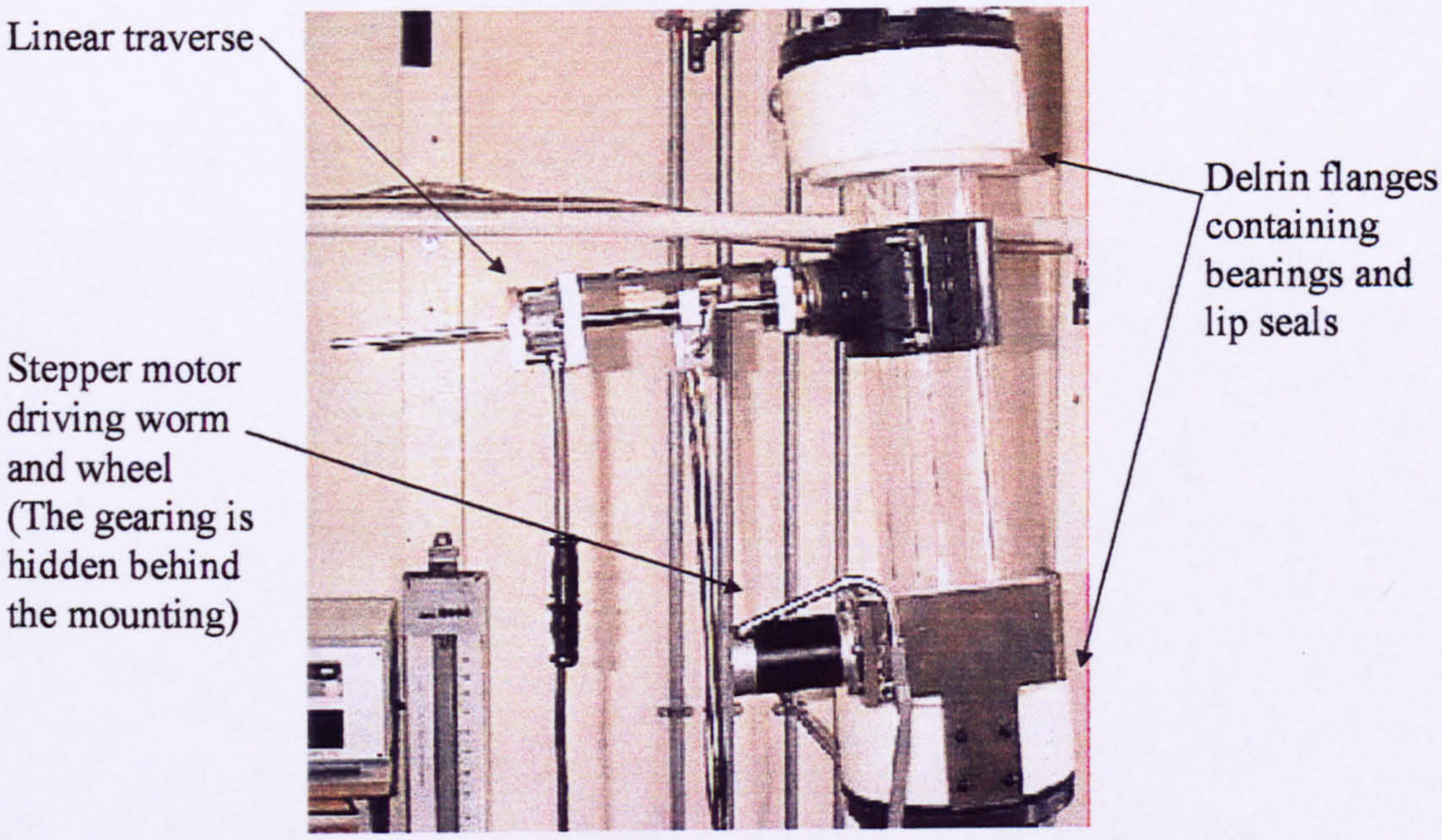

Figure 4-8. The two axis traversing mechanism.

4.3.3 The two axis stepper control system.

As mentioned in the previous two sections, both traverse axes were driven by stepper motors. Stepper motors must be powered by a stepper motor driver that supplies a train of pulses to each phase of the motor in the correct order. In turn a controller, that supplies signals containing information on the appropriate direction and speed of travel, must manage the drivers.

Many manufacturers supply component stepper motor control systems that allow a wide variety of motors to be easily controlled via an RS232 link from a PC. The system used in the current investigation was supplied by RS Components Ltd. It was a modular system that was housed in a shielded rack. It allowed both the small (1 Amp) linear traverse motor, and the large (5 Amp) rotary traverse motor to be easily controlled whilst minimising any electrical noise.

4.4 The probe control, data acquisition and initial data analysis software.

In order to determine the detailed profiles of $\alpha_{s,i}$ and $u_{s,i}$ it was necessary to acquire measurements at a large number of spatial locations in the flow cross-section. Data was acquired at one hundred and twenty-eight spatial locations for each cross-section in the

current investigation. At each spatial location data was acquired from reference measurement devices and from the local probe. Initially it was necessary for an operator to position the probe using instructions sent via the RS232 interface and then initiate data acquisition using the data acquisition software manually. Obviously this was a very repetitive process. Therefore software was written in QuickBasic 4.5 to control it. The following sections of this chapter briefly introduce the techniques used to control the movement of the local probe and acquire data from it. The program written to integrate these processes is then described.

4.4.1 Controlling the stepper motor system.

Instructions were transmitted to the traverse controller using the RS232 interface from the PC. Initially the controller was accessed using an RS232 terminal emulator supplied by RS Components Ltd. However in order to integrate the controller into the QuickBasic program it was necessary to communicate with it directly.

The motion increment used by the stepper motor controller was a "step". Each step corresponded to one pulse of power being sent to the stepper motor. The linear, or rotational movement that this caused depended on the gearing of the mechanical drive. In the current investigation the linear stepper motor moved 0.0254mm per step whilst the gear ratio of the worm and wheel allowed the rotary axis to move 0.015° per step. For the final traverse motion control software all the movements of the probe were calculated in mm and degrees and then converted, using the factors given above, into motor steps.

4.4.2 Acquiring data automatically using GlobalLab.

The data acquisition software used was GlobalLab. This is a DOS based data acquisition and analysis package supplied by Data Translation. GlobalLab allowed the data acquisition card to be automatically controlled via a pre-written chain of commands called a macro. In this case the data acquisition card was a DT2821A supplied by Data Translation.

The DT2821A was unable to acquire data at more than one frequency at a time. Therefore in the current investigation separate macros were written to acquire data at different frequencies. This was necessary because the cross-correlation velocity estimate required data acquired at a high sampling frequency, whereas all other data could be acquired at a lower sampling frequency. The macros were run sequentially at each spatial location of the probe. Whilst this increased the total data acquisition time it reduced the volume of data acquired. The macros

were written in such a way that data from each spatial location was stored in an individual binary data file.

4.4.3 The QuickBasic motor and data acquisition control program.

Before writing the control software it was important to define the requirements which would be placed on it. The software had to allow the user to define the number of spatial locations, in both the radial and angular axes, at which data should be acquired. It then had to be capable of positioning the probe at the relevant spatial locations and of acquiring the relevant data. Finally, the program had to inform the user of what it was doing and of the position of the probe at all times. It also needed to run from a simple and easy to understand menu system so that it could be used by a less experienced operator. A flow diagram of the complete program is shown in Figure 4-9. This explains the main functions of the software. In addition the functioning of the program is explained below.

1. Initially the user was prompted to choose from a menu of options. Option 1 allowed the manual resetting of the probe to the datum position. This was an important function for initial setting up of the probe. Option 2 allowed the probe to acquire data at a single spatial location. Option 3 allowed the probe to acquire data at a number of spatial locations within the flow cross-section under computer control. As this was the most common function of the program it is detailed below.

2. Following the initial menu the user was prompted as to whether the conditions in the pipe were static or dynamic. As described in Section 4.2.1.2, it was necessary to acquire calibration data from the probe in water in order to be able to calculate $\sigma_{m,i}$. The static condition option allowed this calibration data to be acquired. It controlled the movement of the probe to the required positions and acquired data from the local probe volume fraction sensor and from reference measurement devices (see Chapter 6) for one minute at each location at a sampling frequency of 100Hz. This option did not acquire data from the local probe velocity sensors as no calibration data was required from these.

The dynamic condition option used the same movement control functions as before. It also acquired the same quantity of data from the local probe volume fraction measurement sensor and from reference measurement devices (see Chapter 6) as before. However, in addition it acquired data for one minute from the local probe velocity measurement

sensors at the higher sampling frequency of 3750Hz. This high frequency data allowed accurate cross-correlation velocity estimates to be made.

3. The user was then prompted to enter the number of number of spatial locations at which data was required. To do this the user was prompted to specify the number of angular probe positions required and then the number of linear probe positions required. Using this information the program calculated a rotational increment and a linear increment. The rotational increment was based on a maximum 180° rotation, since once it had rotated 180° the linear traverse was at the diametrically opposite position from its start position. The linear increment was based on 76mm of possible travel, which was equal to the pipe inside diameter (80mm) minus the diameter of the probe (4mm).

4. With this information the program was able to begin the automatic movement and acquisition process. Following initial experimentation it was discovered that if the probe moved through a solids-liquid flow to the pipe wall there was a possibility that it could trap a particle at the wall. This could have resulted in damage to the probe and in data being acquired at the wrong positions. Therefore the program first prompted for the working section of the flow loop to be emptied of solids. It then moved the probe to the pipe wall and prompted for the flow to be restarted. Following a settling time of 10 minutes the program began the acquisition of data at the pipe wall for each rotational position in turn through 360° of rotation. By using 360° of rotation all the spatial locations in contact with the pipe wall could be acquired without having to move the probe away from the wall.

5. Once data had been acquired for every rotational position at the pipe wall the program moved the probe across the flow into the centre of the pipe. It then acquired "normalisation" data at this position. The purpose of this data is explained in Section 6.4. Following the collection of the normalisation data the program moved the probe and acquired data, for every linear position across the pipe diameter except those touching the pipe wall, for the 0° rotational position. The probe was then moved to the centre of the pipe at the second rotational position. Stage 5 was then repeated for all the required rotational positions.

4. Construction of the local probe and ancillaries.

---

6. When data had been acquired at all the necessary spatial positions the program returned the probe to the centre of the pipe at the 0° rotational position and returned the software to the initial menu.

The output of the program was a series of binary data files. These were analysed as described in Section 6.4.

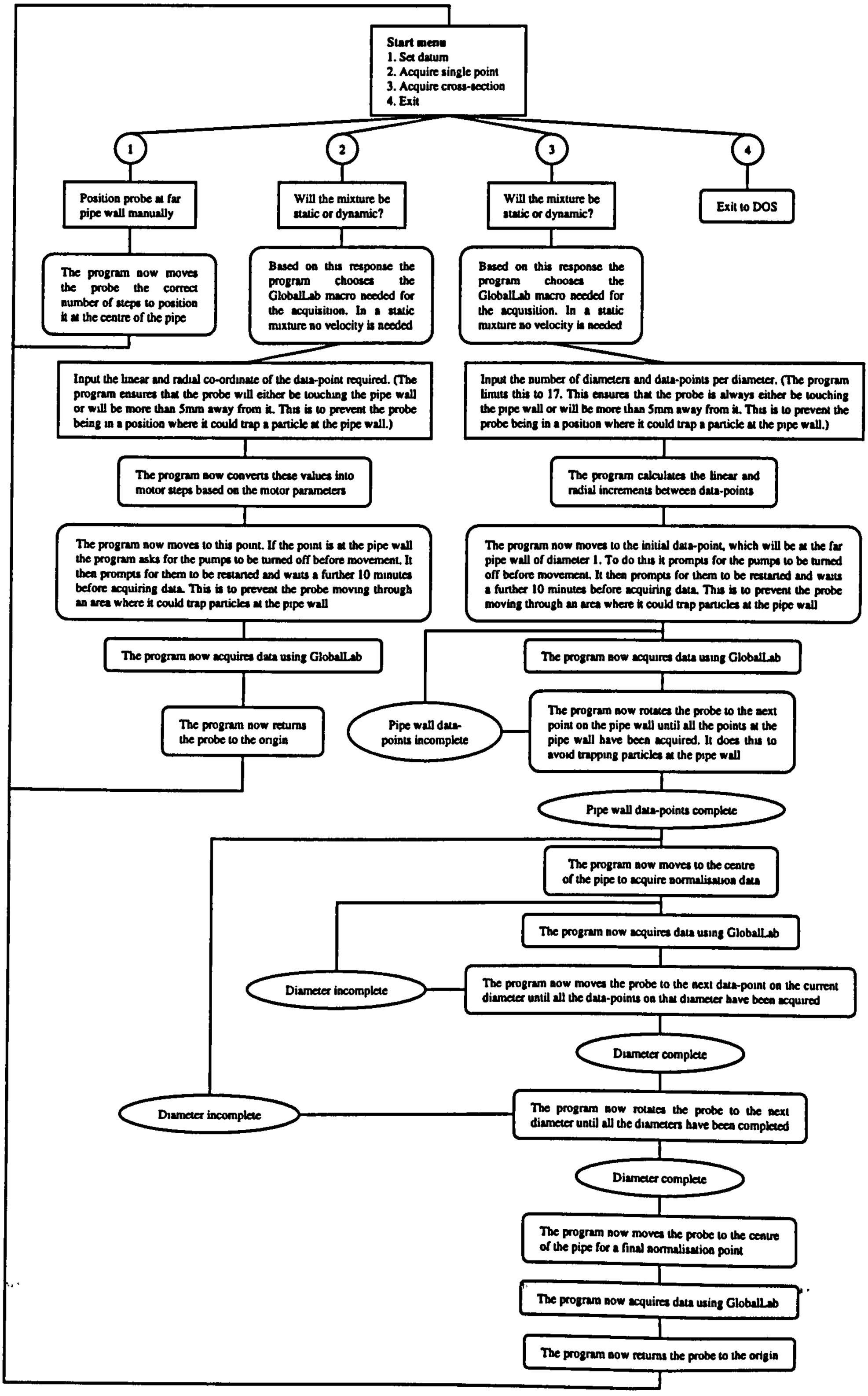

Figure 4-9. Flow diagram of the probe movement and data acquisition control program.

5. Static testing of the probe.

5.1 Reasons for carrying out static testing of the probe.

Before the local probes were used dynamically in the flow loop a number of experimental static testing procedures were carried out. These are detailed in this chapter. The static testing was carried out to achieve the objectives given below.

1. The effect on the response of the probe of the variation of its proximity to the pipe wall had been investigated during the finite element modelling (see Section 3.2.5). The results had suggested that the pipe wall could cause a large change in the response of the probe. Therefore it was important that experimental static testing was carried out to quantify this.

2. The finite element modelling (see Section 3.2.6) had led to a 6-electrode SEMM array being selected for the experimental probe. This array can be configured to give measurements of both $\alpha_{s,i}$ and $u_{s,i}$ as shown in Figure 3-7 and described in Section 3.1.3.3. Because this configuration had been selected the finite element modelling results for both 4-electrode SEMM arrays and 6-electrode SEMM arrays were relevant. These results had suggested that varying the geometry of both types of electrode array could substantially affect their responses. It was important that these results were verified experimentally. This was carried out by recreating the finite element model conditions in the laboratory and measuring the response of probes configured as both 4-electrode and 6-electrode SEMM arrays with many of the geometries that had been analysed by finite element analysis. A further intention of this work was to calculate the actual fluid resistances recorded by the probes as the finite element modelling had only allowed the probes response to be represented as a dimensionless relative sensitivity, Ψ. This would verify that the ideal relative sensitivities that had been calculated did not represent mixture resistance changes that would be too low to accurately measure.

3. In order to measure $u_{s,i}$ the responses from two axially displaced sensors are cross-correlated (see Section 4.2.1.1). In order that the measurement is accurate the effective separation of the sensors, L, must be accurately known. Usually this separation is assumed to be equal to the physical separation of the two sensors, j. However the two sensors are integrated into one 6-electrode SEMM array in the present investigation and it was

possible that L was not equal to j. Static testing was carried out to experimentally give this separation.

5.2 Experimental procedure for the static testing.

5.2.1 The static test rig.

A test rig was designed and built that would allow all the experimental work described above to be carried out. The rig allowed a probe to be positioned at different radial and axial positions within a water filled section of pipe. Solid particles and other objects could then be positioned statically within the vessel to allow the response of the probe to be investigated.

The static test rig is shown in Figure 5-1. The probe was clamped to the movable bed of a linear slide-way which allowed the probe to be moved in the radial direction, r. The micrometer scale on this axis allowed r to be measured to an accuracy of 0.05mm. This radial positioning device was mounted on two cylindrical rails using linear bearings which allowed the probe to be moved in an axial direction, y. A millimetre scale was used which allowed y to be measured to an accuracy of ±0.5mm. A cap on the pipe section had a number of mounting points which allowed different solid objects to be suspended within the vessel using 0.1mm diameter nylon line.

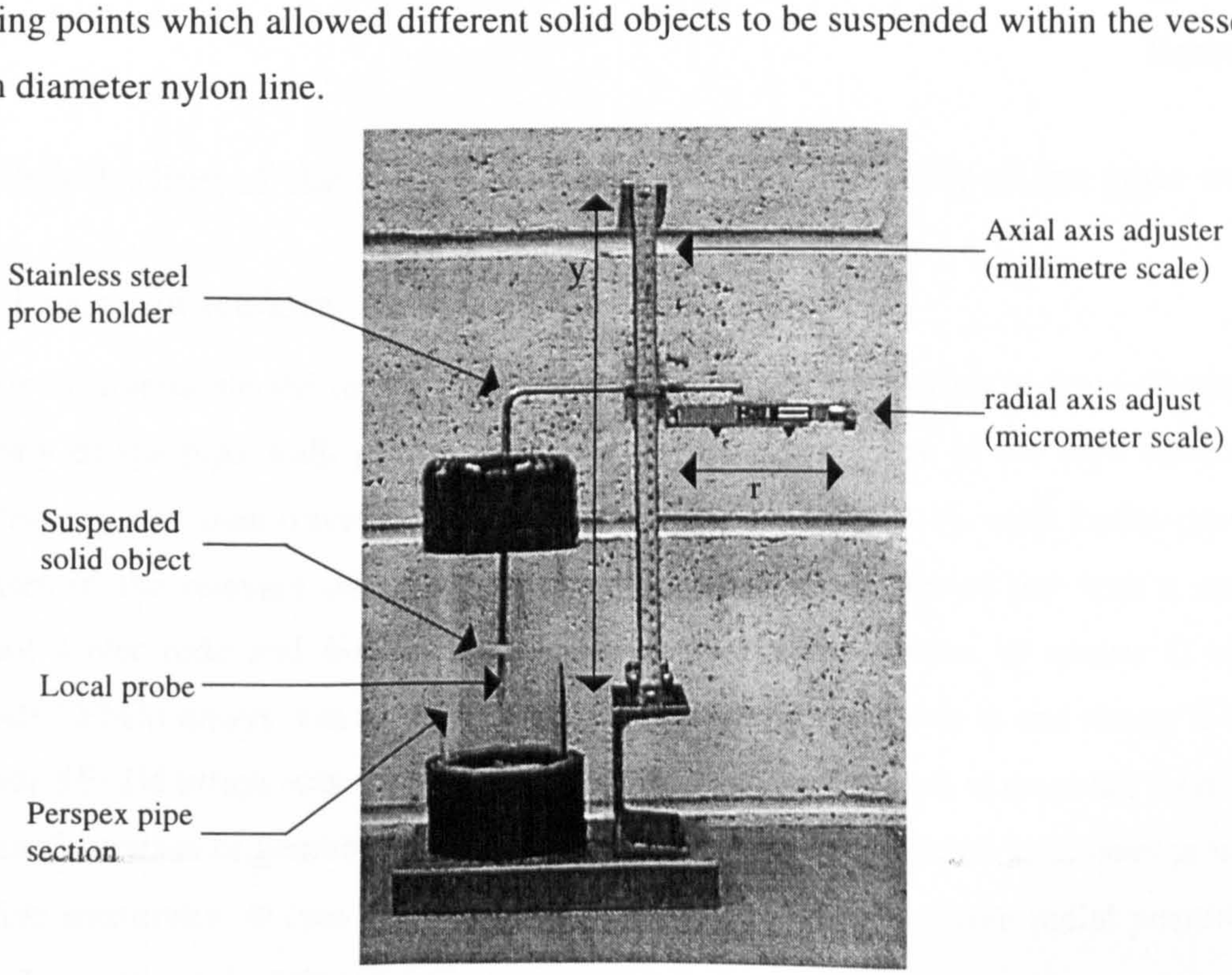

Figure 5-1. The experimental static test rig.

5. Static testing of the probe.

5.2.2 Analysis of the probe response.

The probes used in the static testing were constructed to give a number of different 4-electrode and 6-electrode SEMM arrays. These arrays and the notation used to describe them are described in Section 3.2.1. The measurement method used with the SEMM arrays is shown in Figure 4-3. To allow comparisons of the experimental static testing results from different probes to be made it was necessary to calculate the mixture resistances at all the relevant sensors of each probe. For a 4-electrode SEMM array the mixture resistance R_m^C must be measured at sensor C. For a 6-electrode SEMM array the mixture resistances R_m^A and R_m^B, must be measured at sensors A and B respectively. In order to do this it was necessary to measure the potential differences at these sensors. Equation 4-3 shows the format in which these potential differences were given by the measurement hardware. The mixture resistance at each sensor was then calculated using the form of Equation 4-6 as shown in Equation 5-1. It is important to note that the mixture resistance at a given sensor is directly proportional to the potential difference at a given sensor which was measured in Chapter 3.

$$\text{(i)}\, R_m^A = R^{ref}\left(\frac{V^A}{V^{ref}}\right)_m \quad \text{(ii)}\, R_m^B = R^{ref}\left(\frac{V^B}{V^{ref}}\right)_m \quad \text{(iii)}\, R_m^C = R^{ref}\left(\frac{V^C}{V^{ref}}\right)_m$$

Equation 5-1

5.3 Static testing of the probe response to the proximity of the pipe wall.

5.3.1 Testing procedure.

In order to investigate the response of different probe configurations to the influence of the proximity of the pipe wall, probes were positioned in the centre of the pipe section of the static test rig, and then traversed towards each pipe wall in turn. At each radial position the responses of the relevant sensors were recorded. Tests were carried out with a number of different 4-electrode and 6-electrode SEMM arrays. The response of sensor C of the 4-electrode SEMM arrays was recorded whilst the responses of sensor A and sensor B of the 6-electrode SEMM arrays was recorded. This allowed any differences in response caused by the array configuration or geometry to be identified. The sensor responses have been presented as a relative sensitivity, Φ (see Equation 5-3), plotted against the relative radial position of the probe, r^* (see Equation 5-2).

$$r^* = \frac{r}{0.5D}$$

Equation 5-2

r = Radial distance from the probe surface to the pipe centre.

D = Diameter of the pipe.

$$\Phi = \frac{(R_r - R_u)}{(R_{max} - R_u)} \times \frac{100}{1}$$

Equation 5-3

Φ = Relative sensitivity at a given radial position.

R_{r^*} = Measured resistance at the given sensor with the probe at radial position r^*.

R_{max} = Maximum measured resistance at the given sensor for any radial position of the probe.

R_u = Measured resistance at the given sensor with the probe positioned at $r^*=0$.

5.3.2 Results of the testing.

5.3.2.1 The effect of the pipe wall on the response of sensor C of 4-electrode SEMM arrays.

In order to measure $\alpha_{s,i}$ the mixture conductivity $\sigma_{m,i}$ must be calculated as shown in Section 4.2.1.2. This requires that the cell constant, K^C, must be calculated. In Section 4.2.1.2 it was stated that K^C would vary with r^*. However it was important to investigate the extent of this effect. In order to do this the responses of 4-electrode SEMM arrays with different field electrode separation, f, and sense electrode separation, s_α (see Figure 3-8), were tested as r^* was varied. Figure 5-2 shows the responses of five different SEMM arrays at varying r^*.

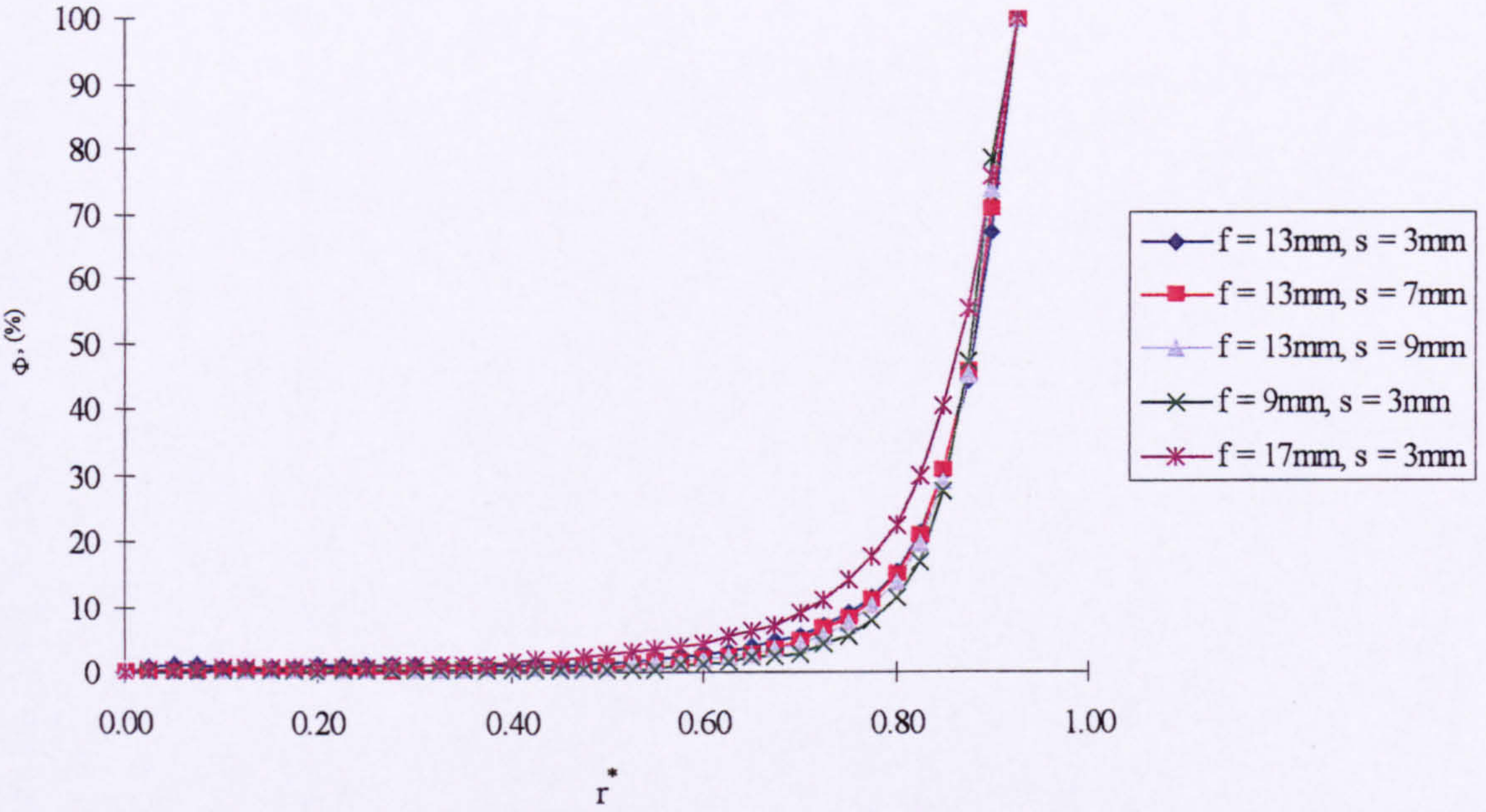

Figure 5-2. The variation of Φ with r^* for 4-electrode SEMM arrays.

The responses of all the SEMM arrays show qualitative agreement with the finite element modelling results (see Section 3.2.5). In Figure 5-2 the responses of the arrays are not significantly affected by the wall until $r^* \approx 0.7$. Above this value Φ rises to a maximum value when the probe contacts the pipe wall.

Although the responses are all qualitatively similar some variations in the array response can be identified for the different array geometries. Figure 5-3 shows four of the responses over a small range of r^*. This shows that some of the arrays began to react to the pipe wall at a lower value of r^* than others. If the finite element modelling sensitivity volumes (see Section 3.2.6.2) for these arrays are examined the reason for this becomes apparent. The arrays which were most sensitive to the proximity of the pipe wall were those whose sensitivity volumes protruded furthest radially away from the probe body.

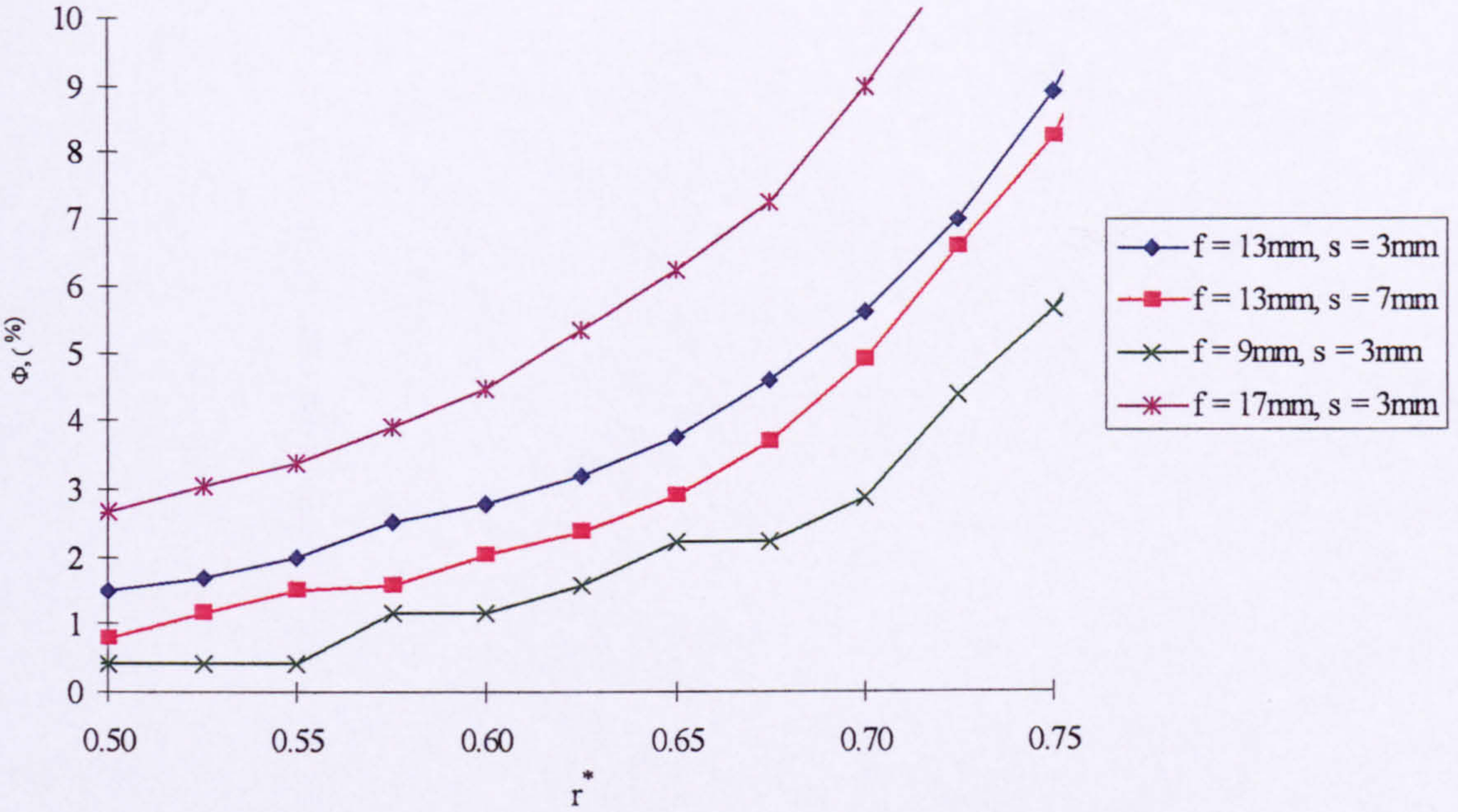

Figure 5-3. Enlarged view of the variation of Φ with r^* for 4-electrode SEMM arrays.

Despite the slight variations in curve shape these results all confirm the hypothesis made in section 3.2.5. This was that the pipe wall compresses the electric field around the array as the probe approaches it causing an increase in the current density around the probe. This in turn causes the measured resistance to rise. The results also confirm this effect can cause a large variation in the probe response. This confirms that the cell constant of the sensor, K^C, will vary significantly with r^* (see Section 4.2.1.2).

5.3.2.2 The effect of the pipe wall on the responses of sensor A and sensor B of 6-electrode SEMM arrays.

The output signals of the velocity sensors, sensor A and sensor B, of a 6-electrode SEMM array are directly cross-correlated in order to give a measurement of $u_{s,i}$ (see Section 4.2.1.1). In order to achieve the best possible cross-correlation the effect of the pipe wall should be the same on both sensor A and sensor B. To investigate whether this condition was met the responses of a number of different 6-electrode SEMM arrays were investigated. Arrays with sensor separation, $2\text{mm} \le j \le 10\text{mm}$, and field electrode separation, $13\text{mm} \le f \le 19\text{mm}$, were tested (see Figure 3-9). The sense electrode separation, s_v, was not varied as the finite element modelling had shown that varying s_v had little effect on the sensitivity of the sensors (see Section 3.2.6.3.3). Plots showing the effect of the proximity to the pipe wall of arrays with different j are shown in Figure 5-4. Plots showing the effect of the proximity to the pipe

wall of arrays with different f are shown in Figure 5-5. In each case the responses of both Sensor A and Sensor B are shown.

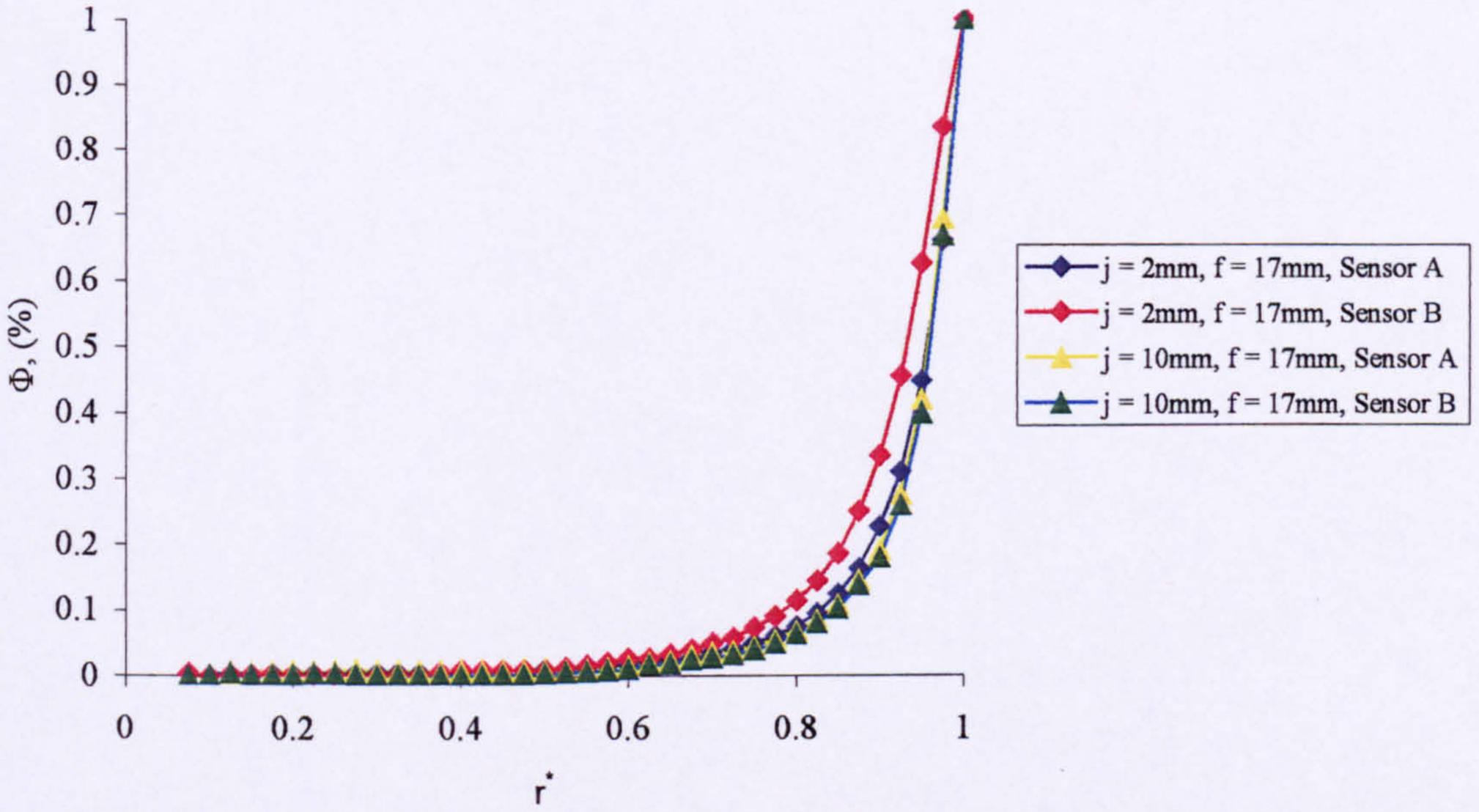

Figure 5-4. The variation of Φ with r^* for both sensors of 6-electrode SEMM arrays with varying j.

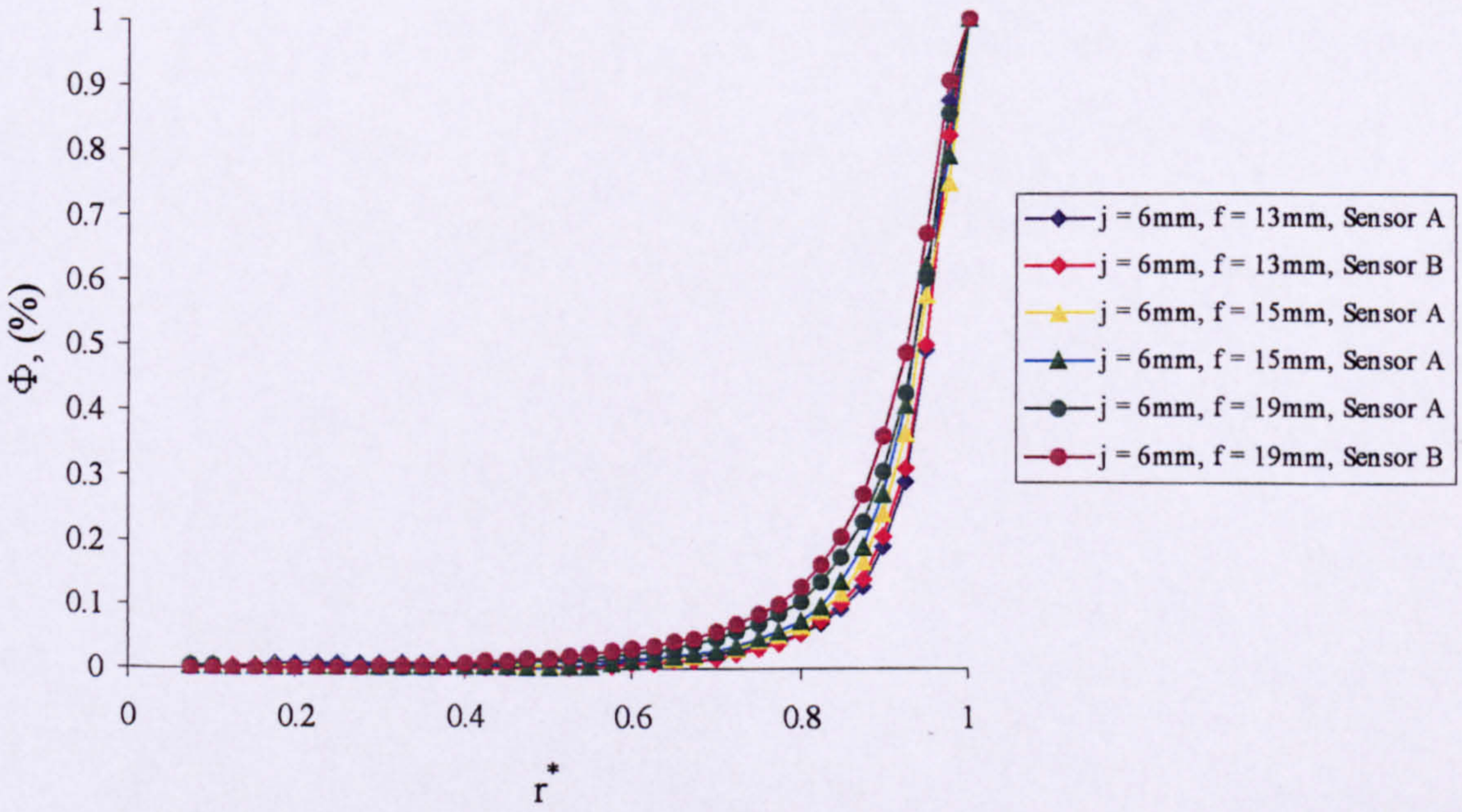

Figure 5-5. The variation of Φ with r^* for both sensors of 6-electrode SEMM arrays with varying f.

Again the responses of all the arrays show qualitative agreement with the finite element modelling results (see Section 3.2.5). The responses of the arrays were not significantly affected by the wall until $r^* \approx 0.7$. Above this value Φ increases to a maximum at the pipe wall.

Although the responses are all qualitatively similar some variations in the array response can be identified for the different array geometries. If j is high the responses for both Sensor A and Sensor B agree very closely (see Figure 5-4). As j is decreased the difference between the responses for the two sensors becomes more pronounced and the effect of the pipe wall at a given value of r^* increases. The same trends in response can be seen as f is increased. If the finite element modelling results (see Section 3.2.6.3.3) are examined these effects can be simply explained. The arrays with the most compact, symmetrical sensitivity volumes for each sensor, A and B, are less affected by the proximity of the pipe wall and show a more even effect at both sensors A and B. Therefore the geometry that was identified as offering the optimum sensitivity distribution for the measurement of $u_{s,i}$ is also less severely affected by the proximity of the pipe wall.

5.4 Static testing of the probe response to a ring of non-conducting material.

5.4.1 Testing procedure.

In Chapter 3 finite element modelling was described that led to the identification of the 6-electrode SEMM array as the optimum array type for the combination measurement of $\alpha_{s,i}$ and $u_{s,i}$ in the current investigation. The modelling had also suggested some optimum geometries of the array to be selected. In order to validate these results experimental static testing was carried out as described in this section.

The axisymmetric finite element modelling in Chapter 3 simulated a geometry in which a ring of solid, non-conducting, material was positioned at different axial and radial positions relative to the probe. The simulated ring had a 5mm × 5mm cross-section in order to represent 5mm diameter solid particles. To recreate this geometry as closely as possible for static testing eight nylon rings were manufactured with 5mm × 5mm cross-section and internal diameters, d, ranging from 6mm to 20mm in 2mm increments (see Figure 5-6).

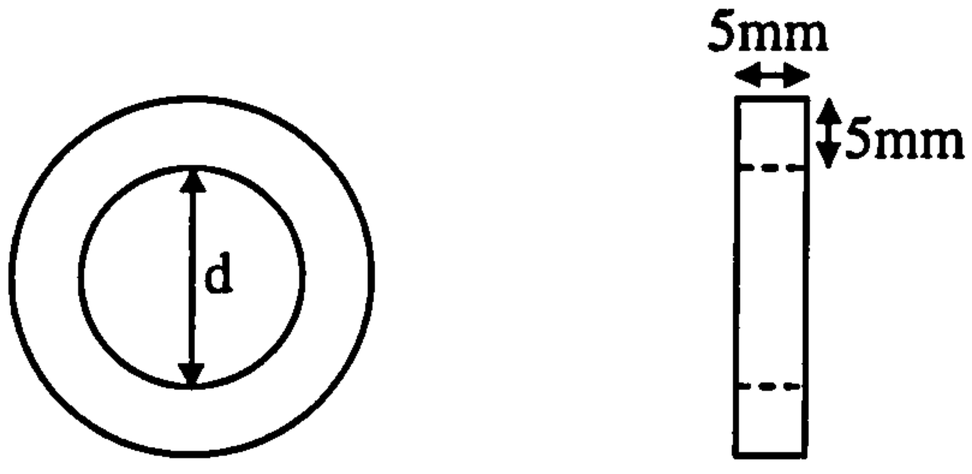

Figure 5-6. The geometry of the nylon rings used in the experimental static testing.

The rings were suspended, one at a time, in the centre of the static test rig vessel. The probe being investigated was then moved through the centre of each ring in 1mm axial steps. At each position the mixture resistance at the relevant sensors of the array was recorded. Tests were carried out with a number of different 4-electrode and 6-electrode SEMM arrays. The response of sensor C of the 4-electrode SEMM arrays was recorded whilst the responses of sensor A and sensor B of the 6-electrode SEMM arrays was recorded. This allowed any differences in response caused by the array configuration or geometry to be identified.

The measured mixture resistances are presented in two ways. In Sections 5.4.2.1 and 5.4.3.1 the sensor responses are presented in terms of the relative sensitivity, Ψ. The relative sensitivity is calculated using a similar method as that used in the finite element modelling (see Section 3.2.6.1). Ψ is plotted against the radial and axial co-ordinates of the centre of the ring cross-section relative to the probe (see Figure 3-19). Ψ is defined in Equation 5-4. It should be noted that the mixture resistances measured in this testing are directly proportional to the potential differences measured in Chapter 3. Therefore Equation 5-4 is equivalent to Equation 3-6.

$$\Psi = \frac{\left(R_{(r,z)} - R_w\right)}{\left(R_{max} - R_w\right)} \times 100$$

Equation 5-4

Ψ = Relative sensitivity.

$R_{(r, z)}$ = Measured mixture resistance at a given sensor with a nylon ring at position (r, z).

R_{max} = Maximum measured mixture resistance at a given sensor for any position of the nylon rings..

R_w = Measured mixture resistance at a given with the probe in water with no nylon ring.

In Sections 5.4.2.2 and 5.4.3.2 the sensor responses are presented in terms of the change in resistance, ΔR. Unlike Ψ this allows a quantitative comparison of the SEMM arrays to be made. ΔR is defined in Equation 5-5, where $R_{(r,z)}$ and R_w are defined above.

$$\Delta R = R_{(r,z)} - R_w$$

Equation 5-5

5.4.2 Static testing of the response of sensor C of 4-electrode SEMM arrays.

The geometry of the 4-electrode SEMM array allows two variable dimensions (see Figure 3-8). These are the field electrode separation, f, and the sense electrode separation, s_α. During the finite element modelling the axial field electrode length, a, was also varied. However in the experimental probes this dimension is fixed. From the finite element modelling trends were identified in the sensitivity of the array with variation of all three variable dimensions (see Section 3.2.6.2). In order to verify these trends experimental static testing was carried out using 4-electrode SEMM arrays with different values of f and s_α. The results of this testing are presented in this section.

5.4.2.1 Qualitative comparison of the static testing and the finite element modelling.

<u>The effect on the sensitivity volume shapes of varying the axial field electrode length, a.</u>

The finite element modelling had allowed the simulation of field electrodes with values of a between 6mm and effectively 0mm. This modelling had suggested that the sensitivity volume shape would become more asymmetrical as a was increased (see 3.2.6.2). However it was considered that these results were possibly unreliable. As described above it was not possible to vary a in the experimental probes. The probe construction method fixed it at approximately 0.3mm. If the results presented in Section 3.2.6.2 were reliable this should have resulted in a sensitivity volume with a small degree of asymmetry. Figure 5-7 shows the static testing sensitivity volumes for two different 4-electrode SEMM arrays. Also shown are the finite element modelling sensitivity volumes for arrays with the same values of f and s_α but with varying values of a.

Experimental static testing results

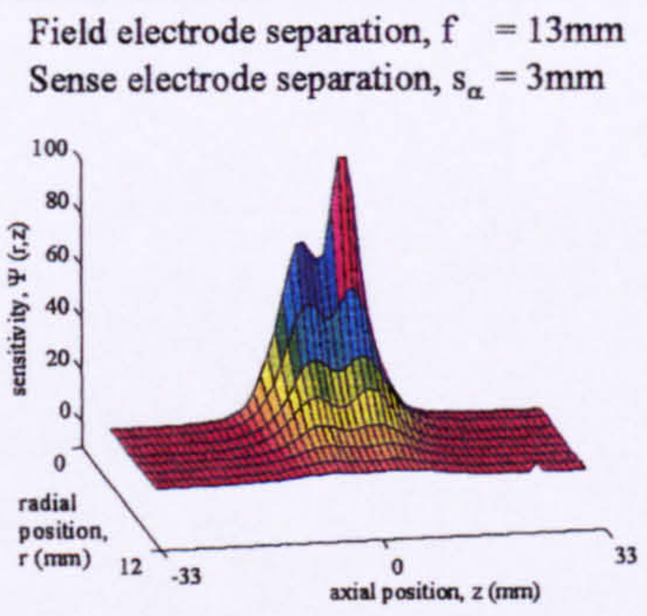

Finite element modelling results assuming an axial field electrode length, a, of 0mm

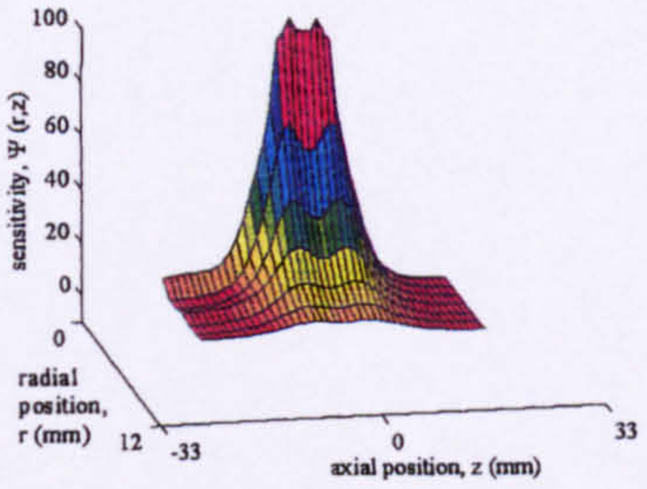

Finite element modelling results assuming an axial field electrode length, a, of 5mm

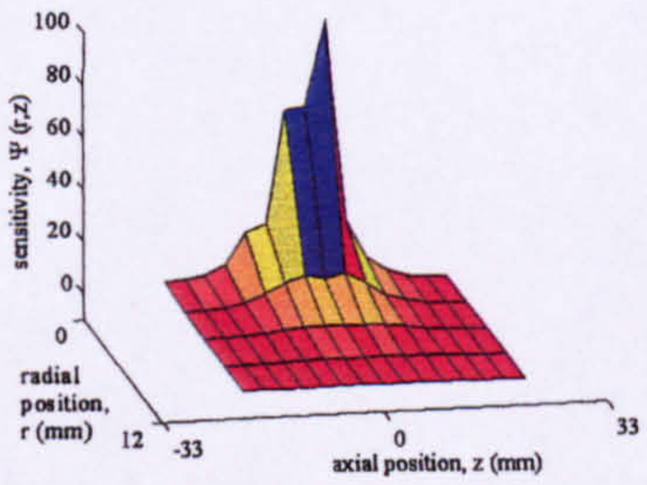

Figure 5-7. Comparison of experimental and modelling sensitivity volumes for 4-electrode SEMM arrays with increasing a.

From Figure 5-7 the experimental sensitivity volumes show a similar degree of asymmetry as the finite element modelling sensitivity volumes for an array with a = 5mm. This is significantly larger than the actual a = 0.3mm of the experimental probes. Because of this disagreement, and the lack of experimental static testing with varying a, it was not considered that these results confirmed the accuracy of the finite element modelling.

It is possible that the asymmetry of the experimental static testing sensitivity volumes is a result of charge dissipation. The side of the array that showed a lower sensitivity was found to be the side closest to the grounded field electrode. If some charge was sunk to another ground in the test vessel it would result in low sensitivity at this side of the probe. The static test rig had been designed to avoid this. However it was considered that this was still the likely cause of the asymmetry. Because of this conclusion and the conclusions drawn in Section 3.2.6.2 the results of the testing of the effect of a on the array sensitivity were not applied in the

current investigation. It is suggested that further work should be carried out to investigate these effects.

The effect on the sensitivity volume shapes of varying the field electrode separation, f.

The finite element modelling had suggested that variation of f had a significant effect on the sensitivity volume of a 4-electrode SEMM array. Three different sensitivity volume shapes were identified as the value of the field electrode separation increased. Of these shape 2 was identified as the most desirable shape for a volume fraction measurement sensor (see Section 3.2.6.2). It was important to check that these sensitivity volume shapes occurred, at the same values of f, in the experimental probes. Experimental static testing sensitivity volumes for arrays with varying f are shown in Figure 5-8. The sensitivity volumes predicted by the finite element modelling are also shown for each array geometry for comparison.

Figure 5-8 shows that the static test results are qualitatively similar to the finite element modelling results. The three sensitivity volume shapes observed in the finite element modelling (see Section 3.2.6.2) can all be identified in the experimental static testing results at approximately the same geometry, strongly suggesting that the finite element modelling results are reliable.

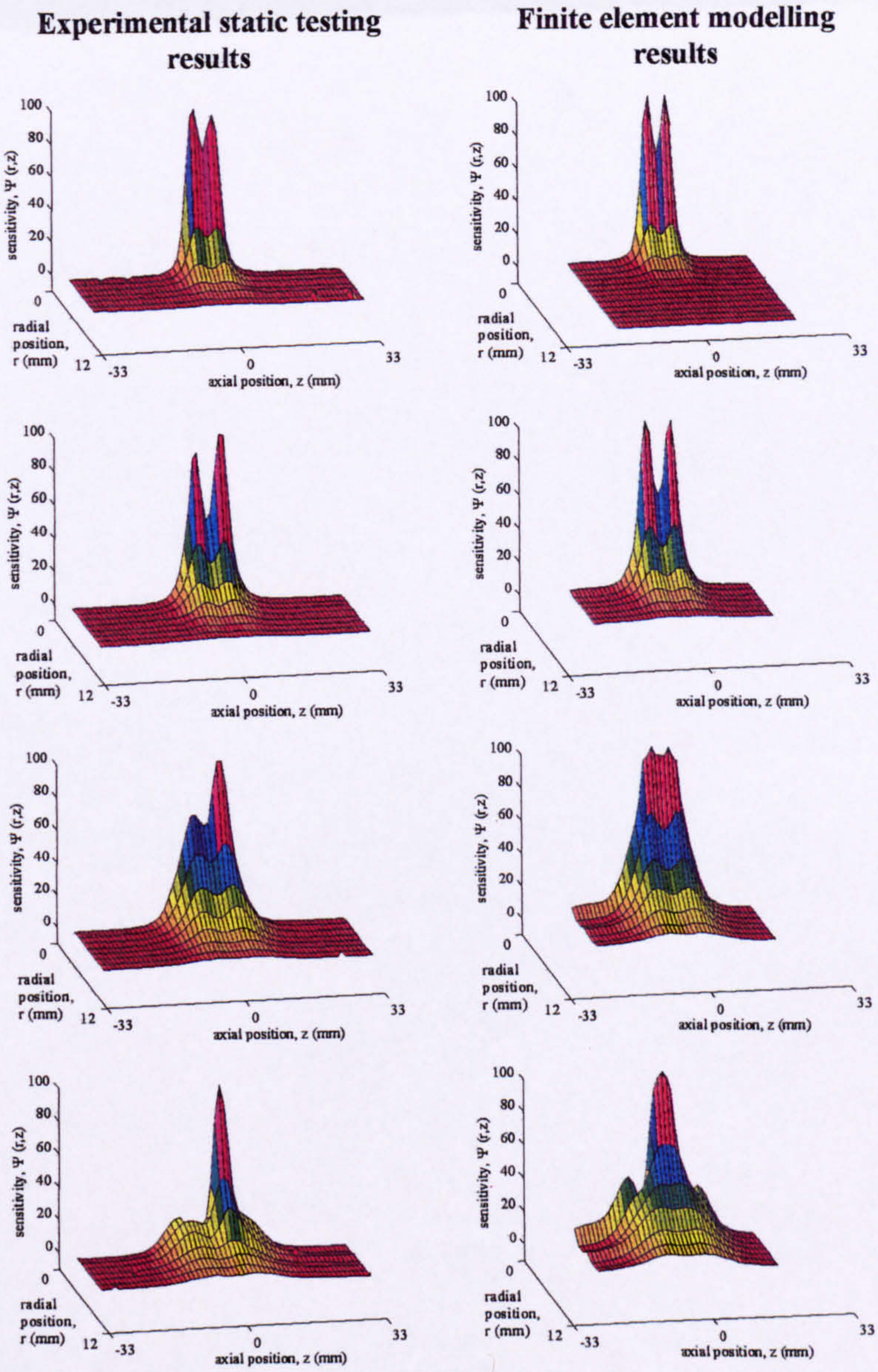

Figure 5-8. Qualitative comparison of sensitivity volumes from finite element modelling and experimental static testing for 4-electrode SEMM arrays with increasing f.

<u>The effect on the sensitivity volume shapes of varying the sense electrode separation, s_α.</u>

From the finite element modelling the optimum sensitivity volume shape for measurement of $\alpha_{s,i}$ had been selected as shape 2 (see Section 3.2.6.2). The modelling showed that a shape 2 sensitivity volume occurred at increasing values of f as s_α increased and that to achieve a shape 2 sensitivity volume the combination of f and s_α should be chosen carefully. To verify these results experimental static testing was carried out using probes configured as 4-electrode SEMM arrays with varying s_α. Representative sensitivity volumes are shown in Figure 5-9 alongside the relevant finite element modelling sensitivity volumes for comparison.

	Experimental static testing results	Finite element modelling results
$\omega = 0.69$, shape 1 Field electrode separation, f = 13mm Sense electrode separation, s_α = 9mm	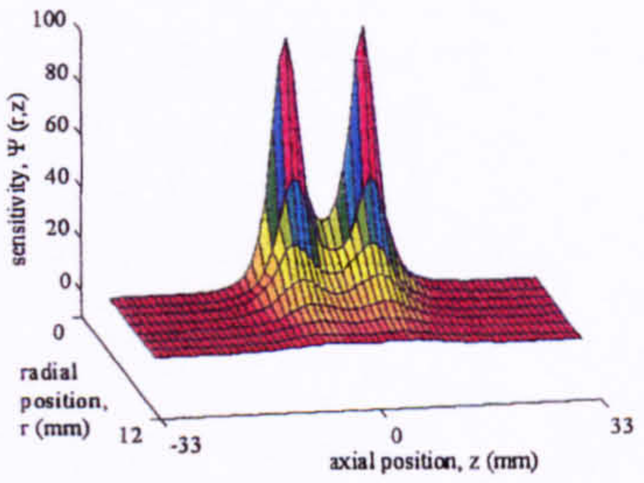	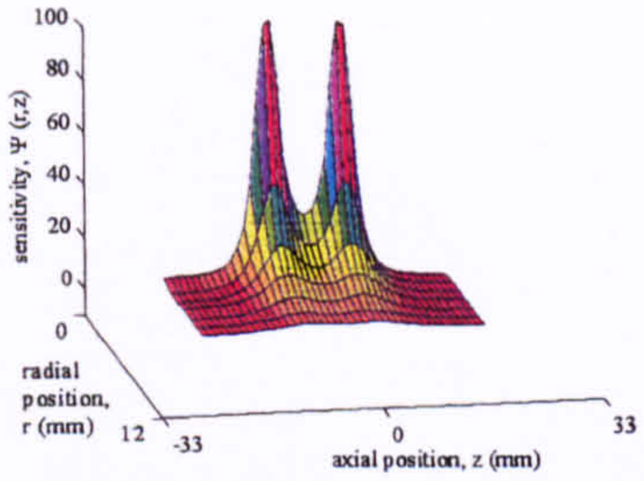
$\omega = 0.54$, shape 1 Field electrode separation, f = 13mm Sense electrode separation, s_α = 7mm	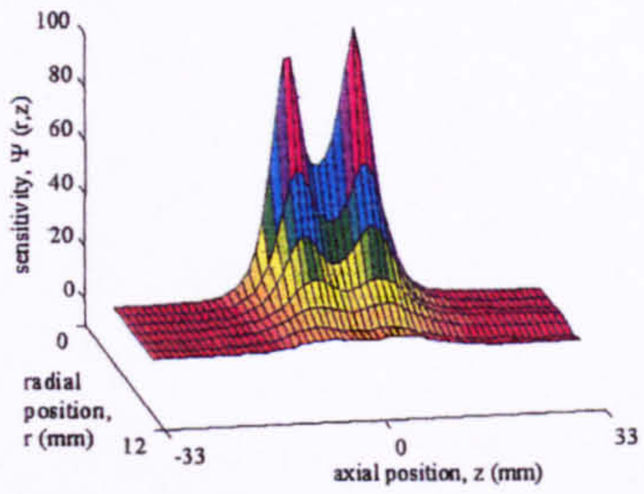	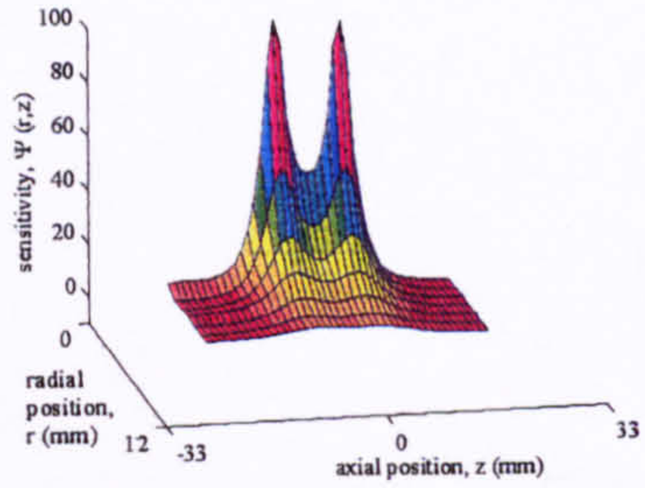
$\omega = 0.23$, shape 2 Field electrode separation, f = 13mm Sense electrode separation, s_α = 3mm	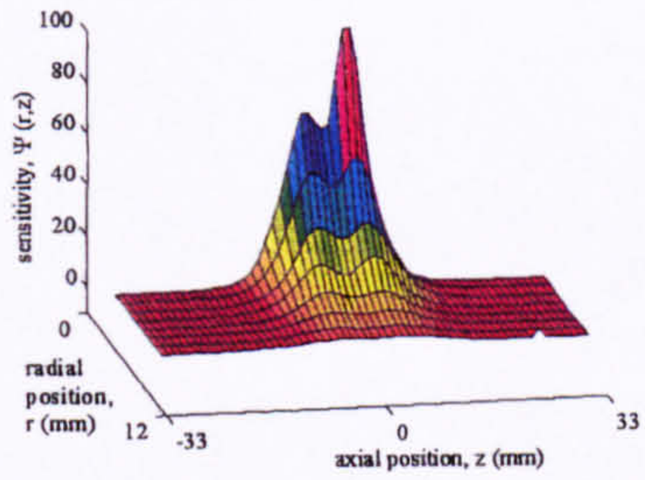	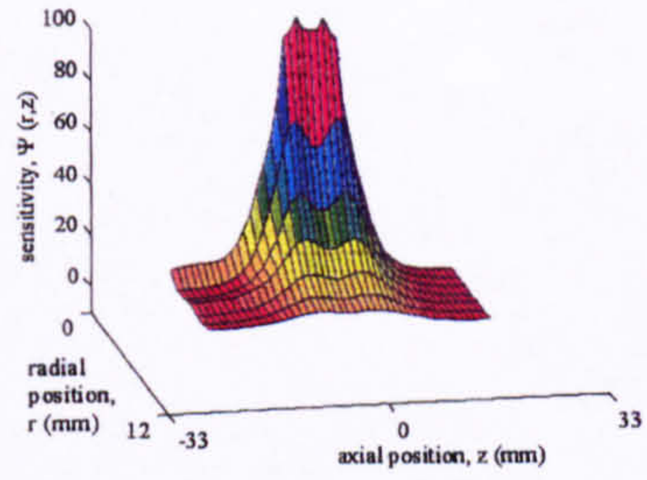

Figure 5-9. Qualitative comparison of sensitivity volumes from finite element modelling and experimental static testing for 4-electrode SEMM arrays with increasing s_α.

In Figure 5-9 the static testing sensitivity volumes again show qualitative agreement with the finite element modelling sensitivity volumes. The sensitivity volumes from each method are approximately the same when the array is configured with the same combination of f and s_α This suggests that a 4-electrode SEMM array will exhibit a shape 2 sensitivity volume if its geometry is as predicted in Section 3.2.6.2.

5.4.2.2 Quantitative analysis of the static testing.

Qualitative analysis of the array's sensitivity as the geometry was varied showed the electrode geometries that gave the best sensitivity volume shape. However it was important to verify that the measured changes in mixture resistance acquired by these arrays were large enough to measure accurately. For the purposes of this quantitative analysis the response of the array has been presented as a change in mixture resistance, ΔR (see Equation 5-5). Therefore the sensitivity volumes for each array geometry presented in this section show ΔR as a function of the position of the nylon ring.

The finite element modelling showed that the shape of the sensitivity volume of a 4-electrode SEMM array evolved as f was increased (see Section 3.2.6.2) and three general shapes of sensitivity volume were identified (see Figure 3-22). The appearance of these shapes in the sensitivity volumes from finite element modelling (defined in terms of Ψ) and experimental static testing (defined in terms of Ψ) was compared in Figure 5-8. In Figure 5-10 their appearance in the sensitivity volumes from finite element modelling (defined in terms of Ψ) and experimental static testing (defined in terms of ΔR) is compared.

At first examination the sensitivity volumes from experimental static testing shown in Figure 5-10 appear the same as those in Figure 5-8. However if the sensitivity scales are examined differences can be seen.

1. The shape 1 sensitivity volumes shown in Figure 5-10 show a peak value of ΔR of approximately 1000Ω. However these plots show a rapid fall-off in ΔR as the radial position of the ring is increased.
2. The shape 2 sensitivity volume shown in Figure 5-10 shows a lower peak value of ΔR of approximately 500Ω. However as the radial position of the ring is increased ΔR does not fall away as rapidly as in the shape 1 sensitivity volumes.
3. The shape 3 sensitivity volumes show a significantly lower value of ΔR at all the positions of the ring. In Figure 5-10 the peak value of ΔR for the shape 3 sensitivity volume is less than 400Ω. This response falls away rapidly as either the radial or axial position of the ring is increased.

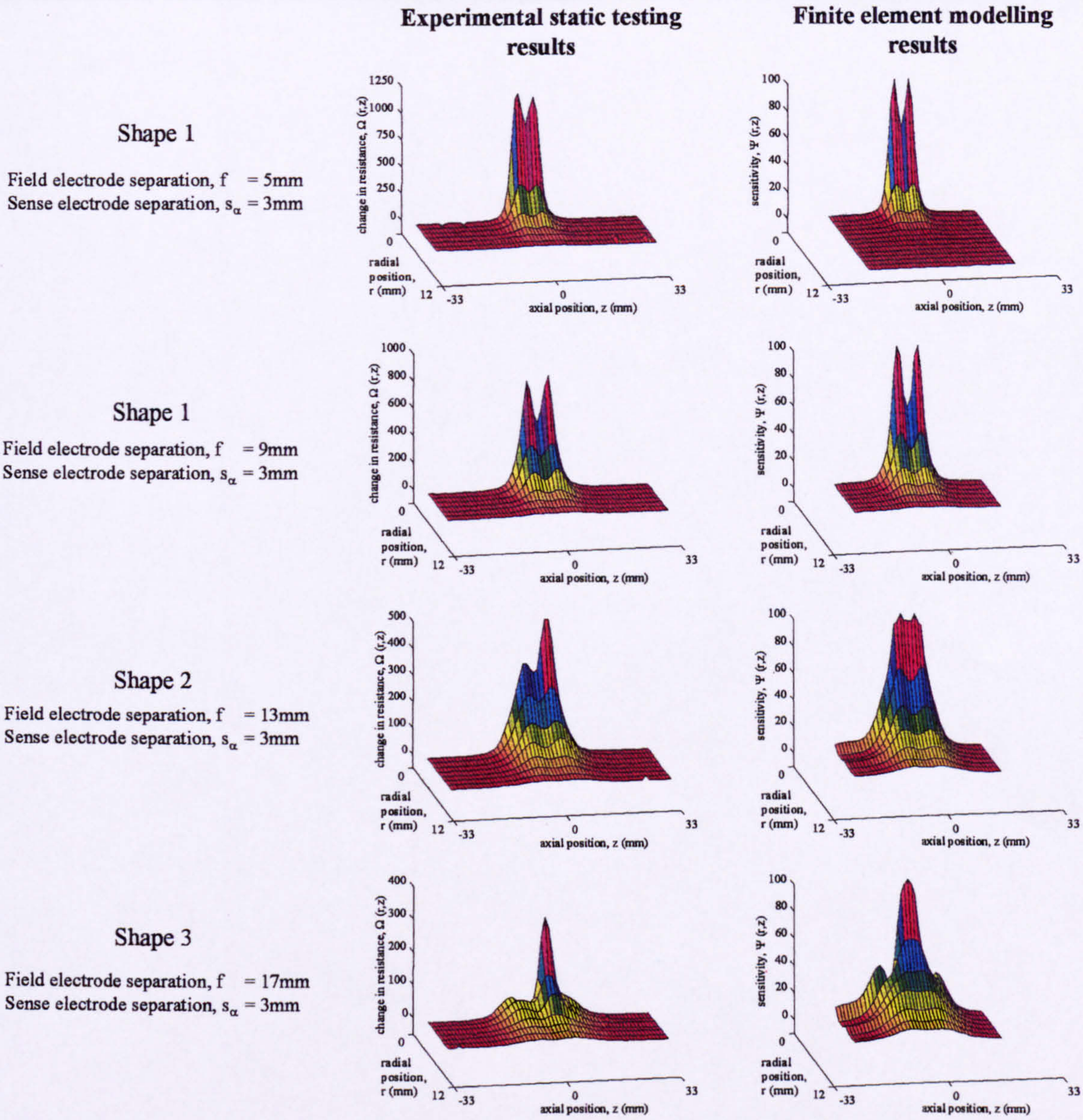

Figure 5-10. Comparison of quantitative experimental static testing sensitivity volumes with finite element modelling sensitivity volumes.

These results confirm that an array with a shape 3 sensitivity volume is unsuitable for the measurement of $\alpha_{s,i}$ in the current investigation as the value of ΔR is low and highly variable. The results show that an array with a shape 1 sensitivity volume will result in the highest value of ΔR. However this high ΔR will only be recorded if the particle is close to the array. The results show that an array with a shape 2 sensitivity volume will give a larger value of ΔR at increased radial positions of the particle, and will give a more uniform response to a particle at a wide range of radial and axial positions. In conclusion the results support the

findings of the finite element modelling that a shape 2 sensitivity volume is the most ideal for measurement of $\alpha_{s,i}$ in the current investigation.

5.4.3 Static testing of the response of sensor A and sensor B of 6-electrode SEMM arrays.

The geometry of a 6-electrode SEMM array allows three dimensions to be varied to change the geometry of the sensors. These are the sensor separation, j, the field electrode separation, f, and the sense electrode separation, s_v (see Figure 3-9). From the finite element modelling trends were noticed in the sensitivity of the array with variation of all these dimensions (see Section 3.2.6.3.3). In order to verify these trends static testing was carried out using 6-electrode SEMM arrays with different j, f and s_v.

5.4.3.1 Qualitative comparison of the static testing with the finite element modelling.

<u>The effect on the sensitivity volume shapes of varying the sensor separation, j.</u>

The finite element modelling had suggested that the axial and radial size of the sensitivity volumes of sensors A and B of 6-electrode SEMM arrays reduced as j was increased. In order to validate this finding experimental static testing was carried using arrays with different j. Figure 5-11 and Figure 5-12 show representative experimental static testing sensitivity volumes for 6-electrode SEMM arrays as j is varied. Also shown are the sensitivity volumes from finite element modelling of arrays with the same geometry.

Figure 5-11 and Figure 5-12 show that the experimental static testing sensitivity volumes are qualitatively similar to the finite element modelling sensitivity volumes. Any differences can be explained by considering that the tolerances of the positions of the electrodes of the experimental probes are not as high as those of the modelled arrays. The axial and radial size of the sensitivity volumes clearly reduces as j is increased and therefore it is considered that the finite element modelling results are reliable.

sensor separation, j **=2mm**
field electrode separation, f =17mm
sense electrode separation, s_v =1mm

Experimental static testing results

Finite element modelling results

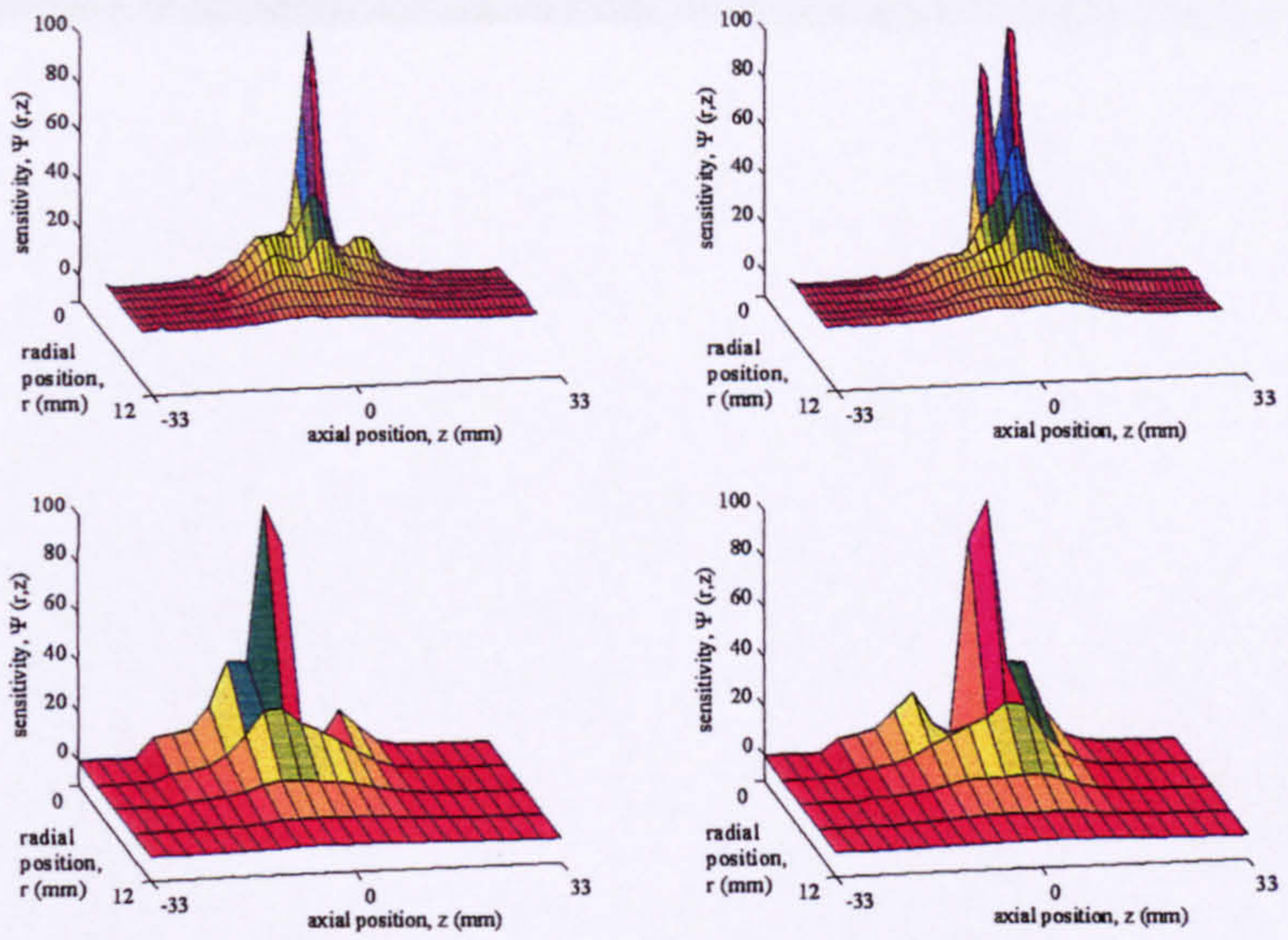

sensor separation, j **=10mm**
field electrode separation, f =17mm
sense electrode separation, s_v =1mm

Experimental static testing results

Finite element modelling results

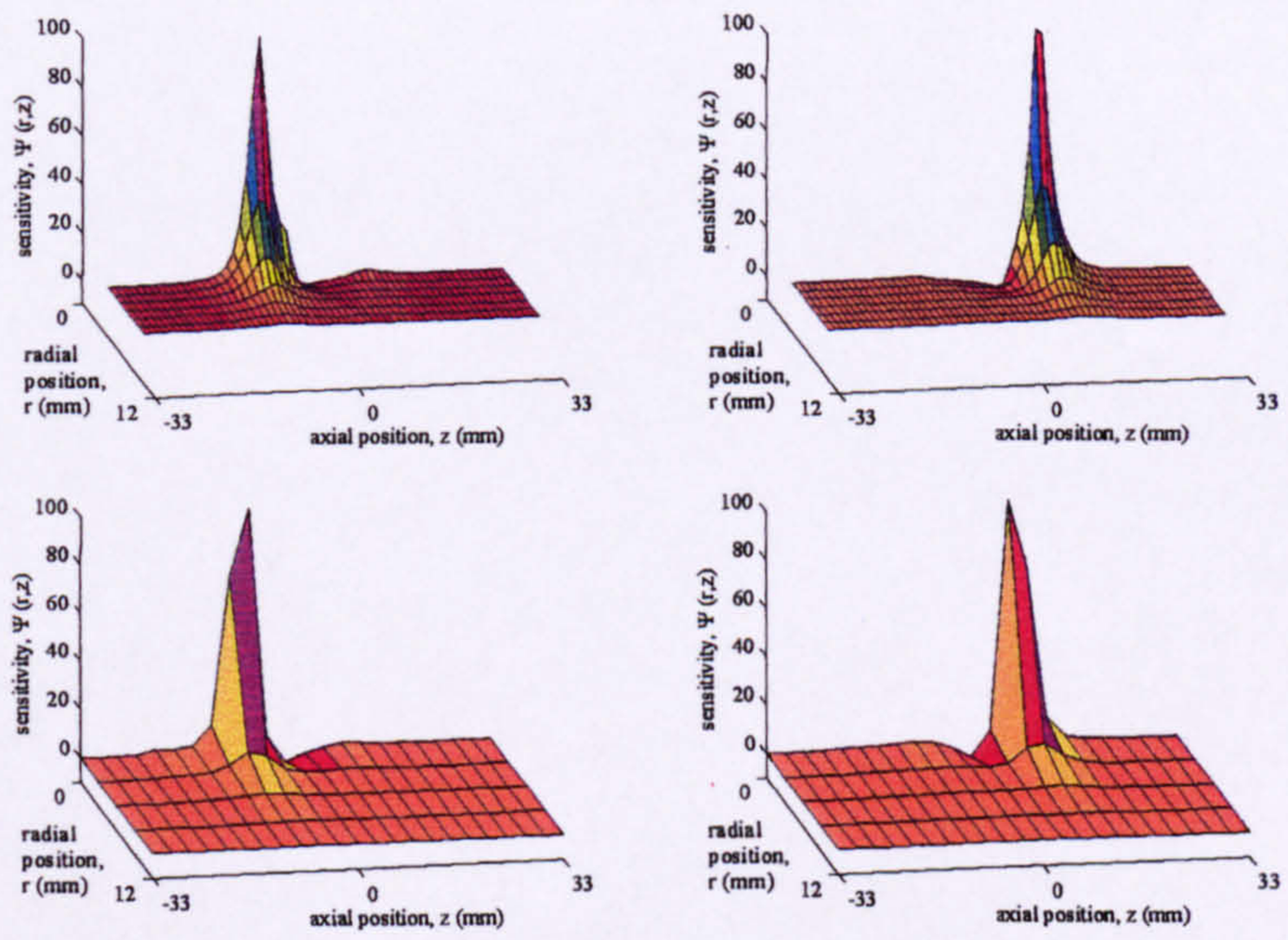

Figure 5-11. Qualitative comparison of sensitivity volumes from static testing and finite element modelling for 6-electrode SEMM arrays as j is varied.

sensor separation, j **=6mm**
field electrode separation, f =15mm
sense electrode separation, s_v =3mm

Experimental static testing results

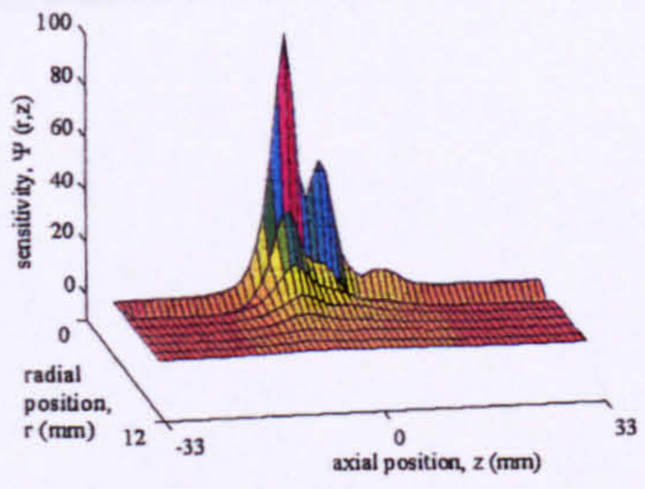

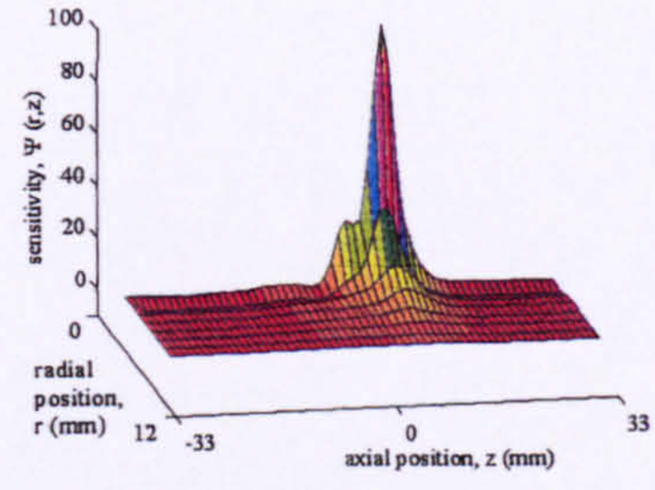

Finite element modelling results

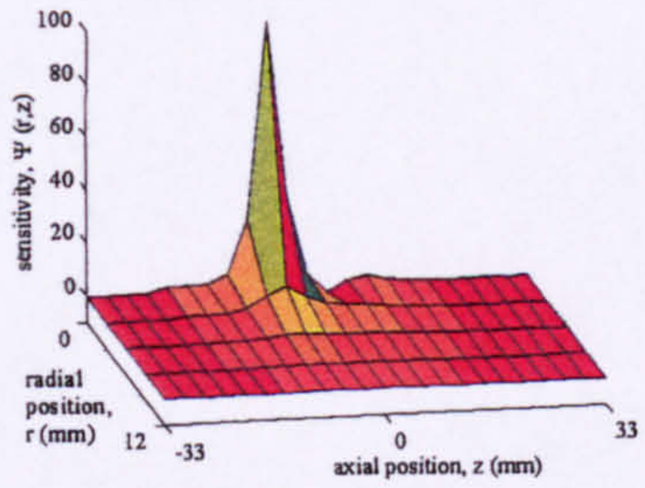

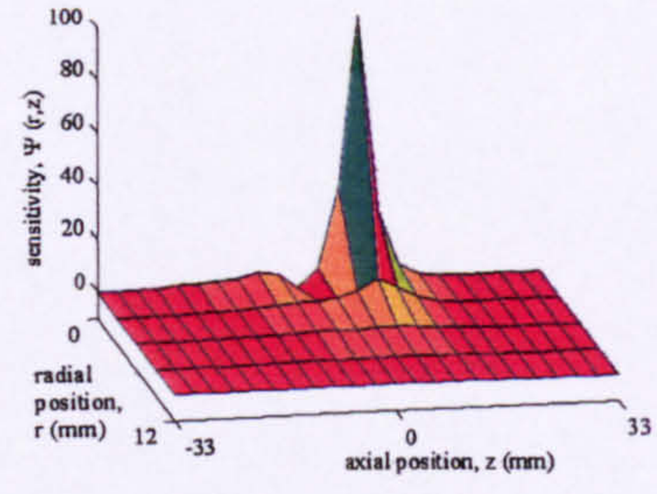

sensor separation, j **=8mm**
field electrode separation, f =15mm
sense electrode separation, s_v =3mm

Experimental static testing results

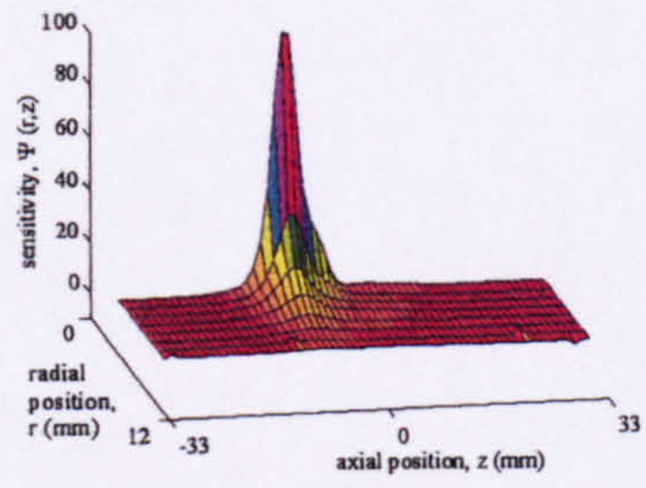

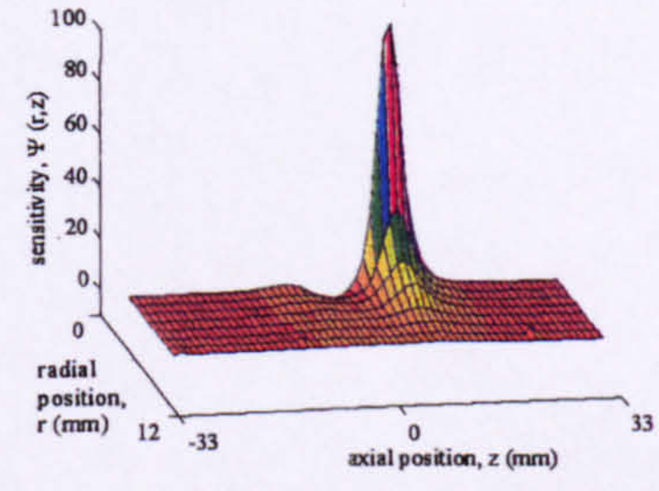

Finite element modelling results

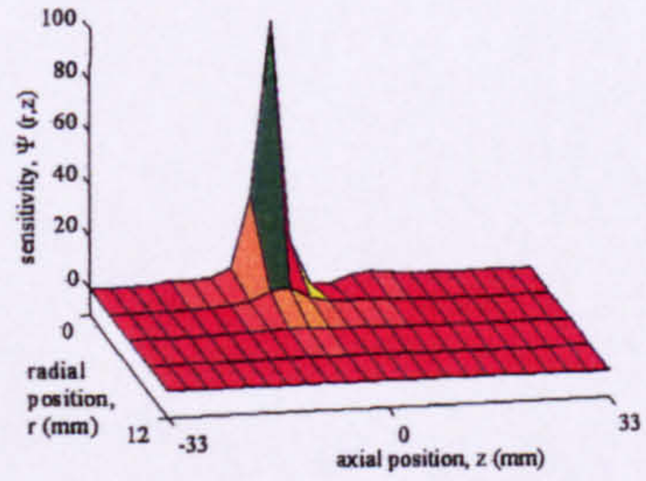

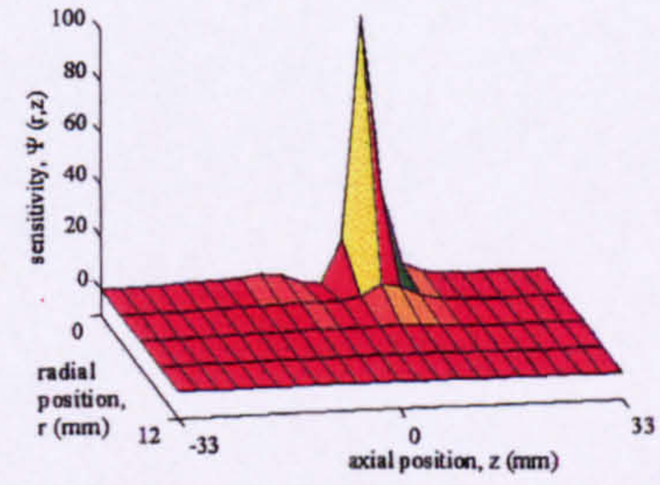

Figure 5-12. Qualitative comparison of sensitivity volumes from static testing and finite element modelling for 6-electrode SEMM arrays as j is varied.

The effect on the sensitivity volume shapes of varying the field electrode separation, f.

The finite element modelling had suggested that the axial and radial size of the sensitivity volumes of sensors A and B of 6-electrode SEMM arrays reduced as f was reduced with respect to j (see Section 3.2.6.3.3). This trend was considered of fundamental importance to the array optimisation, as it suggested that optimised sensitivity could be achieved with a low value of j, therefore reducing the effects of flow pattern dispersion on the cross-correlation (see Section 3.2.6.3). In order to validate these findings experimental static testing was carried out using probes configured as 6-electrode SEMM arrays with different values of f. Representative experimental static testing sensitivity volumes are shown in Figure 5-13 and Figure 5-14. The finite element modelling sensitivity volumes for arrays with the same

geometry are also shown for comparison. In Figure 5-14 the sense electrode separation, s_v, also varies slightly between the two arrays. However, it will be shown in the following section that s_v has little effect on the sensitivity volume shape and that these two arrays can be used to show the effect of variation of f.

Figure 5-13 and Figure 5-14 show that the experimental static testing sensitivity volumes show qualitative agreement with the finite element modelling sensitivity volumes. This suggests that the results of the finite element modelling are reliable and that an optimised sensitivity volume shape can be achieved as long as f is minimised with respect to j.

sensor separation, j =2mm
field electrode separation, f =5mm
sense electrode separation, s_v =1mm

Experimental static testing results

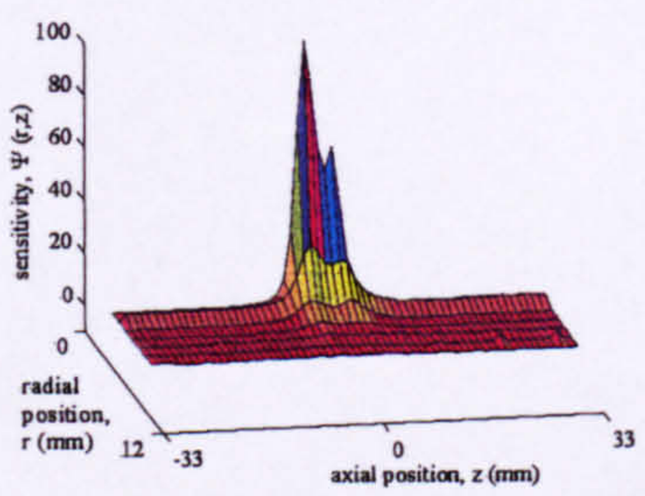

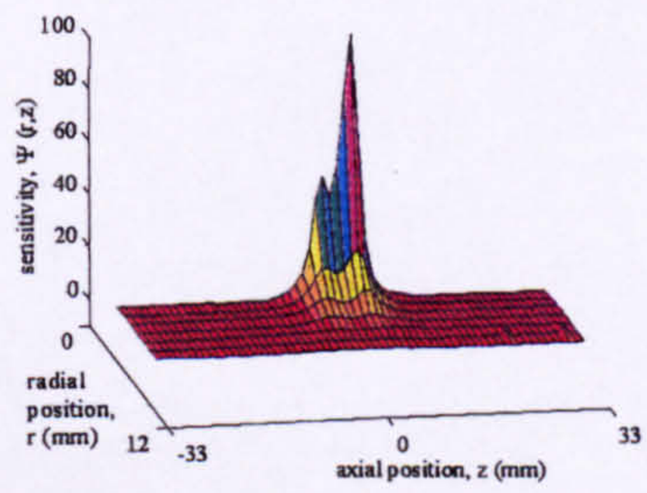

Finite element modelling results

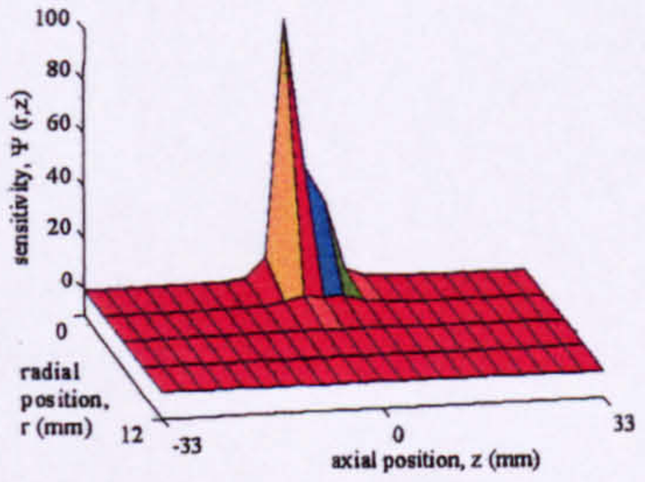

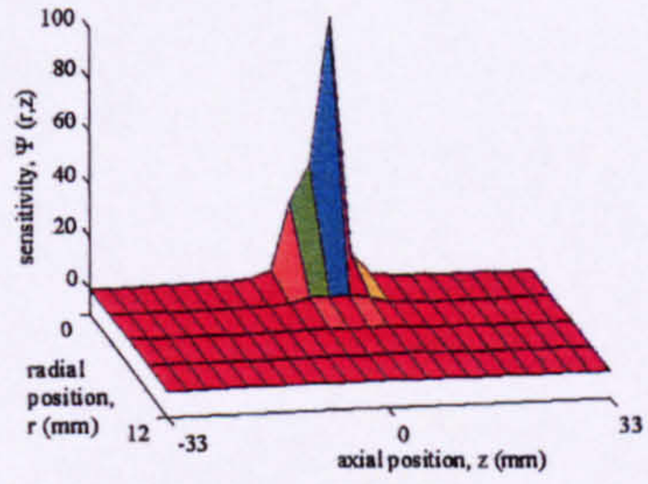

sensor separation, j =2mm
field electrode separation, f =17mm
sense electrode separation, s_v =1mm

Experimental static testing results

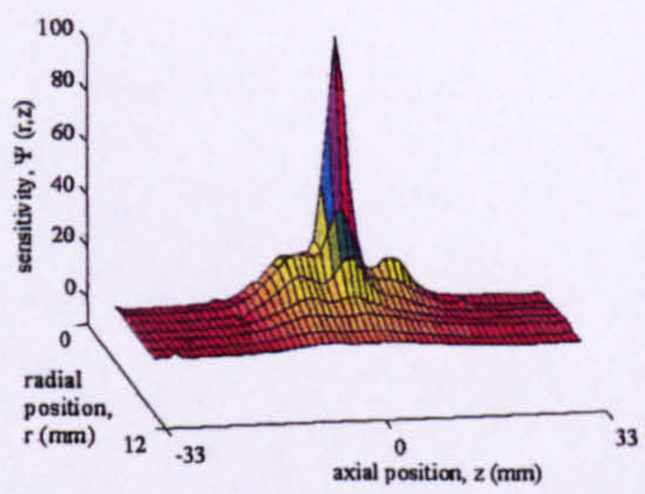

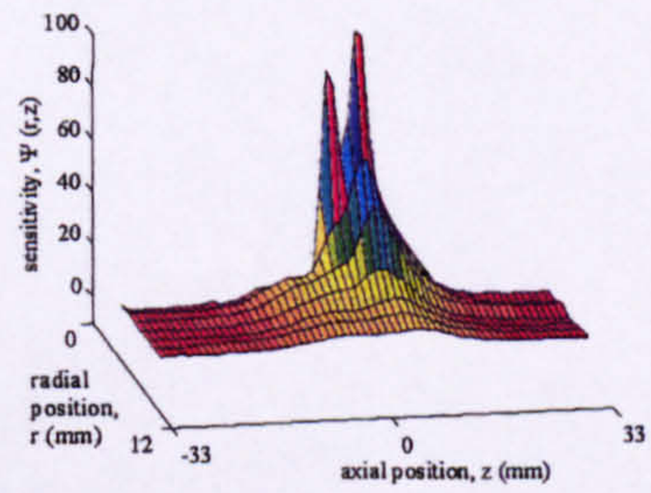

Finite element modelling results

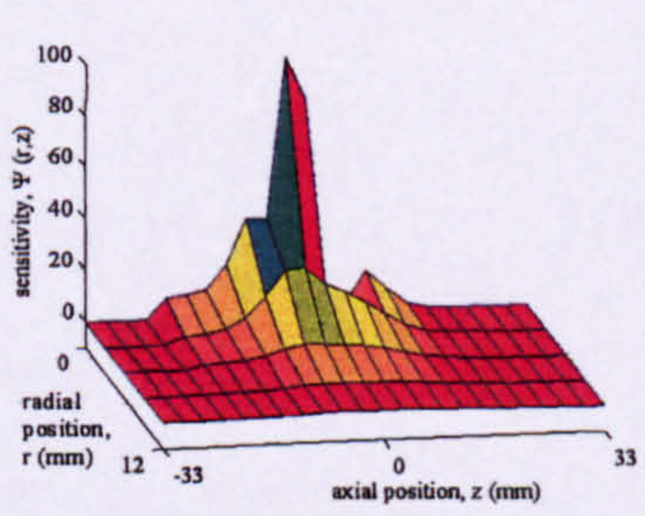

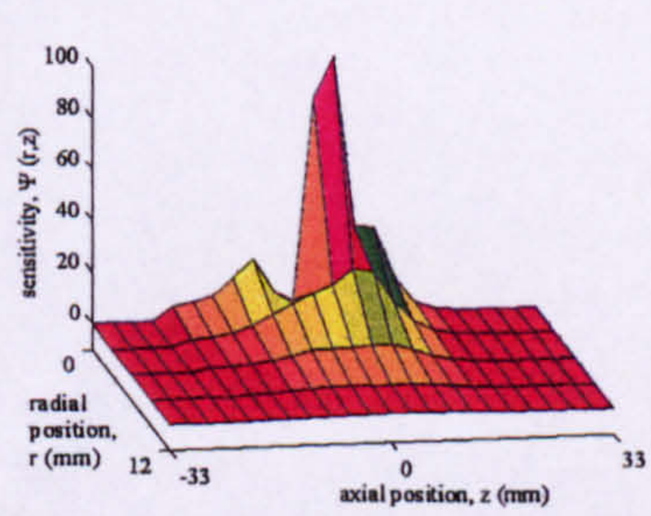

Figure 5-13. Qualitative comparison of sensitivity volumes from static testing and finite element modelling for 6-electrode SEMM arrays as f is varied.

sensor separation, j =6mm
field electrode separation, f =13mm
sense electrode separation, s_v =3mm

Experimental static testing results

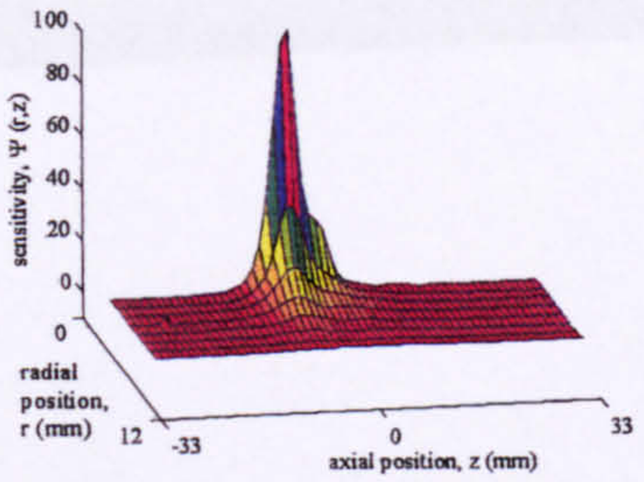

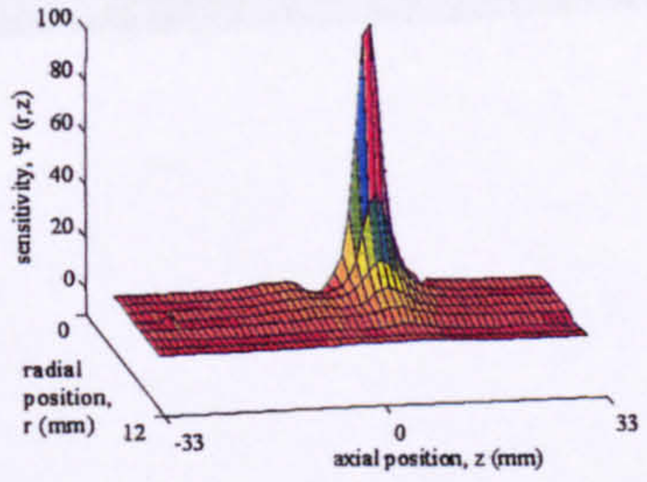

Finite element modelling results

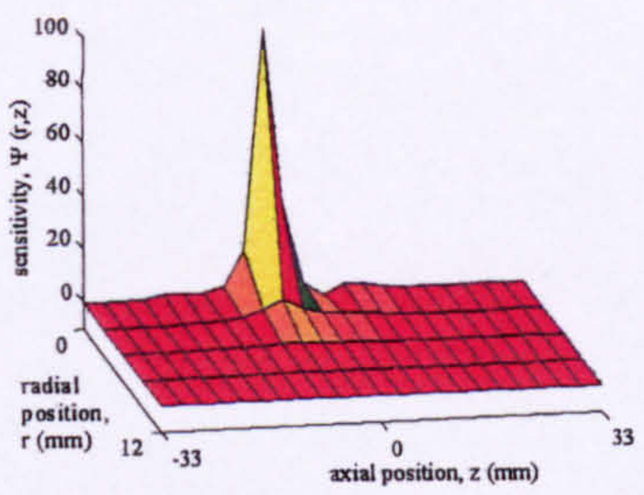

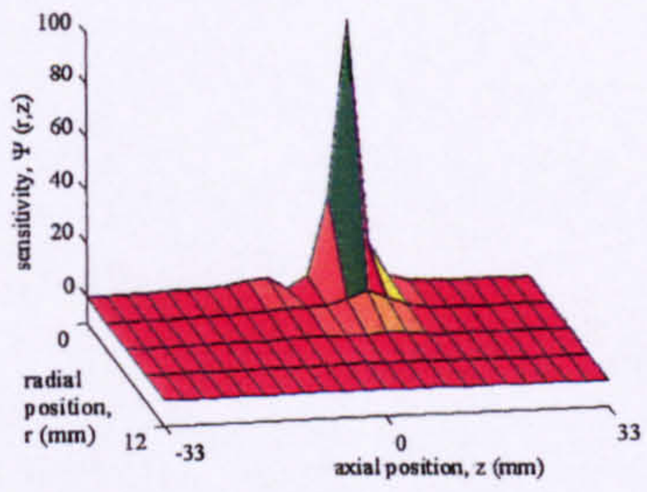

sensor separation, j =6mm
field electrode separation, f =19mm
sense electrode separation, s_v =5mm

Experimental static testing results

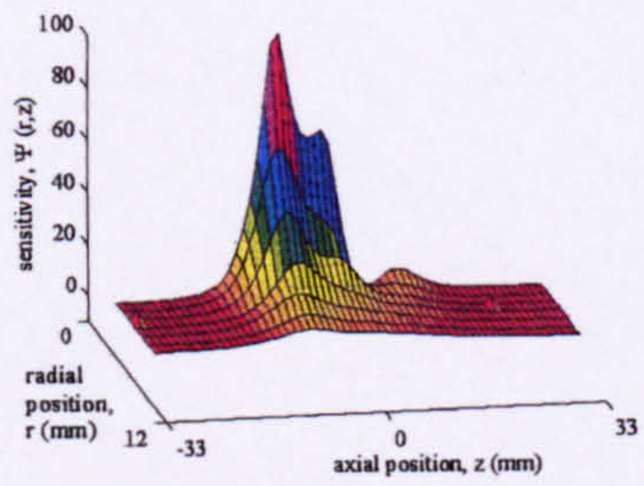

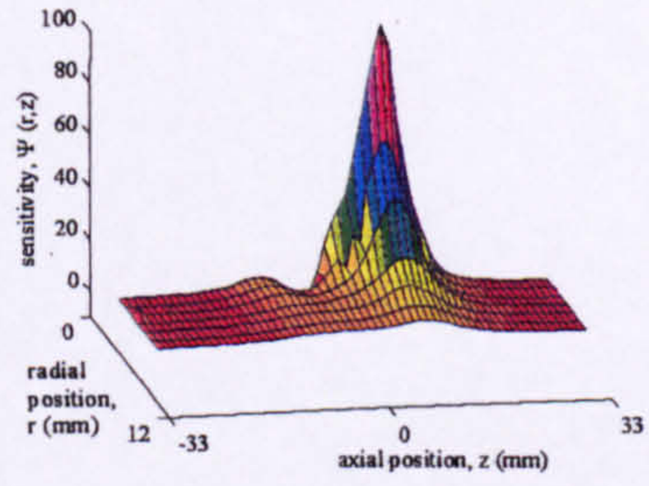

Finite element modelling results

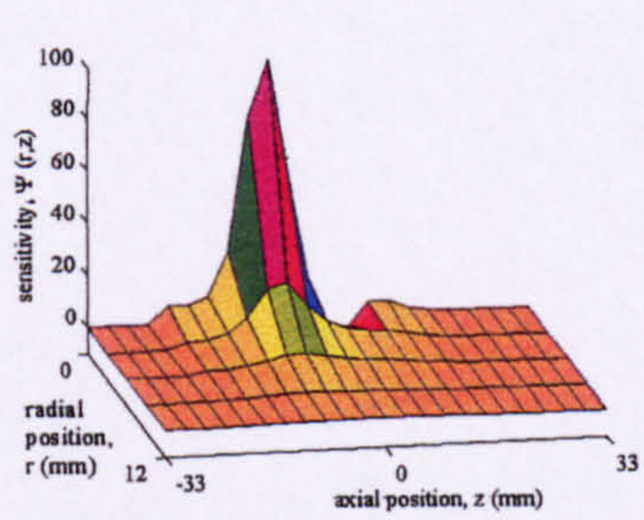

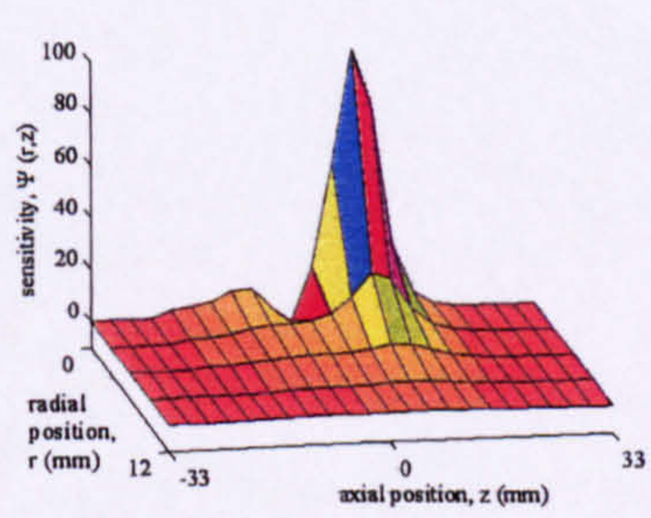

Figure 5-14. Qualitative comparison of sensitivity volumes from static testing and finite element modelling for 6-electrode SEMM arrays as f is varied.

<u>The effect on the sensitivity volume shapes of varying the sense electrode separation, s_v</u>

The finite element modelling suggested that the sensitivity volume shapes of sensors A and B of a 6-electrode SEMM array are affected very little by variation of s_v (see Section 3.2.6.3.3). If this was the case it would allow much greater freedom for design of combination measurement probes, capable of acquiring simultaneous measurements of $\alpha_{s,i}$ and $u_{s,i}$ (see Figure 3-7) by allowing a wider possible range of s_α. To verify these findings experimental static testing was carried out using probes configured as 6-electrode SEMM arrays with varying s_v. Representative static testing sensitivity volumes are shown in Figure 5-15. The finite element modelling sensitivity volumes for arrays with the same geometry are shown for comparison. In Figure 5-15 it can be seen that f also varies slightly between the two arrays but

it was not expected that this slight change would have a large effect on the sensitivity volume shapes.

Figure 5-15 shows qualitative agreement between the static testing sensitivity volumes and the finite element modelling sensitivity volumes. This shows that the finite element modelling results are reliable and that the variation of s_v has little effect on the sensitivity volume shape.

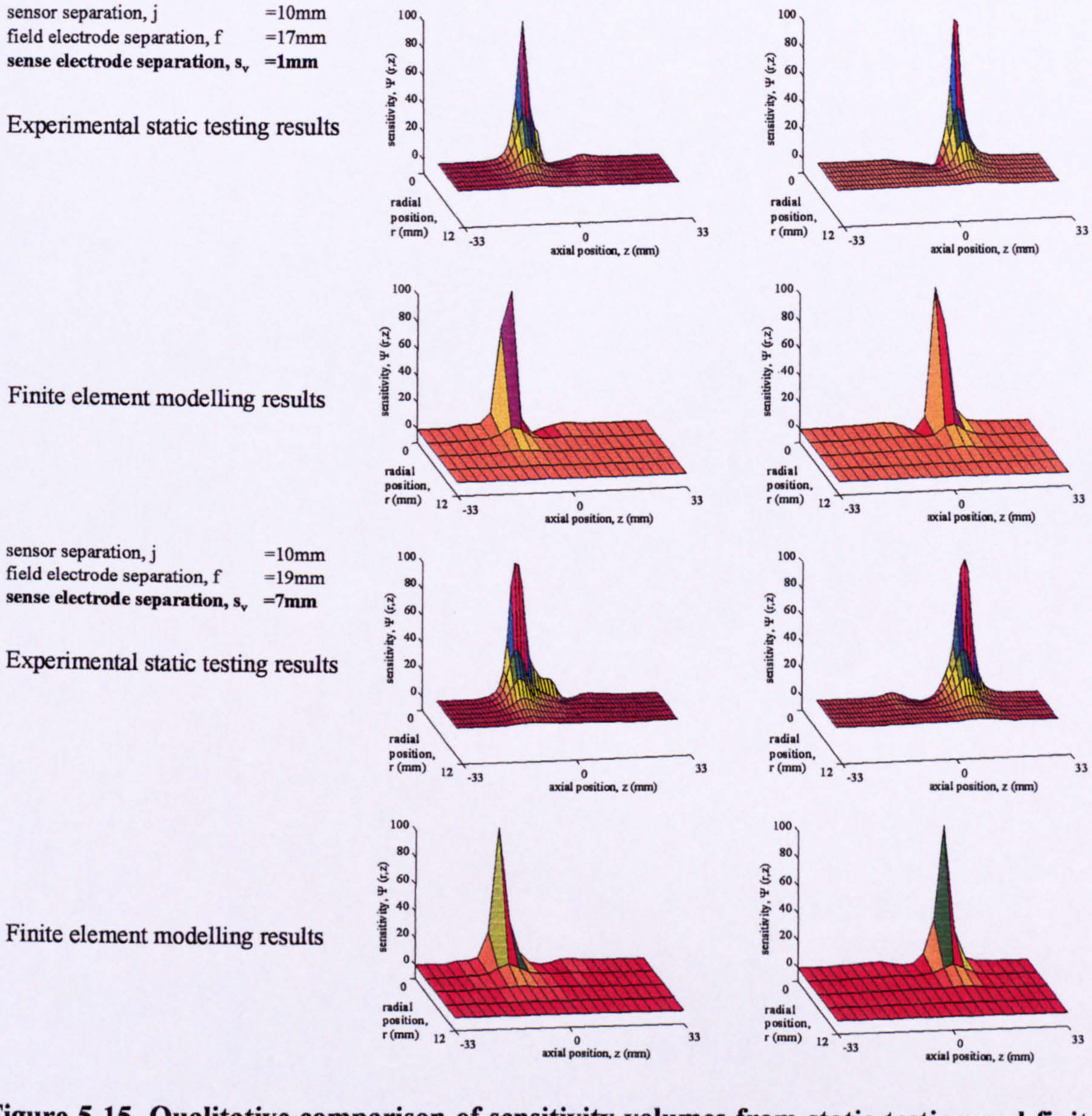

Figure 5-15. Qualitative comparison of sensitivity volumes from static testing and finite element modelling for 6-electrode SEMM arrays as s_v is varied.

5.4.3.2 Quantitative analysis of the static testing.

Qualitative analysis of the array's sensitivity as the geometry was varied showed the electrode geometries that gave the best sensitivity volume shape. However it was important to verify

that the measured changes in mixture resistance acquired by these arrays were large enough to measure accurately. For the purposes of this quantitative analysis the response of the array has been presented as a change in mixture resistance, ΔR (see Equation 5-5). Therefore the sensitivity volumes for each array geometry presented in this section show ΔR as a function of the position of the nylon ring.

The finite element modelling showed that the shape of the sensitivity volume of a 6-electrode SEMM array was optimised as the sensor separation, j, was increased (see Section 3.2.6.3.3). The appearance of this trend in the sensitivity volumes from finite element modelling (defined in terms of Ψ) and experimental static testing (defined in terms of Ψ) was compared in Figure 5-11 and Figure 5-12. In Figure 5-16 the appearance of the trend in the sensitivity volumes from experimental static testing (defined in terms of ΔR) is shown.

The experimental static testing sensitivity volumes in Figure 5-16 show that the axial and radial size of the sensitivity volume reduces as j is increased. If the sensitivity scales of the plots is examined it can also be seen that the maximum value of ΔR for each sensor increases as j is increased. This reinforces the conclusion drawn in Section 3.2.6.3.3 that j should be increased in order to optimise the sensitivity of the sensors.

sensor separation, j **=2mm**
field electrode separation, f =17mm
sense electrode separation, s_v =1mm

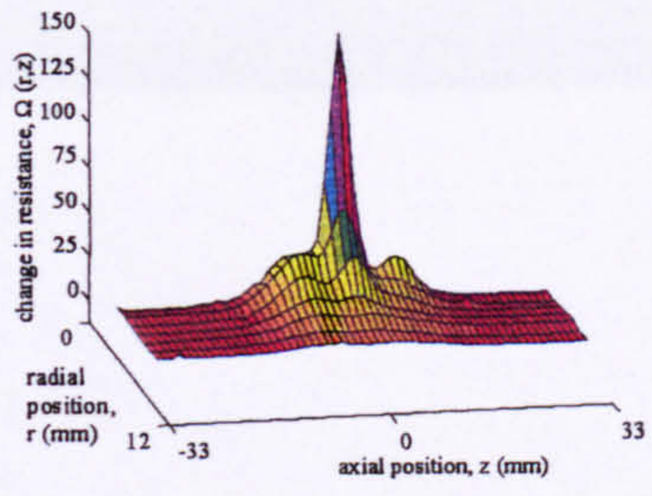

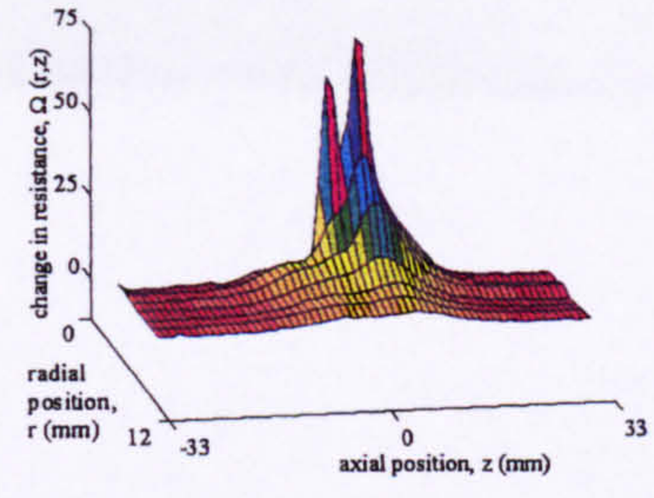

sensor separation, j **=10mm**
field electrode separation, f =17mm
sense electrode separation, s_v =1mm

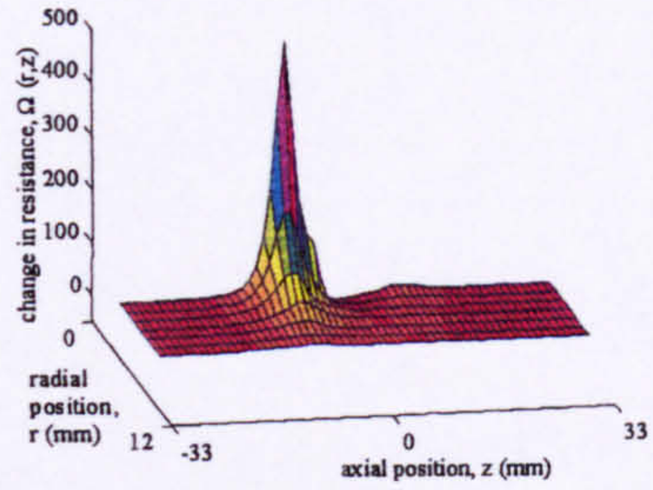

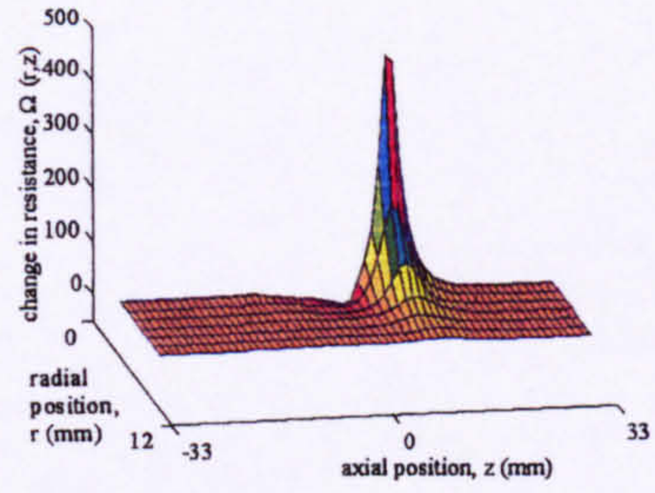

sensor separation, j **=6mm**
field electrode separation, f =15mm
sense electrode separation, s_v =3mm

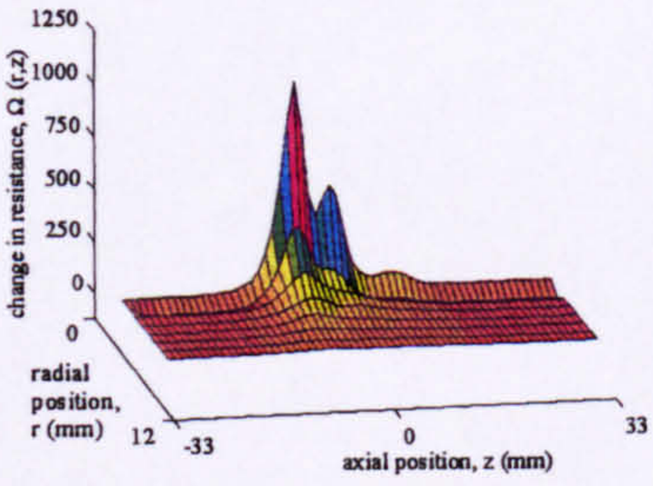

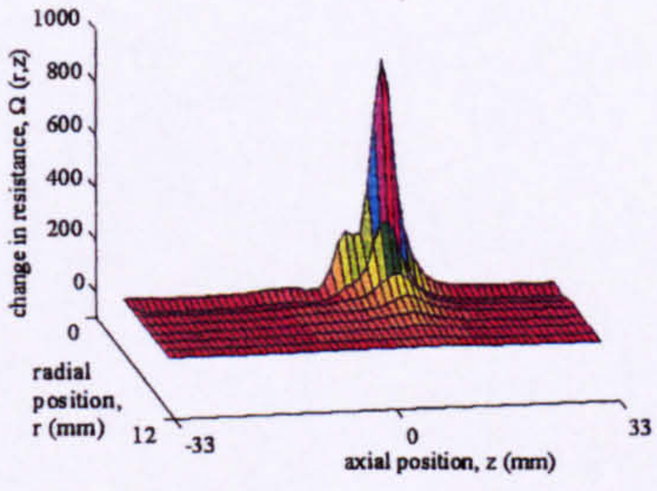

sensor separation, j **=8mm**
field electrode separation, f =15mm
sense electrode separation, s_v =3mm

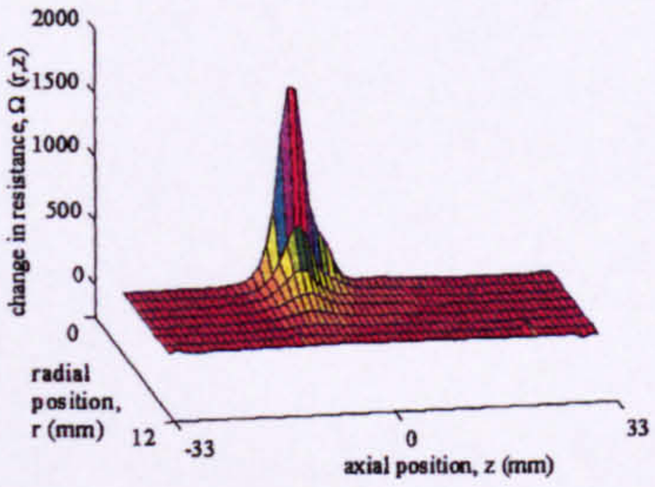

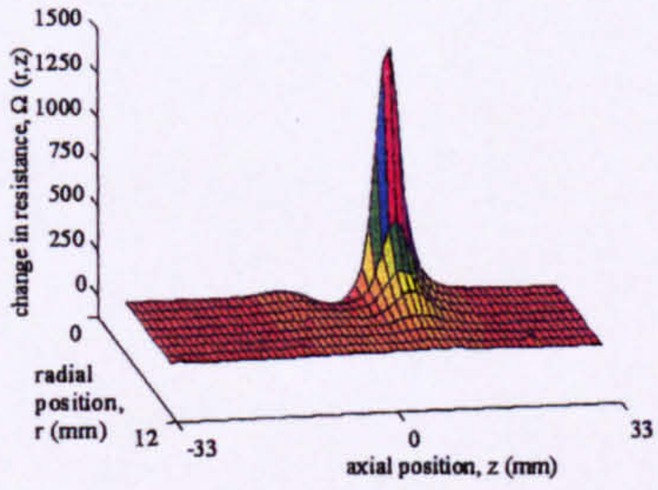

Figure 5-16. Quantitative sensitivity volumes for 6-electrode SEMM arrays as j is varied.

The finite element modelling also showed that the sensitivity volumes for sensors A and B of a 6-electrode SEMM array were optimised if the field electrode separation, f, was minimised with respect to j (see Section 3.2.6.3.3). The appearance of this trend in the sensitivity volumes from finite element modelling (defined in terms of Ψ) and experimental static testing (defined in terms of Ψ) was compared in Figure 5-13 and Figure 5-14. In Figure 5-17 the appearance of the trend in the sensitivity volumes from experimental static testing (defined in terms of ΔR) is shown.

sensor separation, j =2mm
field electrode separation, f =5mm
sense electrode separation, s_v =1mm

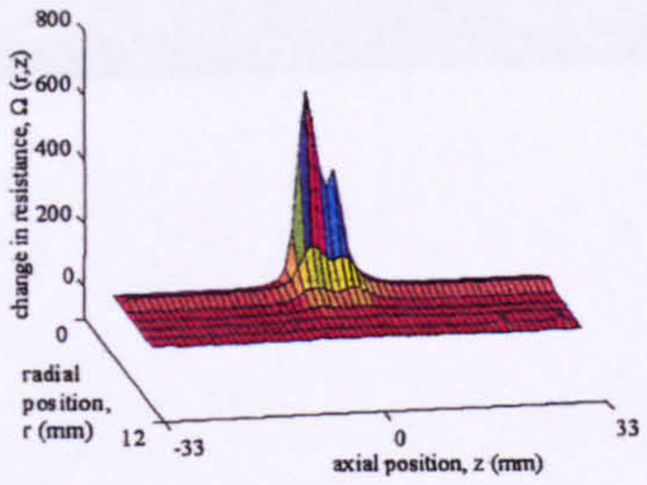

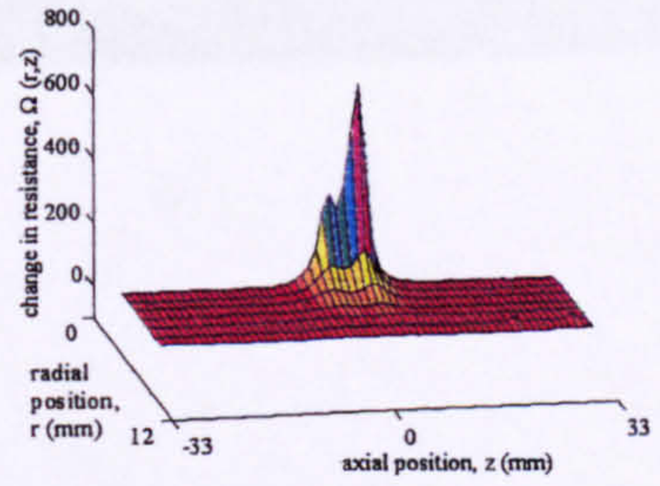

sensor separation, j =2mm
field electrode separation, f =17mm
sense electrode separation, s_v =1mm

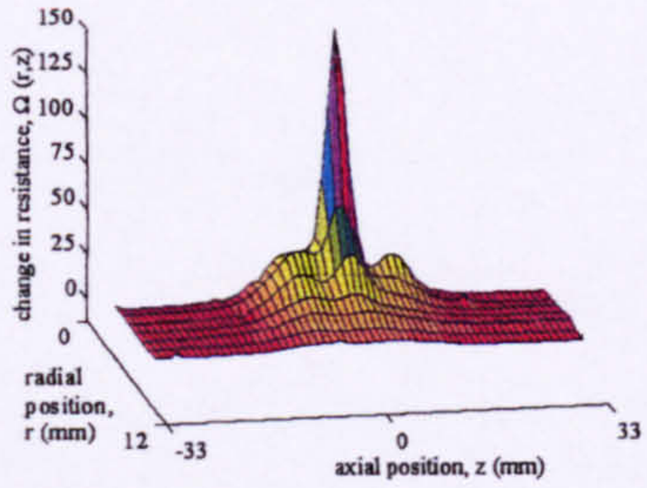

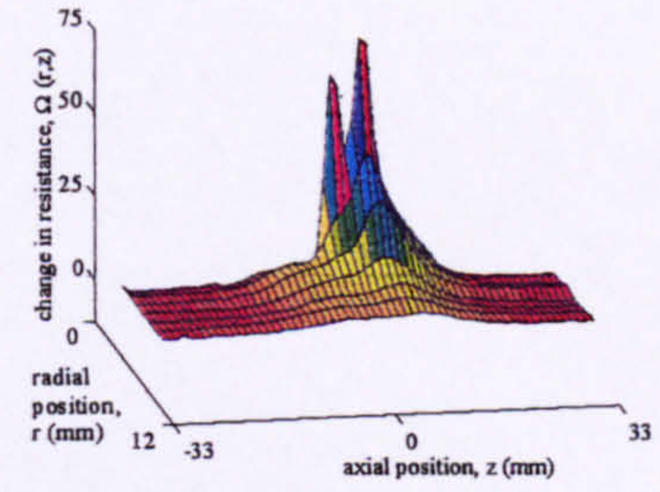

sensor separation, j =6mm
field electrode separation, f =13mm
sense electrode separation, s_v =3mm

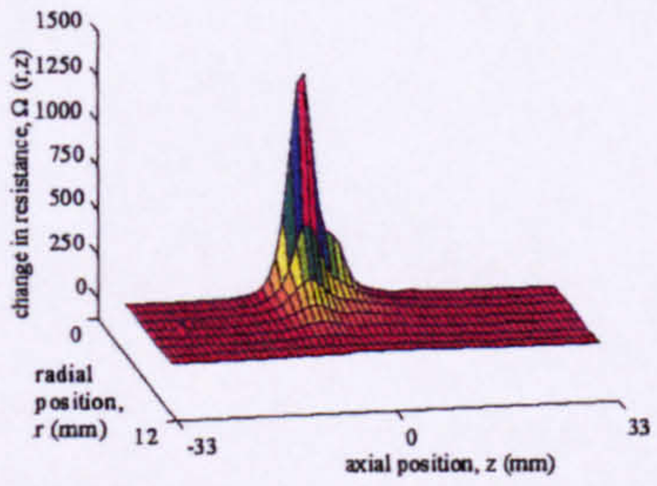

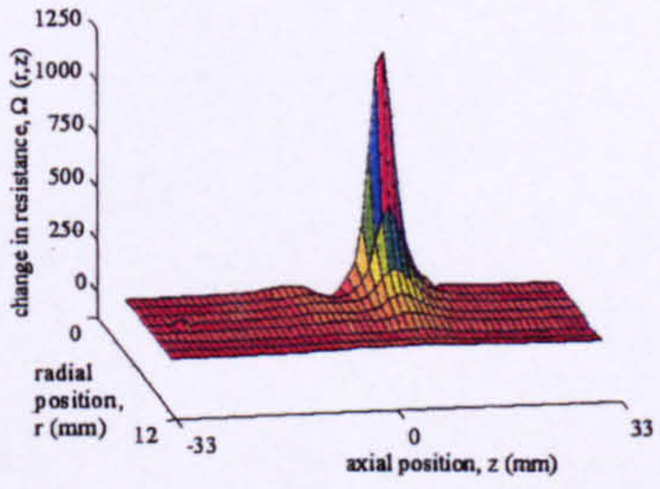

sensor separation, j =6mm
field electrode separation, f =19mm
sense electrode separation, s_v =5mm

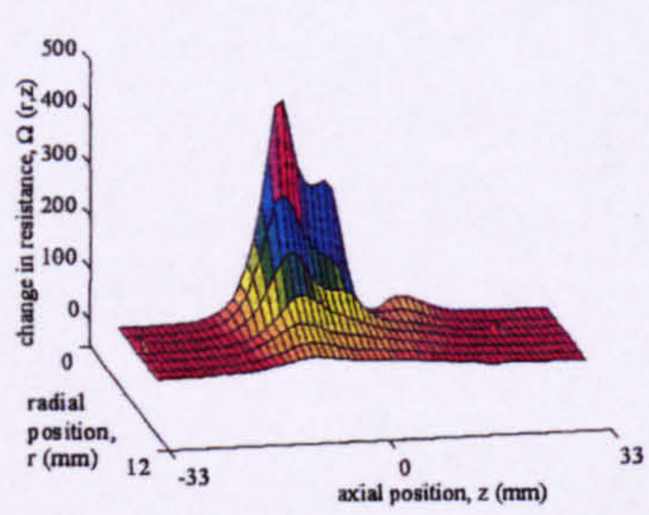

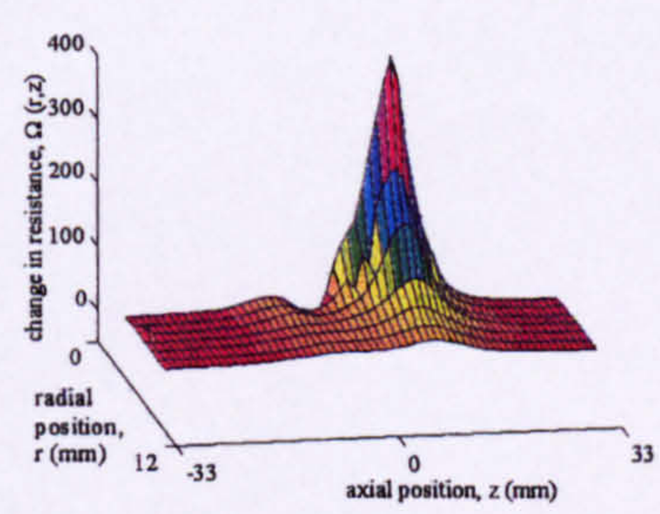

Figure 5-17. Quantitative sensitivity volumes for 6-electrode SEMM arrays as f is varied.

The static testing sensitivity volumes in Figure 5-17 show that the axial and radial size of the sensitivity volume reduces as f is reduced. If the sensitivity scales of the plots are examined it can also be seen that the maximum value of ΔR recorded by each sensor increases as f is reduced. This reinforces the conclusion drawn in Section 3.2.6.3.3 that f should be minimised with respect to j in order to optimise the sensitivity of the sensor.

Finally the finite element modelling showed that variation of the sense electrode separation, s_v, had little effect on the sensitivity volumes of sensors A and B of a 6-electrode SEMM array (see Section 3.2.6.3.3). The appearance of this trend in the sensitivity volumes from finite element modelling (defined in terms of Ψ) and experimental static testing (defined in

terms of Ψ) was compared in Figure 5-15. Figure 5-18 shows sensitivity volumes from experimental static testing (defined in terms of ΔR) for arrays with different s_v to enable this trend to be investigated.

sensor separation, j =10mm
field electrode separation, f =17mm
sense electrode separation, s_v =1mm

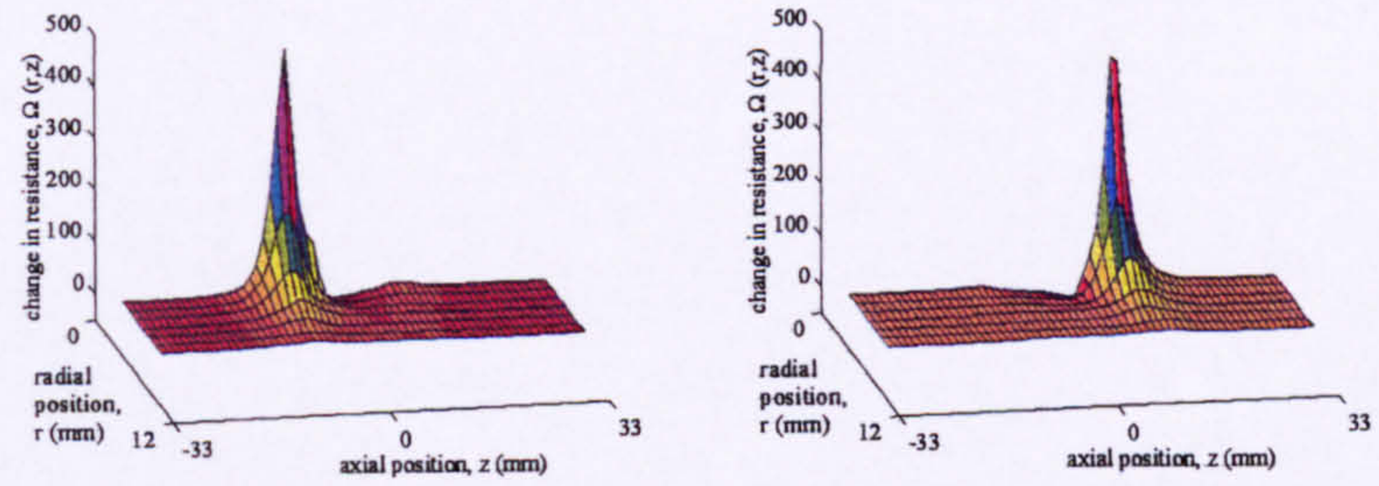

sensor separation, j =10mm
field electrode separation, f =19mm
sense electrode separation, s_v =7mm

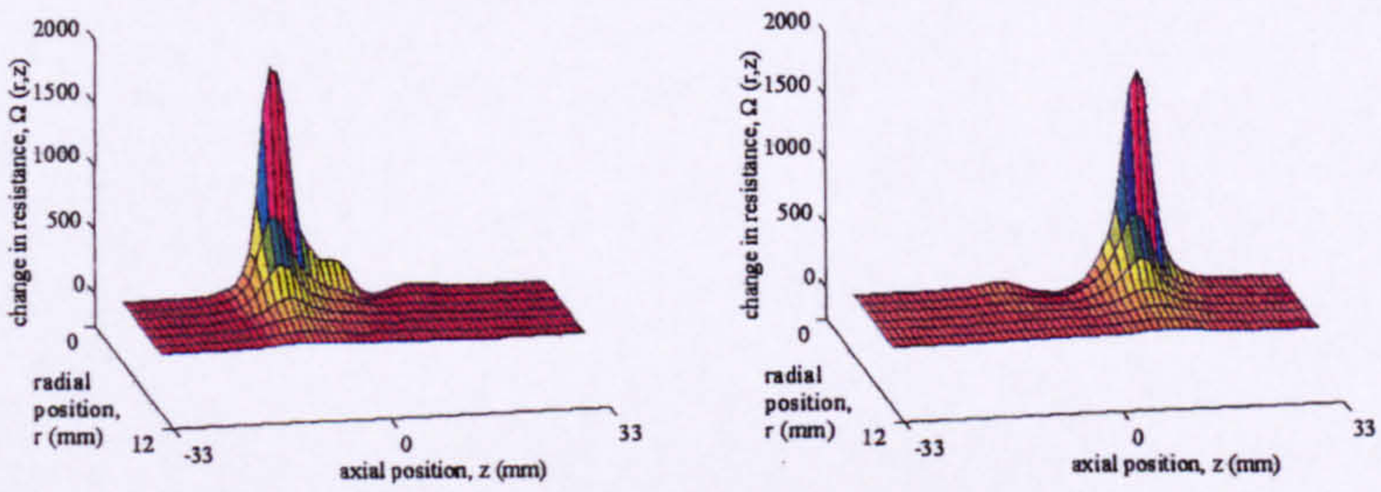

Figure 5-18. Quantitative sensitivity volumes for 6-electrode SEMM arrays as s_v is varied.

Figure 5-18 shows that the response of the array is affected as s_v is increased. Although the sensitivity volume shape is not greatly altered, the peak value of ΔR recorded increases as s_v is increased. This shows that s_v should be maximised in order to achieve an optimum response.

5.4.4 Conclusions of the experimental static testing of the probe response.

In Chapter 3 a number of guidelines were suggested for selecting optimum geometries for 4-electrode SEMM arrays (see Figure 3-8) and 6-electrode SEMM arrays (see Figure 3-9). These conclusions are summarised in Section 3.2.7. In general these conclusions have been supported by the experimental static testing in this chapter. The addition to this is that the experimental static testing reported in Section 5.4.3.2 showed that s_v should be maximised in order to optimise the response of the array.

In Chapter 3 four probe geometries were selected for acquiring combination measurements of $\alpha_{s,i}$ and $u_{s,i}$ (see Figure 3-7 for a description of the combination measurement principle). The geometries of these devices and their finite element modelling sensitivity volumes are given in Table 3-2 and Figure 3-33. Following the experimental static testing it was decided that

two of these devices would not be ideal for experimental use because they would result in low values of s_v. It was decided to build probes with the remaining two geometries to obtain profiles of $\alpha_{s,i}$ and $u_{s,i}$ in experimental testing. The geometries of these probes are given in Table 5-1. Their experimental static testing sensitivity volumes are shown in Figure 5-19. The finite element modelling sensitivity volumes are shown for comparison.

Table 5-1. Optimum array geometries for acquiring combination measurements of $\alpha_{s,i}$ and $u_{s,i}$ selected following experimental static testing.

Geometry	Sensor Separation (j), (mm)	Field electrode separation (f), (mm)	Sense electrode separation (s_α), (mm)	Sense electrode separation (s_v), mm
1	6	13	3	3
2	8	15	5	3

Sensor separation, j = 6mm
Field electrode spacing, f = 13mm
Sense electrode spacing, s_α = 3mm
Sense electrode spacing, s_v = 3mm

Experimental static testing results

Sensor α

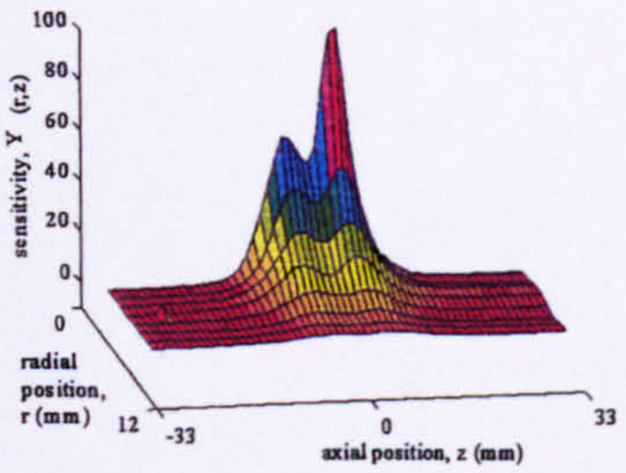

Sensor A

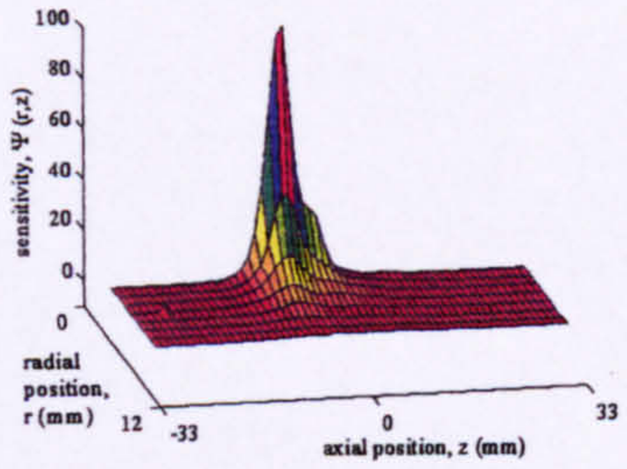

Sensor B

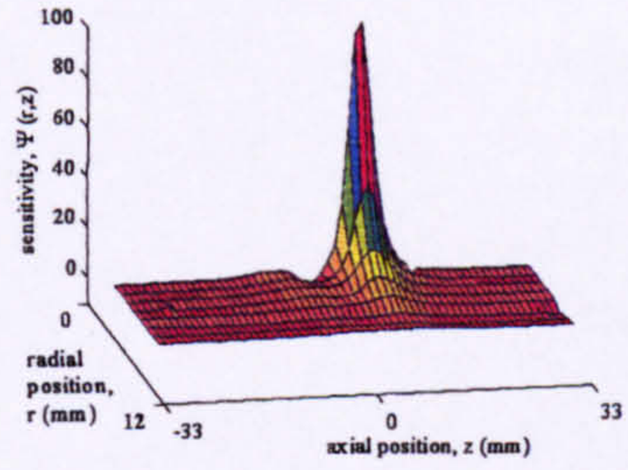

Finite element modelling results

Sensor α

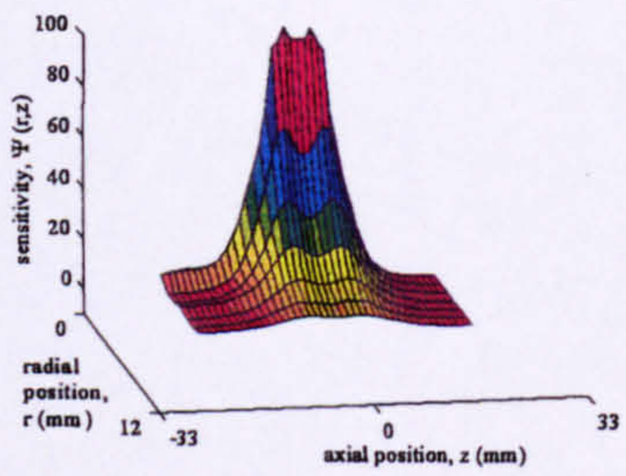

Sensor A

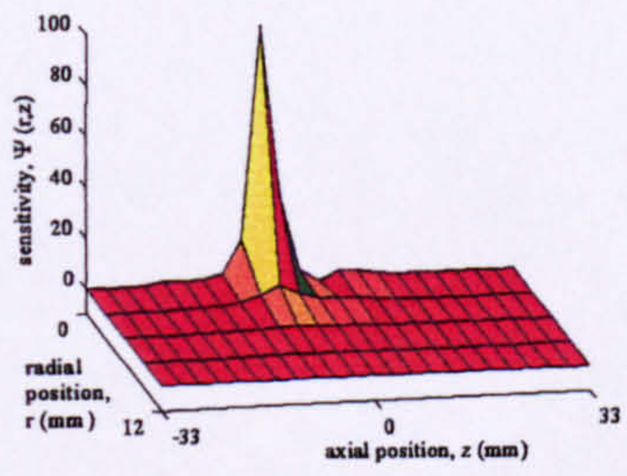

Sensor B

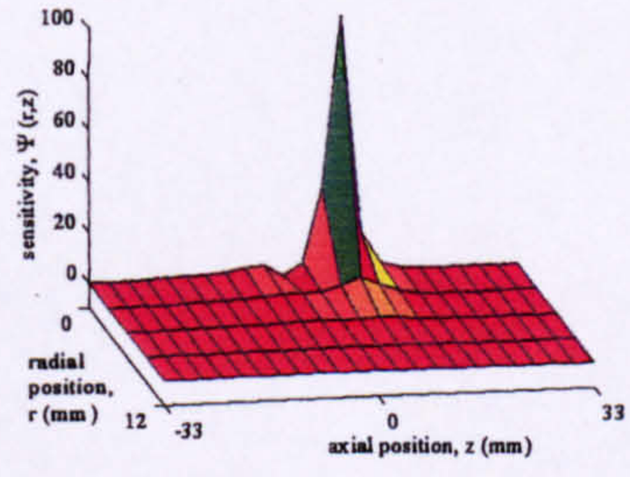

Sensor separation, j = 6mm
Field electrode spacing, f = 13mm
Sense electrode spacing, s_α = 3mm
Sense electrode spacing, s_v = 3mm

Experimental static testing results

Sensor α

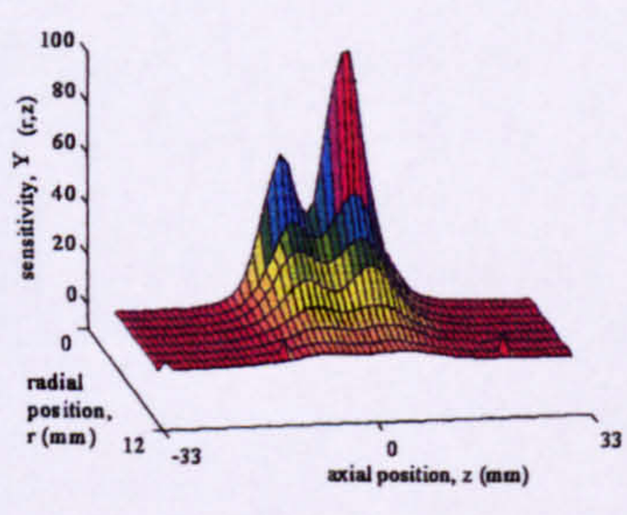

Sensor A

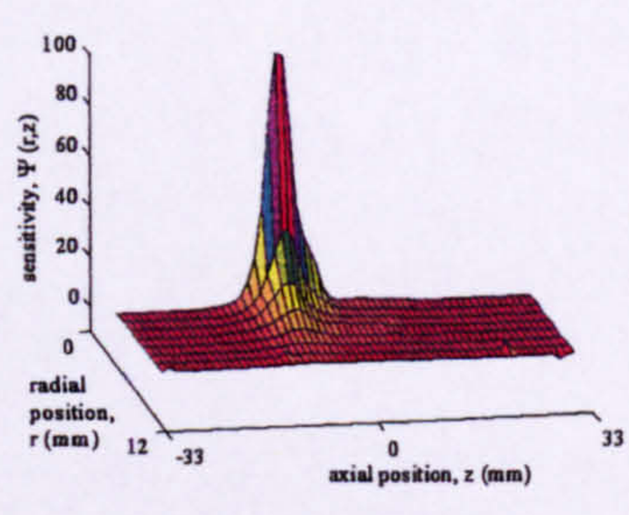

Sensor B

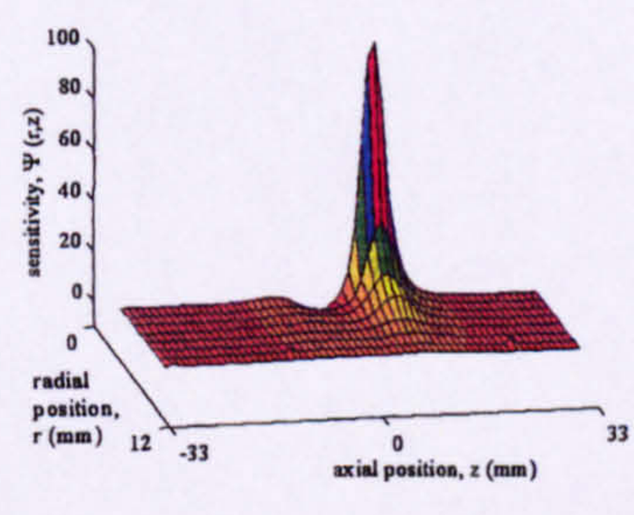

Finite element modelling results

Sensor α

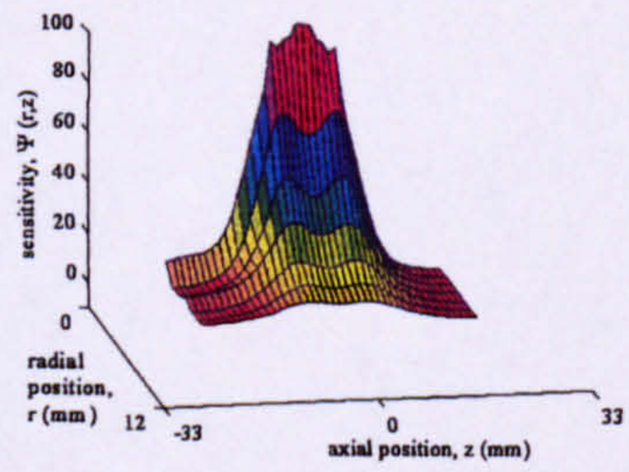

Sensor A

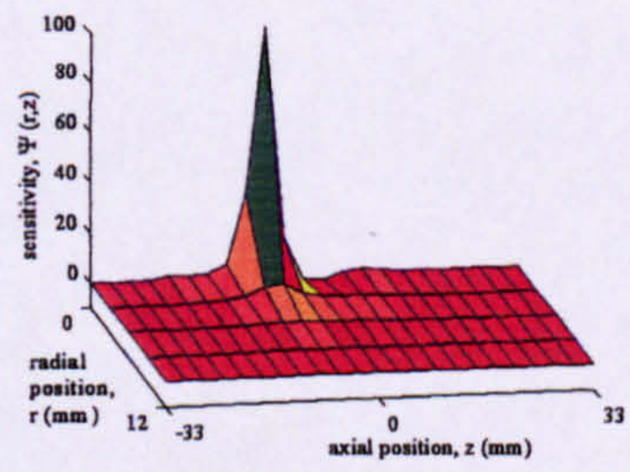

Sensor B

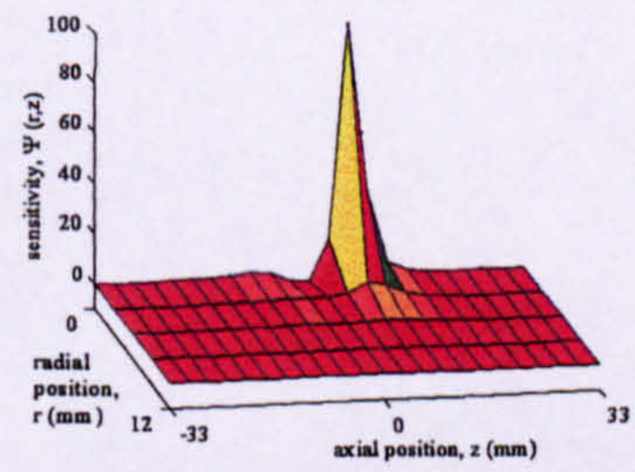

Figure 5-19. Comparison of static testing sensitivity volumes and finite element modelling sensitivity volumes for optimised 6-electrode array geometries.

In Figure 5-19, as in all the static testing, the sensitivity volumes show good agreement with the finite element modelling sensitivity volumes. This suggests that the finite element modelling results are reliable. It is therefore concluded that either of these two probe geometries would be ideal for a probe capable of a combination solids volume fraction and solids velocity measurement.

5.4.5 Static testing to determine the effective sensor separation, L, between sensors A and B of the optimised probe geometries.

Cross-correlation allows the time delay, δ, between two axially displaced signals to be estimated. The process is described in detail in Section 2.3. Applied to the current investigation δ is equal to the time taken for a particle to pass between sensor A and sensor B of the 6-electrode SEMM array. In order to be able to estimate $u_{s,i}$ from cross-correlation of the responses from sensor A and sensor B of a 6-electrode SEMM array it is necessary to know the effective sensor separation, L, between the two sensors. If δ and L are known $u_{s,i}$ is given by Equation 5-6.

$$u_{s,i} = \frac{L}{\delta}$$

Equation 5-6

In the previous research investigated the effective sensor separation, L, was assumed to be equal to the physical sensor separation, j. However it was decided that this assumption should be verified using the experimental static testing results. In order to do this values of the relative sensitivity, Ψ, were plotted, for a radial position r = 1mm, and varying axial positions, z, of the nylon ring, for sensor A and sensor B of ideal geometry 1 (see Figure 5-20) and ideal geometry 2 (see Figure 5-21)(see Section 5.4.4 for optimised array geometries).

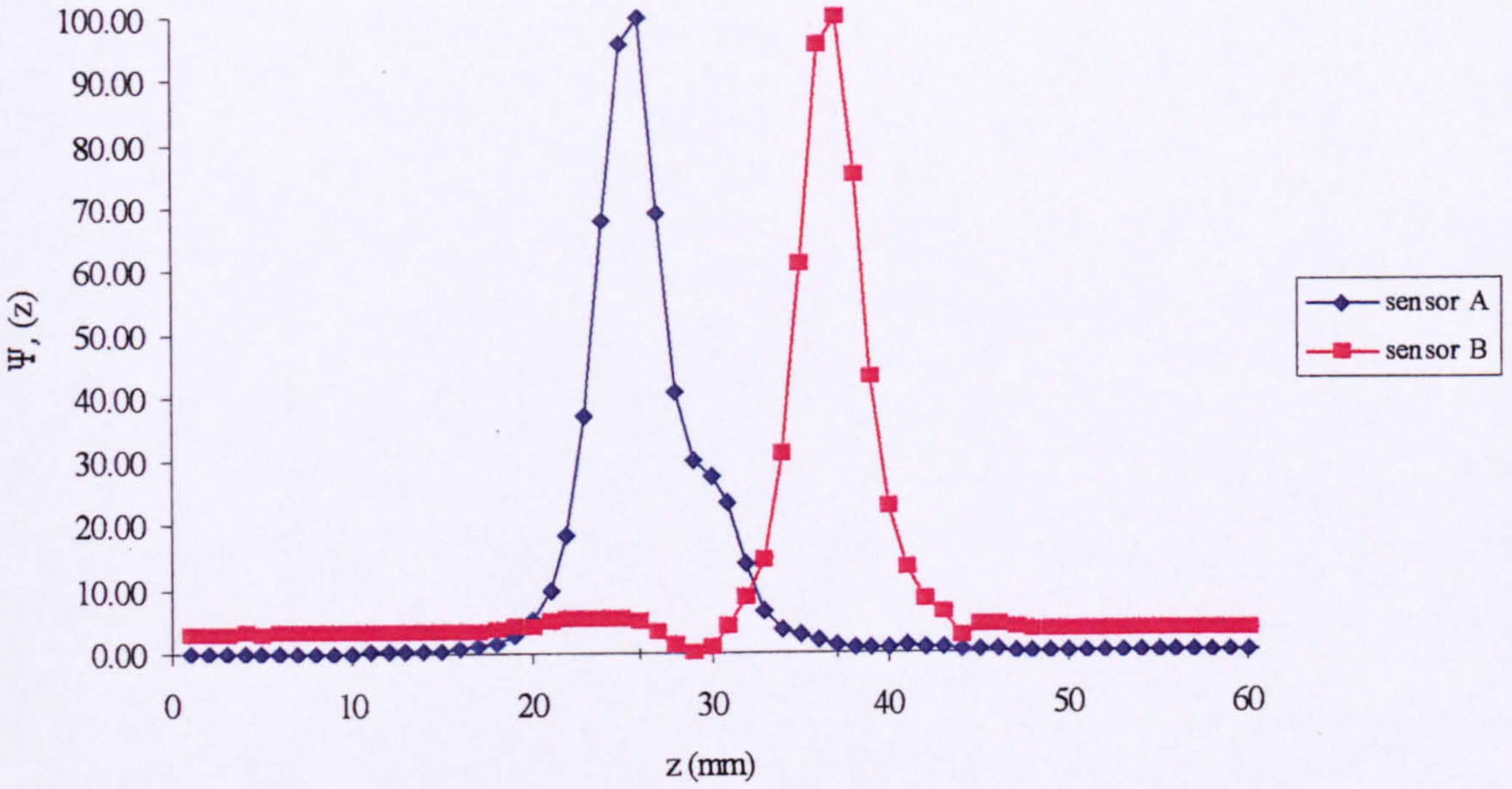

Figure 5-20. Values of relative sensitivity, Ψ, for simulated particles at the probe wall, for optimised probe geometry 1.

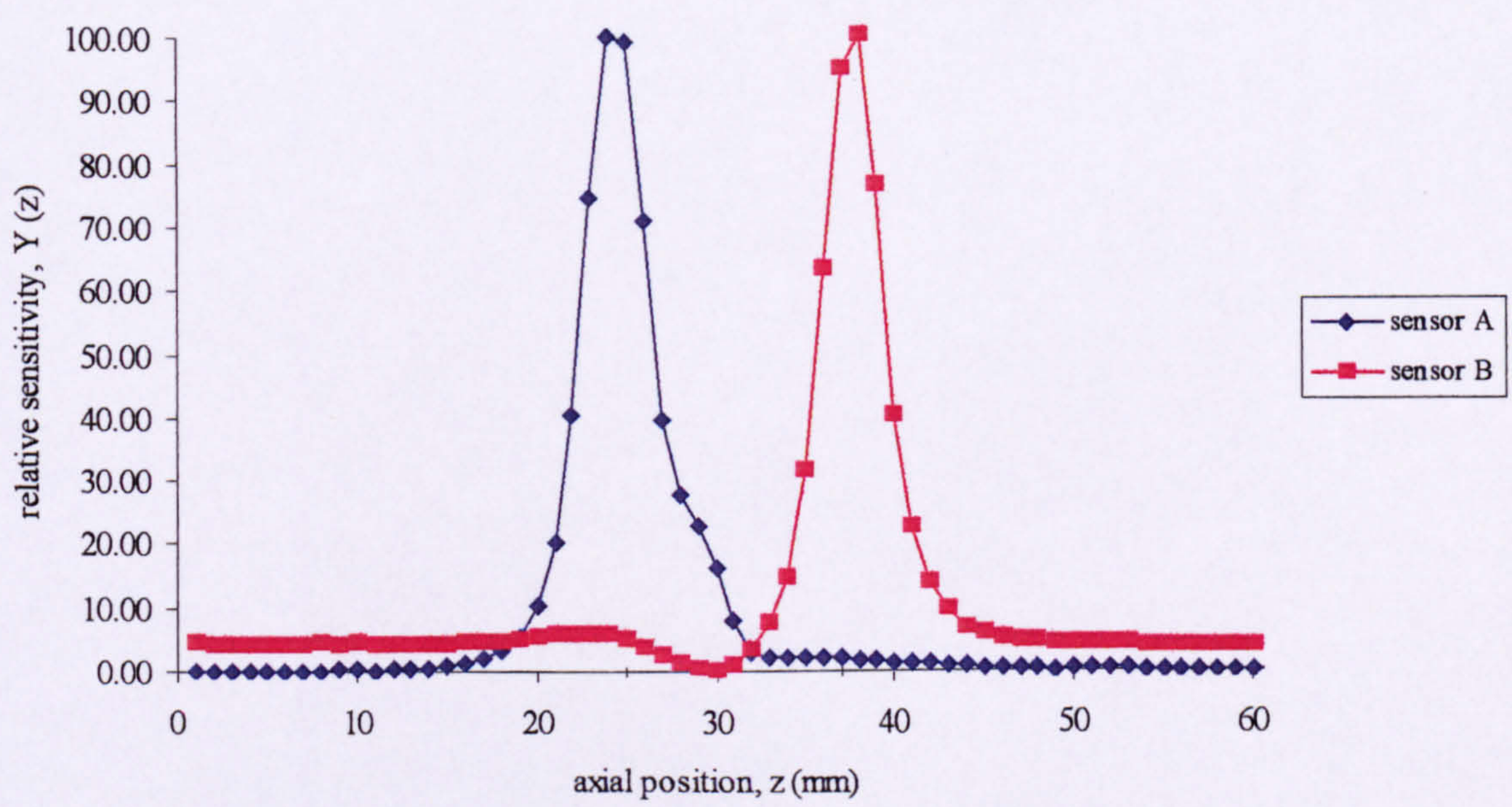

Figure 5-21. Values of relative sensitivity, Ψ, for simulated particles at the probe wall, for optimised probe geometry 2.

Optimised probe geometry 1 has a physical sensor separation, j, of 6mm. The effective sensor separation, L, measured from Figure 5-20, is 11mm. Optimised probe geometry 2 has a physical sensor separation, j, of 8mm. The effective sensor separation, L, measured from Figure 5-21 is 12mm.

In conclusion the value of j for a given probe geometry is unlikely to give an accurate estimate of the value of L. The experimental static testing reported in this chapter has predicted L for two optimised probe geometries. These predicted values of L are accurate to ±1mm. This will result in a possible error being introduced into the estimate of $u_{s,i}$. In the case of optimised array geometry 1 this will result in a possible velocity error of ±12.5%. In the case of optimised array geometry 2 this will result in a possible velocity error of ±8.3%. The error in this case is defined as in Equation 5-7.

$$\text{error} = \frac{u_{s,i,estimated} - u_{s,i,actual}}{u_{s,i,actual}}$$

Equation 5-7

In order to minimise the error it was decided to use the second probe geometry presented in Section 5.4.5 for experimental testing in the flow loop. If necessary L could be measured to a higher accuracy using a modified static testing method. However it was decided to use the measured values of L given above initially.

6. Experimental Apparatus and Procedures.

6.1 The multiphase flow loop.

In order to carry out dynamic testing of the measurement probes a multiphase flow loop was required. This facility had to be capable of producing the necessary solids-water flows relevant to the present investigation. The flow conditions required a variety of different solids flow rates, water flow rates, and solids volume fractions. In addition to these requirements the working section of the flow loop had to be capable of being positioned at different inclinations from vertical. This would allow the highly non-uniform flows described in Section 1.2 to be established. The instrumentation on the flow loop had to be capable of providing reference measurements of the flow parameters listed below.

1. Water volumetric flow rate, Q_w.
2. Solids volumetric flow rate, Q_s.
3. Mean solids volume fraction in the working section, α_s.
4. Mean solids velocity in the working section, u_s.
5. Water conductivity, σ_w.

The equipment used to acquire these reference measurements is described in Section 6.3. At the start of the current investigation the flow loop at the University of Huddersfield was capable of producing liquid and gas-liquid vertical flows. Some of the plant to extend this capability to include solids flows was in place. Also many of the reference measurement devices were in place. The flow loop was further developed as part of the current investigation.

A schematic diagram and photograph of the flow loop are shown in Figure 6-1. Details of the flow rate capabilities and loop dimensions are given in Section 6.2. Details of the reference measurement devices are given in Section 6.3.

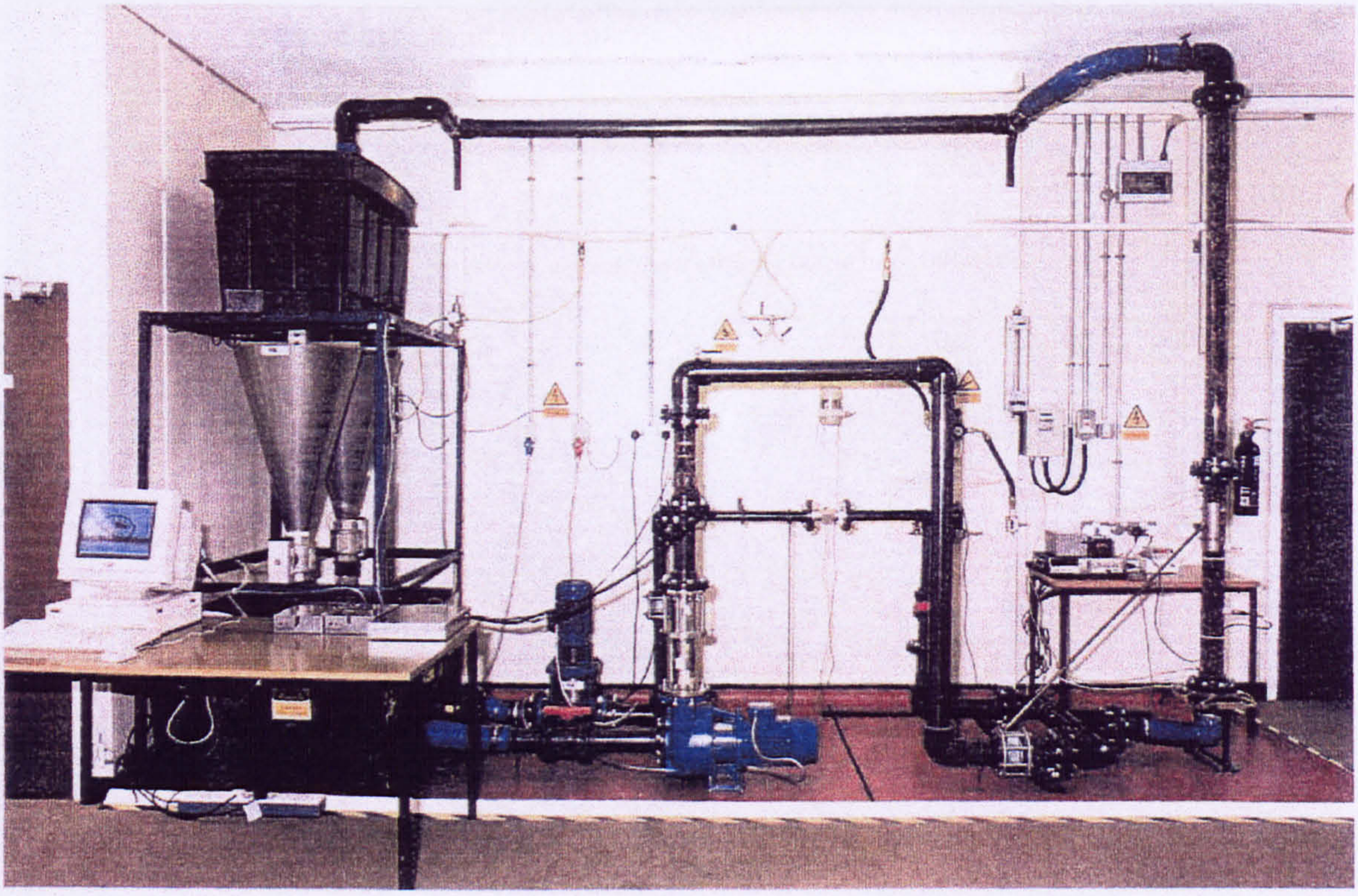

All symbols in accordance with BS1553:Part 1 and BS1646:Part 3

Figure 6-1. Schematic diagram and photograph of the University of Huddersfield flow loop.

6.2 Flow capabilities of the multiphase flow loop.

The flow loop is capable of producing flows with water as the continuous phase. The disperse phase can be solid particles (plastic spheres) and/or air. For the current investigation the working section was constructed of 80mm inside diameter acrylic pipe and was

approximately 2.5m long. The working section can be positioned to give upward flows which are either vertical or inclined from vertical. For the current investigation inclinations of 0°, 5° and 30° degrees from vertical were used. However it is possible to set up other inclination angles as required.

The solids phase consists of 5mm diameter plastic spheres with a density of 1340 kgm^{-3}. The particles are pumped from a reservoir using a Wemco solids handling pump which pumps a mixture of solids and water. A homogeneous solids-water mixture is maintained in the solids reservoir using a 1kW tank mixer. Using this system flows with Q_s up to 1.75 m^3h^{-1} can be produced. Water can also be pumped through the working section using a vertical multistage in-line centrifugal pump from a reservoir containing water only. The pump can deliver up to 22 m^3h^{-1}. By using the two pumps in conjunction both Q_s and Q_w can be independently set allowing α_s in the working section to be varied. The relative positions in the flow loop of both the pumps are shown in Figure 6-1.

After flowing through the working section the solid particles are separated from the liquid using a stainless steel separator developed as part of the current investigation. The separator consists of a rectangular cross-section chute of stainless steel mesh. Baffles are positioned at intervals along the chute which partially block the flow of the solids-liquid mixture. By breaking up and slowing the flow of the mixture they improve the efficiency of the separation.

6.3 Reference measurement devices.

6.3.1 Gravimetric flow measurement system.

6.3.1.1 Hopper load cell system.

Q_s and Q_w are measured using gravimetric systems. After flowing through the separator (see Figure 6-1) the separated solids and water pass into conical stainless steel hoppers. Each hopper has a pneumatic ball valve at its base and is suspended from a load cell. Both the load cells and the valve control system are interfaced to a PC. By closing the valves at the base of the hoppers and recording the time taken for a given mass of material to collect in the hopper the mass flow rate, $\dot{M}$, of that material can be calculated. By combining $\dot{M}$ with the density of the material, ρ, as in Equation 6-1, the volumetric flow rate, Q, can be calculated.

$$Q = \frac{\dot{M}}{\rho}$$

Equation 6-1

Because the separator is not 100% efficient some liquid flows into the solids hopper. The volumetric flow rate of water into the solids hopper, Q_w^*, is measured using a separate system which is described in Section 6.3.1.3. By accounting for Q_w^* more accurate estimates of Q_s and Q_w can be obtained.

A program written in QuickBasic 4.5 is used to control the operation of the pneumatic ball valves and to obtain readings from the load cells. This program enables Q_s and Q_w to be automatically acquired at intervals during the experimental testing. This program, and the method used to calculate Q_s and Q_w are detailed in 6.3.1.5.

6.3.1.2 Weighed hopper load cell calibration.

The load cells were calibrated twice during the course of this investigation. The first calibration took place before the experimental testing and the second took place after the experimental testing in order to check for any drift in the calibration.

The calibration procedure involves adding known masses of water to the solids hopper, M_s, and the water hopper, M_w, and recording the resulting response of the solids hopper load cell, V_s, and the water hopper load cell, V_w. For each of the hoppers the mass of water added is increased in increments over the full range of the load cells, 0kg to 40kg. In order to ensure the accuracy of each calibration the hopper filling procedure was carried out three times for each calibration. The calibration was checked at intervals during the current investigation by applying a single known mass of water to each hopper and ensuring the load cell response fell on the existing calibration curve. The results for the calibrations are presented in the following sections.

December 1997 calibration.

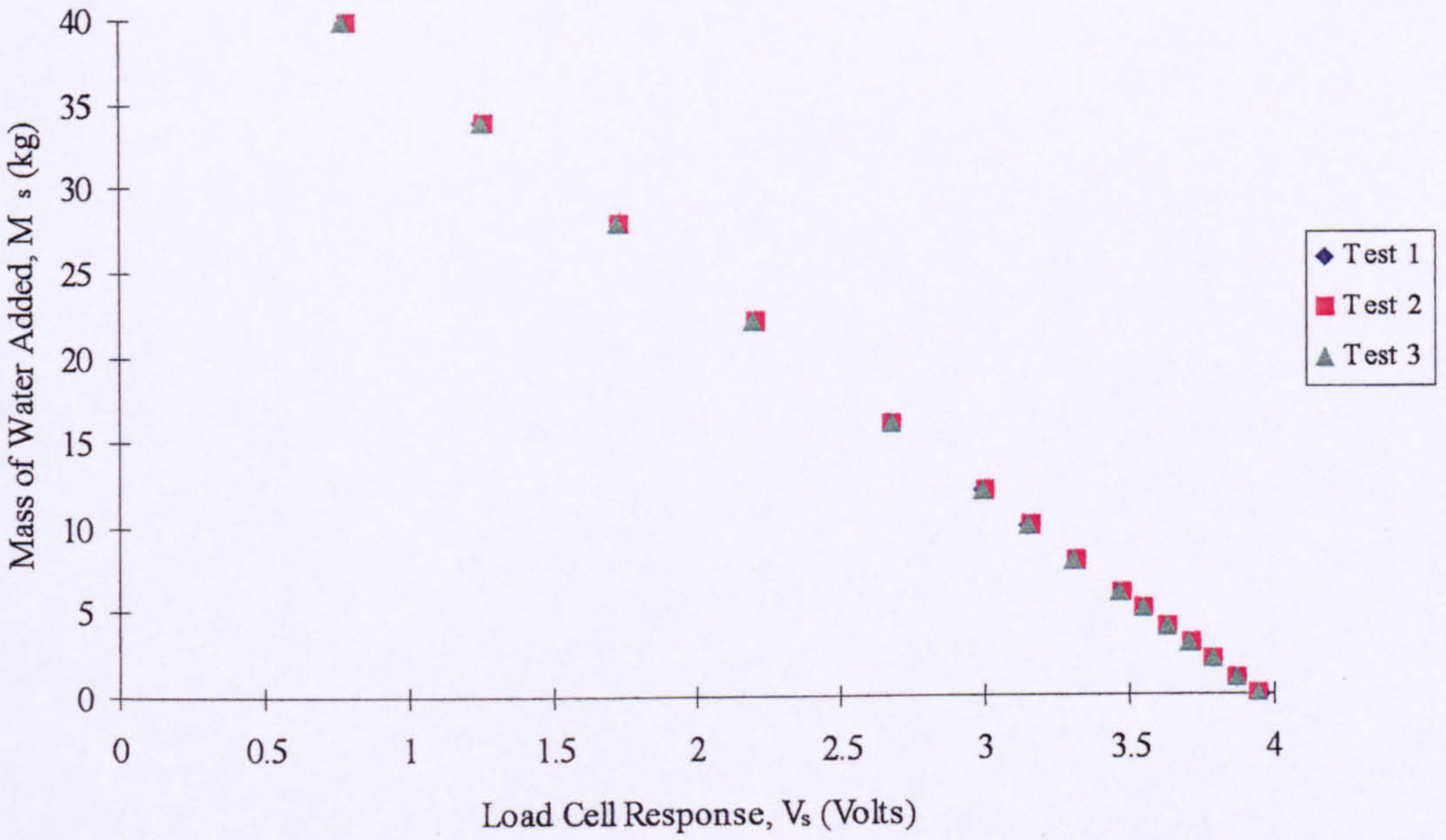

Figure 6-2. December 1997 solids hopper load cell calibration.

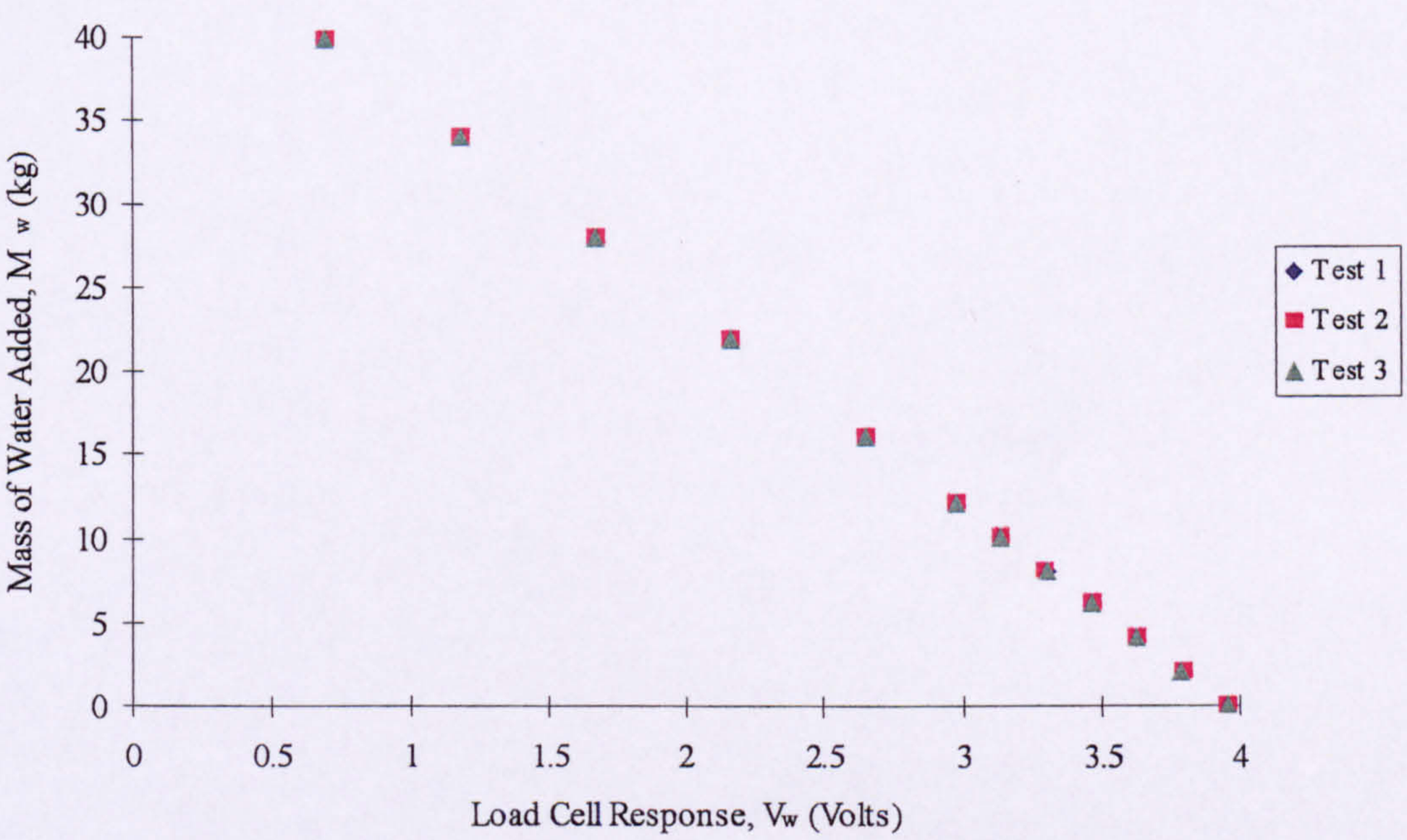

Figure 6-3. December 1997 water hopper load cell calibration.

The hopper calibration curves in Figure 6-2 and Figure 6-3 both show excellent linearity with very little difference between the three consecutive tests. Linear regression was used to obtain the relationships between M_w and V_w, and M_s and V_s. These relationships were integrated into the gravimetric flow measurement system control program used during flow loop tests (see

Section 6.3.1.5). Equation 6-2 gives the relationship for the solids hopper load cell whilst Equation 6-3 gives the relationship for the water hopper load cell.

$$M_s = 49.618 - 12.578V_s$$

Equation 6-2

$$M_w = 48.403 - 12.248V_w$$

Equation 6-3

September 1998 calibration.

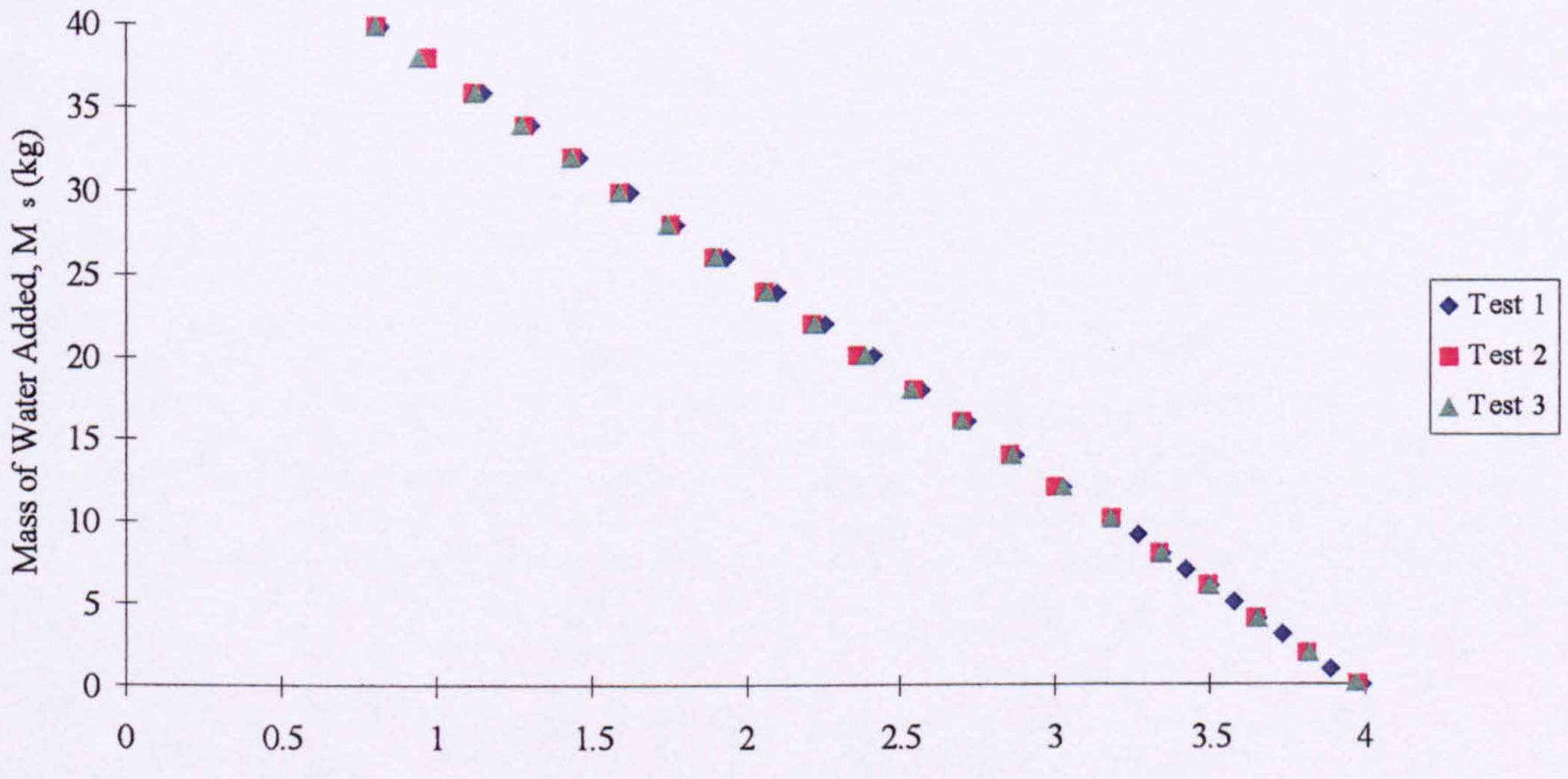

Figure 6-4. September 1998 solids hopper load cell calibration.

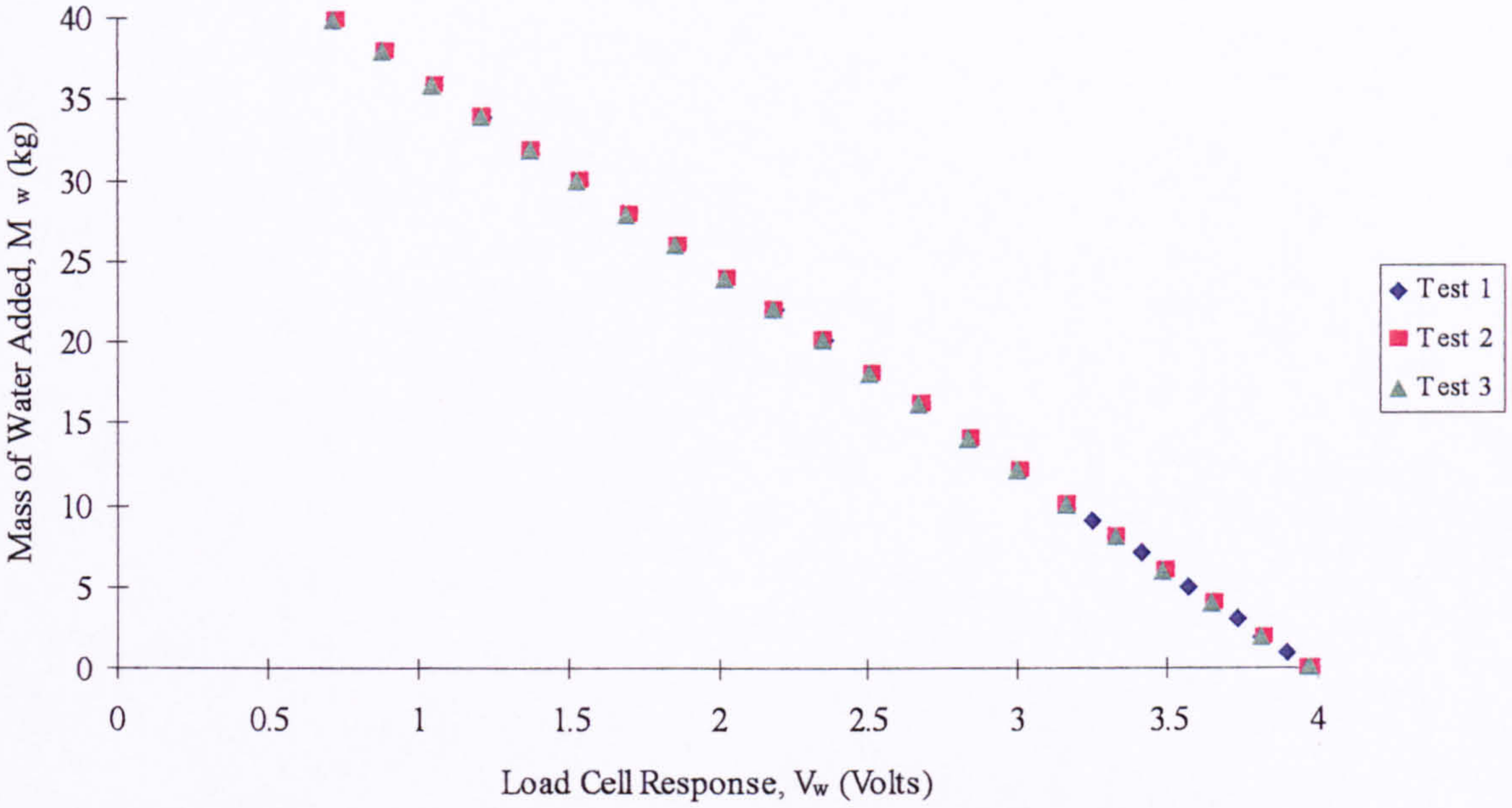

Figure 6-5. September 1998 water hopper load cell calibration.

In Figure 6-4 and Figure 6-5 both the hopper calibration curves again show excellent linearity with very little difference between the three consecutive tests. Linear regression was used to obtain the relationships between M_w and V_w, and M_s and V_s as with the earlier calibration. Equation 6-4 shows the relationship for the solids hopper load cell whilst Equation 6-5 shows the relationship for the water hopper load cell.

$$M_s = 50.006 - 12.589V_s$$

Equation 6-4

$$M_w = 48.755 - 12.267V_w$$

Equation 6-5

There is little difference between the 1997 and 1998 calibrations for either load cell. The 1997 calibrations will have introduced a maximum error of 0.09% into measurements of M_s and 0.15% into measurements of M_w.

6.3.1.3 Solids hopper water level measurement system.

As mentioned in the previous section the solids-liquid separator is not 100% efficient. Some water will always adhere to the surface of the solid particles and will flow into the solids hopper. In order to measure the volumetric flow rate of this water, Q_w^*, a water level measurement system has been installed in the solids hopper.

The system consists of two parallel copper strips, mounted on a layer of insulating material, running up the wall of the hopper as shown in Figure 6-6.

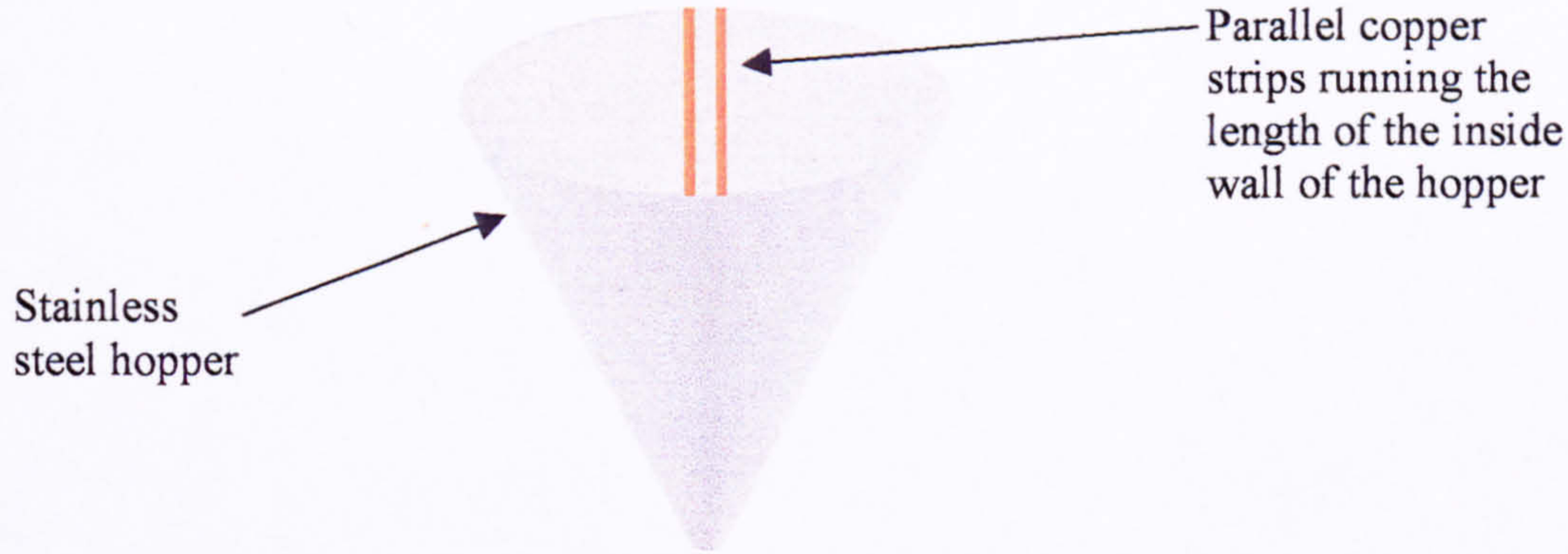

Figure 6-6. The position of water level measurement device inside the solids hopper.

As water fills the hopper it will form an electrical connection between the strips. Above the water level no current will flow between the strips. The electrical resistance, R_x, between the strips will be related to the level of water in the hopper, h, as described below.

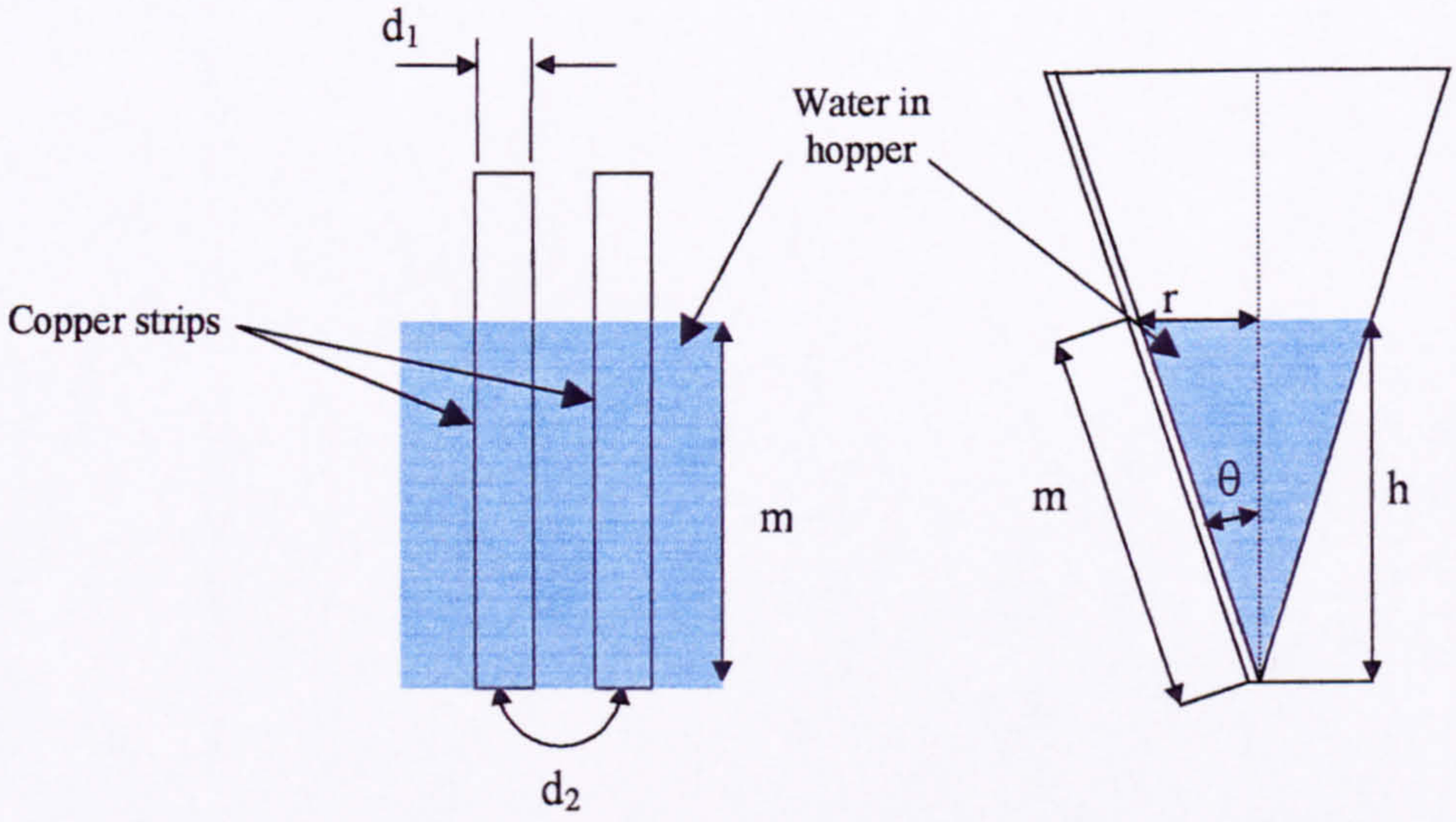

Figure 6-7. Schematic representation of the solids hopper water level measurement device.

The resistance, R, of a conductor can be calculated using Equation 6-6, where η is the resistivity of the material, L is the length of the conductor, and A is its cross-sectional area.

$$R = \frac{\eta L}{A}$$

Equation 6-6

Although this equation is not directly applicable to the present case it will allow an estimate to be made of the relationship between R_x and h. The conductor is the solids-liquid mixture

between the strips through which current passes. The cross-sectional area of the conductor is the wetted length of the strips, m, multiplied by their width, d_1. The length of the current path is d_2 (see Figure 6-7). Using these dimensions Equation 6-6 can be rearranged to give Equation 6-7.

$$R_x = \frac{\eta d_2}{d_1 m}$$

Equation 6-7

From Equation 6-7 it is clear that R_x is proportional to $\frac{1}{m}$. In order to relate the value of R_x to the volume of water, υ_w^*, present in the solids hopper it is necessary to consider the mixture present in the hopper and the geometry of the hopper, as shown in Figure 6-7. The mixture present in the solids hopper will consist of both solids and water. Because the mixture has already been partially separated the level of water in the hopper is less than the level of the solids. Therefore the volume of the hopper, υ_{wet}, in which water is present will actually contain a mixture of close packed solids and water. The close packed solids volume fraction for the particles in the current investigation has been calculated experimentally as 0.62. Therefore υ_{wet} is related to υ_w^*, by Equation 6-8.

$$\upsilon_w^* = 0.62\upsilon_{wet}$$

Equation 6-8

υ_{wet} is related to m and therefore R_x by considering the geometry of the hopper as shown in Figure 6-7. The volume of the cone in which water is present is given by Equation 6-9.

$$\upsilon_{wet} = \frac{\pi r^2 h}{3}$$

Equation 6-9

By substituting for r and h Equation 6-9 can be rearranged to give Equation 6-10.

$$\upsilon_{wet} = \frac{\pi m^3 \sin^2\theta\cos\theta}{3}$$

Equation 6-10

Equation 6-7, Equation 6-8 and Equation 6-10 can be combined to give Equation 6-11.

$$\upsilon_w^* = 0.62 \times \frac{\rho^3 d_2^3 \pi \sin^2\theta\cos\theta}{2d_1^3} \frac{1}{R_x^3}$$

Equation 6-11

From Equation 6-11 it can be seen that υ_w^* is proportional to $\frac{1}{R_x^3}$.

R_x is measured using the measurement principle described in Section 4.2.1. A sinusoidal excitation is applied across the parallel copper strips and a known reference resistor in series as shown in Figure 6-8.

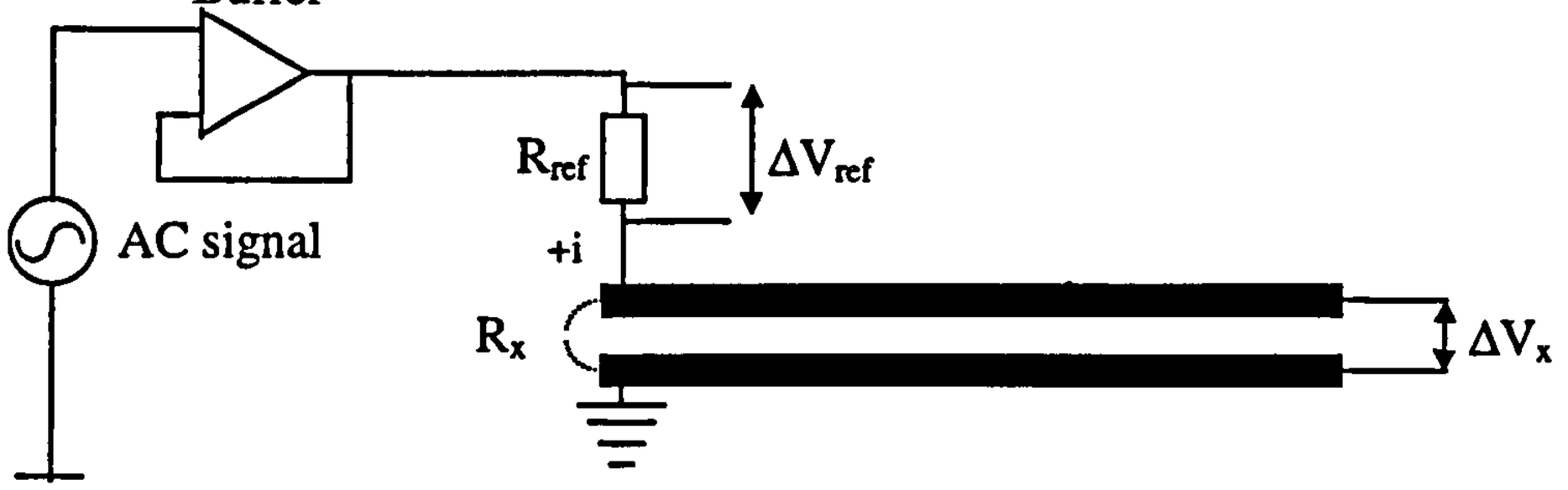

Figure 6-8. The electrical principle used in the solids hopper water level measurement system.

The applied sinusoidal excitation causes sinusoidal voltage drops to exist across the parallel copper strips, and across the reference resistor R_{ref}. These are shown in Figure 6-8 as ΔV_x and ΔV_{ref}. The amplitude of ΔV_x is proportional to R_x as shown in Equation 6-12. The amplitude of ΔV_{ref} is similarly proportional to R_{ref}.

$$\text{(i)}\ R_x = \frac{|\Delta V_x|}{|i|} \qquad \text{(iv)}\ R_{ref} = \frac{|\Delta V_{ref}|}{|i|}$$

Equation 6-12

The electronic hardware used to acquire measurements of R_x and R_{ref} is very similar to that used with the local measurement probe (see Section 4.2.2 and Figure 4-4). The circuit rectifies the sinusoidal voltage drops, ΔV_x and ΔV_{ref}, and gives a DC output, referenced to ground, that is proportional to the amplitude of each. These DC output voltage drops are V_x and V_{ref} respectively.

In order to calculate R_x, the DC output voltages, V_x and V_{ref} are measured. R_x is then calculated using the principle shown in Equation 6-13. In Equation 6-13 k is the rectifier gain. As the circuitry was carefully matched it was assumed that k was the same for both measurements.

$$\frac{V_{ref}}{V_x} = \frac{k|i|R_{ref}}{k|i|R_x} \therefore R_x = \frac{V_x R_{ref}}{V_{ref}}$$

Equation 6-13

If Equation 6-13 is substituted into Equation 6-11 Equation 6-14 is given.

$$\upsilon_w^* = 0.62 \times \frac{\rho^3 d_2^3 \pi \sin^2\theta \cos\theta}{3 d_1^3 R_{ref}^3} \left(\frac{V_{ref}}{V_x} \right)^3$$

Equation 6-14

During experimental testing V_x and V_{ref} are measured. Equation 6-14 shows that the volume of water in the solids hopper, υ_w^* should then be proportional to $\left(\frac{V_{ref}}{V_x} \right)^3$. Because the other dimensions in Equation 6-14 cannot be easily measured the exact relationship was determined using experimental calibration. The results of these calibrations are shown below. The calibration allows υ_w^* to be accurately measured. If the time taken for this measured volume of water to accumulate is measured then the volumetric flow rate of water into the solids hopper, Q_w^*, can be calculated.

6.3.1.4 Solids hopper water level meter calibration.

Calibration of the solids hopper water level meter has been carried out on two occasions during the current investigation. The first calibration took place before the experimental testing and the second took place after the experimental testing in order to check for any drift in the calibration.

The calibration was carried out by adding dry solids to the hopper and then adding measured volumes of water whilst recording the value of $\left(\frac{V_{ref}}{V_x} \right)^3$ given by the level meter. At all times it was ensured that the solids level in the hopper exceeded the water level.

December 1997 calibration.

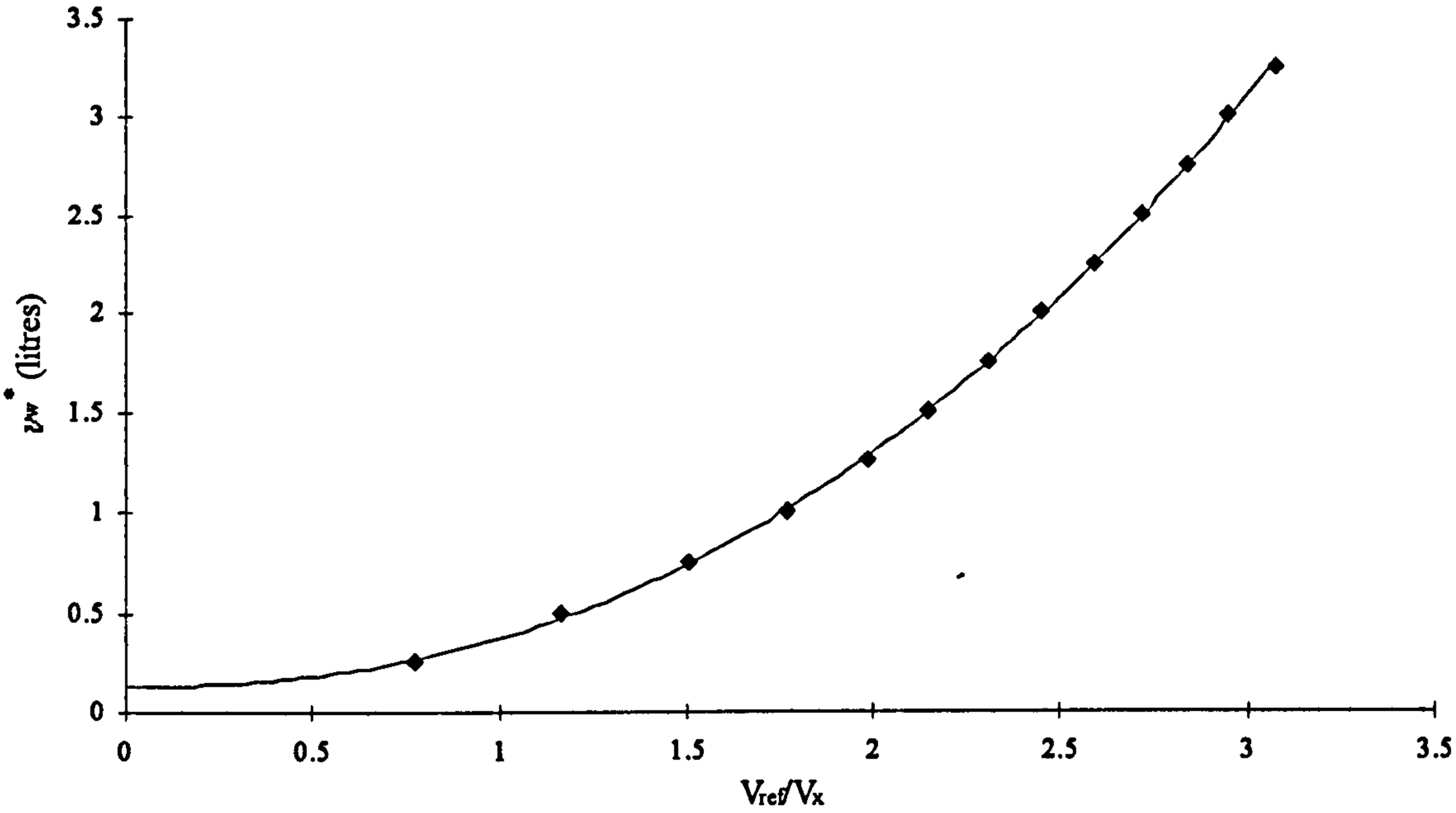

Figure 6-9. December 1997 solids hopper water level meter calibration.

A cubic polynomial was fitted to the experimental data-points in Figure 6-9. The data fits this applied cubic polynomial well. Equation 6-15 gives the equation of this cubic polynomial.

$$\upsilon_w^* = 0.0333\left(\frac{V_{ref}}{V_x}\right)^3 + 0.2412\left(\frac{V_{ref}}{V_x}\right)^2 - 0.0331\left(\frac{V_{ref}}{V_x}\right) + 0.1304$$

Equation 6-15

Equation 6-15 was integrated into the gravimetric flow measurement system control software (see Section 6.3.1.5) to estimate the volume of water in the solids hopper, υ_w^*.

September 1998 calibration.

Before this second calibration was carried out the pneumatically actuated ball valve at the base of the solids hopper was replaced because of wear. This replacement caused the geometry at the base of the hopper to change. Therefore it was not expected that the calibration curve would be identical. Additionally it was noticed during experimental testing after the first calibration that the volume of water in the hopper, υ_w^*, never exceeded 0.2 litres. Therefore in the second calibration extra data points were acquired for lower added volumes of water.

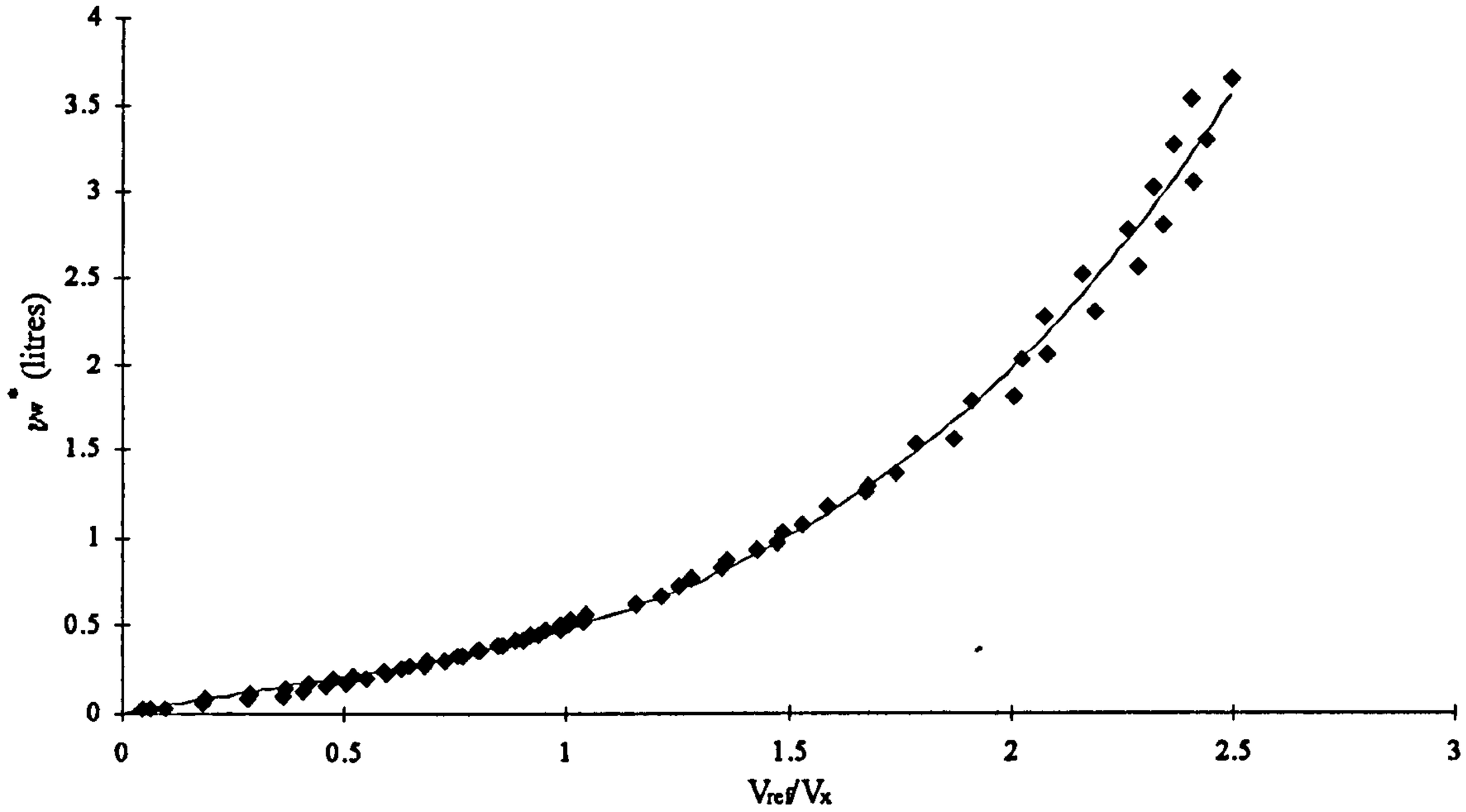

Figure 6-10. September 1998 solids hopper water level meter calibration.

As before a cubic polynomial was fitted to the experimental data-points in Figure 6-10. As with the previous calibration this data also shows a good fit to the estimated cubic calibration curve. This applies with both low and high applied volumes of water. Equation 6-16 gives the equation of the updated calibration curve.

$$\upsilon_w^* = 0.2885\left(\frac{V_{ref}}{V_x}\right)^3 - 0.3994\left(\frac{V_{ref}}{V_x}\right)^2 + 0.6477\left(\frac{V_{ref}}{V_x}\right) + 0.0474$$

Equation 6-16

This equation has been used to replace the previous calibration in the gravimetric flow measurement system control software (see Section 6.3.1.5).

6.3.1.5 The gravimetric flow measurement system control program.

In order to automatically acquire measurements of Q_s and Q_w, corrected to allow for Q_w^* at known intervals during extended experimental testing a program was written in QuickBasic 4.5. A flow diagram of the program is shown in Figure 6-11. It is explained below.

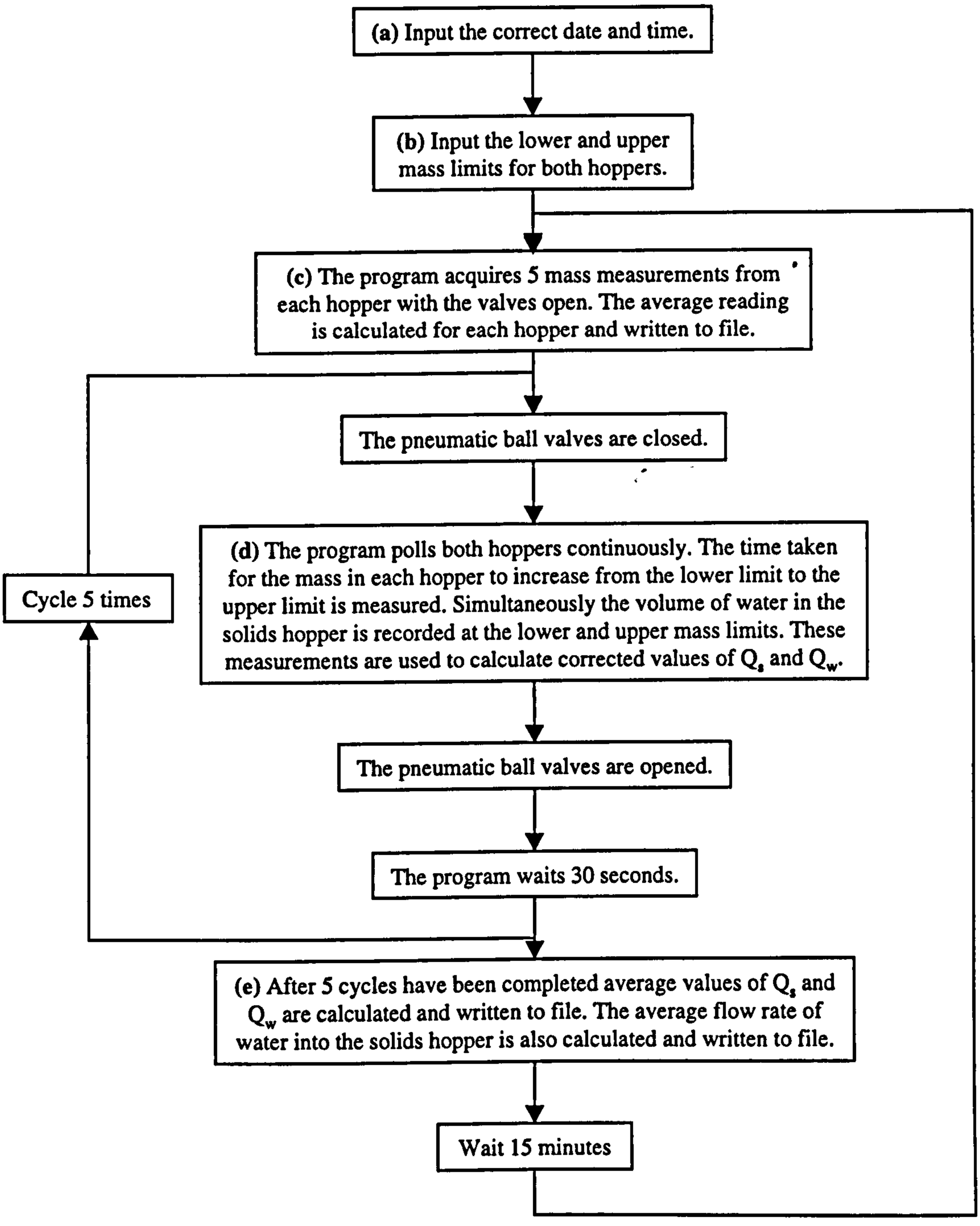

Figure 6-11. Flow diagram for the gravimetric flow measurement system control program.

a) The program first prompts the user for the correct date and time. It is important that the data from the hoppers can be compared with data from other devices. Therefore it is important that the time the data was acquired is accurately known.

b) The program now prompts the user for the lower mass limit for the solids hopper, $M_{s(l)}$, the lower mass limit for the water hopper, $M_{w(l)}$, the upper mass limit for the solids hopper, $M_{s(u)}$ and the upper mass limit for the water hopper, $M_{w(u)}$. In each measurement cycle the time taken for the mass in each hopper to vary between the lower and upper limits is measured. The upper limit is the total mass that will be collected in the hopper before the valves are reopened in each measurement cycle. It is important that the upper limit for each hopper is set so that the total amount of material that will be collected in each cycle is small compared to the capacity of the flow loop. It is important to also set a lower limit above zero. This is because the material flowing into the hoppers causes a load to be registered by the load cells even with the valves open. It is important that the lower limit for each hopper is set so that it is above this load.

c) The program now acquires 5 measurements from each hopper with the valves open. The average value for each hopper is written to file. This data can be used to ensure that the lower limit for each hopper is set adequately high.

d) Once the valves are closed the program polls each load cell continuously. As the mass in the water hopper reaches $M_{w(l)}$ the program begins a timer. As the mass in the solids hopper reaches $M_{s(l)}$ the program begins a second timer. As the second timer is started the program measures the volume of water, $\upsilon^{*}_{w(l)}$, in the solids hopper. When the mass in the water hopper reaches $M_{w(u)}$ the program stops the first timer to give the time taken, ΔT_w, for the pre-set mass of water to collect. When the mass in the solids hopper reaches $M_{s(u)}$ the program stops the second timer to give the time taken, ΔT_s, for the pre-set mass of solids to collect. When the second timer stops the program again measures the volume of water, $\upsilon^{*}_{w(u)}$, in the solids hopper. The pneumatic ball valves are then reopened.

From these measurements Q_w is given by the volumetric flow rate of water into the water hopper plus the volumetric flow rate of water into the solids hopper as shown in Equation 6-17.

$$Q_w = \frac{M_{w(u)} - M_{w(l)}}{\rho_w \Delta T_w} + \frac{\upsilon^{*}_{w(u)} - \upsilon^{*}_{w(l)}}{\Delta T_s}$$

Equation 6-17

Q_s is given by the volumetric flow rate of solids into the solids hopper minus the volumetric flow rate of water into the solids hopper as shown in Equation 6-18.

$$Q_s = \frac{M_{s(u)} - M_{s(l)}}{\rho_s \Delta T_s} - \frac{\upsilon^*_{w(u)} - \upsilon^*_{w(l)}}{\Delta T_s}\left(\frac{\rho_w}{\rho_s}\right)$$

Equation 6-18

The corrected volumetric flow rates are stored by the program.

e) The program now loops and carries out step d four more times. This can be seen in Figure 6-11. The program then calculates the average values of Q_w and Q_s which are written to file. Additionally an average value of the volumetric water flow rate into the solids hopper is calculated and written to file. This allows the efficiency of the solids-liquid separator to be analysed.

The program now waits for 15 minutes before beginning the cycle again at step (c). This can be seen in Figure 6-11. The complete data written to file can be used to calculate the average flow rate during an experimental run and also to show any variation in flow rates that may have occurred during the test.

6.3.2 Turbine meter.

A turbine meter is installed in the liquid line of the flow loop (see Figure 6-1). It can be used to give a measurement of the liquid volumetric flow rate, Q_w, delivered by the vertical multistage in-line centrifugal pump. This measurement is not relevant during solids-liquid flow as a separate quantity of liquid is also delivered by the solids handling pump. However during this investigation the turbine meter was used in order to calculate the pipe friction factor (see Section 6.3.3). The calibration of the turbine meter itself was checked during the current investigation by comparing it with measurements taken using the gravimetric flow measurement system described in 6.3.1. The results of this calibration are given below.

6.3.2.1 Turbine meter calibration

Measurements of volumetric flow rate, Q, are acquired from turbine meters by counting the rotations of the turbine. Turbine meters are designed so that the rotation frequency, f, of the turbine is directly proportional to Q over the specified range of operation of the meter. This relationship is given by Equation 6-19.

$$Q = mf$$

Equation 6-19

In Equation 6-19 m is the meter factor for the device which can vary as the meter begins to wear. Additionally, although the meter only has constant value of m over a specified range of flow rates, it will behave in a repeatable way over a larger range. The turbine meter installed on the flow loop was calibrated over the full range of operation of the vertical in-line multistage liquids pump to check the factory meter factor over the specified range and to give a calibration curve for the meter factor over the wider range of flow rates that can be obtained from the pump. The calibration was carried out by comparing the turbine meter response with the water flow rate read from the gravimetric flow measurement system (see Sections 6.3.1). The data acquired from this calibration is presented in Figure 6-12.

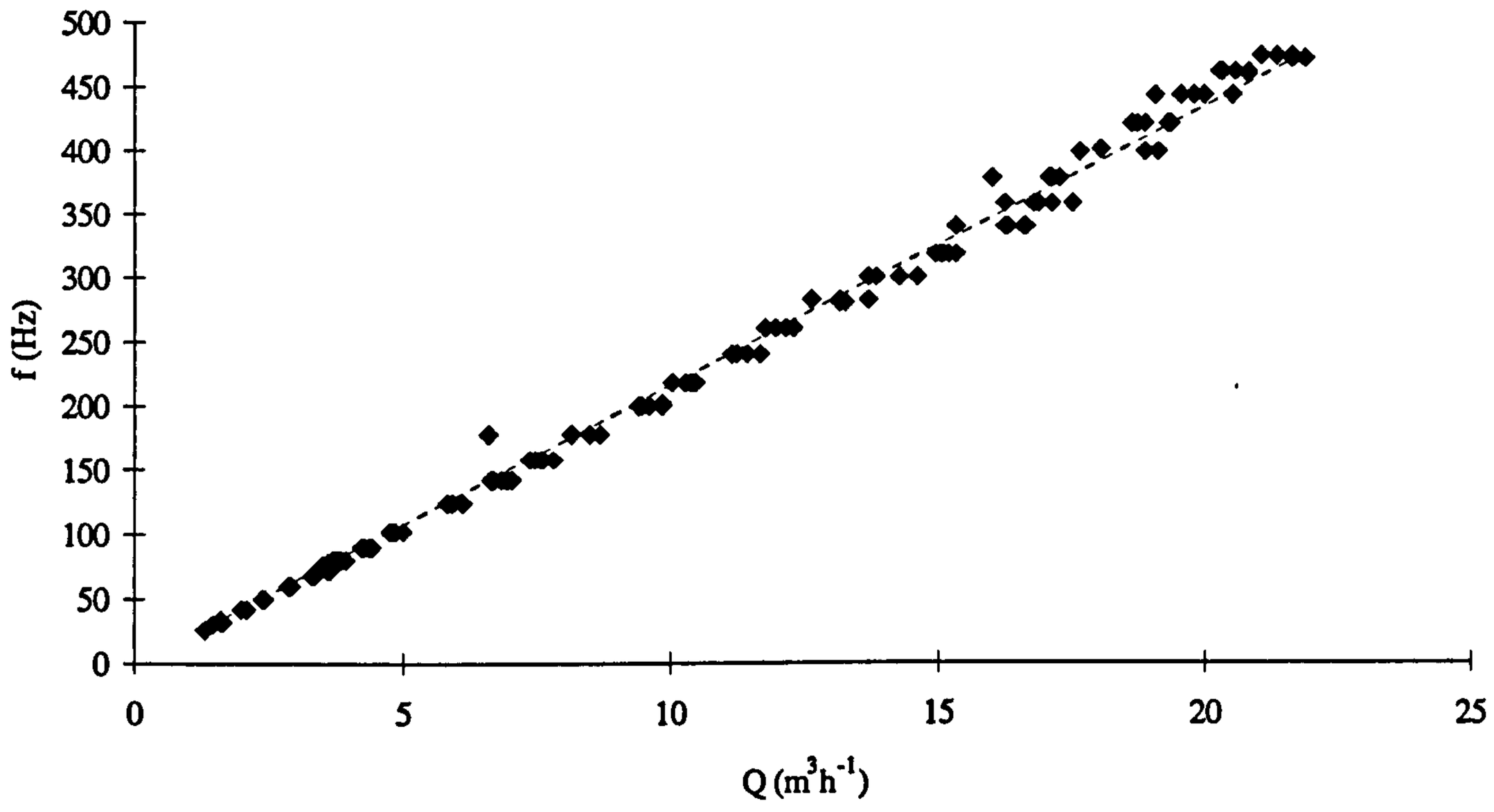

Figure 6-12. Turbine meter calibration.

Figure 6-12 shows that there is a linear variation of f as Q is increased. The factory calibration for this meter was $0.0462 m^3 h^{-1} Hz^{-1}$ over a design range of $3.41 m^3 h^{-1}$ to $40.88 m^3 h^{-1}$. The meter factor calculated from the calibration experiments is $0.0462 m^3 h^{-1} Hz^{-1}$. This is valid over a range of $1.29 m^3 h^{-1}$ to $21.92 m^3 h^{-1}$. This shows that the meter has experienced little wear and that it is also usable at lower flow rates than the manufacturer's specifications suggest.

6.3.3 Differential pressure sensor.

A Honeywell ST-3000 differential pressure sensor is installed on the flow loop (see Figure 6-1). This device is used to measure the differential pressure across a one metre length of the

working section. A flushing system is installed in order to ensure that no air can become trapped in either the transducer or the measurement lines (see Figure 6-1). The differential pressure (DP) cell can be used to estimate the solids volume fraction, α_s. The method used to do this is explained in this section.

A representation of the DP cell installation is shown in Figure 6-13.

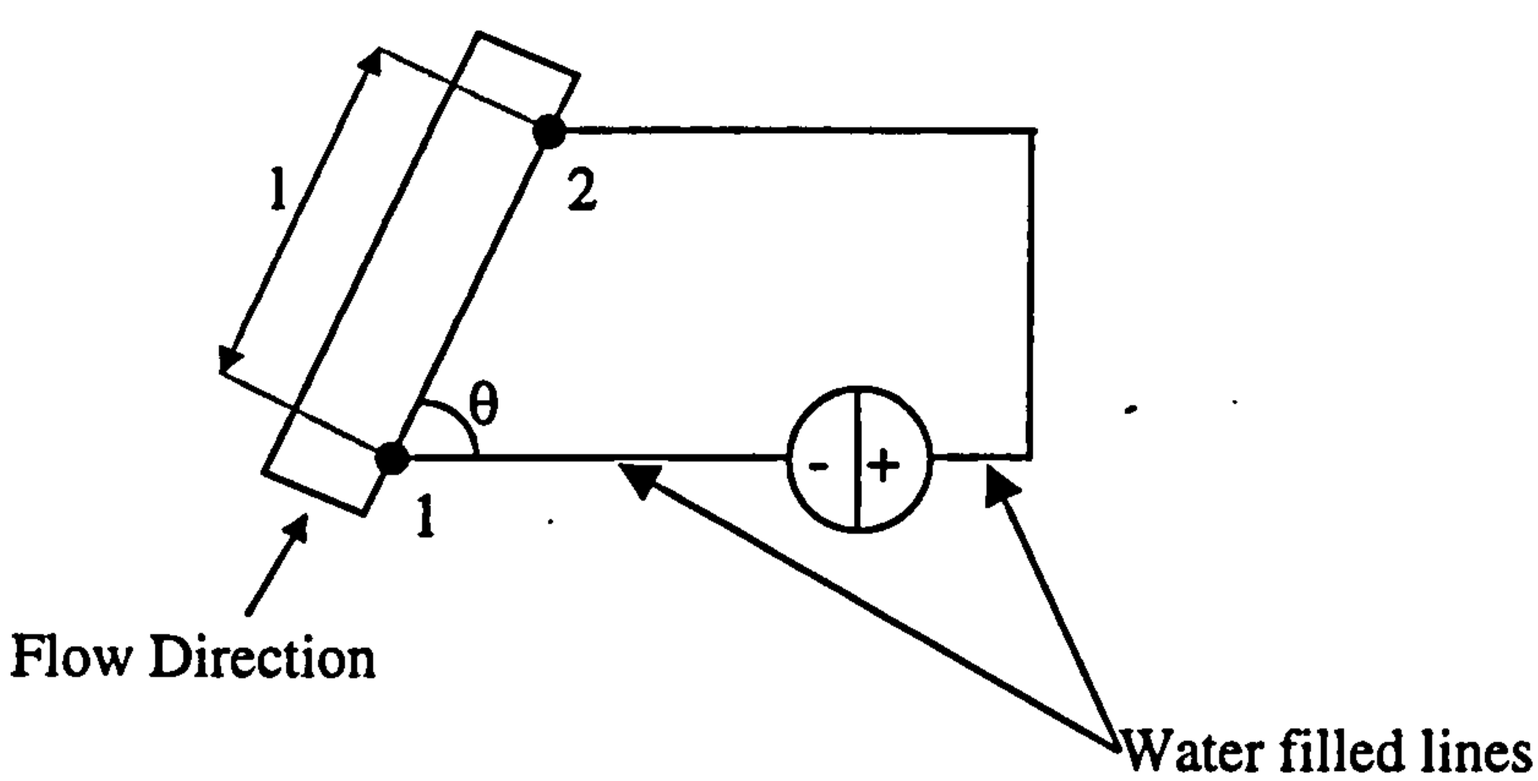

Figure 6-13. The DP cell installation.

It is assumed that there is a stable flow in the pipe with no acceleration of the flow along the pipe length. In this situation the pressure drop along length of pipe is made up of two components as in Equation 6-31.

$$\Delta P = \Delta P_{PE} + \Delta P_F$$

Equation 6-20

In Equation 6-20 ΔP_{PE} is the pressure drop due to the change in potential energy of the flow which is a function of the mixture density, ρ_M, as in Equation 6-21.

$$\Delta P_{PE} = \rho_M g l \cos\theta$$

Equation 6-21

Equation 6-20 and Equation 6-21 can be combined to give Equation 6-22.

$$\rho_M = \frac{\Delta P - \Delta P_F}{g l \cos\theta}$$

Equation 6-22

In turn ρ_M can be used to calculate the solids volume fraction, α_s. The density of a multiphase mixture is related to the densities of the solid and liquid components, ρ_s and ρ_w, and the solids volume fraction, α_s. This relationship is given by Equation 6-23.

$$\rho_M = \alpha_s \rho_S + (1 - \alpha_s)\rho_w$$

Equation 6-23

Equation 6-23 can be rearranged to give Equation 6-24.

$$\alpha_s = \frac{\rho_M - \rho_w}{\rho_s - \rho_w}$$

Equation 6-24

Application of Equation 6-22 and Equation 6-24 allows α_s to be calculated as long as the other component of the pressure difference given in Equation 6-20, ΔP_F, is known. ΔP_F is the pressure drop due to frictional losses in the flow. These losses are discussed below.

In order to discuss the frictional losses in solids-liquid flow it is first important to discuss the frictional losses in single phase liquid flow. Discussions of friction effects in single phase flows are given by Benedict [91] and Massey [92]. In a laminar flow the fluid flows in the axial direction only and the flow can be assumed to be structured in layers. The velocity across the cross-section of the pipe will vary from zero at the pipe wall to the core velocity in the central section of the pipe. This results in different layers of the flow having different velocities. This difference in velocities causes shear stresses to exist between the layers. The shear is resisted by the fluid. The degree to which the fluid resists shear is related to its viscosity. The resistance to shear between the layers results in frictional pressure losses occurring.

In a turbulent flow the fluid flows erratically in all directions within the pipe in structures referred to as eddies. This results in far more structures within the flow moving at different velocities than found in a laminar flow. Therefore a greater shear, referred to as the turbulent shear stress, occurs. The degree of shear is related to the eddy viscosity of the flow. The eddy viscosity of the flow can be many times larger than the viscosity of the fluid. Therefore the frictional pressure losses in a turbulent flow can be many times larger than those in a laminar flow. Additionally the eddies interact with the surface of the pipe causing extra pressure losses.

In a solids-liquid flow additional interactions occur. As described by Roco & Shook [93] these are particle-particle, particle-fluid, and particle-wall interactions. In a vertical flow particle-fluid interactions can act to modify the turbulence in the fluid and cause a mixing

effect which in turn modifies the shear stresses in the flow. Additionally particle-particle and particle-wall interactions directly increase the frictional pressure losses. In an inclined flow some of the solid particles form a densely packed layer against the lower wall of the pipe. If these particles are no longer supported by the fluid they do not contribute to the density of the mixture. Therefore they do not contribute to ΔP_{PE}, the pressure drop due to the change in potential energy of the flow.

A wide range of opinion has been published in the literature on the effect of the addition of solids on the frictional pressure losses in vertical and inclined flows. For vertical flow Govier & Aziz [94] report the findings of Newitt et al that if particle diameter ≥0.01″ the effect is minimal and a single phase friction factor allows a reasonable approximation of the pressure losses. This is supported by Durand (as reported in Govier & Aziz [94]) and Mizukami et al [95] for gas-solid flow. Durand and Newitt also claim that the same effect is found in inclined flows as long as the particles remain suspended in the flow. Other authors find that the frictional pressure losses in a two-phase flow will be lower than in a single phase flow. They include Newitt et al (as reported in Govier & Aziz [94]) for mixtures containing fine particles, and Serizawa et al [49] for gas-liquid flow. Additionally Roco & Shook [93] report that the effect of the pipe wall supporting some particles in an inclined flow will decrease the pressure drop in the flow. Finally a number of authors find that the frictional pressure losses in a two-phase flow will be higher than in a single phase flow. Beggs & Brill [96] report that the losses can be up to three times those in single phase flow. Chen & Kadambi [33], Turian & Yuan [97] and Akagawa et al [4] all show an increase in losses which becomes larger as the solids volume fraction is increased, but which decreases as the mixture velocity increases. In particular Chen & Kadambi report that if solids volume fraction <0.15 the increase in frictional pressure loss is not significant.

Although there is little agreement in the above literature review it was noted that ΔP_F is generally substantially less than ΔP_{PE}. Therefore it was decided to assume that a single phase friction factor would adequately represent the frictional losses in the current investigation.

The frictional losses in both laminar and turbulent single phase flow were quantified by Darcy who carried out experiments using the fully developed flow of water in long straight pipes. Darcy's formula, as reported by Massey [92], is given in Equation 6-25.

$$\Delta P_F = \frac{2\rho_w l \cos\theta f u^2}{D}$$

Equation 6-25

Here u is the flow velocity, D is the pipe diameter, and f is a coefficient referred to as the friction factor. The other nomenclature is as already defined. A number of correlations have been developed that allow the value of f to be estimated. A review of some of these is given by Massey [92]. However the relationship is hard to quantify and factors, such as the pipe roughness, can be difficult to evaluate. Therefore it is usually advisable to calculate f experimentally for each flow condition in each application. This is the methodology used in the current investigation.

In a single phase liquid flow ρ_m is equal to ρ_w. Therefore Equation 6-20 and Equation 6-21 can be combined to give Equation 6-26.

$$\Delta P_F = \Delta P - \rho_w g l \cos\theta$$

Equation 6-26

Similarly rearranging Equation 6-25 gives Equation 6-27.

$$f = \frac{\Delta P_F D}{2\rho_w l \cos\theta u^2}$$

Equation 6-27

Using Equation 6-27 it is now possible to experimentally determine the relationship between f and u for the flow loop working section in the present investigation. Single phase water flows were set up with known Q_w measured using the turbine meter described in Section 6.3.2. From Q_w it is possible to calculate u, the mean water velocity in the pipe using Equation 6-28 where A is the cross-sectional area of the working section.

$$u = \frac{Q_w}{A}$$

Equation 6-28

ΔP for these flows was measured using the differential pressure sensor and ΔP_F was calculated using Equation 6-26. It was then possible to produce a calibration curve of friction factor, f , against velocity, u, for water flow. The results of this calibration are presented in Section 6.3.3.1.

In order to estimate the value of f, for the two phase flows in the current investigation, from this calibration it was necessary to calculate the fluid velocity in the working section. In a solids-liquid flow the relevant velocity is the homogeneous velocity, u_h. It is given by Equation 6-29.

$$u_h = \frac{(Q_w + Q_s)}{A}$$

Equation 6-29

In the current investigation Q_w and Q_s were measured during experimental testing using the gravimetric hopper system described in Section 6.3.1. These measurements, combined with the single-phase friction factor calibration, measurements of ΔP acquired from the differential pressure cell, and Equation 6-22 and Equation 6-24 were used to give a measure of α_s in the working section of the flow loop.

6.3.3.1 Flow loop friction factor calculation.

In order to calculate the single phase friction factor, f, Q_w and therefore the water velocity in the working section, u, was measured, using the turbine meter, over a wide range of flow conditions. By combining the measured pressure gradient in the working section, ΔP, with Equation 6-26 and Equation 6-27 it was possible to calculate the value of f for these flow conditions. The resulting calibration curve is shown in Figure 6-14.

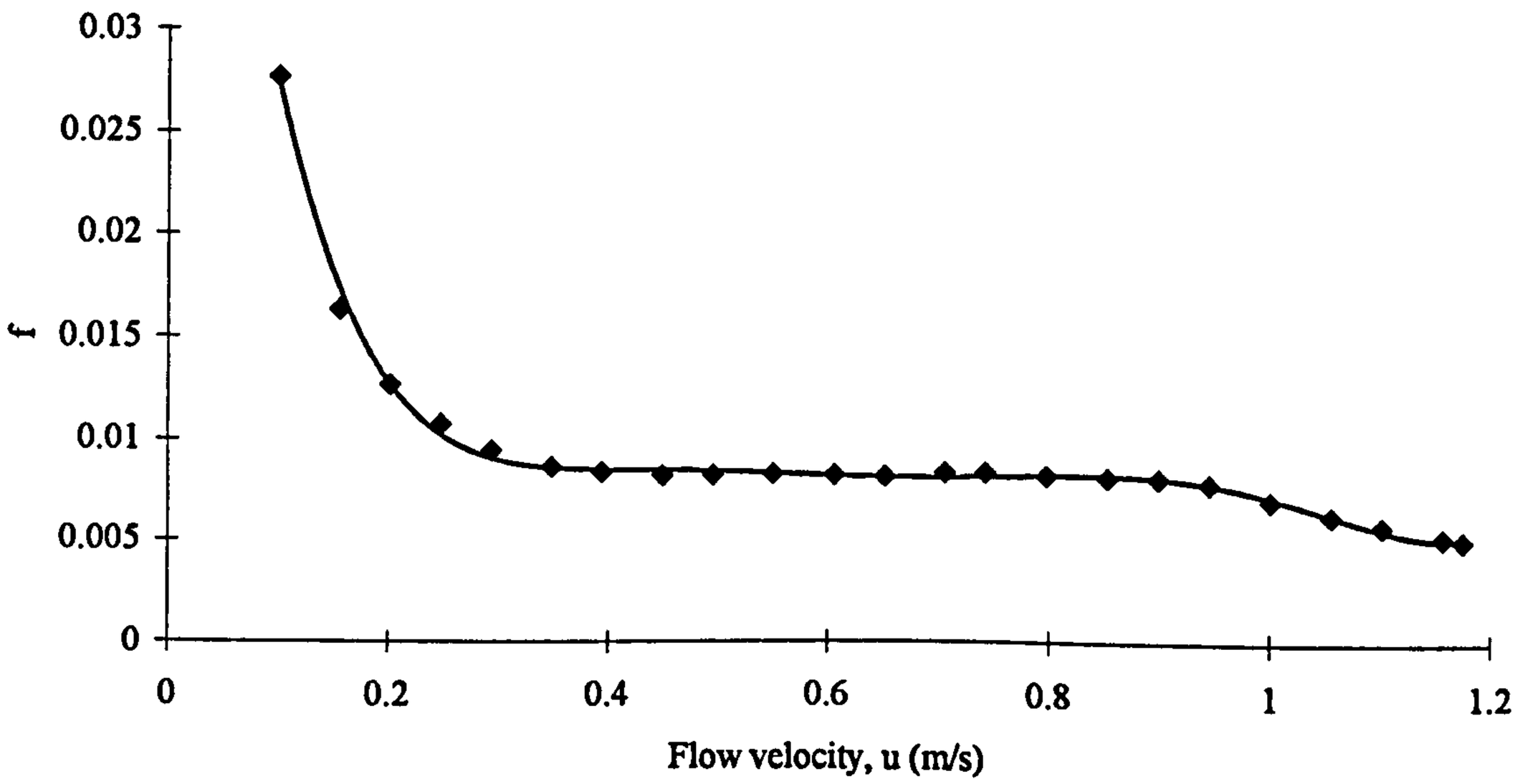

Figure 6-14. Variation of friction factor, f, with flow velocity, u.

The experimental data in Figure 6-14 shows a classic increase in f as the flow velocity decreases. This can be seen by comparing this plot with those given by Massey [92]. In the current investigation a sixth order polynomial approximation, Equation 6-30, was used to relate f to u. Equation 6-30 has been plotted with the experimental data in Figure 6-14 and shows a good fit to the data over the full range of flow velocities.

$$f = 0.852u^6 - 3.604u^5 + 6.114u^4 - 5.320u^3 + 2.505u^2 - 0.607u + 0.068$$

Equation 6-30

6.3.4 Reservoir water conductivity meter.

In order to relate the measurements of $\sigma_{m,i}$ acquired by the local probe to $\alpha_{s,i}$ the water conductivity must be known at all times, as shown by Maxwell's [65] equation, (see Equation 2-3). This has also been shown by a number of previous researchers including Nasr-el-Din et al [52] and Asakura et al [54]. The water conductivity changes during long experimental runs due to temperature changes in the water. In order to correct for this effect on the measurements obtained from the local probe a water conductivity cell was installed in the main water reservoir. Additionally a proprietary conductivity meter was used to measure the conductivity of water samples drawn off at intervals during experimental testing.

The water conductivity cell consists of a sealed box with four 5mm×5mm gold plated electrodes, each separated by 5mm, on its surface. The connections to these electrodes are brought to the surface through a water-tight conduit as shown in Figure 6-15.

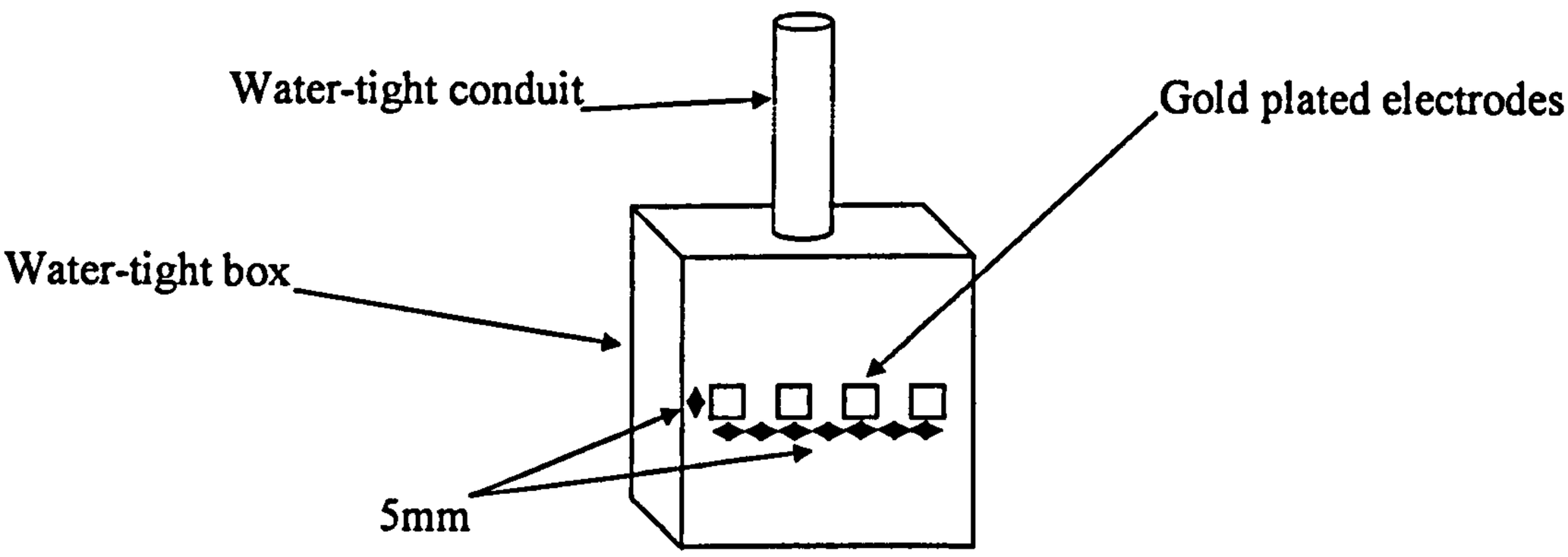

Figure 6-15. The reservoir water conductivity meter.

The electrodes are configured as a 4-electrode SEMM array. This configuration and the measurement principle are the same as those used for sensor C of the local conductivity probe (see Section 4.2.1 and 4.2.1.2). The electrical principle for the measurements is shown in Figure 6-16.

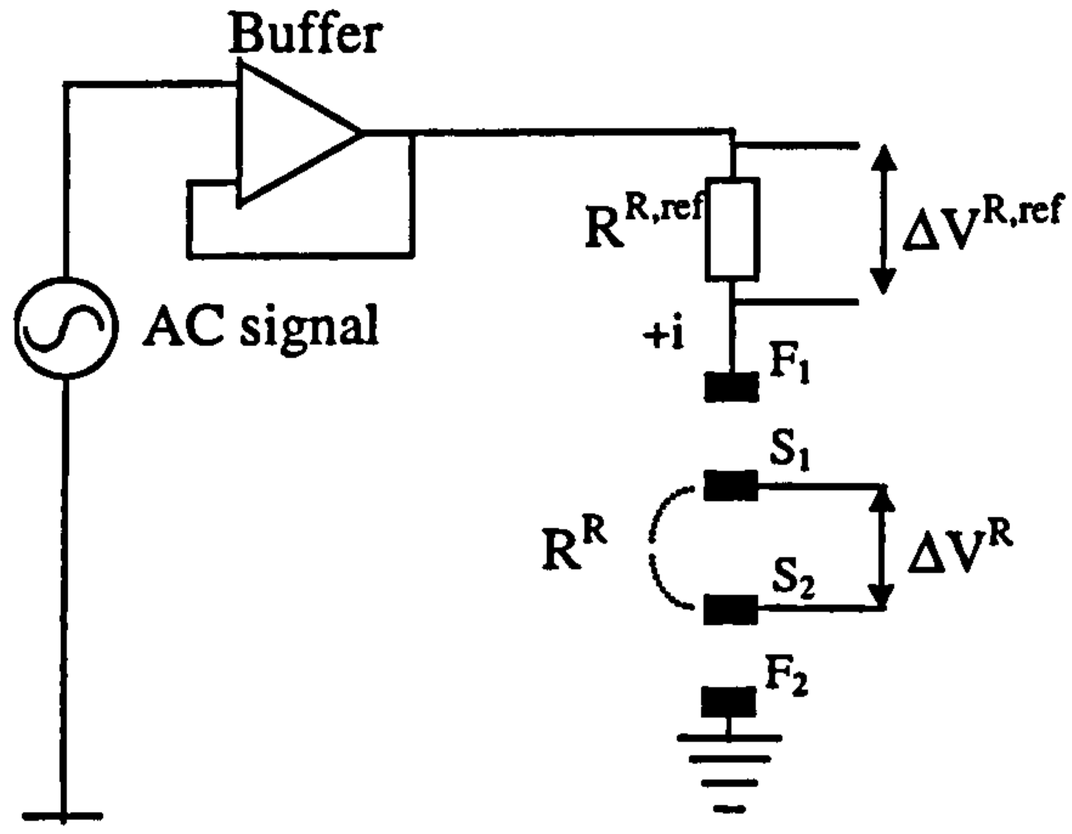

Figure 6-16. The electrical principle of the measurement used in the reservoir water conductivity meter.

An AC excitation is applied to field electrode F_1. Field electrode F_2 is held at ground. This applied sinusoidal excitation causes sinusoidal voltage drops to exist across the sense electrodes, S_1 and S_2, and across the reference resistor R_{ref}. These are shown in Figure 6-16 as ΔV^R and $\Delta V^{R,ref}$. The amplitude of ΔV^R is proportional to the fluid resistance, R^R, between the pair of sense electrodes as in Equation 6-31. The amplitude of $\Delta V^{R,ref}$ is similarly proportional to $R^{R,ref}$.

$$R^R = \frac{|\Delta V^R|}{|i|} \qquad R^{R,ref} = \frac{|\Delta V^{R,ref}|}{|i|}$$

Equation 6-31

R^R is inversely proportional to the electrical conductivity, σ_w^R, of the water between the sense electrodes as shown in Equation 6-32 where K^R is the cell constant of the sensor pair.

$$\frac{1}{R^R} = K^R \sigma_w^R$$

Equation 6-32

It should be noted at this point that the electronic measurement hardware, which is described in 4.2.2, rectifies the sinusoidal voltage drops, ΔV^R and $\Delta V^{R,ref}$, and gives a DC output, referenced to ground, that is proportional to the amplitude of each. These DC output voltage drops are V^R and $V^{R,ref}$ respectively.

In order to calculate the fluid resistance, R^R, the DC output voltages, V^R and $V^{R,ref}$ are measured. With reference to Figure 6-16 R^R is then calculated using the principle shown in Equation 6-33 where k is the gain of the rectifier. As the measurement circuits were closely matched it was assumed that k was equal for each rectifier.

$$\frac{V^{R,ref}}{V^R} = \frac{k|i|R^{R,ref}}{k|i|R^R} \therefore R^R = \frac{V^R R^{R,ref}}{V^{R,ref}}$$

Equation 6-33

From Equation 6-32 and Equation 6-33 it can be seen that σ_w^R is given by Equation 6-34.

$$\sigma_w^R = \frac{V^{R,ref}}{V^R} \frac{1}{K^R R^{R,ref}}$$

Equation 6-34

In the current investigation the relative variation of σ_w^R over the experimental testing period was required. From Equation 6-35 it can be seen that the relative change in σ_w^R between times 1, $\sigma_{w(1)}^R$, and 2, $\sigma_{w(2)}^R$, is given by Equation 6-35.

$$\frac{\sigma_{w(2)}^R}{\sigma_{w(1)}^R} = \left(\frac{V_{(2)}^{R,ref}}{V_{(2)}^R} \frac{1}{K^R R^{R,ref}} \right) \left(K^R R^{R,ref} \frac{V_{(1)}^R}{V_{(1)}^{R,ref}} \right) = \left(\frac{V_{(2)}^{R,ref}}{V_{(2)}^R} \right) \left(\frac{V_{(1)}^R}{V_{(1)}^{R,ref}} \right)$$

Equation 6-35

The advantages of this device over the proprietary meter are that it can be used to acquire a reading automatically without requiring a water sample to be drawn off from the flow loop. Drawing off a water sample into a beaker could introduce errors due to impurities in the sampling line and beaker. The reservoir conductivity meter response was checked by comparing the variation in its output, $\frac{V^R}{V^{R,ref}}$, with readings of water conductivity and temperature acquired by the proprietary conductivity meter. This data is presented below.

6.3.4.1 Reservoir water conductivity meter testing.

The output of the reservoir water conductivity meter, $\frac{V^R}{V^{R,ref}}$, was checked by comparing it with measurements taken using a proprietary conductivity meter. It was also compared with temperature measurements taken using the same proprietary meter. The testing was carried out in a solids-liquid flow over a long time period in order to accurately simulate the

experimental conditions. The two conductivity readings and the temperature are plotted against time as relative values. The method used to give X_r, the relative value for a given device, is given in Equation 6-36 where X_t is the value at time t, and X_i is the initial value.

$$X_r = \frac{X_t - X_i}{X_i}$$

Equation 6-36

This method of presenting the data allows the variation in each of the three readings to be easily compared on the same axes (see Figure 6-17).

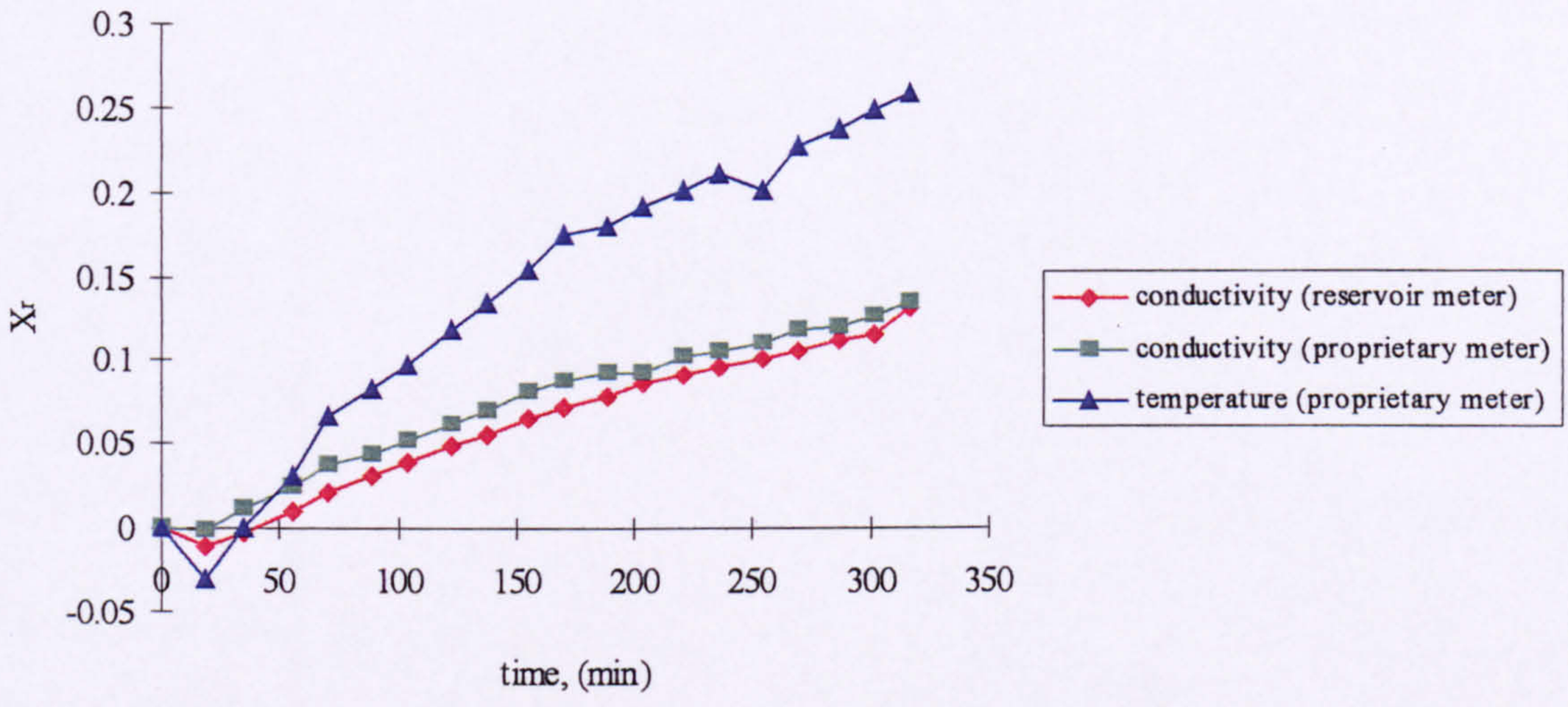

Figure 6-17. Relative variation of water conductivity and temperature.

Figure 6-17 shows that the three sets of readings show the same trends over the experimental test period. Therefore it was decided that the reservoir conductivity meter should be used in the experimental testing. The reservoir water conductivity cell allowed σ_w to be acquired automatically whilst the local probe was positioned at each spatial location which allowed a detailed plot of the variation to be assembled. This was not possible with the proprietary device.

6.4 Experimental procedure.

The experimental procedure can be divided into three sections. These are the initial data acquisition, followed by initial and secondary data analysis. The procedures are detailed in this section.

6.4.1 Experimental data acquisition.

In the current investigation measurements were acquired from the local probe at 128 spatial locations within the pipe. This operation was carried out using the probe control and data acquisition software described in Section 4.4.3. The spatial locations were arranged as 8 diametrical traverses of the pipe with 16 radial points on each as shown in Figure 6-18. Additionally data was acquired at the centre of the pipe cross-section before each diametrical traverse. This data was used to normalise the results using a procedure described in Section 6.4.3. Data was also acquired at 16 radial points along 1 diametrical traverse in static water before and after each experimental test. This data allows the effect of the probes proximity to the pipe wall to be corrected for as described in Section 4.2.1.2 and Section 6.4.3.

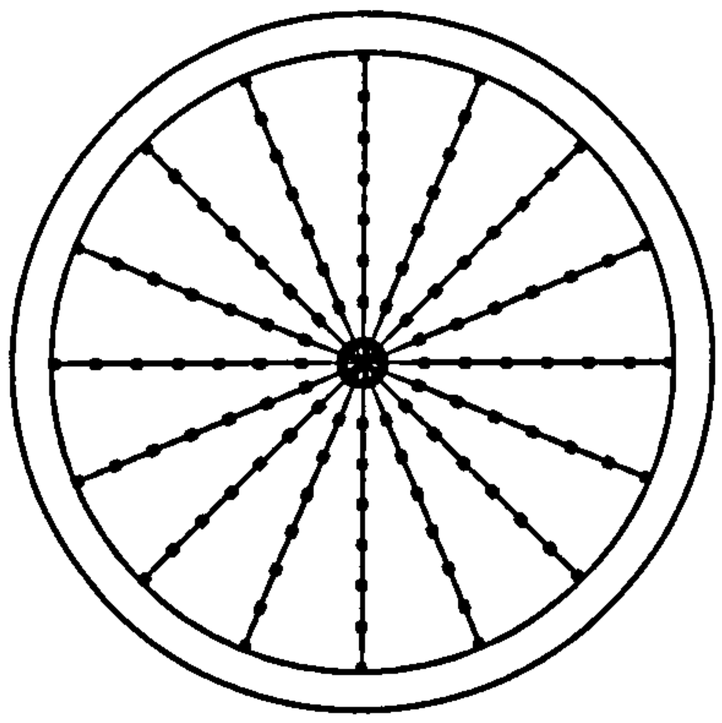

Figure 6-18. The arrangement of the probe data acquisition locations.

The measurements acquired at each spatial location both in static water and the flowing mixture are listed in Table 6-1.

Table 6-1. Measurements acquired at each spatial location during experimental testing

	Acquisition frequency (Hz)	Acquisition time period (s)
Acquired from the local probe		
Sensor C - V^C	100	60
Sensor C - V^{ref}	100	60
Sensor A - V^A	3750	60
Sensor B – V^B	3750	60
Acquired from reference measurement devices		
Differential pressure cell - ΔP	100	60
Reservoir water conductivity meter - V^R	100	60
Reservoir water conductivity meter – $V^{R,ref}$	100	60

Additionally the time at which the data was acquired from each spatial location was recorded. This allowed the data to be synchronised with data acquired from the gravimetric hopper system described in Section 6.3.1. In the current investigation the gravimetric hopper system was used to acquire corrected measurements of Q_s^{ref} and Q_w^{ref}, the solids and water volumetric flow rates, at intervals of 15 minutes during the experimental testing. Finally σ_w and T_w, the water conductivity and temperature, were acquired at intervals of 30 minutes using a proprietary meter.

6.4.2 Initial data analysis.

As described in Section 4.4.3 the probe control and data acquisition software outputs two binary data files for each of the 128 spatial positions of the probe. The first contains the local probe solids volume fraction measurement data, the reservoir water conductivity cell measurement data and the differential pressure measurement data. The second contains the local probe solids velocity data. Additionally a pair of data files exists for each of the normalisation points, where there is one normalisation point for each of the 8 rotational positions of the local probe. The purpose of this normalisation data is explained in Section 6.4.3.

A series of GlobalLab text macros and a QuickBasic control program were written to carry out some initial analysis on this data. The procedures are summarised below. The results files from this analysis are detailed in Table 6-2.

The measurements V^A and V^B from sensors A and B of the local probe were AC coupled to remove any DC offset from the signals. The signals were then cross-correlated using FFT techniques. The time delay, δ_i, of the peak of the resulting cross correlation function was then written to a text file. This procedure was repeated for each spatial location of the probe during experimental testing.

The measurements V^C and V^{ref} from sensor C of the local probe and the reference resistor were combined within GlobalLab to give a single measurement, $\left(\frac{V^{ref}}{V^C}\right)$. In Equation 4-7 it was shown that this value is proportional to σ^C, the fluid conductivity at sensor C. The mean value of $\left(\frac{V^{ref}}{V^C}\right)$ was calculated from the 60 seconds of measurement data for each spatial location of the probe. These mean values were then written to a text results file. This procedure was repeated for the measurements acquired in both static water and flowing mixture.

The measurements V^R and $V^{R,ref}$ from the reservoir water conductivity sensor were combined within GlobalLab to give a single measurement, $\left(\frac{V^{R,ref}}{V^R}\right)$. In Equation 6-34 it was shown that this value is proportional to σ_w^R, the water conductivity. The mean value of $\left(\frac{V^{R,ref}}{V^R}\right)$ was calculated from the 60 seconds of measurement data acquired whilst the local probe was positioned at each spatial location. These mean values were then written to a text results file.

The differential pressure measurement data required little initial analysis. The only procedure used involves calculating the mean value of ΔP for each spatial location of the probe and

writing these values to a text file. This procedure was repeated for the measurements acquired in both static water and flowing mixture.

Table 6-2. Data output from the initial analysis

Local probe	
Sensor C	Text file containing mean values of $\left(\frac{V^{ref}}{V^{C}}\right)_{w,0}$ for 16 radial locations of the probe within 1 diametrical traverse acquired in static water before experimental testing. From Equation 4-7 these measurements are equal to $K^{C}\sigma^{C}_{w,0}R^{ref}$ where K^{C} is the cell constant for sensor C which is different for each radial position of the probe.
	Text file containing mean values of $\left(\frac{V^{ref}}{V^{C}}\right)_{m,t}$ for 128 spatial locations of the probe within 8 diametrical traverses acquired during flow. From Equation 4-7 these measurements are equal to $K^{C}\sigma^{C}_{m,t}R^{ref}$ where K^{C} is the cell constant for sensor C which is different for each radial location of the probe.
	Text file containing mean values of $\left(\frac{V^{ref}}{V^{C}}\right)_{m,n}$ acquired at the centre of the pipe for each of the 8 diametrical traverses during flow. From Equation 4-7 these measurements are equal to $K^{C}_{n}\sigma^{C}_{m,n}R^{ref}$ where K^{C}_{n} is the cell constant for sensor C with the probe at the centre of the pipe.
	Text file containing mean values of $\left(\frac{V^{ref}}{V^{C}}\right)_{w,f}$ for 16 radial locations of the probe within 1 diametrical traverse acquired in static water after experimental testing. From Equation 4-7 these measurements are equal to $K^{C}\sigma^{C}_{w,f}R^{ref}$ where K^{C} is the cell constant for sensor C which is different for each radial location of the probe.

	to $K^C\sigma^C_{w,f}R^{ref}$ where K^C is the cell constant for sensor C which is different for each radial location of the probe.
Sensors A and B	Text file containing the time delay δ_i between the signals from sensor A and sensor B. These values were produced by cross-correlation of the signals from sensors A and B acquired at 128 spatial locations within 8 diametrical traverses during flow. Text file containing mean values of the time delay, δ_n, between the signals from sensor A and sensor B. These values were produced by cross-correlation of the signals from sensors A and B acquired at the centre of the pipe for each of the 8 diametrical traverses during flow
Reference devices	
Reservoir water conductivity meter	Text file containing mean values of $\left(\frac{V^{R,ref}}{V^R}\right)_{w,0}$ acquired whilst the probe was positioned at 16 radial locations within 1 diametrical traverse in static water before experimental testing. From Equation 4-7 these measurements are equal to $K^R\sigma^R_{w,0}R^{R,ref}$ where K^R is the cell constant for the reservoir conductivity cell. Text file containing mean values of $\left(\frac{V^{R,ref}}{V^R}\right)_{w,t}$ acquired whilst the probe was positioned at 128 spatial locations within 8 diametrical traverses during flow. From Equation 4-7 these measurements are equal to $K^R\sigma^R_{w,t}R^{R,ref}$ where K^R is the cell constant for the reservoir conductivity cell. Text file containing mean values of $\left(\frac{V^{R,ref}}{V^R}\right)_{w,f}$ acquired whilst the probe was positioned at 16 radial locations within 1 diametrical traverse in static water after experimental testing. From Equation 4-7 these measurements are equal to $K^R\sigma^R_{w,f}R^{R,ref}$ where K^R is the cell constant for the reservoir conductivity cell.

Differential pressure cell	Text file containing mean values of ΔP acquired in static water whilst the probe was positioned at each of the 16 radial positions before and after experimental testing. Text file containing mean values of ΔP acquired in the flowing mixture whilst the probe was positioned at each of the 128 spatial locations of during experimental testing.
Gravimetric hopper system	Text file containing mean values of Q_s^{ref} and Q_w^{ref} acquired at 15 minute intervals during experimental testing.
Proprietary conductivity meter	Readings of σ_w and T_w acquired at 30 minute intervals during experimental testing.

6.4.3 Secondary data analysis.

This section describes the procedures used to give final measurements of the flow parameters from the data given in Table 6-2.

6.4.3.1 Local probe solids volume fraction.

In order to calculate $\alpha_{s,i}^{probe}$ using Maxwell's relationship it is necessary to use measured values of σ_m^C and σ_w^C as shown in Equation 4-4 which is reproduced here.

$$\alpha_{s,i}^{probe} = \frac{1-\left(\frac{\sigma_m^C}{\sigma_w^C}\right)}{1+0.5\left(\frac{\sigma_m^C}{\sigma_w^C}\right)}$$

Equation 4-4

From Table 6-2 it can be seen how the outputs of the local probe can be related to both σ_m^C and σ_w^C. However before these outputs can be used to calculate $\alpha_{s,i}^{probe}$ they must be corrected to account for drifting flow parameters as described below.

In order to calculate σ_w^C, the measurements of $\sigma_{w,0}^C$ and $\sigma_{w,f}^C$ must first be corrected for any drift in σ_w that took place over the period of the experimental test. This was carried out using the measurements of $\sigma_{w,t}^R$ acquired during testing. The correction is shown in Equation 6-37.

$$\text{(i)}\ \sigma_{w,0}^{C,corr} = \sigma_{w,0}^{C}\frac{\overline{\sigma}_{w,t}^{R}}{\sigma_{w,0}^{R}} \qquad \text{(ii)}\ \sigma_{w,f}^{C,corr} = \sigma_{w,f}^{C}\frac{\overline{\sigma}_{w,t}^{R}}{\sigma_{w,f}^{R}}$$

Equation 6-37

Equation 6-37 normalises $\sigma_{w,0}^{C}$ and $\sigma_{w,f}^{C}$ to the mean value of $\sigma_{w,t}^{R}$ during the test. Following this correction the mean measurement of σ_{w}^{C} was calculated for each radial position of the probe using $\sigma_{w,0}^{C,corr}$ and $\sigma_{w,f}^{C,corr}$ as shown in Equation 6-38.

$$\sigma_{w}^{C} = \frac{\sigma_{w,0}^{C,corr} + \sigma_{w,f}^{C,corr}}{2}$$

Equation 6-38

In order to calculate σ_{m}^{C} the measurements of $\sigma_{m,t}^{C}$ must also be corrected for any drift in σ_{w} that took place over the period of the experimental test. This was also carried out using measurements of $\sigma_{w,t}^{R}$ acquired during testing. The correction is shown in Equation 6-39.

$$\sigma_{m,t}^{C,corr1} = \sigma_{m,t}^{C}\frac{\overline{\sigma}_{w,t}^{R}}{\sigma_{w,t}^{R}}$$

Equation 6-39

Next it is necessary to correct $\sigma_{m,t}^{C,corr1}$ for any drift in the mean solids volume fraction that could have occurred during the test period. In the current investigation each experimental test took several hours to complete. Over this time the flow conditions fluctuated slightly. For this correction it was assumed that the fluctuation of the local solids volume fraction at the centre of the pipe represented the fluctuation of the mean solids volume fraction. Therefore the correction was carried out using the normalisation measurements, $\sigma_{m,n}^{C}$, acquired at the centre of the pipe at intervals during the experimental testing. This correction is shown in Equation 6-40.

$$\sigma_{m,t}^{C,corr2} = \sigma_{m,t}^{C,corr1}\frac{\overline{\sigma}_{m,n}^{C}}{0.5\left(\sigma_{m,n1}^{C} + \sigma_{m,n2}^{C}\right)}$$

Equation 6-40

Equation 6-40 normalises each measurement $\sigma_{m,t}^{C}$ to the mean of all the normalisation data acquired. It should be noted that as the normalisation data was acquired before each diametrical traverse of the pipe took place no data exactly conforms to the time that a given

measurement of $\sigma_{m,t}^{C}$ was acquired. Therefore in Equation 6-40 the mean of the immediately preceding, $\sigma_{m,n1}^{C}$, and following, $\sigma_{m,n2}^{C}$, normalisation measurements was used.

Following this correction $\sigma_{m,t}^{C,corr2}$ was assumed to give an accurate measurement of σ_{m}^{C}. The corrected measurements of σ_{m}^{C} and σ_{w}^{C} were then substituted into Equation 4-4. In terms of the actual output signals of the probe this is shown by Equation 6-41 where $\left(\frac{V^{C}}{V^{ref}}\right)_{m}$ and $\left(\frac{V^{C}}{V^{ref}}\right)_{w}$ are the corrected outputs.

$$\alpha_{s,i}^{probe} = \frac{1-\left(\left(\frac{V^{ref}}{V^{C}}\right)_{m}\left(\frac{V^{C}}{V^{ref}}\right)_{w}\right)}{1+0.5\left(\left(\frac{V^{ref}}{V^{C}}\right)_{m}\left(\frac{V^{C}}{V^{ref}}\right)_{w}\right)}$$

Equation 6-41

It is important to note that only measurements of $\left(\frac{V^{C}}{V^{ref}}\right)_{m}$ and $\left(\frac{V^{C}}{V^{ref}}\right)_{w}$ acquired at the same radial position of the local probe can be paired in Equation 6-41 as the cell constant, K^{C}, varies with the proximity of the pipe wall. If this condition is not met the effect of the proximity of the pipe wall on the sensitivity of the sensor will not be corrected for.

6.4.3.2 Local solids axial velocity.

In order to calculate the local solids axial velocity, $u_{s,i}^{probe}$, it is necessary to measure the time taken, τ_i, for the particles to pass between sensor A and sensor B of the local probe. $u_{s,i}^{probe}$ is then given by Equation 6-42 where L is the effective sensor separation.

$$u_{s,i}^{probe} = \frac{L}{\delta_i}$$

Equation 6-42

From Table 6-2 it can be seen that δ_i is given by cross-correlation of the signals from sensor A and sensor B. However before these measurements can be used to calculate $u_{s,i}^{probe}$ it is

necessary to correct δ_i for any drift in the mean solids axial velocity that could have occurred during the test period. In the current investigation each experimental test took several hours to complete. Over this time the flow conditions fluctuated slightly. For this correction it was assumed that the variations in the local solids axial velocity at the centre of the pipe represented the fluctuation of the mean solids axial velocity. Therefore the correction was carried out using the normalisation measurements, δ_n, acquired at the centre of the pipe at intervals during the experimental testing. This correction is shown in Equation 6-43.

$$\delta_i^{corrl} = \delta_i \frac{\delta_n}{0.5(\delta_{n1} + \delta_{n2})}$$

Equation 6-43

Equation 6-43 normalises each measurement δ_i to the mean of all the normalisation data acquired. It should be noted that as the normalisation data was acquired before each diametrical traverse of the pipe took place no data exactly conforms to the time that a given measurement of δ_i was acquired. Therefore in Equation 6-43 the mean of the immediately preceding, δ_{n1}, and following, δ_{n2}, normalisation measurements was used. $u_{s,i}^{probe}$ was now calculated by substituting δ_i^{corrl} into Equation 6-42 as shown in Equation 6-44.

$$u_{s,i}^{probe} = \frac{L}{\delta_i^{corrl}}$$

Equation 6-44

6.4.3.3 Integrated global measurements of solids volume fraction, solids axial velocity and solids volumetric flow rate from the local probe.

In order to calculate the mean global values of these flow parameters it is necessary to integrate the local values determined in the previous two sections. This is done using Equation 1-1, Equation 1-4 and Equation 1-5. These are all reproduced here.

$$Q_s^{probe} = \int_A u_{s,i}^{probe} \alpha_{s,i}^{probe} dA$$

Equation 1-1

$$\alpha_s^{probe} = \frac{1}{A} \int_A \alpha_{s,i}^{probe} dA$$

Equation 1-4

$$u_s^{probe} = \frac{\int_A \alpha_{s,i}^{probe} u_{s,i}^{probe} dA}{\int_A \alpha_{s,i}^{probe} dA} = \frac{Q_s^{probe}}{A\alpha_s^{probe}}$$

Equation 1-5

6.4.3.4 Reference measurements.

Reference measurements of Q_s^{ref} and Q_w^{ref} were obtained by calculating the mean values of the variables (measured using the gravimetric hopper system described in Section 6.3.1) over the period of the experimental testing. In order to calculate reference measurements of α_s^{ref} and u_s^{ref} it was also necessary to use the acquired differential pressure data. This procedure is detailed below.

Initially it was necessary to estimate f, the friction factor for the flow. The principle of the friction factor is described in Section 6.3.3. The calibration carried out for the current investigation is given in Equation 6-30 which is reproduced here.

$$f = 0.852u_h^6 - 3.604u_h^5 + 6.114u_h^4 - 5.320u_h^3 + 2.505u_h^2 - 0.607u_h + 0.068$$

Equation 6-30

In order to apply this calculation it is necessary to calculate the mean homogeneous velocity, u_h, of the flow. This is done using Equation 6-29 which is reproduced here.

$$u_h = (Q_w + Q_s)\frac{4}{\pi D^2}$$

Equation 6-29

From the value of f calculated using Equation 6-30 and Equation 6-29 it is possible to estimate the frictional pressure loss, ΔP_F, in the flow using Darcy's equation which is shown as Equation 6-25 and reproduced here.

$$\Delta P_F = \frac{2\rho_w l\cos\theta f u_h^2}{D}$$

Equation 6-25

It is then possible to calculate the reference solids volume fraction, α_s^{ref}, by combining Equation 6-20, Equation 6-21 and Equation 6-23 to give Equation 6-45.

$$\alpha_s^{ref} = \frac{\Delta P - \Delta P_F}{gl\cos\theta(\rho_s - \rho_w)} - \frac{\rho_w}{\rho_s - \rho_w}$$

Equation 6-45

It is also now possible to calculate the reference solids axial velocity, u_s, using Equation 6-46 where A is the pipe cross-sectional area.

$$u_s = \frac{Q_s}{\alpha_s A}$$

Equation 6-46

It should be noted at this point that these reference measurements of α_s, u_s and Q_s are global values and can only be compared with the integrated values of the local probe measurements as shown in Section 6.4.3.3.

6.5 The Electrical Resistance Tomography (ERT) system.

The principles of tomography including ERT have been described in Section 2.1.5. In this section the device used in the current parallel investigation is explained in more detail. More complete descriptions of the device are given by Loh [56] and Lucas [57,58]. The device used had three planes of 16 stainless steel electrodes equispaced around the internal circumference of an 80m diameter pipe. Each electrode measured 5mm in the axial direction and 10mm in the circumferential direction. The electrode planes were separated by 2cm and 3cm as shown in Figure 6-19.

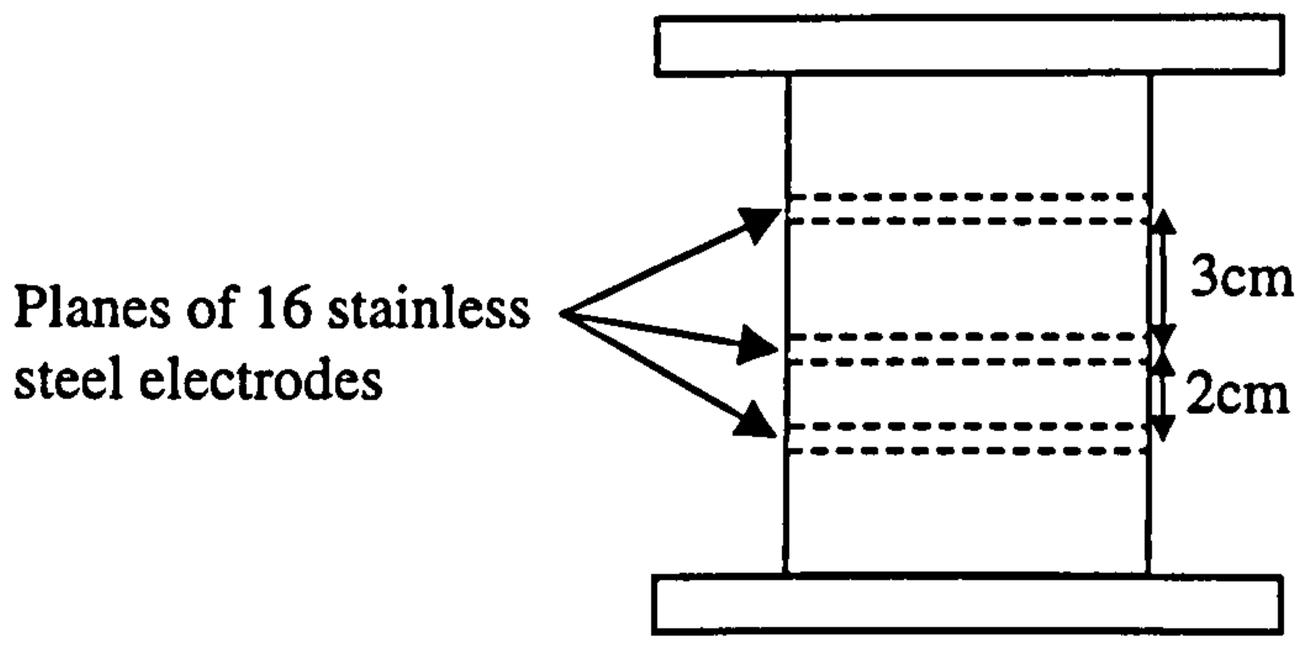

Figure 6-19. The electrode configuration of the ERT system.

Using this electrode assembly plane separations of 2cm, 3cm and 5cm could be achieved. The device was configured as a dual-plane system. Measurements were simultaneously acquired from two of the electrode planes. After reconstruction the measurements give profiles of the conductivity distribution within the flow cross-section at the axial positions of the electrode planes. The level of detail given by each profile is a function of the number of electrodes in each plane. A 16 electrode plane gives conductivity measurements for 104 "pixels" within the cross-section. Variations in conductivity recorded in pixels of the first plane were then cross-correlated with variations in conductivity recorded in the corresponding pixel of the second plane. This allowed a profile of the solids velocity to be calculated.

Previous ERT systems did not have the capability to acquire data fast enough to measure the solids velocity. The device used in the current investigation had been optimised to increase the possible data acquisition rate. This development is described by Loh [56] and Lucas [57,58]. It included optimisation of the measurement electronics to reduce settling times and it involved an "interleaved" protocol for the data acquisition. Using the interleaved protocol the system acquired consecutive voltage measurements alternately from each plane. This eliminated cross-talk as only one plane of electrodes is active at a time. Also it simplified the cross-correlation as the *i'th* frame of data from each plane is effectively acquired over the same period of time.

To obtain the solids velocity profiles data was acquired at 50 frames per second from two of the electrode planes for 20 seconds. This data was then reconstructed using the linear back-projection method (see Section 2.1.5.2). These images were then cross-correlated using the pixel-pixel cross-correlation method described by Beck & Plaskowski [68] to obtain the solids velocity profile. In order to obtain a profile of the solids volume fraction the measurements acquired from one plane of electrodes were reconstructed using the modified Newton-Raphson technique (see Section 2.1.5.2).

From these profiles it was possible to calculate values of the global solids volume fraction, α_s, the global solids axial velocity, u_s, and the solids volumetric flow rate, Q_s, using Equation 1-1, Equation 1-4 and Equation 1-5. In order to validate these measurements reference data was acquired from the gravimetric flow measurement system (see Section 6.3.1) and the differential pressure sensor (see Section 6.3.3).

7. Experimental results.

7.1 The experimental testing program.

7.1.1 The Format of the experimental results.

This chapter presents the results of the experimental testing carried out using the local probe. The results were acquired using the experimental methodology described in Section 6.4. They cover the range of solids-liquid flow conditions detailed in Section 7.1.2. The results have been validated qualitatively and quantitatively as described below.

7.1.1.1 Qualitative comparison of the results with ERT data.

The shapes of the solids volume fraction and solids velocity profiles obtained by the local probe were qualitatively compared with results acquired using a dual-plane ERT system. This ERT system is as described in Section 6.5 and by Loh [56] and Lucas et al [57,58].

The profiles acquired from each system used different data-point co-ordinates. The co-ordinates of the data-points for each system are shown in Figure 7-1. To qualitatively compare the profiles an interpolation routine was used to plot profiles from the two systems using the same co-ordinates. The interpolation was carried out in Matlab using an inverse distance method within the 2D function described by the data. The interpolated data-grid is also shown in Figure 7-1.

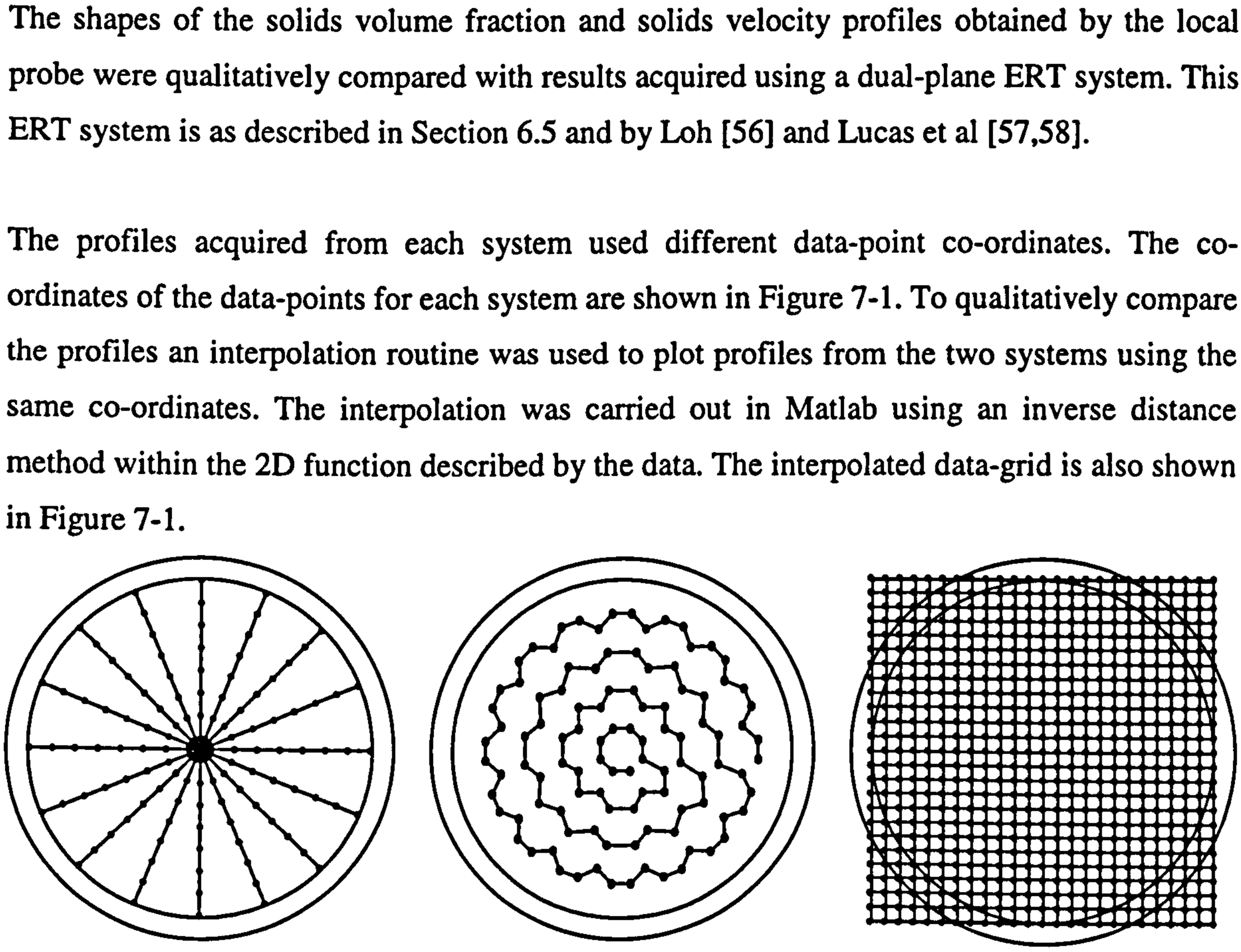

Figure 7-1. The measurement data grids and the interpolated data grid.

It should be stressed at this point that the results were only interpolated for the purposes of visual comparison and presentation. Wherever results have been integrated to give global measurement values, as described in Section 6.4.3.3, the original data were used.

7.1.1.2 Quantitative comparison of the results with reference measurement data.

In order to quantitatively validate the results from the local probe and the ERT system they were compared with global measurements acquired using the reference measurement systems described in Chapter 6. To allow the local measurements to be compared with these global measurements the results were integrated over the pipe cross-section. The details and methods used are presented in Section 6.4.3.3.

7.1.2 Flow conditions tested with the local probe system.

For each flow condition tested with the local probe the mean values of Q_s^{ref}, Q_w^{ref}, α_s^{ref}, u_s^{ref} and σ_w, obtained using the reference measurement systems are given in Table 7-1. The measurement nomenclature is described below.

Q_s^{ref}, solids volumetric flow rate - The average solids volumetric flow over the experimental test run measured using the gravimetric hopper system as described in Sections 6.3.1.

Q_w^{ref}, water volumetric flow rate - The average water volumetric flow rate over the experimental test run measured using the gravimetric hopper system as described in Section 6.3.1.

α_s^{ref}, solids volume fraction - The average solids volume fraction over the experimental test run measured using pressure gradient method corrected for frictional pressure loss as described in Sections 6.3.3.

u_s^{ref}, solids velocity - The average solids velocity over the experimental test run measured by combining the solids volumetric flow rate and solids volume fraction measurements as described in Section 6.4.3.4.

σ_w, water conductivity - The average water conductivity over the experimental test run measured using the proprietary conductivity meter as described in Section 6.3.4

Flow condition numbers have been assigned to the flow conditions that were used. It is important to realise that this does not mean that experimental tests with the same flow condition number are identical. Each experimental test took place on a separate occasion. Due to the pump control being open-loop, and because of slight variations in the temperature and therefore viscosity of the water, it is extremely difficult to reproduce identical flow conditions during different tests. Therefore experimental tests have been assigned the same flow condition number if the actual flow conditions were approximately the same.

Table 7-1. Flow conditions for which data was acquired using the local probe system.

Flow condition no.	Data -set	Angle of inclination of flow	Solids volumetric flow rate, Q_s^{ref} (m^3h^{-1})	Water volumetric flow rate, Q_w^{ref} (m^3h^{-1})	Solids volume fraction, α_s^{ref}	Solids velocity, u_s^{ref} (ms^{-1})	Water conductivity, σ_w (μScm^{-1})
1	1	0°	1.07	6.69	0.18	0.32	139.5
1	2	0°	1.00	7.94	0.16	0.34	137.6
2	1	0°	1.37	7.93	0.17	0.44	157.6
3	1	0°	0.70	5.37	0.18	0.22	158.9
4	1	0°	0.38	3.41	0.20	0.10	154.7
4	2	0°	0.35	3.09	0.20	0.10	152.7
4	3	0°	0.38	3.50	0.20	0.11	157.0
7	1	5°	0.35	3.72	0.21	0.09	145.1
7	2	5°	0.43	4.28	0.20	0.12	131.1
8	1	5°	0.79	5.89	0.20	0.22	146.9
8	2	5°	0.86	6.44	0.19	0.26	134.0
9	1	5°	1.12	7.50	0.18	0.34	144.8
10	1	0°	1.11	14.79	0.08	0.79	157.4
11	1	0°	0.47	20.31	0.05	0.57	172.4
12	1	30°	1.05	7.55	0.34	0.17	145.2
12	2	30°	0.78	6.67	0.33	0.13	176.4
13	1	30°	1.11	7.92	0.33	0.19	163.2
13	2	30°	1.01	7.94	0.36	0.18	137.6
14	1	30°	0.90	10.33	0.22	0.23	184.1
15	1	30°	1.15	15.12	0.10	0.66	177.1
16	1	30°	1.28	11.92	0.17	0.41	180.4

7.1.3 Flow conditions tested with the ERT system.

For each flow condition tested with the ERT system the mean values of Q_s^{ref}, Q_w^{ref}, α_s^{ref}, u_s^{ref} and σ_w, obtained using the reference measurement systems are given in Table 7-2. Additionally the plane separation is given. This is the separation between the two electrode

planes of the ERT system. It is analogous to the sensor separation of the local probe and therefore has an effect on the velocity resolution.

Flow condition numbers have been assigned to the flow conditions that were used. It is important to realise that this does not mean that experimental tests with the same flow condition number are identical. The reasons for this are given in the previous section Experimental tests have been assigned the same flow condition number if the actual flow conditions were approximately the same.

Table 7-2. Flow conditions for which data was acquired using the ERT system.

Flow condition no.	Angle of inclination of flow	ERT plane separation (cm)	Solids volumetric flow rate, Q_s^{ref} (m^3h^{-1})	Water volumetric flow rate, Q_w^{ref} (m^3h^{-1})	Solids volume fraction, α_s^{ref}	Solids velocity, u_s^{ref} (ms^{-1})	Water conductivity, σ_w (μScm^{-1})
1	0°	3	0.96	6.96	0.15	0.36	158.5
1	0°	5	1.11	6.84	0.16	0.39	148.5
2	0°	5	1.27	8.35	0.15	0.47	147.3
3	0°	2	0.66	4.61	0.17	0.21	162.8
3	0°	3	0.62	5.79	0.15	0.23	160.8
3	0°	5	0.76	5.90	0.15	0.28	149.3
4	0°	3	0.35	4.28	0.13	0.15	158.2
4	0°	5	0.36	3.90	0.17	0.13	150.2
5	0°	2	0.61	12.03	0.06	0.56	167.6
5	0°	5	0.61	10.17	0.06	0.58	152.2
6	0°	2	0.77	8.51	0.11	0.39	164.5
6	0°	5	0.96	9.51	0.11	0.55	153.3
7	5°	3	0.43	4.50	0.18	0.13	152.1
7	5°	5	0.41	4.04	0.19	0.12	135.1
8	5°	3	0.79	6.32	0.17	0.26	156.3
8	5°	5	0.86	6.23	0.18	0.26	135.1
9	5°	3	1.05	7.37	0.17	0.34	152.1
9	5°	5	1.01	6.84	0.18	0.31	135.4
10	0°	2	0.74	17.09	0.03	1.36	169.3
12	30°	3	0.84	7.30	0.22	0.21	152.8
13	30°	3	1.01	8.29	0.25	0.22	155.3
14	30°	3	0.97	10.72	0.21	0.26	155.1

7.2 Comparison of experimental results from the local probe system with experimental results from the ERT system.

The aim of this section of the thesis is to give a qualitative comparison of the shapes of the flow profiles acquired using the local probe system with the shapes of the flow profiles acquired using the dual plane ERT system under similar flow conditions.

Profiles of local solids volume fraction from both the local probe, $\alpha_{s,i}^{probe}$, and the ERT system, $\alpha_{s,i}^{ERT}$, are shown in Section 7.2.1. Profiles of local solids axial velocity from both the local probe, $u_{s,i}^{probe}$, and the ERT system, $u_{s,i}^{ERT}$, are shown in Section 7.2.2. The profiles are shown for vertical upward flows and upward flows inclined at 5° and 30° from vertical. The profiles are presented for each flow condition as given in Table 7-1 and Table 7-2. Where more than one data set was available from the local probe they are all presented. The ERT profiles are sorted according to plane separation. Changing the plane separation has a substantial effect on the profiles of $u_{s,i}^{ERT}$ as the velocity resolution of the device is highly dependent on plane separation (see Section 2.3). Changing the plane separation has no effect on profiles of $\alpha_{s,i}^{ERT}$. Therefore the profiles of $\alpha_{s,i}^{ERT}$ for each plane separation should be regarded as extra data sets for the same flow condition. The profiles are discussed at the end of the section.

7.2.1 Comparison of profiles of solids volume fraction from each system.

7.2.1.1 Solids volume fraction profiles for vertical flow.

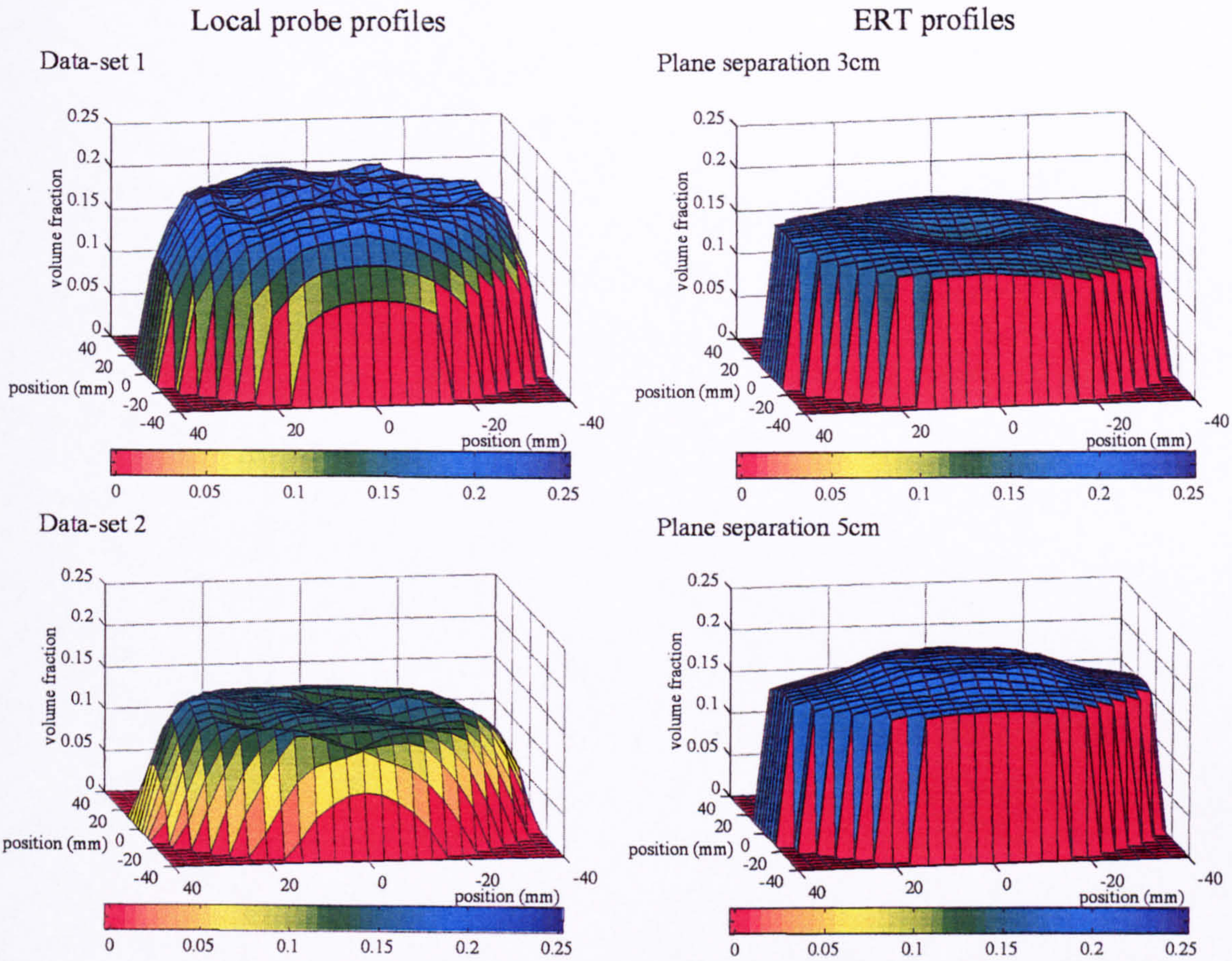

Figure 7-2. Solids volume fraction profiles for vertical flow, flow condition 1.

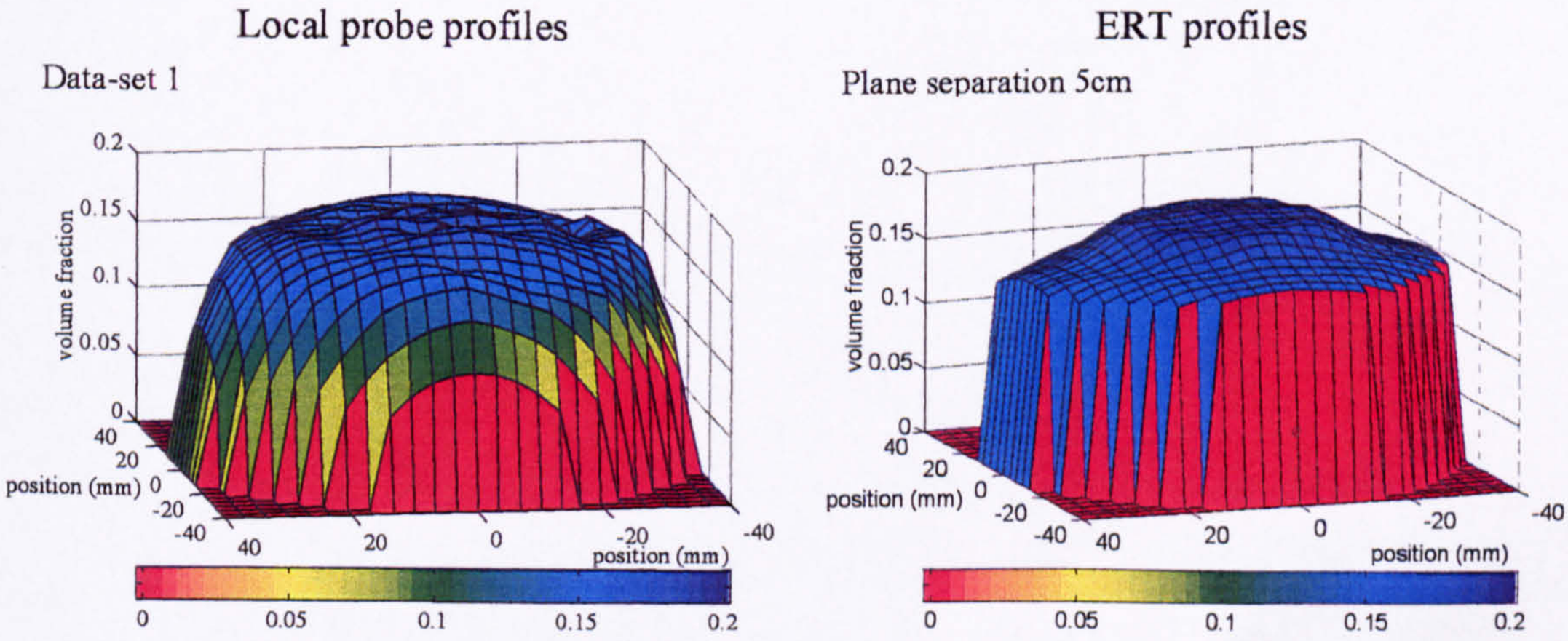

Figure 7-3. Solids volume fraction profiles for vertical flow, flow condition 2.

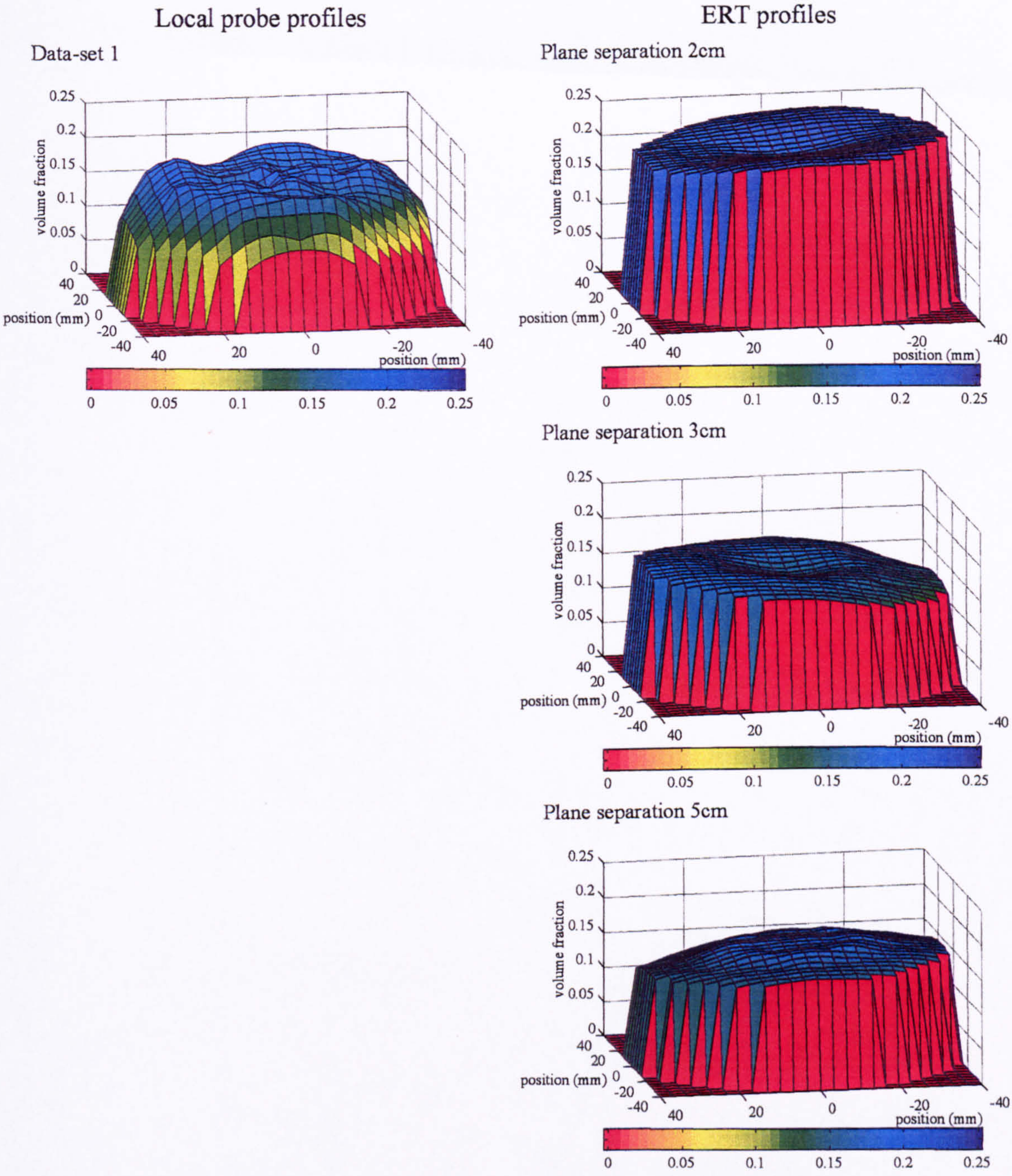

Figure 7-4. Solids volume fraction profiles for vertical flow, flow condition 3.

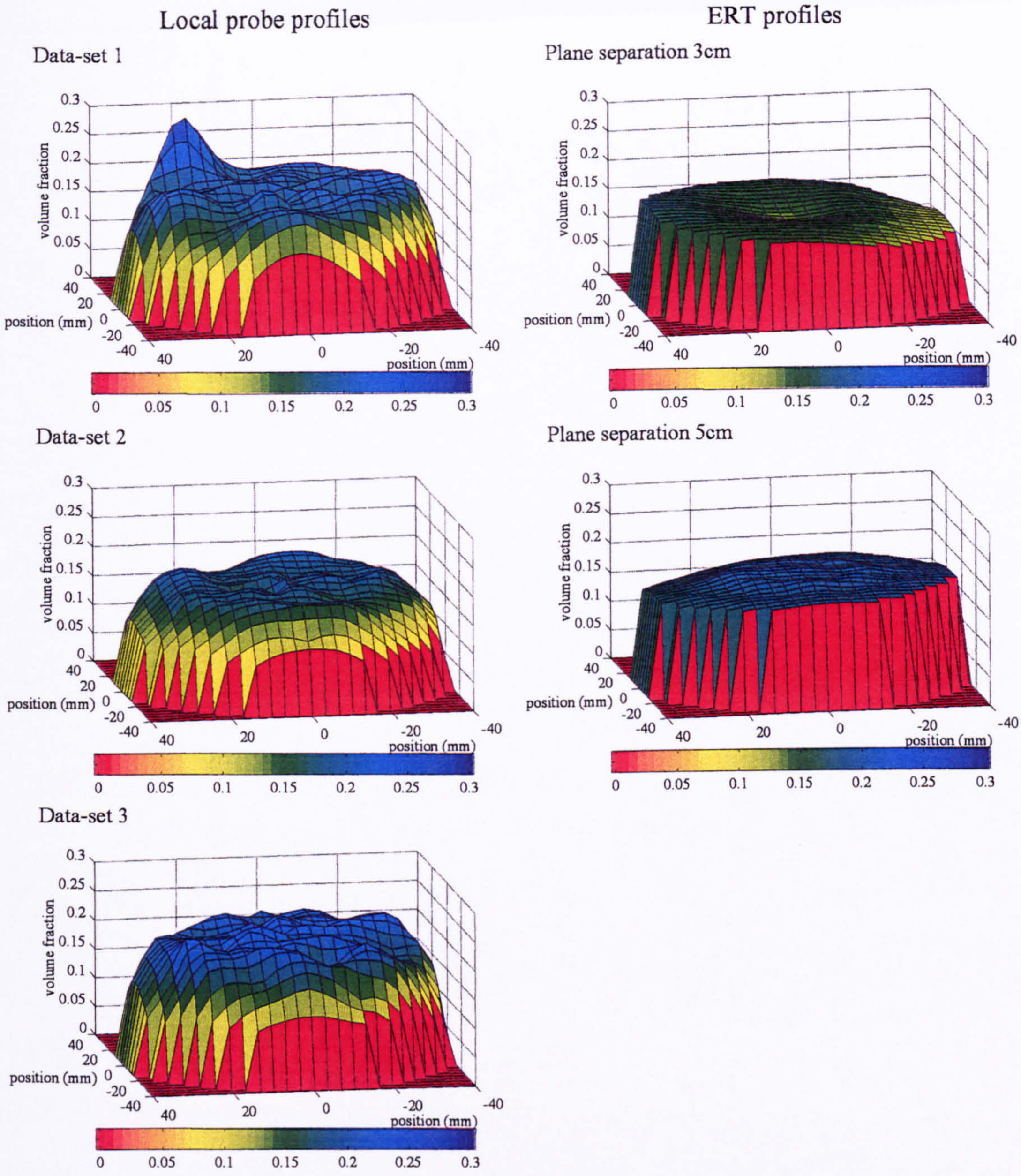

Figure 7-5. Solids volume fraction profiles for vertical flow, flow condition 4.

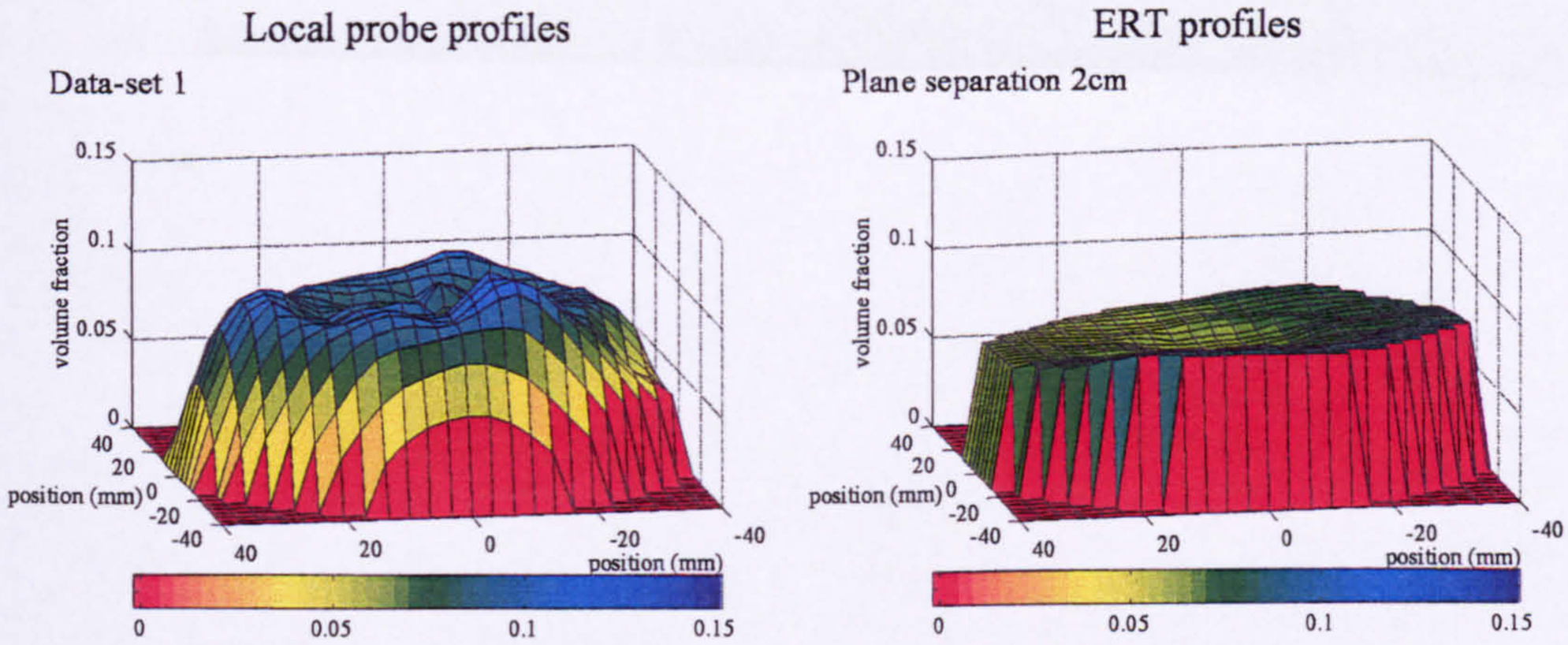

Figure 7-6. Solids volume fraction profiles for vertical flow, flow condition 10.

7.2.1.2 Solids volume fraction profiles for flow inclined 5° from vertical.

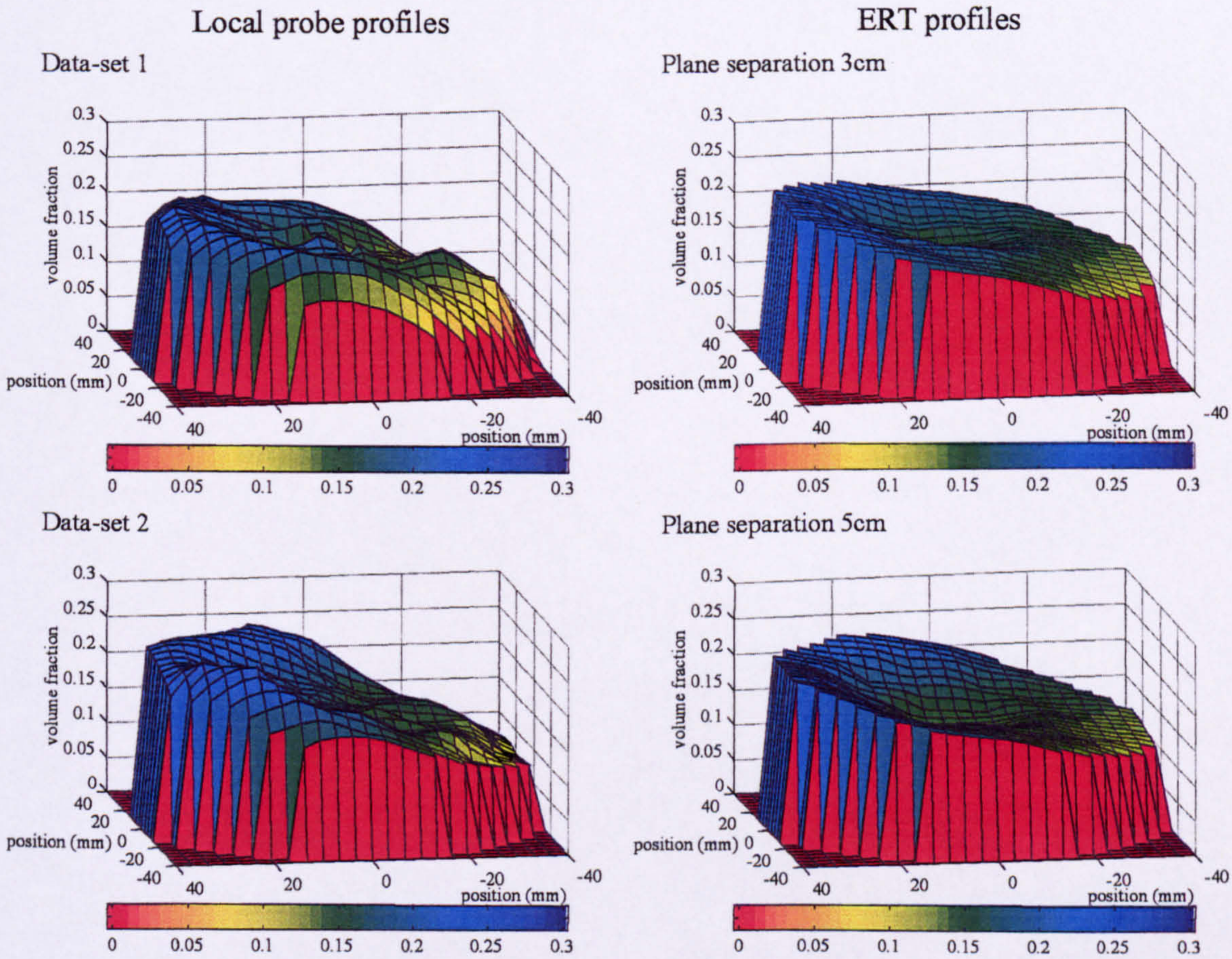

Figure 7-7. Solids volume fraction profiles for flow inclined 5° from vertical, flow condition 7.

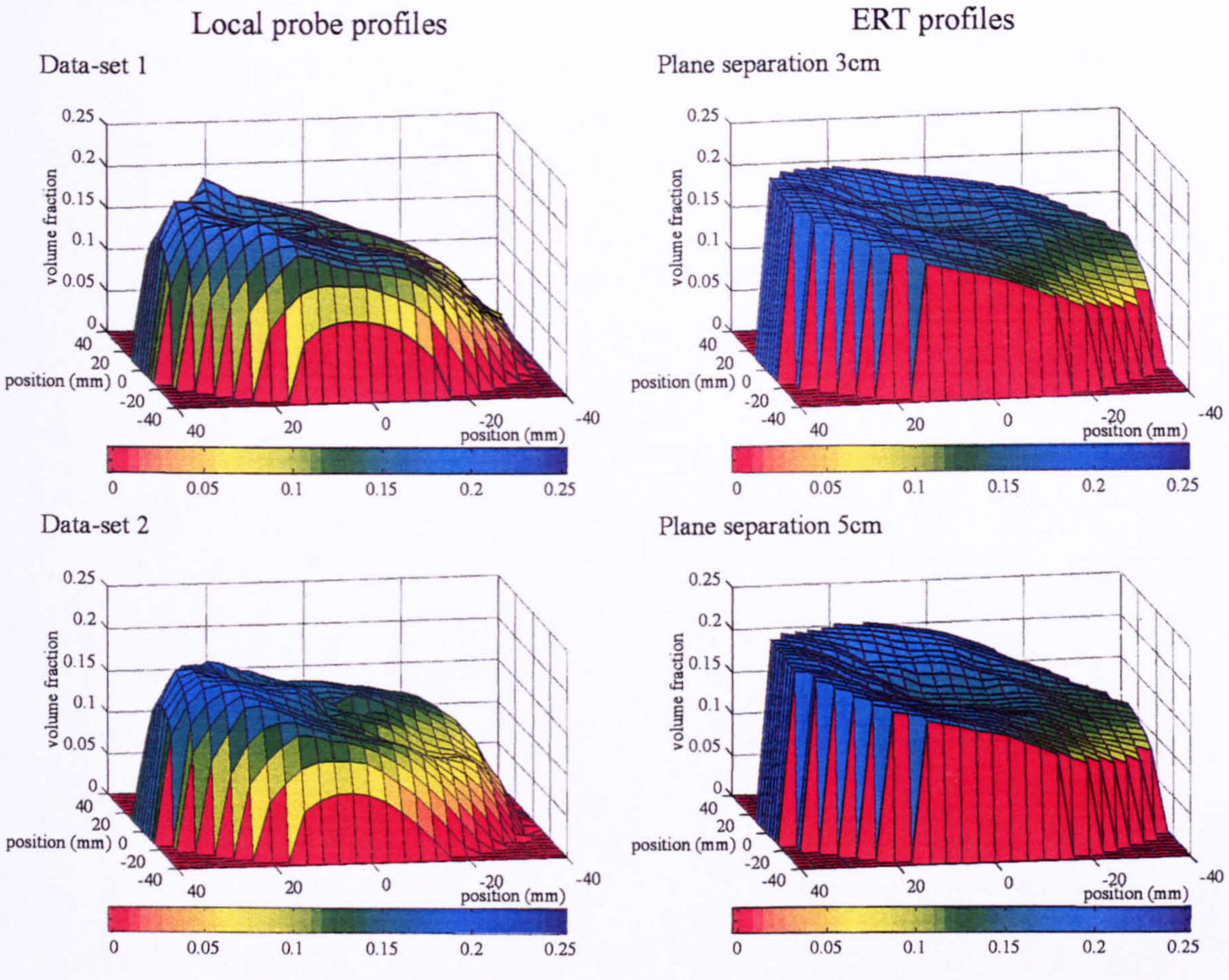

Figure 7-8. Solids volume fraction profiles for flow inclined 5° from vertical, flow condition 8.

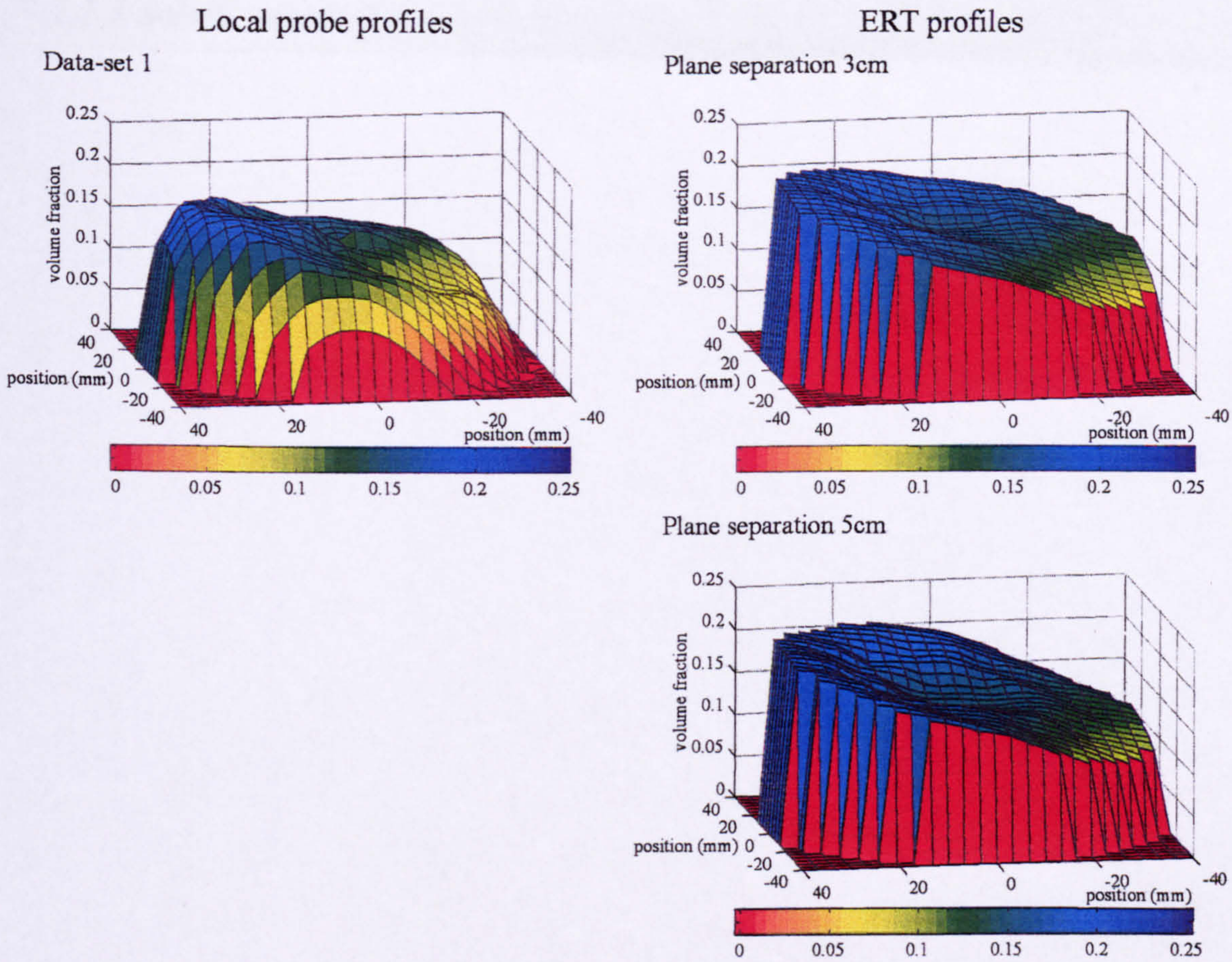

Figure 7-9. Solids volume fraction profiles for flow inclined 5° from vertical, flow condition 9.

7.2.1.3 Solids volume fraction profiles for flow inclined 30° from vertical.

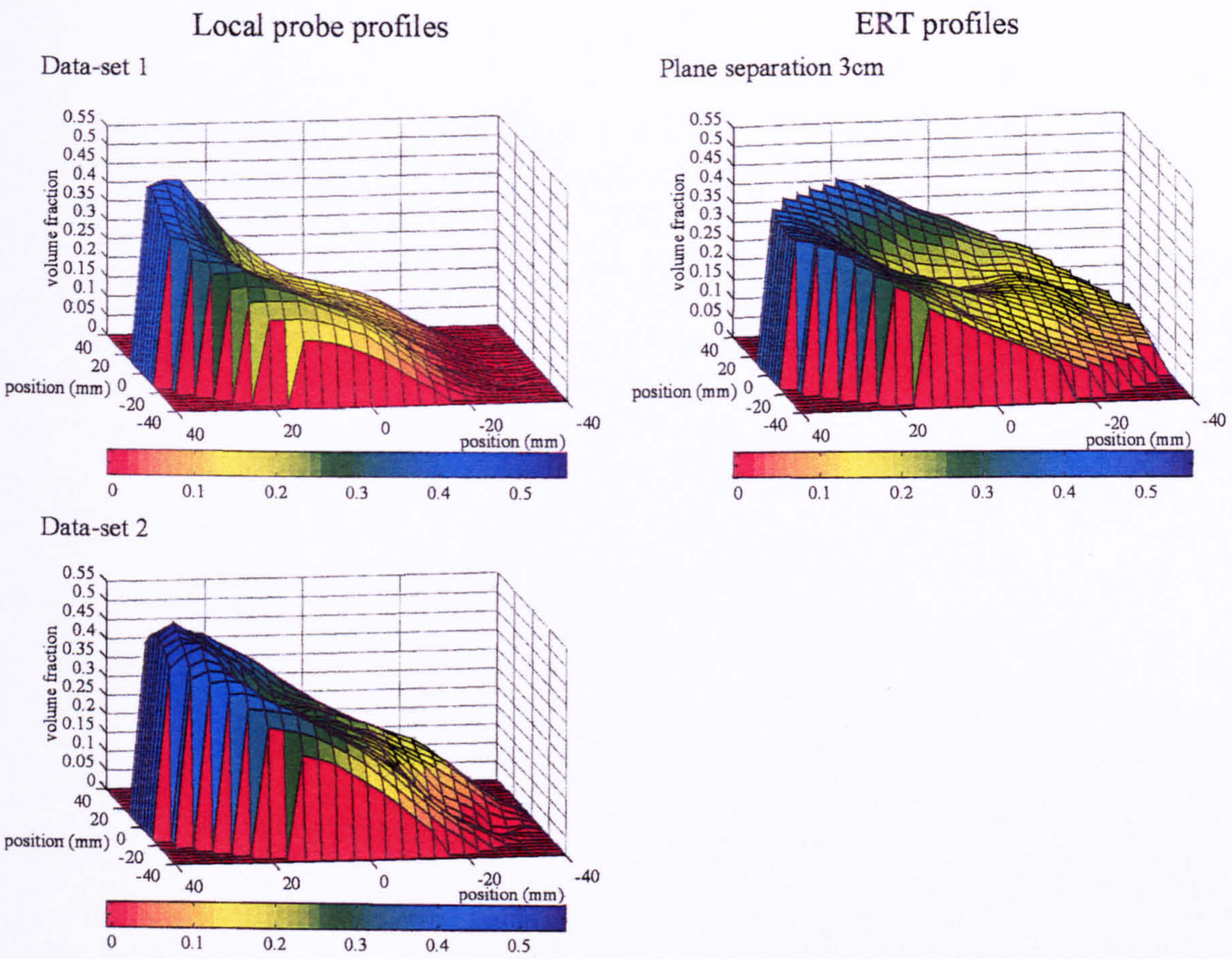

Figure 7-10. Solids volume fraction profiles for flow inclined 30° from vertical, flow condition 12.

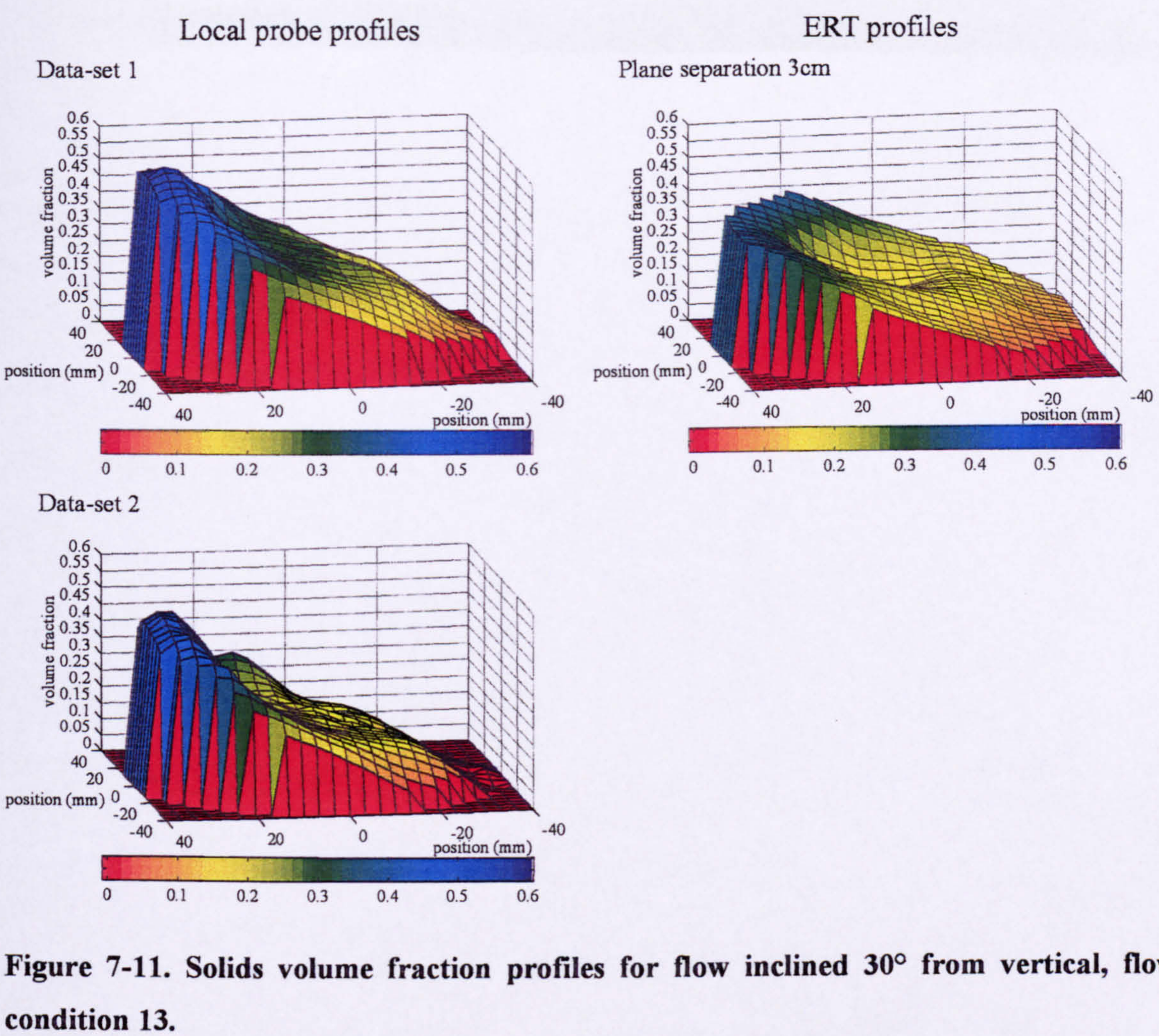

Figure 7-11. Solids volume fraction profiles for flow inclined 30° from vertical, flow condition 13.

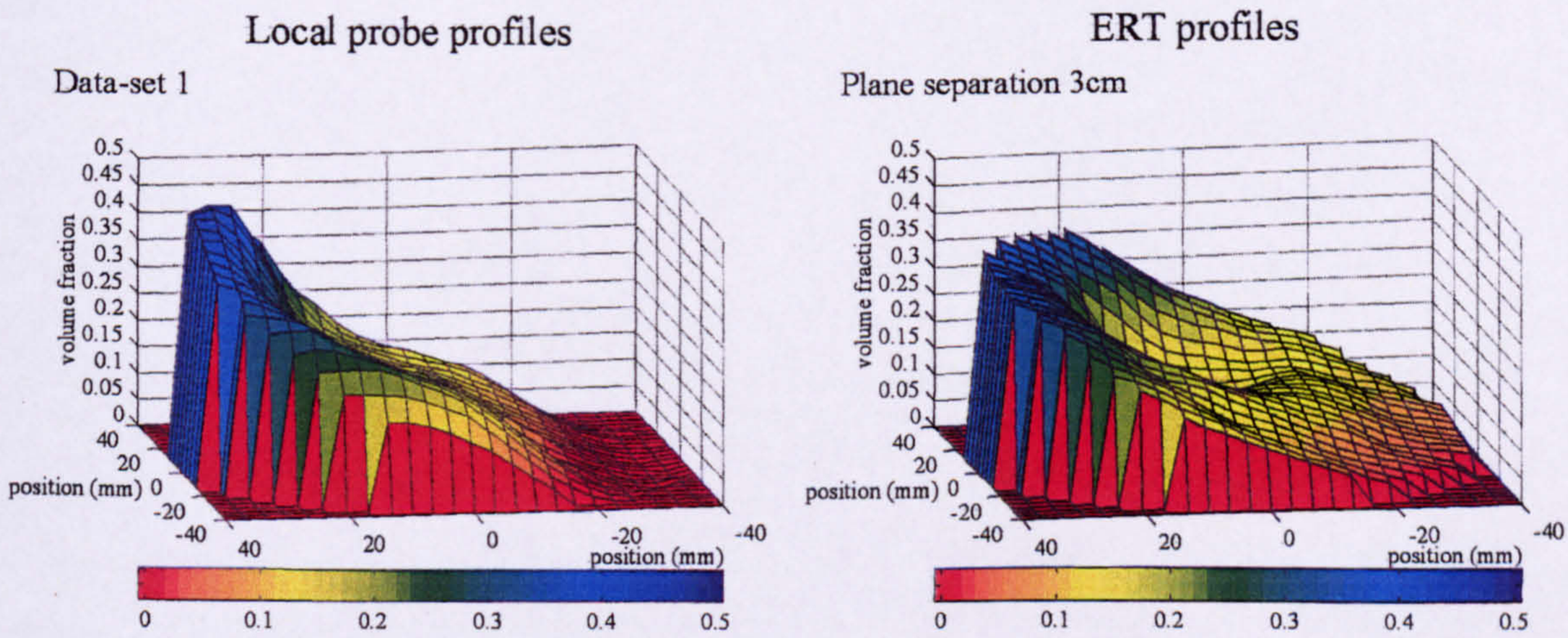

Figure 7-12. Solids volume fraction profiles for flow inclined 30° from vertical, flow condition 14.

7.2.1.4 Discussion of the solids volume fraction profiles.

It is clear that there is qualitative agreement between the profiles acquired from each system. Profiles of $\alpha_{s,i}$ in vertical upward flow (see Figure 7-2 to Figure 7-6) all show only small variations of $\alpha_{s,i}$ across the central area of the flow cross-section. Complete cross-sectional profiles of $\alpha_{s,i}$ in vertical upward flow could not be found in the literature. However results showing $\alpha_{s,i}$ relatively constant across the pipe have previously been published by Asakura et al [54], Alajbegovic et al [98], Bartosik & Shook [99] and Akagawa et al [4]. Profiles of $\alpha_{s,i}$ in inclined upward flows (see Figure 7-7 to Figure 7-12) all show an almost one-dimensional shape, with $\alpha_{s,i}$ only varying as a function of co-ordinate Z, where Z is as defined in Figure 7-13.

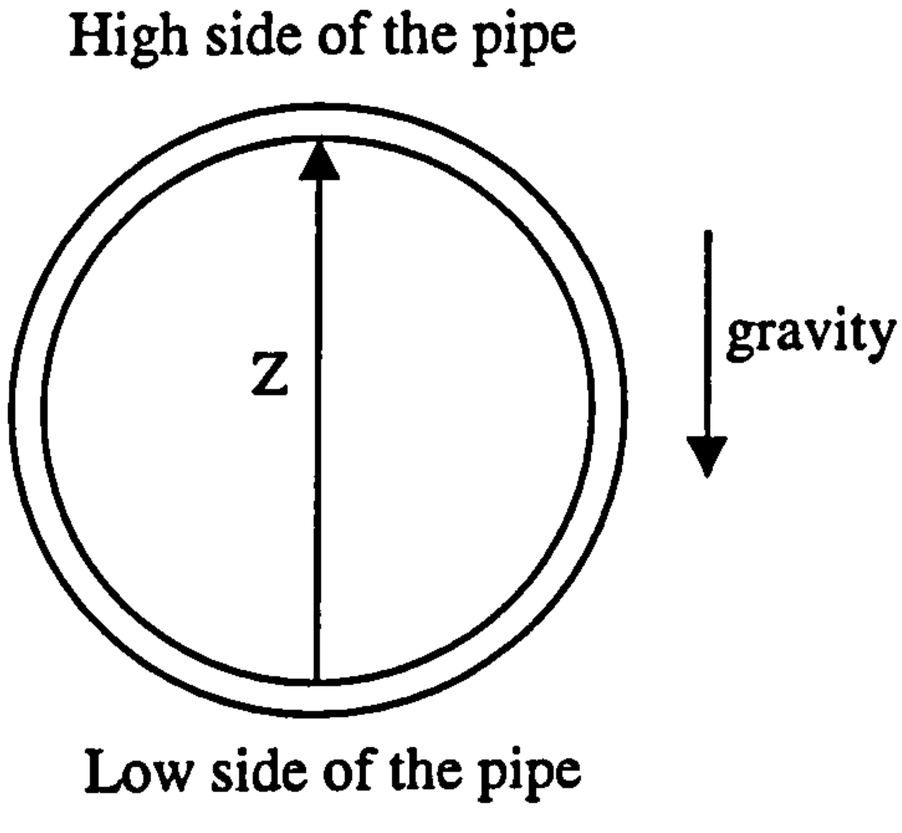

Figure 7-13. The position of the Z axis relative to the pipe cross-section.

At the high side of the pipe $\alpha_{s,i}$ is low, reducing to zero in Figure 7-10 and Figure 7-12. At the low side of the pipe $\alpha_{s,i}$ is high, almost reaching close packing ($\alpha_{s,i}\approx0.62$) for flow condition 13 (see Figure 7-11). This variation of α_i can be seen in the results of Matousek [100] which are the only published profiles of $\alpha_{s,i}$ in upward inclined solids-liquid flow that could be found. However similar profile shapes have been reported by Lucas [101] and Tabeling et al [102] for the dense phase volume fraction in inclined oil-water flows. Vigneaux et al [43] give full cross-sectional profiles for this type of flow which reinforce the assumption that $\alpha_{s,i}$ only varies in the Z direction. These flow profiles also show qualitative agreement with those reported by Roco & Shook [93] and Chen & Kadambi [33] for horizontal solids-liquid flow. They also agree with the full cross-sectional profiles of horizontal solids-liquid flow reported by Hsu et al [103] and Scarlett & Grimley [25]. The causes of this profile shape are described in Section 1.2. Despite this qualitative agreement between the profiles there are some

differences between those given by the local probe and those given by the ERT system as discussed below.

The most obvious difference is that the profiles acquired by the local probe show a drop in solids volume fraction close to the pipe wall whilst the profiles acquired by the ERT system do not. This is true for all flow inclinations, but it is most easily observable in the vertical flow profiles. This "wall effect" can be seen in the results published by Asakura et al [54], Alajbegovic et al [98] and Akagawa et al [4] for vertical solids-liquid flow. Bartosik & Shook [99] also report that the wall effect increases with global solids volume fraction, α_s, and the particle diameter, d_p. Similarly the profiles reported by Matousek [100] in inclined solids-liquid flow and Lucas [101], Vigneaux et al [43] and Tabeling et al [102] in liquid-liquid inclined flow show wall effects at the low side of the pipe where $\alpha_{s,i}$ is high. At the high side of the pipe $\alpha_{s,i}$ is often negligible and therefore the wall effect cannot be seen. In horizontal solids-liquid flow wall effects are reported by Chen & Kadambi [33] and Roco & Shook [93] who also report that the effect increases with increasing d_p.

In summary the bulk of the previous research suggests that there will be a drop in $\alpha_{s,i}$ close to the pipe wall. The most likely cause of the disagreement between the two systems used in the current investigation is the increased spatial resolution of the local probe at the pipe wall. The local probe acquires a measurement directly at the pipe wall. In contrast the ERT data is averaged over a pixel which extends 7mm into the flow. The measurement positions closest to the pipe wall can be seen by looking at the data-grid for each device shown in Figure 7-1. Because of this it is considered that the local probe profiles give a more accurate representation of the solids volume fraction close to the pipe wall.

Another feature, which can be observed in many of the local probe profiles, is a slight reduction in solids volume fraction in the central portion of the pipe. This is noticeable at all flow inclinations. In vertical flow it can most clearly be seen in Figure 7-4 and Figure 7-6. In flow inclined at 5° from vertical it is most apparent in Figure 7-7. Finally in flow inclined at 30° from vertical it is obvious in all the presented profiles, Figure 7-10, Figure 7-11, and Figure 7-12.

Unfortunately it is difficult to verify this feature from the ERT profiles. This is because of the way in which the profiles are reconstructed. A common factor in tomographic systems is a drop in sensitivity at the centre of the vessel. In the ERT system used in the current investigation a weighting function based on the radial distance of the measurement pixel from the pipe wall was used in the reconstruction algorithms as reported by Loh [104]. This weighting function preferentially increases $\alpha_{s,i}^{ERT}$ at the centre of the pipe. Before application of the weighting function many of the profiles of $\alpha_{s,i}^{ERT}$ showed a large dip in the centre of the pipe. After application of the weighting function this artefact was not as apparent. If the profiles acquired by the ERT system for vertical flow are considered, a dip is still present in some cases, whilst in others an increase in $\alpha_{s,i}^{ERT}$ is noticeable in the central portion of the pipe (see Figure 7-2, Figure 7-4, and Figure 7-5). All the presented profiles acquired by the ERT system for inclined flow (see Figure 7-7 to Figure 7-12) show a strong dip feature in the centre of the pipe.

The arbitrary nature of the ERT weighting function makes it difficult to prove whether a dip in $\alpha_{s,i}$ does actually exist from the profiles acquired by the ERT system alone. However the appearance of this feature in profiles obtained by the local probe and the ERT system suggests that such a dip is present. "Saddle" shaped profiles have been previously reported by Asakura et al [54], Alajbegovic et al [98] and Akagawa et al [4] for vertical upward solids-liquid flows. These authors reported that the size of the dip in $\alpha_{s,i}$ decreased as u_s increased. Additionally Asakura et al [54] reported that the size of the dip increased as d_p increases and Akagawa et al [4] reported that its size increased with increasing ρ_s. The highly varying profiles for inclined and horizontal flows result in the feature being harder to identify in published data. However it is possible to identify similar shapes from the data of Matousek [100], Lucas [101], Vigneaux et al [43], Tabeling et al [102], Hsu et al [103] and Chen & Kadambi [33]. Additionally the data of Roco & Shook [93] and Scarlett & Grimley [25] suggests that the saddle shape becomes more noticeable as α_s increases. In the light of this published data, it seems reasonable to accept the saddle shape in the profiles of $\alpha_{s,i}$ as a genuine feature. This suggests that the weighting function applied to the profiles acquired by the ERT system may be over-compensating for the sensitivity variation of the device.

The final difference between the profiles obtained from the local probe and the ERT system can be seen in the inclined flow results (see Figure 7-7 to Figure 7-12). Both systems give similar average values of $\alpha_{s,i}$. Visually this can be seen by looking at the value of $\alpha_{s,i}$ in the centre of the pipe cross-section. However the profiles acquired by the local probe system consistently show a steeper gradient of $\alpha_{s,i}$ across the pipe. This results in a higher peak value of $\alpha_{s,i}$ at the low side of the pipe and a lower value of $\alpha_{s,i}$ at the high side of the pipe (see Figure 7-13). This can most clearly be seen in the profiles for flow inclined 30° from vertical (see Figure 7-10 to Figure 7-12).

In order to decide which of the two systems gave the most accurate profile of $\alpha_{s,i}$ the arrangement of solid particles in the inclined pipe was considered. Visual observation of flow inclined 30° from vertical showed a packed layer of solids at the low side of the pipe. At close packing $\alpha_{s,i}$ should be approximately 0.62. Examination of the experimental profiles showed that the profiles acquired by the local probe show values of $\alpha_{s,i}$ closer to 0.6 than the profiles acquired by the ERT system. Therefore it was considered that the profiles acquired by the local probe show a truer representation of the distribution of $\alpha_{s,i}$ across the pipe.

In conclusion both sets of solids volume fraction profiles show qualitative agreement with each other and with the expected profile shapes. The profiles acquired by the local probe appear to show greater detail although the fact that the local probe acquired one minute of data at each point whilst the ERT system acquired a full data-set in 20 seconds will be partly responsible. This is because the longer acquisition time allows temporal variations in $\alpha_{s,i}$ to be averaged out. More obvious differences include an improved resolution at the pipe wall in the profiles acquired using the local probe. Also the local probe is able to measure a steeper solids volume fraction gradient across the pipe than the ERT system. However against these advantages must be weighed the fact that the local probe has a large data acquisition time, and is also an intrusive instrument, whilst the non-intrusive ERT system acquires data for the entire cross-section over a shorter time interval.

7.2.2 Comparison of profiles of solids velocity from each system.

7.2.2.1 Solids velocity profiles for vertical flow.

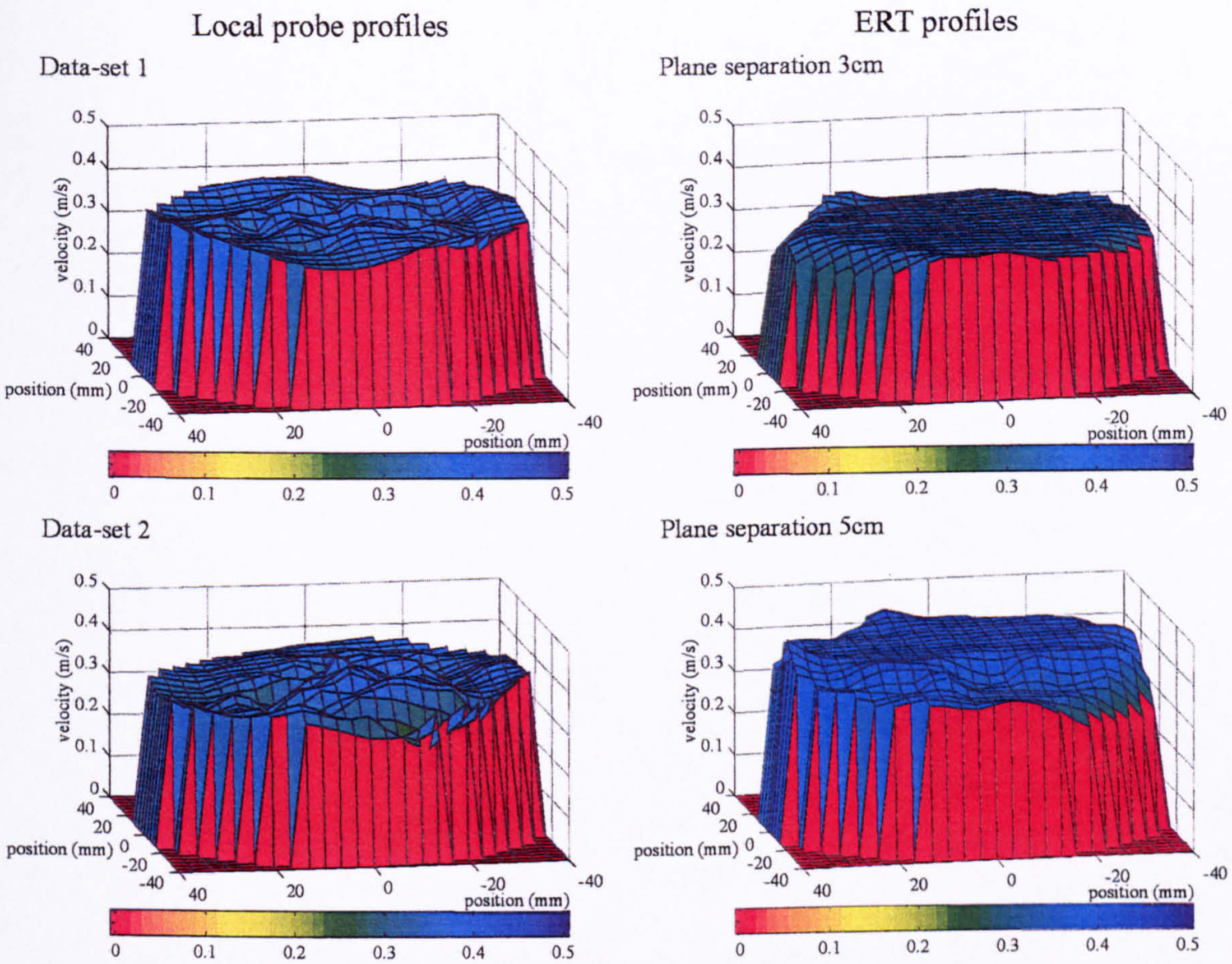

Figure 7-14. Solids velocity profiles for vertical flow, flow condition 1.

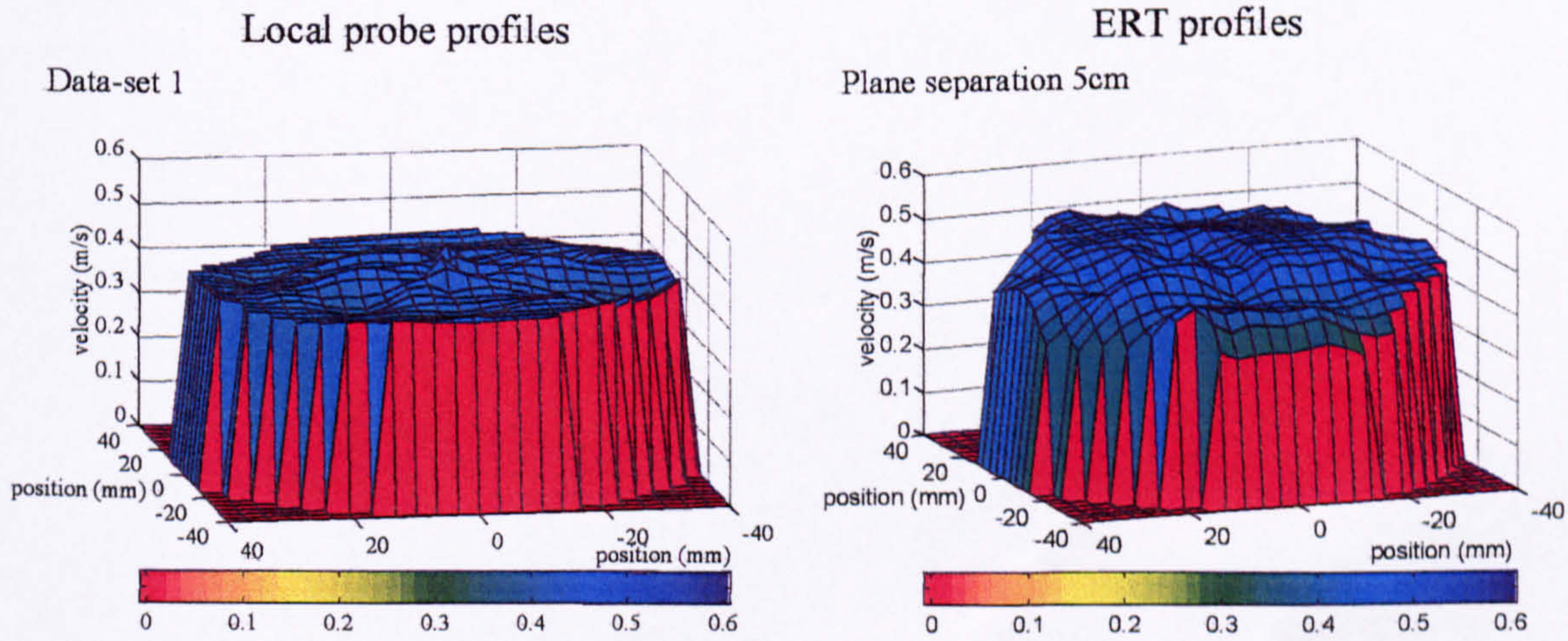

Figure 7-15. Solids velocity profiles for vertical flow, flow condition 2.

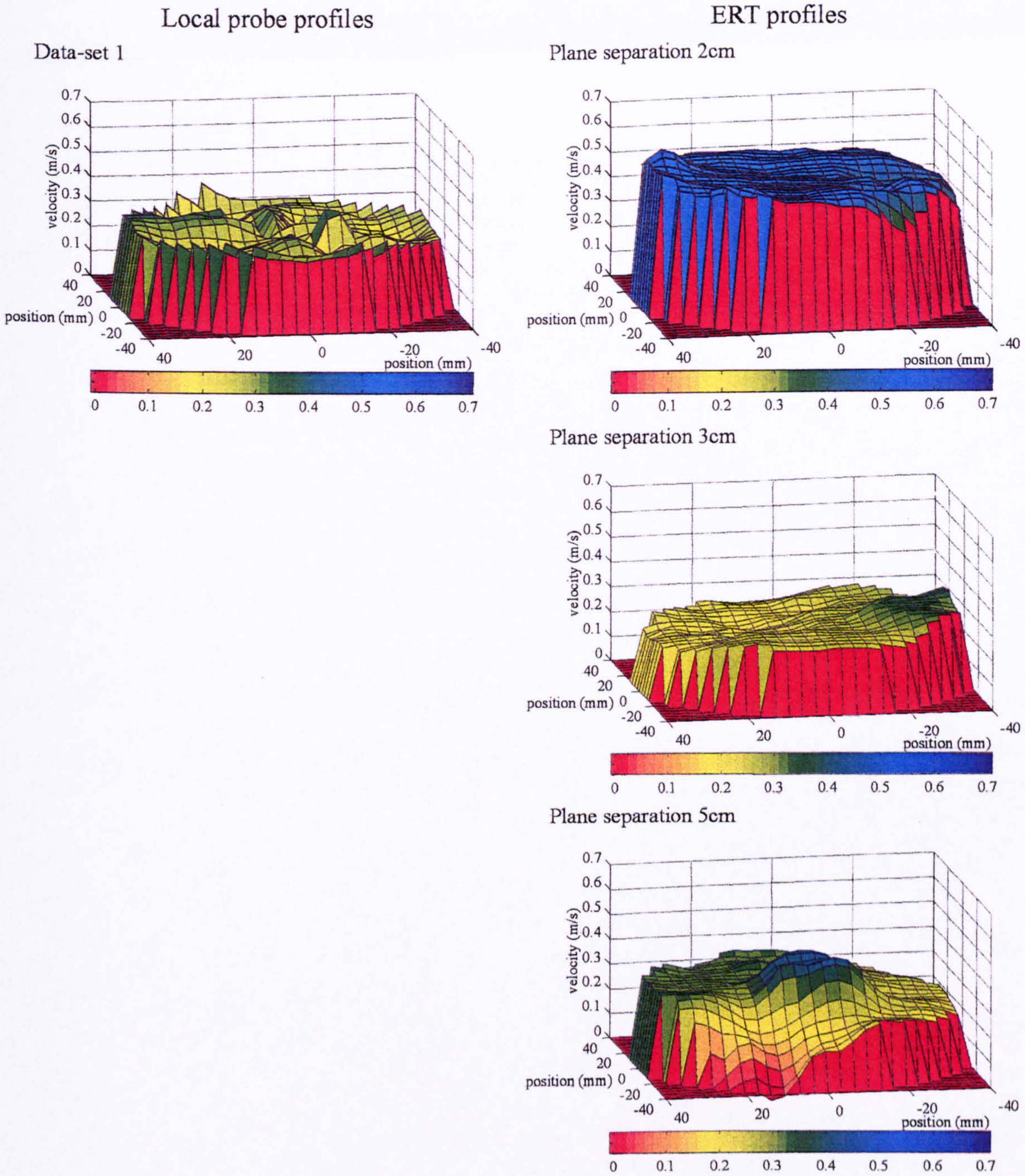

Figure 7-16. Solids velocity profiles for vertical flow, flow condition 3.

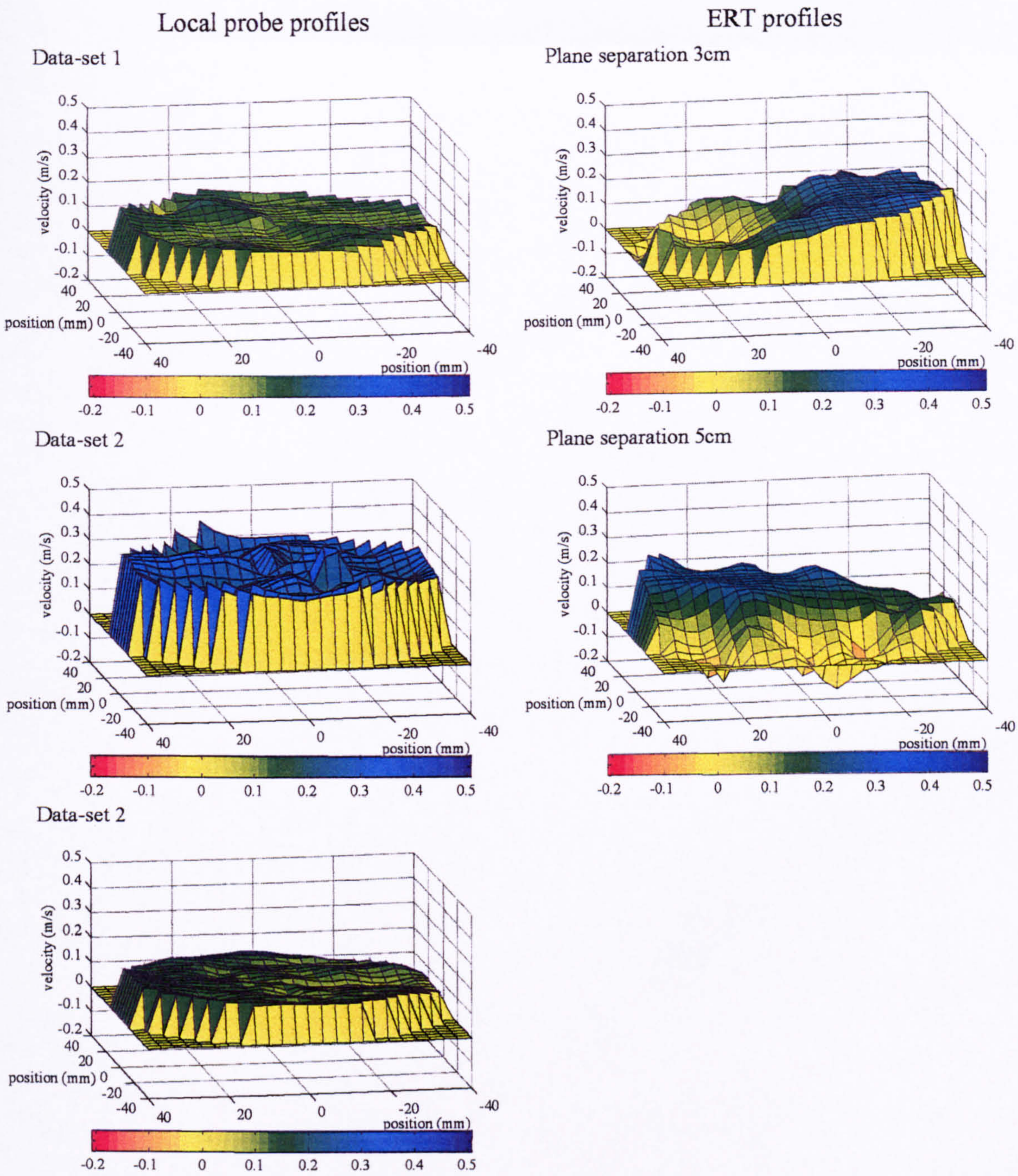

Figure 7-17. Solids velocity profiles for vertical flow, flow condition 4.

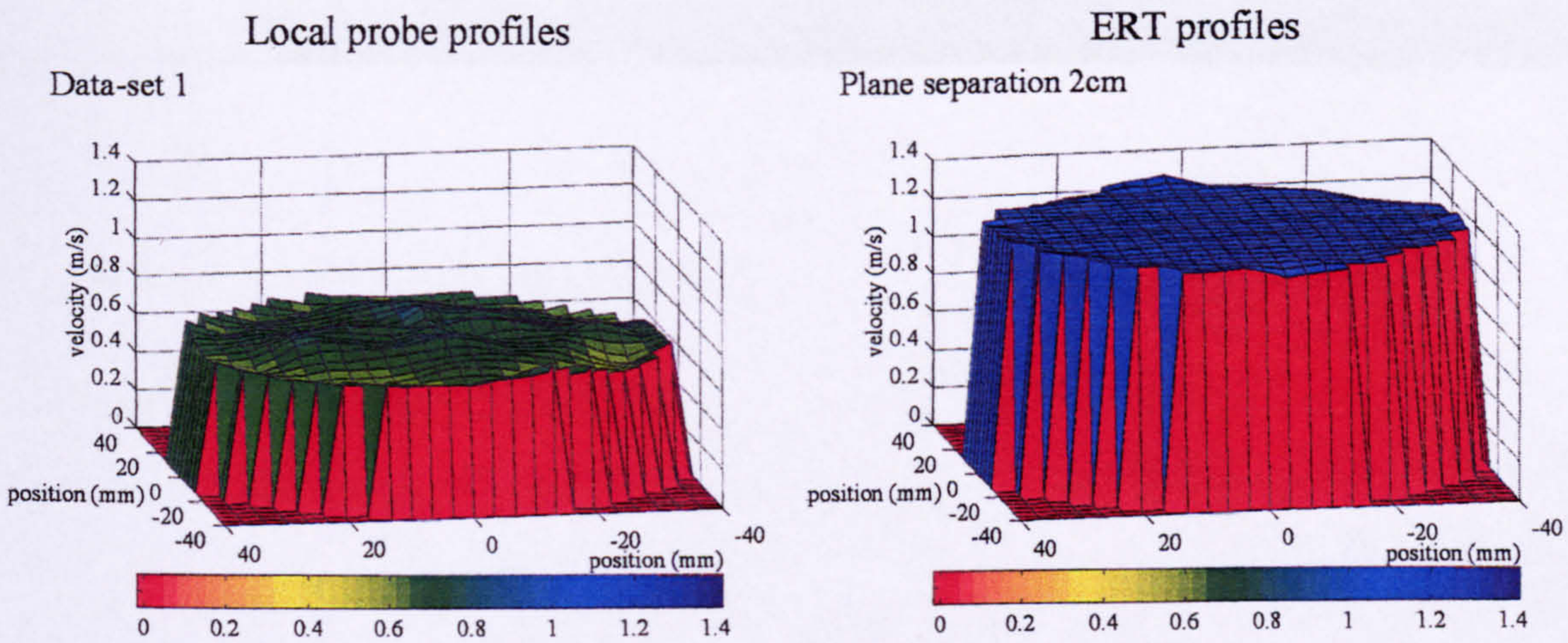

Figure 7-18. Solids velocity profiles for vertical flow, flow condition 10.

7.2.2.2 Solids velocity profiles for flow inclined 5° from vertical.

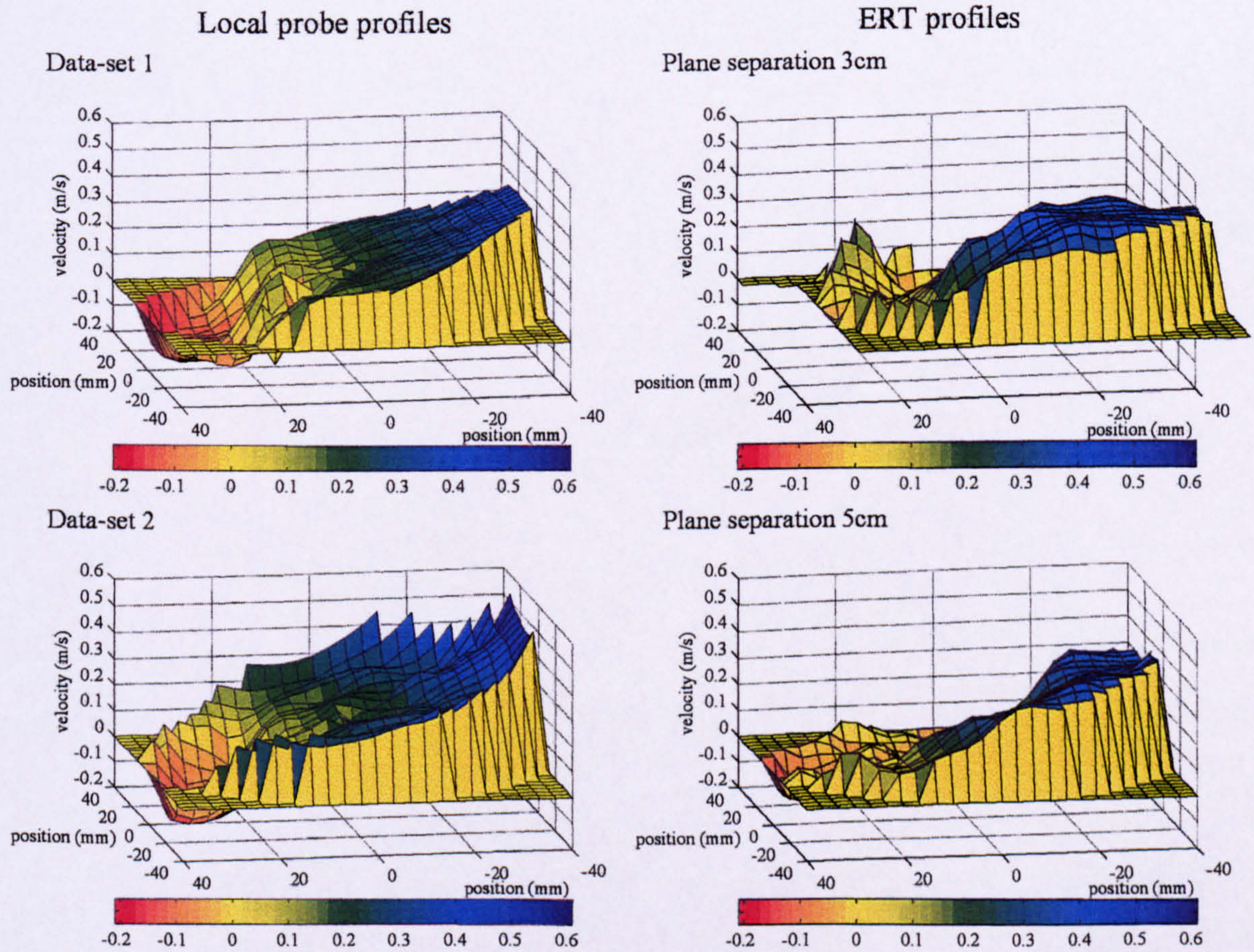

Figure 7-19. Solids velocity profiles for flow inclined 5° from vertical, flow condition 7.

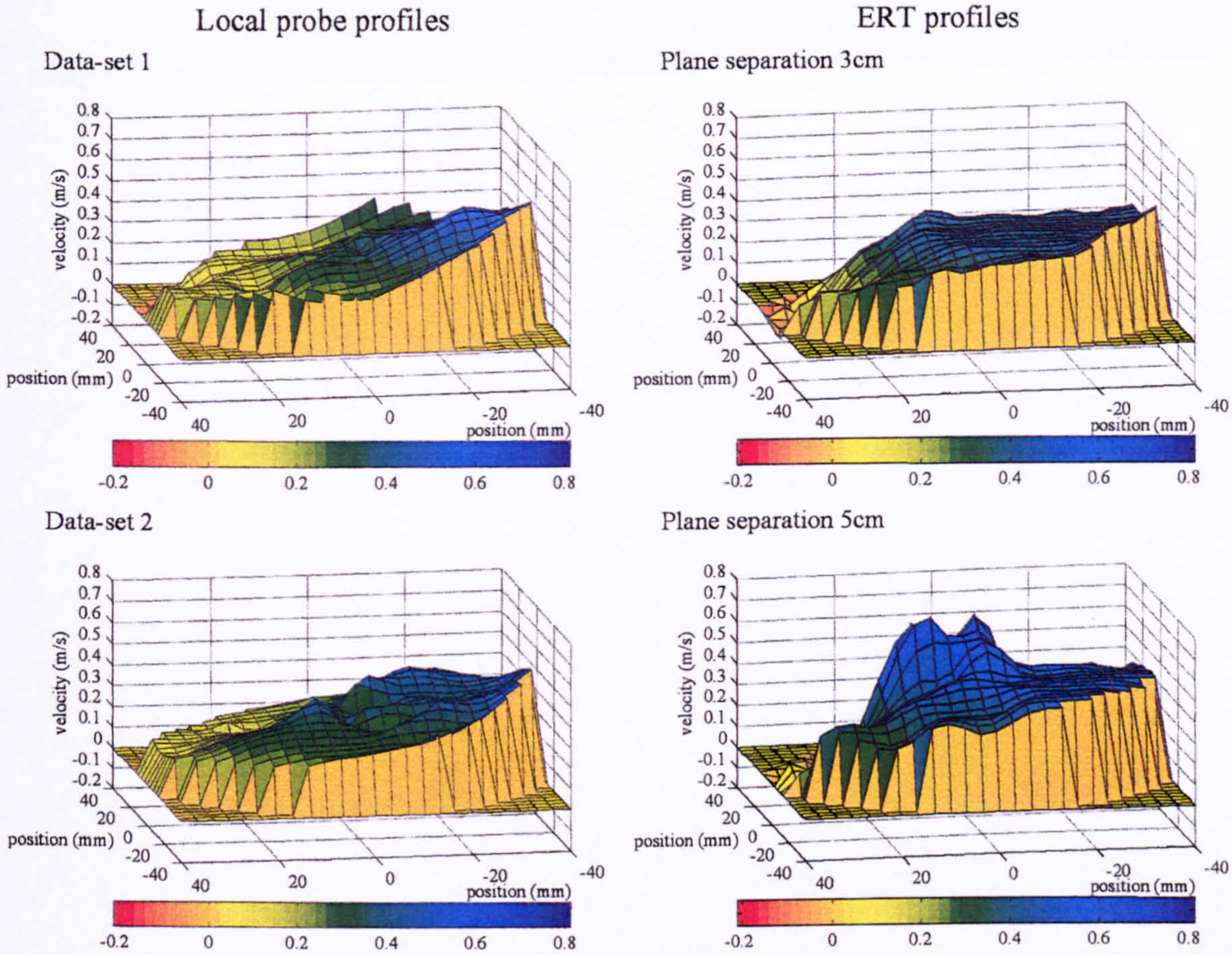

Figure 7-20. Solids velocity profiles for flow inclined 5° from vertical, flow condition 8.

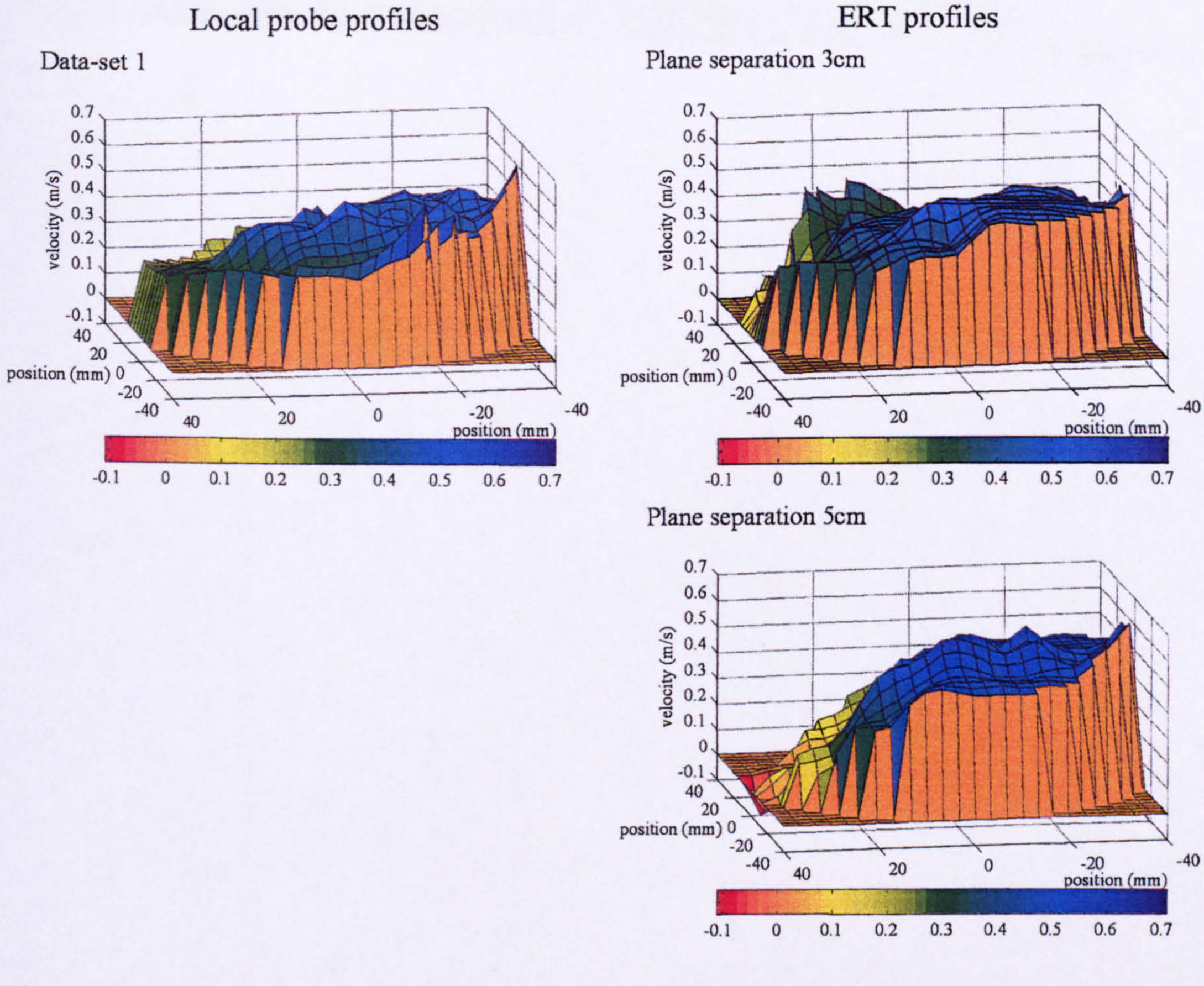

Figure 7-21. Solids velocity profiles for flow inclined 5° from vertical, flow condition 9.

7.2.2.3 Solids velocity profiles for flow inclined 30° from vertical.

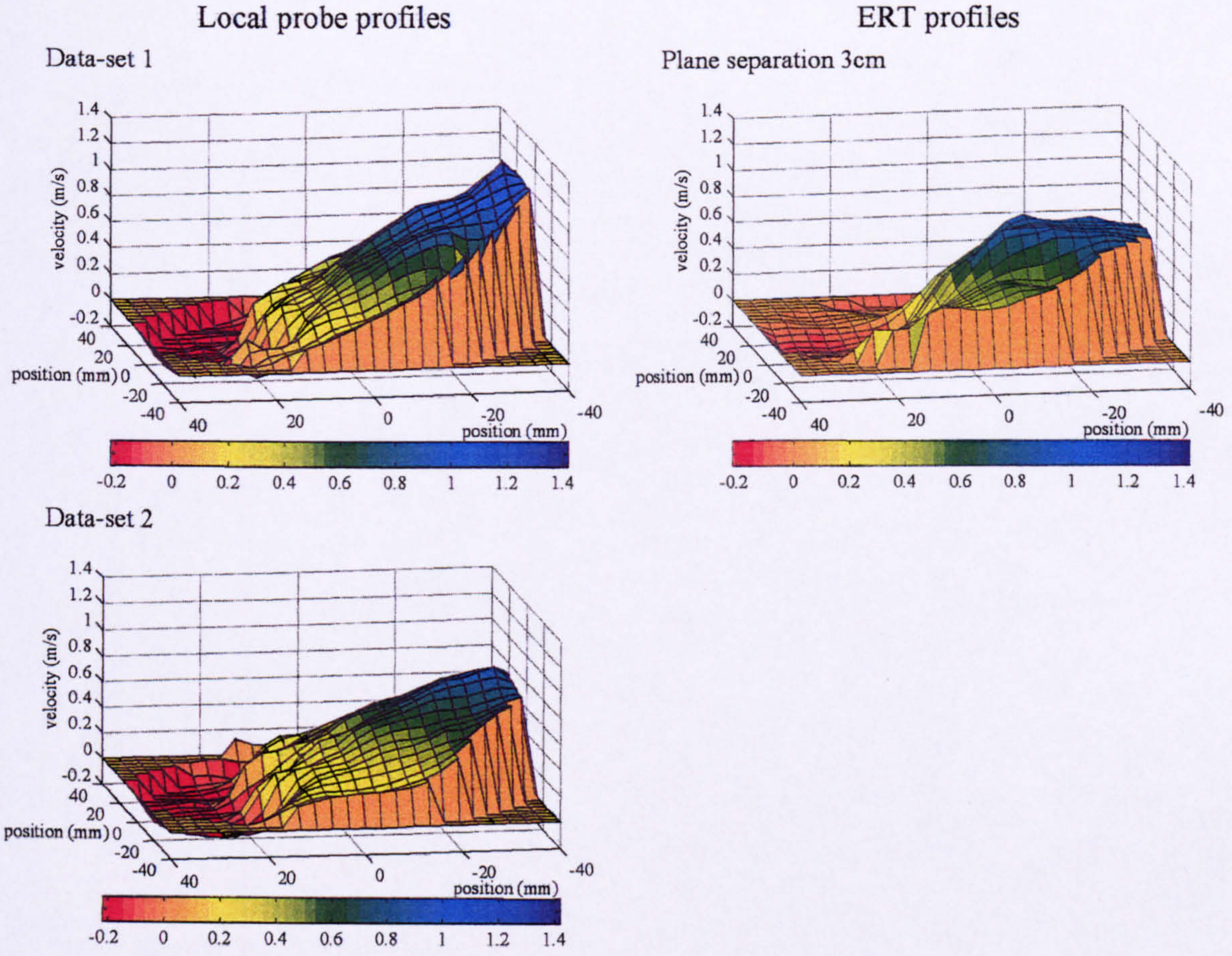

Figure 7-22. Solids velocity profiles for flow inclined 30° from vertical, flow condition 12.

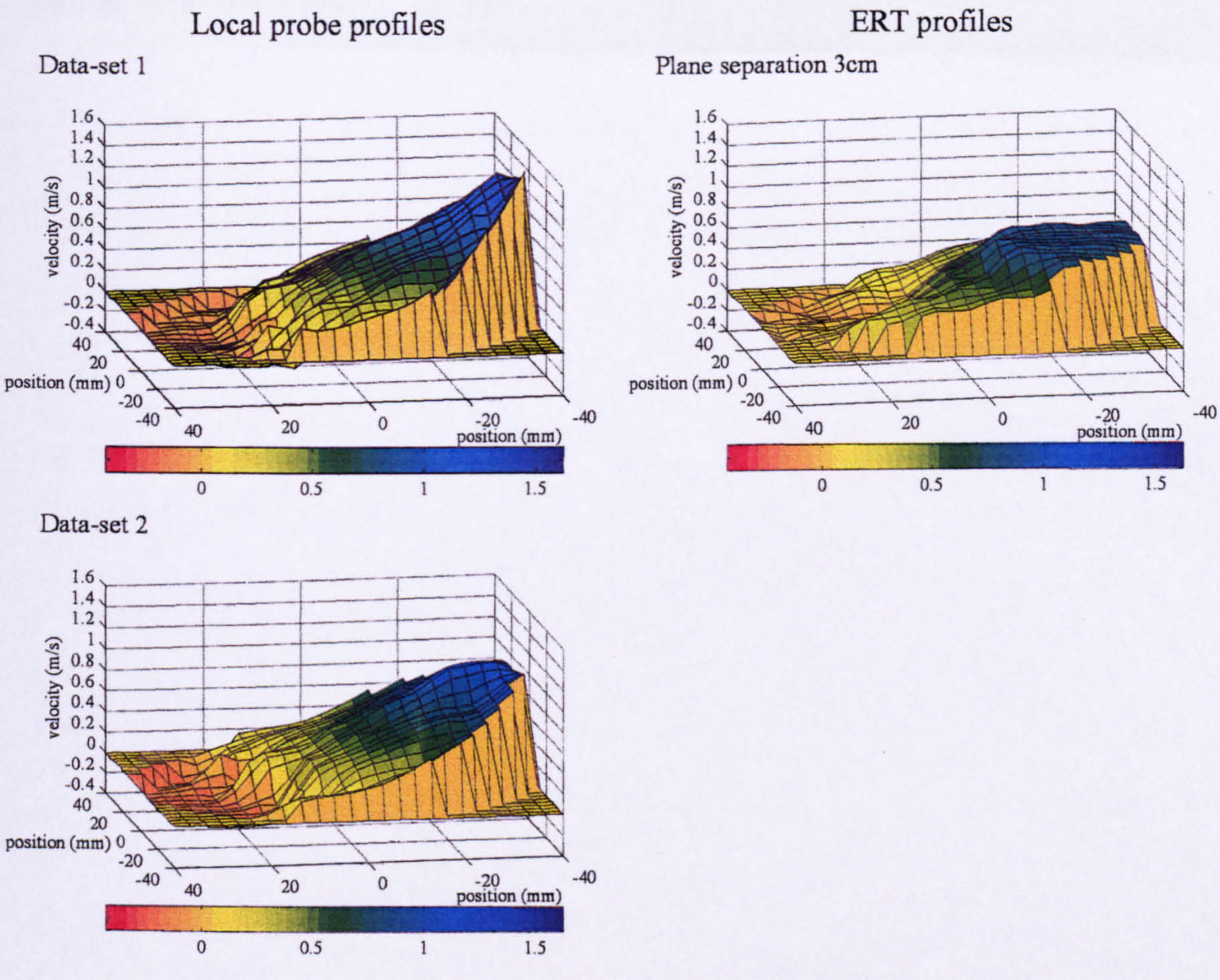

Figure 7-23. Solids velocity profiles for flow inclined 30° from vertical, flow condition 13.

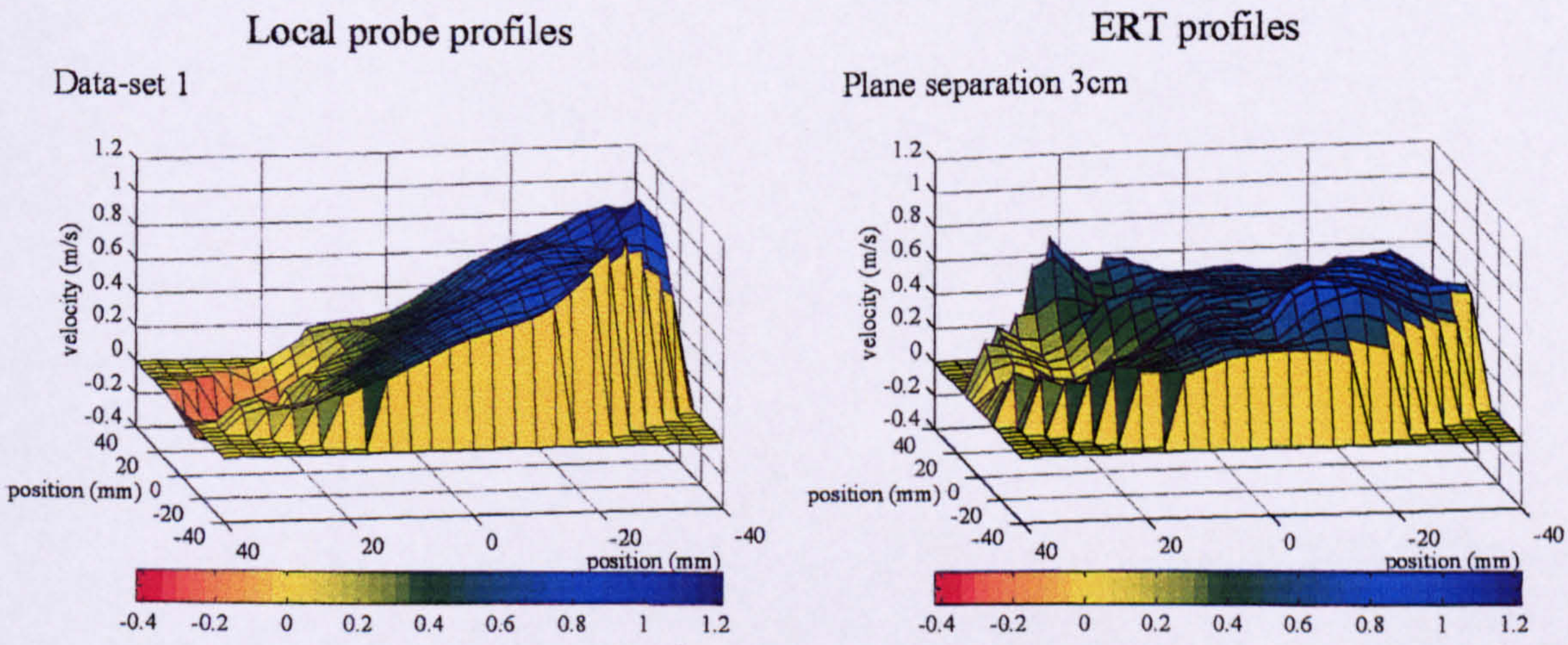

Figure 7-24. Solids velocity profiles for flow inclined 30° from vertical, flow condition 14.

7.2.2.4 Discussion of the solids velocity profiles.

As with the profiles of $\alpha_{s,i}$ there is qualitative agreement between profiles of local solids axial velocity, $u_{s,i}$, acquired by the local probe system and the ERT system. Profiles of $u_{s,i}$ in

vertical flow (see Figure 7-14 to Figure 7-18) show only small variations of $u_{s,i}$ within the cross-section for a given flow condition. The profiles are flatter than those of $\alpha_{s,i}$ with no drop in $u_{s,i}$ at the pipe wall shown by either system. Complete cross-sectional profiles of $u_{s,i}$ in vertical upward flow could not be found in the literature. However results showing only small variations of $u_{s,i}$ across the diameter of the pipe have been reported by Akagawa et al [4], Bartosik & Shook [99], Asakura et al [54] and Liu [105]. Liu [105] reported a drop in $u_{s,i}$ close to the wall that increased as the wall roughness increased. Asakura et al [54] reported that this "wall effect" increased as α_s decreased. Additionally Asakura et al [54] and Akagawa et al [4] reported that this "wall effect" increased as the mean solids axial velocity, u_s, increased. These trends are not noticeable in the profiles from the current investigation. However the ranges of α_s and u_s in the current investigation are much smaller than those used by the authors quoted above.

The profiles of $u_{s,i}$, for upward flows inclined from the vertical (see Figure 7-19 to Figure 7-24) show an almost one-dimensional shape also with $u_{s,i}$ varying as a function of co-ordinate Z (see Figure 7-13). This complements the almost one-dimensional profiles of $\alpha_{s,i}$ shown in Section 7.2.1. In the flows inclined 5° from vertical with high u_s (see Figure 7-20 and Figure 7-21) $u_{s,i}$ is low in the packed layer which exists at the low side of the pipe where Z is low. In the flow inclined 5° from vertical with low u_s, and in all the flows inclined 30° from vertical $u_{s,i}$, is negative at the low side of the pipe. This means that the solid particles are flowing down the pipe even though the net solids flow is upward. Therefore the particles which flow down the pipe must at some stage be re-circulated into the upward flow. At the high side of the pipe $u_{s,i}$ is high, reaching $1.5ms^{-1}$ in the profile acquired by the local probe for flow condition 13 (see Figure 7-23). No profiles of $u_{s,i}$ in inclined solids-liquid flow could be found in the literature. However a steep gradient of dense phase velocity with negative flow at the low side of the pipe was reported by Lucas [106] and Tabeling et al [102] for inclined liquid-liquid flow. Complete cross-sectional profiles of $u_{s,i}$ were reported by Scarlett & Grimley [25] and Hsu et al [103] for horizontal solids-liquid flow but since the flow was horizontal no reverse flow was observed. Both Scarlett & Grimley [25] and Hsu et al [103] showed a steep gradient of $u_{s,i}$ as a function of co-ordinate Z. This suggests that the profile shapes calculated during the current investigation are reliable. However although the profiles from each system show qualitative agreement there are some differences as discussed below.

For vertical flow the profiles all show qualitative agreement except those for flow condition 4 (see Figure 7-17). This can be explained by examination of the profiles and the flow conditions in Table 7-1 and Table 7-2. Flow condition 4 has a low value of u_s. This causes the measured data to be affected in two ways. First, the mean water velocity, u_w, at this flow condition is only just above the critical velocity, u_c, necessary to suspend the solid particles. During experimental testing Q_s and Q_w both fluctuated slightly. At flow condition 4 this fluctuation occasionally caused u_w to fall below u_c thereby causing the liquid to be unable to suspend the solids. This caused significant fluctuations and in some cases reverse flow to be exhibited in the profiles shown in Figure 7-17. Secondly it was observed that at the low value of u_s of flow condition 4 radial motion of the particles became more significant resulting in a degraded cross-correlation function. In order to achieve an accurate measurement of $u_{s,i}$ the peak of the cross-correlation function must be accurately located and any degradation of the function results in errors in the velocity measurement.

In inclined flow the profiles of $u_{s,i}^{probe}$ generally show a smoother variation across the pipe than the profiles of $u_{s,i}^{ERT}$. This is most likely to be due to the length of the time period over which data was acquired by each device. The ERT system acquired data over the complete flow cross-section for 20 seconds. The local probe acquired data for 60 seconds at each probe location. This results in time dependent variations being averaged out by the local probe which results in a smoother profile of $u_{s,i}^{probe}$.

Also from the inclined flow profiles (see Figure 7-19 to Figure 7-24) it is possible to see the effect of varying the plane separation of the ERT system. The profiles acquired by the local probe show a steep gradient of $u_{s,i}^{probe}$ between the lower and upper sides of the pipe. This was the profile shape that was expected as discussed previously in this section. If the profiles of $u_{s,i}^{ERT,3cm}$, acquired by the ERT system with 3cm plane separation, are examined it is obvious that this profile shape is not reproduced. The minimum value of $u_{s,i}^{ERT,3cm}$ measured agrees well with the minimum value of $u_{s,i}^{probe}$ measured. However the profiles of $u_{s,i}^{ERT,3cm}$ appear to show $u_{s,i}^{ERT,3cm}$ deviating from the expected profile as the top of the pipe is approached and the expected value of $u_{s,i}$ increases. When the plane separation is increased to 5cm this plateau effect is less noticeable (see Figure 7-19).

This feature of the profiles can be explained by considering the velocity resolution of each device. In Section 2.3 the velocity estimate, v_{est}, given by a cross-correlation flow meter for a given actual flow velocity, v_a, was defined by Equation 2-15 which is reproduced here.

$$v_{est} = \frac{v_a}{1 \pm \left(\frac{\tau v_a}{L} \right)}$$

Equation 2-15

In Equation 2-15 τ is equal to 1/f where f is the sampling frequency of the device. L is the effective separation between the sensors of the device. From Equation 2-15 it can be seen that in order for v_{est} to be equal to v_a the condition shown in Equation 7-1 must be true.

$$\frac{\tau v_a}{L} \equiv 0$$

Equation 7-1

From Equation 7-1, as v_a increases the error in v_{est} will increase. This effect is responsible for the profiles of $u_{s,i}^{ERT}$ deviating further from the local probe profile shape towards the top of the pipe as the true local axial velocity increases. The reason why the profiles of $u_{s,i}^{ERT,5cm}$ show this effect less, and why the profiles of $u_{s,i}^{probe}$ do not show it to a recognisable extent can also be seen from Equation 7-1. The condition shown in Equation 7-1 can be approached by either maximising L, or minimising τ. The relevant values of L, τ, and $\frac{\tau}{L}$, for the local probe system and the ERT system with both plane separations are shown below.

Device	L (cm)	τ (s)	$\frac{\tau}{L}$ (scm^{-1})
Local probe system	0.012	0.00027	0.023
ERT system with 3cm plane separation	0.03	0.02	0.667
ERT system with 5cm plane separation	0.05	0.02	0.400

This shows that the local probe system has a significantly lower value of $\frac{\tau}{L}$ than the ERT system. This results in v_{est} being close to v_a for all values of v_a. The ERT system has a significantly higher value of $\frac{\tau}{L}$ which gives a larger error in v_{est}, particularly at high values of

v_a. However this error is reduced by increasing L from 3cm to 5cm. It is also important to note that this error can be reduced by interpolating the cross-correlation function.

To conclude this section, in order to acquire accurate local solids axial velocity, $u_{s,i}$, profiles it is preferable to minimise τ. Similarly the total acquisition period of the correlation device should be large to enable time dependent variations in $u_{s,i}$ to be averaged out. The local probe allows both of these criteria to be met. However it results in a device with a large acquisition time that also needs to be able to store and process a large amount of data. The ERT system allows profiles to be acquired quicker but gives less accurate profiles. In conclusion it appears that a compromise must be made in the design of a cross-correlation flow meter.

7.3 Comparison of experimental results acquired by the local probe system with reference measurements.

The aim of this section is to allow the integrated values of $\alpha_{s,i}^{probe}$ and $u_{s,i}^{probe}$ to be compared with reference data. The data acquired using the local probe at all flow conditions was integrated using the methods described in Section 6.4.3.3 to give global average values of α_s^{probe}, u_s^{probe} and Q_s^{probe}. The reference data was acquired using the reference data devices as described in chapter 6.

It should be noted at this point that the data integrated was the actual data acquired from the local probe. In the profiles presented in section 7.2 interpolated data was plotted as interpolated profiles allow a better qualitative comparison to be made between the profiles acquired by the two different systems.

For the purposes of the quantitative comparison the percentage error, e^{probe}, between a value obtained from integrated local probe measurements and the relevant global reference value is defined as in Equation 7-2.

$$e^{probe} = \frac{X^{probe} - X^{ref}}{X^{ref}} \times 100$$

Equation 7-2

In Equation 7-2 X is the flow parameter in question, and the superscripts ^{probe} and ^{ref} refer to the value obtained from integrated local probe measurements and the reference measurement

respectively. Another error value that will be referred to is the absolute error, e_{abs}^{probe}, which is given by Equation 7-3.

$$e_{abs}^{probe} = X^{probe} - X^{ref}$$

Equation 7-3

For the purposes of examining trends in the errors two other error values will be referred to. The first is the systematic, or mean, error which is defined by Equation 7-4. This is denoted by e_{sys}^{probe} for the systematic percentage error, and $e_{abs,sys}^{probe}$ for the systematic absolute error as shown.

$$e_{sys}^{probe} = \frac{\sum_{i=1}^{i=n} e_i^{probe}}{n} \qquad e_{abs,sys}^{probe} = \frac{\sum_{i=1}^{i=n} e_{abs,i}^{probe}}{n}$$

Equation 7-4

The second is the random error which is the standard deviation of the error as defined by Equation 7-5. This is denoted by e_{ran}^{probe} for the random percentage error, and $e_{abs,ran}^{probe}$ for the random absolute error as shown.

$$e_{ran}^{probe} = \sqrt{\frac{\sum_{i=1}^{i=n}\left(e_i^{probe} - \overline{e}^{probe}\right)^2}{n}} \qquad e_{abs,ran} = \sqrt{\frac{\sum_{i=1}^{i=n}\left(e_{abs,i}^{probe} - \overline{e}_{abs}^{probe}\right)^2}{n}}$$

Equation 7-5

In addition to this notation an additional superscript has been added to each reported error value to allow errors in different flow parameters to be defined separately. These are $^{\alpha}$ for errors in the value of α_s, ^{u} for errors in the value of u_s, and ^{Q} for errors in the value of Q_s.

7.3.1 Comparison of reference measurements of mean solids volume fraction with integrated measurements from the local probe.

7.3.1.1 Results for vertical upward flow.

The integrated solids volume fraction data obtained from the local probe data for each vertical upward flow condition, and the relevant reference data, are presented in Table 7-3.

Table 7-3. Integrated solids volume fraction data from the local probe and reference devices for vertical upward flow.

Flow condition	Reference Data	Integrated Local Probe Data	Errors	
	α_s^{ref}	α_s^{probe}	$e^{probe,\alpha}$, (%)	$e_{abs}^{probe,\alpha}$
1	0.18	0.18	0.00	0.00
1	0.16	0.12	-25.00	-0.04
2	0.17	0.15	-11.76	-0.02
3	0.18	0.16	-11.11	-0.02
4	0.20	0.18	-10.00	-0.02
4	0.20	0.20	0.00	0.00
4	0.20	0.19	5.00	0.01
10	0.08	0.08	0.00	0.00
11	0.05	0.03	-40.00	-0.02

For the upward, vertical flow conditions tested the errors between the integrated local probe values and the reference values of mean solids volume fraction over the whole data set are given below.

Systematic error, $e_{sys}^{probe,\alpha}$	-11.43%
Random error, $e_{ran}^{probe,\alpha}$	13.40%
Systematic absolute error, $e_{abs,sys}^{probe,\alpha}$	-0.01
Random absolute error, $e_{abs,ran}^{probe,\alpha}$	0.02

7.3.1.2 Results for upward flow inclined 5° from vertical.

The integrated solids volume fraction values obtained from the local probe data for each upward flow condition inclined 5° from vertical, and the relevant reference data, are presented in Table 7-4.

Table 7-4. Integrated solids volume fraction data from the local probe and reference devices for upward flow inclined 5° from vertical.

Flow condition	Reference Data	Integrated Local Probe Data	Errors	
	α_s^{ref}	α_s^{probe}	$e^{probe,\alpha}$, (%)	$e_{abs}^{probe,\alpha}$
7	0.21	0.16	-23.81	-0.05
7	0.20	0.18	-10.00	-0.02
8	0.20	0.13	-35.00	-0.07
8	0.19	0.12	-36.84	-0.07
9	0.18	0.12	-33.33	-0.06

For the upward flow conditions inclined 5° from vertical that were tested the errors between the integrated local probe values and the reference values of mean solids volume fraction over the whole data set are given below.

Systematic error, $e_{sys}^{probe,\alpha}$	-27.80%
Random error, $e_{ran}^{probe,\alpha}$	11.15%
Systematic absolute error, $e_{abs,sys}^{probe,\alpha}$	-0.05
Random absolute error, $e_{abs,ran}^{probe,\alpha}$	0.02

7.3.1.3 Results for upward flow inclined 30° from vertical.

The integrated solids volume fraction values obtained from the local probe data for each upward flow condition inclined 30° from vertical, and the relevant reference data, are presented in Table 7-5.

Table 7-5. Integrated solids volume fraction data from the local probe and reference devices for upward flow inclined 30° from vertical.

Flow condition	Reference Data	Integrated Local Probe Data	Errors	
	α_s^{ref}	α_s^{probe}	$e^{probe,\alpha}$, (%)	$e_{abs}^{probe,\alpha}$
12	0.34	0.26	-23.53	-0.08
12	0.33	0.25	-24.24	-0.08
13	0.33	0.29	-12.12	-0.04
13	0.36	0.21	-41.67	-0.15
14	0.22	0.17	-22.73	-0.05
15	0.10	0.09	-10.00	0.01
16	0.17	0.18	-5.88	0.01

For the upward flow conditions inclined 30° from vertical that were tested the errors between the integrated local probe values and the reference values of mean solids volume fraction over the whole data set are given below.

Systematic error, $e_{sys}^{probe,\alpha}$	-6.40%
Random error, $e_{ran}^{probe,\alpha}$	13.41%
Systematic absolute error, $e_{abs,sys}^{probe,\alpha}$	-0.05
Random absolute error, $e_{abs,ran}^{probe,\alpha}$	0.06

7.3.1.4 Discussion of the solids volume fraction data.

Before discussing the solids volume fraction results it is useful to give the systematic and random errors between the integrated local probe values and the reference values for all flow inclinations combined.

Systematic error, $e_{sys}^{probe,\alpha}$	-17.63%
Random error, $e_{ran}^{probe,\alpha}$	14.35%
Systematic absolute error, $e_{abs,sys}^{probe,\alpha}$	-0.04
Random absolute error, $e_{abs,ran}^{probe,\alpha}$	0.04

Initially it appears that the integrated local probe data under-predicts the reference measurement data at all flow conditions. This under-prediction is more pronounced in upward flows inclined 5° from vertical. Both $e_{ran}^{probe,\alpha}$ and $e_{abs,ran}^{probe,\alpha}$ are large at all flow conditions pointing to a large scatter in the data.

In order to discuss the differences between the integrated local probe values, α_s^{probe}, and the reference values, α_s^{ref}, in more detail it was important to identify any trends in the results. For this purpose $e_{abs}^{probe,\alpha}$ was plotted against different reference measurements (see Figure 7-25 to Figure 7-27.) Figure 7-25 is a plot of $e_{abs}^{probe,\alpha}$ against the reference volume fraction measurement, α_s^{ref}. Figure 7-25 also shows the chronological order in which the data was acquired using a colour axis. This plot type is used in order to attempt to de-couple any trends caused by more than one influence. Figure 7-26 is a plot of $e_{abs}^{probe,\alpha}$ against the reference solids velocity, u_s^{ref}. Figure 7-26 also shows α_s^{ref} for each data-set. Finally Figure 7-27 is a plot of $e_{abs}^{probe,\alpha}$ against the number of experimental test runs completed. This plot gives a presentation of the variation in error over time. Figure 7-27 also shows α_s^{ref} for each data-set. Again this is to allow any trends caused by more than one influence to be de-coupled.

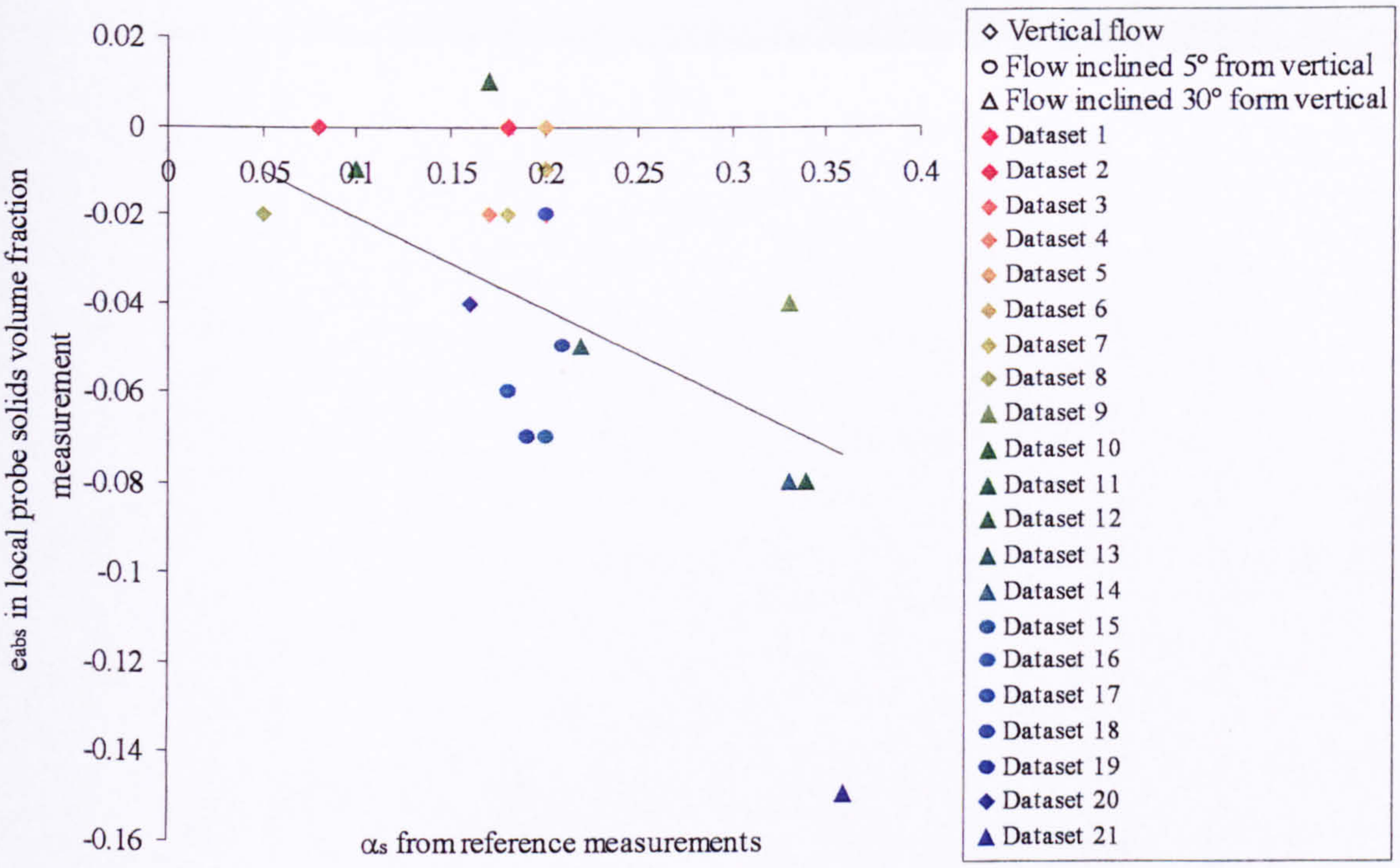

Figure 7-25. Plot of $e_{abs}^{probe,\alpha}$ against α_s^{ref}.

Figure 7-26. Plot of $e_{abs}^{probe,\alpha}$ against u_s^{ref}.

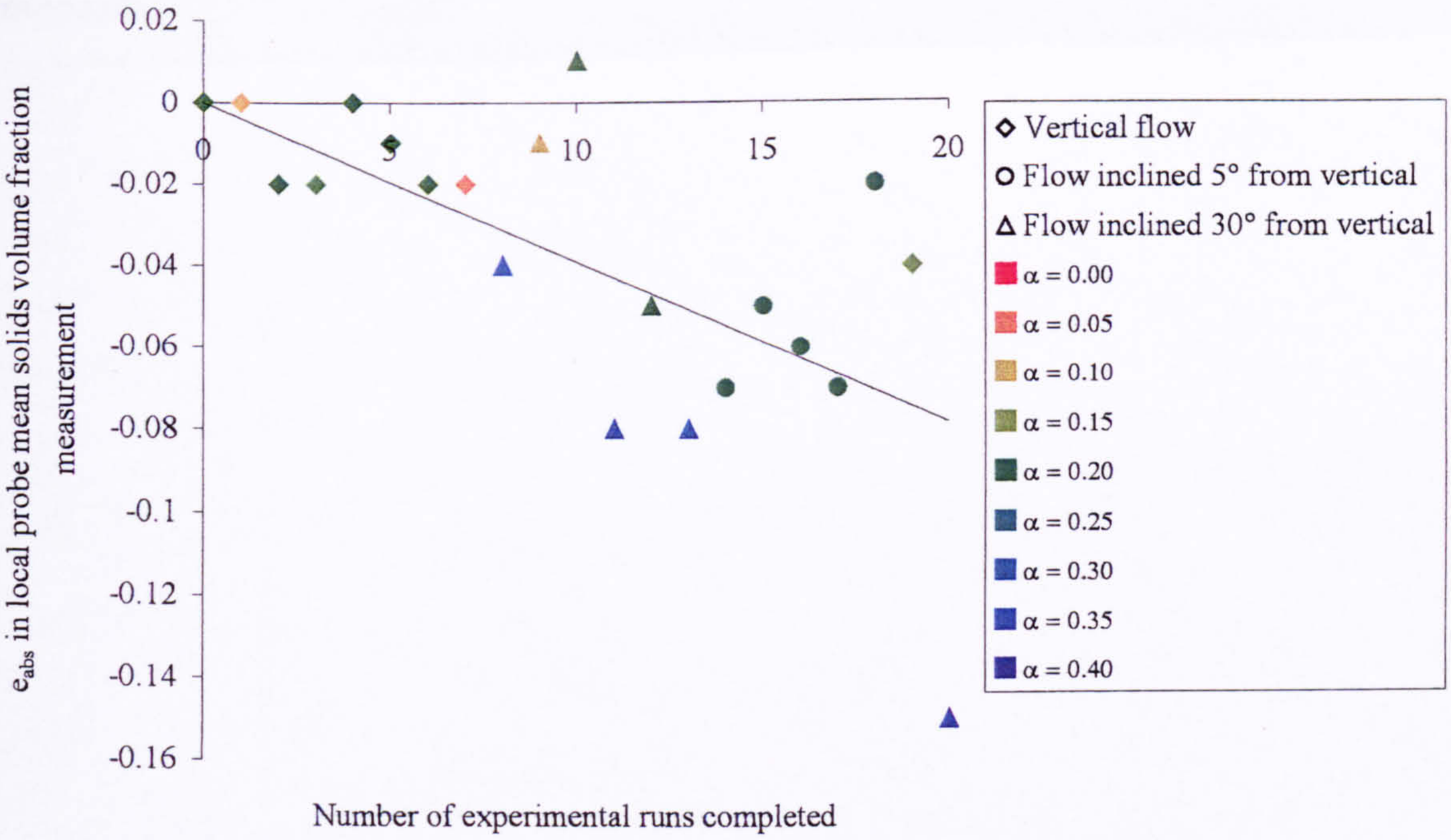

Figure 7-27. Plot of $e_{abs}^{probe,\alpha}$ against number of experimental runs completed.

From Figure 7-25 it is clear that there is a trend in $e_{abs}^{probe,\alpha}$ when referenced to α_s^{ref}. A line of best fit has been added to Figure 7-25 to highlight this. This clearly shows that α_s^{probe} tends to be lower than α_s^{ref} and that this error tends to increase as α_s^{ref} is increased. However if the chronological order in which the data was acquired is examined in Figure 7-25, using the colour scale of the data-points, a complementary trend can also be identified.

This increasing difference between α_s^{probe} and α_s^{ref} over time can be more clearly seen in Figure 7-27 where the number of experimental runs completed is plotted as the x-axis. A line of best fit has been added to Figure 7-27 to highlight this trend. Again the coupled trend, showing increasing difference between α_s^{probe} and α_s^{ref} as α_s^{ref} is increased, can be identified using the colour scale applied to the data-points.

It is difficult from Figure 7-25 and Figure 7-27 to identify whether both trends actually appear in the data. The flow conditions acquired early in the experimental testing were all vertical flows whilst the later flow conditions tested were inclined flows where α_s tended to be higher. Because of this difficulty in de-coupling the trends they have both been investigated in the current investigation.

Increasing $e_{abs}^{probe,\alpha}$ over time.

Increasing $e_{abs}^{probe,\alpha}$ over the time period of the experimental testing could be caused by a combination of increasing wear on the probe and the effect of the probe on the flow in the pipe. As the solids flow past the probe some will always come into collision with its tip. The effect of a collision will be to deflect the particle away from the surface of the probe. This effect has been observed in the flow loop. Unfortunately it is difficult to quantify the effect. However the combined effect of particle collisions could be to form a thin "boundary" layer around the probe containing no particles. The existence of this layer would cause $\alpha_{s,i}^{probe}$ to be low and therefore α_s^{probe} to be low compared to α_s^{ref} .

At the beginning of the experimental test period the probe configuration had been optimised to give a relatively large sensitivity volume for volume fraction measurement in order to give a reasonable depth of investigation. This would minimise any effect on the measurement of a boundary layer around the probe. The experimental sensitivity volume for sensor C of the probe (see Figure 3-9) acquired before the experimental testing took place is shown in Figure 7-28. Also shown in Figure 7-28 is the experimental sensitivity volume for the same sensor acquired after the completion of the experimental testing. For details of the format of this static testing see Chapter 5.

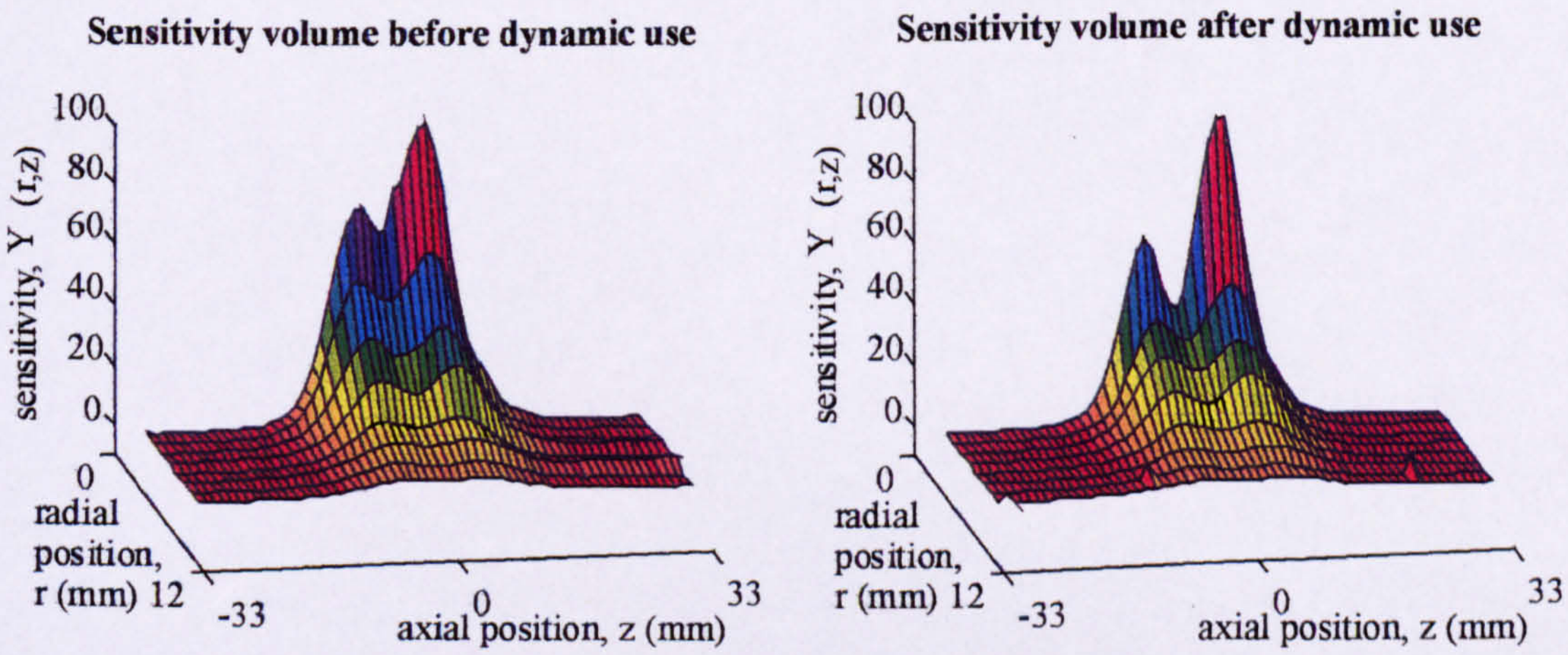

Figure 7-28. Local probe volume fraction measurement sensitivity volumes before and after the experimental test period.

The later sensitivity volume shown in Figure 7-28 shows a slightly steeper fall off in sensitivity with distance from the probe. This could result in the volume fraction measurement acquired by the probe becoming more dependent on the solids volume fraction close to the

probe surface, and less dependent on the solids volume fraction further away from the probe surface. This would result in the particle free layer affecting the measured result and causing a drop in measured volume fraction.

This degradation in probe response is likely to be due to the nature of the probe construction (see Chapter 4). The ring electrodes of the probe are formed from silver plated, copper wire. They are held in a ring shape and at a particular axial position by an epoxy resin which forms the bulk of the probe body. It is possible, through wear, that the position of the ring electrodes could have changed slightly over the experimental testing period. It is also possible that water was able to work its way behind the ring electrodes during experimental testing. This could also affect the sensitivity of the probe.

A possible problem with this hypothesis is that the thickness of the boundary layer around the probe would be expected to vary with u_s. However no such effect is identifiable in Figure 7-26. Despite this it was felt that a general trend in $e_{abs}^{probe,\alpha}$ over time could be justified. In order to investigate it further a correction was applied to the local probe $\alpha_{s,i}^{probe}$ data based on the chronological position of the data-set. The correction is based on the line of best fit applied in Figure 7-27. This correction factor was applied to each measurement of $\alpha_{s,i}^{probe}$ in each data-set. These corrected measurements were then integrated over the pipe cross-section as described in Section 6.4.3.3 in order to give a modified measurement of mean solids volume fraction, $\alpha_s^{probe,*}$. The differences between the values of $\alpha_s^{probe,*}$ and the measurements of α_s^{ref} are shown in the error statistics below. It should be noted that an additional superscript * denotes that the error values relate to differences between $\alpha_s^{probe,*}$ and α_s^{ref}.

Systematic error, $e_{sys}^{probe,\alpha*}$	3.30%
Random error, $e_{ran}^{probe,\alpha*}$	12.82%
Systematic absolute error, $e_{abs,sys}^{probe,\alpha*}$	0.00
Random absolute error, $e_{abs,ran}^{probe,\alpha*}$	0.03

The correction has removed the systematic error in the data. It has not improved the random error of the data. However considering the simplicity of the correction, and the hypothesis on which it is based, this is not surprising.

Increasing $e_{abs}^{probe,\alpha}$ with increasing α_s^{ref}.

An increase in $e_{abs}^{probe,\alpha}$ with increasing α_s^{ref} could be a result of errors in the reference measurement data. This can be explained by considering the method used to calculate α_s^{ref} from the reference measurement data (see Section 6.3.3). α_s^{ref} is calculated from a measurement of the pressure gradient, ΔP, along the working section. As described in Section 6.3.3 this pressure gradient is made up of two components, ΔP_{PE} and ΔP_F as shown in Equation 6-20.

$$\Delta P = \Delta P_{PE} + \Delta P_F$$

Equation 6-20

ΔP_{PE} is the pressure drop due to the change in potential energy of the flow. This is proportional to the mixture density, ρ_M, which is proportional to α_s^{ref} (see Section 6.3.3). ΔP_F is the pressure drop due to frictional losses in the flow. In Section 6.3.3 a survey of previous work to calculate these losses in two phase flows was reported. This showed that there was a wide variety of opinion in the previous research. For the purposes of the experimental testing it was assumed that the effect of the solids on the frictional losses in the flow would be minimal. Therefore it was assumed that the losses would be the same as those in a single phase flow of water with the same homogeneous velocity, u_h (see Section 6.3.3). For the purposes of this error analysis it was assumed that ΔP_F in the solids-liquid flow is higher than that in single phase flow. If this is the case the procedure detailed in Section 6.3.3 would result in an underestimation of ΔP_F and therefore an overestimation of ΔP_{PE}. In turn this would result in an overestimation of ρ_M which would then yield an overestimation of α_s^{ref}.

This trend was further investigated by applying a correction to α_s^{ref} at each flow condition based on the line of best fit shown in Figure 7-25. This yielded modified values of the reference solids volume fraction, $\alpha_s^{ref,\#}$. The differences between the values of α_s^{probe} and $\alpha_s^{ref,\#}$ are shown in the error statistics below. It should be noted that an additional superscript $^{\#}$ denotes that these values relate to differences between α_s^{probe} and $\alpha_s^{ref,\#}$.

Systematic error, $e_{sys}^{probe,\alpha\#}$	3.66%
Random error, $e_{ran}^{probe,\alpha\#}$	16.69%
Systematic absolute error, $e_{abs,sys}^{probe,\alpha\#}$	0.00
Random absolute error, $e_{abs,ran}^{probe,\alpha\#}$	0.03

As before the correction has improved the systematic error but failed to improve the random error. Again this is not surprising considering the complexity of the flow and the simplicity of the correction.

In conclusion, both of the trends in the difference between α_s^{probe} and α_s^{ref} can be explained, and applying a simple correction resulted in similar reductions in the differences between α_s^{probe} and α_s^{ref}. The first trend identified, which corrected for the possible variation of $e_{sys}^{probe,\alpha}$ as a function of the age of the probe, suggests that the local probe measurements are in error. The second correction, based on the hypothesis that $e_{abs}^{probe,\alpha}$ increased as a function of α_s, suggests that the reference measurements of solids volume fraction are in error. The only way to show whether either hypothesis is correct would be to carry out further experimental tests. These could include an investigation of the solids flow around the probe and an investigation of the frictional pressure losses in solids-liquid flows.

7.3.2 Comparison of reference measurements of solids velocity with integrated measurements from the local probe.

7.3.2.1 Results for vertical flow.

The integrated solids axial velocity values obtained from the local probe for each vertical upward flow condition, and the relevant reference data, are presented in Table 7-6.

Table 7-6. Integrated solids axial velocity data from the local probe and reference devices for vertical upward flow.

Flow condition	Reference Data	Local Probe Data	Errors	
	u_s^{ref}, (ms^{-1})	u_s^{probe}, (ms^{-1})	$e^{probe,u}$, (%)	$e_{abs}^{probe,u}$, (ms^{-1})
1	0.32	0.36	12.50	0.04
1	0.34	0.37	8.82	0.03
2	0.44	0.43	-2.23	-0.01
3	0.22	0.28	27.27	0.06
4	0.10	0.13	30.00	0.03
4	0.10	0.13	30.00	0.03
4	0.11	0.13	18.18	0.02
10	0.79	0.69	-12.66	-0.10
11	0.57	0.93	63.16	0.36

For the upward, vertical flow conditions that were tested the errors between the integrated local probe values and the reference values of axial solids velocity over the whole data set are given below.

Systematic error, $e_{sys}^{probe,u}$	19.45%
Random error, $e_{ran}^{probe,u}$	20.71%
Systematic absolute error, $e_{abs,sys}^{probe,u}$	0.05ms^{-1}
Random absolute error, $e_{abs,ran}^{probe,u}$	0.12ms^{-1}

7.3.2.2 Results for flow inclined 5° from vertical.

The integrated axial solids velocity values obtained from the local probe for each upward flow condition inclined 5° from vertical, and the relevant reference data, are presented in Table 7-7.

Table 7-7. Integrated solids axial velocity data from the local probe and reference devices for upward flow inclined 5° from vertical.

Flow condition	Reference Data	Local Probe Data	Errors	
	u_s^{ref} (ms^{-1})	u_s^{probe}, (ms^{-1})	$e^{probe,u}$, (%)	$e_{abs}^{probe,u}$, (ms^{-1})
7	0.09	0.11	22.22	0.02
7	0.12	0.17	41.67	0.05
8	0.22	0.25	13.64	0.03
8	0.26	0.30	15.34	0.04
9	0.34	0.43	26.47	0.09

For the upward flow conditions inclined 5° from vertical that were tested the errors between the integrated local probe values and the reference values of axial solids velocity over the whole data set are given below.

Systematic error, $e_{sys}^{probe,u}$	23.87%
Random error, $e_{ran}^{probe,u}$	10.04%
Systematic absolute error, $e_{abs,sys}^{probe,u}$	$0.05ms^{-1}$
Random absolute error, $e_{abs,ran}^{probe,u}$	$0.02ms^{-1}$

7.3.2.3 Results for flow inclined 30° from vertical.

The integrated axial solids velocity values obtained from the local probe for each upward flow condition inclined 30° from vertical, and the relevant reference data, are presented in Table 7-8.

Table 7-8. Integrated flow data from the local probe and reference devices for upward flow inclined 30° from vertical.

Flow condition	Reference Data	Local Probe Data	Errors	
	u_s^{ref} (ms^{-1})	u_s^{probe}, (ms^{-1})	$e^{probe,u}$, (%)	$e_{abs}^{probe,u}$, (ms^{-1})
12	0.17	0.20	17.65	0.03
12	0.13	0.13	0.00	0.00
13	0.19	0.21	10.53	0.02
13	0.18	0.17	-5.56	-0.01
14	0.23	0.22	-4.35	-0.01
15	0.66	0.58	-12.12	-0.08
16	0.41	0.34	-17.07	-0.07

For the vertical flow conditions inclined 30° from vertical tested the errors between the integrated local probe values and the reference values of solids velocity over the whole data set are given below.

Systematic error, $e_{sys}^{probe,u}$	-1.56%
Random error, $e_{ran}^{probe,u}$	12.20%
Systematic absolute error, $e_{abs,sys}^{probe,u}$	$-0.02ms^{-1}$
Random absolute error, $e_{abs,ran}^{probe,u}$	$0.04ms^{-1}$

7.3.2.4 Discussion of the solids velocity data.

Before discussing the solids velocity results it is important to note the method used to integrate the local measurements of $u_{s,i}^{probe}$ over the pipe cross-section to obtain an estimate of u_s^{probe} (see Section 6.4.3.3). u_s^{probe} is given by Equation 1-5.

$$u_s^{probe} = \frac{\int_A \alpha_{s,i}^{probe} u_{s,i}^{probe} dA}{\int_A \alpha_{s,i}^{probe} dA} = \frac{Q_s^{probe}}{A\alpha_s^{probe}}$$

Equation 1-5

It is clear from Equation 1-5 that the value of u_s^{probe} is dependent upon the value of α_s^{probe}. Any errors in the value of α_s^{probe} will have an effect on the value of u_s^{probe} and because of this effect it was difficult to isolate sources of error in the determination of u_s^{probe}. In the following section plots similar to those presented in Section 7.3.1.4 are presented. These are intended to highlight any trends in the velocity measurement data.

Before presenting the plots and discussing the solids velocity results in detail it is useful to give the systematic and random errors between the integrated local probe values and the reference values of axial solids velocity for all flow inclinations combined. These are given below.

Systematic error, $e_{sys}^{probe,u}$	13.50%
Random error, $e_{ran}^{probe,u}$	19.62%
Systematic absolute error, $e_{abs,sys}^{probe,u}$	$0.03ms^{-1}$
Random absolute error, $e_{abs,ran}^{probe,u}$	$0.09ms^{-1}$

It is clear that there is a significant systematic difference between u_s^{probe} and u_s^{ref}. Additionally there is a significant amount of scatter in the data. These differences are shown in more detail in the following error plots (see Figure 7-29 to Figure 7-31). Figure 7-29 is a plot of $e_{abs}^{probe,u}$ against u_s^{ref}. The chronological order in which the data-sets were acquired can be seen using the secondary colour axis. Figure 7-30 is a plot of $e_{abs}^{probe,u}$ against α_s^{ref}. The variation with u_s^{ref} can be seen simultaneously using the secondary colour axis. Finally Figure 7-31 is a plot of the variation in $e_{abs}^{probe,u}$ over the experimental time period. In this plot the secondary colour axis shows the variation with u_s^{ref} as in Figure 7-30.

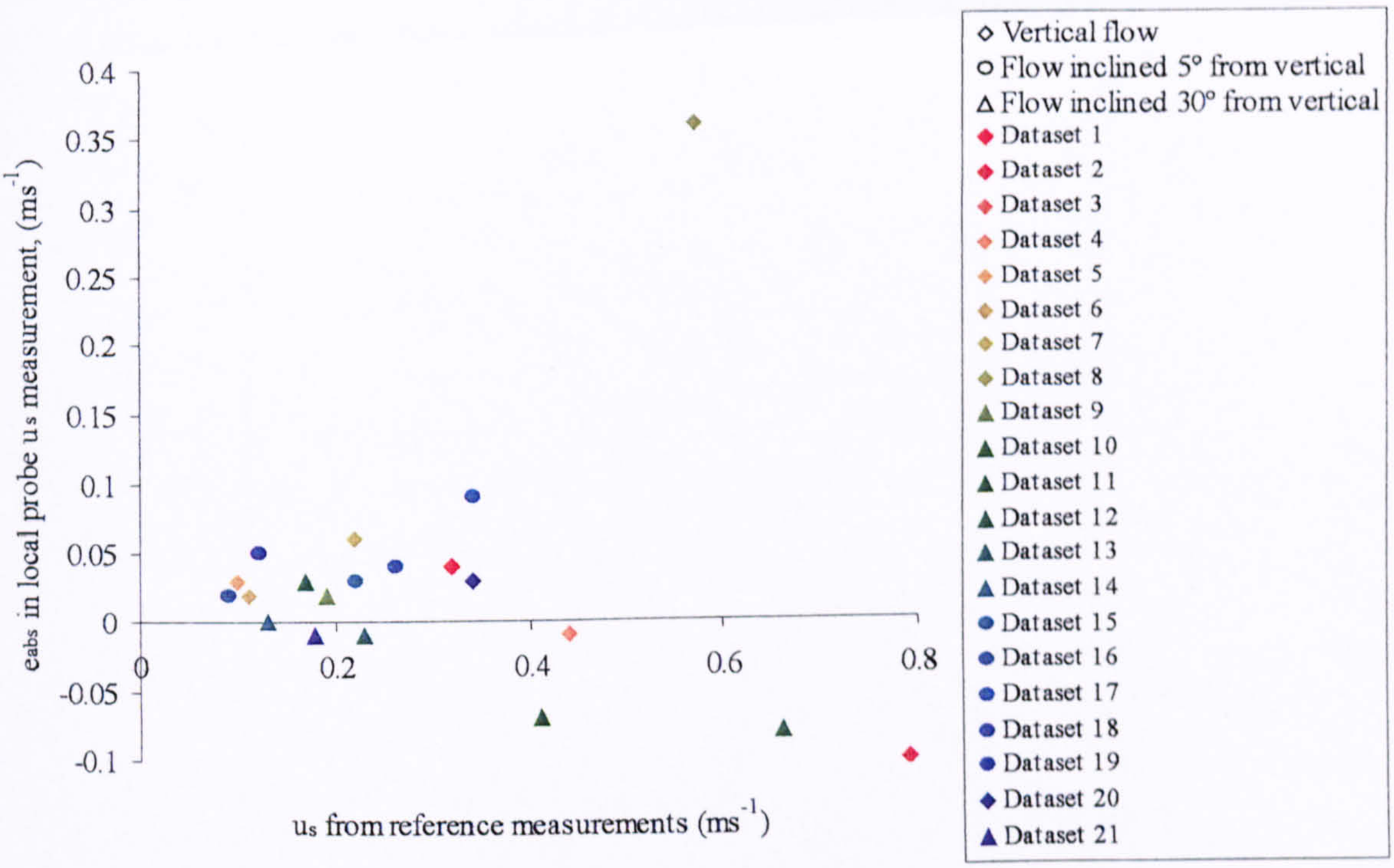

Figure 7-29. Plot of $e_{abs}^{probe,u}$ against u_s^{ref}.

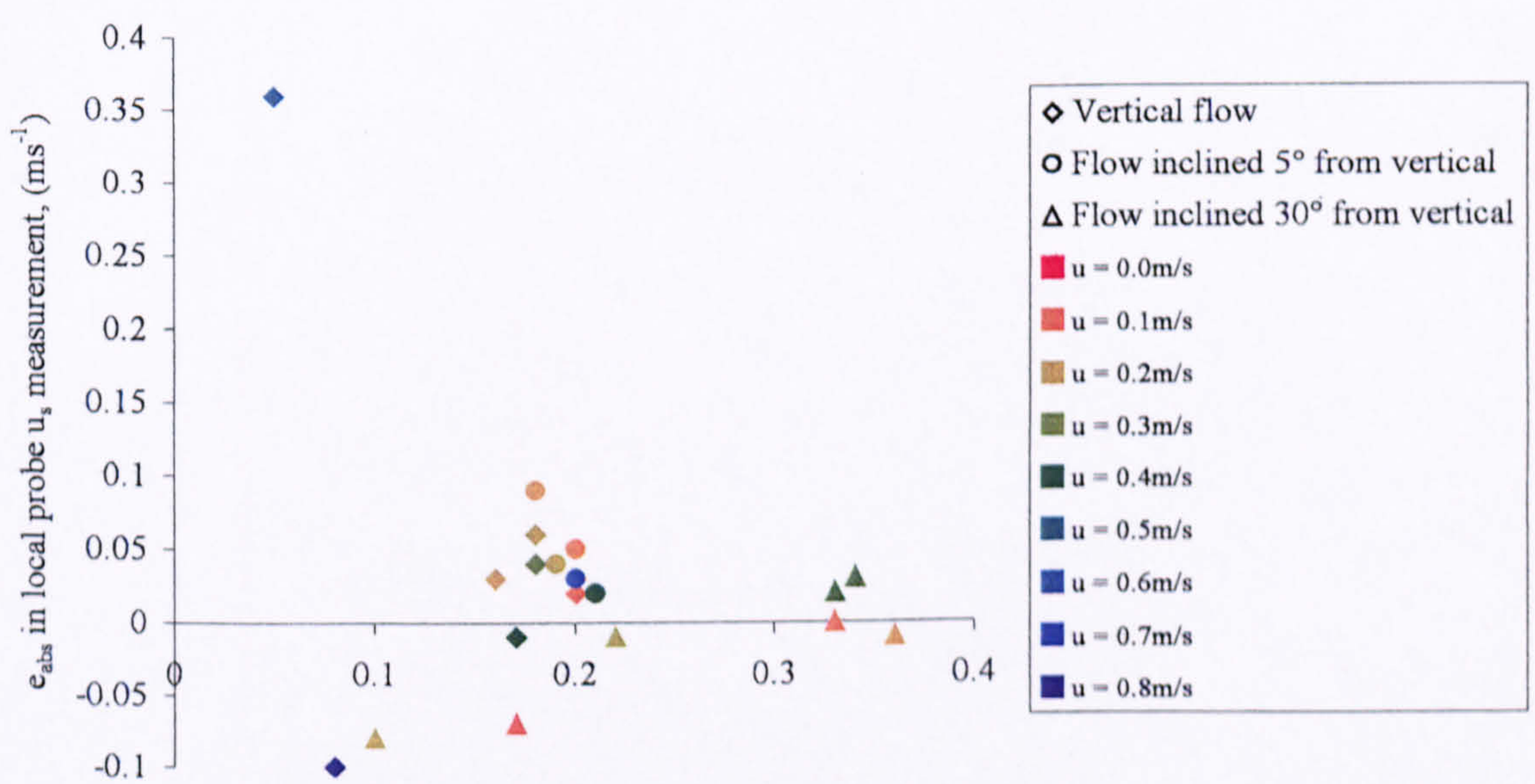

Figure 7-30. Plot of $e_{abs}^{probe,u}$ against α_s^{ref}.

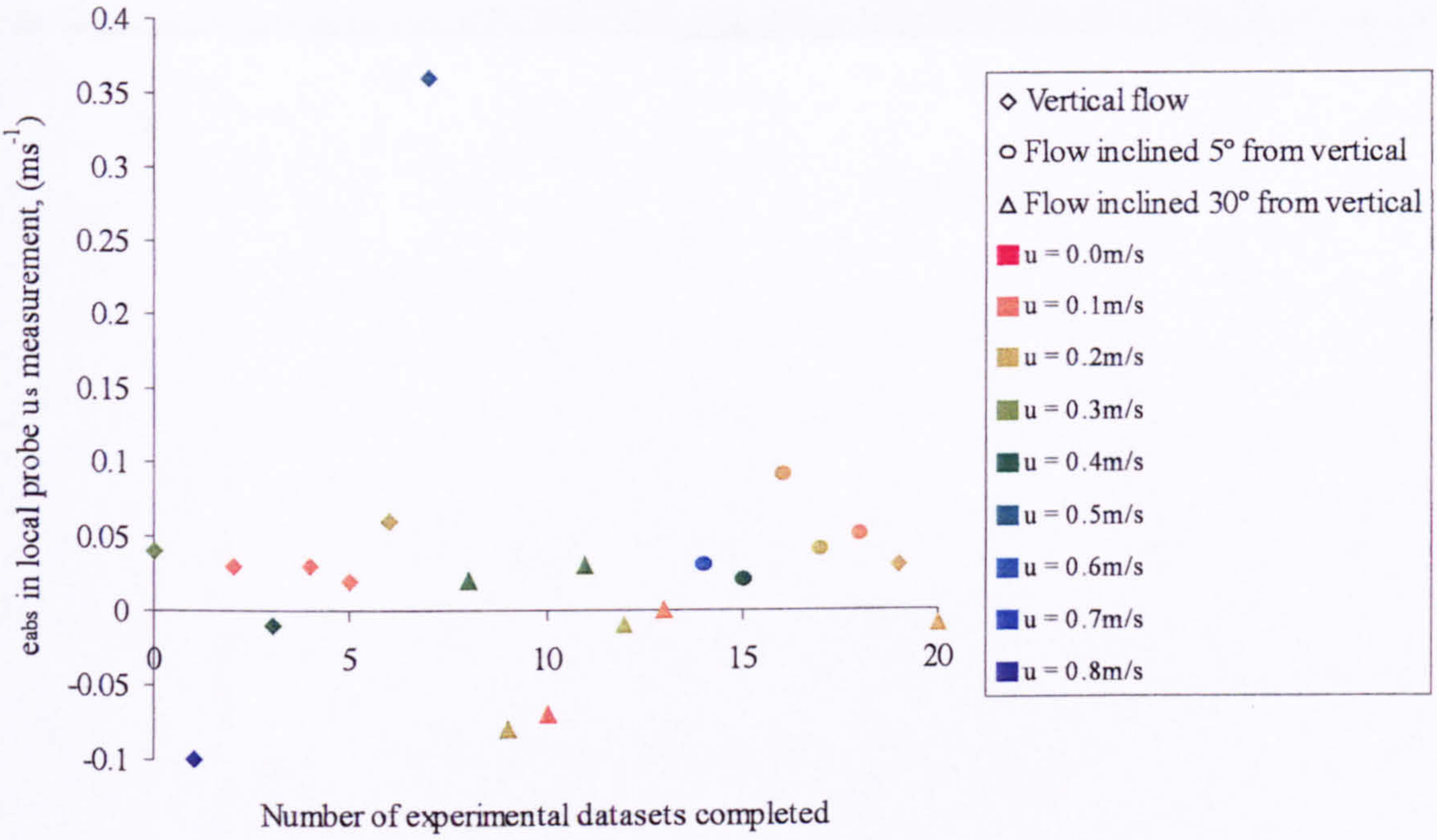

Figure 7-31. Plot of $e_{abs}^{probe,u}$ against the number of experimental data-sets completed.

Because of the link between α_s^{probe} and u_s^{probe} values of the mean axial solids velocity, $u_s^{probe,*}$, have been calculated using the measured local axial solids velocity $u_{s,i}^{probe}$ and the modified values of local solids volume fraction, $\alpha_{s,i}^{probe,*}$, obtained by applying the first correction described in Section 7.3.1.4. Similarly, modified reference values of the mean axial solids velocity, $u_s^{ref,\#}$, have been calculated using the measurements of reference solids volumetric flow rate, Q_{ref}^{s}, and the modified values of reference mean solids volume fraction, $\alpha_s^{ref,\#}$, obtained by applying the second correction described in Section 7.3.1.4. The differences between $u_s^{probe,*}$ and u_s^{ref}, and the differences between u_s^{probe} and $u_s^{ref,\#}$ are shown in the error statistics below. It should be noted that an additional superscript * denotes differences between $u_s^{probe,*}$ and u_s^{ref}, and an additional superscript $^\#$ denotes differences between u_s^{probe} and $u_s^{ref,\#}$.

Systematic error,	$e_{sys}^{probe,u*}$	17.30%	$e_{sys}^{probe,u\#}$	-9.15%
Random error,	$e_{ran}^{probe,u*}$	18.10%	$e_{ran}^{probe,u\#}$	15.04%
Systematic absolute error,	$e_{abs,sys}^{probe,u*}$	$0.03ms^{-1}$	$e_{abs,sys}^{probe,u\#}$	$-0.05ms^{-1}$
Random absolute error,	$e_{abs,ran}^{probe,u*}$	$0.08ms^{-1}$	$e_{abs,ran}^{probe,u\#}$	$0.10ms^{-1}$

It is clear that an offset exists between the integrated local probe values of axial solids velocity and the reference values of axial solids velocity for the majority of flow conditions. This is true for the unmodified values u_s^{probe} when compared to either u_s^{ref} (see Figure 7-29) or $u_s^{ref,\#}$. It is also for the modified values, $u_s^{probe,*}$, when compared to u_s^{ref}. The likely cause of the offsets is an error in the value of the effective sensor separation, L, assumed for the cross-correlation. The cross-correlation yields an estimate of the time taken, δ, for a particle to pass between two axially displaced sensors which is then combined with L, the effective separation of the two sensors, sensor A and sensor B, to give a measurement of the solids velocity as in Equation 7-6.

$$u_{s,i} = \frac{L}{\delta}$$

Equation 7-6

The physical separation between sensor A and sensor B on the local probe is 8mm. However static testing presented in Section 5.4.5 had suggested that the effective separation was 12mm. Unfortunately the measurement resolution of the static testing only allowed the estimate of L to be made to an accuracy of ±1mm.

An iterative routine was written in Matlab to enable an ideal value of effective sensor separation to be calculated for each flow condition in the current investigation. For the case where the unmodified local probe measurements were compared to the unmodified reference values this routine is described as below. Profiles of $u_{s,i}^{probe}$ were first calculated using a pre-set value of L. Predicted values of the mean axial solids velocity, $u_s^{probe,pred}$, were then calculated by integrating these profiles with values of $\alpha_{s,i}^{probe}$ over the flow cross-section. This loop was repeated with an incrementing value of L, until $u_s^{probe,pred}$ was equal to u_s^{ref}, to give L_{corr}. The routine was also used with the modified values of the local solids volume fraction, $\alpha_{s,i}^{*}$, to give modified values of the mean axial solids velocity, $u_s^{probe,*,pred}$, which were compared with u_s^{ref} to give predicted values of the effective sensor separation, L_{corr}^{*}. Also, the predicted values of $u_s^{probe,pred}$ were compared with the modified reference solids velocity values, $u_s^{ref,\#}$, to obtain a predicted effective sensor separation, $L_{corr}^{\#}$. The relevant mean values of L for all flow conditions are given below.

Calculated by comparing:		
$u_s^{probe,pred}$ with u_s^{ref}	L_{corr}	11.1mm
$u_s^{probe,*,pred}$ with u_s^{ref}	L^*_{corr}	10.4mm
$u_s^{probe,pred}$ with $u_s^{ref,\#}$	$L^{\#}_{corr}$	13.9mm

Using these three modified values of the effective sensor separation modified profiles of the local axial solids velocity were calculated for each of the three cases and modified values of the mean axial solids velocity were calculated. These were $u_s^{probe,L=11.1}$, $u_s^{probe,*L=10.4}$ and $u_s^{probe,L=13.9}$ where the superscript * denotes the use of the modified volume fraction profiles, $\alpha_{s,i}^{probe,*}$, and the additional superscript gives the assumed value of sensor separation used to calculate the local solids velocity profile. The differences between these integrated local probe axial solids velocity values and the relevant reference axial solids velocity values are shown in the error statistics below where the relevant reference values are u_s^{ref} for $u_s^{probe,L=11.1}$ and $u_s^{probe,*L=10.4}$ and $u_s^{ref,\#}$ for $u_s^{probe,L=13.9}$.

Systematic error,	$e_{sys}^{probe,u,L=11.1}$	1.89%	$e_{sys}^{probe,u,*L=10.4}$	1.14%	$e_{sys}^{probe,u,L=13.9}$	2.64%
Random error,	$e_{ran}^{probe,u,L=11.1}$	18.43%	$e_{ran}^{probe,u,*L=10.4}$	16.52%	$e_{ran}^{probe,u,L=13.9}$	18.16%
Systematic absolute error,	$e_{abs,sys}^{probe,u,L=11.1}$	$0.00ms^{-1}$	$e_{abs,sys}^{probe,u,*L=10.4}$	$-0.01ms^{-1}$	$e_{abs,sys}^{probe,u,L=13.9}$	$-0.01ms^{-1}$
Random absolute error,	$e_{abs,ran}^{probe,u,L=11.1}$	$0.09ms^{-1}$	$e_{abs,ran}^{probe,u,*L=10.4}$	$0.08ms^{-1}$	$e_{abs,ran}^{probe,u,L=13.9}$	$0.11ms^{-1}$

It is clear that modifying the value of the effective sensor separation significantly reduces the difference between the local probe mean axial solids velocity estimate and the reference mean axial solids velocity measurement for all three cases. This suggests that more accurate measurement of the effective sensor separation should be carried out using static tests.

Another obvious feature of the error plots (see Figure 7-29 to Figure 7-31) is that whilst the difference between u_s^{probe} and u_s^{ref} is relatively small for most flow conditions, it is high for

flow conditions with u_s^{ref} greater than approximately $0.4ms^{-1}$. If the flow conditions with values of u_s^{ref} greater than $0.4ms^{-1}$ are removed from the initial error analysis the error statistics are as below. It should be noted that these errors are based on the difference between u_s^{probe} and u_s^{ref}.

Systematic error, $e_{sys}^{probe,u}$	16.53%
Random error, $e_{ran}^{probe,u}$	13.02%
Systematic absolute error, $e_{abs,sys}^{probe,u}$	$0.03ms^{-1}$
Random absolute error, $e_{abs,ran}^{probe,u}$	$0.03ms^{-1}$

Removing the flow conditions with u_s^{ref} greater than $0.4ms^{-1}$ from the error analysis clearly reduces the random error significantly leaving a large systematic error which can be removed by applying a corrected value of the effective sensor separation as previously shown.

In conclusion, sources of error have been identified in the local probe axial solids velocity measurements. Principally these point to the importance of accurately calculating the effective sensor separation for use in cross-correlation, and the importance of increasing the accuracy of the local probe axial solids velocity measurement at high values of u_s^{ref}. However both the reference and the integrated local probe estimations of u_s^{probe} are dependent on measurements of solids volume fraction and it has proved to be difficult to decouple the velocity measurement errors from the solids volume fraction measurement errors. For this reason the main recommendation of this section is that it is important to address sources of error in the reference and local probe solids volume fraction measurements before the solids velocity measurements can be addressed.

7.3.3 Comparison of reference measurements of solids volumetric flow rate with integrated measurements from the local probe.

7.3.3.1 Results for vertical flow.

The integrated solids volumetric flow rate values from the local probe for each vertical upward flow condition, and the relevant reference data, are presented in Table 7-9.

Table 7-9. Integrated solids volumetric flow rate data from the local probe and reference devices for vertical upward flow.

Flow condition	Reference Data	Local Probe Data	Errors	
	Q_s^{ref}, (m^3h^{-1})	Q_s^{probe}, (m^3h^{-1})	$e^{probe,Q}$, (%)	$e_{abs}^{probe,Q}$, (m^3h^{-1})
1	1.07	1.17	9.35	0.10
1	1.00	0.80	-20.00	-0.20
2	1.37	1.17	-14.60	-0.20
3	0.70	0.80	14.29	0.10
4	0.38	0.43	-13.16	0.05
4	0.35	0.46	31.43	0.11
4	0.38	0.45	18.42	0.07
10	1.11	0.99	-10.81	-0.12
11	0.47	0.52	-10.64	0.05

For the upward, vertical flow conditions that were tested the errors between the integrated local probe values and the reference measurements of solids volumetric flow rate for the whole data set are given below.

Systematic error, $e_{sys}^{probe,Q}$	5.76%
Random error, $e_{ran}^{probe,Q}$	17.09%
Systematic absolute error, $e_{abs,sys}^{probe,Q}$	0.00m^3h^{-1}
Random absolute error, $e_{abs,ran}^{probe,Q}$	0.13m^3h^{-1}

7.3.3.2 Results for flow inclined 5° from vertical.

The integrated solids volumetric flow rate values from the local probe for each upward flow condition inclined 5° from vertical, and the relevant reference data, are presented in Table 7-10.

Table 7-10. Integrated solids volumetric flow rate data from the local probe and reference devices for upward flow inclined 5° from vertical.

Flow condition	Reference Data	Local Probe Data	Errors	
	Q_s^{ref}, (m^3h^{-1})	Q_s^{probe}, (m^3h^{-1})	$e^{probe,Q}$, (%)	$e_{abs}^{probe,Q}$, (m^3h^{-1})
7	0.35	0.32	-8.57	-0.03
7	0.43	0.57	32.56	0.14
8	0.79	0.58	-26.58	-0.21
8	0.86	0.67	-22.09	-0.19
9	1.12	0.79	-29.46	-0.33

For the upward flow conditions inclined 5° from vertical that were tested the errors between the integrated local probe values and the reference measurements of solids volumetric flow rate for the whole data set are given below.

Systematic error, $e_{sys}^{probe,Q}$	-10.83%
Random error, $e_{ran}^{probe,Q}$	25.54%
Systematic absolute error, $e_{abs,sys}^{probe,Q}$	$-0.12m^3h^{-1}$
Random absolute error, $e_{abs,ran}^{probe,Q}$	$0.18m^3h^{-1}$

7.3.3.3 Results for flow inclined 30° from vertical.

The integrated solids volumetric flow rate values from the local probe for each upward flow condition inclined 30° from vertical, and the relevant reference data, are presented in Table 7-11.

Table 7-11. Integrated solids volumetric flow rate data from the local probe and reference devices for upward flow inclined 30° from vertical.

Flow condition	Reference Data	Local Probe Data	Errors	
	Q_s^{ref}, (m^3h^{-1})	Q_s^{probe}, (m^3h^{-1})	$e^{probe,Q}$, (%)	$e_{abs}^{probe,Q}$, (m^3h^{-1})
12	1.05	0.90	-14.29	-0.15
12	0.78	0.62	-20.51	-0.16
13	1.11	1.08	-3.70	-0.03
13	1.01	0.65	-35.64	-0.36
14	0.90	0.64	-28.89	-0.26
15	1.15	0.83	-27.83	-0.32
16	1.28	1.12	-12.50	-0.16

For the vertical flow conditions inclined 30° from vertical that were tested the errors between the integrated local probe values and the reference measurements of solids volumetric flow rate over the whole data set are given below.

Systematic error, $e_{sys}^{probe,Q}$	-20.34%
Random error, $e_{ran}^{probe,Q}$	11.35%
Systematic absolute error, $e_{abs,sys}^{probe,Q}$	$-0.21 m^3h^{-1}$
Random absolute error, $e_{abs,ran}^{probe,Q}$	$0.11 m^3h^{-1}$

7.3.3.4 Discussion of the solids volumetric flow rate data.

Before discussing the solids volumetric flow rate results it is important to reiterate the method used to integrate the local measurements of $\alpha_{s,i}^{probe}$ and $u_{s,i}^{probe}$ over the pipe cross-section to get the value of Q_s^{probe} (see Section 6.4.3.3). Q_s^{probe} is given by Equation 1-1.

$$Q_s^{probe} = \int_A \alpha_{s,i}^{probe} u_{s,i}^{probe} dA$$

Equation 1-1

It is clear from Equation 1-1 that the value of Q_s^{probe} is dependent upon both $\alpha_{s,i}^{probe}$ and $u_{s,i}^{probe}$. Any errors in either measurement will have an effect on Q_s^{probe}. This section will concentrate on identifying any trends in the error of the measurement of Q_s^{probe} as before. However these trends will be discussed in the context of error sources in the measurement of $u_{s,i}^{probe}$ and $\alpha_{s,i}^{probe}$.

Before discussing the measurements of Q_s^{probe} in detail it is useful to give the systematic and random errors for the entire set of data for all flow inclinations combined. If the measured local solids volume fraction data, $\alpha_{s,i}^{probe}$, and the measured local solids velocity data, $u_{s,i}^{probe}$, is used in the calculation of Q_s^{probe} the errors between Q_s^{probe} and Q_s^{ref} are as given below.

Systematic error, $e_{sys}^{probe,Q}$	-6.85%
Random error, $e_{ran}^{probe,Q}$	20.57%
Systematic absolute error, $e_{abs,sys}^{probe,Q}$	$-0.10 m^3 h^{-1}$
Random absolute error, $e_{abs,ran}^{probe,Q}$	$0.16 m^3 h^{-1}$

It is immediately obvious that there is a larger scatter in the values of Q_s^{probe} than shown for the values of either α_s^{probe} or u_s^{probe}. Also there is a small offset between the values of Q_s^{probe} and Q_s^{ref}. In order to investigate the differences between the values of Q_s^{ref} and Q_s^{probe} error plots were made as described below. The error plots take the same format as in Sections 7.3.1.4 and 7.3.2.4. The absolute error, $e_{abs}^{probe,Q}$, is plotted against different flow variables. Within each plot a colour axis is used to show the value of an additional flow variable. Figure 7-32 shows $e_{abs}^{probe,Q}$ plotted against Q_s^{ref}. The secondary colour axis shows how $e_{abs}^{probe,Q}$ varies when referenced against the number of experimental data-sets completed. This shows the effect of age on the probe. Figure 7-33 shows $e_{abs}^{probe,Q}$ plotted against α_s^{ref}, Figure 7-34 shows $e_{abs}^{probe,Q}$ plotted against u_s^{ref} and Figure 7-35 shows $e_{abs}^{probe,Q}$ plotted against the number of experimental data-sets that had been acquired. As stated above this shows how the response of the probe varies with its age. For Figure 7-33, Figure 7-34 and Figure 7-35 the secondary colour axis shows variation with Q_s^{ref}.

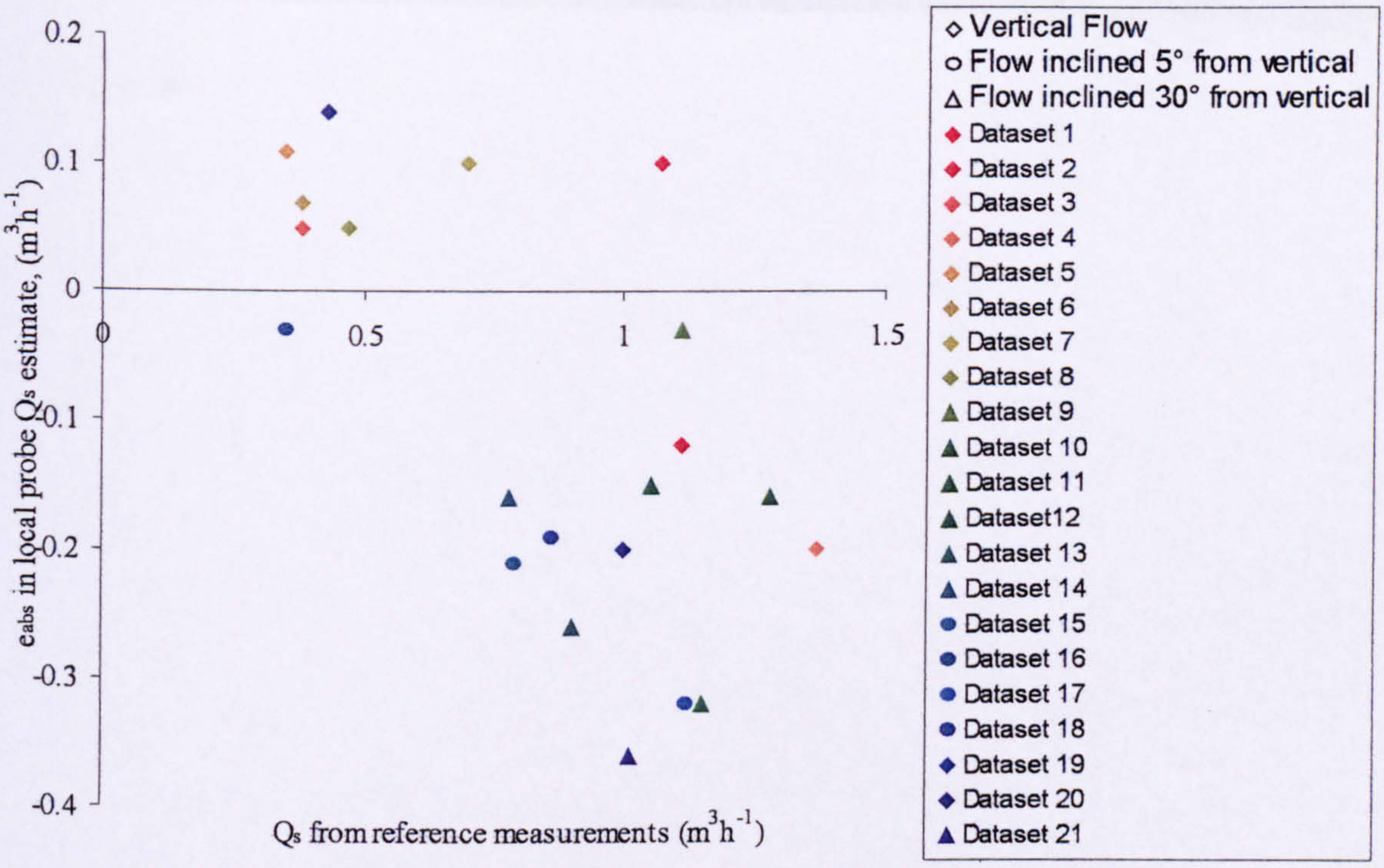

Figure 7-32. Plot of $e_{abs}^{probe,Q}$ against Q_s^{ref}.

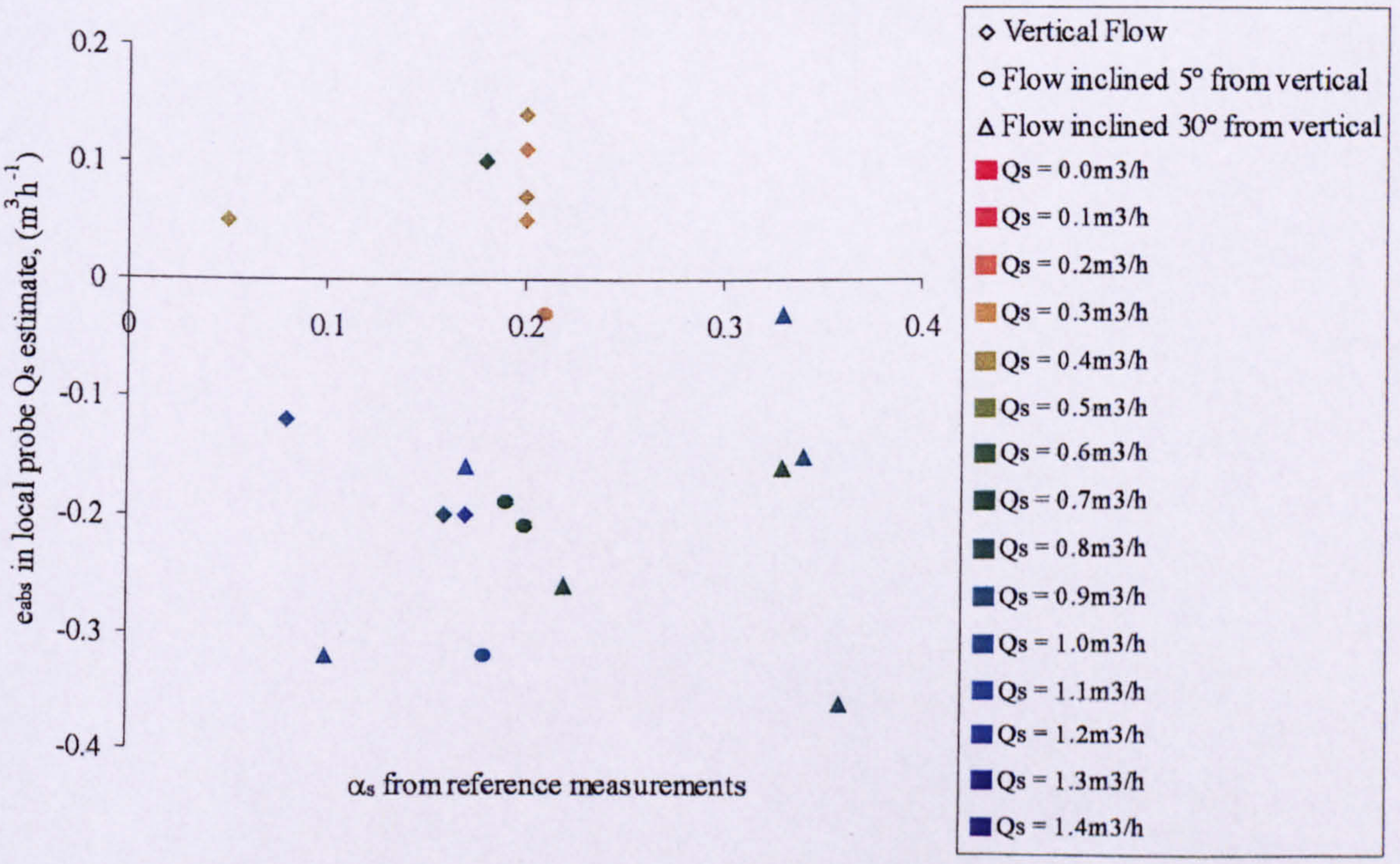

Figure 7-33. Plot of $e_{abs}^{probe,Q}$ against α_s^{ref}.

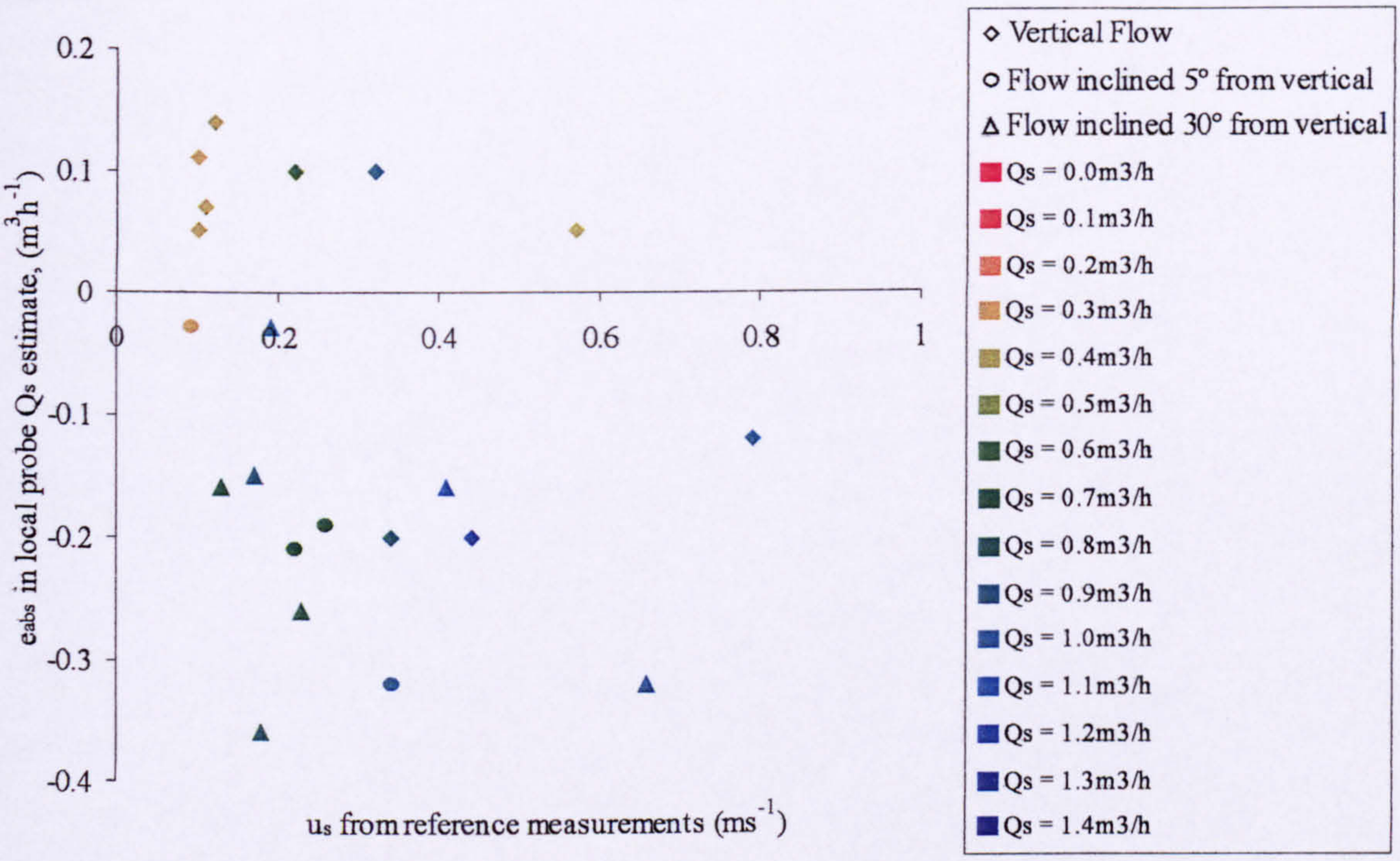

Figure 7-34. Plot of $e_{abs}^{probe,Q}$ against u_s^{ref}.

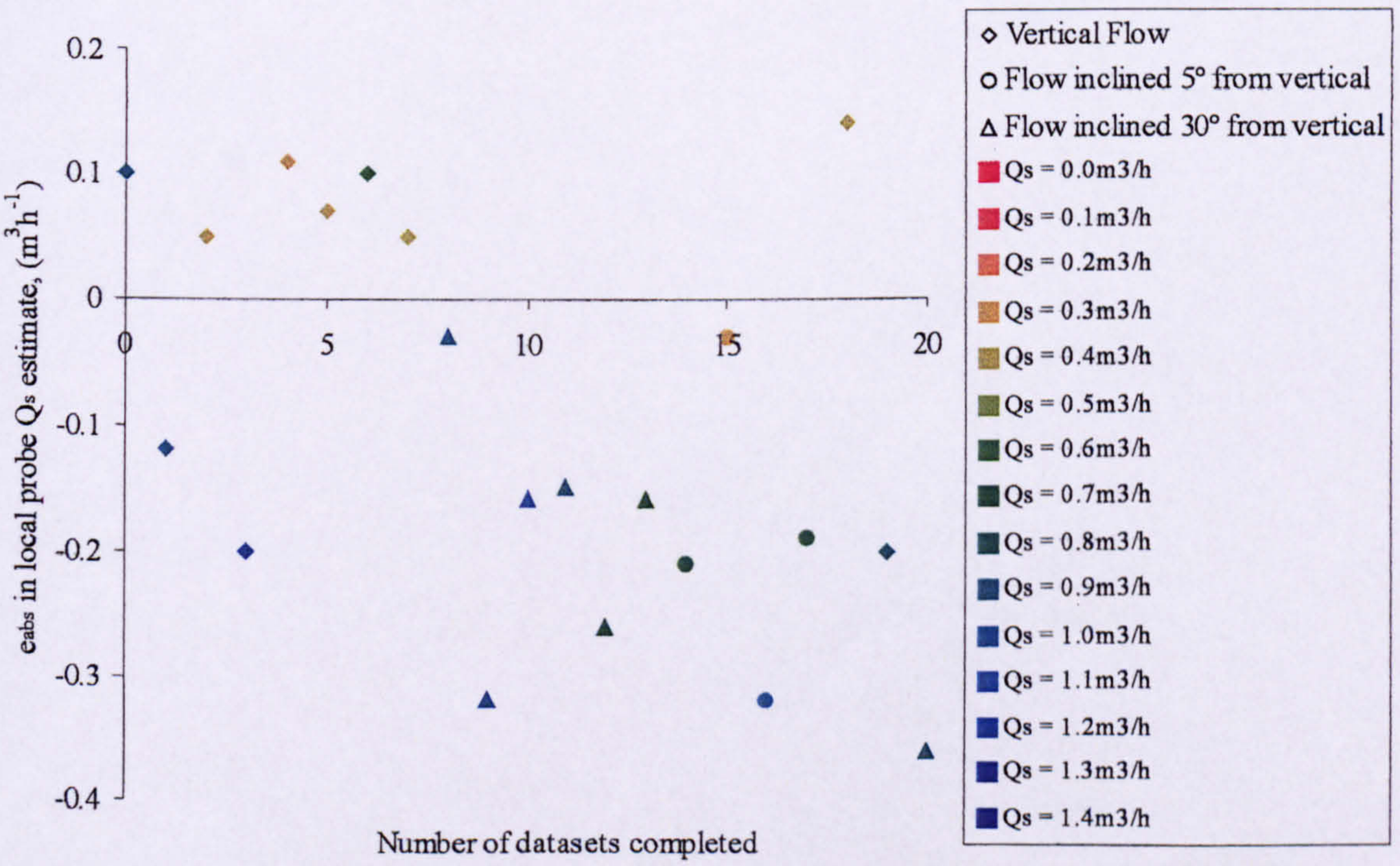

Figure 7-35. Plot of $e_{abs}^{probe,Q}$ against the number of experimental runs completed.

All the error plots show that there are no obvious trends in the difference between Q_s^{probe} and Q_s^{ref} (see Figure 7-32 to Figure 7-35). To further investigate these errors three sets of modified solids volumetric flow rates were calculated using the corrected values calculated in

the previous two sections. Values of $Q_s^{probe,L=11.1}$ were calculated using the measured values of local solids volume fraction, $\alpha_{s,i}^{probe}$, and the corrected values of local solids velocity, $u_{s,i}^{probe,L=11.1}$ (see Section 7.3.2.4). Values of $Q_s^{probe,*L=10.4}$ were calculated the modified values of local solids volume fraction, $\alpha_{s,i}^{probe,*}$ (see Section 7.3.1.4), and the modified values of local solids velocity, $u_{s,i}^{probe,*L=10.4}$ (see Section 7.3.2.4). Finally values of $Q_s^{probe,L=13.9}$ were calculated using the measured values of local solids volume fraction, $\alpha_{s,i}^{probe}$, and the corrected values of local solids velocity, $u_{s,i}^{probe,L=13.9}$ (see Section 7.3.2.4). The errors between these values and the reference solids volumetric flow rate measurements, Q_s^{ref} are shown below. It should be noted that all the integrated local probe values are compared with Q_s^{ref} as this is a direct physical measurement and should contain little error.

Systematic error,	$e_{sys}^{probe,Q,L=11.1}$	-15.27%	$e_{sys}^{probe,Q,*L=10.4}$	0.91%	$e_{sys}^{probe,Q,L=13.9}$	6.03%
Random error,	$e_{ran}^{probe,Q,L=11.1}$	19.31%	$e_{ran}^{probe,Q,*L=10.4}$	20.61%	$e_{ran}^{probe,Q,L=13.9}$	23.96%
Systematic absolute error,	$e_{abs,sys}^{probe,Q,L=11.1}$	$-0.17m^3h^{-1}$	$e_{abs,sys}^{probe,Q,*L=10.4}$	$-0.03m^3h^{-1}$	$e_{abs,sys}^{probe,Q,L=13.9}$	$0.00m^3h^{-1}$
Random absolute error,	$e_{abs,ran}^{probe,Q,L=11.1}$	$0.17m^3h^{-1}$	$e_{abs,ran}^{probe,Q,*L=10.4}$	$0.15m^3h^{-1}$	$e_{abs,ran}^{probe,Q,L=13.9}$	$0.16m^3h^{-1}$

It is clear from the results shown above that there is a significant offset between values of $Q_s^{probe,L=11.1}$ and the measurements of Q_s^{ref}. This suggests that any error in the assumed value of effective sensor separation is not solely responsible for the difference between the integrated local probe values and the reference measurements of solids volumetric flow rate. Both $Q_s^{probe,*L=10.4}$ and $Q_s^{probe,L=13.9}$ show the same order of difference from Q_s^{ref} as shown by the unmodified local probe results, Q_s^{probe}. Additionally values of solids volumetric flow rate predicted by all three modified methods show a similar amount of scatter as the unmodified local probe results.

In conclusion the comparison of solids volumetric flow rates obtained from the local probe and measured by reference instruments has shown that differences between Q_s^{probe} and Q_s^{ref}

were not significantly improved by the application of simple correction factors to correct for errors in the solids volume fraction and axial solids velocity measurements. In particular a significant scatter remains in the errors. The results presented in this section have suggested that errors in both solids volume fraction and axial solids velocity measurements need to be addressed by further work. Only when any error mechanisms involved with the measurement of $\alpha_{s,i}^{probe}$, $u_{s,i}^{probe}$ and α_s^{ref} are understood will it be possible to directly address the accuracy of the measurement of Q_s^{probe}.

7.4 Quantitative comparison of experimental results from the ERT system with reference measurements.

The aim of this section is to allow the integrated measurements of local solids volume fraction, $\alpha_{s,i}^{ERT}$, and local axial solids velocity, $u_{s,i}^{ERT}$, acquired by the ERT system to be quantitatively compared with reference data. The ERT data was integrated in the same way as the local probe data to give global measurements of mean solids volume fraction, α_s^{ERT}, mean axial solids velocity, u_s^{ERT}, and solids volumetric flow rate, Q_s^{ERT}. This procedure is described in Section 6.4.3.3. The reference data was acquired using the reference data devices as described in Chapter 6.

It should be noted at this point that the data integrated for this section was the actual data acquired from the ERT system. The profiles presented in Section 7.2 were interpolated data. This allowed a better qualitative comparison to be made between the profiles acquired by the two different systems. For the purposes of this quantitative comparison the errors between the ERT values and the reference values are as defined in Section 7.3. The relevant equations describing these error relationships are Equation 7-2, Equation 7-3, Equation 7-4 and Equation 7-5. It should be noted that the superscript ^{ERT} denotes that the values relate to the ERT system.

7.4.1 Comparison of reference measurements of mean solids volume fraction with integrated measurements from the ERT system.

7.4.1.1 Results for vertical flow.

The integrated solids volume fraction values from the ERT system for each vertical upward flow condition and the relevant reference data are presented in Table 7-12.

Table 7-12. Integrated solids volume fraction data from the ERT system and reference devices for vertical upward flow.

Flow condition	Plane Separation	Reference data	ERT system data	Errors	
	(cm)	α_s^{ref}	α_s^{ERT}	$e^{ERT,\alpha}$, (%)	$e_{abs}^{ERT,\alpha}$
1	3	0.15	0.16	6.67	0.01
1	5	0.16	0.18	12.50	0.02
2	5	0.15	0.17	13.33	0.02
3	2	0.17	0.22	29.41	0.05
3	3	0.15	0.16	6.67	0.01
3	5	0.15	0.16	6.67	0.01
4	3	0.13	0.15	15.38	0.02
4	5	0.17	0.18	5.88	0.01
5	2	0.06	0.11	83.33	0.05
5	5	0.06	0.07	16.67	0.01
6	2	0.11	0.16	45.45	0.05
6	5	0.11	0.13	18.18	0.02
10	2	0.03	0.07	133.33	0.04

For the upward, vertical flow conditions that were tested the errors between the integrated solids volume fraction values and the reference measurements over the whole data set are given below.

Systematic error, $e_{sys}^{ERT,\alpha}$	30.27%
Random error, $e_{ran}^{ERT,\alpha}$	37.74%
Systematic absolute error, $e_{abs,sys}^{ERT,\alpha}$	0.02
Random absolute error, $e_{abs,ran}^{ERT,\alpha}$	0.02

7.4.1.2 Results for flow inclined 5° from vertical.

The integrated solids volume fraction values from the ERT system for each upward flow condition inclined at 5° from vertical, and the relevant reference data, are presented in Table 7-13.

Table 7-13. Integrated solids volume fraction data from the ERT system and reference devices for upward flow inclined 5° from vertical.

Flow condition	Plane Separation	Reference data	ERT system data	Errors	
	(cm)	α_s^{ref}	α_s^{ERT}	$e^{ERT,\alpha}$, (%)	$e_{abs}^{ERT,\alpha}$
7	3	0.18	0.18	0.00	0.00
7	5	0.19	0.17	-10.13	-0.02
8	3	0.17	0.16	-5.88	-0.01
8	5	0.18	0.16	-11.11	-0.02
9	3	0.17	0.17	0.00	0.00
9	5	0.18	0.16	-11.11	-0.02

For the upward flow conditions inclined 5° from vertical that were tested the errors between the integrated solids volume fraction values from the ERT system and the reference measurements over the whole data set are given below.

Systematic error, $e_{sys}^{ERT,\alpha}$	-6.37%
Random error, $e_{ran}^{ERT,\alpha}$	5.30%
Systematic absolute error, $e_{abs,sys}^{ERT,\alpha}$	-0.01
Random absolute error, $e_{abs,ran}^{ERT,\alpha}$	0.01

7.4.1.3 Results for flow inclined 30° from vertical.

The integrated solids volume fraction values from the ERT system for each upward flow condition inclined at 30° from vertical, and the relevant reference data, are presented in Table 7-14.

Table 7-14. Integrated solids volume fraction data from the ERT system and reference devices for upward flow inclined 30° from vertical.

Flow condition	Plane Separation	Reference data	ERT system data	Errors	
	(cm)	α_s^{ref}	α_s^{ERT}	$e^{ERT,\alpha}$, (%)	$e_{abs}^{ERT,\alpha}$
12	3	0.22	0.23	4.55	0.01
13	5	0.25	0.22	-12.00	-0.03
14	3	0.21	0.18	-14.29	-0.03

For the upward flow conditions inclined 30° from vertical that were tested the errors between the integrated solids volume fraction values from the ERT system and the reference measurements over the whole data set are given below.

Systematic error, $e_{sys}^{ERT,\alpha}$	-7.25%
Random error, $e_{ran}^{ERT,\alpha}$	10.28%
Systematic absolute error, $e_{abs,sys}^{ERT,\alpha}$	-0.02
Random absolute error, $e_{abs,ran}^{ERT,\alpha}$	0.02

7.4.1.4 Discussion of the solids volume fraction data.

It is not within the scope of the current investigation to offer a detailed analysis of the ERT data. For a more complete analysis see Lucas et al [57,58] and Loh [56].

What is immediately apparent is that the estimate of the mean solids volume fraction obtained from the ERT system, α_s^{ERT}, tends to be higher than the value obtained from reference

measurements, α_s^{ref}, in vertical flows. This is the opposite of the trend in the local probe data. Aside from this, the errors in data acquired by both systems are of the same order although the data acquired by the ERT system shows higher values of $e_{sys}^{ERT,\alpha}$ and $e_{ran}^{ERT,\alpha}$ due to some large percentage differences between α_s^{ERT} and α_s^{ref} at flow conditions with low α_s^{ref}. The high measurements acquired by the ERT system could be due in part to the weighting function applied to the data to redress a lack of sensitivity in the centre of the pipe (see Section 7.2.1.4). The profiles acquired by the local probe show a saddle shape dipping at the pipe centre. The profiles acquired by the ERT system show a slight peak at the pipe centre with the region affected by the weighting function easily identifiable. As discussed in Section 7.2.1.4 it is possible that the weighting function has resulted in $\alpha_{s,i}^{ERT}$ being artificially high towards the centre of the pipe, giving an estimate of α_s^{ERT} which is too high.

In inclined flows α_s^{ERT} tends to be low compared to α_s^{ref} which mirrors the trend in the measurements acquired by the local probe. In flows inclined 5° from vertical the measurements acquired by the local probe show a larger offset to the data. However the scatter of data is comparable. In flows inclined 30° from vertical the absolute errors in the measurements acquired by the local probe are larger. However the percentage errors are comparable. This is because the local probe could be used over a larger range of α_s than the ERT system. As the sign of the errors here agree it is possible that an error in the reference measurement, particularly the estimate of ΔP_F as discussed in Section 7.3.1.4, is partly responsible.

7.4.2 Comparison of reference measurements of mean solids velocity with integrated measurements from the ERT system.

7.4.2.1 Results for vertical flow.

The integrated axial solids velocity values from the ERT system for each vertical upward flow condition and the relevant reference data are presented in Table 7-15.

Table 7-15. Integrated axial solids velocity data from the ERT system and reference devices for vertical upward flow.

Flow condition	Plane Separation	Reference data	ERT system data	Errors	
	(cm)	u_s^{ref}, (ms^{-1})	u_s^{ERT}, (ms^{-1})	$e^{ERT,u}$, (%)	$e_{abs}^{ERT,u}$, (ms^{-1})
1	3	0.36	0.33	6.67	-0.03
1	5	0.39	0.40	12.50	0.01
2	5	0.47	0.47	13.33	0.00
3	2	0.21	0.50	29.41	0.29
3	3	0.23	0.26	6.67	0.03
3	5	0.28	0.29	6.67	0.01
4	3	0.15	0.15	15.38	0.00
4	5	0.13	0.12	5.88	-0.01
5	2	0.56	0.86	83.33	0.30
5	5	0.58	0.51	16.67	-0.09
6	2	0.39	0.65	45.45	0.26
6	5	0.55	0.48	18.18	-0.07
10	2	1.36	1.25	133.33	-0.11

For the upward, vertical flow conditions that were tested the errors between the integrated vales obtained from the ERT system and the reference measurements over the whole data set are given below. As the results were acquired using the ERT system configured with 3 different plane separations three different sets of error statistics have been presented. This is because the plane separation has a significant effect on the accuracy of the velocity measurement as discussed in Section 7.2.2.4. An additional superscript denotes the plane separation relevant to the error values.

Plane separation		2cm		3cm		5cm
Systematic error	$e_{sys}^{ERT,u2}$	72.88%	$e_{sys}^{ERT,u3}$	9.57%	$e_{sys}^{ERT,u5}$	12.21%
Random error	$e_{ran}^{ERT,u2}$	46.21%	$e_{ran}^{ERT,u3}$	5.03%	$e_{ran}^{ERT,u5}$	5.05%
Systematic absolute error	$e_{abs,sys}^{ERT,u2}$	0.19ms^{-1}	$e_{abs,sys}^{ERT,u3}$	0.00ms^{-1}	$e_{abs,sys}^{ERT,u5}$	-0.03ms^{-1}
Random absolute error	$e_{abs,ran}^{ERT,u2}$	0.20ms^{-1}	$e_{abs,ran}^{ERT,u3}$	0.03ms^{-1}	$e_{abs,ran}^{ERT,u5}$	0.04ms^{-1}

7.4.2.2 Results for flow inclined 5° from vertical.

The integrated axial solids velocity from the ERT system for each upward flow condition inclined 5° from vertical, and the relevant reference data, are presented in Table 7-16.

Table 7-16. Integrated axial solids velocity data from the ERT system and reference devices for upward flow inclined 5° from vertical.

Flow condition	Plane Separation	Reference data	ERT system data	Errors	
	(cm)	u_s^{ref}, (ms^{-1})	u_s^{ERT}, (ms^{-1})	$e^{ERT,u}$, (%)	$e_{abs}^{ERT,u}$, (ms^{-1})
7	3	0.13	0.19	46.15	0.06
7	5	0.12	0.11	8.33	-0.01
8	3	0.26	0.28	7.69	0.02
8	5	0.26	0.30	15.38	0.04
9	3	0.34	0.38	11.76	0.04
9	5	0.31	0.35	12.90	0.04

For the upward flow conditions inclined 5° from vertical that were tested the errors between the integrated axial solids velocity values obtained from the ERT system and the reference measurements over the whole data set are given below. As the results were acquired using the ERT system configured with 2 different plane separations two different sets of error statistics have been presented. This is because the plane separation has a large effect on the accuracy of

the velocity measurement as discussed in Section 7.2.2.4. An additional superscript denotes the plane separation relevant to the error values.

Plane separation		3cm		5cm
Systematic error	$e_{sys}^{ERT,u3}$	21.87%	$e_{sys}^{ERT,u5}$	12.20%
Random error	$e_{ran}^{ERT,u3}$	21.13%	$e_{ran}^{ERT,u5}$	3.58%
Systematic absolute error	$e_{abs,sys}^{ERT,u3}$	0.04ms^{-1}	$e_{abs,sys}^{ERT,u5}$	0.02ms^{-1}
Random relative error	$e_{abs,ran}^{ERT,u3}$	0.02ms^{-1}	$e_{abs,ran}^{ERT,u5}$	0.03ms^{-1}

7.4.2.3 Results for flow inclined 30° from vertical.

The integrated axial solids velocity values from the ERT system for each upward flow condition inclined 30° from vertical and the relevant reference data are presented in Table 7-17.

Table 7-17. Integrated axial solids velocity data from the ERT system and reference devices for upward flow inclined 30° from vertical.

Flow condition	Plane Separation	Reference data	ERT system data	Errors	
	(cm)	u_s^{ref}, (ms^{-1})	u_s^{ERT}, (ms^{-1})	$e^{ERT,u}$, (%)	$e_{abs}^{ERT,u}$, (ms^{-1})
12	3	0.21	0.23	9.52	0.02
13	3	0.22	0.30	36.36	0.08
14	3	0.26	0.44	69.23	0.18

For the upward flow conditions inclined 30° from vertical that were tested the errors between the integrated axial solids velocity values obtained from the ERT system and the reference measurements over the whole data set are given below. As the results were acquired using the ERT system configured with only one different plane separation only one set of error statistics has been presented. An additional superscript denotes the plane separation relevant to the error values.

Plane separation		3cm
Systematic error	$e_{sys}^{ERT,u3}$	38.37%
Random error	$e_{ran}^{ERT,u3}$	29.91%
Systematic absolute error	$e_{abs,sys}^{ERT,u3}$	$0.09ms^{-1}$
Random relative error	$e_{abs,ran}^{ERT,u3}$	$0.08ms^{-1}$

7.4.2.4 Discussion of the axial solids velocity data.

Again, it is not within the scope of the current investigation to offer a detailed analysis of the ERT data. For a more complete analysis see Lucas et al [57,58] and Loh [56].

It is clear that u_s^{ERT} is high compared to u_s^{ref}. As expected increasing the plane separation improves the velocity resolution and therefore increases the accuracy of the velocity measurements. This was discussed in Section 7.2.2.4. Unfortunately, even at the largest plane separation the lower sampling frequency (100 frames per second) of the ERT system restricts its use to lower axial velocities than the local probe system. This can particularly be seen in the results for flows inclined 30° from vertical. At these flow conditions the errors are high and only a limited amount of data was collected for this reason.

In vertical flows and flows inclined 5° from vertical the errors in the measurements acquired by the ERT system are comparable with those in the measurements acquired by the local probe. The measurements acquired by the local probe show a larger systematic error but this is probably due to an error in the assumed value of the effective sensor separation (see Section 7.3.2.4). The scatter of the two sets of results is similar although in vertical flow the measurements acquired by the local probe do show higher scatter than those acquired by the ERT system.

7.4.3 Comparison of reference measurements of solids volumetric flow rate with integrated measurements from the ERT system.

7.4.3.1 Results for vertical flow.

The integrated solids volumetric flow rate values from the ERT system for each vertical upward flow condition and the relevant reference data are presented in Table 7-18.

Table 7-18. Integrated solids volumetric flow rate data from the ERT system and reference devices for vertical upward flow.

Flow condition	Plane Separation	Reference data	ERT system data	Errors	
	(cm)	Q_s^{ref}, (m^3h^{-1})	Q_s^{ERT}, (m^3h^{-1})	$e^{ERT,Q}$, (%)	$e_{abs}^{ERT,Q}$, (m^3h^{-1})
1	3	0.96	0.94	2.08	-0.02
1	5	1.11	1.31	18.02	0.20
2	5	1.27	1.40	10.24	0.13
3	2	0.66	2.01	204.55	1.35
3	3	0.62	0.76	22.58	0.14
3	5	0.76	0.82	7.89	0.06
4	3	0.35	0.39	11.43	0.04
4	5	0.36	0.39	8.33	0.03
5	2	0.61	1.76	188.52	1.15
5	5	0.61	0.66	8.20	0.05
6	2	0.77	1.80	133.77	1.03
6	5	0.96	1.10	14.58	0.14
10	2	0.74	1.64	121.62	0.90

For the upward, vertical flow conditions that were tested the errors between the integrated solids volumetric flow rate values obtained from the ERT system and the reference measurements over the whole data set are given below. As the results were acquired using the ERT system configured with 3 different plane separations three different sets of error statistics have been presented. This is because the plane separation has a large effect on the accuracy of the velocity measurement, and therefore the solids volumetric flow rate measurement, as

discussed in Section 7.2.2.4. An additional superscript denotes the plane separation relevant to the error values.

Plane separation		2cm		3cm		5cm
Systematic error	$e_{sys}^{ERT,Q2}$	162.12%	$e_{sys}^{ERT,Q3}$	12.03%	$e_{sys}^{ERT,Q5}$	11.21%
Random error	$e_{ran}^{ERT,Q2}$	40.58%	$e_{ran}^{ERT,Q3}$	10.26%	$e_{ran}^{ERT,Q5}$	4.17%
Systematic absolute error	$e_{abs,sys}^{ERT,Q2}$	$1.11m^3h^{-1}$	$e_{abs,sys}^{ERT,Q3}$	$0.05m^3h^{-1}$	$e_{abs,sys}^{ERT,Q5}$	$0.10m^3h^{-1}$
Random absolute error	$e_{abs,ran}^{ERT,Q2}$	$0.19m^3h^{-1}$	$e_{abs,ran}^{ERT,Q3}$	$0.08m^3h^{-1}$	$e_{abs,ran}^{ERT,Q5}$	$0.07m^3h^{-1}$

7.4.3.2 Results for flow inclined 5° from vertical.

The integrated solids volumetric flow rate values from the ERT system for each upward flow condition inclined 5° from vertical and the relevant reference data are presented below, Table 7-19.

Table 7-19. Integrated solids volumetric flow rate data from the ERT system and reference devices for upward flow inclined 5° from vertical.

Flow condition	Plane Separation	Reference data	ERT system data	Errors	
	(cm)	Q_s^{ref}, (m^3h^{-1})	Q_s^{ERT}, (m^3h^{-1})	$e^{ERT,Q}$, (%)	$e_{abs}^{ERT,Q}$, (m^3h^{-1})
7	3	0.43	0.62	44.19	0.19
7	5	0.41	0.34	17.07	-0.07
8	3	0.79	0.81	2.53	0.02
8	5	0.86	0.89	3.49	0.03
9	3	1.05	1.14	8.57	0.09
9	5	1.01	1.01	0.00	0.00

For the upward flow conditions at 5° from vertical that were tested the errors between the integrated values of solids volumetric flow rate obtained from the ERT system and the reference measurements over the whole data set are given below. As the results were acquired

using the ERT system configured with 2 different plane separations two different sets of error statistics have been presented. This is because the plane separation has a large effect on the accuracy of the velocity measurement, and therefore the solids volumetric flow rate measurement, as discussed in Section 7.2.2.4. An additional superscript denotes the plane separation relevant to the error values.

Plane separation		3cm		5cm
Systematic error	$e_{sys}^{ERT,Q3}$	18.43%	$e_{sys}^{ERT,Q5}$	6.85%
Random error	$e_{ran}^{ERT,Q3}$	22.51%	$e_{ran}^{ERT,Q5}$	9.02%
Systematic absolute error	$e_{abs,sys}^{ERT,Q3}$	$0.10m^3h^{-1}$	$e_{abs,sys}^{ERT,Q5}$	$-0.01m^3h^{-1}$
Random absolute error	$e_{abs,ran}^{ERT,Q3}$	$0.09m^3h^{-1}$	$e_{abs,ran}^{ERT,Q5}$	$0.05m^3h^{-1}$

7.4.3.3 Results for flow inclined 30° from vertical.

The integrated solids volumetric flow rate from the ERT system for each upward flow condition inclined 30° from vertical and the relevant reference data are presented below, Table 7-20.

Table 7-20. Integrated solids volumetric flow rate data from the ERT system and reference devices for upward flow inclined 30° from vertical.

Flow condition	Plane Separation	Reference data	ERT system data	Errors	
	(cm)	Q_s^{ref}, (m^3h^{-1})	Q_s^{ERT}, (m^3h^{-1})	$e^{ERT,Q}$, (%)	$e_{abs}^{ERT,Q}$, (m^3h^{-1})
12	3	0.84	0.96	14.29	0.12
13	3	1.01	1.18	16.83	0.17
14	3	0.97	1.39	43.30	0.42

For the upward flow conditions at 5° from vertical tested the errors between the integrated values of solids volumetric flow rate obtained from the ERT system and the reference measurements over the whole data set are given below. As the results were acquired using the ERT system configured with only one different plane separation only one set of error statistics has been presented. An additional superscript denotes the plane separation relevant to the error values.

Plane separation		3cm
Systematic error	$e_{sys}^{ERT,Q3}$	24.81%
Random error	$e_{ran}^{ERT,Q3}$	16.07%
Systematic absolute error	$e_{abs,sys}^{ERT,Q3}$	$0.24m^3h^{-1}$
Random absolute error	$e_{abs,ran}^{ERT,Q3}$	$0.16m^3h^{-1}$

7.4.3.4 Discussion of the solids volumetric flow rate results.

From the solids volumetric flow rate results it is again possible to see the effect of increasing the plane separation. As the plane separation increases the accuracy of the measurement of u_s^{ERT} increases and therefore the accuracy of the measurement of Q_s^{ERT} increases.

For flow inclined 30° from vertical the systematic errors and random errors from both the local probe and the ERT system are comparable. However Q_s^{ERT} is generally high relative to the reference measurements, mainly because both α_s^{ERT} and u_s^{ERT} are overestimated relative to the reference values. Q_s^{probe} is generally low relative to the reference measurements because α_s^{probe} is generally underestimated relative to the reference values.

For vertical flow and flow inclined 5° from vertical the local probe and the ERT system both show comparable systematic errors. Again Q_s^{probe} is low whilst Q_s^{ERT} is high. The local probe shows a larger amount of scatter than the ERT system with either plane separation. This suggest that there is a larger amount of random error in the local probe system.

In conclusion both the local probe and the ERT system show errors for which possible sources can be identified. Generally the ERT system gives artificially high measurements of α_s^{ERT} and u_s^{ERT}. The high reading of α_s^{ERT} is possibly due to an error in the weighting function applied during reconstruction. However this cannot be confirmed without further experimentation. The high reading of u_s^{ERT} is not so easily explicable. However as discussed in Section 7.2.2.4 there are a number of inherent inaccuracies in the ERT solids velocity estimate. Again these could be best quantified with further experimentation.

8. Flow modelling.

8.1 The aim of the flow modelling.

The local probe system enables measurements to be made of $\alpha_{s,i}^{probe}$, the local solids volume fraction, and $u_{s,i}^{probe}$, the local solids axial velocity. From these measurements α_s^{probe}, the area averaged solids volume fraction, u_s^{probe}, the area averaged solids axial velocity, and Q_s^{probe}, the solids volumetric flow rate can be estimated.

The local probe system cannot be considered to be a complete two-phase flow meter because it cannot enable an estimate of the water volumetric flow rate, Q_w, to be made. This is because it cannot obtain a profile of the local water velocity, $u_{w,i}$. If a profile of $u_{w,i}$ were measured Q_w could be calculated as shown in Equation 1-2.

$$Q_w = \int_A u_{w,i}\left(1 - \alpha_{s,i}^{probe}\right)dA$$

Equation 1-2

One of the aims of the current research was to enable estimates of $u_{w,i}$ to be made enabling Q_w to be predicted. This would result in the local probe system being significantly more desirable for laboratory and industrial applications.

Traditionally two phase flow measurement has been achieved by using two different devices in conjunction. A device sensitive to the flow of phase A is used to measure the relative volume fraction of each phase and the velocity of phase A. Simultaneously a second device, sensitive to the flow of phase B is used to measure the velocity of phase B. In a flow consisting of non-conducting solids dispersed in a conducting liquid, as in the current investigation, appropriate devices could be a conductivity measurement device, and an electromagnetic flow meter. The conductivity measurement device could be used to measure solids volume fraction and solids velocity. Meanwhile an electromagnetic flow meter, such as reported by Bernier & Brennen [107] in vertical bubbly flows, could be used to measure the liquid velocity. Combining the measurements would give a full two phase flow measurement.

However the costs of the second device add significantly to the overall costs of the flow meter. If the liquid velocity could be predicted from the known solids volume fraction and

velocity this would dramatically reduce the costs of two phase flow measurement. Therefore it was decided to investigate the relationship between the solids and liquid velocities.

8.2 Review of previous work.

In a solids-liquid flow where there is a density difference between the two components the solid particles and the liquid flow at different velocities. In the current investigation the solid particles have a density of 1340kgm^{-3} whilst the water has a density of 997kgm^{-3}. Therefore in an upward flow the lower density water will flow at a higher velocity than the solids. The difference between the local axial solids and water velocities is defined as the axial slip velocity, as given in Equation 1-3.

$$v_{slip,i} = u_{w,i} - u_{s,i}$$

Equation 1-3

A great deal of previous research has be carried out to attempt to quantify $v_{slip,i}$ for different flow conditions. Before carrying out the modelling work in this chapter a review of this work was carried out for both vertical and inclined flow.

8.2.1 Slip velocities in vertical flows.

A wide range of previous research has been carried out to determine $v_{slip,i}$, the axial slip velocity, in solids-liquid flows in vertical pipes. In a number of studies, particularly involving small particles, particles with densities close to that of the liquid and flows with very high Reynolds numbers, the slip was found to be negligible. An example is the work of Yianneskis & Whitelaw [34]. Their work involved a particle to liquid density ratio of 1.18 and flows with Reynolds numbers greater than 40,000. In such flows $v_{slip,i}$ is insignificant compared to the high mean flow velocity due to the small density ratio. In the current investigation the density ratio is higher, 1.35, and the flow Reynolds number is lower. Therefore $v_{slip,i}$ is significant compared to the mean flow velocity.

Generally $v_{slip,i}$ is derived as a function of v_t, the terminal settling velocity of a single particle in an unbounded liquid. If a particle is allowed to fall unhindered by either the vessel or other particles only two forces act upon it. These are the downward force due to gravity and the drag force which opposes motion (see Govier & Aziz [94]). The particle will reach its terminal velocity when these forces are in equilibrium. A more detailed discussion of v_t and its calculation for the current flow conditions is presented in Section 8.2.3. As $\alpha_{s,i}$ increases, particle-particle interactions cause a reduction in $v_{slip,i}$ when compared to v_t. The models

derived in the literature attempt to take account of this hindered settling effect and are referred to as hindered settling models.

At this point it is important to note that the hindered settling models reviewed only take account of particle-particle interactions. The effects of the pipe wall and diffusion effects caused by the variation of the flow across the pipe are not included. The models allow $v_{slip,i}$ to vary from v_t to 0. In some experimental studies this range is not found to be accurate. Govier & Aziz [94] report that Doig & Roper found that velocity does lag the liquid velocity, as expected, across much of the pipe cross-section. However they also found that the particle velocity was greater than the liquid velocity at the pipe wall. Alajbegovic et al [98] also present results showing this pattern. However these effects are small in a relatively large pipe such as in the current investigation.

A review of some early hindered settling models is given by Govier & Aziz [94]. They present hindered settling models which apply to either laminar or turbulent flows. For laminar flows of random suspensions the model of Burgess, as reported by Govier & Aziz [94], is shown in Equation 8-1.

$$v_{slip,i} = \frac{v_t}{1+6.88\alpha_{s,i}}$$

Equation 8-1

For laminar flows of random suspensions of spherical particles the model of Famularo & Happel, as reported by Govier & Aziz [94], is shown in Equation 8-2.

$$v_{slip,i} = \frac{v_t}{1+\gamma\alpha_{s,i}^3} \qquad \gamma = 1.30 \pm 0.24$$

Equation 8-2

For turbulent flow the Carmen-Kozeny equation, as reported by Govier & Aziz [94], is shown in Equation 8-3.

$$v_{slip} = \frac{v_t(1-\alpha_{s,i})^3}{10\alpha_{s,i}}$$

Equation 8-3

More recently Zuber [108] showed that v_{slip} is proportional to v_t as shown in Equation 8-4.

$$v_{slip} = v_t(1-\alpha_{s,i})f(\alpha_{s,i})$$

Equation 8-4

In Equation 8-4 $f(\alpha_{s,i})$is a function which is derived from the assumed relationship between the liquid viscosity and the bulk mixture viscosity. Zuber [108] compared a number of previously reported relationships of this type. Two of these are presented here. The Mooney relationship, shown in Equation 8-5, accounts for both hydrodynamic interaction and particle collisions.

$$f(\alpha_{s,i}) = \frac{1}{e^{\left[\frac{2.5\alpha_{s,i}}{1-s\alpha_{s,i}}\right]}} \qquad 1.35 \le s \le 1.91$$

Equation 8-5

The Brinkman-Roscoe, given in Equation 8-6, relationship assumes that hydrodynamic interactions take place. However the effects of particle collisions are not accounted for.

$$f(\alpha_{s,i}) = (1-\alpha_{s,i})^{2.5}$$

Equation 8-6

Combining Equation 8-4 and Equation 8-6 gives Zuber's relationship to predict slip velocity which is shown in Equation 8-7.

$$v_{slip,i} = v_t(1-\alpha_{s,i})^{3.5}$$

Equation 8-7

Zuber [108] presents a number of comparisons with experimental data which show that this relationship gives reasonable predictions. In a later paper Zuber & Findlay [109] claim that Equation 8-7 is of the correct form but that the exponent 3.5 is not always applicable. In this later paper Zuber alters Equation 8-7 to give Equation 8-8 where q varies between 0 an 3 depending on the particle size.

$$v_{slip,i} = v_t(1-\alpha_{s,i})^{q}$$

Equation 8-8

Similar equations have also been reported by other authors. Galvin et al [110] report the Richardson-Zaki model, shown in Equation 8-9, with $n \approx 4.65$ if the Reynolds number of the flow is below 1.

$$v_{slip,i} = v_t(1-\alpha_{s,i})^{n-1}$$

Equation 8-9

Liu reports the Richardson-Zaki model as Equation 8-10, although in this case no Reynolds number condition is given.

$$v_{slip,i} = v_t(1-\alpha_{s,i})^{16/3}$$

Equation 8-10

Finally Shook & Roco [111] also report a relationship the same as Equation 8-8 although they claim that the value of coefficient q will vary as the particle Reynold's number varies. They state that q = 4.7 for particle Reynold's numbers below 0.2 and that q = 2.35 for particle Reynold's numbers above 1,000.

In conclusion the weight of evidence in the literature suggests that a relationship similar to that given in Equation 8-8 will be most relevant. However there appears to be little agreement on the value of the coefficient q. Because of this Equation 8-8 will be used for the majority of the slip velocity modelling, although some other relationships will be briefly examined.

8.2.2 Slip velocities in inclined and horizontal flows.

Less previous research has been carried out into the value of $v_{slip,i}$ in horizontal and inclined flows. In an inclined or horizontal flow the action of gravity on the particles does not act along the axis of the pipe. The resulting flow pattern has been described in detail in Chapter 1. The particles will tend to settle towards the bottom side of the pipe. At the same time the fluid will tend to re-suspend the particles. This results in an equilibrium condition with both a solids volume fraction and solids velocity gradient along the Z axis of the pipe (see Figure 7-13). In extreme cases in upward inclined flows the settled layer of solids will become dense and heavy enough to begin to slide back down the pipe, even though the net flow of solids is in the upward direction. In these conditions it is expected that the liquid velocity profile will be highly non-uniform.

Vigneaux et al [43] have shown that in an inclined oil-water flow that $v_{slip,i}$ is a function of $\alpha_{s,i}$ at a given angle of inclination and that $v_{slip,i}$ is not a function of volumetric flow rate. This variation with $\alpha_{s,i}$ is found in the hindered settling models applied to vertical flows. Turian & Yuan [97] state that $v_{slip,i}$ will be close to zero in a horizontal flow as long as the flow rate is high enough to suspend all the solids. These results suggest that $v_{slip,i}$ in inclined flows can be calculated in a similar way as $v_{slip,i}$ in a vertical flow as long as the solids are relatively evenly suspended. The only modification necessary is to take account of the indirect action of gravity

on the flow. The modified version of Equation 8-8 is shown in Equation 8-11 below where θ is the angle of inclination of the pipe from vertical.

$$v_{slip,i} = v_t \cos\theta (1 - \alpha_{s,i})^q$$

Equation 8-11

As the pipe is inclined further from vertical Vigneaux et al [43] show that $v_{slip,i}$ increases in oil-water flows. They show that in these cases $v_{slip,i}$ can exceed v_t. They state that this is due to the oil agglomerating at the top of the pipe. The large concentrated oil structures do not act as single bubbles, and rise at a much higher velocity. In a solids-liquid flow the solids will begin to form a concentrated layer at the bottom of the pipe. In some cases this layer can flow back down the pipe resulting in high $v_{slip,i}$.

Stratified flows cannot be modelled as simply as fully suspended flows. In order to model stratified solids-liquid flows many researchers apply a two-layer model. The lower layer assumes the flow to be a packed bed which applies a force on the pipe wall due to its effective weight. At the same time the upper layer is assumed to behave in the same way as a fully suspended flow. Examples of two layer models are given by Roco & Shook [93], Shook & Roco [111] and Matousek [100]. Although many of these models assume that no slip occurs within each layer it is assumed that slip takes place between the layers. This leads to a more accurate model of a stratified flow than a single layer model would be able to give.

In conclusion it is reasonable to assume that a two-layer type slip model should be applicable in cases where a significant solids bed exists at the bottom of the pipe. In fully suspended flows it is reasonable from the published literature to assume that a slip model of the type shown in Equation 8-11 will be applicable.

8.2.3 Terminal settling velocity of a spherical particle.

A good discussion of the terminal settling velocity of a spherical particle is given by Govier & Aziz [94]. This is summarised in this section. The terminal settling velocity of the particles, v_t, is defined as the velocity at which a single particle will settle due to gravity alone. This requires that no other particles interact with it and that no external force is applied. The theory applied in this section (and in Govier & Aziz [94]) also assumes that the particles are smooth, regular, rigid spheres. Whilst this is not strictly the case in this investigation it is a reasonable assumption.

Under these conditions two forces act on the particles. These are a downward gravitational force, F_g, given by Equation 8-12 and the drag force resisting the motion of the particles, F_D, which is given by Equation 8-13.

$$F_g = \frac{\pi d_p^3}{6}(\rho_s - \rho_w)g$$

Equation 8-12

$$F_D = C_D \frac{\rho_w u_p^{\ 2}}{2} \frac{\pi d_p^2}{4}$$

Equation 8-13

In Equation 8-12 and Equation 8-13 ρ_s and ρ_w are the densities of the solids and the water respectively. C_D is the drag coefficient, d_p is the particle diameter and u_p is the particle velocity. At the terminal settling velocity these forces become equal so that no acceleration takes place. At this point $u_p = v_t$.

In order to calculate v_t it is necessary to calculate C_D, the drag coefficient. The value of C_D is a function of the particle Reynolds number, Re_p. This is given by Equation 8-14 where μ_w is the viscosity of the water.

$$Re_p = \frac{du_p\rho_w}{\mu_w}$$

Equation 8-14

If Re_p is less than about 1.0 the motion of the particle through the fluid will be laminar. In this case Stokes' law holds and C_D is given by Equation 8-15(a). If Re_p is between 1 and 1000 the flow is in a transitional region with some turbulence. In this case the value of C_D must be acquired from a purely empirical equation like that of Allen which is given by Equation 8-15(b). Finally, if Re_p is greater than 1000 the flow is purely turbulent and the value of C_D is given by Equation 8-15(c).

$$\text{(a) } C_D = \frac{24\mu_w}{du_p\rho_w} \qquad \text{(b) } C_D = 30\left(\frac{du_p\rho_w}{\mu_w}\right)^{-0.625} \qquad \text{(c) } C_D = 0.44$$

Equation 8-15

These three relationships can be represented by a family of lines such as plotted by Govier & Aziz [94]. The particles in the current research fall in the transition region. The value of v_t for this combination of solids and liquid has been calculated to be $0.210 ms^{-1}$.

8.3 Application to the current research.

From the review of existing literature it is clear that $v_{slip,i}$ will vary across the pipe cross-section as $\alpha_{s,i}$ varies across the pipe cross-section. However in order to get a rough idea of $v_{slip,i}$ in the current flow conditions two "boundary" slip values were applied at all points in the pipe to give profiles of the maximum and minimum predicted $u_{s,i}$ using Equation 1-3. It should be noted that this analysis ignores any effect the variation of $\alpha_{s,i}$ across the pipe may have. Maximum, $Q_w^{pred,max}$, and minimum, $Q_w^{pred,min}$, values of water volumetric flow rate were then calculated using Equation 1-2. From the literature two reasonable boundary conditions exist. The lowest predicted value of $v_{slip,i}$ in the literature is $0 ms^{-1}$. From Section 8.2 many previous researchers claim that there will be negligible slip between the phases. The highest predicted value of $v_{slip,i}$ is always given as less than v_t. v_t in the current research has been determined to be $0.210 ms^{-1}$. In the current investigation $v_t \cos\theta$ has been used in place of v_t, where θ is the inclination angle. This is in order to take account of the indirect action of gravity in inclined flows. Figure 8-1 shows $Q_w^{pred,max}$ and $Q_w^{pred,min}$ plotted against Q_w^{ref}. A solid line is plotted in Figure 8-1 where $Q_w^{pred} = Q_w^{ref}$.

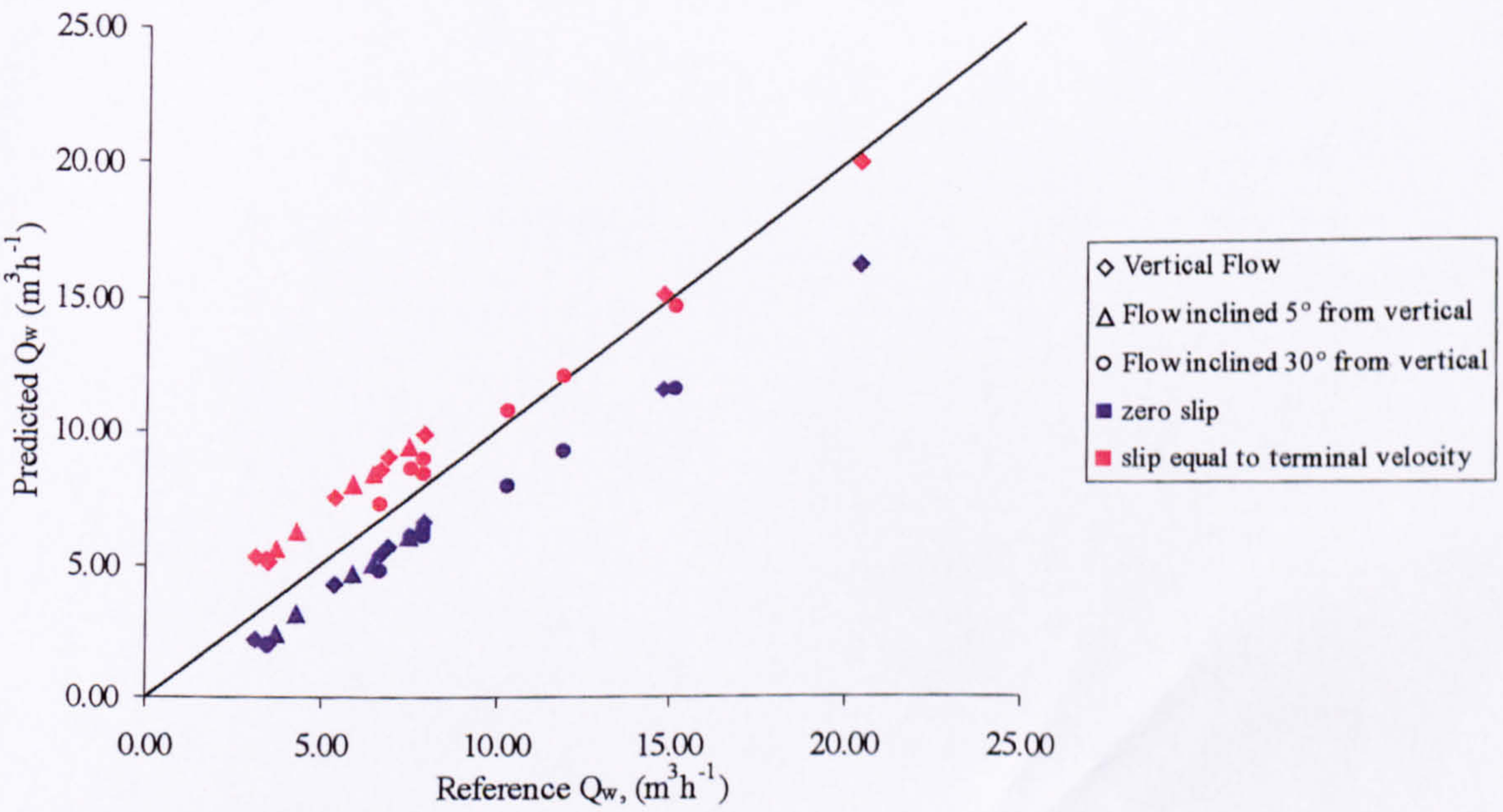

Figure 8-1. $Q_w^{pred,max}$ and $Q_w^{pred,min}$ plotted against Q_w^{ref}.

Figure 8-1 shows a number of definite trends in the data. For the majority of the vertical flow conditions and for flows inclined at 5° from vertical the ideal mean slip velocity must lie fairly centrally between the minimum and maximum boundaries. This is not the case for two of the vertical flow conditions with high Q_w. This could be due to the slip altering as the flow turbulence increases. Alternately it could be due to spurious data at these points. For all the flows inclined at 30° from vertical $Q_w^{pred,max}$ appears to be close to Q_w^{ref}. This suggests that $v_{slip,i}$ for these flows is close to $v_t\cos\theta$. Again the ideal $v_{slip,i}$ appears to increase as Q_w increases. Following this initial investigation of $v_{slip,i}$ it was decided to perform further modelling to attempt to identify the actual slip behaviour. As two distinct approximate values of slip had been identified for flows at different inclinations they were each investigated separately.

8.3.1 Vertical flow and flow inclined at 5° from vertical.

In upward vertical flows and upward flows inclined 5° from vertical the ideal $v_{slip,i}$ appears from Figure 8-1 to fall between 0ms^{-1} and $v_t\cos\theta$ (0.210ms^{-1} in vertical flow and 0.209ms^{-1} in flows inclined 5° from vertical). This suggests that a hindered settling model as introduced in Section 8.2.1 is appropriate.

Following the literature review carried out in Section 8.2.1 it was decided to attempt to calculate $v_{slip,i}$ using two different approaches. Initially a hindered settling model of the form of Equation 8-4 was applied to the data. The viscosity relationships given by Equation 8-5 and Equation 8-6 were both used. In addition a $\cos\theta$ term was included to allow for any inclination away from vertical. This results in the slip velocity models given by Equation 8-16 for the Mooney viscosity relationship and Equation 8-17 for the Brinkman-Roscoe viscosity relationship.

$$v_{slip,i}^{Mny} = v_t\cos\theta\frac{(1-\alpha_{s,i})}{e^{\left[\frac{2.5\alpha_{s,i}}{1-1.63\alpha_{s,i}}\right]}}$$

Equation 8-16

$$v_{slip,i}^{B\text{-}R} = v_t\cos\theta(1-\alpha_{s,i})^{3.5}$$

Equation 8-17

Using these hindered settling models profiles of $v_{slip,i}^{Mny}$ and $v_{slip,i}^{B\text{-}R}$ were calculated for each data-set based on the measured profiles of $\alpha_{s,i}^{probe}$. Then profiles of $u_{w,i}^{Mny}$ and $u_{w,i}^{B\text{-}R}$ were calculated using Equation 1-3 and values of Q_w^{Mny} and $Q_w^{B\text{-}R}$ were calculated using Equation 1-2. Figure 8-2 shows Q_w^{Mny} and $Q_w^{B\text{-}R}$ plotted against Q_w^{ref}. As with Figure 8-1 a solid line has been plotted where $Q_w^{pred} = Q_w^{ref}$.

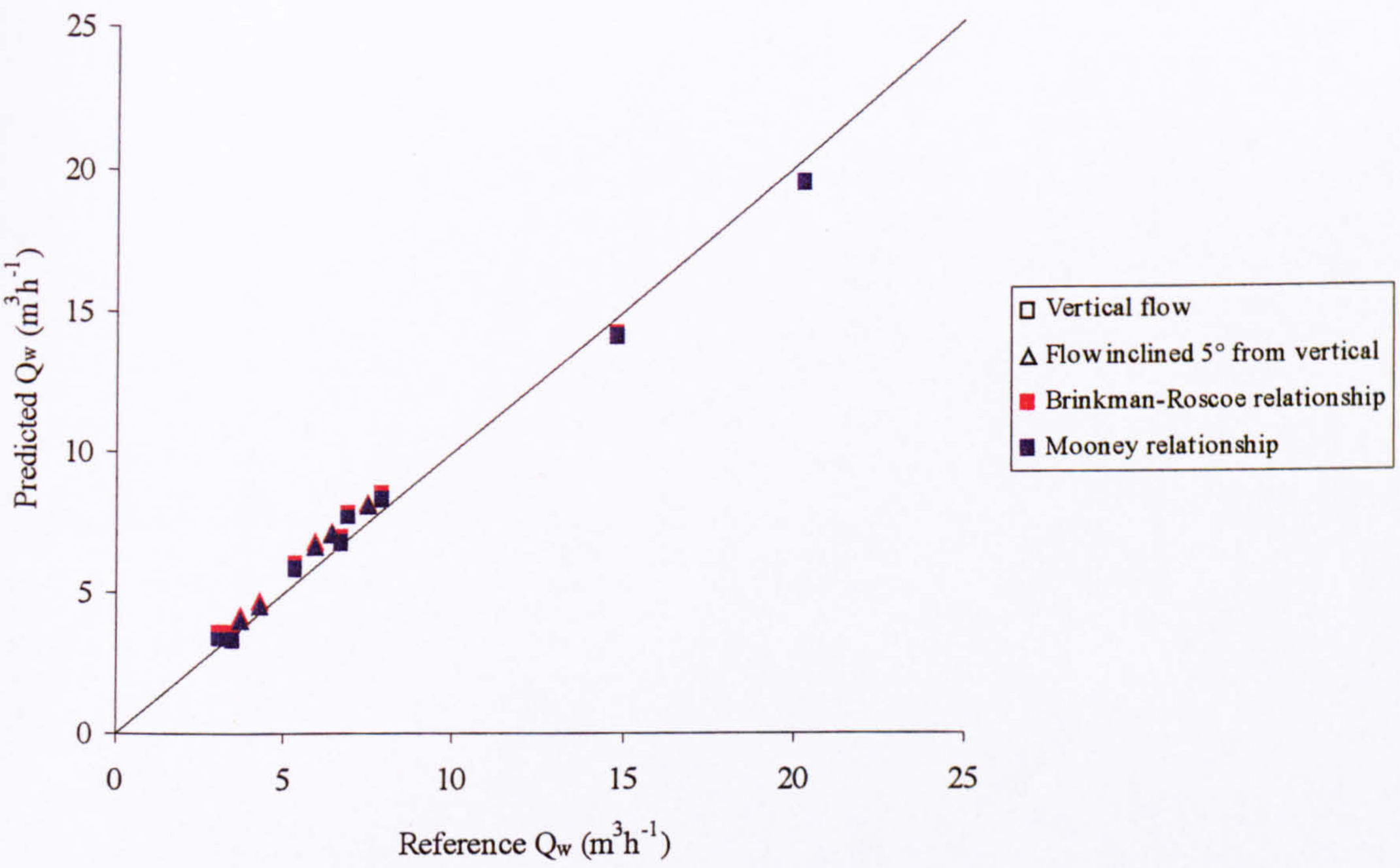

Figure 8-2. Q_w^{Mny} and $Q_w^{B\text{-}R}$ plotted against Q_w^{ref}.

It is clear from Figure 8-2 that both relationships give similar results. The error statistics from each are presented in Table 8-1. In Table 8-1 the error notation is as given by Equation 7-2, Equation 7-3, Equation 7-4 and Equation 7-5. The superscripts ^{Mny} and $^{B\text{-}R}$ denote errors referring to differences between the reference measurements and Q_w^{Mny} and $Q_w^{B\text{-}R}$ respectively.

Table 8-1. Errors in Q_w^{Mny} and $Q_w^{B\text{-}R}$.

		Vertical flow	Flow inclined 5° from vertical		Vertical flow	Flow inclined 5° from vertical
Systematic error	$e_{sys}^{Q_w,Mny}$	2.68%	7.83%	$e_{sys}^{Q_w,B\text{-}R}$	5.97%	10.87%
Random error	$e_{ran}^{Q_w,Mny}$	6.87%	2.97%	$e_{ran}^{Q_w,B\text{-}R}$	7.96%	2.23%
Absolute systematic error	$e_{abs,sys}^{Q_w,Mny}$	$0.05m^3h^{-1}$	$0.45m^3h^{-1}$	$e_{abs,sys}^{Q_w,B\text{-}R}$	$0.20m^3h^{-1}$	$0.60m^3h^{-1}$
Absolute random error	$e_{abs,ran}^{Q_w,Mny}$	$0.54m^3h^{-1}$	$0.23m^3h^{-1}$	$e_{abs,ran}^{Q_w,B\text{-}R}$	$0.58m^3h^{-1}$	$0.20m^3h^{-1}$

It is clear from Table 8-1 that both relationships give better predictions in vertical flow than in flow inclined 5° from vertical. It can also be seen that the Mooney relationship, which accounts for particle collisions, gives better accuracy than the Brinkman-Roscoe relationship. This suggests that particle collisions may be significant in the current flow conditions.

The second approach used to predict $v_{slip,i}$ was to use the model given by Zuber as Equation 8-8. Using this relationship a number of different authors have calculated different values of coefficient q to fit particular flow conditions. In the current investigation an ideal value of q was calculated for each flow condition.

In order to determine the ideal value of q to fit the experimental data in each flow condition a iterative Matlab routine was written. The routine applies a pre-set value of q to each data-point in the flow cross-section. It should be noted that q is assumed to be the same at all points in the flow cross-section. A profile of the predicted local axial slip velocity, $v_{slip,i}^{Zub}$ was then calculated for each flow condition using Equation 8-8 from which a profile of the predicted local axial water velocity, $u_{w,i}^{Zub}$, was then calculated using Equation 1-3. Equation 1-2 was then used to calculate a value of the predicted water volumetric flow rate, Q_w^{Zub}. The routine compared Q_w^{Zub} with Q_w^{ref} and then adjusted the value of q and repeated the procedure.

This loop continued until $Q_w^{Zub} = Q_w^{ref}$. Figure 8-3 shows the resulting values of q plotted against Q_w^{ref}.

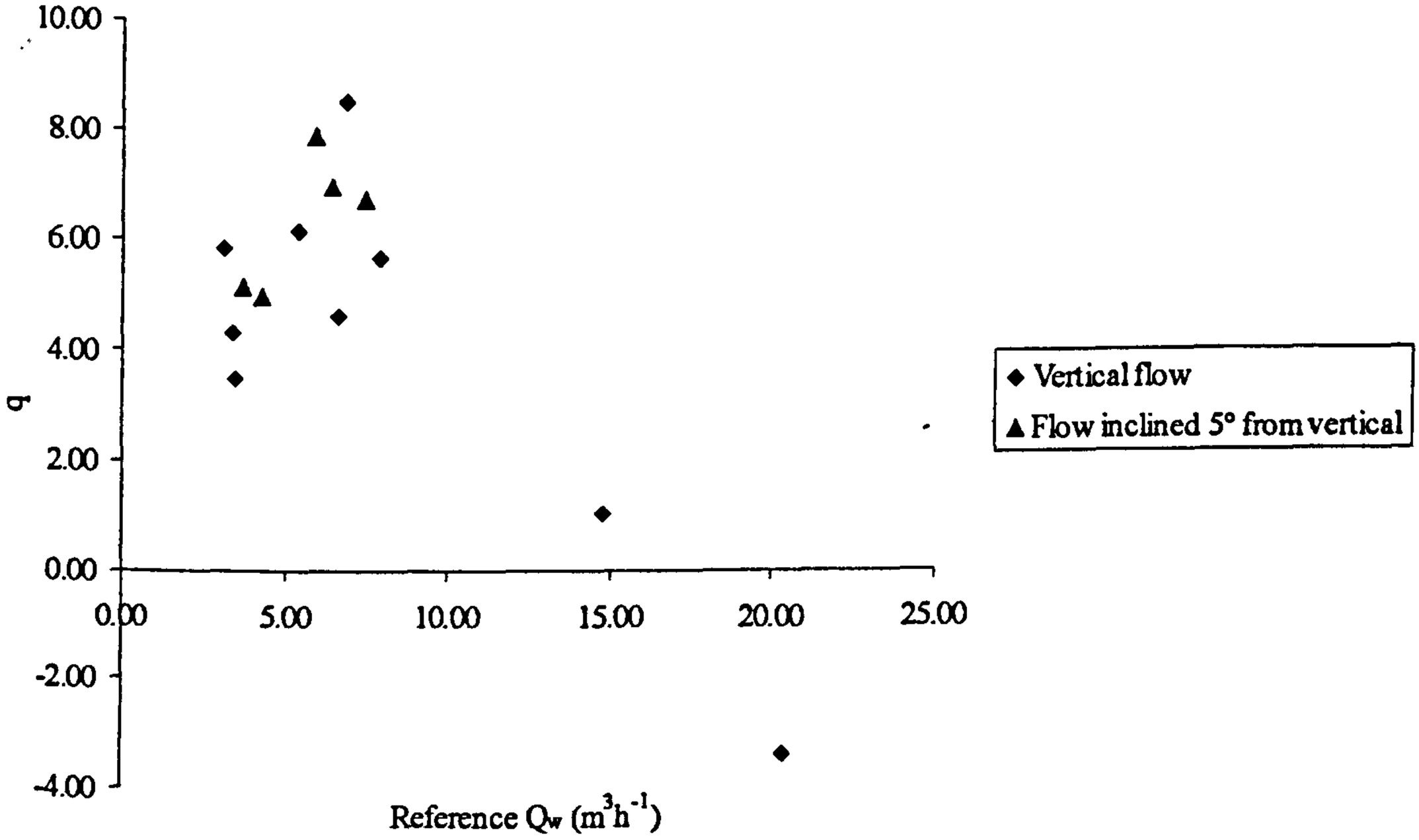

Figure 8-3. Ideal values of coefficient q plotted against Q_w^{ref}.

From Figure 8-3 two observations can be made. First it is clear that there is a significant degree of scatter in the values. This is to be expected considering the errors present in both α_s^{probe} (see Section 7.3.1) and u_s^{probe} (see Section 7.3.2). Second it appears possible to identify a reduction in the value of q as Q_w^{ref} increases. This trend has previously been noted by Shook & Roco [111] (see Section 8.2.1). Unfortunately in the current investigation it is only represented by two flow conditions and it was decided that this was not enough evidence for the trend to be confirmed.

Following examination of these results it was decided that a single average value of q could be used to predict Q_w for the current flow conditions. In this case the mean value of q for all flow conditions is equal to 4.84. Predicted values of the water volumetric flow rate, $Q_w^{q=4.84}$, were calculated using this value of q. The values of $Q_w^{q=4.84}$ and Q_w^{ref} are given in Table 8-2. The error statistics, using the same notation as in Table 8-1, are presented in Table 8-3. An

additional superscript $^{q=4.84}$ denotes that the errors relate to the difference between $Q_w^{q=4.84}$ and Q_w^{ref}.

Table 8-2. $Q_w^{q=4.84}$ and Q_w^{ref} for vertical flow and flow inclined 5° from vertical.

Vertical flow		Flow inclined 5° from vertical	
Q_w^{ref}, (m^3h^{-1})	$Q_w^{q=4.84}$, (m^3h^{-1})	Q_w^{ref}, (m^3h^{-1})	$Q_w^{q=4.84}$, (m^3h^{-1})
3.09	3.30	3.72	3.79
3.41	3.28	4.28	4.31
3.50	3.14	5.89	6.42
5.37	5.65	6.44	6.83
6.69	6.64	7.50	7.85
6.88	7.52		
7.93	8.11		
14.79	13.93		
20.31	19.37		

Table 8-3. Error statistics for $Q_w^{q=4.84}$ for vertical flow and flow inclined 5° from vertical.

		Vertical flow	Flow inclined 5° from vertical
Relative systematic error	$e_{sys}^{Q_w,q=4.84}$	-0.19%	4.46%
Relative random error	$e_{ran}^{Q_w,q=4.84}$	6.53%	3.32%
Absolute systematic error	$e_{abs,sys}^{Q_w,q=4.84}$	$-0.11m^3h^{-1}$	$0.27m^3h^{-1}$
Absolute random error	$e_{abs,ran}^{Q_w,q=4.84}$	$0.53m^3h^{-1}$	$0.22m^3h^{-1}$

From Table 8-3 the Zuber model, given by Equation 8-8 with q=4.84, gives comparable errors to the Zuber model incorporating the Mooney relationship, which is given by Equation 8-16. The errors also compare favourably to the errors achieved in the measurement of Q_s^{probe} (see Section 7.3.3). This suggests that the local probe can be used to measure both Q_s and Q_w within the range of flow conditions reported here in upward flows inclined up to 5° from vertical. It suggests that either the Zuber model incorporating the Mooney relationship (see

Equation 8-16) or the later Zuber model (see Equation 8-11) with a value of q of 4.84 will give comparable accuracies.

8.3.2 Flow inclined at 30° from vertical.

In more highly deviated flows the flow structure is more complicated. A two-dimensional profile across the Z axis (see Figure 7-13) of the solids velocity profile of a flow inclined 30° from vertical from the current investigation is shown in Figure 8-4.

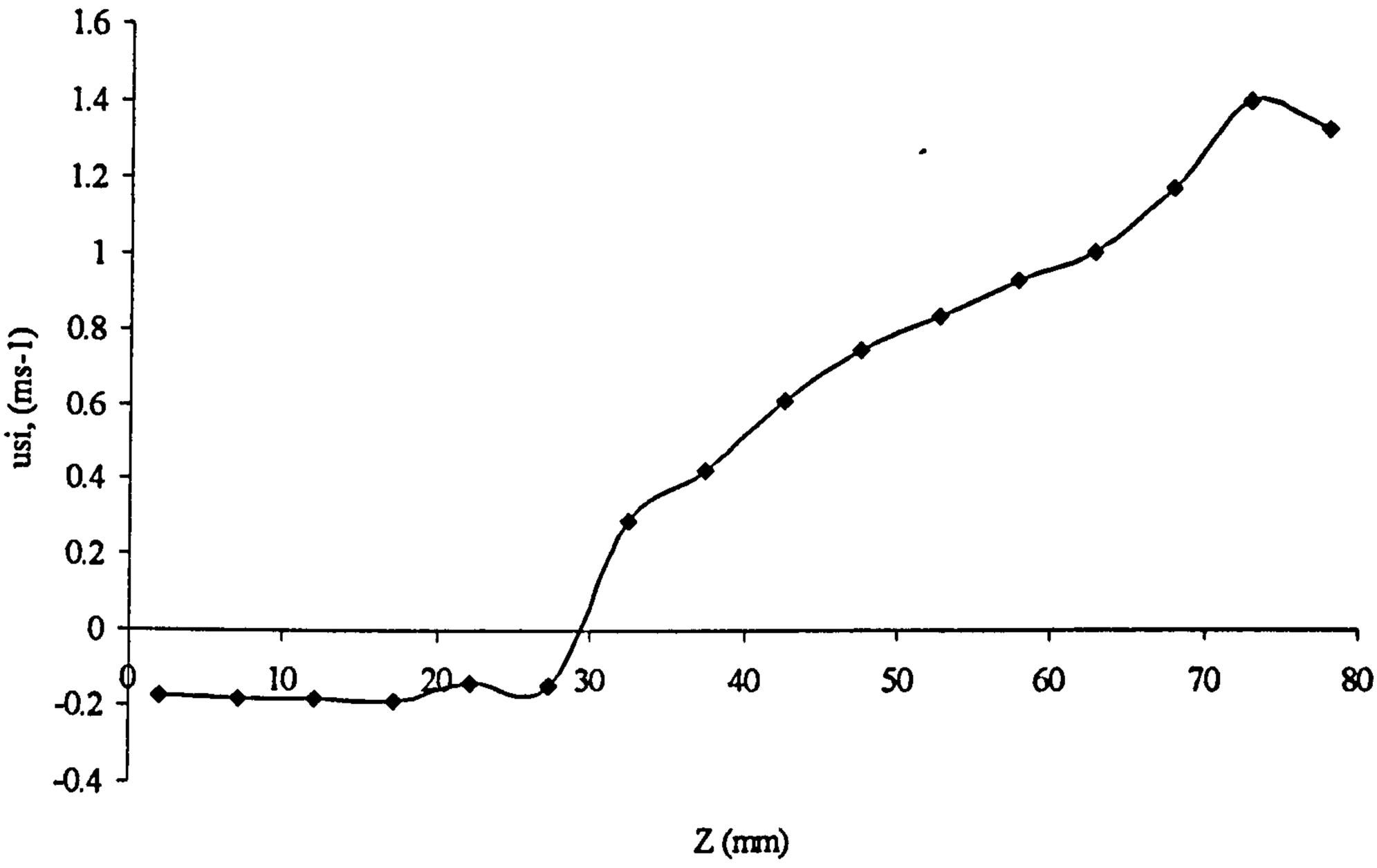

Figure 8-4. Two dimensional profile of $u_{s,i}^{probe}$ for a flow inclined 30° from vertical.

From Figure 8-4 the two-layer structure of the flow can be easily identified. At the low side of the pipe, where, Z is less than 30mm, $u_{s,i}$ is uniform and negative. This is the lower layer where a concentrated bed of solids is flowing down the pipe. For Z greater than 30mm $u_{s,i}$ is positive and a steep gradient of $u_{s,i}$ can be seen. In this region the solids are suspended. In order to predict $v_{slip,i}$ accurately in this two layer structure, and in view of the references cited in Section 8.2.2, it was decided to apply a two layer type slip model.

This was investigated in two ways. Before either method could be attempted the position of the interface of the two layers had to be determined. In order to do this it was assumed that, within a given cross-section, $u_{s,i}$ and $\alpha_{s,i}$ only vary across the Z axis of the pipe (see Figure 7-13). This assumption has been made by a wide range of previous researchers (see Section

7.2). If the flow profiles presented in Section 7.2 are examined it can also be seen that this assumption is reasonable. Given this assumption, the point at which the interface exists was identified for each flow condition from graphs similar to Figure 8-4. From Figure 7-1 it can be seen that it is not possible to assemble a chord across the pipe at constant Z using the measured data-points only. Therefore the flow cross section was interpolated into a large number of points, similar to the interpolated grid shown in Figure 7-1 so that the interfacial line could be positioned accurately at constant Z. It was now possible to accurately apply different slip models to the different layers in the flow.

The first model used (model A) assumes that the flow in the upper layer can be described using the same slip model as used for vertical flows and fully suspended inclined flows, i.e. a Zuber type model as given by Equation 8-8. Following the modelling of vertical flows and flows inclined 5° from vertical the value of q was set as 4.84. The model was then used to calculate profiles of $v_{slip,i}^{A,upper}$ from which profiles of the local axial water velocity in the upper layer, $u_{w,i}^{A,upper}$, were calculated using Equation 1-3. From these it was possible to calculate the water volumetric flow rate in the upper layer, $Q_w^{A,upper}$, using Equation 1-2. It was now assumed that the local axial slip velocity in the lower layer, $v_{slip,i}^{A,lower}$, was constant at all positions. This assumption was made because $u_{s,i}$ was relatively constant in the lower layer. A Matlab routine was written to increment the value of $v_{slip,i}^{A,lower}$ and therefore calculate values of the local axial water velocity in the lower layer, $u_{w,i}^{A,lower}$, and therefore values of the water volumetric flow rate in the lower layer, $Q_w^{A,lowerr}$, and thus the total water volumetric rate, $Q_w^{A,total}$, until $Q_w^{A,total}$ was equal to Q_w^{ref}. The resulting "ideal" values of $v_{slip,i}^{A,lower}$ for each flow condition are shown in Figure 8-5.

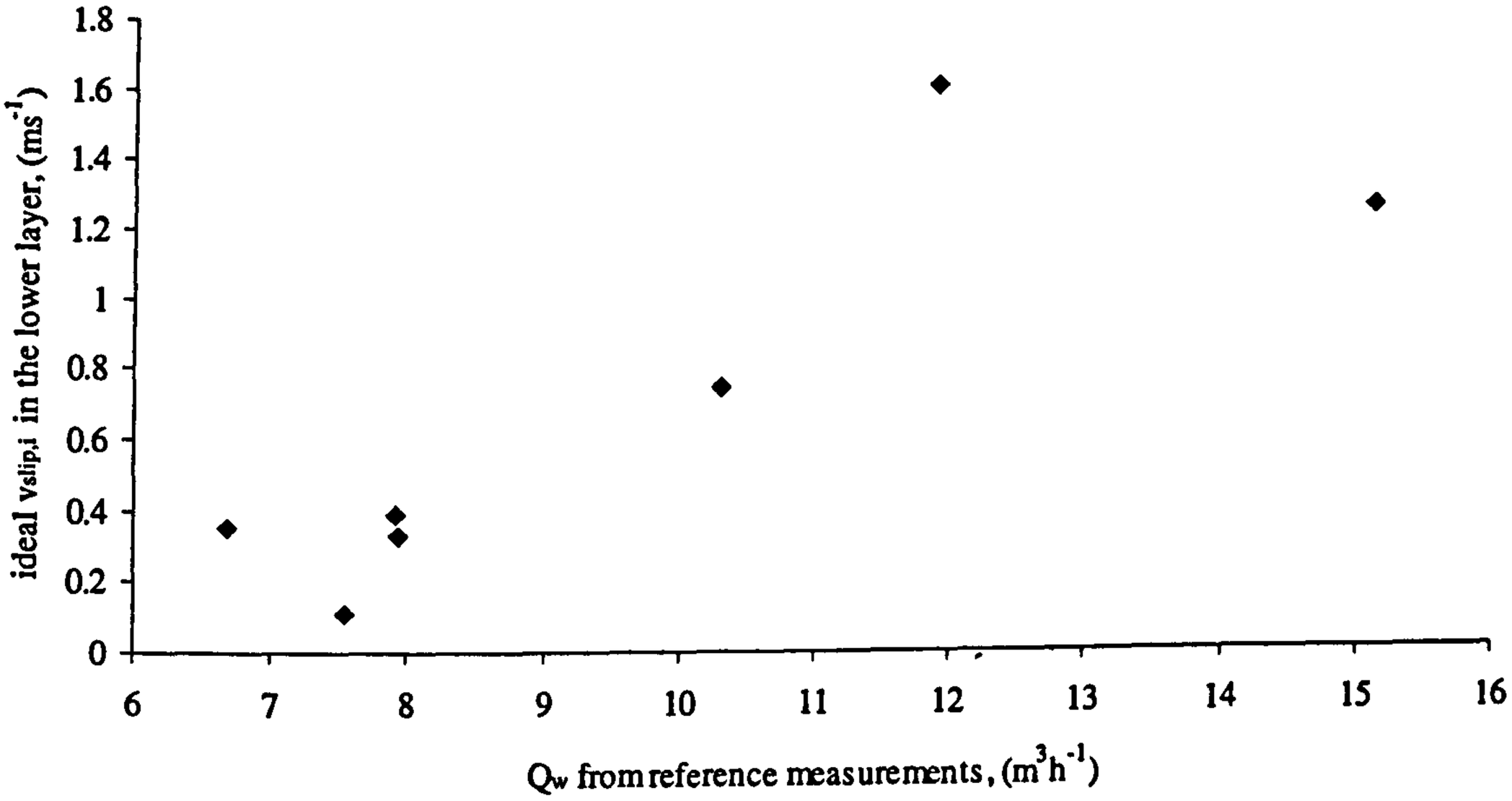

Figure 8-5. Ideal values of $v_{slip,i}^{A,lower}$ for flow inclined 30° from vertical.

From Figure 8-5 the mean value of $v_{slip,i}^{A,lower}$ is 0.68ms^{-1} although it is clear that there is substantial scatter about this value. It appears that $v_{slip,i}^{A,lower}$ tends to increase as Q_w^{ref} increases. This would suggest that $u_{w,i}^{lower}$ would increase substantially more than $u_{s,i}^{lower}$ as Q_w^{ref} increased. However there are too few data-points to confirm this trend.

The second model used (model B) assumed that the local axial slip velocity in the lower layer, $v_{slip,i}^{lower}$, was approximately equal to 0.18ms^{-1}. This assumption was made because Figure 8-1 shows that the average value of $v_{slip,i}$ must be close to the terminal velocity, which is approximately equal to 0.18ms^{-1} for this angle of inclination. As the majority of the solids are present in the sedimented lower layer it is reasonable to assume that this is where this high slip exists. Using this slip value in Equation 1-3 a profile of the axial water velocity in the lower layer, $u_{w,i}^{B,lower}$, was calculated from which the water volumetric flow rate in the lower layer, $Q_w^{B,lower}$, was calculated using Equation 1-2. It was now assumed that the Zuber model, see Equation 8-8, was valid in the upper layer. A Matlab routine was written to increment the value of $\bar{q}$ in the upper layer, $q^{B,upper}$, and therefore calculate profiles of the local axial water velocity in the upper layer, $u_{w,i}^{B,upper}$, and therefore values of the water volumetric flow rate in

the upper layer, $Q_w^{B,upper}$, and thus the total water volumetric flow rate, $Q_w^{B,total}$, until $Q_w^{B,total}$ was equal to Q_w^{ref}. The resulting "ideal" values of $q^{B,upper}$ are presented in Figure 8-6.

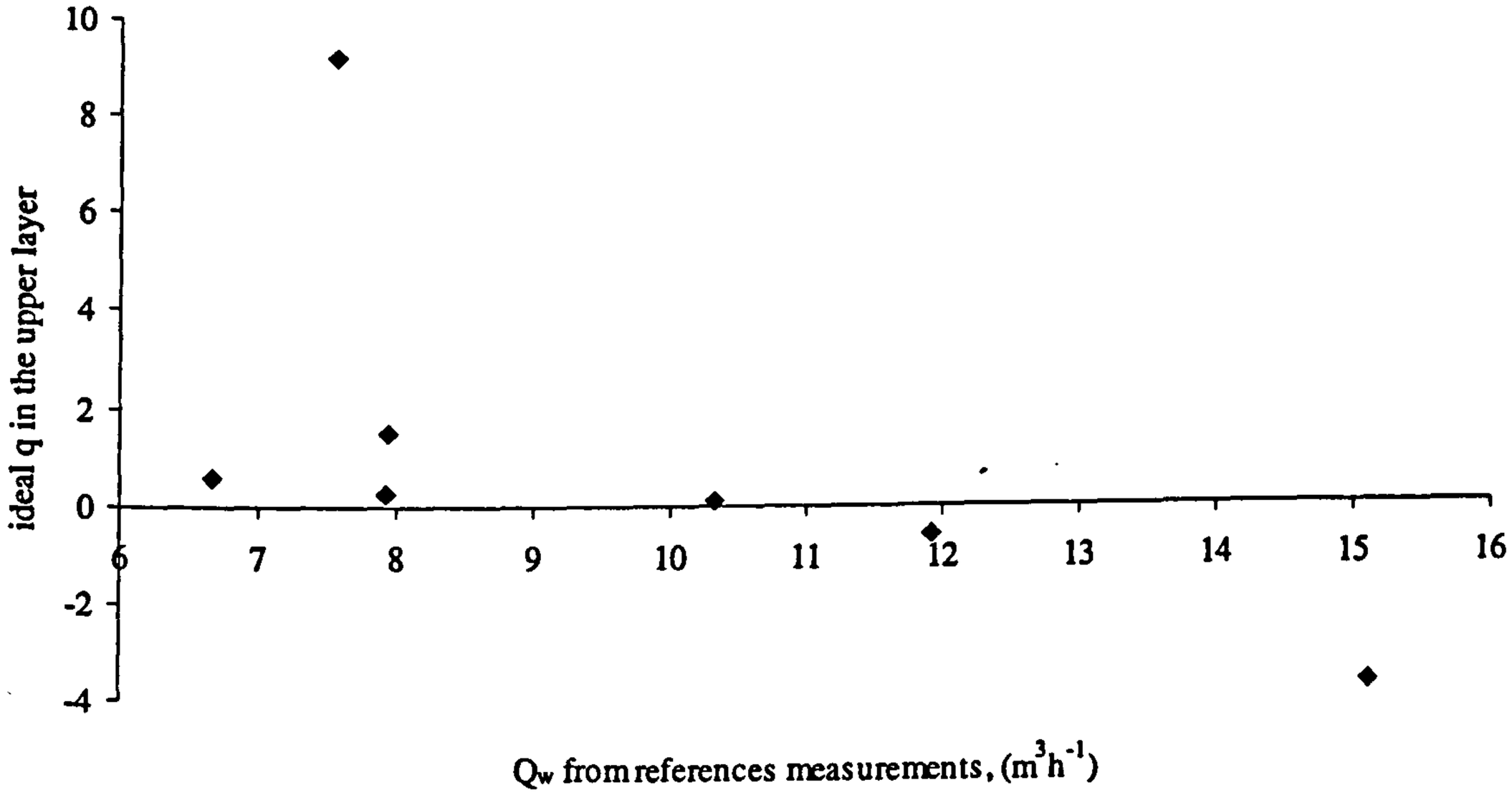

Figure 8-6. Ideal values of q in the upper layer predicted using model B.

From Figure 8-6 the mean value of $q^{B,upper}$ in the upper layer is 1.05 although it is clear that there is substantial scatter about this value. It appears that $q^{B,upper}$ tends to decrease as Q_w^{ref} increases. This would agree with the analysis of Shook & Roco [111] and would also agree with the possible trend identified for vertical flows and flows inclined at 5° from vertical.

In order to compare the two models values of $Q_w^{A,total}$ were calculated using the mean value of $v_{slip,i}^{A,lower}$ given by Model A. Also values of $Q_w^{B,total}$ were calculated using the mean value of $q^{B,upper}$ given by Model B. The values of $Q_w^{A,total}$ and $Q_w^{B,total}$ are given in Table 8-4. The error values between $Q_w^{A,total}$, $Q_w^{B,total}$ and Q_w^{ref} using the same notation as in Table 8-1 are given in Table 8-5. It should be noted that the superscript A denotes errors between $Q_w^{A,total}$ and Q_w^{ref} whilst the superscript B denotes errors between $Q_w^{B,total}$ and Q_w^{ref}.

Table 8-4. $Q_w^{pred,A}$ and $Q_w^{pred,B}$ for flow inclined 30° from vertical.

Q_w^{ref}, (m^3h^{-1})	$Q_w^{pred,A}$, (m^3h^{-1})	$Q_w^{pred,B}$, (m^3h^{-1})
7.92	9.41	7.57
15.12	12.59	11.18
11.92	10.84	11.15
7.55	10.14	8.68
10.33	10.19	9.94
6.67	8.46	6.48
7.94	9.46	8.12

Table 8-5. Error statistics for $Q_w^{pred,A}$ and $Q_w^{pred,B}$ for flow inclined 30° from vertical.

		Flow inclined 30° from vertical		Flow inclined 30° from vertical
Systematic error	$e_{sys}^{Q_w,A}$	10.28%	$e_{sys}^{Q_w,B}$	-3.76%
Random error	$e_{ran}^{Q_w,A}$	19.33%	$e_{ran}^{Q_w,B}$	12.20%
Absolute systematic error	$e_{abs,sys}^{Q_w,A}$	$0.52m^3h^{-1}$	$e_{abs,sys}^{Q_w,B}$	$-0.62m^3h^{-1}$
Absolute random error	$e_{abs,ran}^{Q_w,A}$	$1.83m^3h^{-1}$	$e_{abs,ran}^{Q_w,B}$	$1.58m^3h^{-1}$

From Table 8-5 the absolute errors shown by both models are comparable. However the relative errors given by Model B are significantly smaller than those from Model A. Additionally the possible trend identified in the variation of $q^{B,upper}$ agrees with that identified in vertical flows and flows inclined 5° from vertical. This trend also agrees with the published analysis of Shook & Roco [111]. For these reasons it was decided that Model B, where the local axial slip velocity in the lower layer was set as $0.18ms^{-1}$ and the value of q used in the Zuber hindered settling model in the upper layer was set as 1.05, would be the best two-layer slip model to use for these flow conditions. The errors reported in Table 8-5 are larger than those reported for predicted values of Q_w in vertical flows and flows inclined 5° from vertical. However they are still comparable to the errors in measurement of Q_s for flows inclined 30° from vertical.

9. Conclusions.

The current investigation has achieved the primary objectives listed in Chapter 1. An optimised local conductivity probe has been developed that is capable of acquiring measurements of the local solids volume fraction, $\alpha_{s,i}$, and the local solids axial velocity, $u_{s,i}$, in non-uniform solids-liquid flows. This device is configured as a 6-electrode Separated Excitation and Measurement Method (SEMM) array. In addition electronic measurement hardware and a computer controlled two-axis positioning and data acquisition system have been developed. Measurements of the area averaged solids volume fraction, α_s, the area averaged solids axial velocity, u_s, and the solids volumetric flow rate, Q_s, have been calculated from measurements acquired by the local probe. Finally flow modelling has been carried out that has allowed the liquid volumetric flow rate, Q_w, to be predicted.

In addition the multiphase flow loop at the University of Huddersfield has been developed to allow these flows to be established. Reference measurement devices have been integrated and calibrated which allow reference measurements of the mean solids volume fraction, α_s, the mean axial solids velocity, u_s, the solids volumetric flow rate, Q_s and the water volumetric flow rate, Q_w, to be measured.

The measurements acquired by the local probe have been used to qualitatively validate measurements of the local solids volume fraction, $\alpha_{s,i}$ and the local axial solids velocity, $u_{s,i}$, acquired using a dual-plane Electrical Resistance Tomography (ERT) system developed as part of a parallel investigation. The measurements acquired by the local probe and by the reference measurement devices have been used to validate the measurements of the mean solids volume fraction, α_s, the mean axial solids velocity, u_s and the solids volumetric flow rate, Q_s obtained from the ERT data.

In addition to achieving the primary objectives a number of specific conclusions have been reached as a result of the optimisation of the local probe, and as a result of experimental comparisons between it, the dual-plane ERT system and the reference measurement systems. These are detailed in the following sections.

9.1 Conclusions from the local probe optimisation.

In order to optimise the local probe for the current investigation finite element modelling and experimental static testing was carried out. As a result of this work a number of specific conclusions were reached with regard to different configurations of local SEMM conductivity probe. These are detailed below:

- 4-electrode SEMM arrays

  The finite element modelling and experimental static testing showed that the sensitivity of a 4-electrode SEMM array can be optimised for the measurement of the local solids volume fraction, $\alpha_{s,i}$. In order to do this the combination of field electrode separation, f, and the sense electrode spacing, s_α, must be carefully selected. The modelling showed that a direct relationship probably exists between f and s_α. However the quantity of modelling carried out in the current investigation was not adequate to calculate it.

- 6-electrode SEMM arrays

  The finite element modelling and experimental static testing showed that a 6-electrode SEMM array can be optimised for the measurement of the local axial solids velocity, $u_{s,i}$, and it showed that operating the two axially displaced sensors simultaneously can enhance their sensitivity for this measurement. In order to optimise the array the field electrode separation, f, must be minimised with respect to the sensor separation, j. The sense electrode separation, s_v, is not critical. It was also shown that a 6-electrode SEMM array can be configured to acquire simultaneous measurements of both $\alpha_{s,i}$ and $u_{s,i}$ from sensors optimised for this purpose. In this case f must be minimised with respect to j, whilst the combination of f and s_α must be carefully selected.

- 8-electrode probes

  The finite element modelling showed that an 8-electrode probe can be optimised for the measurement of the local axial solids velocity, $u_{s,i}$ and it showed that operating the two axially displaced sensors simultaneously can enhance their sensitivity for this measurement. In order to optimise the array the sensor separation, j, and the sense electrode separation, s_v, should be minimised. These conclusions were not validated by experimental static testing.

9.2 Conclusions from experimental testing in the flow loop.

Following experimental testing of both the local probe system and the dual-plane ERT system in the University of Huddersfield multiphase flow loop a number of conclusions were made regarding both systems and the reference measurement devices. These are detailed below.

- The local probe system

  The profiles of local solids volume fraction, $\alpha_{s,i}$, and local axial solids velocity, $u_{s,i}$, suggested that the local probe has a higher spatial resolution than the ERT system used in the current investigation. When compared with the reference measurement systems the local probe tended to underestimate the mean solids volume fraction, α_s. It was suggested that this could either be caused by the effect of a boundary layer around the probe or alternatively by inherent errors in the reference measurement of mean solids volume fraction, α_s, which was acquired using a differential pressure measurement corrected for frictional pressure losses. When compared with the reference measurements the local probe tended to overestimate the mean axial solids velocity, u_s. It was suggested that this was a result of an inadequate measurement of the effective sensor separation, L. Application of a correction appeared to support this. When compared with reference measurements integrated data from the local probe gave generally good estimates of Q_s although significant scatter was identifiable. The mean differences that were achieved between the integrated local probe values and the reference measurements are given below.

Angle of inclination from vertical	0°	5°	30°
Mean percentage difference between the integrated local probe values and the reference measurements of			
Mean solids volume fraction	-11.43%	-27.80%	-6.40%
Mean axial solids velocity	19.45%	23.87%	-1.56%
Solids volumetric flow rate	5.76%	-10.83%	-20.34%

Applying simple corrections for the error sources suggested above resulted in a reduction in these mean percentage differences. For all flow inclinations combined the mean solids volume fraction was reduced to 3.66%, the mean axial solids velocity error was reduced to 2.64% and the solids volumetric flow rate error was reduced to 6.03%.

Flow modelling showed that the water volumetric flow rate, Q_w, could be predicted to the same degree of accuracy as the solids volumetric flow rate, Q_s, could be measured. It was found that a hindered settling model of the type proposed by Zuber [109] with a value of coefficient q of 4.84 allowed the water volumetric flow rate to be predicted to an accuracy of –0.19% in vertical flow, and 4.46% in upward flow inclined 5° from vertical. In upward flows inclined 30° from vertical where a solids bed formed in the pipe it was found that a two layer model predicted the water volumetric flow rate to an accuracy of –3.76%. In this model the axial slip velocity was set at $0.18ms^{-1}$ in the solids bed and a Zuber type hindered settling model was applied in the suspended layer with a value of coefficient q of 1.05.

- The ERT system

  Although the current investigation was not directly concerned with the ERT system some conclusions were drawn from the experimental data presented. The profiles of local solids volume fraction, $\alpha_{s,i}$, and local axial solids velocity, $u_{s,i}$, suggested that the ERT system had a lower spatial resolution than the local probe. They also suggested that the weighting function applied as part of the reconstruction of the local solids volume fraction profile could be overcompensating for the sensitivity deficiency of the device at the centre of the pipe and masking features of the profile. It was suggested that this could also be responsible for the fact that the ERT system tended to overestimate the mean solids volume fraction when compared to the reference measurements. The effect of altering the plane separation was clear from the results which showed that the current system is not capable of measuring the mean axial solids velocity in highly deviated flows. This is because the local velocities in these flows can be very high. When compared with the reference measurements the ERT system tended to overestimate the solids volumetric flow rate although this error was reduced by reducing the plane separation. The mean errors that were found between the integrated ERT values and the reference measurements at each plane separation are given below.

Angle of inclination from vertical	0°	5°	30°
Mean percentage difference between the integrated local probe values and the reference measurements of			
Mean solids volume fraction	30.27%	-6.37%	-7.25%
Mean axial solids velocity, plane separation = 2cm	72.88%	N/A	N/A
Mean axial solids velocity, plane separation = 3cm	9.57%	21.87%	38.37%
Mean axial solids velocity, plane separation = 5cm	12.21%	12.20%	N/A
Solids volumetric flow rate, plane separation = 2cm	162.12%	N/A	N/A
Solids volumetric flow rate, plane separation = 3cm	12.03%	18.43%	24.81%
Solids volumetric flow rate, plane separation = 5cm	11.21%	22.51%	N/A

- The reference measurement systems

  Generally the reference measurement systems performed well. However it was suggested that the measurement of the mean solids volume fraction using a differential pressure measurement corrected for frictional pressure losses was unreliable. This is most likely due to an incomplete understanding of the frictional pressure losses in the particular solids-liquid flows established in the current investigation and the extent to which the pipe walls can support the solids load.

10. Further work.

As a result of the current investigation, and the conclusions reached, a number of suggestions for further work can be made. These are detailed below:

- Construction of the local probe

  A method of constructing the local probe to higher tolerances could be developed. The manufacturing method used in the current investigation allowed large numbers of probes to be manufactured quickly and at a low cost. Using the design guidelines developed in the current investigation a single optimised probe would be viable at a higher unit cost.

- Local probe optimisation.

  The local probe finite element modelling could be extended to enable the calculation of an optimised relationship between the field electrode separation and the sense electrode separation of a 4-electrode SEMM array for measurement of local solids volume fraction. Insufficient finite element modelling was carried out in the current investigation to allow this. A more detailed understanding of the behaviour of the array could simplify scaling up of the device for other applications.

  The experimental static testing could be extended to investigate the effect on the response of the local probe of a single particle. This would allow a more accurate understanding of the probe's behaviour and could improve the optimisation. The static testing carried out in the current investigation was not an exact simulation of the experimental flow conditions.

  The experimental static testing could also be extended to allow a more accurate measurement of the effective sensor separation between sensors A and B to be made. This would increase the accuracy of the measurements of the local axial solids velocity that could be made by the local probe.

- Experimental use of the local probe system.

  Experimental investigation of the flow of a solids-liquid mixture around the probe could be carried out. This would allow the quantification of any boundary layer effects which

could increase the accuracy of the measurement of local solids volume fraction by the local probe.

- Reference measurement devices.

  An investigation of the relationship between the mean solids volume fraction and the pressure gradient in the working section could be carried out. This could quantify the frictional pressure losses that arise from particle-particle and particle-wall interactions. It could also investigate the extent to which the solids are supported by the pipe wall. The effects of variables, such as the mean solids volume fraction, the mean axial solids velocity, the flow Reynolds number and the inclination angle on these pressure losses could be determined. This would allow more accurate reference measurements to be acquired.

- The ERT system

  A detailed investigation of the effect of the weighting function applied during reconstruction of the images could be carried out. This could increase the accuracy of the profiles of the local solids volume fraction obtained by the system. Development of higher speed ERT systems could be carried that would allow the measurement of local axial solids velocity profiles in inclined flows with high axial velocities to be carried out.

- Flow modelling

  The improvement of both hindered settling models and two-layer models could be investigated. In particular this could involve the development of more generic models that could be applied to a wider range of flow conditions. As part of this work an investigation could be carried to measure local axial slip velocities in vertical and inclined solids-liquid flow.

References

1. PRIDDY W.J. BP multiphase meter application experience. *Measurement & Control*, vol. 32, February 1999, pp. 9-15.
2. THORN R., JOHANSEN G.A., HAMMER E.A. Three-phase flow measurement in the offshore oil industry - is there a place for process tomography? *Proceedings of the 1st World Congress on Industrial Process. Tomography*, Buxton, U.K., 1999, pp. 228-235.
3. JAMIESON A.W. Multiphase metering – the challenge of implementation. *Measurement & Control*, vol. 32, February 1999, pp.5-9.
4. AKAGAWA K., FUJII T., TAKENAKA N. The effects of the density ratio in a vertically rising solid-liquid two-phase flow. *International Conference on the Mechanics of Two-Phase Flows*. Taipei, Taiwan, 1989, pp. 203-208.
5. CONSTANTINI R., PARSONS R.H. The economic and environmental impact of long distance slurry pipelines. *Hydrotransport 3, Proceedings of the 3rd International Conference on the Hydraulic Transport of Solids in Pipes*, Golden, Colorado, U.S.A., 1974, pp. K1-K12.
6. GOOSEN P.E., COOKE R. Design and construction of the Noordhoek kaolin slurry pipeline. *Hydrotransport 13, Proceedings of the 13th International Conference on Slurry Handling and Pipeline Transport,* Johannesburg, South Africa, 1996, pp. 405-417.
7. KAKKA R.S. Review of instruments for measuring flow rate and solids concentration in steelworks slurry pipeline. *Hydrotransport 3, Proceedings of the 3rd International Conference on the Hydraulic Transport of Solids in Pipes*, Golden, Colorado, U.S.A., 1974, pp. F81-F92.
8. LJUBICIC B., BUKUROV Z., CVIJANOVIC P., STAJNER K. Coal-dredging efficiency – The underwater mining experience at Kovin coal mine. *Hydrotransport 13, Proceedings of the 13th International Conference on Slurry Handling and Pipeline Transport,* Johannesburg, South Africa, 1996, pp. 391-404.
9. CHU C.P., LEE D.J. Moisture distribution in sludge: Effects of polymer conditioning. *ASCE Journal of Environmental Engineering*, vol. 125, no. 4, 1999, pp. 340-345.
10. ABU-ORF M., DENTEL S.K. Polymer dose assessment using the streaming current detector. *Water Environment Research*, vol. 69, no. 6, 1997, pp. 1075-1085.
11. CHOU S., LIN S., HUANG C. Application of optical monitor to evaluate the coagulation of pulp wastewater. *Proceedings of the 7th International Workshop on*

Instrumentation, Control and Automation of Water and Wastewater Treatment and Transport Systems, Brighton, U.K., 1997, pp. 162-171.

12. GRIEVE B.D., DYAKOWSKI T., MANN R., WANG M. Interfacing of EIT into an industrial pressure filter – a practical example. *Proceedings of the 1st World Congress on Industrial Process Tomography*, Buxton, U.K., 1999, pp. 113-119.

13. WEI F., LIN H., CHENG Y., WANG Z., JIN Y. Profiles of particle velocity and solids fraction in a high-density riser. *Powder Technology*, vol. 100, 1998, pp. 183-189.

14. YANG H., GAUTAM M. Influence of annulus reflux on the pressure drop and voidage profile along the riser of a circulating fluidised bed. *Proceedings of the ASME/JSME Fluids Engineering and Laser Anemometry Conference and Exhibition*, 1999, pp. 233-240.

15. BOND J., CULLIVAN J.C., CLIMPSON N., DYAKOWSKI T., FAULKS I., JIA X., KOSTUCH J.A., PAYTON D., WANG M., WANG S.J., WEST R.M., WILLIAMS R.A. Industrial monitoring of hydrocyclone operation using electrical resistance tomography. *Proceedings of the 1st World Congress on Industrial Process. Tomography*, Buxton, U.K., 1999, pp. 102-112.

16. SCHÜLLER R.B., HALLERAKER M., ENGEBRETSEN B. Advanced profile gauge for multiphase systems. *Proceedings of the 1st World Congress on Industrial Process. Tomography*, Buxton, U.K., 1999, pp. 126-139.

17. HULBERT M.H., LAMBERT D.N., BENNETT R.H., FREELAND G.L., BURNS J.T., SAWYER W.B., FIELD P. In situ electrical resistivity measurements of calcareous sediments. *ASTM Special Publication STM777*, 1982, pp. 414-428.

18. LAUER-LEREDDE C., PEZARD P.A., DEKEYSER I. FICUS, a new in-situ probe for resistivity measurements in unconsolidated marine sediments. *Marine Geophysical Researches*, vol. 20, no. 2, 1998, pp. 95-107.

19. RIDD P.V. A sediment level sensor for erosion and siltation detection. *Estuarine, Coastal and Shelf Science*, vol. 35, 1992, pp. 353-362.

20. GRIFFITHS D.H., KING R.F. Applied geophysics for geologists and engineers. *Pergamon Press*, Oxford, 2nd edition, 1983.

21. LAGACE P.J., FORTIN J., CRAINIC, E.D. Interpretation of resistivity sounding measurements in N-layer soil using electrostatic images. *IEEE Transactions on Power Delivery*, vol. 11, no. 3, 1996, pp. 1349-1354.

22. BINLEY A., DAILY W., RAMIREZ A. Detecting leaks from waste storage ponds using electrical tomographic methods. *Proceedings of the 1st World Congress on Industrial Process Tomography*, Buxton, U.K., 1999, pp. 6-13.

23. JORDANA J., GASULLA M., PALLÁS-ARENY R. Leakage detection in buried pipes by electrical resistance imaging. *Proceedings of the 1st World Congress on Industrial Process Tomography*, Buxton, U.K., 1999, pp. 28-34.

24. CHAOUKI J., LARACHI F., DUDUKOVIC M.P. Noninvasive tomographic and velocimetric monitoring of multiphase flows. *Industrial and Engineering Chemistry Research*, vol. 36, no. 11, 1997, pp. 4476-4503

25. SCARLETT B., GRIMLEY A. Particle velocity and concentration profiles during hydraulic transport in a circular pipe. *Hydrotransport 3, Proceedings of the 3rd International Conference on the Hydraulic Transport of Solids in Pipes*, Golden, Colorado, U.S.A., 1974, pp. D23-D37.

26. GUNN D.J., AL-DOORI H.H. The measurement of bubble flows in fluidised beds by electrical probe. *International Journal of Multiphase Flow*, vol. 11, no. 4, 1985, pp. 535-551.

27. POLONSKY S., BARNEA D., SHEMER L. Experimental study of the motion of an elongated bubble by means of image processing technique. *Development of Measuring Techniques for Multiphase Flows, Proceedings of the 2nd International Symposium on Measuring Techniques for Multiphase Flows*, Beijing, China, 1998, pp. 251-256.

28. YAMAMOTO F., OHTA J., MURAI Y., SONG X.Q. PIV Measurement of Multiphase Flows. *Development of Measuring Techniques for Multiphase Flows, Proceedings of the 2nd International Symposium on Measuring Techniques for Multiphase Flows*, Beijing, China, 1998, pp. 3-20.

29. HASSAN Y., BLANCHAT T. Full-field bubbly flow velocity measurements by digital image pulsed laser velocimetry. *Experiments in Fluids*, vol. 11, 1991, pp.293-301.

30. JONES O.C., DELHAYE J-M. Transient and statistical measurement techniques for two-phase flows – a critical review. *International Journal of Multiphase Flow*, vol. 3, 1976, pp.89-116.

31. SHENG Y.Y., IRONS G.A. A combined laser doppler anemometry and electrical probe diagnostic for bubbly two-phase flow. *International Journal of Multiphase Flow*, vol. 17, no. 5, 1991, pp. 585-598.

32 . MARIÉ J.L. Investigation of two-phase bubbly flows using laser doppler anemometry. *Physicochemical Hydrodynamics*, vol. 4, no. 2, 1983, pp. 103-118.

33 . CHEN R.C., KADAMBI J.R. Experimental and numerical studies of solid-liquid pipe flow. *Proceedings of the ASME Fluids Engineering Division*, vol. 189, 1994, pp. 123-135.

34 . YIANNESKIS M., WHITELAW J.H. Velocity characteristics of pipe and jet flows with high particle concentration. *Proceedings of the ASME Energy Sources Technology Conference*, 1984, pp. 12-15.

35 . MENDES DE MOURA L.F., MARVILLET C. Local measurements in gas-liquid two-phase flows: A review of different techniques. *Experimental and Numerical Flow Visualisation and Laser Anemometry, Proceedings of the ASME Fluids Engineering Division Conference*, vol. 239, no. 4, 1996, pp. 363-370.

36 . CARTELLIER A., ACHARD J.L. Local phase detection probes in fluid/fluid two-phase flows. *Review of Scientific Instrumentation*, vol. 62, no.2, 1991, pp. 279-303.

37 . TALLON S., DAVIES C.E., BARRY B. Slip velocity and axial dispersion measurements in a gas-solid pipeline using particle tracer analysis. *Powder Technology*, vol. 99, 1998, pp. 125-131.

38 . MILLER A., GIDASPOW D. Dense, vertical gas-solid flow in a pipe. *AIChE Journal*, vol. 38, no. 11, 1992, pp. 1801-1815.

39 . NASR-EL-DIN H., SHOOK C.A. Sampling from slurry pipelines: Thick walled and straight probes. *Journal of Pipelines*, vol. 5, 1985, pp. 113-124.

40 . RAO C.S., DUKLER A.E. The isokinetic-momentum probe. A new technique for measurement of local voids and velocities in flow of dispersions. *Industrial and Engineering Chemistry Fundamentals*, vol. 10, no. 3, 1971, pp. 520-526.

41 . CECCIO S.L., GEORGE D.L. A review of electrical impedance techniques for the measurement of multiphase flows. *Journal of Fluids Engineering, Transactions of the ASME*, vol. 118, June 1996, pp. 391-399.

42 . ANGELI P., HEWITT G.F. Phase distribution measurements in liquid-liquid pipeline flows using an impedance probe. *Proceedings of the ASME Heat Transfer Division*, vol. 334, no. 3, 1996, pp.149-156.

43 . VIGNEAUX P., CHENAIS P., HULIN J.P. Liquid-liquid flows in an inclined pipe. *AIChE Journal*, vol. 34, no. 5, 1988, pp. 781-789.

44 . CLARK N.N., SEISS R., TURTON R. Probe measurements in gas-liquid systems. *Flow Measurement & Instrumentation*, vol. 3, no. 1, 1992, pp. 17-23.

45 . TEYSSEDOU A., TAPUCU A., LORTIE M. Impedance probe to measure local void fraction profiles. *Review of Scientific Instrumentation*, vol. 59, no. 4, 1988, pp. 631-639.

46 . THANG N.T., DAVIS M.R. The structure of bubbly flow through venturis. *International Journal of Multiphase Flow*, vol. 5, no. 1, 1979, pp. 17-37.

47 . VAN DER WELLE R. Void fraction, bubble velocity and bubble size in two-phase flow. *International Journal of Multiphase Flow*, vol. 11, no. 3, 1985, pp. 317-345.

48 . REVANKAR S.T., ISHII M. Theory and measurement of local interfacial area using a four sensor probe in two-phase flow. *International Journal of Heat and Mass Transfer*, vol. 36, no. 12, 1993, pp. 2997-3007.

49 . SERIZAWA A., KATAOKA I., MICHIYOSHI I. Turbulence structure of air-water bubbly flow – 1. Measuring techniques. *International Journal of Multiphase Flow*, vol. 2, no. 3, 1975, pp. 221-233.

50 . CASTELLO-BRANCO M.A.S.C., SCHWERDTFEGER K., Large-scale measurements of the physical characteristics of round vertical bubble plumes in liquids. *Metallurgical and Materials Transactions B*, vol. 25, no. 3, 1994, pp. 359-371.

51 . SUN K.X., ZHANG M.Y., CHEN X.J. An investigation of double-sensor resistivity probe techniques for the measurement of gas-liquid bubbly flow. *Development of Measuring Techniques for Multiphase Flows, Proceedings of the 2nd International Symposium on Measuring Techniques for Multiphase Flows*, Beijing, China, 1998, pp. 111-116.

52 . NASR-EL-DIN H., SHOOK C.A., COLWELL J. A conductivity probe for measuring local concentrations in slurry systems. *International Journal of Multiphase Flow*, vol. 13, no. 3, 1987, pp. 365-378.

53 . MACTAGGART R.S., NASR-EL-DIN H.A., MASLIYAH J.H. A conductivity probe for measuring local solids concentration in a slurry mixing tank. *Separations Technology*, vol. 3, no. 3, 1993, pp. 151-160.

54 . ASAKURA K., ITO M., NAKAJIMA I. Local mean profiles of velocity, concentration and concentration fluctuations of solid phase in a vertical pipe. *Proceedings of the International Conference on Bulk Materials Storage, Handling & Transportation: Symposium on Freight Pipelines*, Wollongong, Australia, vol. 1, no. 92/7, 1992, pp. 123-127.

55. XIE T., TJIN S.C., YANG Q., NG S.L. Effect of blood's velocity on blood resistivity. *IEEE Transactions on Instrumentation and Measurement*, vol. 47, no. 5, 1998, pp. 1197-1200.

56. LOH W.W. Real-time monitoring of drilling cuttings transport using electrical resistance tomography. *PhD Thesis*, UMIST, U.K., 1998.

57. LUCAS G.P., CORY J., WATERFALL R.C., LOH W.W. On-line monitoring of drilling cuttings transport using electrical resistance tomography. *Development of Measuring Techniques for Multiphase Flows, Proceedings of the 2nd International Symposium on Measuring Techniques for Multiphase Flows*, Beijing, China, 1998, pp. 239-244.

58. LUCAS G.P., CORY J., WATERFALL R.C., LOH W.W., DICKIN F.J. Measurement of the solids volume fraction and velocity distributions in solids-liquid flows using dual-plane electrical resistance tomography. *Flow Measurement & Instrumentation*, (to be published).

59. DICKIN F.J., HOYLE B.S., HUNT A., HUANG S.M., ILYAS O., LENN C., WATERFALL R.C., WILLIAMS R.A., XIE C.G., BECK M.S. Tomographic imaging of industrial process equipment: techniques and applications. *IEE Proceedings – G*, vol. 139, no. 1, 1992, pp. 72-82.

60. YANG W.Q. An appraisal of three electrical tomography techniques. *Development of Measuring Techniques for Multiphase Flows, Proceedings of the 2nd International Symposium on Measuring Techniques for Multiphase Flows*, Beijing, China, 1998, pp. 285-290.

61. PENG L.H., YAO D.Y., SU B.L., ZHANG B.F. Research on electrical capacitance tomography system. *Development of Measuring Techniques for Multiphase Flows, Proceedings of the 2nd International Symposium on Measuring Techniques for Multiphase Flows*, Beijing, China, 1998, pp. 245-250.

62. PRIMROSE K. QIU C. Performance and application studies of an electrical resistance tomography system, *Proceedings of the 1st World Congress on Industrial Process Tomography*, Buxton, U.K., 1999, pp. 133-139.

63. CILLIERS J.J., WANG M., NEETHLING S.J. Measuring flowing foam density distributions using ERT. *Proceedings of the 1st World Congress on Industrial Process Tomography*, Buxton, 1999, pp. 108-112.

64. DE LA RUE R.E., TOBIAS C.W. On the conductivity of dispersions. *Journal of the Electrochemical Society*, vol. 106, no. 9, 1959, pp. 827-832.

65. MAXWELL J.C. A treatise on electricity and magnetism. *Calendar Press*, Oxford, 1881.

66. TURNER J.C.R. Electrical conductivity of liquid-fluidised beds. *AIChE Symposium Series*, vol. 69, no. 128, 1973, pp. 115-122.

67. BRUGGEMAN D.A.G. Calculation of different physical constants of heterogeneous substances. *Annalen Physica*, vol. 24, 1935, pp. 636-679.

68. BECK M.S., PLASKOWSKI A. Cross correlation flowmeters – their design and application. *Adam Hilger*, Bristol, 1987.

69. RAJAN V.S.V., RIDLEY R.K., RAFA K.G. Multiphase flow measurement techniques – a review. *Journal of Energy Resources Technology, Transactions of the ASME*, vol. 115, no. 3, 1993, pp. 151-160.

70. LUCAS G.P., ALBUSAIDI K. An axial scanning system for investigating vertical gas-liquid flows in the slug and bubbly-slug transition regimes. *Flow Measurement & Instrumentation*, vol. 9, 1998, pp. 171-181.

71. LONGONI A., BUSSOLATI C., FRANCESCHINI G. A non-invasive flowmeter based on electrical conductivity measurements. *Proceedings of the 9th IMEKO World Congress on Technological and Methodological Advances in Measurement*, Berlin, Germany, vol. 2, 1982, paper 7.1, pp. 271-277.

72. GU N., LIU X.B. Improvement on flow rate measurement with correlation flowmeter. *Development of Measuring Techniques for Multiphase Flows, Proceedings of the 2nd International Symposium on Measuring Techniques for Multiphase Flows*, Beijing, China, 1998, pp. 61-65.

73. VOLANSCHI A., OLTHUIS W., BERGVELD P. Electrolyte conductivity measured with an ISFET. *Proceedings of Trends in Electrochemical Biosensors Conference*, Trieste, Italy, 1992, pp. 147-154.

74. VOLANSCHI A., OLTHUIS W., BERGVELD P. Design of a miniature electrolyte conductivity probe using ISFETs in a four point configuration. *Sensors & Actuators B*, vol. 18-19, 1994, pp. 404-407.

75. NCUBE F., KASTRINAKIS E.G., NYCHAS S.G., LAVDAKIS K.E. Drifting behaviour of a conductivity probe. *Journal of Hydraulic Research*, vol. 29, no. 5, 1991, pp. 643-654.

76. HOLTZKNECHT L.J., MARK JR. H.B., RIDGWAY T.H., ZIMMER H. Design and characterisation of a four point probe for conducting polymer electrode studies. *Analytical Instrumentation*, vol. 18, no. 1, 1989, pp. 23-35.

77. DAILY W., RAMIREZ A. The role of electrical resistance tomography in the U.S. nuclear waste site characterisation program. *Proceedings of the 1st World Congress on Industrial Process Tomography*, Buxton, 1999, pp. 2-5.

78. RIDD P.V. Electric potential due to a ring electrode. *IEEE Journal of Oceanic Engineering*, vol. 19, no. 3, 1994, pp. 464-467.

79. WON I.J. The geometrical factor of a marine resistivity probe with four ring electrodes. *IEEE Journal of Oceanic Engineering*, vol. OE-12, no. 1, 1987, pp. 301-303.

80. MA J., DAWALIBI F.P. Influence of inductive coupling between leads on resistivity measurements in multilayer soils. *IEEE Transactions on Power Delivery*, vol. 13, no. 4, 1998, pp. 999-1004.

81. GASULLA-FORNER M., JORDANA-BARNILS J., PALLÁS-ARENY R., TORRENTS J.M. Subsurface resistivity measurements using square waveforms. *IEEE Transactions on Instrumentation & Measurement*, vol. 47, no. 1, 1998, pp. 74-77

82. COULSON J. M., RICHARDSON J. F. Chemical Engineering, *Pergamon Press*, Oxford, 3rd edition, 1991.

83. TRETHEWAY K.R., CHAMBERLAIN J. Corrosion for Science & Engineering. *Longman*, U.K., 2nd edition, 1995.

84. LEE K.T., BECK M.S., MCKEOWN. An on-line instrument for measuring small quantities of dispersed non-conducting liquid in a conducting liquid. *Measurement & Control*, vol. 7, 1974, pp. 341-345.

85. RAO S.S. The finite element method in engineering. *Pergamon Press*, Oxford, U.K., 2nd edition, 1992.

86. LUCAS G.P. The measurement of two-phase flow parameters in vertical and deviated flows. *PhD thesis*, UMIST, 1987.

87. LUCAS G.P., WALTON I.C. Flow rate measurement by kinematic wave detection in vertically upward, bubbly two-phase flows. *Flow Measurement & Instrumentation*, vol. 8, no. 3-4, 1997, pp. 133-143.

88. KYTÖMAA H.K., BRENNEN C.E. Small amplitude kinematic wave propagation in two-component media. *International Journal of Multiphase Flow*, vol. 17, no. 1, 1991, pp. 13-26.

89. SERIZAWA A., KATAOKA I., MICHIYOSHI I. Turbulence structure of air-water bubbly flow – 3. Transport properties. *International Journal of Multiphase Flow*, vol. 2, 1975, pp. 247-259.

90. AL-KURDI H.S. The Design of a Multiphase Solid/Liquid Flowmeter. *Final Year Project*, University of Huddersfield, 1996.

91. BENEDICT R.P. Fundamentals of Pipe Flow. *John Wiley & Sons*, New York, U.S.A., 1980.

92. MASSEY B.S. Mechanics of Fluids. *Chapman & Hall*, London, U.K., 6th edition, 1990.

93. ROCO M.C., SHOOK C.A. Modelling of slurry flow: the effect of particle size. *The Canadian Journal of Chemical Engineering*, vol. 16, August 1983, pp. 494-503.

94. GOVIER G.W., AZIZ K. The flow of complex mixtures in pipes. *Van Nostrand Reinhold*, New York, 1972.

95. MIZUKAMI M., PARTHASARATHY R.N., FAETH G.M. Particle-generated turbulence in homogeneous dilute dispersed flows. *International Journal of Multiphase Flow*, vol. 18, no. 3, 1992, pp. 397-412.

96. BEGGS H.D., BRILL J.P. An experimental study of two-phase flow in inclined pipes. *47th Annual Fall Meeting of the Society of Petroleum Engineers of AIME*, San Antonio, Texas, U.S.A., 1972, Paper SPE 4007, .

97. TURIAN R.M., YUAN T. Flow of slurries in pipelines. *AIChE Journal*, vol. 23, no. 3, 1977, pp. 232-243.

98. ALAJBEGOVIC A., ASSAD A., BONETTO F., LAHEY JR. R.T. Phase distribution and turbulence structure for solid/fluid upflow in a pipe. *International Journal of Multiphase Flow*, vol. 20, no. 3, 1994, pp. 453-479.

99. BARTOSIK A.S., SHOOK C.A. Prediction of vertical liquid-solid pipe flow using measured concentration distribution. *Particulate Science & Technology*, vol. 13, no. 2, 1995, pp. 85-104.

100. MATOUSEK V. Internal structure of slurry flow in inclined pipe. Experiments and mechanistic modelling. *Hydrotransport 13, Proceedings of the 13th International Conference on Slurry Handling and Pipeline Transport*, Johannesburg, South Africa, 1996, pp. 187-210.

101. LUCAS G.P. Modelling complex phase distributions in highly deviated oil-water flows to reduce the complexity of image reconstruction. *Proceedings of the European Concerted Action on Process Tomography Conference*, Bergen, Norway, 1995.

102 . TABELING P., POULIQUEN O., THERON B., CATALA G. Oil water flows in deviated pipes : experimental study and modelling. *Proceedings of the 5th International Conference on Multiphase Production*, Cannes, France, 1991, pp. 292-306.

103 . HSU F-L., TURIAN R.M., MA T-W. Flow of noncolloidal slurries in pipelines. *American Institute of Chemical Engineers Journal*, vol. 35, no. 3, 1989, pp. 429-442.

104 . LOH W.W. Personal communication. 1997.

105 . LIU S. Particle dispersion for suspension flow. *Chemical Engineering Science*, vol. 54, 1999, pp. 873-891.

106 . LUCAS G.P. Modelling velocity profiles in inclined multiphase flows to provide a-priori information for flow imaging. *Proceedings of the European Concerted Action on Process Tomography Conference*, Oporto, Portugal, 1994.

107 . BERNIER R.N., BRENNEN C.E. Use of the electromagnetic flowmeter in a two-phase flow. *International Journal of Multiphase Flow*, vol. 9, no. 3, 1983, pp. 252-257.

108 . ZUBER N. On the dispersed two-phase flow in the laminar flow regime. *Chemical Engineering Science*, vol. 19, 1964, pp. 897-917.

109 . ZUBER N., FINDLAY J.A. Average volumetric concentration in two-phase flow systems. *Journal of Heat Transfer, Transactions of the ASME*, vol. 87, November 1965, pp. 453-468.

110 . GALVIN K.P., PRATTEN S., NGUYEN TRAN LAM G. A generalised empirical description for particle slip velocities in liquid fluidised beds. *Chemical Engineering Science*, vol. 54, 1999, pp. 1045-1052.

111 . SHOOK C.A., ROCO M.C. Slurry flow: Principles and practice. *Butterworth-Heinemann*, Boston, 1991.